Electrochemical study of redox enzymes and their utilization on modified electrodes

Dimitrios Zouraris

National technical university of athens
school of chemical engineering

PhD THESIS

«Η έγκριση της διδακτορικής διατριβής από την Ανωτάτη Σχολή Χημικών Μηχανικών του Ε.Μ.Πολυτεχνείου δεν υποδηλώνει αποδοχή των γνωμών του συγγραφέα. (Ν. 5343/1932, Άρθρο 202)»

This research is co-financed by Greece and the European Union (European Social Fund- ESF) through the Operational Programme «Human Resources Development, Education and Lifelong Learning» in the context of the project "Strengthening Human Resources Research Potential via Doctorate Research" (MIS-5000432), implemented by the State Scholarships Foundation (IKY)

σὰν ἔτοιμος ἀπὸ καιρό, σὰ Θαρραλέος,
ἀποχαιρέτα την, τὴν αλεξάνδρεια Ποῦ φεύγει.

Απόσπασμα από ποίημα του Κ. Π. Καβάφη:
Απολείπειν ο θεός Αντώνιον

Prologue - Aknowledgement

Disclaimer: The reader is advised to skip this part due to the high risk of finding it "cringeworthy".

The journey of this thesis began three and half years ago somewhere between the Laboratory of Physical Chemistry and Applied Electrochemistry and the Lab of Biotechnology of the School of Chemical Engineering, NTUA, with the main part of the work being carried out in the first one. It started with one principal aspiration: to discover new things, learn and to enjoy the process - not in this particular order. The first two goals shall be judged through the process of reading this work and during the defending of the thesis. The third one is only the writer can really know.

Before moving on to the main part of the thesis, the people who helped/contributed - in different ways - in the completion of this thesis shall be credited. The reader at this point has another chance to skip the rest of the prologue and move on to the actual thesis. In case the reader insists on reading this "part of the thesis", they should also be prepared that it is written in an unconventional bottom-up structure, instead of the common top-bottom one, for reasons of climax, as I consider the top-bottom structure of such texts quite anticlimatic.

Hence, the acknowledgments shall start by thanking my parents - Georgia and Zacharias - and my friends - Dimitra, Christina, George, Michalis, Kyriaki, Ioanna, Demi, Anna and Lefteris - for all the moral support they have offered me all these years. One of the main lessons of these three and a half years is that, no matter how good the working conditions are and no matter how much you are willing to try and give it your all, in case you have no people outside the working environment to help you morally, it is not really possible to make it through.

Next, I shall thank two laboratories for their cooperation. The first one is the Laboratory of Inorganic Chemical Technology of the School of Chemical Engineering, NTUA and Professor C. Argirousis for providing the immobilization matrix used in the experimental section of this thesis. The second one is the Laboratory of Biochemical Process Engineering, Division of Chemical Engineering, Department of Civil, Environmental and Natural Resources Engineering, Luleå University of Technology and professor P. Christakopoulos for the cooperation in the study of lignin as an electron donor for the LPMO enzymes.

Moving on, another person than played a major role in this work is Sotiria Kiafi who carried out her diploma thesis in the Laboratory of Physical Chemistry and Applied electrochemistry, NTUA and was of great help with the experiments regarding the multi copper laccase oxidase. The experimental results of her systematic and persistent work were the starting point of one of the most challenging parts of this PhD, the study and mathematical modeling of a Michaelis-Menten reaction kinetic scenario of an immobilized species using FTacV. I shall also admit that it will be difficult to find in the future a lab partner with whom I will cooperate that effectively and effortlessly.

I also feel obliged to express my gratitude to the people from the Laboratory of Biotechnology and more specifically three people, Christina Pentari, Natasa Zerva and Anthi Karnaouri. Christina for helping with HPAEC-PAD - and basically for putting so much effort so that it would finally work correctly - and for helping out with finding

out what was going wrong with the electroporation experiments. Natasa for starting this interaction of the electrochemistry and the biotechnology lab with her peroxidase six years ago and for her contribution in this work with the multi copper laccase oxidase. Last but not least, Anthi, for her work with the LPMOs, her idea for studying the electron donors electrochemically, the introduction of pGAPZα C vector in the laboratory, her patience and constant support during the enzyme production and purification processes.

At this point I would like to express my gratitude to the Associate Professor E. Topakas and the Assistant Professor M. Dimarogona who are also a part of my "3-person" counseling PhD committee. They were indeed a counseling committee and were eager to respond to my questions and they did not have a decorative role, which sadly is the most common characteristic in our days.

Finally, the time has come to say a big thank you to supervisor of this thesis, associate professor A. Karantonis. (The reader at this point has one last change to abandon the reading of this section, and move on to the main thesis.) This collaboration started back - in the now distant - 2015 when I started working on my diploma thesis. Ever since, he has been everything a supervisor should be, a professor. When I say professor, I imply the Greek work καθηγητής, which is derived from the word καθοδηγώ which means guide. In that sense, a professor is the one who shall guide you through knowledge and experience, shall make you think, discuss with you and make you conquer what is necessary for your next step.[1] And for these past years, indeed A. Karantonis has guided me through the world of electrochemistry, while at the same giving me experimental freedom as to where this work would go. I do not know if under any other circumstances would I find a supervisor that would not only let me, but also encourage me, do what I did in this PhD. My aspiration ever since understanding what instrumental chemical analysis is and its principles, was to contribute to the development of an analytical technique, and this work at least let me believe that I achieved this with what I report for FTacV. No matter what, without Prof. Karantonis, I do not know if I would even come close this. Now, if the contribution of this work will indeed be useful for others in the future only time will tell. So again one big thank you - or better in greek "ευχαριστώ" - do not know if is enough. Thank you for the knowledge, thank you for trusting me, thank you for the conversations, thank you for the clash of opinions, thank you for collaborating, thank you for putting up with me...

For a closing remark of this prologue now. Most people misinterpret - in my opinion - Cavathys poem "Ithaka", by considering only the first verses and reach the conclusion that it is not the destination that matters but the journey. However, they forget that if it weren't for the destination, the journey would have never happened. And as the poet explicitly mentions in the same poem " Ithaka gave you the marvelous journey./ Without her you wouldn't have set out." So, it's been a great journey. A journey that ends just at the right moment before it starts withering. A journey where I met the right people, at the right time. A journey which lead to the final destination. And even

[1] I do not use the word teacher, δάσκαλος in Greek, due to the fact that it implies an absolute center of knowledge which is not susceptible to defiance or questioning and is not as open to dialog as a professor - καθηγητής. Moreover, the word teacher is closely connected to primary education, which although essential and still basic, is not what will help a person face the real world.

though the journey was exciting, there is nothing more pleasing and cleansing than reaching the destination. And this is how the verse which appears at the first pages of this manuscript connects with the situation. “As one long prepared, and graced with courage / say goodbye to her, the Alexandria that is leaving.”. We should be ready for the end and we should be happy about it, because it shaped us. So let us move on to the Ithaka of this journey, the Alexandria that is leaving. The manuscript of this PhD.

Abstract

The present work focuses on the extraction of thermodynamic and kinetic information of redox enzymes and molecules they interact with, through electrochemical techniques. In the introduction, a quick overview is made on redox enzymes in general and how they can be exploited electrochemically together with the challenges faced. As one of the most prominent problems when using cyclic voltammetry for the study of redox enzymes is the existence capacitance currents, a major part of this work focuses on exploring an alternative, large amplitude fast Fourier transform alternating current voltammetry (FTacV), so as to overcome this obstacle. The investigation of FTacV takes place for both free in a solution and immobilized on an electrode surface electroactive species. The respective results for cyclic voltammetry are presented as well for comparison.

Starting with the free species, the chief observables, *i.e.* peak height, peak width and peak potential of the principal peaks, are determined for FTacV for a reversible reaction of free electroactive species. The values of the chief observables are derived from a semi-analytic solution as well as from the solution of the full initial-boundary value problem. A condition under which FTacV is independent of scan rate, up to the fifth harmonic, is introduced. The dependence of the chief observables on the parameters of the system is shown. Then, the case of quasi reversible and irreversible kinetics is studied correlating the chief observables with the electrode kinetics. Moreover two step electron reactions are examined in order to get a visual representation of the resulting voltammograms. Two mechanisms are also explored when coupling an electroactive species with a homogeneous reaction. The first is the EC mechanism and the second the homogeneous catalytic reaction scheme. Convolution voltammetry is also introduced in this work as some of its aspects would of use in the experimental part of this work.

The analysis that comes right after that concerns the immobilized species. Starting from an one step reaction of an electroactive speceis doing a similar study to the one conducted for the free species, moving on to two step reactions. As a next step, the coupling of the redox reaction of the immobilized species with a reaction that concerns a species free in the bulk solution shall follow. More specifically the Michaelis-Menten kinetics of an immobilized enzyme shall be thoroughly analyzed as the case of an electrochemical-chemical (EC) mechanism. Methodologies regarding the extraction of kinetic constants are also introduced.

Moving on to the experimental section of this work, Lytic polysaccharide monooxygenases (LPMOs) are introduced and the expression process of three LPMOs with two different expression vectors is analyzed. These expressed LPMOs are then immobilized with two different methodologies and kinetic information is obtained regarding both the interaction of the immobilized enzyme with the electrode and the interaction of the enzyme with phosphoric acid swollen cellulose (PASC) using FTacV. The methodologies that are introduced earlier are utilized in this case.

The next step is to examine possible electron donors that work with the LPMOs electrochemically using cyclic voltammetry, FTacV and convolution voltammetry. Various phenolic compounds and lingin from wheat straw are first examined as electron donors with an LPMO analyzing their reaction products with high-performance anion-exchange chromatography with pulsed amperometric detection (HPAEC-PAD). Then,

based on the elution patterns and the presence and intensity of the oxidized products, in combination with the voltammetric data, an interpretation was given to the interaction of these substrates as reducing agents for the LPMOs.

In the last part of the work, a laccase like multi copper oxidase from the fungus *Thermothelomyces Thermophila* is examined immoblized on an electrode surface and its interaction with epinephrine using FTacV. The application of the theory of probing an immobilized redox enzyme reacting with a free in the solution substrate following a Michaelis-Menten kinetic scheme is thoroughly examined.

Περίληψη

Η παρούσα εργασία εστιάζει στην εξαγωγή θερμοδυναμικών και κινητικών δεδομένων οξειδοαναγωγικών ενζύμων καθώς και μορίων που αντιδρούν με αυτά, μέσω ηλεκτροχημικών τεχνικών. Στην εισαγωγή της εργασίας αυτής, πραγματοποιείται μία γενική επισκόπηση για τα οξειδοαναγωγικά ένζυμα και του πως μπορούν να αξιοποιηθούν ηλεκτροχημικά, καθώς και των δυσκολιών που εμφανίζονται.

Καθώς ένα από τα κύρια προβλήματα όταν χρησιποιείται η κυκλική βολταμμετρία για την μελέτη οξειδοαναγωγικών ενζύμων είναι τα ρεύματα λόγω χωρητικότητας, ένα μεγάλο μέρος της δουλειάς αυτής επικεντρώνεται στην διερεύνηση της χρήσης της κυκλικής βολταμμετρίας εναλασσόμενου ρεύματος διαταραχής μεγάλου πλάτους με μετασχηματισμό Φουριέ, (large amplitude fast Fourier transform alternating current voltammetry - FTacV), ως εναλλακτική για την άρση του προαναφερθέντος εμποδίου. Η διερεύνηση της FTacV γίνεται και για ελεύθερα στο διάλυμα και για ακινητοποιημένα σε ηλεκτροδιακή επιφάνεια, ηλεκτροενεργά είδη. Παρατίθενται και τα αντίστοιχα αποτελέσματα για την κυκλική βολταμμετρία για σύγκριση.

Ξεκινώντας από το ελεύθερο είδος, τα κυρίως παρατηρούμενα μεγέθη, δηλαδή το ύψος, το πλάτος και το δυναμικό των κορυφών, προσδιορίζονται για ελεύθερα στο διάλυμα ηλεκτροενεργά είδη όταν χρησιμοποιείται η FTacV. Οι τιμές των κυρίως παρατηρούμενων μεγεθών προσδιορίζονται από μία ημιαναλυική λύση καθώς και από την ολοκληρωμένη λύση του προβλήματος αρχικών-συνοριακών τιμών. Είσαγεται επίσης μία συνθήκη κατά της οποία η FTacV καθίσταται ανεξάρτητη της ταχύτητας σάρωσης και εξάγονται οι εξαρτήσεις των κυρίως παρατηρούμενων μεγεθών από το πλάτος της διαταραχής. Κατόπιν εξετάζεται η περίπτωση ημιαντιστρεπτών και αναντίστρεπτων κινητικών, συσχετίζοντας τα κυρίως παρατηρούμενα μεγέθη με την ηλεκτροχημική κινητική. Επίσης, μελετώνται δράσεις δύο σταδίων και γίνεται γραφική αναπαράσταση των βολταμμογραφημάτων που προκύπτουν. Ακόμα δύο μηχανισμοί εξερευνώνται κατά την σύζευξη ενός ηλεκτροχημικού είδους με μία ομογενή χημική δράση. Πραγματοποιείται ακόμα μία εισαγωγή στην βολταμμετρία συνέλιξης, η οποιά θα χρησιμοποιηθεί σε κομμάτι της ανάλυσης πειραματικών αποτελεσμάτων.

Η αμέσως επόμενη ανάλυση αφορά σε ακινητοποιημένα είδη. Η ανάλυση ξεκινάει από δράσεις ενός σταδίου για ακινητοποιημένα ηλεκτροενεργά είδη, κάνοντας παρόμοια ανάλυση με αυτήν για το ελεύθερο είδος, φτάνοντας σε δράσεις δύο σταδίων. Σε επόμενη φάση μελετάται η σύζευξη της οξειδοαναγωγικής δράσης ακινητοποιημένου είδους με μία δράση που αφορά σε χημικό είδος που βρίσκεται ελεύθερο στον κύριο όγκο του διαλύματος. Ειδικότερα, οι κινητικές που αναλύονται είναι η κινητική Michaelis-Menten και το σενάριο όπου μία χημική αντίδραση έπεται της ηλεκτροχημικής (μηχανισμός EC). Αναλύονται οι αντίστοιχες μεθοδολογίες που αφορούν στην εξαγωγή κινητικών σταθερών.

Συνεχίζοντας στο πειραματικό κομμάτι της εργασίας, εισάγονται οι βασικές έννοιες γύρω από τις λυτικές μονοξυγενάσες των πολυσακχαριτών (Lytic polysaccharide monooxygenases - LPMOs) και αναλύεται η διαδιακασία ετερόλογης έκφρασης τριών τέτοιων ενζύμων σε δύο διαφορετια συστήματα. Τα εκφρασμένα ένζυμα κατόπιν ακινητοποιούνται με δύο διαφορετικές μεθοδολογίες και εξάγονται κινητικές πληροφορίες σχετικά με την αλληλεπίδραση τόσο της δράσης του ακινητοποιημενου ενζύμου με το ηλεκτρόδιο καθώς και με διογκωμένη με φωσφορικό οξύ κυτταρίνης (phosphoric acid swollen cellulose - PASC).

Η χρησιμοποιούμενη τεχνική για αυτήν την μελέτη είναι η FTacV. Οι μεθοδολογίες που χρησιμοποιούνται είναι αυτές που έχουν ήδη παρουσιαστεί.

Το επόμενο βήμα είναι η ηλεκτροχημική μελέτη πιθανών δοτών ηλεκτρονίων για τις LPMO με τη χρήση κυκλικής βολταμμετρίας, βολταμμετρίας συνέλιξης και FTacV. Διαφορετικές φαινολικές ουσίες και λιγνίνη από άχυρο εξετάζονται ως προς την αποτελεσματικότητά τους ως δότες ηλεκτρονιών χρησιμποιώντας χρωματογραφία ιοντοεναλλαγής υψηλής απόδοσης συζευυγμένη με παλμικό αμπερομετρικό ανιχνευτή (high-performance anion-exchange chromatography with pulsed amperometric detection, HPAEC-PAD). Κατόπιν, βασιζόμενοι στα οξειδωμένα προϊόντα και την ένταση των κορυφών των χρωματογραφημάτων, σε συνδυασμό με βολταμμετρικά δεδομένα, δίνεται ερμηνεία για την αλληλεπίδραση των εξεταζόμενων ουσιών ως δότες ηλεκτρονίων και τις LPMOs.

Στο τελευταίο κομμάτι αυτής της δουλειάς το ένζυμο που αναλύεται είναι μία οξειδάση πολλαπλών χαλκών με ενεργότητα λακάσης από το μύκητα *Thermothelomyces Thermophila* ενώ είναι ακινητοποιημένο στην επιφάνεια ενός ηλεκτροδίου και αλληλεπιδρά με επινεφρίνη. Για τη μελέτη αυτή χρησιμοποιείται η FTacV. Γίνεται η εφαρμογή της θεωρίας της μελέτης ενός ακινητοποιημένμου οξειδοαναγωγικού ενζύμου που αντιδρά με ένα είδος ελεύθερο στο διάλυμα και ακολουθεί κινητική Michaelis-Menten.

List of Symbols

A_0	perturbation amplitude	V
a	transfer coefficient	
b_a	anodic exponent	V^{-1}
b_c	cathodic exponent	V^{-1}
$c^{(i)}$	Fourier coefficient	
c_dl	specific capacitance of the double layer	$\mathrm{F\ mol}^{-1}$
c_k	concentration of electroactive species k on the electrode surface	$\mathrm{mol\ m}^{-3}$
c_k^*	concentration of electroactive species k in the bulk solution	$\mathrm{mol\ m}^{-3}$
$\hat{c}_\mathrm{s}$	dimensionless substrate concentration	
D_k	diffusion coefficient of electroactive species k	$\mathrm{m}^2\ \mathrm{s}^{-1}$
E	electrode potential	V
E^0	standard electrode potential	V
$E^{0\prime}$	formal electrode potential	V
$E^{0\prime}_\mathrm{app}$	formal electrode potential affected by the immobilization matrix	V
E_I	initial scanning potential potential	V
E_F	final scanning potential potential	V
E_R	reversal scanning potential potential	V
$E_\mathrm{p,CV}$	peak potential for cyclic votlammetry	V
$E_\mathrm{p,c,CV}$	cathodic peak potential for cyclic votlammetry	V
$E_\mathrm{p,a,CV}$	anodic peak potential for cyclic votlammetry	V
$E_{\frac{\mathrm{p}}{2},\mathrm{CV}}$	peak half wave potential for cyclic votlammetry	V
f	perturbation frequency	s^{-1}
f_min	minimum applied frequency for the respective scan rate in FTacV	s^{-1}
h	harmonic order	
I	convolution (corellation) current)	$\mathrm{C\ s}^{-1/2}$
I_L	limiting convolution (corellation) current)	$\mathrm{C\ s}^{-1/2}$
i_F	Faradaic current density	$\mathrm{A\ m}^{-2}$
$i_\mathrm{p,CV}$	peak current density for cyclic voltammetry	$\mathrm{A\ m}^{-2}$
i_c	capacitance current density	$\mathrm{A\ m}^{-2}$
$i_\mathrm{p,irrev,CV}$	cathodic peak current density for cyclic voltammetry	$\mathrm{A\ m}^{-2}$
j_k	flux of electroactive species k	$\mathrm{m}^{-2}\ \mathrm{s}^{-1}$
k	dimensionless electron transfer kinetic constant	
k^0	standard electron transfer kinetic constant	$\mathrm{m\ s}^{-1}$ or $1\ \mathrm{s}^{-1}$
k_CV	dimensionless kinetic parameter for cyclic voltammetry	
k_ac	dimensionless kinetic parameter for FTacV voltammetry	
k_a	anodic kinetic constant	$\mathrm{m\ s}^{-1}$
k_c	cathodic kinetic constant	$\mathrm{m\ s}^{-1}$
k_EC	kinetic constant in the EC mechanism	s^{-1}
k_3	kinetic constant in homogeneous catalysis	$\mathrm{m}^3\ \mathrm{mol}^{-1}\ \mathrm{s}^{-1}$
k_r1	dimensionless kinetic constant for EC mechanism	
M	linear convolutinon of the dimensionless current	
M_L	limiting linear convolutinon of dimensionless current	
n	number of transfered electrons	

r_i	reaction rate	$m^3\ mol^{-1}\ s^{-1}$
$\hat{r}_i$	dimensionless reaction rate	
R_Ω	Resistance between working and reference electrode	Ω
P	Power spectrum magnitude	
q	constant	$A\ m^{-2}$
S	electrode surface area	m^2
T	temperature	K
t	time	s
t_R	reversal time	s
u	dimensionless applied potential	
v	scan (sweep) rate	$V\ s^{-1}$
x	distance from the electrode surface	m
y	dimensionless distance from the electrode surface	
$\hat{\alpha}$	dimensionless concentration of the oxidant	
$\hat{\beta}$	dimensionless concentration of the reductant	
α_0	dimensionless perturbation amplitude	
γ	concentration ratio	
Γ_i	Surface concentration of species i	$mol\ cm^{-2}$
Γ^0	Total surface concentration	$mol\ cm^{-2}$
Δ	step of the trapezoidal rule	
$\Delta\xi_\mathrm{p}, h$	Width at half maximumfor odd harmonics	
δ	diffusion coefficient ratio	
θ_i	surface coverage of species i	
Λ_EC	Dimensionless kinetic parameter in homogeneous catlysis	
μ	dimensionless double layer capacitance	
ξ	dimesnionless potential	
ξ^0	dimesnionless standard (formal) potential	
ξ_I	initial dimensionless electrode potential	
ξ_R	reversal dimensionless electrode potential	
ξ_p, h	Peak potential of the principal peak	
$\xi_\mathrm{p,CV}$	dimesnionless peak potential for cyclic votlammetry	
$\xi_{\frac{\mathrm{p}}{2},\mathrm{CV}}$	dimensionless half wave peak potential for cv	
σ	dimensionless scan rate	
$\bar{\sigma}$	specific conductivity of the electrolyte	$S\ m^{-1}$
τ	dimensionless time	
τ_ac	dimensionless time for FTacV	
τ_AC	time constant of the ac perturbation	
τ_CV	dimensionless time for cyclic voltammetry	
τ_MM	time constant of the catalytic reaction	
τ_R	reversal dimensinoless time	
τ_RC	time constant of the RC circuit	
Ψ_{EC}	dimensionless catalytic current peak	
Ψ	dimensionless current	
ψ	dimensionless current density	
ψ_ac	dimensionless total current density for FTacV	

$\psi_{\mathrm{ac,F}}$	dimensionless Faradaic current density for FTacV
$\psi_{\mathrm{ac,C}}$	dimensionless capacitance current density for FTacV
$\psi_{\mathrm{p},h}$	dimensionless peak current density for harmonic h
$\psi_{\mathrm{p},n}$	dimensionless peak current density for different electrons
ψ_{CV}	dimensionless current density for cyclic voltammetry
$\psi_{\mathrm{p,irev,CV}}$	dimensioless cathodic peak current for cyclic voltammetry
$\psi_{\mathrm{p,CV}}$	dimensionless peak current density for cyclic voltammetry

1. Introduction

The primary scope of this thesis is to exploit electrochemical methods in order to get some insight into the reaction mechanisms of certain redox enzymes. But before getting there we shall present a quick overview of redox enzymes, how they have been exploited in electrochemistry up to now, the main challenges one can come up against and what is proposed in this work as an alternative that can help in overcoming these problems.

To begin with, in general what we can define as redox enzymes, are proteins that catalyze electron transfer by reduction or oxidation of substrates within a redox network (*i.e.*, glutathione peroxidases, glutathione reductases, peroxiredoxins, thioredoxin reductases, glucose 6-phosphate dehydrogenase, catalase, etc.) [1]. These enzymes can get involved in various biological processes, the most important of which may be the bioenergetic metabolism [2].

Although such enzymes are very attractive to study ectrochemically since there is electron exchange implicated in their action, there has been an important discouraging factor, their size. Redox enzymes tend to have high molecular weights and their active site is usually buried inside their structure making their study rather difficult as the rate of electron transfer through the protein drops exponentially with distance. More specifically, regarding the distance between the electrode surface and the enzyme's active center, fast electron transfer (sufficient to sustain substrate limited currents) is restricted to around 0.8 nm or less, with the rate of direct electron transfer decreasing by around 10^4 when the distance is increased from 0.8 to 1.7 nm [3].

One of the most common techniques employed in order to study such enzymes is cyclic voltammetry. However problems that arise when using such a technique include relative lack of sensitivity, the frequent appearance of broad ill-defined waves from which potential values are difficult to ascertain as well as high capacitance currents.

1.1 Mediated Electron Transfer

One way to study redox enzymes electrochemically avoiding such problems is to use mediators[1] which shuttle the electrons between the redox enzyme and the electrode surface. A schematic representation of such a process is presented in Fig. 1.1.1. Examples of mediators include ferrocene derivatives, quinones, organic salts and metal bipyridine complexes [5]. In such a system, the consumption of the mediator is detected as a current wave resulting from its electrochemical recycling on the electrode. This means that if for example the mediator is oxidized on the electrode surface and the reduced form is constantly being produced from the reaction with the enzyme, the oxidation current shall increase as it is a function of the concentration of the reduced form of the mediator. The only species that interacts with the electrode surface is the mediator, and the homogeneous catalytic process which occurs in the bulk of the electrochemical cell is fundamentally the same as that in common solution assays where the enzyme may be mixed in a cuvette with its substrate and a redox partner and a cosubstrate, providing a source or a sink of electrons for the redox transformation of the substrate and whose absorbance depends on its redox state [2].

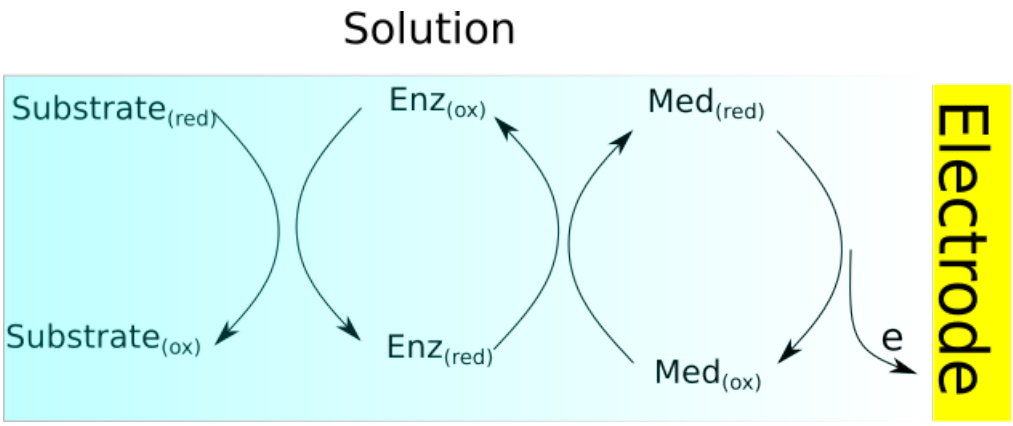

Figure 1.1.1: Mediated electron transfer example with the substrate, the enzyme and the mediator free in the solution. The reduced form of the enzyme's substrate reacts with the oxidizeded form of the redox enzyme giving the oxidized form of the substrate and the reduced form of the enzyme. Then the reduced form of the enzyme reacts with the oxidized form of the mediator, leading to the oxidized form of the enzyme and the reduced one of the mediator. As a last step, the mediator is oxidized on the electrode surface.

Strong theoretical backgorund of such systems and how to extract the respective kinetic constants from a mediated system in which the enzyme can be found free in the solution, has been presented in the works of Savéant. The most notable works include the study of a glucose oxidase with ferromethanol as a mediator [6] and the study of horseradish peroxidase (HRP) using $[Os(bpy)_2pyCl]^+$ as a mediator [7]. The

[1] Mediators are low molecular weight electroactive species which have large heterogeneous rate constatns, react fast with the redox enzymes, have stable oxidized and reduced forms, and do not autooxidate [4].

kinetic constants implicated in the various steps were calculated and a methodology is introduced for the determination of the kinetic consntants using cyclic voltametry which has been useful and exploited in other enzymes as well [8].

Another variation includes the study of *Desulfovibrio gigas* cyt c_3 in solution was oxidized at a basal plane pyrolytic carbon (PG) electrode, and its catalytic oxidation of hydrogenase from *D. gigas* [9, 10]

Another approach when it comes to mediated electrochemistry of enzymes is the immobilization of the enzyme on an electrode surface together with the mediator. Ferrocyanide, ferrocene carboxylic acid and other anions have been incorporated into electropolymerized polypyrole (PPy) films as counteranions without significant results due to leakage of the mediator and stability issues [11].

1.2 Direct Electron Transfer

The second - and more difficult to achieve - method in order to study enzymes electrochemically is via direct electron transfer of the enzymes. This feat can only be achieved in case that the active site of the enzymes is not burried deep within the enzyme structure.

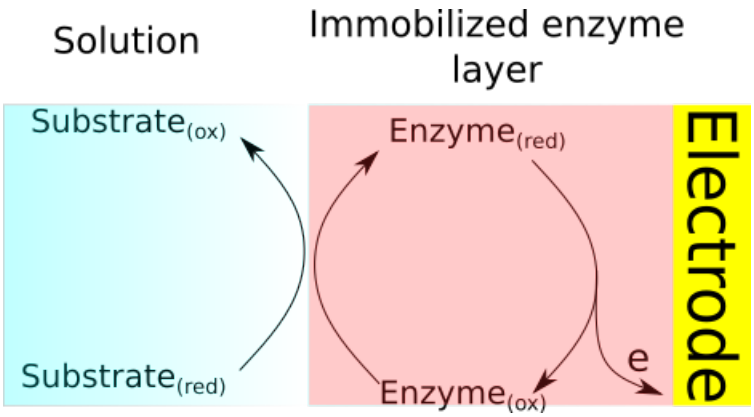

Figure 1.2.1: Direct electron transfer of an enzyme immobilized on an electrode surface. The substrate is free in the solution. The reduced form of the substrate reacts with the oxidized form of the enzyme resulting in the oxidized form of the substrate and the reduced form of the enzyme. The enzyme then is oxidized on the electrode surface.

To achieve this feat, over the years a number of methods have been employed in order to immobilize enzymes on electrodes by adsorption or in thin films. These approaches allow the direct study of electrochemical properties of redox enzymes and enzyme catalysis by direct voltammetry without the use of mediators. Such thin-film methods include adsorption or coadsorption of enzymes onto electrodes [12], adsorption onto self-assembled monolayers [13], covalent linkage onto electrodes, incorporation into lipid or polyion films, and layer-by-layer construction of enzymes with polyions or nanoparticles [14, 15]. A schematic representation of direct electron transfer of an immobilized enzyme with the substrate free in the solution is presented in Fig. 1.2.1.

The efficiency of the redox conversion in the films which have immobilized redox enzymes depends on: (a) the thermodynamics of the potential-driven redox reaction in the film as controlled by the standard electrode potential E^0,[2], (b) the kinetics of electron transfer at the film-electrode interface (c) the rate of charge transport within the film, which may depend on counter ion entry and exit rates, and electron self-exchange between redox sites, and (d) structural transformations coupled to electron transfer, such as conformational changes [11].

Early electrochemical studies of redox enzymes that implicated direct electron transfer suffered from adsorption and denaturation of the enzymes on the electrode surface as well as irreversibility of the reactions [5]. Over the next decades the electrochemical study of enzymes started focusing more on immobilization methods with redox polymers being the prevailing one [17]. Still however, direct electron transfer was not the most common option as a carrier maintaining high enzymatic catalytic activity was something that was not achieved to a great degree of satisfaction.

Two of the main issues encountered during cyclic voltammetry of immobilized species are the greater than the expected peak separation and the capacitive (charging) currents due to the charge and discharge of the double layer on the electrode-solution interface, with the second one being more prominent. Regarding the the peak separation, usually enzyme films on electrode surfaces are diluted with electrochemically inert materials and redox centers are rather far apart. Consequently, peak widths are usually larger than the expected ones[3]. Furthermore, an even greater peak separation appears in the case of increased scan rate which can be attributed to slow electron transfer between electrode and redox sites, slow transport of charge within the film limited by electron or counter ion transport, uncompensated voltage drop within the film, and structural reorganization of the film or enzyme accompanying the redox reactions.

When it comes to capacitance, it can be considered a problem of greater importance, as when the enzyme concentration is low, the Faradaic signal under steady state conditions following a Michaelis Menten reaction scheme is masked by the capacitance. One example of how a signal of an immobilized enzyme can be distorted when capacitance is implicated can be found in Fig. 1.2.2. In the absence of substrate (black line) the signal is masked by the capacitance giving misleading information for the peak magnitude. In the presence of a substrate one can also see that the sigmoidal expected signals in the case where capacitance is absent, are also altered in the second scenario. Moreover the effect of the catalysis is underestimated in the second case as the percentage of the current increase in the presence of the substrate is decreased.

Thus, even though it is very common in the literature for such voltammograms to be presented, they are not a precise source to extract kinetic data of the immobi-

[2] E^0 represents the equilibrium potential of an electrode under standard-state conditions, *i.e.*, in solutions with the relative activities of all components being unity and a pressure being 1 atm (ignoring the deviations of fugacity and activity from pressure and concentration, respectively) at a temperature T. In the case where the activities of the components deviate from the unity, the formal electrode potential $E^{0\prime}$ is used instead [16]. It is a measure of the tendency of a chemical species to acquire or lose electrons and thereby be reduced or oxidized, respectively.

[3] More details about the peak separation in cyclic voltammetry shall be presented in the following chapters.

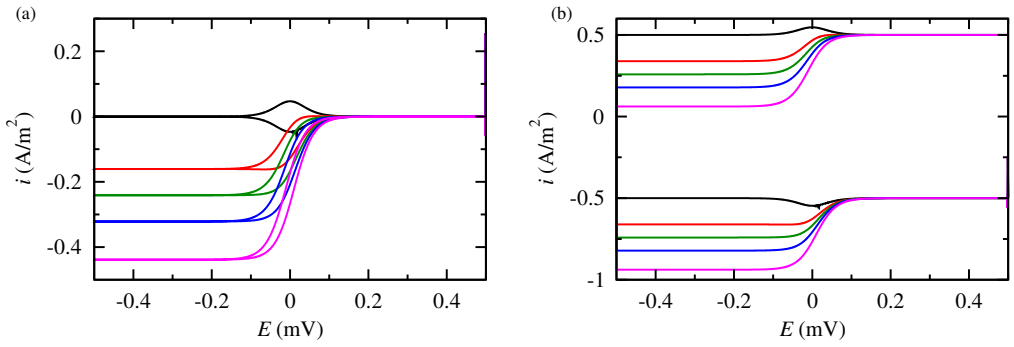

Figure 1.2.2: Computational example of a cyclic voltammogram of an immobilized species reacting with a free in a solution substrate at increasing substrate concentrations under steady state conditions following a Michaelis Menten reaction scheme (a) in the absence and (b) in the presence of potential independent capacitive current.

lized enzymes. In case the capacitance is absent in the cyclic voltammetry, numerical studies have been performed by Limoges and Savéant, giving a thorough analysis and methodology to extract the desired kinetic information [18, 19].

1.3 FTacV

Although it is common practice to subtract the capacitative current form a cyclic voltammogram, the procedure can be quite painstaking and result might still not be the desired one.

In the past, techniques that perturb the applied potential, such as square wave voltammetry (SWV), differential pulse voltammetry (DPV) and small amplitude ac voltammetry have been employed to overcome the issue of capacitance of cyclic voltammetry with examples of the employment of SWV on molecules of biological importance [20, 21]. In the case of ac voltammetry, for reasons of simplicity, small amplitude sinusoidal signals have been applied, as for high amplitudes, the responses tend to be nonlinear [22, 23]. Nevertheless, due to the development of both analytical and numerical methods, large amplitude signals are applied in ac voltammetry, similarly with DPV and SWV, leading to the rise of large amplitude Fourier transform alternating current cyclic voltammetry (FTacV) [22, 24].

An intensive effort has been made for the development of FTacV [25, 26, 24]. As in other alterations of cyclic voltammetry (*i.e.* DPV, SQW) in which the concept is to perturb the applied potential of cyclic voltammetry in order to amplify the electrochemical signal, in FTacV a constant frequency f sine wave with amplitude A_0 is imposed on the cyclic voltammetry potential dc ramp generating an alternate current (ac) waveform, as depicted in Fig. 1.3.1. However, the method does not stop at this point. The resulting ac voltammogram undergoes a Fourier transformation so as to convert the current-time data to the frequency domain. Then, in the resulting power spectrum, peaks (bursts) appear around the multiples of the applied frequency. At each distinct peak of the power spectrum inverse Fourier transformation is applied.

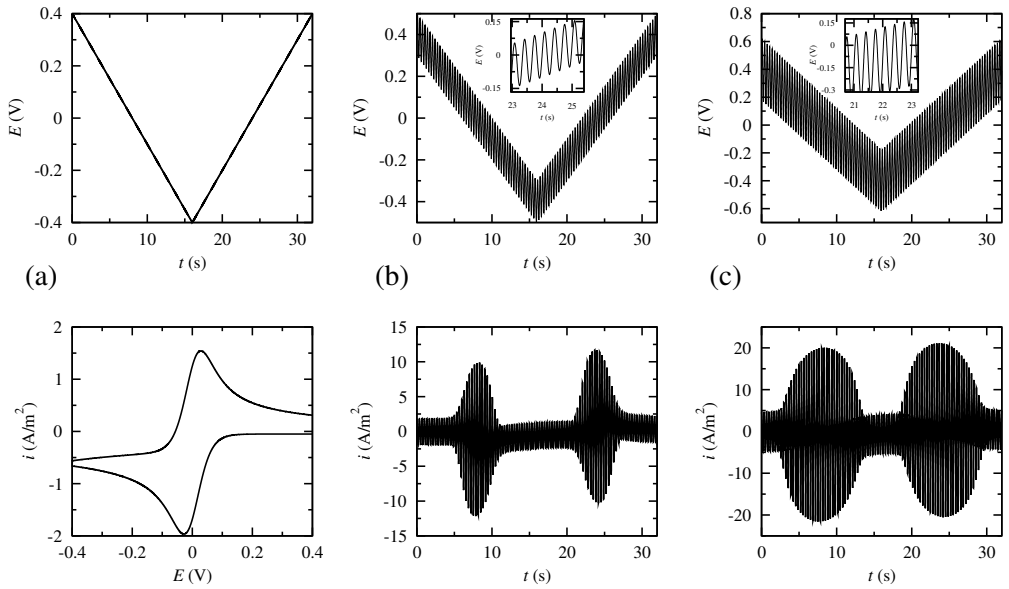

Figure 1.3.1: Potential ramp and respective voltammogram for (a) cyclic voltammetry (b) FTacV for a pertrubation amplitude $A_0 = 100$ mV and frequency of $f = 3$ Hz (c) FTacV for a pertrubation amplitude $A_0 = 250$ mV and frequency $f = 3$ Hz.

The resulting voltammograms are called the harmonic components of the analysis. The order of the harmonic is defined by the order of the burst from the power spectrum that underwent inverse Fourier transform. For example if applied f was 4 Hz and the burst that undergoes the inverse Fourier is at 20 Hz, then the resulting harmonic shall be the 5th one as it is the 5th burst in the power spectrum. Now for the case of an electrochemically reversible reaction, the resulting harmonics have peaks equal to the order of the harmonic. Regarding the odd harmonics their characteristic is that they have one dominant peak while the even ones have two identical dominant peaks. An interesting point is that in the case of the odd harmonic the E^0 can e extracted from the potential value of the dominant peak, while for the even ones, from the minimum that lies between the identical dominant peaks. An example of the process of the signal processing along with the resulting harmonics is presented in Fig. 1.3.2.

The main advantage of this method is that in the higher harmonic components resulting from the analysis, the background current, i.e. capacitative current, is diminished, thus leading to a clear Faradaic current response due to the electrochemical reaction, which could be very useful in the study of redox active proteins where the background currents prevail over the faradaic ones [25, 26].

Over the last decades, several approaches have been followed for the analysis of large amplitude ac-voltammograms. Among them, the works of Mooring and Kies [27], Engblom *et al.* [28] and Gavaghan and Bond [29] stand out, for the description of reversible electrode reactions. Regarding the immobilized species approximate analytic solutions for the reversible case have been published in the past, as well as numerical calculations for quasi-reversible conditions [30]. Similar simulations have been performed for the redox reaction of azurin, immobilized on a paraffin-impregnated graphite electrode

[26]. The effect of the transfer coefficient and kinetic constant on the shape of the harmonics has been shown and the effect of perturbation frequency and amplitude has been discussed. A methodology for the determination of kinetic and thermodynamic parameters has been proposed, based on the peak separation of the analytic signal, obtained by Hilbert transform [23]. An elegant methodology, based on analytic or approximate solutions for high perturbation frequencies has been analyzed both for the case of large amplitude sinusoidal voltammetry [31], as well as large amplitude ac voltammetry [32]. An alternative methodology was also proposed, mainly based on direct numerical simulation and comparison of theoretical harmonics with experimental ones [25, 33]. Numerical simulations and experimental studies concerning the case of a two-electron process of immobilized species [34] as well as theoretical analysis for more complex chemical scenarios [35] are worth mentioning.

One of the scopes of the present work is to analyze further large amplitude FTacV response for both free and immobilized species and examine various kinetic scenarios of coupling electrochemical reactions with chemical ones while monitoring the electrochemical ones.

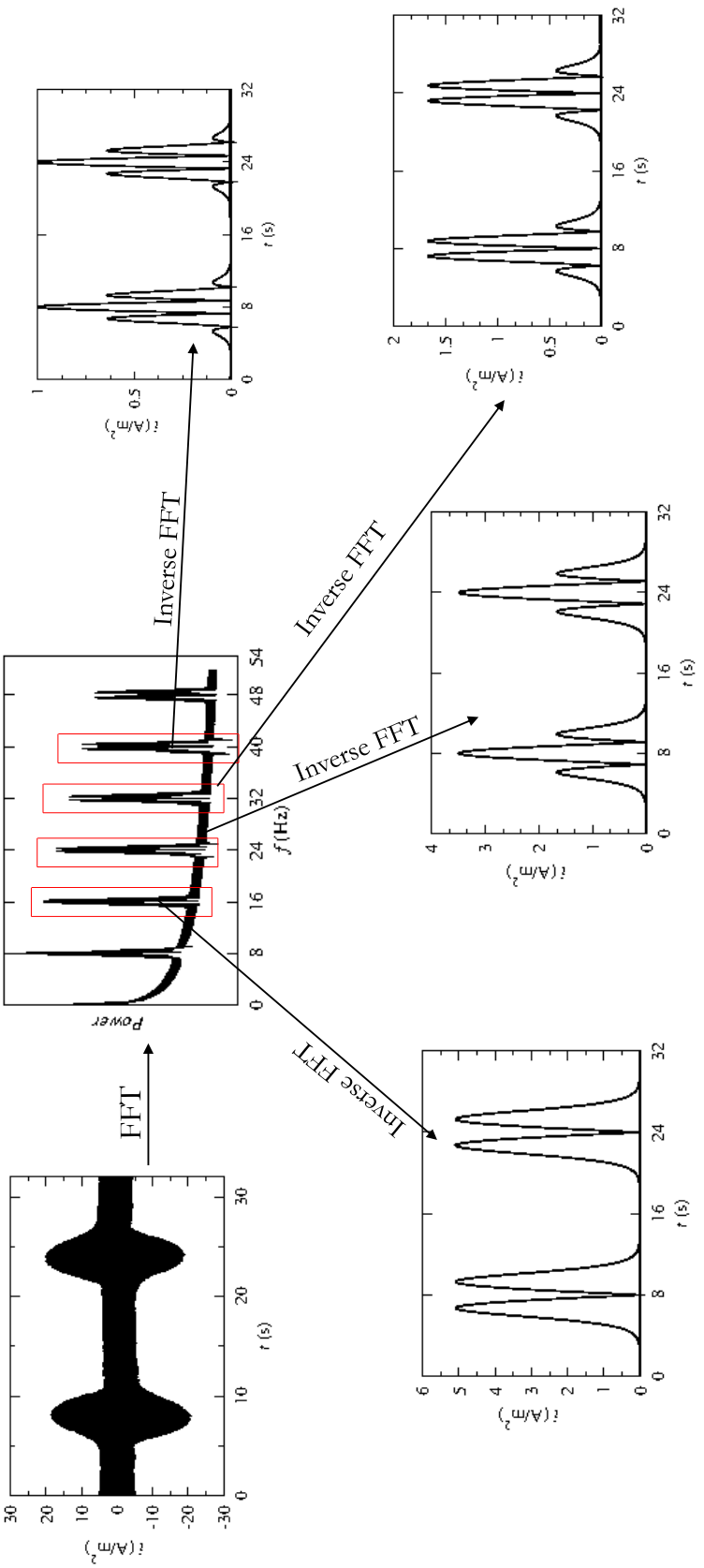

Figure 1.3.2: Schematic representation of FTacV signal processing.

Bibliography

[1] M. L. Kemp. *Redox Enzymes*, pages 1825–1825. Springer New York, New York, NY, 2013.

[2] C. Leger and P. Bertrand. Direct electrochemistry of redox enzymes as a tool for mechanistic studies. *Chem. Rev.*, 108:2379 – 2438, 2008.

[3] Y. Degani and A. Heller. Direct electrical communication between chemically modified enzymes and metal electrodes. I. electron transfer from glucose oxidase to metal electrodes via electron relays, bound covalently to the enzyme. *"J. Phys. Chem.*, 91(6):1285–1289, 1987.

[4] P. N. Bartlett, P. Tebbutt, and R. G. Whitaker. Kinetic aspects of modified electrodes and mediators in bioelectrochemistry. *Prog. Reaction Kinetics.*, 16:55–155, 1991.

[5] F. A. Armstrong. Probing metalloproteins by voltammetry. *Bioinorg. Chem.*, 72:137–221, 1990.

[6] C. Bourdillon, C. Demaille, J. Moiroux, and J. M. Saveant. New insights into the enzymic catalysis of the oxidation of glucose by native and recombinant glucose oxidase mediated by electrochemically generated one-electron redox cosubstrates. *Journal of the American Chemical Society*, 115(1):1–10, 1993.

[7] M. Dequaire, B. Limoges, J. Moiroux, and J.-M. Savéant. Mediated electrochemistry of horseradish peroxidase. Catalysis and inhibition. *J. Am. Chem. Soc.*, 124(2):240–253, 2002.

[8] D. Zouraris, A. Zerva, E. Topakas, and A. Karantonis. Kinetic and amperometric study of the *Mt*perII peroxidase isolated from the ascomycete fungus *Myceliophthora Thermophila*. *Bioelectrochem.*, 118:19–24, 2017.

[9] V. Niviere, E. C. Hatchikian, P. Bianco, and J. Haladjian. Kinetic studies of electron transfer between hydrogenase and cytochrome c3 from *Desulfovibrio gigas*. electrochemical properties of cytochrome c3. *Biochim. Biophys. Acta*, 935(1):34–40, 1988.

[10] C. Moreno, R. Franco, I. Moura, J. Le Gall, and Jo. J. G. Moura. Voltammetric studies of the catalytic electron-transfer process between the *desulfovibrio gigas* hydrogenase and small proteins isolated from the same genus. *Eur. J. Biochem.*, 217(3):981–989, 1993.

[11] P. N. Bartlett. *Bioelectrochemistry: fundamentals, experimental techniques and applications*. John Wiley & Sons, 2008.

[12] F. A. Armstrong, H. A. Heering, and J. Hirst. Reactions of complex metalloproteins studies by protein film voltammetry. *J. Chem. Soc. Rev.*, 26:169–179, 1997.

[13] K. Niki and B. W. Gregory. Monolayers of organothiols. *Biomolecular Films: Design, Function, and Applications*, 111:65, 2003.

[14] J. F. Rusling and Z. Zhang. Thin films on electrodes for direct protein electron transfer. In *Handbook of surfaces and interfaces of materials*, pages 33–71. Elsevier, 2001.

[15] J. F. Rusling and Z. Zhang. Polyion and surfactant films on electrodes for protein electrochemistry. *Electroanalytical Methods for Biological Materials*, page 195, 2002.

[16] A. J. Bard, Gy. Inzelt, and F. Scholz. *Electrochemical dictionary*. Springer Science & Business Media, 2008.

[17] George G Guilbault and Marco Mascini. *Uses of immobilized biological compounds*, volume 252. Springer Science & Business Media, 2012.

[18] B Limoges, J. Moiroux, and J. M. Savéant. Kinetic control by the substrate and/or the cosubstrate in electrochemically monitored redox enzymatic homogeneous systems. catalytic responses in cyclic voltammetry. *J. Electroanal. Chem.*, 521(1):1 – 7, 2002.

[19] B. Limoges and J. M. Savéant. Catalysis by immobilized redox enzymes. Diagnosis of inactivation and reactivation effects through odd cyclic voltammetric responses. *J. Electroanal. Chem.*, 562(1):43 – 52, 2004.

[20] L. J. C. Jeuken, J. P. McEvoy, and F. A. Armstrong. Insights into gated electron transfer kinetics at the electrode protein interface. *J. Phys. Chem. B*, 106(9):2304–2313, 2002.

[21] E. T. Smith and B. A. Feinberg. Redox properties of several bacterial ferredoxins using square wave voltammetry. *J. Biol. Chem.*, 265(24):1437–14376, 1990.

[22] H. Adamson, A. M. Bond, and A. Parkin. Probing biological redox chemistry with large amplitude Fourier transformed ac voltammetry. *Chem. Commun.*, 53:9519–9533, 2017.

[23] C. Anastassiou and K. Parkerand D. O'Hare. Determination of kinetic and thermodynamic parameters of surface confined species through ac voltammetry and a nonstationary signal processing technique: The hilbert transform. *Anal. Chem.*, 77:3357–64, 06 2005.

[24] A. M. Bond, N. W. Duffy, S.-X. Guo, J. Zhang, and D. Elton. Changing the look of voltammetry. *Anal. Chem.*, 77:186A–195A, 2005.

[25] S.-X. Guo, A. M. Bond, and J. Zhang. Fourier transformed large amplitude alternating current voltammetry: Principles and applications. *Review of Polarography*, 61:21–32, 2015.

[26] S. Guo, J. Zhang, D. M. Elton, and A. M. Bond. Fourier transform large-amplitude alternating current cyclic voltammetry of surface-bound azurin. *Anal. Chem.*, 76:166–177, 2004.

[27] C. I. Mooring and H. L. Kies. A.C. voltammetry at large amplitudes. a simplified theoretical approach. *J. Electroanal. Chem.*, 78:219–227, 1977.

[28] S. O. Engblom, J. C. Myland, and K. B. Oldham. Must ac voltammetry employ small signals? *J. Electroanal. Chem.*, 480:120–132, 2000.

[29] D. J. Gavaghan and A. M. Bond. A complete numerical simulation of the techniques of alternative current linear sweep and cyclic voltammetry: Analysis of a reversible process by conventional and fast Fourier transform methods. *J. Electroanal. Chem.*, 480:133–149, 2000.

[30] M.J. Honeychurch and A.M. Bond. Numerical simulation of fourier transform alternating current linear sweep voltammetry of surface bound molecules. *J. Electroanal. Chem.*, 529:3–11, 2002.

[31] Ch.G. Bell, C.A. Anastasiou, D. O'Hare, K.H. Parker, and J.H. Siggers. Theory of high frequency, large-amplitude sinusoidal voltammetry for ideal surface-confined redox species. *Electrochim. Acta*, 56:7569–7579, 2011.

[32] Ch.G. Bell, C.A. Anastassiou, D. O'Hare, K.H. Parker, and J.H. Siggers. Theoretical treatment of high-frequency, large-amplitude ac voltammetry applied to ideal surface-confined redox systems. *Electrochim. Acta*, 64:71–80, 2012.

[33] B. D. Fleming, J. Zhang, D. Elton, and A. M. Bond. Detailed analysis of the electron-transfer properties of azurin adsorbed on graphite electrodes using dc and large-amplitude Fourier transformed ac voltammetry. *Anal. Chem.*, 79:6515–6526, 2007.

[34] G.P. Stevenson, Ch.-Y. Lee, G.F. Kennedy, A. Parkin, R.E. Baker, K. Gillow, F.A. Armostrong, D.J. Gavaghan, and A.M. Bond. Theoretical analysis of the two-electron transfer reaction and experimental studies with surface-confined cytochrome *c* peroxidase using large-amplitude fourier transformed ac voltammetry. *Langmuir*, 28:9864–9877, 2012.

[35] J. Zhang and A.M. Bond. Theoretical studies of large amplitude alternating current voltammetry for a reversible surface-confined electron transfer process coupled to a pseudo first-order electrocatalytic process. *J. Electroanal. Chem.*, 600:23–34, 2007.

2. Voltammetry of Free Electroactive Species

One of the most commonly examined systems in electrohcemistry is that of a free in a solution electroactive species reacting on an electrode surface. In such a case, reactive species are diluted in the electrolytic solution and transported to and from the electrode surface by diffusion. In this section, different cases concerning the reaction of free electroactive species shall be examined. A comparison shall be made between the already established analysis of cyclic voltammetry with new ones that concern FTacV, regarding one step and two step electrochemical reaction processes, the EC mechanism and the monitoring homogeneous reactions.

In the last section of this Chapter, convolution voltammetry shall be introduced for a number of possible scenarios as well. Although there is an already established methodology concerning convolution voltammetry, in this work it was considered useful to gather and reproduce some of the most common scenarios since there was no previous experience with this technique. The analysis of convolution voltammetry will be supplementary to other techniques and could be useful in the interpretation of some experimental results in the following Chapters.

The analysis introduced in this Thesis starts with the free in a solution electroactive species and not the immobilized one, because although the second occasion could be considered more accessible and less complex in the analysis, most are acquainted with the fundamental aspects of cyclic voltammetry in free species.

The results that will be introduced in this chapter are computational and are derived either from calculations and solving differential equations with the use of the software XPPaut [1], as well as with the Finite Elements Method (FEM) in more complex cases.

After this Chapter is concluded, one shall have a basic understanding of FTacV in comparison with cyclic voltammetry and shall be in position to interpret basic as well as more complex voltammograms of free electroactive species. Regarding the exploitation of these results in this work, they shall be of most help in the interpretation of the electrochemical behavior and oxidation mechanism of compounds working as electron donors for the enzymes belonging to the family of the LPMOs.

2.1 One step electron transfer

2.1.1 General formulation for CV and FTacV

Let us assume a redox reaction of a free in a solution electroactive species that exchanges electrons with a solid electrode surface. In the simplest case, a one step n electrode redox reaction is considered,

$$\mathrm{Ox} + ne \underset{}{\overset{k^0}{\rightleftharpoons}} \mathrm{Red}$$

where the chemical species is initially in its oxidized form Ox, and can be reduced to Red. For the first part of the analysis, a sufficiently large standard electron transfer kinetic constant k^0 is considered, so as the mass transfer of the electroactive species is the rate determining step of the process and thus electrochemical kinetics shall be ignored. Convection of the species are also absent, *i.e.* the electrode is stagnant and natural convection is ignored.

Some additional assumptions are considered for the analysis of the aforementioned system and they are listed below:

- The electrode is uniformly accessible by the electroactive species, ignoring effects at the edges of the electrode resulting in an one dimensional problem
- Flow due to migration of electroactive species shall be ignored due to the presence of supporting electrolyte.[1] Uncompensated resistance (IR-drop) effects are also considered negligible
- No adsorption of electroactive species is considered and surface coverage is also regarded as zero
- Capacitance of the electrochemical double layer is considered potential independent, and thus charging currents are assumed proportional to the scan rate

Under the above assumptions, the mass balance equation can be written as

$$\frac{\partial c_k}{\partial t} = -\frac{\partial j_k}{\partial x} \tag{2.1.1}$$

where the flux j_k is given by Fick's law,

$$j_k = -D_k \frac{\partial c_k}{\partial x} \tag{2.1.2}$$

for $k = 1, 2$. Thus, $c_1(x,t)$ and $c_2(x,t)$ correspond to the concentrations of the oxidant and the reductant, respectively.

The concentrations are expressions of both space and time $c_\mathrm{k}(x,t)$ and the initial conditions for this particular problem are $c_1(x,0) = c_1^*$ and $c_2(x,0) = 0$ signifying that

[1] Supporting electrolyte is an electrolyte containing non electroactive species - in the potential range examined - and has an ionic strength much higher than the electroactive species of the species in the solution [2].

only the Ox species are initially present in the solution, with the concentration on the electrode surface being the same as the concentration in the bulk solution, while there is no Red species in the solution.[2] Moreover, equal diffusion coefficients are considered for the Red and the Ox species, $D = D_1 = D_2$.

Far[3] from the electrode surface ($x = L$) the boundary conditions for the concentrations are $c_1(L,t) = c_1^*$ and $c_2(L,0) = 0$, *i.e.* the amount of the produced reductant can be considered negligible.

At the electrode surface (at $x = 0$) the flux of the Ox species is equal and opposite of that of the Red species which translates to the following boundary conditions,

$$j_1(0,t) = -j_2(0,t) = \frac{i_\mathrm{F}}{nF} \tag{2.1.3}$$

where the Faradaic current[4] density obeys the Butler-Volmer law and is given by the following equation,

$$i_\mathrm{F} = nFk^0\left[c_2(0,t)e^{\frac{(1-a)nF}{RT}(E(t)-E^0)} - c_1(0,t)e^{-\frac{anF}{RT}(E(t)-E^0)}\right] \tag{2.1.4}$$

where a is the transfer coefficient and E^0 the standard (or formal) electrode potential.

The term $E(t)$ represents the electrode potential which is scanned with a scan rate[5], v, beginning at initial value value of E_I, more positive than E^0 to a reversal value E_R more negative than E^0. The time that corresponds to the instant that the potential reaches E_R is called reversal time t_R and is equal to $\frac{E_\mathrm{I}-E_\mathrm{R}}{v}$.

After the potential reaches the value of t_R , the potential is reversed back to E_I. In the case of FTacV, the potential is also perturbed by a sinusoidal perturbation of frequency f and amplitude A_0. The expression of the potential dependence against time is presented below,[6]

$$E(t) = E_\mathrm{I} - vt_\mathrm{R} + v|t - t_\mathrm{R}| + A_0 \sin 2\pi ft \qquad \text{for } 0 \le t \le 2t_\mathrm{R} \tag{2.1.5}$$

For the case of cyclic voltammetry the last term is omitted

$$E(t) = E_\mathrm{I} - vt_\mathrm{R} + v|t - t_\mathrm{R}| \qquad \text{for } 0 \le t \le 2t_\mathrm{R} \tag{2.1.6}$$

[2]Concentrations in the bulk solution are symbolized with an asterisk and are considered time and space independent.

[3]By this term, a distance L from the electrode surface is considered over which the concentration of species can be assumed time and space independent.

[4]The current generated by the reduction or oxidation of some chemical substance at an electrode.

[5]Also referred as sweep rate.

[6]In case of the reverse process- starting from a potential more negative than E^0 reaching a reversal potential more positive than E^0, the equations for FTacV and CV respectively are,

$$E(t) = E_\mathrm{I} + vt_\mathrm{R} - v|t - t_\mathrm{R}| + A_0 \sin 2\pi ft \qquad \text{for } 0 \le t \le 2t_\mathrm{R}$$
$$E(t) = E_\mathrm{I} + vt_\mathrm{R} - v|t - t_\mathrm{R}| \qquad \text{for } 0 \le t \le 2t_\mathrm{R}$$

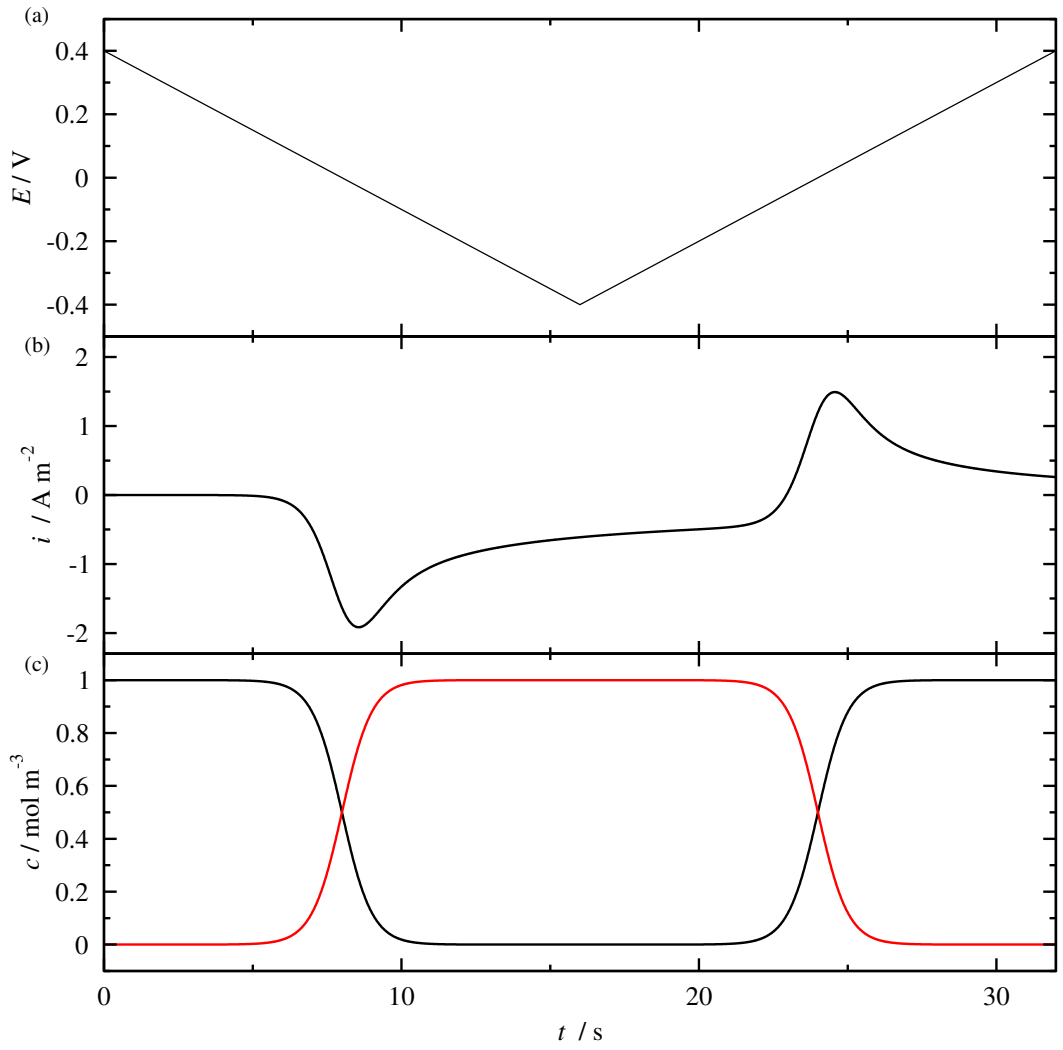

Figure 2.1.1: Example of cyclic voltammetry for free species,for $c_1^* = 1$ mol/m^3, $v = 50$ mV/s, $D = 1 \times 10^{-9}$ m/s. (a) Potential E against time t, (b) current density i against time t and (c) c_1 concentration of Ox (black line) and c_2 of Red species (red line), against time t.

By summing up the Faradaic and the non-Faradaic current density (capacitance current density), $i_C = C_{dl}\frac{dE}{dt}$ the following expression is obtained for the total current density,

$$i(t) = i_F(t) + C_{dl}\left(v\frac{t - t_R}{|t - t_R|} + 2\pi f A_0 \cos 2\pi f t\right) \tag{2.1.7}$$

where C_{dl} is the specific capacitance of the double layer.

As the sum of the fluxes on the electrode surface shall be equal to zero, the boundary conditions for very fast kinetics are

$$j_1(0,t) + j_2(0,t) = 0 \tag{2.1.8}$$

$$c_1(0,t) = c_2(0,t)e^{\frac{nF}{RT}(E(t)-E^0)} \tag{2.1.9}$$

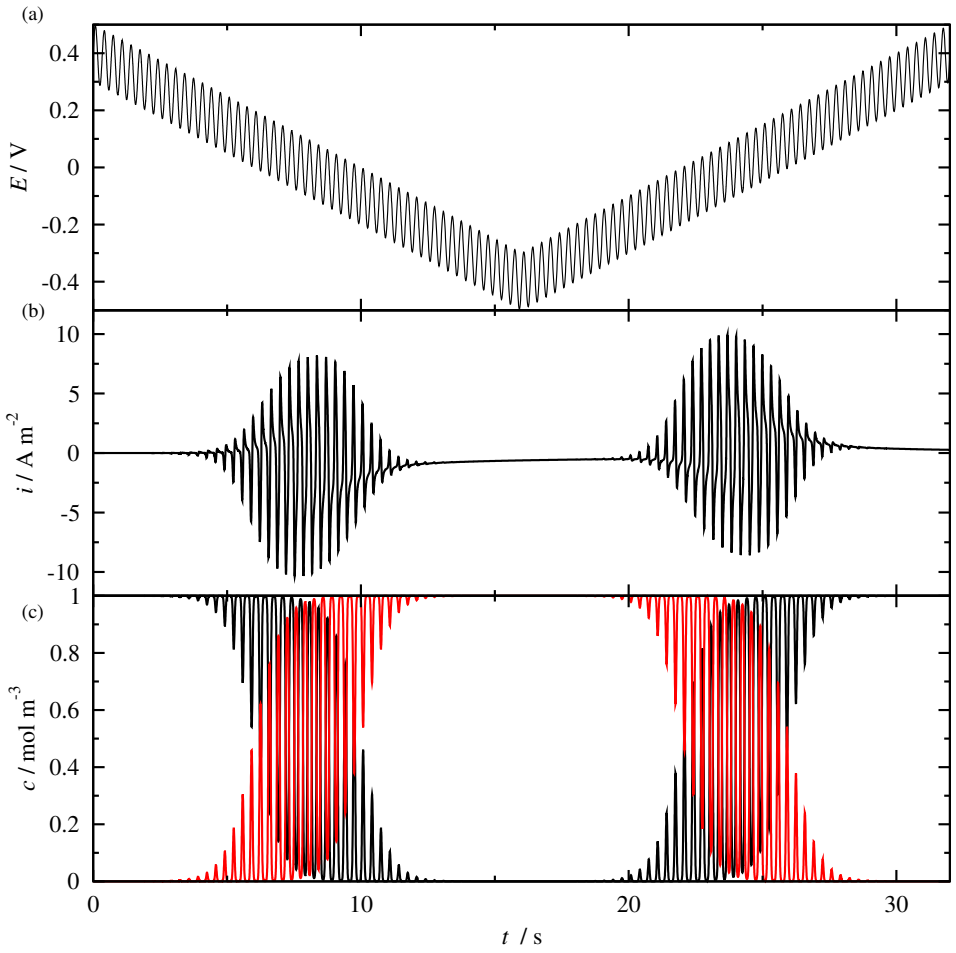

Figure 2.1.2: Example of FTacV for free species for $c_1^* = 1$ mol/m^3, $v = 50$ mV/s, $A = 0.1$ V, $f = 3$ Hz and $D = 1 \times 10^{-9}$ m/s. (a) Potential E against time t, (b) current density i against time t and (c) c_1 concentration of Ox (black line) and c_2 of Red species (red line), against time t.

where, in the second equation, we recognize Nernst equation.

Schematically these scenarios are presented in Figs 2.1.1 and 2.1.2 for cyclic voltammetry and FTacV, respectively, where in both cases the first diagram refers to the sweep of the potential, the second to the current response and the third to the concentration of both forms of the electroactive species on the electrode surface. For the case of cyclic voltammetry one can see that as the potential is swept towards negative (cathodic) values, a peak appear in the current diagram. The currents during the reduction are negative. Looking at the concentration profile on the electrode surface it is also apparent that as the potential is swept cathodically, the concentration of the Ox species is decreased whereas that of the Red species increases. The current peak appears when the two concentrations have the same value. Respectively, when the scan is reversed and the potential is swept to more positive (anodic) values, again a current peak is observed. The anodic currents are positive and by observing the concentration profiles at the surface, as the concentration of the Red species decreases, the concentration of

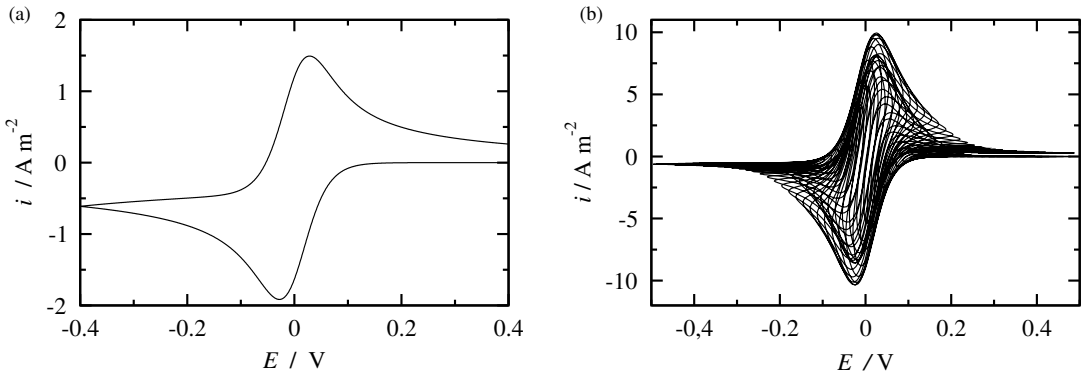

Figure 2.1.3: Example of a (a) cyclic voltammogram and a (b) FTac voltammogram against potential for free species for $c_1^* = 1$ mol/m^3 and $D = 1 \times 10^{-9}$ m/s. For the cyclic voltammogram $v = 50$ mV/s and for the FTac voltammogram $v = 50$ mV/s, $f = 3$ Hz and $A = 100$ mV/s.

the Ox one increases. Again, the oxidation peak appears where the two concentrations have the same value.

By looking at Fig. 2.1.2 and comparing it to Fig. 2.1.1 it is rather clear that the fine lines found in the CV are substituted by perturbed ones, due to the superposition of a sinusoidal signal to the potential ramp. The most interesting part is that the current appears to have positive and negative values during both the anodic and the cathodic scan, as the potential is now shifted towards both anodic and cathodic values while in either the anodic and the cathodic scan.

In Fig. 2.1.3, a comparison between the voltammograms of cyclic voltammetry and FTacV against the potential is shown. One can notice the amplification of the electrochemical signal in the case of FTacV for a perturbation amplitude of 100 mV and frequency of 3 Hz. The resulting peaks are more than 5 times the magnitude of the simple cyclic voltammetry scan, which shows a glimpse of the the advantages FTacV can have when augmenting the electrochemical signal of a reversible reaction.

2.1.2 Semi-Analytical Solution for CV

In cyclic voltammetry, it has been shown that in the case of the reduction of an oxidized form of free species at a initial concentration c_1^*, the current can be expressed in a dimensionless expression as follows [3, 4],

$$\frac{1}{\pi}\int_0^{\tau_{cv}} \frac{\psi_{cv}(\eta)}{\sqrt{(\tau-\eta)}}\mathrm{d}\eta = \frac{1}{1+\exp(-\xi)} \tag{2.1.10}$$

where,

- $\tau_{cv} = \frac{Fv}{RT}t$ is the dimensionless time for cyclic voltammetry
- $\xi = \frac{F}{RT}(E - E^0)$ is the dimensionless electrode potential
- $\psi_{cv} = \frac{i}{FSc_1^*\sqrt{D}\sqrt{\frac{Fv}{RT}}}$ is the dimensionless current for cyclic voltammetry

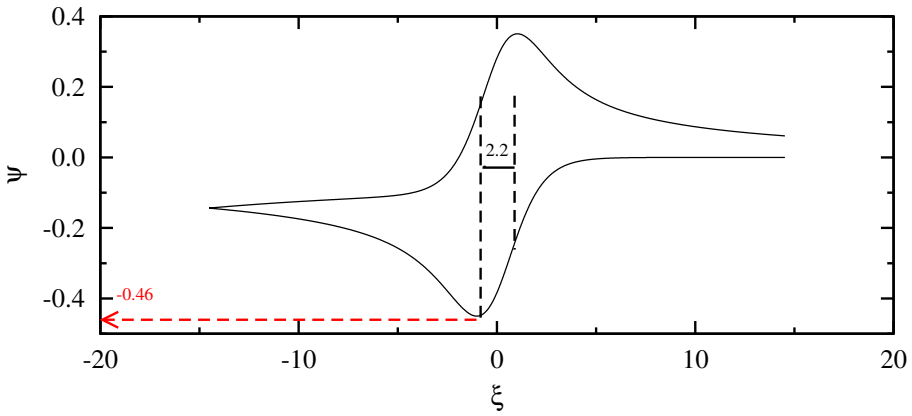

Figure 2.1.4: Dimensionless cyclic voltammogram for a reversible reaction. Annotated magnitues: $\psi_{\mathrm{p,cv}} - \psi_{\frac{\mathrm{p}}{2},\mathrm{cv}}$ (black) and $\psi_{\mathrm{p,cv}}$ (red).

In the dimensionless variable above, S corresponds to the electrode surface area, R to the ideal gas constant, T to the temperature and F to the Faraday constant.

During the cathodic scan the current against the potential is expressed as,

$$\frac{1}{\pi}\int_{-\infty}^{\xi}\frac{\psi_{\mathrm{cv}}(\eta)}{\sqrt{(\tau-\eta)}}\mathrm{d}\eta = \frac{1}{1+\exp(-\xi)} \tag{2.1.11}$$

At a first glimpse of Eq. (2.1.11), the current should depend on the initial potential E_{I}, but as the E_{I} is considerably away from E^0, this dependence vanishes.[7]

The chief observables of a cyclic voltammogram, see Fig. 2.1.4 are,

- $\psi_{\mathrm{p,cv}} = -0.446$ (dimensionless peak current for cyclic voltammetry)
- $\xi_{\mathrm{p,cv}} = 1.1$ (dimensionless peak potential for cyclic voltammetry)
- $\xi_{\mathrm{p,cv}} - \xi_{\frac{\mathrm{p}}{2},\mathrm{cv}} = 2.20$ (dimensionless peak width for cyclic voltammetry)

Taking these dimensionless chief observables, we can revert them back to their respective expressions with dimensions in the following equations,

$$i_{\mathrm{p,cv}} = -0.446FSc_1^*\sqrt{D}\sqrt{\frac{Fv}{RT}} \tag{2.1.12}$$

$$E_{\mathrm{p,cv}} = E^0 - 1.11\frac{RT}{F} \tag{2.1.13}$$

$$E_{\frac{\mathrm{p}}{2},\mathrm{cv}} - E_{\mathrm{p,cv}} = 2.20\frac{RT}{F} \tag{2.1.14}$$

Thus, the current is proportional to the electroactive species concentration in the bulk solution and the square root of the scan rate, according to Eq. (2.1.12). The peak

[7] Experimental experience shows that 400 to 500 mV away from the standard potential are usually sufficient so as the the signal is not disturbed.

potential in the case of a reversible reaction is independent of the scan rate and 28.5 mV more negative than the E^0 at 25 °C, see Eq. (2.1.13). Moreover, at 25 °C the peak width corresponds to 56.5 mV, see Eq. (2.1.14). One more important and widely used criteria from this analysis for checking the reversibility of a system is that the distance between the oxidation and the reduction peak shall be $2.22\frac{RT}{F}$.[8]

2.1.3 Semi-Analytical Solution for FTacV

A similar analysis is to be attempted for the case of FTacV, where the ac-voltammogram can be given from the following expression

$$-\frac{n}{\sqrt{\pi}}\int_0^{\tau}\frac{\psi_{\mathrm{ac,F}}(z)}{\sqrt{\tau_{\mathrm{ac}}-z}}dz = b(\tau_{\mathrm{ac}}) \tag{2.1.15}$$

where

- $\psi_{\mathrm{ac,F}}=\frac{i}{Fc_1^*\sqrt{Df}}$ is the dimensionless current in FTacV
- $\tau_{\mathrm{ac}}=ft$ is the dimensionless time in FTacV
- n the number of electrons
- $\hat{\beta} = \frac{c_2}{c_1^*}$ the dimensionless concentration of the reductant.

Moreover the dimensionless concentration of the reductant can be written as,

$$\hat{\beta}(\tau) = \frac{1}{1+e^{n\xi(\tau)}} \tag{2.1.16}$$

The corresponding dimensionless concentration of the oxidant $\hat{\alpha}(\tau)$ can be expressed as the ratio c_1/c_1^*.

It should noted that in the chosen dimensionless equations, the number of electrons n appears as a parameter, in contrast to the classic choice of dimensionless variables where n appears in the expression of the perturbation amplitude, potential and current [5, 6, 7]. The choice of the present dimensionless equations offers the advantage of a direct comparison of the chief observables for different number of transferred electrons under the same experimental conditions (potential and amplitude).

In Eq. (2.1.16), $\xi = \frac{F}{RT}(E-E^0)$ is the dimensionless electrode potential[9].

Now, the Eq. (2.1.5) shall be rendered dimensionless resulting in Eq. (2.1.17)

$$\xi(\tau) = \xi_{\mathrm{I}} - \sigma\tau_{\mathrm{R}} + \sigma|\tau-\tau_{\mathrm{R}}| + \alpha_0\sin 2\pi\tau \tag{2.1.17}$$

for $0 \le \tau \le 2\tau_{\mathrm{R}}$. In Eq. (2.1.17),

$$\tau_{\mathrm{R}} = \frac{|\xi_{\mathrm{I}}-\xi_{\mathrm{R}}|}{\sigma}$$

[8] In this analysis a one electron process is considered. For an one-step two electron process, the current shall be multiplied with 2 while the peak position, peak width and peak distances shall be divided by 2.

[9] The same dimensionless electrode potential is used as in cyclic voltammetry.

is the reversal time, $\xi_{\rm I} = \frac{F}{RT}(E_{\rm I} - E^0)$ the initial potential, $\xi_{\rm R} = \frac{F}{RT}(E_{\rm R} - E^0)$ the reversal potential and $\sigma = \frac{Fv}{RTf}$ the dimensionless scan rate. The dimensionless perturbation amplitude is $\alpha_0 = \frac{F}{RT}A_0$.

Equation (2.1.15) can be solved for $\psi_{\rm ac,F}(\tau)$, resulting in,

$$\psi_{\rm ac,F}(\tau) = -\frac{n}{\sqrt{\pi}}\Big[\frac{\hat{\beta}(0)}{\sqrt{\tau}} + \int_0^{\tau}\frac{\hat{\beta}'(z)}{\sqrt{\tau - z}}dz\Big] \tag{2.1.18}$$

where the analytic form of the derivative of the concentration is,

$$b'(z) = -\frac{n}{4}\frac{\sigma\frac{z-\tau_{\rm R}}{|z-\tau_{\rm R}|} + 2\pi\alpha_0\cos 2\pi z}{\cosh^2[0.5n(\xi_{\rm I} - \sigma\tau_{\rm R} + \sigma|z-\tau_{\rm R}| + \alpha_0\sin 2\pi z)]} \tag{2.1.19}$$

Setting $y = \sqrt{\tau - z}$, and taking into account that for large values of the initial potential the first term of Eq. (2.1.18) vanishes, we get,

$$\begin{aligned}\psi_{\rm ac,F}(\tau) &= \frac{n^2}{2\sqrt{\pi}}\times \\ &\int_0^{\sqrt{\tau}}\frac{\sigma\frac{\tau-y^2-\tau_{\rm R}}{|\tau-y^2-\tau_{\rm R}|} + 2\pi\alpha_0\cos 2\pi(\tau - y^2)}{\cosh^2[0.5n(\xi_{\rm I} - \sigma\tau_{\rm R} + \sigma|\tau - y^2 - \tau_{\rm R}| + \alpha_0\sin 2\pi(\tau - y^2))]}dy\end{aligned} \tag{2.1.20}$$

The integral above can be evaluated with the trapezoidal rule. Hence, we arrive to the following semi-analytic determination of the Faradaic component of the ac-voltammogram,

$$\begin{aligned}\psi_{ac,\rm F}(\tau) = \frac{n^2\Delta}{2\sqrt{\pi}}\Big\{&\frac{1}{2}\frac{\sigma\frac{\tau-\tau_{\rm R}}{|\tau-\tau_{\rm R}|} + 2\pi\alpha_0\cos 2\pi\tau}{\cosh^2[0.5n(\xi_{\rm I} - \sigma\tau_{\rm R} + \sigma|\tau-\tau_{\rm R}| + \alpha_0\sin\tau)]}\times \\ &\sum_{j=1}\frac{\sigma\frac{\tau-(jh)^2-\tau_{\rm R}}{|\tau-(jh)^2-\tau_{\rm R}|} + 2\pi\alpha_0\cos 2\pi(\tau-(jh)^2)}{\cosh^2[0.5n(\xi_{\rm I} - \sigma\tau_{\rm R} + \sigma|\tau-(jh)^2-\tau_{\rm R}| + \alpha_0\sin 2\pi(\tau-(jh)^2))]}\Big\}\end{aligned} \tag{2.1.21}$$

where Δ is the step of the trapezoidal rule.

Assuming a potential independent double layer capacitance, the capacitive component of the ac-voltammogram is written,

$$\psi_{\rm ac,C} = \mu\Big(\sigma\frac{\tau-\tau_{\rm R}}{|\tau-\tau_{\rm R}|} + 2\pi\alpha_0\cos 2\pi\tau\Big) \tag{2.1.22}$$

where $\mu = \frac{RT\sqrt{f}}{F^2c_1^*\sqrt{D}}C_{\rm dl}$ is the dimensionless double layer capacitance. Therefore, the semi-analytic solution of the complete ac-voltammogram, $\psi_{\rm ac}(\tau) = \psi_{\rm ac,F}(\tau) + \psi_{\rm ac,C}(\tau)$, is,

$$\begin{aligned}\psi_{\rm ac}(\tau) = \frac{n^2\Delta}{2\sqrt{\pi}}\Big\{&\frac{1}{2}\frac{\sigma\frac{\tau-\tau_{\rm R}}{|\tau-\tau_{\rm R}|} + 2\pi\alpha_0\cos 2\pi\tau}{\cosh^2[0.5n(\xi_{\rm I} - \sigma\tau_{\rm R} + \sigma|\tau-\tau_{\rm R}| + \alpha_0\sin\tau)]} \\ &\sum_{j=1}\frac{\sigma\frac{\tau-(jh)^2-\tau_{\rm R}}{|\tau-(jh)^2-\tau_{\rm R}|} + 2\pi\alpha_0\cos 2\pi(\tau-(jh)^2)}{\cosh^2[0.5n(\xi_{\rm I} - \sigma\tau_{\rm R} + \sigma|\tau-(jh)^2-\tau_{\rm R}| + \alpha_0\sin 2\pi(\tau-(jh)^2))]}\Big\}+ \\ &\mu\Big(\sigma\frac{\tau-\tau_{\rm R}}{|\tau-\tau_{\rm R}|} + 2\pi\alpha_0\cos 2\pi\tau\Big)\end{aligned} \tag{2.1.23}$$

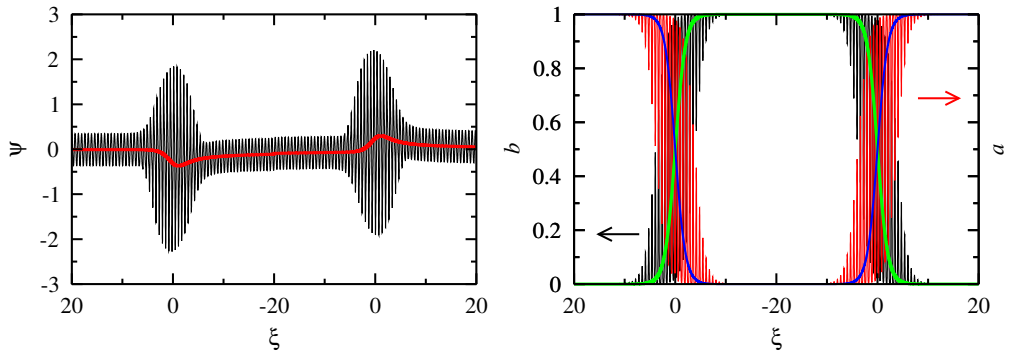

Figure 2.1.5: (a) Dimensionless ac-voltammogram (black) and dimensionless voltammogram (red) for $\alpha_0 = 3.893$, $\mu = 1.458 \times 10^{-2}$, $\sigma = 0.648$, and $n = 1$, together with the dimensionless cyclic voltammogram ($\alpha_0 = 0$). (b) dimensionless concentrations on the electrode surface under the same conditions.

The advantageous aspect of Eq. (2.1.23) is that it can be easily applied iteratively, without the use of additional algorithms. By inspecting this equation, it is evident that the contribution of the capacitance current on the Fourier coefficients of the total current is,

$$\begin{aligned} c^{(0)} &= 2\mu\sigma \frac{\tau - \tau_{\mathrm{R}}}{|\tau - \tau_{\mathrm{R}}|} \\ c^{(1)} &= 2\pi\alpha_0\mu \\ c^{(2)} &= 0 \\ &\vdots \end{aligned}$$

that is, the effect of capacitance current is eliminated for harmonic components higher than one, provided that the capacitance is independent of the electrode potential[10].

Having taken into consideration the correlation between the current and the other factors used in the dimensionless expression of the current (diffusion coefficient D, bulk concentration c_1^* and frequency f), the remaining principal experimental parameters affecting the ac-voltammogram are α_0 and σ, corresponding to the perturbation amplitude and scan rate, respectively, along with the initial potential ξ_{I}, and the reversal time τ_{R}. Moreover, it depends on two physical parameters, *i.e.* the double layer capacitance μ and the number of transferred electrons, n. For large enough values of ξ_{I} and τ_{R}, the chief observables of the voltammogram are independent of these parameters. Moreover, the voltammogram can be independent of the scan rate under specific conditions - we shall discuss this particular subject in the next section. Therefore, the voltammogram actually depends on one experimental parameter, namely, the amplitude and two physical parameters, the double layer capacitance and the number of electrons. As already

[10]In most experimental systems the capacitative currents are not potential independent. Experimental experience shows that while using carbon based electrodes, harmonics higher than the 3rd one are usually needed to get rid of the capacitance.

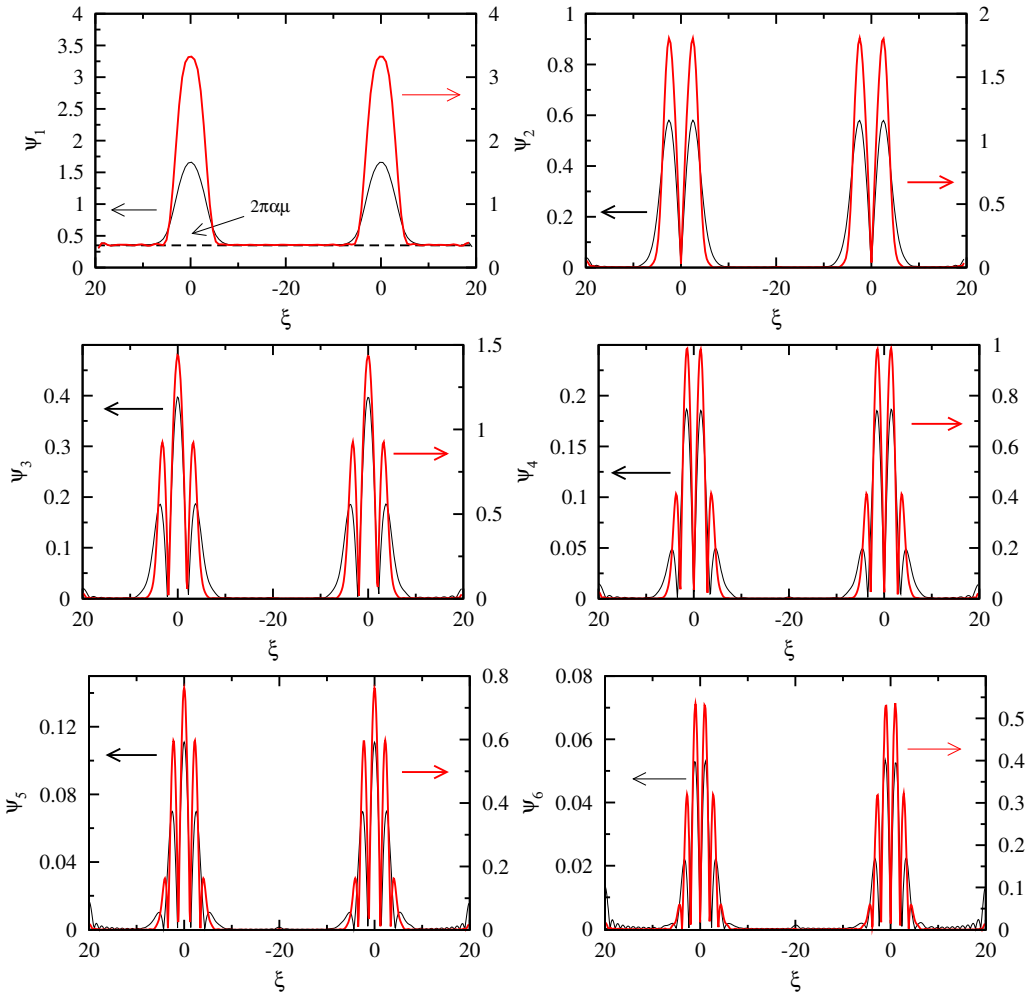

Figure 2.1.6: Dimensionless harmonic components for $\alpha_0 = 3.893$, $\mu = 1.458 \times 10^{-2}$, $n = 1$ (black curve) and $n = 2$ (red curve).

discussed, harmonics higher than the first, tend to be independent of μ. Thus, the chief observables are expected to depend on amplitude and number of electrons only. A typical example of the semi-analytical solution is presented in Fig. 2.1.5(a) together with the corresponding cyclic voltammogram. The concentrations of Red and Ox species on the electrode surface are presented in Fig. 2.1.5(b). In Fig. 2.1.6, the first six harmonics are presented for $\alpha_0 = 3.893$ and $\mu = 1.458 \times 10^{-2}$. Notice that the capacitive component $2\pi\alpha_0\mu$ contributes only to the first harmonic, thus all higher harmonics represent any experiment performed with $\alpha_0 = 3.893$, corresponding to a reversible system with $n = 1$ (black curves) and $n = 2$ (red curves).

By inspecting Eq. (2.1.23), it is realized that the Faradaic current, as it occurs from the dimensionless current ψ will be proportional to the bulk concentration of the oxidant, the square root of the diffusion coefficient and the square root of the frequency. Moreover, a dependence on scan rate, number of electrons and perturbation amplitude exists, which is not evident from the equations. The dependence of ψ on $f^{1/2}$ constitutes

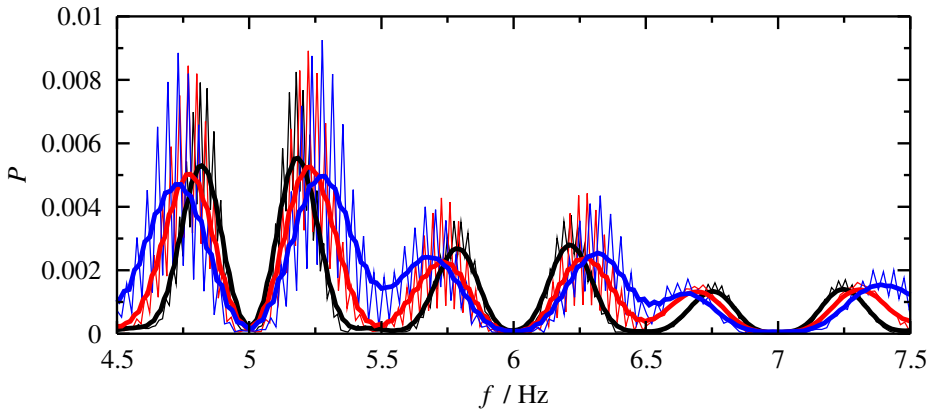

Figure 2.1.7: Effect of the dimensionless scan rate σ on the 5th, 6th and 7th harmonics. Parameter values: $\alpha_0 = 3.89$, $n = 1$ and $\sigma = 1.038$ (black), 1.298 (red) and 1.427 (blue). The smooth lines correspond to the respective moving averages of the bursts for reasons of visualization.

an advantage of the method since the harmonic components are amplified for increasing values of the frequency. In the following section, a condition for independence of scan rate will be derived and the relation of the harmonics on the above mentioned parameters will be investigated numerically. All numerical calculations have been performed by solving both the initial-boundary value problem introduced earlier and the semi-analytical formula, Eq. (2.1.23). The results were identical, provided that k^0 was sufficiently large.

2.1.4 Independence of scan rate

In FTacV, experimentally, the two parameters that are to be altered so as to enhance the electrochemical signal are the amplitude, A_0, and the frequency, f, of the applied sinusoidal perturbation. The signal is resolved in the frequency domain, meaning that the role of frequency analogous to the scan rate is in cyclic voltammetry. Taking this into account, it must be assumed that the FTacV signal is independent of the scan rate. The frequency shall be adequately high for a given value of the scan rate so that the independence holds. Concerning this topic, a thorough analysis has been introduced by Bell *et al.* [5]. Here, an attempt has been made for a more practical approach, by introducing a quantitative relation between the frequency and the scan rate. This relation is valid up to the 5th harmonic, and could be of use while analyzing experimental signals, as the contribution of the capacitance at such high a harmonic is usual absent.

In an attempt to quantify the relation between the perturbation frequency f and the scan rate v, we shall recall that the dimensionless scan rate is $\sigma = \frac{F}{RT}\frac{v}{f}$. This can be translated to $\sigma \approx 38.92\frac{v}{f}$ at $T = 298.15$ K. Thus, the correlation between f and v can be revealed by studying the effect of σ on the dimensionless voltammogram, or more specifically, on the Fourier spectrum of ψ. The present discussion shall be limited

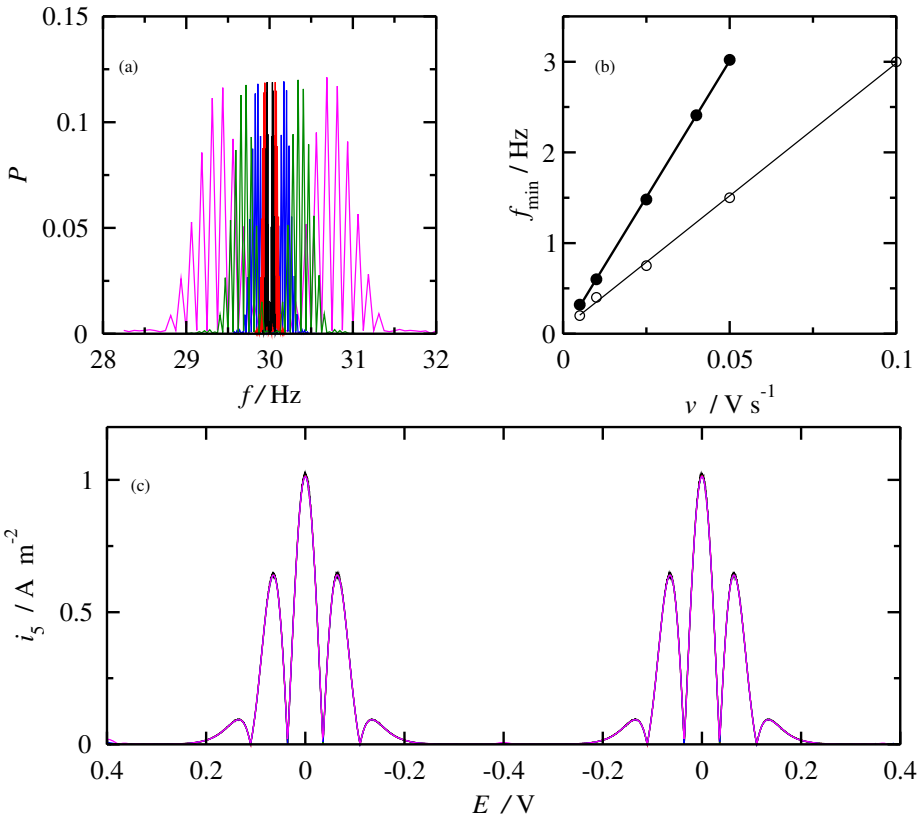

Figure 2.1.8: Effect of scan rate. (a) Power spectra of ac-voltammograms around 30 Hz (5th harmonic) and $n = 1$, (b) minimum frequency against scan rate for $n = 1$ (white circles) and $n = 2$ (black circles), (b) 5th harmonic for different scan rates for $n = 1$. Scan rate values: 5 (black), 10 (red), 25 (blue), 50 (green) and 100 mV/s (magenta). Parameter values: $f = 5$ Hz, $A_0 = 100$ mV, $c_1^* = 1$ mM, $k^0 = 100$ m/s, $E^0 = 0$ V, $D = 10^{-9}$ m^2/s, T=298.15 K.

up to the 5th harmonic, as the experimental experience indicates that above the fifth harmonic the magnitude of the voltammograms drops during the analysis of the results and higher order harmonic components are not easily distinguished.

The effect of σ on the Fourier spectrum is depicted in Fig. 2.1.7, where the 5th, 6th and 7th harmonics are shown together with the corresponding moving averages, for reason of visualization. By paying attention the spectra as well as the corresponding moving average for $\sigma = 1.038$, that is, for $f = 37.49v$ (black curves), it is quite obvious that the harmonic components up to the 7th harmonic are clearly separated. In the case of $\sigma = 1.298$ (red curve) where $f = 29.98v$ all harmonics up to the 6th are separated while an overlap is noticed between the 6th and 7th harmonic components. The situation changes dramatically for a lower value $\sigma = 1.427$ (black curve). In this case, where $f = 27.27v$, the 5th and 6th harmonics overlap and thus, cannot be distinguished.

In order to realize the correlation between the frequency and the scan rate, the 5th

harmonic component of the power spectrum of an ac-voltammogram is presented in Fig. 2.1.8(a), for $f = 6$ Hz, $A_0 = 0.1$ V and different scan rates. In every case, the ac-voltammogram corresponds to a reversible reaction by setting a very large value of k^0 in the initial-boundary value problem. It is evident that as the scan rate increases so does the width of the burst of the 5th harmonic. The analysis of the power spectrum becomes problematic when the bursts of different harmonics start overlapping, thus rendering the inverse Fourier transformation around a certain harmonic component impossible.

In Fig, 2.1.8(b), the minimum frequency for which the 5th and 6th harmonic do not interfere is plotted against the scan rate, for $n = 1$ (white circles) and $n = 2$ (black circles). The slope of this linear curves is $f_{\min}/v = 30.1n$ V^{-1}, which is in close agreement with the results presented in Fig. 2.1.7. Hence, a proposed condition so as that FTacV is independent of the scan rate up to the 5th harmonic is,

$$f \geq 0.77 \frac{nF}{RT} v \tag{2.1.24}$$

provided that the reaction is reversible for the chosen values of f and v.

It should be noted that the width of the bursts is independent of the applied frequency and amplitude and is affected only by the scan rate (results not shown). In Fig. 2.1.8(c) the 5th harmonic component for different scan rates are presented, under the same parameters (notice that the $x-$axis is the electrode potential). It is evident that as long as the bursts do not interfere, there is no difference in the voltammograms that arise from the analysis for the different scan rates.

2.1.5 Effect of amplitude and number of electrons

While the condition of Eq. (2.1.24) is imposed, the two parameters affecting the chief observables, *i.e.* the peak height, the width at half maximum (for the odd harmonics) and the peak potential (for the even harmonics) of the principal peaks, are the amplitude α_0 and the number of electrons n.

In Fig. 2.1.9, the effect of α_0 on the peak height of the principal peak is presented. Figure 2.1.9(a) corresponds to the case of $n = 1$ and Fig. 2.1.9(b) to $n = 2$ transferred electrons. In this, and all subsequent figures, the subscript h indicates the number of the harmonic. In this figure, the slope of the curve for small perturbation amplitudes for $h = 1$ is also shown by a dashed line, corresponding to a typical low amplitude ac-voltammogram. The slopes are $n^2\sqrt{2\pi}/4$, as expected from the theory of low amplitude ac-voltammetry [8].

For $n = 1$, harmonics higher than the 2nd and up to the 6th are detected for $\alpha_0 \geq 1.95$ and are amplified rather drastically in the region from $\alpha_0 = 3.12$ to $\alpha_0 = 9.73$, corresponding to amplitude values of 80 to 250 mV at $T = 298.15$ K. For large values of α_0 all harmonics tend to a saturation, its value determined by the number of the harmonic.

It is interesting to compare the maximum peak height with what is reported in the literature. Thus, according to Mooring and Kies [9] the peak height of the first harmonic for $n = 1$ is $\psi_{\mathrm{p},1} = \sqrt{2\pi}0.50415 = 1.26372$ at $\alpha_0 = 3$. In the present work, the

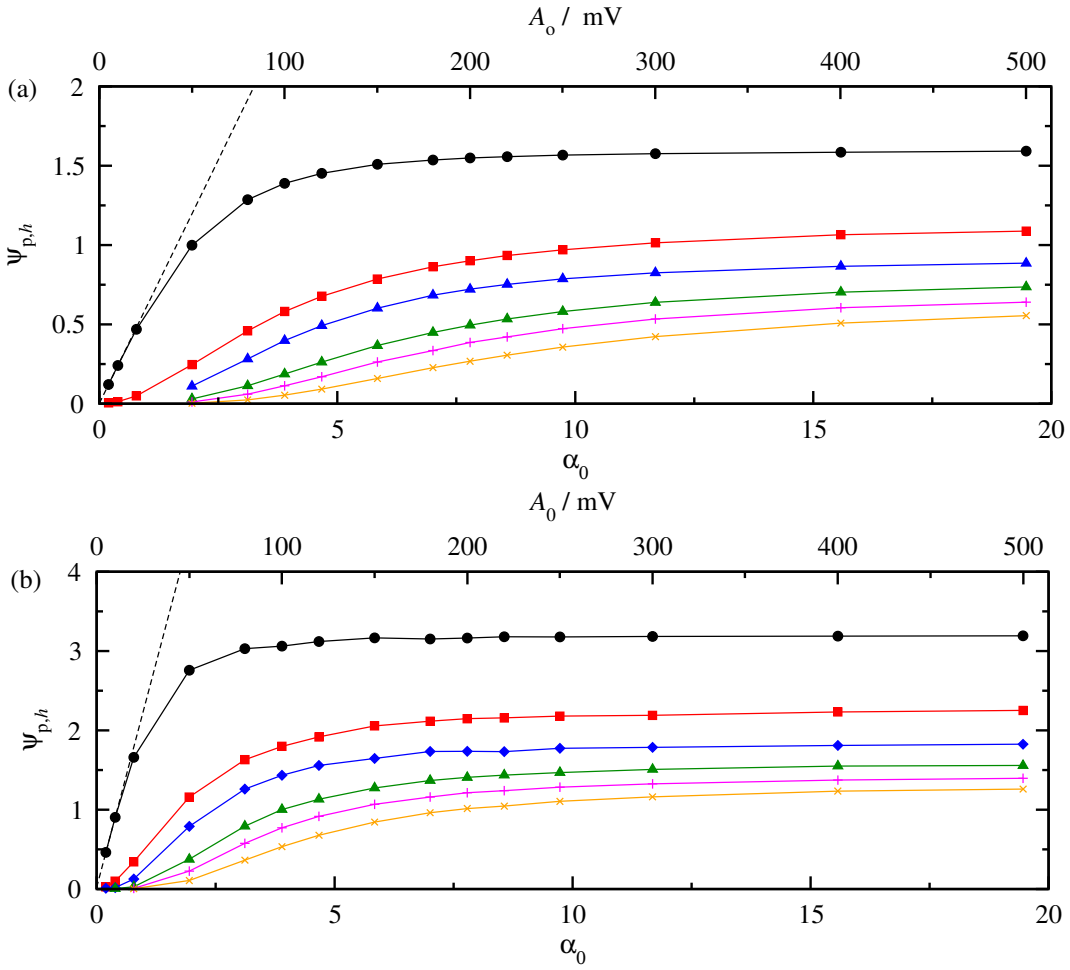

Figure 2.1.9: Maximum peak height for $\mu = 0$, as a function of the perturbation amplitude α_0 for number of electrons transferred (a) $n = 1$ and (b) $n = 2$, together with the dimensional amplitude for $T = 298.15$ K. 1st (black circles), 2nd (red squares), 3rd (blue diamonds), 4th (green triangles), 5th (magenta plus) and 6th harmonic (orange x).

peak height of the first harmonic under the same conditions was found $\psi_{p,1} = 1.2639$, by using the semi-analytical solution. The plot presented in Fig. 2.1.9(a) is practically the same with that presented by Engblom *et al.* for the odd harmonics [10].

For $n = 2$, harmonics higher than the 2nd and up to the 6th are detected for $\alpha_0 \geq 0.77$ and are amplified rather drastically in the region from $\alpha_0 = 1.95$ to $\alpha_0 = 7$, corresponding to amplitude values of 50 to 180 mV at $T = 298.15$ K. A saturation is observed for high values of α_0, its value determined by the number of the harmonic. By comparing the values of $\psi_{p,n}$ it can be seen that the amplification for $n = 2$ is more intense for the same value of α_0.

According to Mooring and Kies [9], the peak height of the first harmonic for $n = 2$ and $\alpha_0 = 1.5$ is $\psi_{p,1} = 2.52743$. The peak height obtained from the semi-analytic

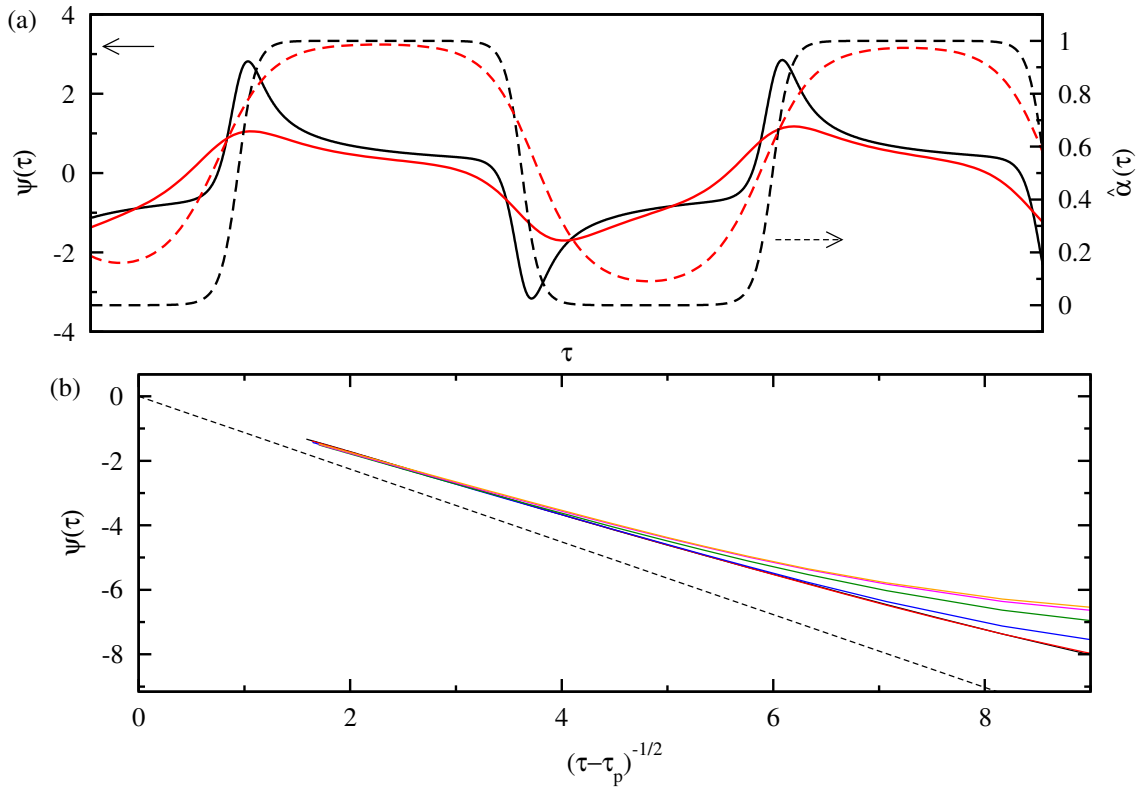

Figure 2.1.10: (a) Fragment of time evolution of the ac-voltammogram (solid lines) together with the corresponding variation of the surface concentration of the oxidant (dashed lines) for different values $\alpha_0 = 3.11$ (red) and 9.77 (black) and $n = 1$, $\sigma = 0.648$. (b) Cottrell plots for $n = 2$ and $\alpha_0 = 19.46$ (black), 15.57 (red), 11.68 (blue), 9.73 (green), 8.56 (magenta) and 7.79 (orange).

solution in this work was $\psi_{\mathrm{p},1} = 2.5155$. The plot shown in Fig. 2.1.9(b) is that of Engblom *et al.* [10] if one sets $\psi_{\mathrm{p},h} \to \psi_{\mathrm{p},h}/n$ and $\alpha_0 \to n\alpha_0$, where $n = 2$.

The saturation of $\psi_{\mathrm{p},h}$ for high values of α_0 can be interpreted qualitatively by comparing the evolution of the current and the surface concentration, for different values of α_0. Such an example is presented in Fig. 2.1.10(a) for $n = 1$ and $\sigma = 0.648$. For a moderate value of the perturbation amplitude $\alpha_0 = 3.11$, the concentration of the oxidant a(τ) oscillates between zero and one, never reaching these limits (red dashed curve). Simultaneously, the current oscillates rather smoothly (red solid line). On the other hand, for large amplitude values, $\alpha_0 = 9.73$, the concentration practically oscillates from zero to one, resembling a "pulse" wave (black dashed line). The current (black solid line) reaches a maximum value and then decays while the concentration is practically either zero or one. Further increase of α_0 results in an insignificant increase of the amplitude since the concentration cannot attain values beyond the limits imposed by the physics of the problem. This situation is illustrated in Fig. 2.1.10(b) for the case $n = 2$, where the decaying part of the current is plotted against the inverse of the square root of time. In this figure, τ_{p} designates the time instant corresponding to the

peak of the current. As can be seen, the relation tends to a "Cottrell condition", which is depicted by a dashed line having a slope of $n/\sqrt{\pi}$.

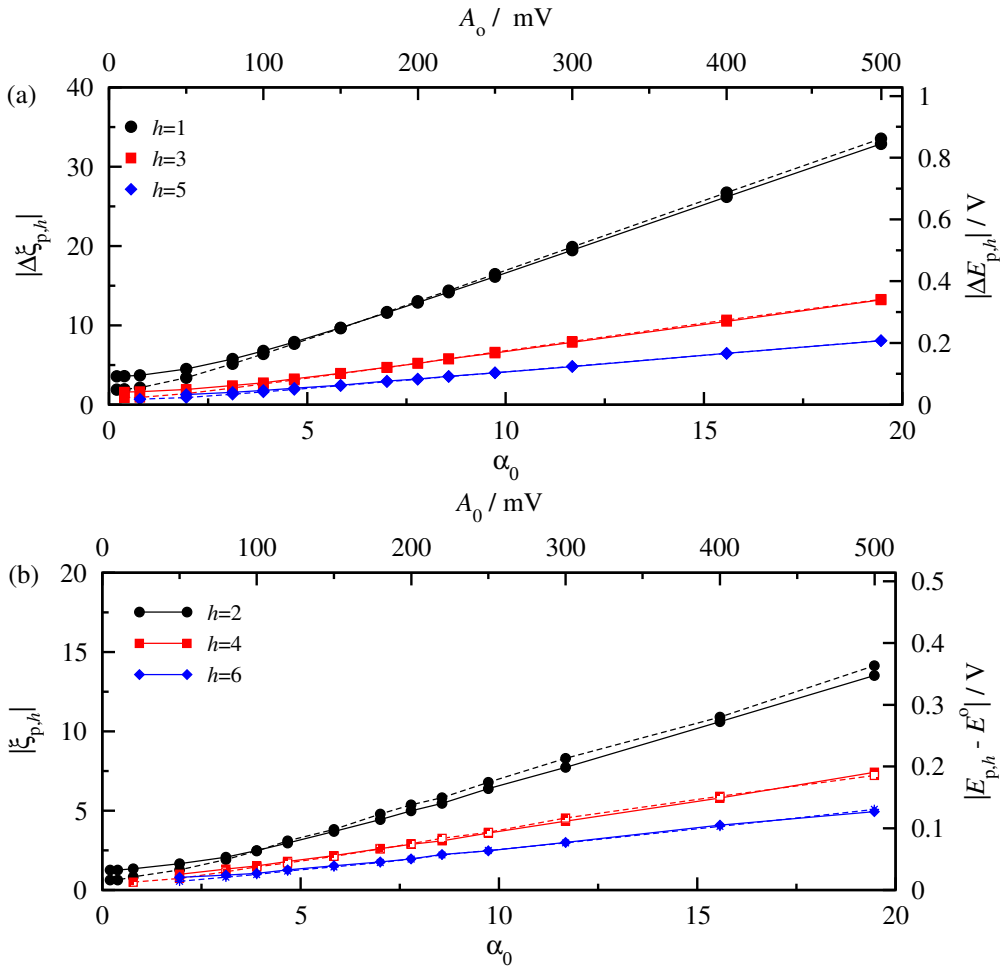

Figure 2.1.11: (a) Width at half maximum for the principal peaks of the odd harmonics and (b) peak potential of the principal peaks of the even harmonics, as a function of the perturbation amplitude α_0 for $\mu = 0$, together with the dimensional amplitude and peak width at $T = 298.15$ K for odd harmonics and different n. Solid lines for $n = 1$ and dashed line for $n = 2$.

The width at half maximum is another observable for the principal peak of the odd harmonics. The width at half maximum $|\Delta\xi_{p,h}|$ for the 1st, 3rd and 5th harmonic as a function of α_0 is presented in Fig. 2.1.11(a). In this figure, hallow symbols correspond to a one electron reaction and black symbols to a two electron reaction. It is evident that for $\alpha_0 > 3.11$, for the case of $n = 1$, and $\alpha_0 > 1.95$, for $n = 2$, the values of $|\Delta\xi_{p,n}|$ tend to vary linearly with α_0 and are practically independent of n. For small values of α_0 the relation is not linear and $|\Delta\xi_{p,1}|$ tends to the value $3.52/n$, as expected from low-amplitude ac-voltammetry [8]. Values of $|\Delta\xi_{p,h}|$ of the 3rd and 5th harmonic, for some values of α_0 are given in Table 2.1.

Table 2.1: Width at half maximum of the principal peak for the 3rd and 5th harmonic.

α_0	$\lvert\Delta\xi_{p,3}\rvert$		$\lvert\Delta\xi_{p,5}\rvert$	
	$n=1$	$n=2$	$n=1$	$n=2$
1.95	1.9	1.4	1.3	0.9
3.89	2.8	2.6	1.8	1.6
5.84	4.0	3.9	2.5	2.4
7.79	5.2	5.2	3.2	3.2
9.73	6.5	6.6	4.0	4.0

Table 2.2: Peak potential of the principal peak for the 2nd and 4th harmonic.

α_0	$\lvert\xi_{p,2}\rvert$		$\lvert\xi_{p,4}\rvert$	
	$n=1$	$n=2$	$n=1$	$n=2$
1.95	1.7	1.25	1.0	0.7
3.89	2.5	2.5	1.5	1.5
5.84	3.7	3.8	2.2	2.1
7.79	5	5.4	2.9	2.9
9.73	6.4	6.8	3.6	3.6

From Fig. 2.1.11(a) as well as Table 2.1, it can be observed that the width at half maximum of odd harmonics depends on both the number of electrons and the harmonic, in contrast to direct current cyclic voltammetry where $|\xi_p - \xi_{p/2}| = 2.2RT/nF$. Moreover, the effect of n on $|\Delta\xi_{p,h}|$ can be traced only for relatively small perturbation amplitudes, while for higher amplitudes the differences tend to be indistinguishable.

Once again, the width at half maximum for the first harmonic can be compared with some of the values tabulated by Mooring and Kies [9]. According to these authors, for $n = 1$, the values of $|\Delta\xi_{p,1}|$ for $\alpha_0 = 0.389$, 1.946 and 3.893 are 3.57, 4.48 and 6.97, respectively. In the present work the corresponding values were 3.59, 4.49 and 6.95. For the case of $n = 2$, the values reported are 1.84, 3.47 and 6.42, whereas in the present work were 1.94, 3.41 and 6.39.

An observable of the principal peaks of the even harmonics is the peak potential, $|\xi_{p,h}|$. This observable is presented in Fig. 2.1.11(b), where, once again, hallow symbols correspond to a one electron reaction and black symbols to a two electron reaction. It can be seen that, linearity is observed for $\alpha_0 > 3.11$ (for $n = 1$) and $\alpha_0 > 1.95$ (for $n = 2$) and the values of $|\xi_{p,n}|$ are practically independent of the number of electrons involved. For small values of α_0 the relation is not linear and $|\xi_{p,2}|$ tends to the value $1.32/n$, as expected from low-amplitude ac-voltammetry [8]. Values of $|\xi_{p,h}|$ of the 2nd and 4th harmonic, for some values of α_0 are given in Table 2.2.

From Fig. 2.1.11(b) as well as Table 2.2, it can be observed that the peak potential of even harmonics depends on both the number of electrons and the harmonic, in contrast to direct current cyclic voltammetry where $|\xi_p| = 1.11RT/nF$. The effect of n on $|\xi_{p,h}|$ can be traced only for relatively small perturbation amplitudes, while for higher amplitudes the differences tend to be eliminated.

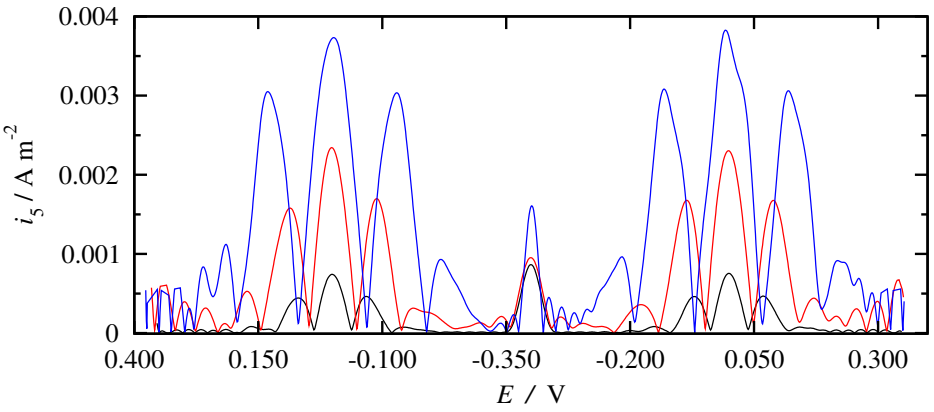

Figure 2.1.12: Effect of amplitude on the 5th harmonic for $c_1^* = 1$ μM. Parameter values: $f = 8$ Hz, $v = 50$ mV/s, $k^0 = 100$ m/s, $n = 1$, $D = 1 \times 10^{-9}$ m^2/s and $T = 298.15$ K. $A_0 = 80$ (black), 150 (red) and 220 mV (blue).

Returning to the variation of $\psi_{\mathrm{p},h}$ with amplitude, it seems to follow a sigmoid relation for $h > 2$, where the region of significant amplification extends approximately from 3.12 to 8.56 (that is, from 80 to 220 mV) for $n = 1$ and 0.77 to 5.84 (that is, from 20 to 150 mV) for $n = 2$. The sigmoidal relations can be fitted, more or less satisfactory, by a variety of analytic functions. Nevertheless, in the region of α_0 values where significant amplification is observed, the curves can be fitted by a rather simple equation,

$$\ln \psi_{\mathrm{p},h} = a_{n,h} - \frac{b_{n,h}}{\alpha_0} \tag{2.1.25}$$

where the constants $a_{n,h}$ and $b_{n,h}$ depend on the number of electrons n and the number of the harmonic h. The corresponding results are shown in Table 3.1.

In case one shall wish to work beyond the limits suggested for the parameters in Table 3.1, they should refer to the diagrams depicted in Fig. 2.1.9 to extract the values they desire.

In Fig. 2.1.12, an example is presented of how the signal of a reversible system of 1 μM can be augmented by increasing the amplitude at a moderate perturbation frequency. By increasing the amplitude from 80 mV up to 220 mV the principal peak

Table 2.3: Fitting parameters for Eq. (3.1.31) in the region from $\alpha_0 = 3.12$ to 8.56 for $n = 1$ and $\alpha_0 = 0.77$ to 5.84 for $n = 2$.

h	$a_{1,h}$	$b_{1,h}$	$a_{2,h}$	$b_{2,h}$
2	0.3470 ± 0.0085	3.480 ± 0.042	0.9960 ± 0.0075	1.611 ± 0.012
3	0.298 ± 0.022	4.80 ± 0.11	0.950 ± 0.021	2.344 ± 0.035
4	0.283 ± 0.016	7.631 ± 0.078	0.850 ± 0.025	3.439 ± 0.043
5	0.280 ± 0.020	9.602 ± 0.097	0.861 ± 0.022	4.477 ± 0.036
6	0.288 ± 0.012	12.483 ± 0.057	0.670 ± 0.078	5.22 ± 0.13

of the fifth harmonic increases from 0.5 mA/m^2 up to 3.7 mA/m^2. For a surface area of 0.00785 cm^2 (*i.e.* 1 mm diameter disk electrode), the current that results is 2.9 nA, which signifies that in order to determine even small quantities, possibly untraceable with cyclic voltammetry, masked by capacitance currents. Similar results could also be obtained by manipulating the frequency of a system, but as suggested by the dimensionless form of the current, the signal is proportional to the square root of the frequency, thus, making the impact of frequency less influential than the one of the amplitude.

It should be emphasized that the above analysis holds for the case of a fully reversible reaction, in the absence of uncompensated resistance and the presence of potential-independent capacitance. In the case where the heterogeneous kinetic constant is not sufficiently high and falls into the category of a quasi reversible reaction, the magnitude of the chief observables is decreased and the shape of the harmonic components starts deforming. This effect is pronounced as the order of the harmonic increases. In the case of an irreversible reaction the shape of the harmonics does not resemble that of the reversible case, nor in magnitude neither in shape. The presence of uncompensated resistance can also have an effect on the shape of higher harmonics, affecting the chief observables, becoming more evident as the order increases. The effect of potential-independent capacitance can be diminished even from harmonics as low as the second one. In the general case, its presence is expected to be eliminated at higher harmonics. In order to analyze signals where the electrode transfer kinetics are slow, IR-drop is present and capacitance does not follow a linear dependence against the scan rate, digital simulation should be considered for the interpretation of the experimental signals. Finally, the relation between scan rate and perturbation frequency determines the number of harmonics which can be extracted from the Fourier spectrum. High scan rates in combination with low frequencies decrease the number of the harmonics that can be analyzed. The proposed equation for the independence of the method from the scan rate can be used for the determination of the first five harmonics, as when we go to higher harmonics, the bursts in the Fourier spectrum start to intertwine and the analysis of the signal is then rendered impossible.

2.1.6 Quasi Reversibility and Irreversibility

We shall now move on to enter the spectrum of quasi reversible and irreversible electrochemical reactions, which are more commonly found in nature, so as to examine what kind of information can be extracted here. Before starting, it should be noted that a semi-analytical solution as the one used for the case of the reversible reaction, is not feasible, or to be more accurate, practical, due to the implication of the electrode kinetics. Thus, a different approach shall be followed from this point on in this chapter.

Starting with cyclic voltammetry again, for the case of an one electron reaction

$$\mathrm{Ox} + \mathrm{e} \underset{\longleftarrow}{\overset{k^0}{\longrightarrow}} \mathrm{Red}$$

where the chemical species is initially in its oxidized form Ox, and can be reduced to Red, we shall consider a heterogeneous standard kinetic constant k^0 winch is not

sufficiently large. Actually its value can vary from 10^{-8} up to 1000 m/s. Of course lower values and higher valued can be employed, but they are not realistic.

Assuming Buttler-Volmer type of kinetics, the current expression shall be given by Eq. (2.1.26),

$$i = Fk^0(c_{\mathrm{R}}\mathrm{e}^{\frac{(1-a)F}{RT}(E-E^0)} - c_{\mathrm{Ox}}\mathrm{e}^{\frac{-aF}{RT}(E-E^0)}) \tag{2.1.26}$$

in which all the symbols have already been analyzed.

In this case the dimensional problem is solved with the FEM method and the quantities are rendered dimensionless afterwards. The dimensionless current and potential for cyclic voltammetry remain the same as in the case of the reversible species, while a new quantity is introduced, the dimensionless kinetic constant k_{cv}

$$k_{\mathrm{cv}} = k^0\sqrt{\frac{RT}{FvD}} \tag{2.1.27}$$

For a dimensional analysis of cyclic voltammetry, one can refer to the works of Savéant [11].

In Fig. 2.1.13, the dimensionless cyclic voltammograms for various kinetic constants are depicted. For the reversible case ($k_{\mathrm{cv}} = 50$) the equations that already have been analyzed. For lower k_{cv} values, entering the quasi reversible region the peak height starts to decrease and the separation of the peaks starts to increase. When total irreversibility is achieved, for a transfer coefficient of 0.5 the peak is 0.248 [11] and the dimensionless cathodic peak of the cyclic voltammogram is given by Eq. (2.1.28),

$$\psi_{\mathrm{cv,irrev,p}} = 0.496\sqrt{a} \tag{2.1.28}$$

In the case of dimensional quantities, Eq. (2.1.28) transforms into Eq. (2.1.29),

$$i_{\mathrm{cv,irrev,p}} = 0.496FSC^0\sqrt{D}\sqrt{\frac{aFv}{RT}} \tag{2.1.29}$$

As already mentioned, for slower kinetics, the peaks shift to a greater degree of separation. The correlations for the cathodic and the anodic peak respectively are given below in a dimensional form,

$$E_{\mathrm{CV,c,p}} = E^{0\prime} - 0.78\frac{RT}{aF} + \frac{RT}{aF}\ln k^0\frac{RT}{aFvD} \tag{2.1.30}$$

$$E_{\mathrm{CV,a,p}} = E^{0\prime} + 0.78\frac{RT}{aF} + \frac{RT}{(1-a)F}\ln k^0\frac{RT}{(1-a)FvD} \tag{2.1.31}$$

The peak width is given by Eq. (2.1.32),

$$E_{\mathrm{CV,c,p/2}} - E_{\mathrm{CV,c,p}} = 1.857\frac{RT}{aF} \tag{2.1.32}$$

Now we shall move on to discover how FTacV works when it comes to quasi reversible and irreversible electron transfer. Regarding the dimensionless parameters in this case,

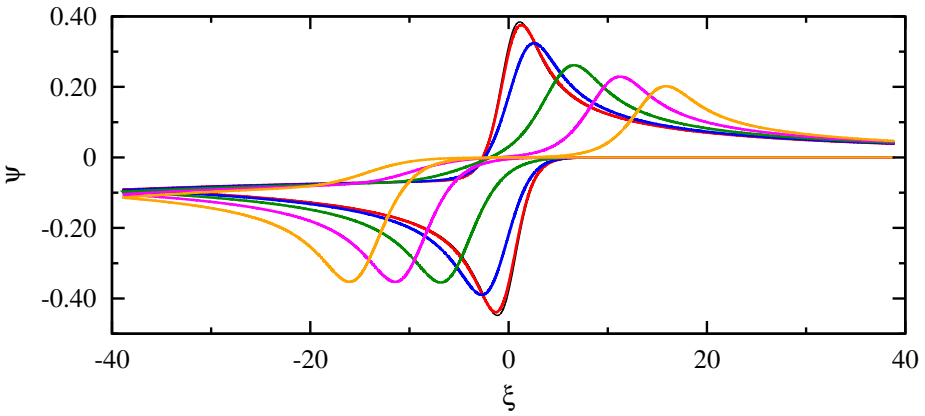

Figure 2.1.13: One step reaction: Dimensionless cyclic voltammograms of free species for $\sigma = 0.4868$, $\alpha_0 = 0.5$, $\xi^0 = 0$ and $k_{\mathrm{CV}} = 50$ (black), 5 (red), 0.5 (blue), 0.05 (green), 0.005 (magenta) and 0.0005 (orange).

the dimensionless current and the dimensionless potential remain the same as in FTacV for the reversible species, while the dimensionless kinetic constant k becomes,

$$k_{\mathrm{ac}} = k^0 \sqrt{\frac{1}{fD}} \tag{2.1.33}$$

The resulting dimensionless first 6 harmonics of such a system can be found in Fig. 2.1.14. As should be noted, going away from the reversible kinetics ($k_{\mathrm{ac}} = 316$) the magnitude of the harmonics decreases drastically and the shape is also deformed. Four regions shall be recognized at this point.

- The region for large values of k_{ac}, which corresponds to the reversible case with all the features already discussed being in effect.
- The quasi reversible region with no dominant peak displacement, where the magnitude of the dominant peaks starts to decrease, but there is no peak shift.
- The quasi reversible region with peak displacement, in which the harmonics continue decreasing in size, but the harmonics start to deform beyond recognition.
- The totally irreversible region, where a minimum harmonic peak has bee reached and the shift of the peaks continues further.

A table with a rough discrimination of the region is included in this work and presented in Table 2.4.

In Fig. 2.1.15, the peaks for the first six harmonics of the totally irreversible case for different amplitudes are depicted. A trend of increase is observed for the first three harmonics, but with an increase not as impactful as the one in presented in the reversible case. As the harmonic order lowers, the increase is much less prominent.

Regarding the effect of the kinetics on the magnitude of the dominant peaks for all the first 6 harmonics, this is presented in Fig. 2.1.16. All first 6 harmonics are presented

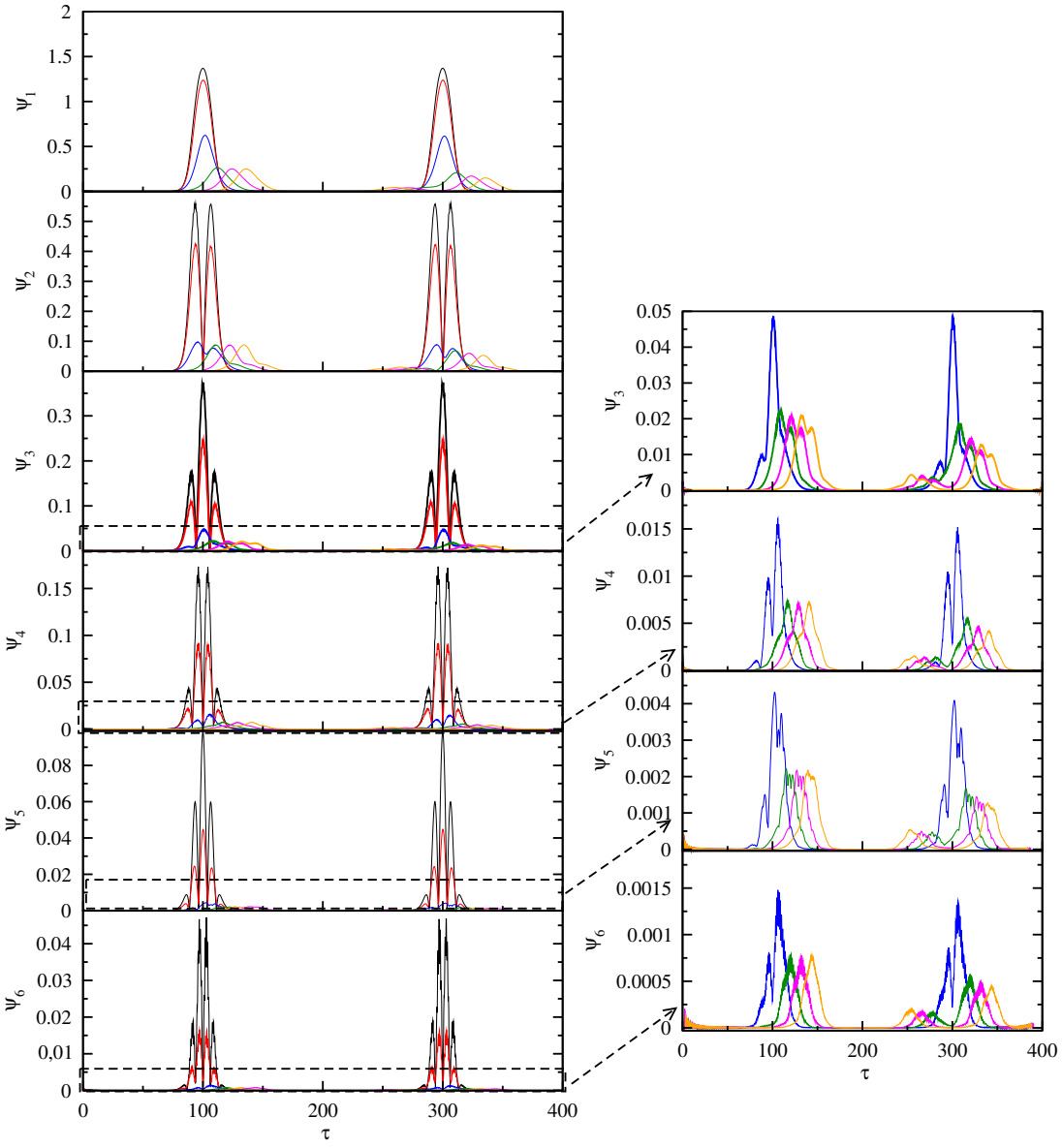

Figure 2.1.14: One step reaction: Dimensionless cyclic voltammograms of free species for $\sigma = 0.4868$, $\alpha_0 = 0.5$, $A_0 = 3.89$, $\xi^0 = 0$ and $k_{ac} = 316$ (black line), 31.6 (red), 3.16 (blue), 0.316 (green), 0.0316 (magenta) and 0.00316 (orange).

for different amplitudes and sigmoidal like dependencies can be observed for the first harmonic, while as the order increases an "anomaly" appears around $k_{ac} = 2$. This is due to around this value starts the deformation of the harmonic components.

With the use of such a diagram, for a system with a know diffusion coefficient, the kinetic constant can be extracted and vice-versa. If both are unknown, with a trial and error procedure, one could find the right combination of D and k^0 in order to fit computational to experimental data. An analytical expression for the correlation of ψ with k is not quite useful, however the values are given in the appendix of this work if one would like to use the values. Such an approach would bot be useful in cyclic

Table 2.4: Kinetic regions for free species

α_0	Reversible	Quasi reversible No Peak Displacement	Irreversible
3.959	$k^0>10^{-2}$	$10^{-2}<k^0<10^{-5}$	$k^0<10^{-7}$
5.939	$k^0>10^{-2}$	$10^{-2}<k^0<10^{-5}$	$k^0<10^{-7}$
7.919	$k^0>10^{-2}$	$10^{-2}<k^0<10^{-5}$	$k^0<10^{-7}$
9.898	$k^0>10^{-2}$	$10^{-2}<k^0<10^{-5}$	$k^0<10^{-7}$
11.878	$k^0>10^{-2}$	$10^{-2}<k^0<10^{-6}$	$k0<10^{-8}$
13.858	$k^0>10^{-2}$	$10^{-2}<k^0<10^{-6}$	$k^0<10^{-8}$
15.838	$k^0>10^{-2}$	$10^{-2}<k^0<10^{-7}$	$k^0<10^{-8}$

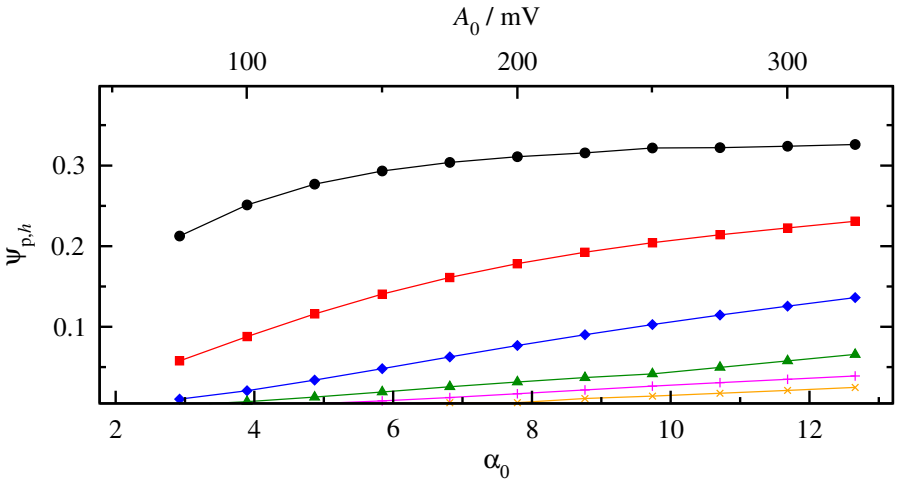

Figure 2.1.15: Maximum peak height for harmonics 1 through 6, as a function of the perturbation amplitude A_0 for free species, together with the dimensional amplitude for $T = 298.15$ K, for an electrochemically irreversible reaction. 1st (black circles), 2nd (red squares), 3rd (blue diamonds), 4th (green triangles), 5th (magenta plus) and 6th harmonic (orange x).

voltammetry due to the fact that the drop of the peak height as the kinetics get slower is not that significant.

Regarding the shift of the dominant peak of the odd harmonics, the dependence can be found in Fig. 2.1.17. It is rather obvious that for large values of $k_{\rm ac}$ the principal peak of the odd harmonics is observed at $\xi = 0$, that is, at E^0. As k becomes smaller, a cathodic (anodic) shift of the principal cathodic (anodic) peak occurs, its value depending on a_0. This effect is depicted in Fig. 2.1.17. It is observed that the region of $k_{\rm ac}$ where the potential of the principal peak is equal to the standard (or formal) potential is wider for large values of a_0. Moreover, for small values of $k_{\rm ac}$ a linear dependence in observed in these semi-logarithmic plots, the slope being $2.303/a$,

$$\xi_{{\rm p},h} = \frac{\beta_h}{a} + \frac{2.303}{a} \log k_{\rm ac} \tag{2.1.34}$$

where β depends on the perturbation amplitude and the order of the harmonic. Indicative values of β for different values of a_0 are presented in Table 2.5.

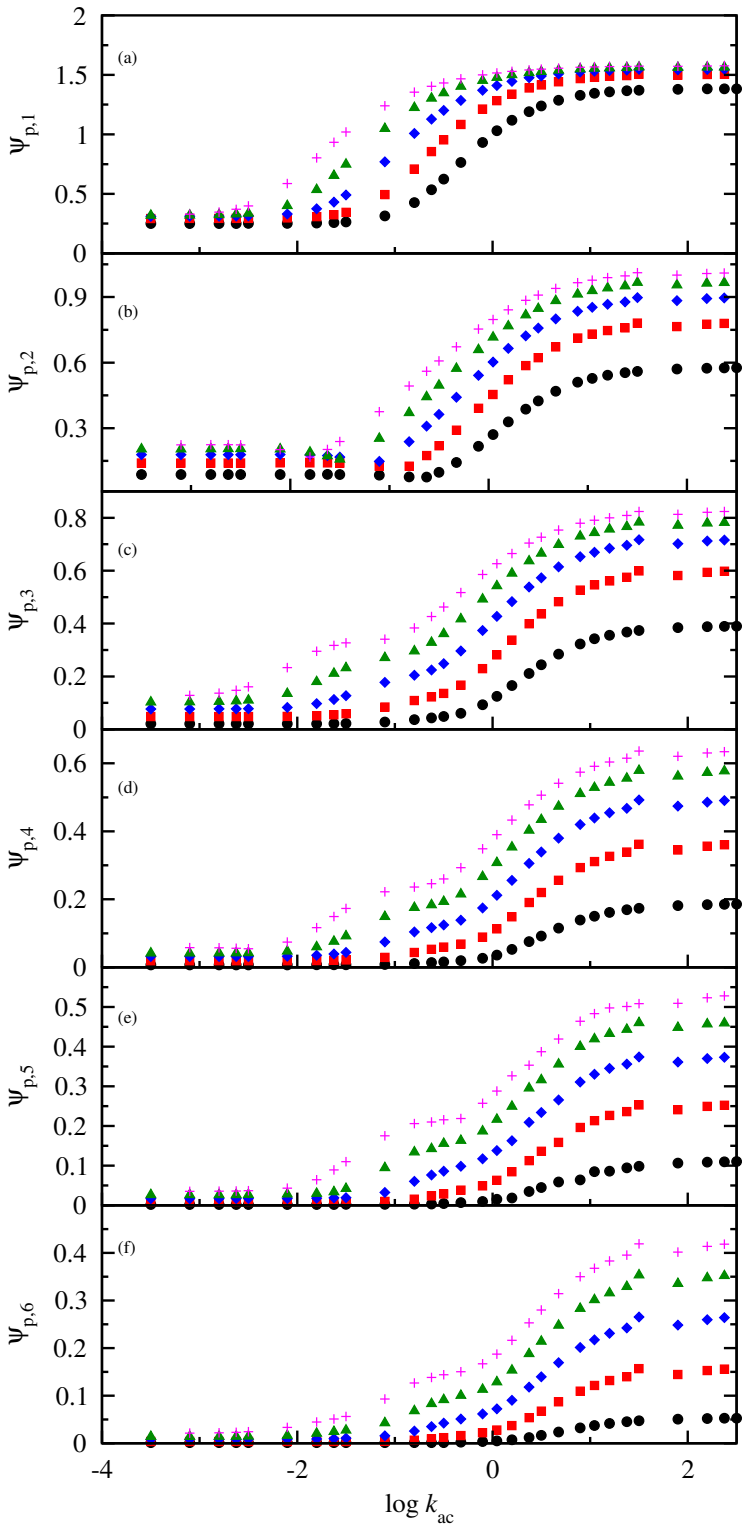

Figure 2.1.16: Maximum peak height for harmonics 1 through 6, as a function of the dimensionless kinetic constant k for a free species. A_0 values: 3.959 (black circles), 5.939 (red squares), 7.919 (blue diamonds), 9.898 (green triangles) and 11.878 (magenta +).

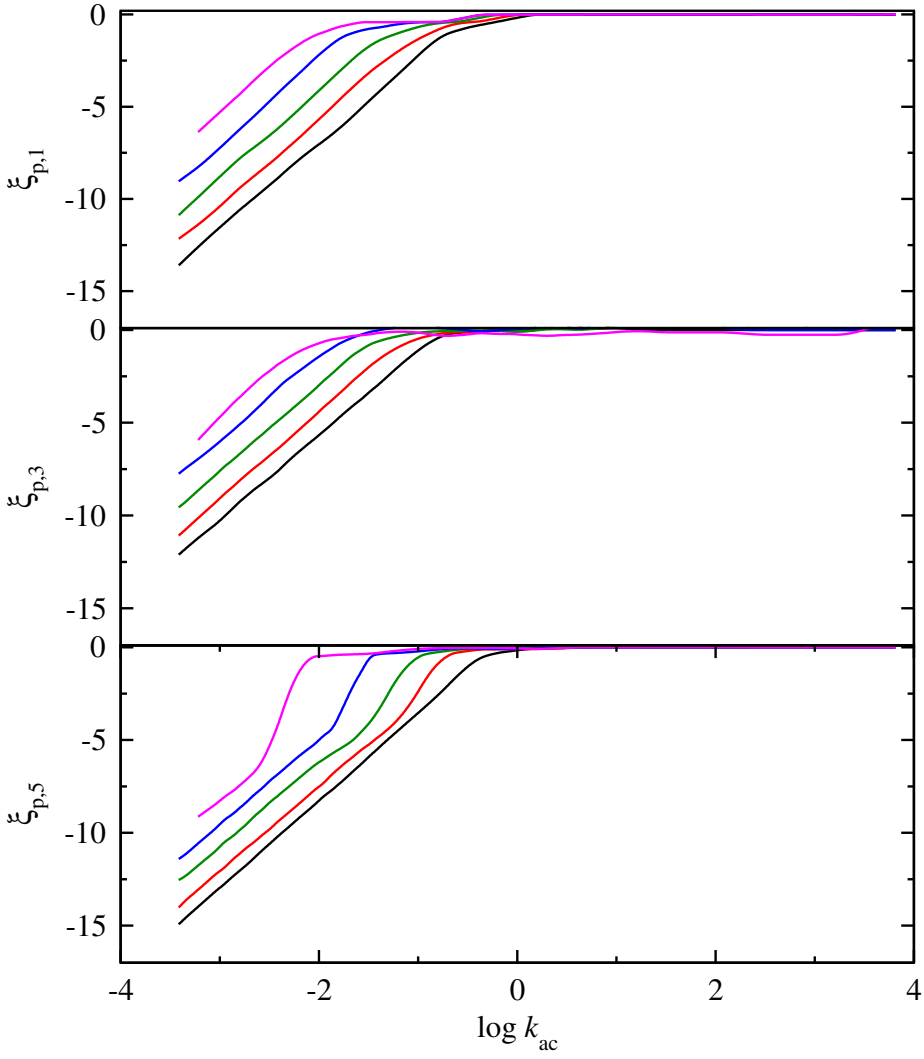

Figure 2.1.17: Principal peak potential as a function of the kinetic constant k of the odd harmonics for a free species. α_0 values: 3.959 (black), 5.939 (red), 7.919 (blue), 9.898 (green) and 11.878 (magenta).

Table 2.5: Values of β_h, Eq. (2.1.34), for different values of a_0

a_0	A_0 (mV at 298 K)	β_1	β_3	β_5
3.894	100	2.06	3.48	1.44
5.842	150	3.69	5.01	1.60
7.789	200	5.31	6.33	3.18
9.736	250	7.62	8.03	4.27
11.683	300	9.44	10.63	4.55

2.2 Two step electron transfer

2.2.1 Two reversible reactions

In the case of a two step reaction, the scenario changes slightly, with the reactions being described in Eqs. (2.2.1) and (2.2.2), where in the first step A is reduced to B and then B is reduced to C. Kinetic constants corresponding to the two steps are k_1^0 and k_2^0 while the formal potentials E_1^0 and E_2^0, respectively,

$$\mathrm{A} + \mathrm{e} \underset{}{\overset{k_1^0}{\rightleftharpoons}} \mathrm{B} \tag{2.2.1}$$

$$\mathrm{B} + \mathrm{e} \underset{}{\overset{k_2^0}{\rightleftharpoons}} \mathrm{C} \tag{2.2.2}$$

Definitions for the dimensionless current and dimensionless scan rate remain the same. The current expressions for each step are expressed as in Eqs. (2.2.3) and (2.2.4). The total dimensionless current ψ_{tot} is the sum of ψ_1 and ψ_2,

$$i_1 = Fk_1^0\left(c_{\mathrm{B}} e^{\frac{(1-a)F}{RT}(E-E_1^0)} - c_{\mathrm{A}} e^{-\frac{aF}{RT}(E-E_1^0)}\right) \tag{2.2.3}$$

$$i_2 = Fk_2^0\left(c_{\mathrm{C}} e^{\frac{(1-a)F}{RT}(E-E_2^0)} - c_{\mathrm{B}} e^{-\frac{aF}{RT}(E-E_2^0)}\right) \tag{2.2.4}$$

.

Again, the scenario shall be initially examined for cyclic voltammetry and then for FTacV. In Fig. 2.2.1 the dimensionless cyclic voltammograms are presented for a two step reaction, with both steps reversible and the standard potential of the second being more negative than the standard potential of the first. When the two formal potentials are well separated it seems like having two cyclic voltammograms with the characteristics discussed before. As the two standard potentials get closer the two voltammograms start to intertwine forming on voltammogram, the peak of which is more than two times the peak of the separate voltammograms, in the case where the two steps have the same standard potential.

In Fig. 2.2.2 the 5th harmonic for different scenarios is presented in the case where both steps are fast. Only the 5th harmonic is presented as all the other harmonics have a similar trend. In Fig. 2.2.2(a) we have the case of two well separated steps with the ξ^0

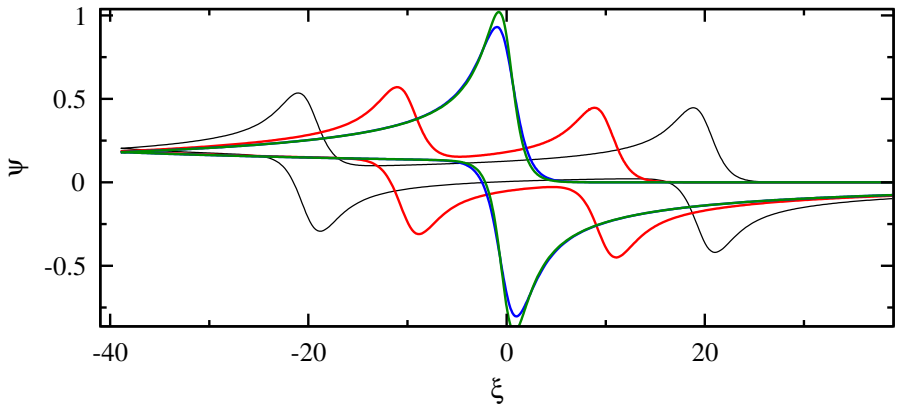

Figure 2.2.1: Two step reaction: Dimensionless cyclic voltammograms of free species for $\sigma = 0.4868$, $k_{\mathrm{CV},1} = k_{\mathrm{CV},1} = 0.031$, $\xi_1^0 = 15$ and $\xi_2^0 = -15$ (black), $\xi_1^0 = 5$ and $\xi_2^0 = -5$ (red), $\xi^0 c_1 = 0.5$ and $\xi_2^0 = -0.5$ (blue), $\xi_1^0 = \xi_2^0 = 0$ (green).

of the second step being more cathodic than the one of the first ($\xi_1^0 = 15$ and $\xi_2^0 = -15$) at different amplitudes. The maxima of each peak correspond to that of a single step fast reversible reaction and as the amplitude increases the harmonics become wider. In such a case, no problem arises in the analysis of the peaks, as the same things that are valid for a one step fast reversible electrochemical reaction, are valid for each step separately. This is as long as the harmonics of the steps are well separated and do not interfere. So, experimentally, when one faces a two step reaction with separated peaks, he shall pay attention to the amplitude used, so that the harmonics do not widen to the extend that they start to interfere with each other.

In Fig. 2.2.2(b) we have the case where we go from two well separated steps (black and red line) to the case where the two steps tend to appear as one (blue line) and finally in the case where the two peaks have the same dimensionless formal potentials. In the latter case, schematically the harmonic resembles that of a single step reaction, but the peak dimensionless current of the harmonic is about 3.7 times higher than that of the single step reaction (2.23 *vs* 0.609, respectively). This difference could act as a diagnostic for the electron transfer mechanism, as if one harmonic appears a single electron transfer but the peak dimensionless current is higher than the expected, probably the reaction is a two-step one.

2.2.2 One reversible and one irreversible reaction

In this section a slightly different scenario shall be examined that the one in the previous section. The difference is that the second step is irreversible, that is C cannot be oxidized back to B. The only equation that changes is Eq. (2.2.4) which is transformed to Eq. (2.2.5),

$$i_2 = -Fk_2^0 c_{\mathrm{b}} e^{-\frac{aF}{RT}(E-E_2^0)} \tag{2.2.5}$$

For the case of cyclic voltammetry, one can find representative voltammograms in Fig. 2.2.3 for a constant value of the dimensionless kinetic constant of the first reaction, while that of the second step is altered. In the case of the highest $k_{\mathrm{CV},2}$ examined, a

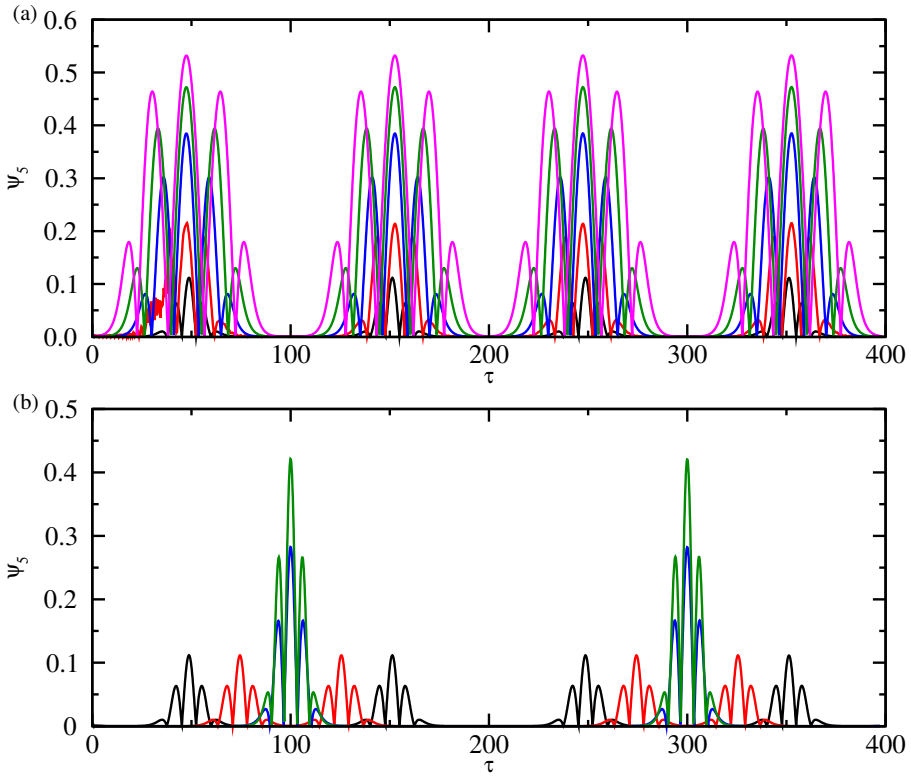

Figure 2.2.2: Different cases of a two step reaction with both steps being electrochemically reversible ($k_{ac,1} = k_{ac,2}$=0.0316): (a) Well seperated steps with $\xi_1^0 = 15$, $\xi_2^0 = -15$ and $\sigma = 0.4868$ for $\alpha_0 = 3.892$ (black), 5.839 (red), 7.785 (blue line), 9.731 (green) and 11.677 (magenta). (b) Decreasing seperation of the steps at $\alpha_0 = 3.892$, $\sigma = 0.4868$, $\xi_1^0 = 5$ and $\xi_1^0 = -5$ (red), $\xi_1^0 = 0.5$ and $\xi_2^0 = -0.5$ (blue) and $\xi_1^0 = \xi_2^0 = 0$ (green).

sole peak appears at a more anodic peak potential value than the formal potential of both of the first reaction step. As the kinetics of the second step become more slow, the peak shifts cathodically and for very small values of $k_{CV,2}$ the peaks are completely separated.

For the respective FTacV case, 1st through 5th harmonic of the forward scan of this case are presented in Fig. 2.2.4.

The fixed parameters in this example are $\sigma = 0.4868$, $\alpha_0 = 3.892$, $\xi_1^0 = 0$, $\xi_2^0 = 5$, $k_{ac,1} = 100$ while $k_{ac,2}$ varies from 10 down to 0.0001. For the highest $k_{ac,2}$ value empoloyed (black line) during the cathodic scan what seems like an irreversible set of peaks appears for all the harmonics. As the value of $k_{ac,2}$ decreases, this peak shifts towards more cathodic potentials (red and blue line). For even lower values of this kinetic parameter, the harmonics start to resemble a reversible kinetics situation. This is due to the fact that the chemically irreversible reaction shifts towards more cathodic peaks when its kinetics get slower, revealing the first fast and reversible step. Now, when the two steps finally start getting separated (magenta and green line), the second step is almost invisible due to the fact that the magnitude of an irreversible reaction in FTacV is order of magnitudes smaller than the one of a reversible one. Experimentally

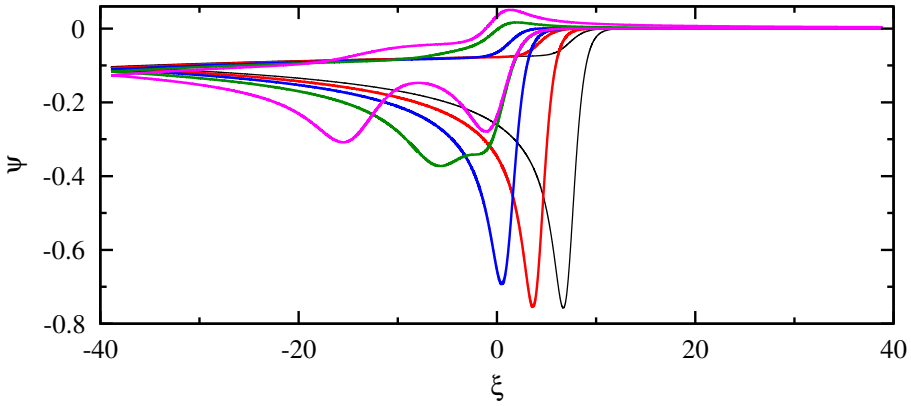

Figure 2.2.3: Two step reaction, with the second being chemically irreversible: Dimensionless cyclic voltammograms of free species for $\sigma = 0.4868$, $\xi_1^0 = 0$, $\xi_2^0 = 5$, $k_{\mathrm{CV},1} = 3.16 \times 10^{-3}$ and $k_{\mathrm{CV},2} = 3.16 \times 10^{-6}$ (black), $k_{\mathrm{CV},2} = 3.16 \times 10^{-8}$ (red), $k_{\mathrm{CV},2} = 3.16 \times 10^{-10}$ (blue), $k_{\mathrm{CV},2} = 3.16 \times 10^{-12}$ (green) and $k_{\mathrm{CV},2} = 3.16 \times 10^{-14}$ (magenta).

such a separation can be achieved by increasing the frequency of the experiment, so that the effective kinetic constant $k_{\mathrm{ac},2}$ (equal to k_2^0/f) gets lowered to a relatively small value and the peak of the second step is shifted more cathodically. Technically, if one would increase the frequency from 1 to 100 Hz, the $k_{\mathrm{ac},2}$ value would be lowered 2 orders of magnitude.

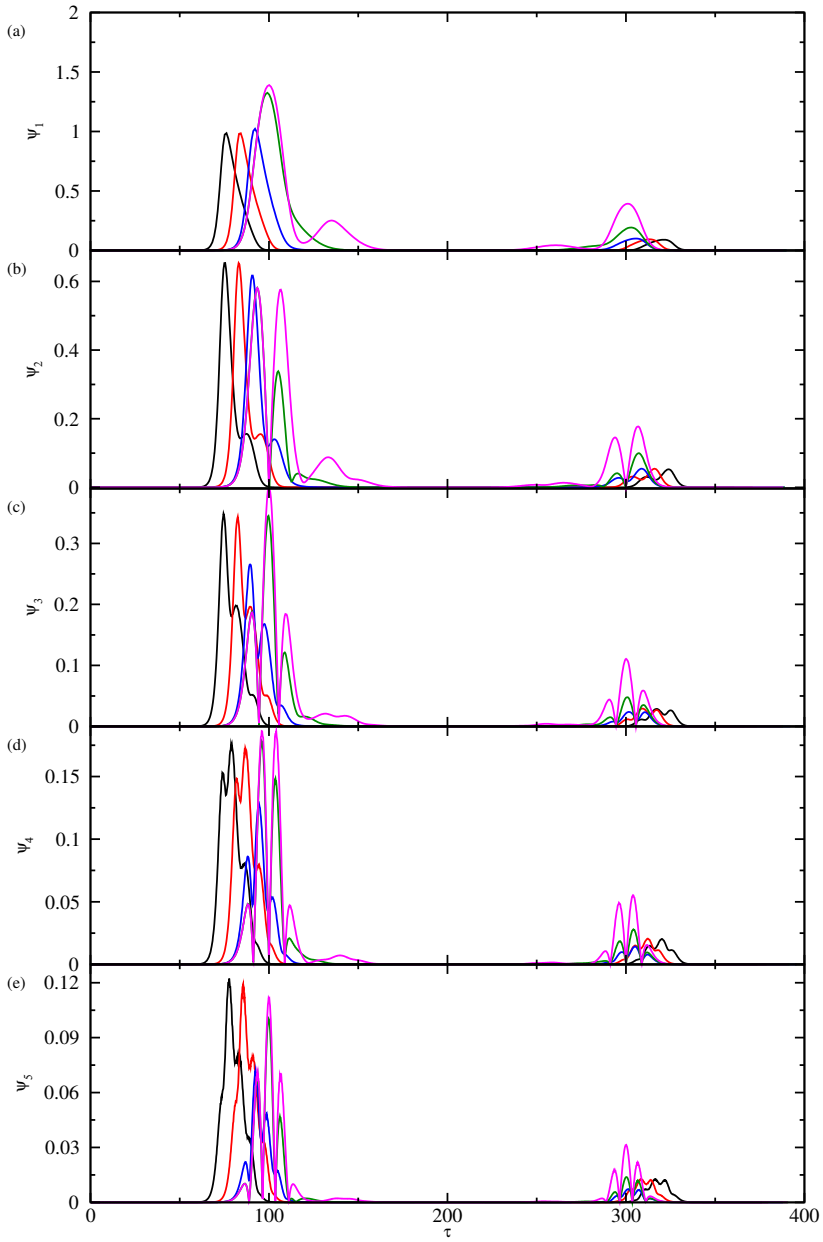

Figure 2.2.4: (a) - (e) 1st through 5th harmonic for a two step reaction with the first being reversible and the second chemically irreversible. $\sigma = 0.48684$, $\alpha_0 = 3.8924$, $\xi^{0_1} = 0$, $\xi_2^0 = 54$, $k_{\mathrm{ac},1} = 3.16 \times 10^{-3}$ and $k_{\mathrm{ac},2} = 3.16 \times 10^{-6}$ (black), $k_{\mathrm{ac},2} = 3.16 \times 10^{-8}$ (red), $k_{\mathrm{ac},2} = 3.16 \times 10^{-10}$ (blue), $k_{\mathrm{ac},2} = 3.16 \times 10^{-12}$ (green) and $k_{\mathrm{ac},2} = 3.16 \times 10^{-14}$ (magenta).

2.3 EC Mechanism

One mechanism of electrochemical reactions that could be of interest is the EC mechanism, in which an electrode electron transfer is followed by a first-order (or pseudo-fist-order) homogeneous reaction. It is one of the simplest scenarios in which a heterogeneous electron transfer is coupled with a reaction taking place in the solution. In this section a subcategory of this kind of mechanisms will be discussed in order to get an idea of the pattern of the voltammograms corresponding to both cyclic voltammetry and FTacV, thus only a qualitative approach shall be made.

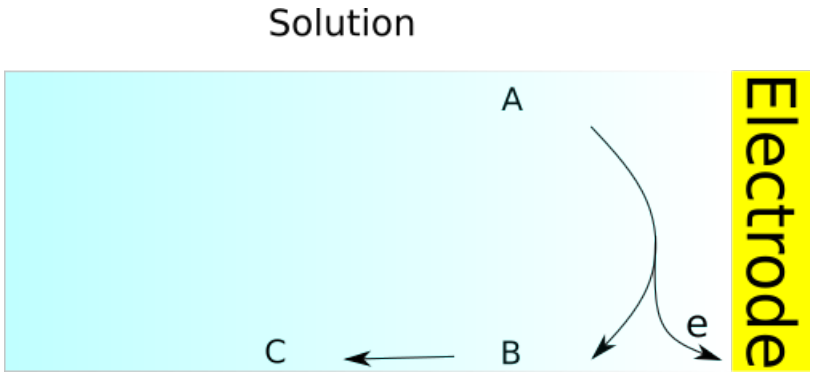

Figure 2.3.1: EC mechanism of a free electroactive species reaction scheme. The reduced form A of the free species is oxidized on the electrode surface to the oxidized form B and is then transformed to the non electroactive species C.

The heterogeneous electron reaction is that found in Eq. (2.3.1) where the reduced form of the electroactive species (A) gives one electron to the electrode resulting in the oxidized form (B). Then the oxidized form of the electroactive species reacts by a first-order (or pseudo-fist-order) reaction, resulting in C, which is electrochemically active in the potential window examined. The kinecti constant of the second step shall be symbolized with k_{EC}. This reaction is treated in this case as an irreversible one. A schematic representation of the scenario is presented in Fig. 2.3.1. Extensive studies have been made for the full scenario, in which this reaction is reversible, and the reverse step is also taken into account [11]. In this work though we shall limit our study to this case, as this shall be of use in the experimental section of this work.

$$\mathrm{A} \underset{}{\overset{k^0}{\rightleftharpoons}} \mathrm{B} + \mathrm{e} \tag{2.3.1}$$

$$\mathrm{B} \xrightarrow{k_{\mathrm{EC}}} \mathrm{C} \tag{2.3.2}$$

The obvious effect of the coupling of the second reaction is that B is consumed for large k_{EC} values, thus it is not able to be reduced again. Consequently, no peaks in the returning scan are expected. In order to visualize this effect, voltammograms for this case are presented in Fig. 2.3.2. Two different scan rates are examined, (10 mV/s and 100 mV/s) for various kinetic constants k_{EC}. For the scan rate of 10 mV/s even

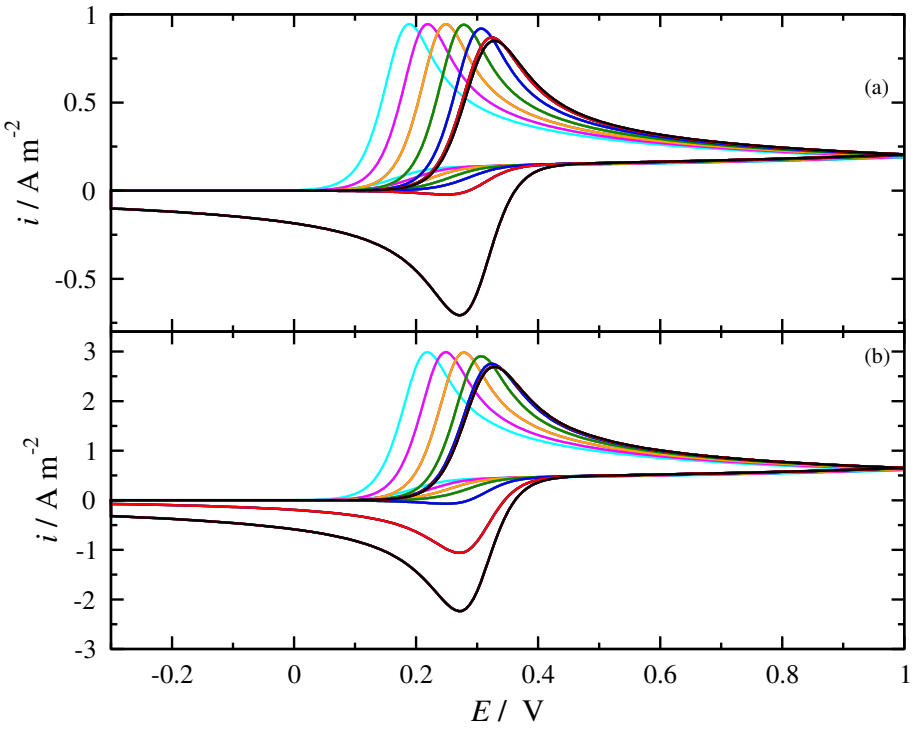

Figure 2.3.2: Example voltammograms of EC mechanism for (a) 10 mV/s and (b) 100 mV/s. Parameters: $c_A^* = 1$ mol m^{-3}, $k^0 = 100$ 1/s , $D = 1 \times 10^{-9}$ m^2/s, $T = 298.15$ K, $k_{EC} = 0$ (black), 0.1 (red), 1 (blue), 10 (green), 100 (magenta), 1000 (orange) and 10000 s^{-1} (cyan).

for a relatively small value of the kinetic constant (0.1 s^{-1}) no reduction peak can be observed in the reverse cathodic scan in addition to a slight increase in the anodic scan. As the k_{EC} increases, the cathodic peak vanishes completely and the anodic one reaches a limiting value and is shifted towards more cathodic potentials. Moving on to the higer scan rate of 100 mV/s, it can be seen that for a k_{EC} value of 0.1 s^{-1} the cathodic peak has not disappeared yet. However, as the k_{EC} value increases, the same trend as in the previous case can be clearly observed. In general a nomogram for both the displacement of the peak as a function of a dimensionless kinetic parameter can be extracted as well as one that takes into account the ration of the oxidation and reduction peak, in order to find the value of k_{EC}. However, the section of this work is to get a grasp of how the waveform of these voltammograms are transformed in an FTacV experiment. Thus, no further analysis shall be made here.

Examining the same scenario by FTacV, using $v = 10$ mV/s, $f = 1$ Hz and $A_0 = 100$ mV, the 1st, 3rd anf 5th harmonics shall be presented in Fig. 2.3.3. In the absence of a subsequent following reaction, the voltammograms are as expected corresponding to those of a reversible reaction. However, when the subsequent chemical reaction starts getting involved, one can observe a drastic change is the reverse scan even for very low values of k_{EC}. Regarding the forward scan, for a k_{EC} value of 0.1 s^{-1} the odd harmonics still resemble that of an uncoupled reversible electrochemical reaction, at a decreased magnitude. As the k_{EC} value starts increasing by orders of magnitude,

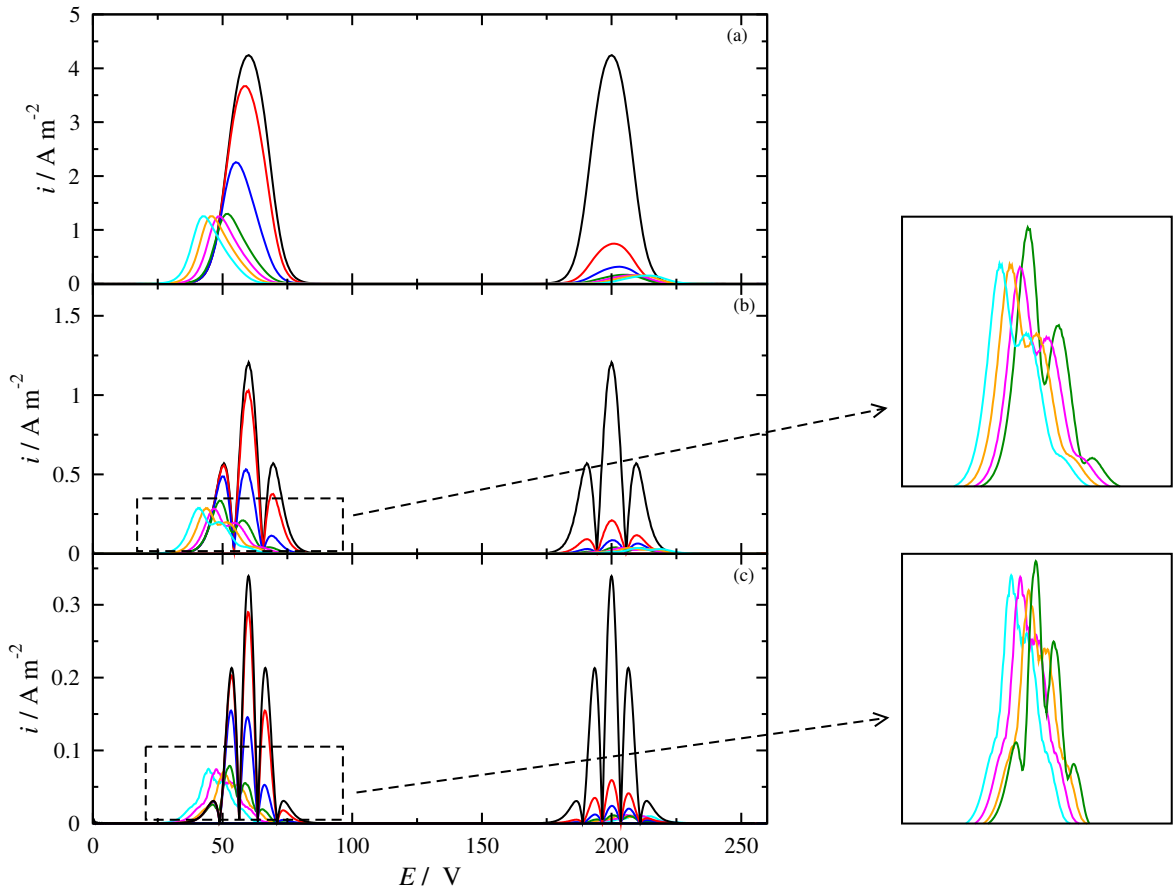

Figure 2.3.3: (a) 1st, (b) 3rd and (c) 5th harmonic examples of EC mechanism for $v = 10$ mV/s, $f = 1$ Hz and $A_0 = 100$ mV. Parameters: $c^*_{\mathrm{A}} = 1$ mol m^{-3}, $k^0 = 100$ 1/s , $D = 1 \times 10^{-9}$ m^2/s, $T = 298.15$ K, $k_{\mathrm{EC}} = 0$ (black), 0.1 (red), 1 (blue), 10 (green), 100 (magenta), 1000 (orange) and 10000 s^{-1} (cyan).

the signal starts deforming and decreasing in magnitude until the harmonics reach a certain waveform of constant magnitude that is shifted more cathodically as the kinetic constant increases. This behavior - the peak shift - is similar to the one observed in the cyclic voltammogram. The harmonics in case of high k_{EC} values, start reminiscing those of an irreversible voltammogram, just like in the case of the cyclic voltammograms. It is also worth noting that for k_{EC} values up to an order of magnitude 1 s^{-1} the central peak in the forward scan although deformed, is not shifted, thus still a value for the formal potential of the electrochemical reaction can be extracted.

2.4 Homogeneous catalytic reaction scheme

One of the most widely studied reaction studied mechanisms with cyclic voltammetry is that of an electroactive species in its oxidized form A being reduced to B, which is coupled with a reaction of a substrate P giving back the oxidized form A and a product Q (Fig. 2.4.1),

$$\mathrm{A} + \mathrm{e} \underset{}{\overset{k^0}{\rightleftharpoons}} \mathrm{B} \tag{2.4.1}$$

$$\mathrm{B} + \mathrm{P} \xrightarrow{k_\mathrm{e}} \mathrm{A} + \mathrm{Q} \tag{2.4.2}$$

In this section some of the most prominent results of this case with cyclic voltammetry will be introduced in order to later have a direct comparison with FTacV in order to see what happens to the signal when the second method applied. Regarding the case of cyclic voltammetry, depending on the the kinetic constant k_e, the scan rate and the ratio of the concentrations of A and P, a wide variety of voltammograms can be obtained. In order to group these results, Savéant has introduced in his work one of his signature zone diagrams. In this thesis, a slightly different (almost) all inclusive diagram is to be presented in Fig. 2.4.2. But before checking this diagram, a few points shall be made clear.

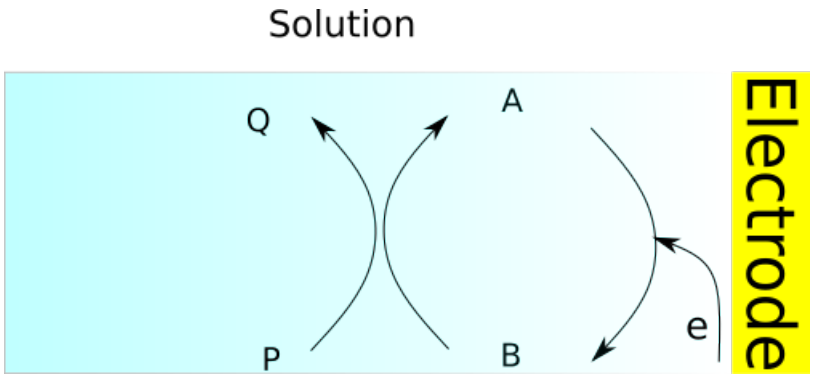

Figure 2.4.1: Homogeneous catalytic reaction scheme of a free electroactive species. The oxidized reactant form A of the free species is reduced on the electrode surface to its reduced form B. It then reacts with the oxidized form of the substrate P, which is free in the solution as well, giving its reduced form Q and regenerating the oxidized form of the reactant A.

Firstly, all the results that are processed come from solving the dimensional problems and not the dimensionless. Then, in order to group the results and give an interpretation to their trends, a few dimensionless quantities are introduced. These are the following,

$$\gamma = \frac{c_{\mathrm{P}}^*}{c_{\mathrm{A}}^*} \qquad \text{(concentration ratio)} \tag{2.4.3}$$

$$\Psi_{\mathrm{EC}} = \frac{i_{\mathrm{p,EC}}\gamma}{i_{\mathrm{p,EC},}^0} \qquad \text{(dimensionless catalytic current peak)} \tag{2.4.4}$$

$$\Lambda_{\mathrm{EC}} = \frac{k_{\mathrm{e}}RTc_{\mathrm{P}}^*}{Fv} \qquad \text{(dimensionless kinetic parameter)} \tag{2.4.5}$$

where c_{P}^* is the concentration of the chemical species P in the bulk solution, c_{A}^* is the concentration of the chemical species A in the bulk solution, $i_{\mathrm{p,EC}}$ the peak/plateau of the reduction peak of the redox reaction. The other symbols have already been discussed.

Now the order of the waveform of the voltammograms in Fig. 2.4.2 are based on the dimensionless kinetic parameter and the concentration ratio. The set of voltammograms presented in Fig. 2.4.2 are arranged in a way corresponding to the change of γ and Λ_{EC}. Starting from a pure cyclic voltammogram for very low values of Λ_{EC}. As the value of Λ_{EC} starts increasing we enter the next zone in which from an increase of the reduction peak and an increase in the oxidation one, as the γ goes up, a sigmoidal curve is reached In the case of a sigmoidal voltamomgram the kinetic constant k_{e} can be directly estimated from the following equation,

$$i_{\mathrm{p}} = FSc_{\mathrm{P}}^*\sqrt{D}\sqrt{k_{\mathrm{e}}c_{\mathrm{A}}^*} \tag{2.4.6}$$

For very large values of Λ_{EC} we leave the region in which the sigmoidal curve can be achieved. When γ is relatively small, two reduction peaks are visible with the one being near the value of the peak found in the cyclic voltammogram in the absence of a chemical reaction, while the other one found in more anodic potentials. The latter peak is also sharper than the first one. Now as γ increases the peak around which resembles the peak in the absence of a reaction, decreases while the other one increases drastically. Finally for high values of both K_{EC} and γ only one sharp peak appears at values more anodic than the E^0 of the redox species.

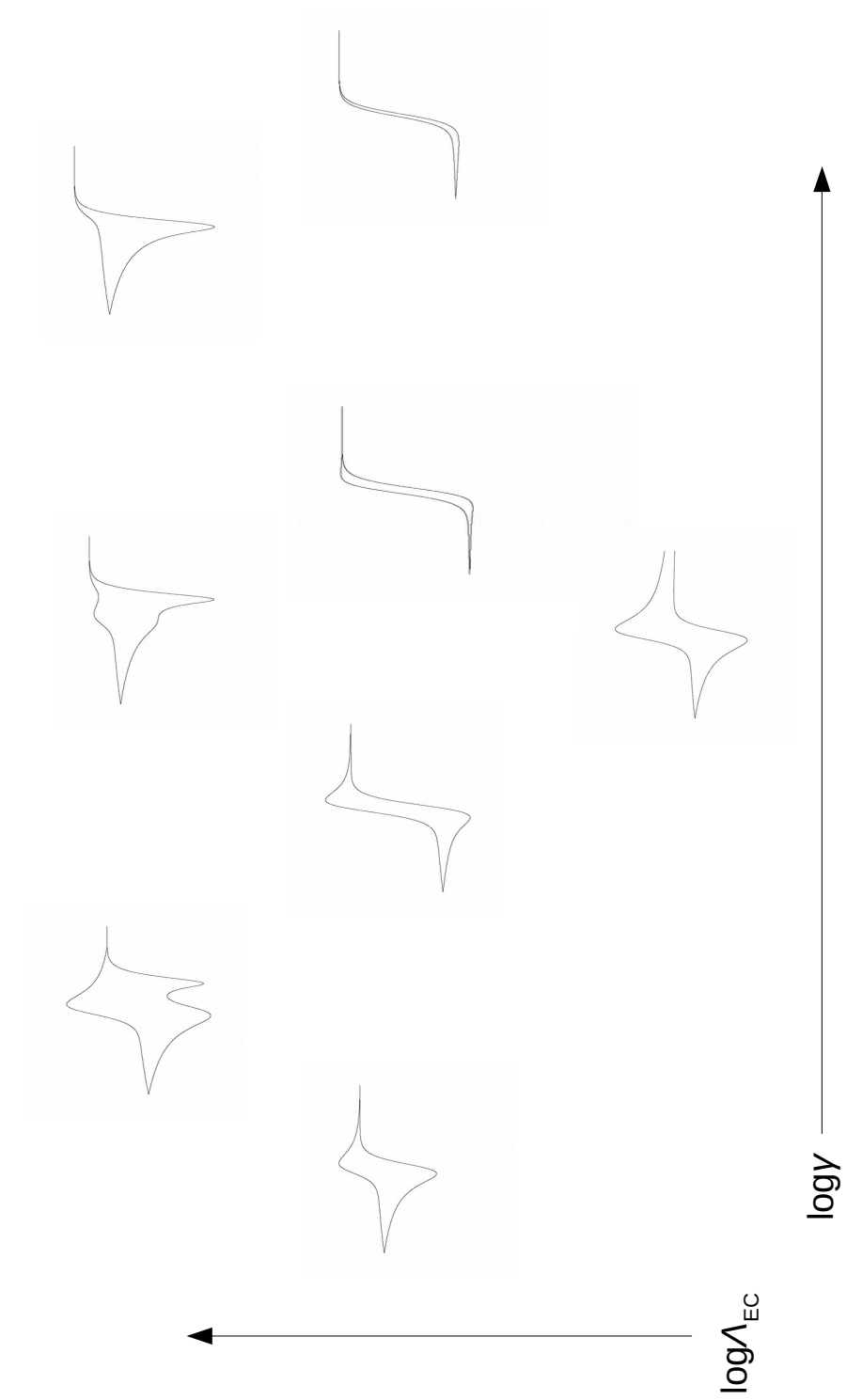

Figure 2.4.2: Examples of different voltammograms resulting from homogeneous catalytic reaction scheme.

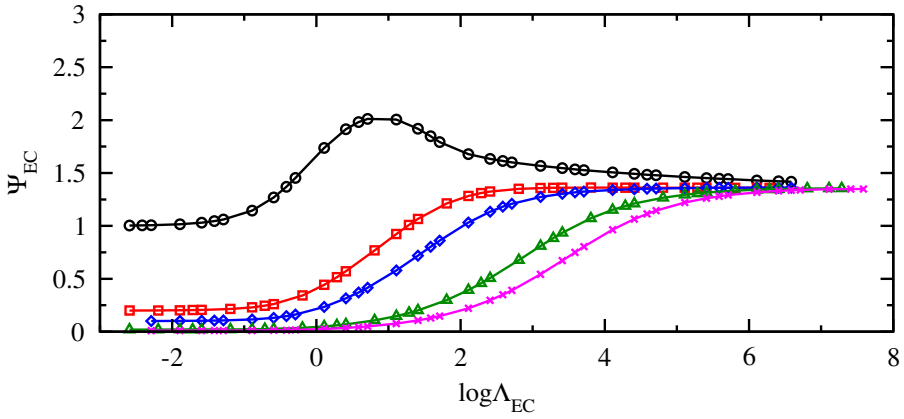

Figure 2.4.3: Homogeneous catalysis electrochemical reactions with the homogeneous electron transfer as a rate-limiting step. Variation of the dimensionless current Ψ_{EC} with the kinetic parameter Λ_{EC} for different values of γ: 1 (black circles), 5 (red squares), 10 (blue diamonds), 50 (green triangles) and 100 (magenta x).

For the case of a reversible electrochemical step at a constant values of γ by plotting the dimensionless catalytic current peak Ψ_{EC} against $\log \Lambda_{EC}$ the resulting diagrams are the ones presented in Fig. 2.4.3. From such a diagram, if one for a certain value of γ has a value of Ψ_{EC}, they shall calculate the value of Λ_{EC}, and thus the kinetic constant k_e can be extracted.

Actually, one of the most significant features of the Fig. 2.4.3 is what happens for a γ value of 1, where one can observe the initial increase of Ψ_{EC} and then its subsequent decrease. This can be better understood if one takes a close look into Fig. 2.4.4(a) where voltammograms at a constant γ of 1 and different k_e values are presented. For k_e we get the typical cyclic voltammogram of a reversible electrochemical reaction. For k_e values of 0.1 and 1 $m^3m^{-1}s$ the reduction peak increases in magnitude while the oxidation one decreases. For a k_e value of 10 $m^3m^{-1}s$ the reduction peak increases slightly from the previous state at a k_e value of 1 $m^3m^{-1}s$ and widens as well For larger values the peak splits and two separate peaks appear, with the first one being stable around the formal potential of the redox species and the other one shifting more anodically as the k_e increases. This change resembles what happens for low values of γ and increasing Λ_{EC} in Fig. 2.4.2.

In Figs. 2.4.4 (b) and (c) the voltammograms of the same parameters but for different c_P^* (thus different γ are presented. The difference between the aforementioned case and the ones observed here is that no decrease is observed in the magnitude of the voltammograms as the k_e increases. The peak just reaches a maximum value. For γ value of 5 the peak separation still appears, but the peak near the formal potential is rather faint in comparison to the other one. Finally for γ at a value of 50 at high k_e values only one reduction peak appears shifting anodically as the kinetic constant increases.

After the analysis of the this mechanism with cyclic voltammetry which has already been established, we shall proceed with the same analysis with FTacV. The dimensionless parameters γ and Ψ_{EC} remain the same, while the kinetic parameter Λ_{EC} changes

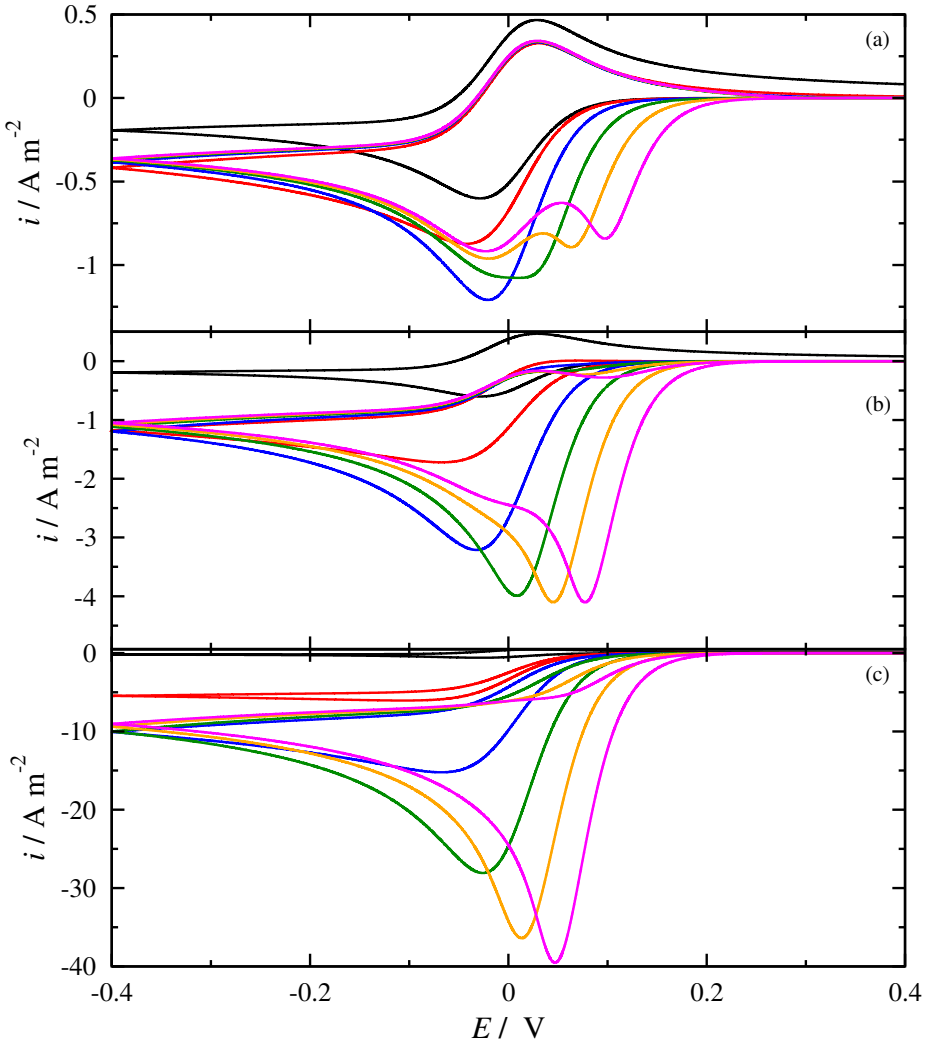

Figure 2.4.4: Example voltammograms of homogeneous catalysis electrochemical reactions with the homogeneous electron transfer as a rate-limiting step. Parameters: $v = 5$ mV/s, $c_A^* = 1$ mol m^{-3}, $T = 298.15$ K, $k_e = 0$ (black), 0.1 (red), 1 (blue), 10 (green), 100 (orange) and 1000 mol m^{-3} s^{-1} (magenta) and (a) $c_P^* = 1$, (b) 5 and (c) 50 mol m^{-3}.

slightly and is now a function of frequency and not of the scan rate - always under the assumption of that the criteria for the independence of the experiment from the scan rate is valid,

$$\Lambda_{\mathrm{EC,FTacV}} = \frac{k_{\mathrm{e}} c_{\mathrm{P}}^{*}}{f} \tag{2.4.7}$$

$\Lambda_{\mathrm{EC,FTacV}}$ corresponds to a certain value of perturbation amplitude. In this analysis only 100 mV shall be examined as an indicative case.

A plot similar to the one in Fig. 2.4.3 is presented in Fig. 2.4.5 corresponding to the 1st, 3rd and 5th harmonic for $A_0 = 100$ mV at different γ values. The dominant peak is taken at each case for the estimation of Ψ_{EC}. A similar analysis can be performed for the even harmonics as well, even though it is not analyzed here. The case of γ equal to 1 is also omitted as no increase in the magnitude of the peaks was observed. In general a trend of increasing currents reaching a plateau is observed as $\Lambda_{\mathrm{EC,FTacV}}$ increases. Some anomalies also occur but we shall get to these by taking each case individually. In general though, these diagrams can be used in the same way as the one in Fig. 2.4.3 to extract the actual kinetic constant k_{e}.

In Fig. 2.4.6 the case of γ equal to 1 is examined. The first 3rd and 5th harmonic are presented in (b) through (d) while the respective cyclic voltammograms without the effect of the perturbation is depicted in (a). Contrary to the increase seen in the cyclic voltammogram, in the harmonics resulting from the FTacV experiments no increase in the dominant peak is observed. However in the region where the split peak appears in the cyclic voltammogram a rather faint peak or set of peaks start appearing as the k_{e} increases. Thus from this case it can be safely concluded that the coupling with the homogeneous reaction has no effect on the set of peaks around the formal potential in the case of FTacV, contrary to cyclic voltammetry. That is why the case of γ equal to 1 is not included in the analysis of Fig. 2.4.5.

Moving on to Fig. 2.4.7 where we have the corresponding case as in Fig. 2.4.6, but with a γ at a value of 5. Again one can see that in the case of FTacV the peak around the formal potential is not affected by the catalysis, whereas the second set of peaks that appear more anodically are the ones to which the increase of the Ψ_{EC} in Fig. 2.4.5 is attributed. Comparing the signals of FTacV to the respective cyclic voltammograms again in the same figure the peaks that appear more anodically in the FTacV correspond to the intense peak that arises in the cyclic voltammogram at high values of k_{e}. This same trend, if not more intense, can be observed in Fig. 2.4.8, where the same voltammograms are presented for a γ value of 10. As long as the second peak does not appear in the cyclic voltammograms, the harmonics remain practically unchanged and only in the case of the split of the peaks in the cyclic voltammograms an increase of the dominant peak appears in FTacV. Again this increase is not due to an increase in the harmonics of the reversible species but due to an set of peaks arising more anodically.

What is interesting is the case of S-shaped cyclic voltammograms and what happens to the respective harmonics resulting from FTacV. Focusing on Fig. 2.4.9, in which for the case of cyclic voltammograms the conditions for an S-Shaped voltammograms are met, no increase is observed in the respective harmonics. This is rather noteworthy, as it indicates that if we have no split of the peak or a very intense peak shifting

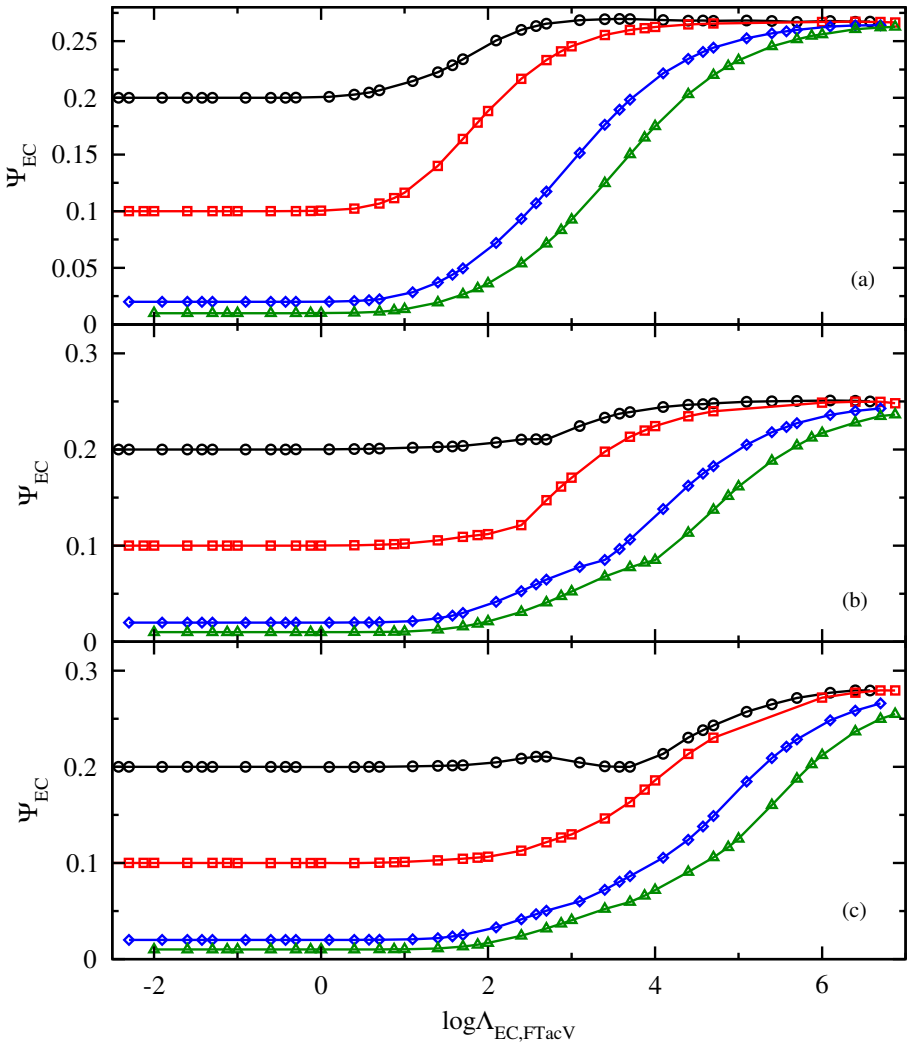

Figure 2.4.5: Homogeneous catalysis electrochemical reactions with the homogeneous electron transfer as a rate-limiting step with FTacV for $A_0 = 100$ mV at $T = 298.15$ K. Variation of the dimensionless current Ψ_{EC} with the kinetic parameter $K_{EC,FTacV}$ for different values of γ: 5 (black circles), 10 (red squares), 50 (blue diamonds) and 100 (green triangles). (a) 1st harmonic, (b) 3rd harmonic and (c) 5th harmonic.

anodically, no difference can be observed in the FTacV. It is as if the redox reaction of the electroactive species is solely monitored.

Finally the case of a very large value of γ is examined in Fig. 2.4.10. In this case for small to intermediate values of k_e a slight increase in the harmonics is observed. However for high values of k_e in which one sole peak appears in the cyclic voltammograms, way more intense than the original voltammograms, in FTacV only then a clear increase in the magnitude of the voltammogram appears. The patterns observed resemble those of a chemically irreversible reaction.

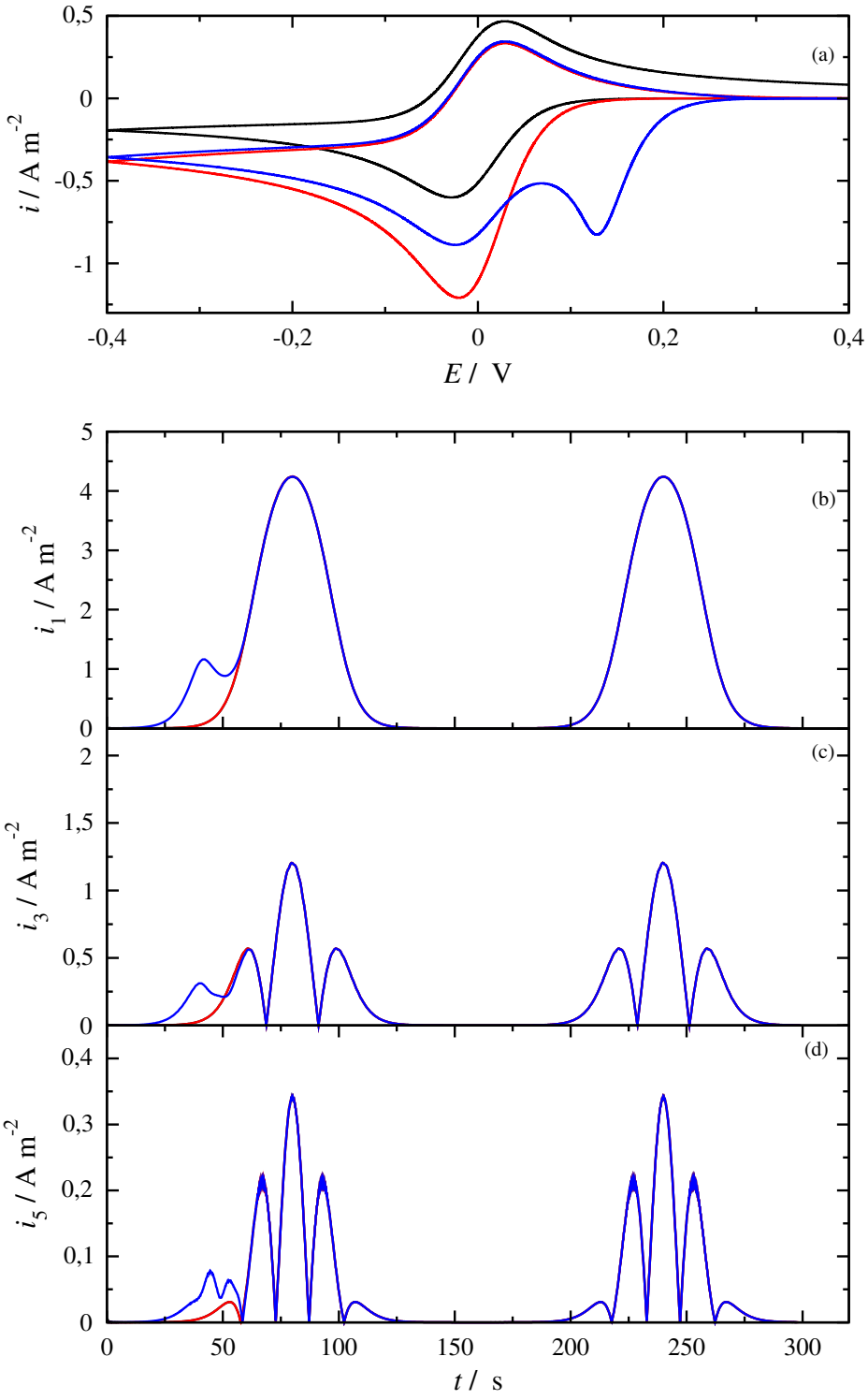

Figure 2.4.6: Homogeneous catalysis electrochemical reactions with the homogeneous electron transfer as a rate determining step. (a) Cyclic voltammetry at $v = 5$ mV/s (b) 1st, (c) 3rd and (d) 5th harmonic for $v = 5$ mV/s, $f = 1$ Hz and $A_0 = 100$ mV. Parameters: $c_A^* = 1$ mol m^{-3}, $c_P^* = 1$ mol m^{-3}, $T = 298.15$ K and $k_e = 0$ (black), 1 (red) and 10000 mol m^{-3} s^{-1} (blue).

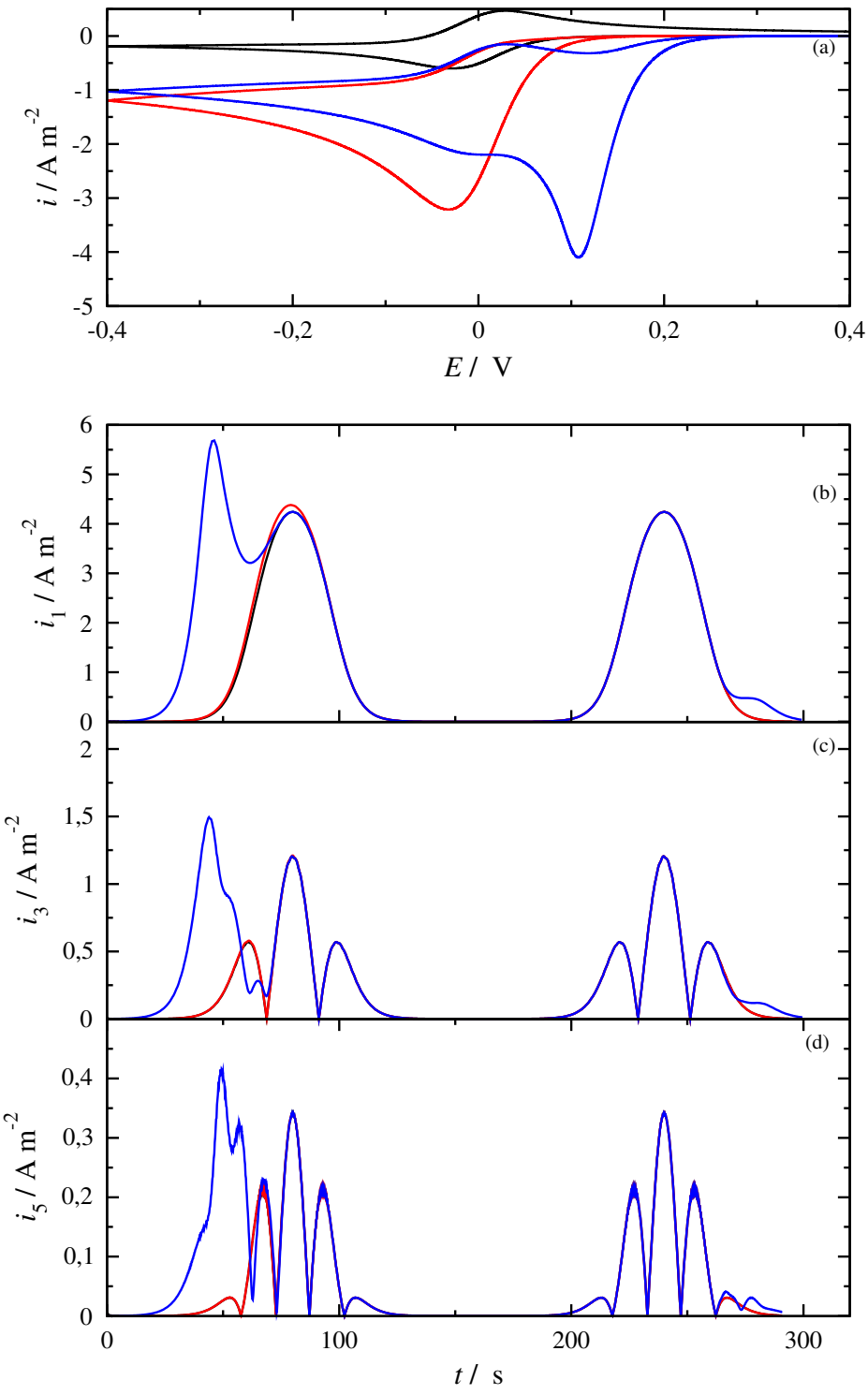

Figure 2.4.7: Homogeneous catalysis electrochemical reactions with the homogeneous electron transfer as a rate determining step. (a) Cyclic voltammetry at $v = 5$ mV/s (b) 1st, (c) 3rd and (d) 5th harmonic for $v = 5$ mV/s, $f = 1$ Hz and $A_0 = 100$ mV. Parameters: $c^*_{\mathrm{A}} = 1$ mol m^{-3}, $c^*_{\mathrm{P}} = 5$ mol m^{-3}, $T = 298.15$ K and $k_{\mathrm{e}} = 0$ (black), 1 (red) and 10000 mol m^{-3} s^{-1} (blue).

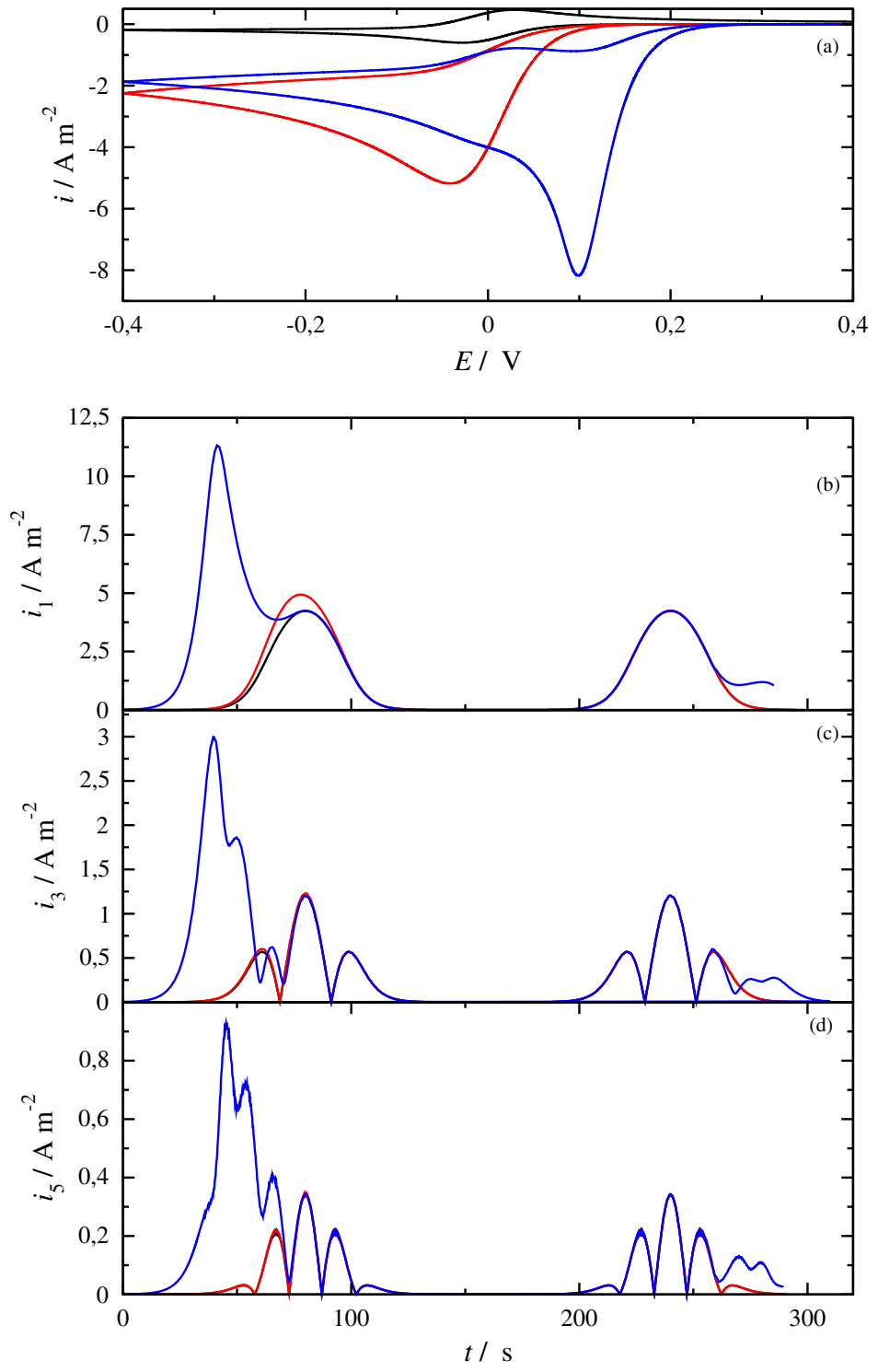

Figure 2.4.8: Homogeneous catalysis electrochemical reactions with the homogeneous electron transfer as a ate determining step. (a) Cyclic voltammetry at $v = 5$ mV/s (b) 1st, (c) 3rd and (d) 5th harmonic for $v = 5$ mV/s, $f = 1$ Hz and $A_0 = 100$ mV. Parameters: $c_A^* = 1$ mol m^{-3}, $c_P^* = 10$ *mol* m^{-3} , $T = 298.15$ K and $k_e = 0$ (black), 1 (red) and 10000 mol m^{-3} s^{-1} (blue).

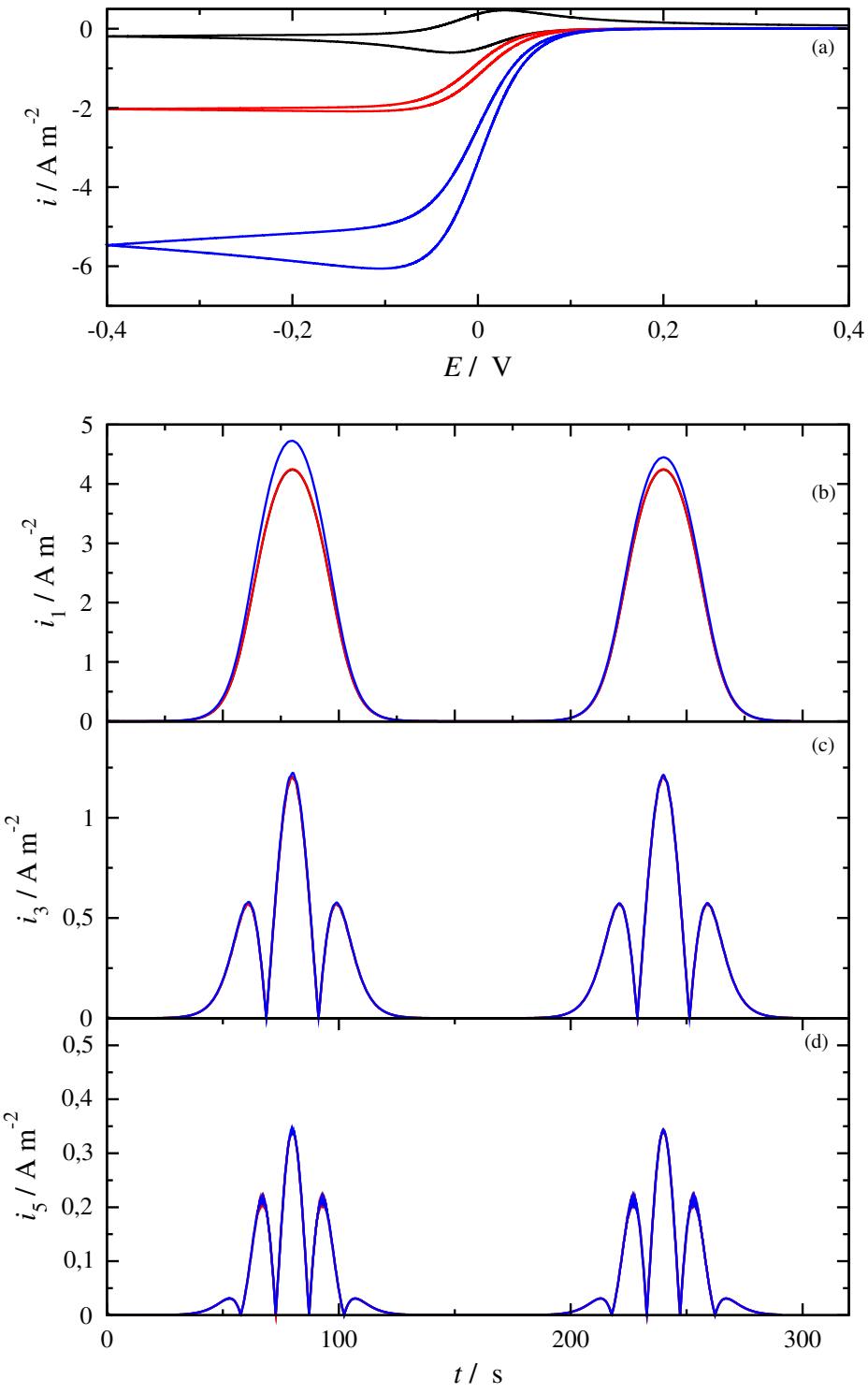

Figure 2.4.9: Homogeneous catalysis electrochemical reactions with the homogeneous electron transfer as a rate determining step. (a) Cyclic voltammetry at $v = 5$ mV/s (b) 1st, (c) 3rd and (d) 5th harmonic for $v = 5$ mV/s, $f = 1$ Hz and $A_0 = 100$ mV. Parameters: $c^*_{\mathrm{A}} = 1$ mol m^{-3}, $c^*_{\mathrm{P}} = 50$ mol m^{-3} , $T = 298.15$ K and $k_{\mathrm{e}}0$ (black), 0.01 (red) and 0.1 mol m^{-3} s^{-1} (blue).

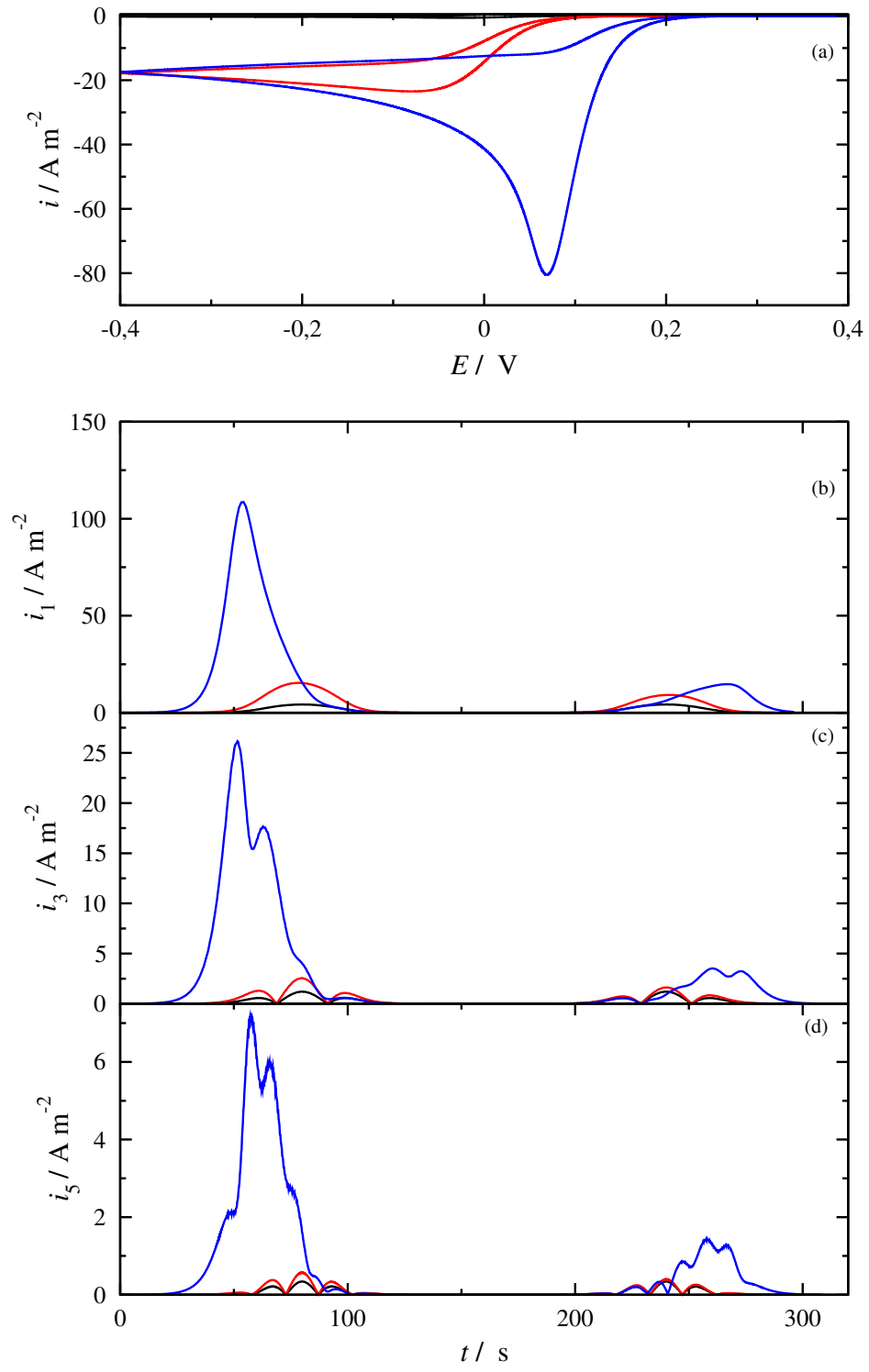

Figure 2.4.10: Homogeneous catalysis electrochemical reactions with the homogeneous electron transfer as a rate determining step. (a) Cyclic voltammetry at $v = 5$ mV/s (b) 1st, (c) 3rd and (d) 5th harmonic for $v = 5$ mV/s, $f = 1$ Hz and $A_0 = 100$ mV. Parameters: $c_A^* = 1$ mol m^{-3}, $c_P^* = 100$ mol m^{-3} , $T = 298.15$ K and $k_e = 0$ (black), 1 (red) and 10000 mol m^{-3} s^{-1} (blue).

2.5 Convolution voltammetry analysis

In this section, convolution voltammetry shall be introduced, as it is a tool that will be used later in this work. It is a tool that can be useful for determining values of the diffusion coefficient of an electroactive species, its bulk concentration, as well as stoichiometric number of electrons exchanged.

2.5.1 One step electron reaction

Let us consider a one step reaction occurring on an electrode surface as described in Eq. (2.5.1), where the oxidized form of an electroactive species (A) takes an electron resulting in the reduced form (B),

$$\mathrm{A} + n\mathrm{e} \underset{k_\mathrm{a}}{\overset{k_\mathrm{c}}{\rightleftharpoons}} \mathrm{B} \tag{2.5.1}$$

We shall consider at this point that the mass transfer of the chemical species A and B happens solely due to diffusion. In this case Fick's second law applies,

$$\frac{\partial c_\mathrm{A}}{\partial t} = D_\mathrm{A} \frac{\partial^2 c_\mathrm{A}}{\partial x^2} \tag{2.5.2}$$

$$\frac{\partial c_\mathrm{B}}{\partial t} = D_\mathrm{B} \frac{\partial^2 c_\mathrm{B}}{\partial x^2} \tag{2.5.3}$$

where $c_\mathrm{A}(x,t)$, $c_\mathrm{B}(x,t)$ are the concentrations of A and B D_A, D_B are the respective diffusion coefficients.

In the case, initially only A is present in the solution, then the initial conditions are,

$$c_\mathrm{A}(x,0) = c_0 \tag{2.5.4}$$

$$c_\mathrm{B}(x,0) = 0 \tag{2.5.5}$$

Considering the electrode surface to be $x = 0$ and the bulk solution to be $x \to \infty$, then the boundary conditions for $x \to \infty$ shall be,

$$c_\mathrm{A}(x \to \infty, t) = c_0 \tag{2.5.6}$$

$$c_\mathrm{B}(x \to \infty, t) = 0 \tag{2.5.7}$$

meaning that the bulk solutions of the electroactive species remain unchanged.

The redox reaction takes place on the electrode surface. Thus at $x = 0$ the flux due to diffusion shall be equal to the change of the concentration per surface unit due to the reaction. Consequently the boundary conditions at $x = 0$ shall be,

$$-D_\mathrm{A} \frac{\partial c_\mathrm{A}}{\partial x}\bigg|_{x=0} = \frac{I}{nSF} \tag{2.5.8}$$

$$-D_\mathrm{B} \frac{\partial c_\mathrm{B}}{\partial x}\bigg|_{x=0} = -\frac{I}{nSF} \tag{2.5.9}$$

where I is the current[11] and S the electrode surface. On the electrode surface the following equations apply,

$$D_{\mathrm{A}}\frac{\partial c_{\mathrm{A}}}{\partial x}\Big|_{x=0} + D_{\mathrm{B}}\frac{\partial c_{\mathrm{B}}}{\partial x}\Big|_{x=0} = 0 \tag{2.5.10}$$

The resulting current obeys to the following equation,

$$I(t) = nAFk^0 e^{-\frac{anF}{RT}(E(t)-E^0)}[c_{\mathrm{B}}(0,t)e^{\frac{nF}{RT}(E(t)-E^0)} - c_{\mathrm{A}}(0,t)] \tag{2.5.11}$$

where E^0 is the formal electrode potential of the reaction, k^0 the reaction rate constant and a the transfer coefficient. The electrode potential is scanned linearly with time

$$E = E_{\mathrm{I}} - vt \tag{2.5.12}$$

where v is the scan rate.

By rendering dimensionless the potential $\xi = nF(E - E^0)/RT$, the time $\tau = Fvt/RT$ as well as the concentrations $\hat{\alpha} = c_{\mathrm{A}}/c_0$ and $\hat{\beta} = c_{\mathrm{B}}/c_0$ then Eq. (2.5.2) and (2.5.3) are rewritten as,

$$\frac{\partial\hat{\alpha}}{\partial\tau} = \frac{\partial^2\hat{\alpha}}{\partial y^2} \tag{2.5.13}$$

$$\frac{\partial\hat{\beta}}{\partial\tau} = \delta\frac{\partial^2\hat{\beta}}{\partial y^2} \tag{2.5.14}$$

where, $\delta = D_{\mathrm{B}}/D_{\mathrm{A}}$ and $y = x\sqrt{\frac{Fv}{D_{\mathrm{A}}RT}}$. Moreover, the initial conditions are,

$$\hat{\alpha}(y,0) = 1 \tag{2.5.15}$$

$$\hat{\beta}(y,0) = 0 \tag{2.5.16}$$

The boundary conditions for $y \to \infty$ are,

$$\hat{\alpha}(y\to\infty,\tau) = 1 \tag{2.5.17}$$

$$\hat{\beta}(y\to\infty,\tau) = 0 \tag{2.5.18}$$

while the boundary conditions for $y = 0$ are,

$$\frac{\partial\hat{\alpha}}{\partial y}\Big|_{y=0} = -\psi \tag{2.5.19}$$

$$\delta\frac{\partial\hat{\beta}}{\partial y}\Big|_{y=0} = \psi \tag{2.5.20}$$

where the dimensionless current is,

$$\psi(\tau) = k_{\mathrm{CV}}e^{-a\xi(\tau)}[\hat{\beta}(0,\tau)e^{\xi(\tau)} - \hat{\alpha}(0,\tau)] \tag{2.5.21}$$

[11] Not the current density

where,

$$\psi = \frac{I}{nFSc_0\sqrt{D_{\mathrm{A}}}\sqrt{\frac{Fv}{RT}}} \tag{2.5.22}$$

and,

$$\xi = \xi_{\mathrm{I}} - \tau \tag{2.5.23}$$

The dimensionless kinetic constant k is given by the equation,

$$k_{\mathrm{CV}} = \frac{k^0}{\sqrt{D_{\mathrm{A}} v \frac{F}{RT}}} \tag{2.5.24}$$

By using Laplace transformation Eq. (2.5.13) and (2.5.14) are rendered,

$$s\bar{\alpha} - \hat{\alpha}(y,0) = \frac{\partial^2 \bar{\alpha}}{\partial y^2} \tag{2.5.25}$$

$$s\bar{\beta} - \hat{\beta}(y,0) = \delta\frac{\partial^2 \bar{\beta}}{\partial y^2} \tag{2.5.26}$$

or, by using Eq. (2.5.17) and (2.5.18),

$$s\bar{\alpha} - 1 = \frac{\partial^2 \bar{\alpha}}{\partial y^2} \tag{2.5.27}$$

$$s\bar{\beta} = \delta\frac{\partial^2 \bar{\beta}}{\partial y^2} \tag{2.5.28}$$

These equations are linear with constant coefficients. The general solution of the second equation is,[12]

$$\bar{\beta}(y,s) = Ae^{\sqrt{\frac{s}{\delta}}y} + Be^{-\sqrt{\frac{s}{\delta}}y}$$

For $y \to \infty$ the $\bar{\beta}$ is equal to zero, and consequently $A = 0$. The coefficient B can be extracted from the condition of Eq. (2.5.20). More specifically,

$$\frac{\partial\bar{\beta}}{\partial y}\Big|_{y=0} = -B\sqrt{\frac{s}{\delta}} = \frac{\bar{\psi}}{\delta} \Rightarrow B = -\bar{\psi}\sqrt{\frac{1}{\delta s}}$$

consequently,

$$\bar{\beta}(y,s) = -\bar{\psi}\sqrt{\frac{1}{\delta s}}e^{-\sqrt{\frac{s}{\delta}}y} \tag{2.5.29}$$

The surface concentration for $y = 0$, $\hat{\beta}(0,t)$, can be found by using the convolution theorem,[13] Consequently,[14]

$$\hat{\beta}(0,\tau) = -\sqrt{\frac{1}{\delta\pi}}\int_0^\tau \frac{\psi(z)}{\sqrt{\tau - z}}dz \tag{2.5.30}$$

[12]The characteristic polyonym is $\delta\lambda^2 - s = 0$, consequently $\lambda = \pm\sqrt{\frac{s}{\delta}}$

[13]For inverse Laplace transform of $f_1(s)\cdot f_2(s)$, $\mathcal{L}^{-1}(f_1(s)\cdot f_2(s)) = \int_0^t F_1(t-z)F_2(z)dz$.

[14]By using inverse Laplace $\mathcal{L}^{-1}(1/\sqrt{s}) = \sqrt{1/\pi t}$.

Respectively, the surface concentrations $\alpha(0,t)$ is,

$$\hat{\alpha}(0,\tau) = 1 + \sqrt{\frac{1}{\pi}} \int_0^\tau \frac{\psi(z)}{\sqrt{\tau - z}} dz \tag{2.5.31}$$

By substituting the dimensionless surface concentrations in the expression of the dimensionless current, Eq. (2.5.21), the result is the cyclic voltammogram,

$$\psi(\tau) = -k_{\mathrm{CV}} e^{-a\xi(\tau)} \left[1 + \frac{1}{\sqrt{\pi}} (\delta^{-1/2} e^{\xi(\tau)} + 1) \int_0^\tau \frac{\psi(z)}{\sqrt{\tau - z}} dz \right] \tag{2.5.32}$$

Equation (2.5.30) can be also written as,

$$\hat{\beta}(0,\tau) = -\delta^{-1/2} M(\tau) \tag{2.5.33}$$

where,

$$M(\tau) = \frac{1}{\sqrt{\pi}} \int_0^\tau \frac{\psi(z)}{\sqrt{\tau - z}} dz \tag{2.5.34}$$

is the linear convolution of the dimensionless current $\psi(z)$ with the function $1/\sqrt{z}$.

Respectively, Eq. (2.5.31), using the function $M(\tau)$, can be rewritten as,

$$\hat{\alpha}(0,\tau) = 1 + M(\tau)$$

The minimum value that $\hat{\alpha}(0,\tau)$ can get is zero, consequently, for this value the function $M(\tau)$ gets a boundary value,

$$M_{\mathrm{L}} = -1$$

The value of $\hat{\beta}(0,\tau)$, when the function $M(\tau)$ gets its boundary value is $\hat{\beta}(0,\tau) = \delta^{-1/2}$.

Finally, exploiting $M(\tau)$, Eq. (2.5.32), can be rewritten as,

$$\psi(\tau) = -k_{\mathrm{CV}} e^{-a\xi(\tau)} \left[1 + (\delta^{-1/2} e^{\xi(\tau)} + 1) M(\tau) \right] \tag{2.5.35}$$

The last equation can also be written as,

$$\psi(\tau) = k_{\mathrm{CV}} e^{-a\xi(\tau)} \left[-1 - \left(\delta^{-1/2} e^{\xi(\tau)} + 1 \right) M(\tau) \right]$$

But, $M_{\mathrm{L}} = -1$, thus,

$$\psi(\tau) = k_{\mathrm{CV}} e^{-a\xi(\tau)} \left[M_{\mathrm{L}} - \left(\delta^{-1/2} e^{\xi(\tau)} + 1 \right) M(\tau) \right] \tag{2.5.36}$$

Eq. (2.5.36) expresses the dependence of the current from the potential of an one step quasi reversible reaction.

Two different cases can be distinguished:

- For large values of the kinetic constant k, that is large k^0 or small v, Eq. (2.5.36) is written as,

$$\xi = \frac{1}{2} \ln \delta + \ln \frac{M_{\mathrm{L}} - M}{M} \tag{2.5.37}$$

  This equation applies to reversible kinetics.

- When $\delta^{-1/2}e^{\xi(\tau)} \ll 1$ then Eq. (2.5.36) is written as,

$$\xi = \frac{1}{a}\ln k_{\mathrm{CV}} + \ln\frac{M_{\mathrm{L}} - M}{\psi(\tau)} \tag{2.5.38}$$

  This dependence stands for irreversible kinetics.

- In the general case of Eq. (2.5.36),

$$\xi = \frac{1}{a}\ln k_{\mathrm{CV}} + \ln\frac{\left[M_{\mathrm{L}} - \left(\delta^{-1/2}e^{\xi(\tau)} + 1\right)M(\tau)\right]}{\psi(\tau)} \tag{2.5.39}$$

Going back to dimensional quantities the function $M(\tau)$ is written as,

$$I(t) = \frac{1}{\sqrt{\pi}}\int_0^{\tau}\frac{i(t)}{\sqrt{t-\tau}}d\tau \tag{2.5.40}$$

where now $I(t)$ denotes the convolution current with units C/s$^{1/2}$. We shall remind that in this case $i(t)$ is the current and not the current density. The current $i(t)$ is recorded experimentlly,thus the correlation curent, $I(t)$, can be calculated by a simple routine *e.g.* in FORTRAN [12],

```
p=f(1)
 do k=2,n
  do j=2,k
   h=t(j)-t(j-1)
   hj=t(k)-t(j)
   sj=sqrt(hj)
   hj1=t(k)-t(j-1)
   sj1=sqrt(hj1)
   p=p+((f(j)*hj1-f(j-1)*hj)*(sj1-sj)
 $           +((f(j)-f(j-1))/3.)*(sj**3-sj1**3))/h
  end do
  write(1,*) t(k), 2.*p/sqrt(pi)
  p=0.
end do
```

where `f(j)` is the current for the time `t(j)`.

The limiting correlation current is ,

$$I_{\mathrm{L}} = -nFA\sqrt{D_{\mathrm{A}}}c_0 \tag{2.5.41}$$

while, the surface concentrations of A and B at every moment are,

$$c_{\mathrm{A}} = -\frac{I_{\mathrm{L}} - I(t)}{nFA\sqrt{D_{\mathrm{A}}}} \tag{2.5.42}$$

$$c_{\mathrm{B}} = -\frac{I(t)}{nFA\sqrt{D_{\mathrm{B}}}} \tag{2.5.43}$$

One can observe that for a known surface area S, the limiting convolution current allows the determination of the diffusion coefficient. The same is valid vice - versa as well - having a known diffusion coefficient, the electrode surface can be calculated. Moreover, one can observe that for a known diffusion coefficient and a known surface area, a cyclic voltammetry experiment allows the determination of the surface concentrations, without the use of another *in situ* technique.

The correlation current *vs.* potential dependencies are,

- Reversible kinetics:

$$E = E^0 + \frac{RT}{2nF} \ln \frac{D_\mathrm{B}}{D_\mathrm{A}} + \frac{RT}{nF} \ln \frac{I_\mathrm{L} - I}{I} \tag{2.5.44}$$

  The above equation can be rewritten as,

$$E = E_{1/2} + \frac{RT}{nF} \ln \frac{I_\mathrm{L} - I}{I}$$

  where,

$$E_{1/2} = E^0 + \frac{RT}{2nF} \ln \frac{D_\mathrm{B}}{D_\mathrm{A}}$$

  is the half wave potential. If the diffusion coefficients are equal, then the half wave potential is equal to the formal potential.

- Irreversible kinetics:

$$E = E^0 + \frac{RT}{anF} \ln \frac{k^0}{\sqrt{D_\mathrm{A}}} + \frac{RT}{anF} \ln \frac{I_\mathrm{L} - I(t)}{i(t)} \tag{2.5.45}$$

- Quasi reversible kinetics:

$$E = E^0 + \frac{RT}{anF} \ln \frac{k^0}{\sqrt{D_\mathrm{A}}} + \frac{RT}{anF} \ln \frac{I_\mathrm{L} - I(t)(1 + \sqrt{\frac{D_\mathrm{A}}{D_\mathrm{B}}} e^{\frac{nF}{RT}(E - E^0)})}{i(t)} \tag{2.5.46}$$

  Using the definition of the half wave potential, the above equation can be rewritten as,

$$E = E^0 + \frac{RT}{anF} \ln \frac{k^0}{\sqrt{D_\mathrm{A}}} + \frac{RT}{anF} \ln \frac{I_\mathrm{L} - I(t)(1 + e^{\frac{nF}{RT}(E - E_{1/2})})}{i(t)}$$

  The last equation can be rewritten as,

$$\ln k_\mathrm{f}(E) = \ln \sqrt{D_\mathrm{A}} - \ln \frac{I_\mathrm{L} - I(t)(1 + e^{\frac{nF}{RT}(E - E_{1/2})})}{i(t)}$$

  where $k_\mathrm{f} = k^0 e^{-\frac{anF}{RT}(E - E^0)}$ the potential dependent kinetic constant of the forward reaction. For k_f what was mentioned for the case of the irreversible reaction is valid here as well.

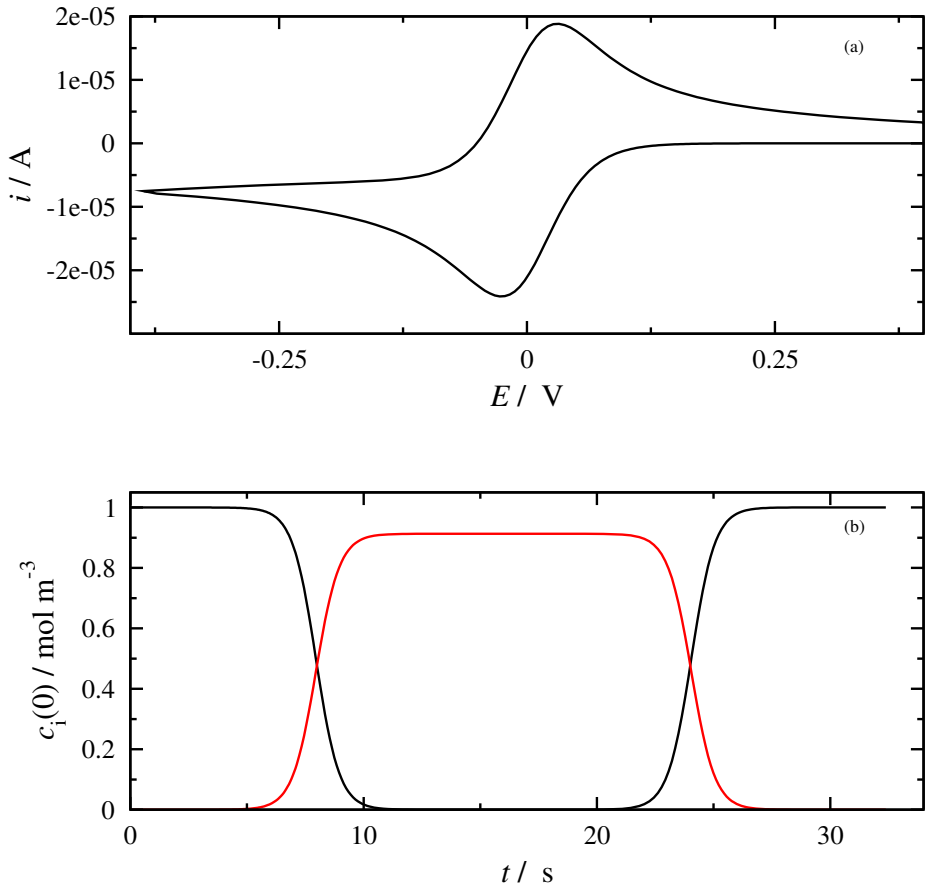

Figure 2.5.1: (a) Cyclic voltammogram and (b) surface concentrations of A (black) and B (red) for reversible kinetics are a scan rate of 50 mV/s. Parameters: $D_{\mathrm{A}} = 1 \times 10^{-9}$ m^2/s, $D_{\mathrm{B}} = 1.2 \times 10^{-9}$ m^2/s, $E^0 = 0$ V, $k^0 = 5 \times 10^3$ m/s, $c^0 = 1$ mol/m^3, $n = 1$ and $S = 1.257 \times 10^{-5}$ m^2 .

2.5.2 Convolution voltammetry examples

In this paragraph, some representative examples will be presented for the case of reversible, irreversible and quasi-reversible kinetics.

We shall commence the analysis from the case of *reversible kinetics*. In Fig. 2.5.1 a cyclic voltammogram as well as the surface concentrations of a reversible cyclic voltammograms are presented for the following parameter values: $D_{\mathrm{A}} = 1 \times 10^{-9}$ m^2/s, $D_{\mathrm{B}} = 1.2 \times 10^{-9}$ m^2/s, $E^0 = 0$ V, $k^0 = 5 \times 10^3$ m/s, $c^0 = 1$ mol/m^3, $n = 1$ and $S = 1.257 \times 10^{-5}$ m^2.

According to what has already been mentioned, the limiting convolution current shall be calculated,

$$I_{\mathrm{L}} = nFS\sqrt{D_{\mathrm{A}}}c^0 = 1 \times 96485 \times \sqrt{1 \times 10^{-9}} \times 1 = 3.83 \times 10^{-5} \text{ C/s}^{1/2}$$

while the dependence of the convolution current with the potential follows Eq. (2.5.44).

In Fig. 2.5.1 the cyclic voltammogram at a scan rate of 50 mV/s is presented as well

as the change in the surface concentrations on the electrode surface as the potential is scanned linearly in time.

In Fig. 2.5.2 the convolution current together with the current as the electrode potential is scanned linearly is presented. One can observe a limiting convolution current equal to the expected one. In the same figure the dependence of $\ln[(I_L - I)/I]$ against the potential E during the cathodic scan is depicted. The dependence is linear with a slope of $nF/RT = 38.9\ V^{-1}$.

The determination of the correlation current allows the calculation of the surface concentrations from the current values though Eq. (2.5.42) and (2.5.43). The surface concentrations appear in Fig. 2.5.3, and are the same as the ones presented in Fig. 2.5.1 (b).

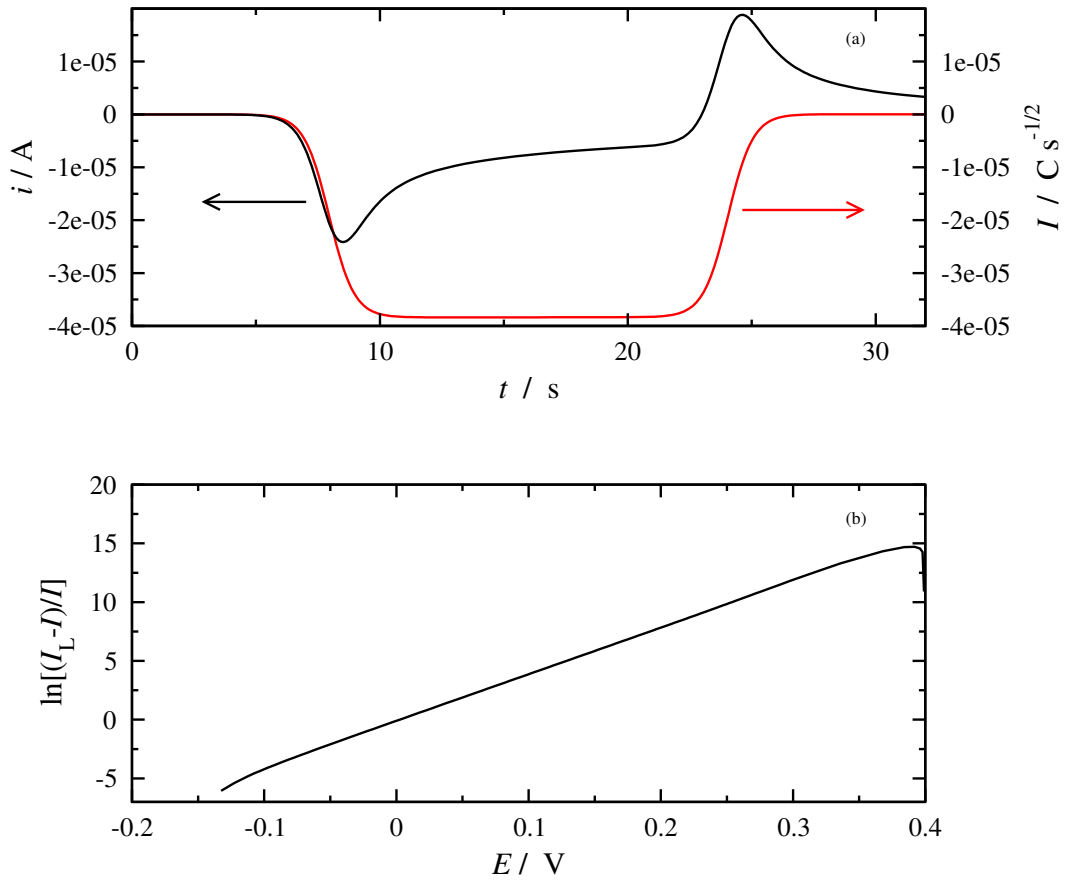

Figure 2.5.2: (a) Cyclic voltammogram (black) together with convolution current (red) for reversible kinetics and (b) ascertainment of Eq. (2.5.44). Parameters: $D_A = 1 \times 10^{-9}\ m^2/s$, $D_B = 1.2 \times 10^{-9}\ m^2/s$, $E^0 = 0\ V$, $k^0 = 5 \times 10^3\ m/s$, $c^0 = 1\ mol/m^3$, $n = 1$ and $S = 1.257 \times 10^{-5}\ m^2$.

The next case concerns *irreversible kinetics*. In Fig. 2.5.4 one can find the cyclic voltammogram and the surface concentrations of an irreversible reaction with the following values: $D_A = 1 \times 10^{-9}\ m^2/s$, $D_B = 1.2 \times 10^{-9}\ m^2/s$, $E^0 = 0\ V$, $k^0 = 5 \times 10^{-8}\ m/s$, $c^0 = 1\ mol/m^3$, $a = 0.5$, $n = 1$ and $S = 1.257 \times 10^{-5}\ m^2$.

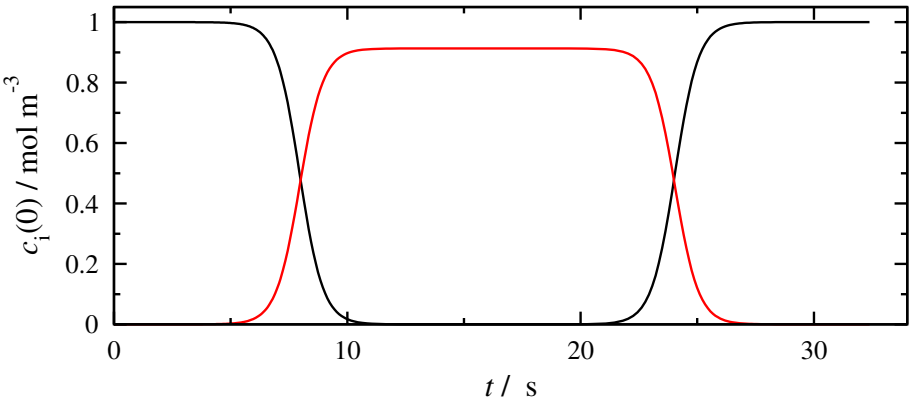

Figure 2.5.3: Surface concentrations as evaluated from convolution current for reversible kinetics.

According to what has already been mentioned, the limiting convolution current should be,

$$I_{\mathrm{L}} = nFS\sqrt{D_{\mathrm{A}}}c^0 = 1 \times 96485 \times \sqrt{1 \times 10^{-9}} \times 1 = 3.83 \times 10^{-5} \ \ \mathrm{C/s^{1/2}}$$

while, the convolution current dependence against the potential shall follow Eq. (2.5.45).

In Fig. 2.5.5 the current together with the convolution current are presented, as the potential is swept linearly. One can observe that the convolution current is equal to the expected.In the same figure the dependence of $\ln[(I_{\mathrm{L}} - I)/I]$ against the potential E during the cathodic scan is depicted.The dependence is linear with a slope of $nF/RT = 19.46\ \mathrm{V}^{-1}$.

The determination of the correlation current allows the calculation of the surface concentrations of the current through Eq. (2.5.42) and (2.5.43). The surface concentrations appear in Fig. 2.5.6, and are the same as the ones in Fig. 2.5.4 (b).

A final example is given for *quasi-reversible kinetics*. In Fig. 2.5.7 one can find the cyclic voltammogram and the surface concentrations of a quasi-reversible reaction with the following values: $D_{\mathrm{A}} = 1 \times 10^{-9}\ \mathrm{m^2/s}$, $D_{\mathrm{B}} = 1.2 \times 10^{-9}\ \mathrm{m^2/s}$, $E^0 = 0\ \mathrm{V}$, $k^0 = 5 \times 10^{-6}\ \mathrm{m/s}$, $c^0 = 1\ \mathrm{mol/m^3}$, $a = 0.5$, $n = 1$ and $S = 1.257 \times 10^{-5}\ \mathrm{m^2}$.

According to what has already been mentioned, the limiting convolution current should be,

$$I_{\mathrm{L}} = nFS\sqrt{D_{\mathrm{A}}}c^0 = 1 \times 96485 \times \sqrt{1 \times 10^{-9}} \times 1 = 3.83 \times 10^{-5}\ \mathrm{C/s^{1/2}}$$

while the dependence of the convolution current against the potential should follow the Eq. (2.5.46). The voltammogram together with the respective surface concentrations appear in Fig. 2.5.7 and the convolution current appears in Fig. 2.5.8.

In the previous section it was shown that for a quasi-reversible reaction, the equation that is valid is the following,

$$\ln k_{\mathrm{f}}(E) = \ln\sqrt{D_{\mathrm{A}}} - \ln\frac{I_{\mathrm{L}} - I(t)(1 + e^{\frac{nF}{RT}(E - E_{1/2})})}{i(t)}$$

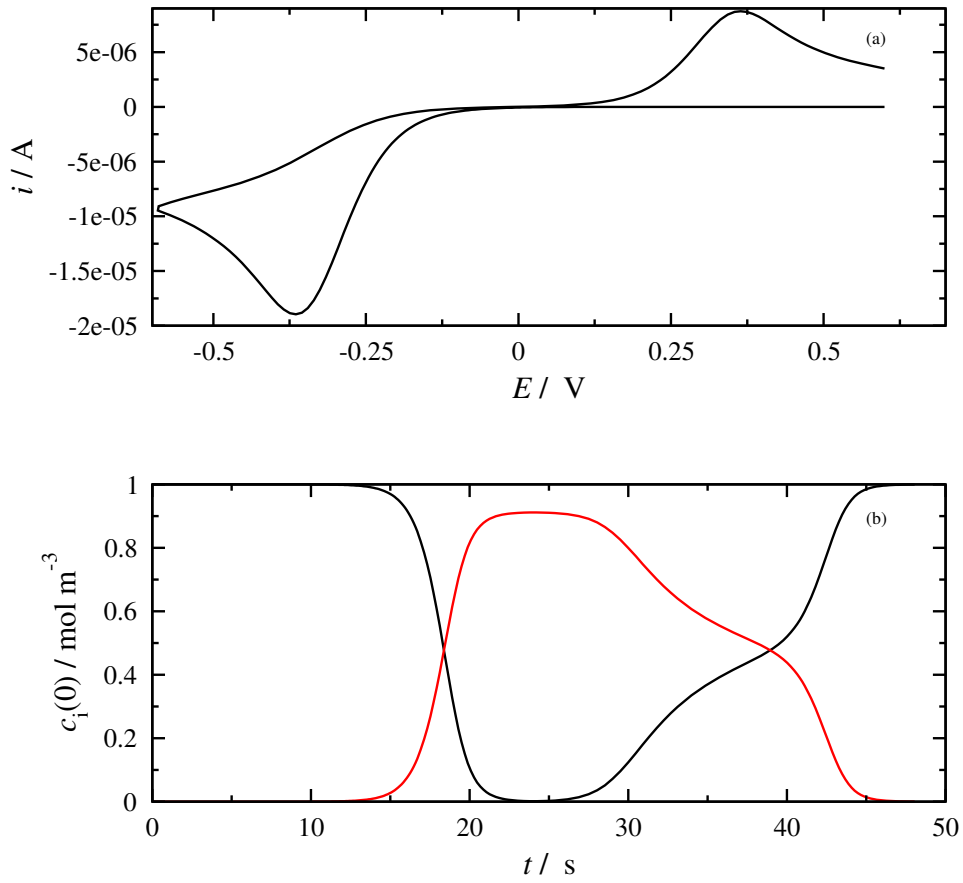

Figure 2.5.4: (a) Cyclic voltammogram and (b) surface concentrations of A (black) and B (red) for irreversible kinetics are a scan rate of 50 mV/s. Parameters:$D_{\mathrm{A}} = 1 \times 10^{-9}$ m^2/s, $D_{\mathrm{B}} = 1.2 \times 10^{-9}$ m^2/s, $E^0 = 0$ V, $k^0 = 5 \times 10^{-8}$ m/s, $c^0 = 1$ mol/m^3, $a = 0.5$, $n = 1$ and $S = 1.257 \times 10^{-5}$ m^2

From the respective cyclic voltammogram one can observe that there is a potential value $E(i = 0)$ where the current reaches zero (during the reverse potential scan). For this potential value the convolution current has a specific value $I(i = 0)$. Taking as a fact that for this potential value $k_{\mathrm{f}}(E)$ has a certain value, the numerator has to be equal to 0 as well.

Consequently we have,

$$E_{1/2} = E(i = 0) - \frac{RT}{nF} \ln \frac{I_{\mathrm{L}} - I(i = 0)}{I(i = 0)}$$

This equation allows the determination of the half wave potential from the convolution current of a quasi reversible reaction. Unfortunately, a similar correlation is not valid for the case of the irreversible kinetics, as there is no clear potential value where the current is rendered zero during the reverse scan.

Now, for the example presented in Fig. 2.5.8, the potential $E(i = 0)$ is -0.042 V while the limiting convolution current is $I_{\mathrm{L}} = -3.837 \times 10^{-5}$ C/s$^{1/2}$. The current $I(i = 0)$ is

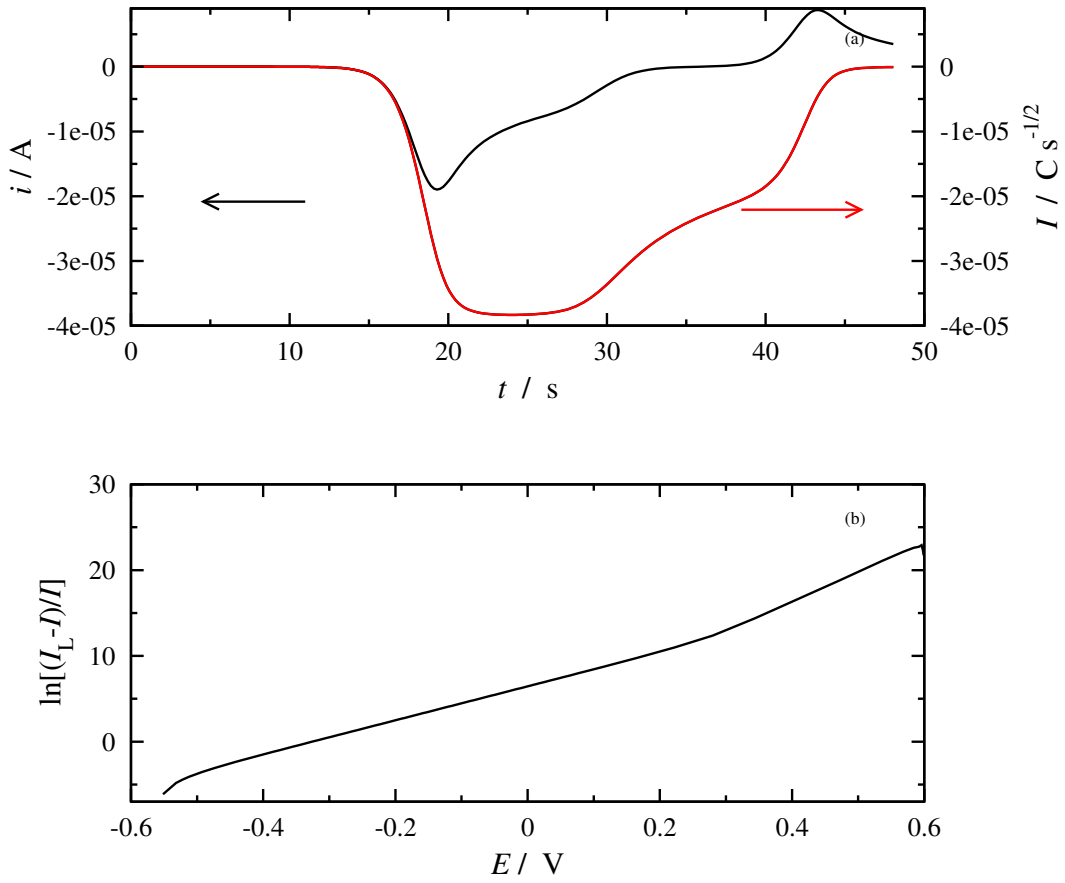

Figure 2.5.5: (a) Cyclic voltammogram (black) together with convolution current (red) for reversible kinetics and (b) ascertainment of Eq. (2.5.44). Parameters: $D_{\mathrm{A}} = 1 \times 10^{-9}$ m^2/s, $D_{\mathrm{B}} = 1.2 \times 10^{-9}$ m^2/s, $E^0 = 0$ V, $k^0 = 5 \times 10^{-8}$ m/s, $c^0 = 1$ mol/m^3, $a = 0.5$, $n = 1$ and $S = 1.257 \times 10^{-5}$ m^2.

equal to -3.274×10^{-5} C/s$^{1/2}$. From these values the resulting half-wave potential is 0.00247 V which is very close to the theoretical value 0.0023 V.

2.5.3 Phenomena affecting of convolution voltammetry

During the previous analysis, the current has been considered to be solely Faradaic due to the redox reaction of the electroactive species. However, the current monitored during a real time experiment is a sum of the Faradaic and a *capacitance current* as mentioned earlier,

$$i_{\mathrm{tot}}(t) = i(t) + i_{\mathrm{C}}(t)$$

where,

$$i_{\mathrm{C}} = C_{\mathrm{dl}} \frac{dE}{dt}$$

and C_{dl} the double layer capacitance, independent of the electrode potential E.

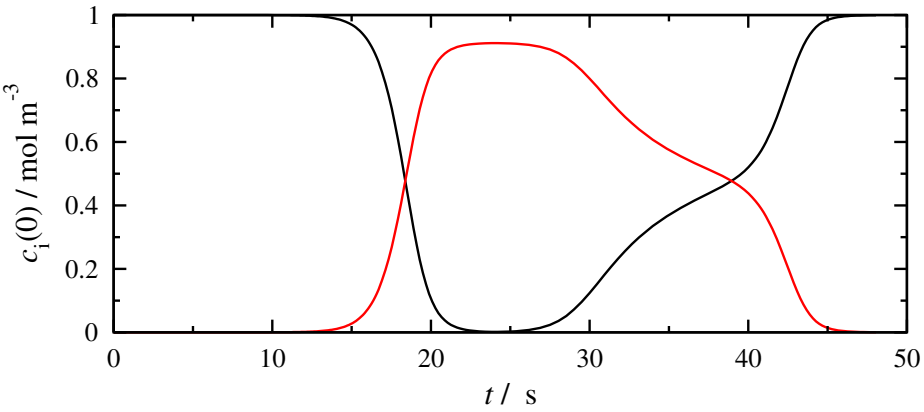

Figure 2.5.6: Surface concentrations as evaluated from convolution current for reversible kinetics.

In Fig. 2.5.9(a) the cyclic voltammogram of a quasi reversible reaction in the presence of capacitance currents is presented, together with the capacitance current (which can be monitored in an experiment in the absence of the redox species in the solution).

In the same figure the convolution current is presented. Now, comparing to Fig. 2.5.8 (b) one can observe a rather significant deviation of the convolution current in the presence of capacitance currents. More specifically, the limiting convolution current is impossible to be determined or even approximated.

A similar effect occurs for the case of the reversible and quasi reversible reaction. Consequently, the application of the relations that give the dependence of the convolution current from the potential is rendered quite impossible.

Thus, the experimental procedure that is prosposed in order to overcome this obstacle is the following

- First, a blank experiment shall be performed, in the absence of A and B, so that the capacitance current is monitored.
- Them, the same experiment under the same conditions shall be performed in the presence of the electroactive species in order to monitor the resulting current.
- The Faradaic current is then determined by subtracting the capacitance current from the total current.
- Finally, the convolution current shall be evaluated.

A common effect on a cyclic voltammogram and consequently on a convolution voltammogram, is that of *uncompensated resistance*, *i.e.* the potential drop between the working and the reference electrode.

In general this effect is considered to be eliminated in the case supporting electrolyte is present in a solution in a large enough concentration and when the reference electrode is really close to the working electrode. In the literature it is suggested that the concentration of the supporting electrolyte is 10 to 100 times greater than that of the analyte. Moreover, the use of Luggin capillary in the reference electrode is suggested.

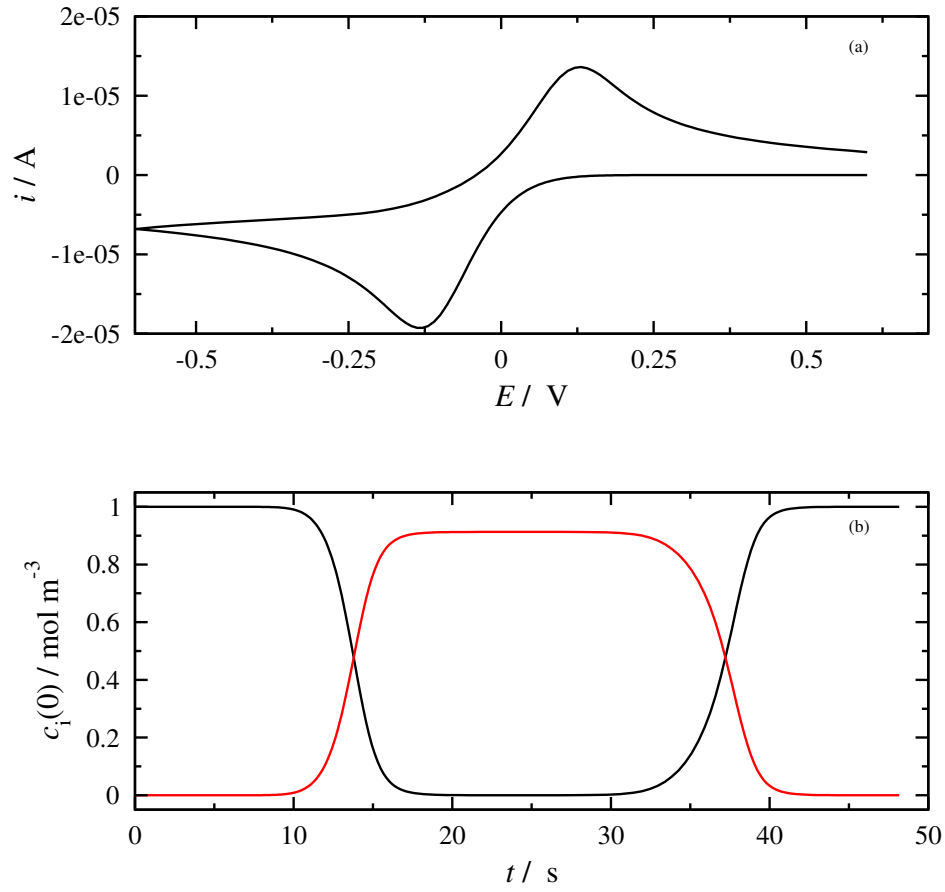

Figure 2.5.7: (a) Cyclic voltammogram and (b) surface concentrations of A (black) and B (red) for quasi reversible kinetics are a scan rate of 50 mV/s. Parameters:$D_{\mathrm{A}} = 1 \times 10^{-9}$ m^2/s, $D_{\mathrm{B}} = 1.2 \times 10^{-9}$ m^2/s, $E^0 = 0$ V, $k^0 = 5 \times 10^{-6}$ m/s, $c^0 = 1$ mol/m^3, $a = 0.5$, $n = 1$ and $S = 1.257 \times 10^{-5}$ m^2.

For the calculations of this section it has been considered that the chemical species A is a result of the complete dissociation of the species AC,

$$\mathrm{AC} \rightarrow \mathrm{A}^+ + \mathrm{C}^-$$

and that the supporting electrolyte DC is completely disdociated ,

$$\mathrm{DC} \rightarrow \mathrm{D}^+ + \mathrm{C}^-$$

Furthermore, for the redox reaction, it has been assumed that the chemical species A is reduced to a neutral specied B,

$$\mathrm{A}^+ + \mathrm{e} \rightarrow \mathrm{B}$$

Consequently, the ion concentrations are c_{A}^* c_{D}^*, and $c_{\mathrm{C}}^* = c_{\mathrm{A}}^* + c_{\mathrm{D}}^*$.

In order to get a better picture of the effect of the supporting electrolyte on a cyclic voltammogram, a distance between the working and the reference electrode of 5 mm

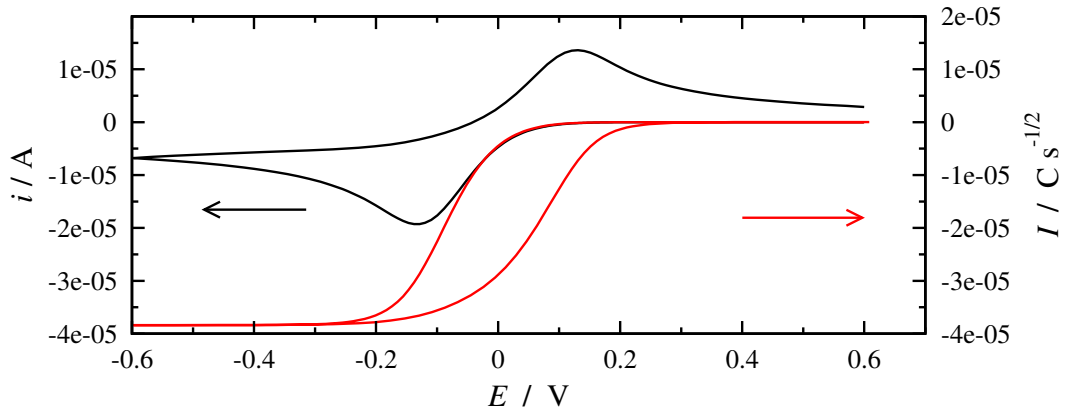

Figure 2.5.8: Cyclic voltammogram (black) together with convolution current (red) for quasi-reversible kinetics. Parameters: $D_A = 1 \times 10^{-9}$ m^2/s, $D_B = 1.2 \times 10^{-9}$ m^2/s, $E^0 = 0$ V, $k^0 = 5 \times 10^{-6}$ m/s, $c^0 = 1$ mol/m^3, $a = 0.5$, $n = 1$ and $S = 1.257 \times 10^{-5}$ m^2 .

shall be considered. The voltammograms are presented in Fig. 2.5.10 for supporting electrolyte concentrations of 0.1, 0.01 and 0.001 M, a surface area of 0.00785 cm^2 and a concentration of the analyte equal to 1×10^{-3} M. One can observe that the cyclic voltammogram for a supporting electrolyte concentration 100 times greater than the analyte is a satisfactory one. However, when the ratio of the electrolyte and the redox species becomes 10 the peaks start seperating and the magnitude of the peaks is decreased. This is due to the increase in the resistance between the working and the reference electrode as well as migration currents.[15] Finally when the concentration of the electrolyte is equal to that of the redox species under analysis, the voltammogram is fully distorted.

From this point on we shall consider a supporting electrolyte concentration of 0.1 M, and the effect of the position of the reference electrode shall be discussed (40, 20 and 5 mm). The cyclic voltammograms are presented in Fig. 2.5.11.

It can be observed that the magnitude of the distance between the reference and the working electrode the current values are lower and the peaks are shifted, while as the distance becomes smaller the voltammogram comes closer to the expected without the effect of uncompensated resistance.

In the presented example the diffusion coefficients of A and B are 1×10^{-5} cm^2/s, the electrode surface 0.00785 cm^2, the number of exchanged electrons is 1 while the charges of A and B are 1 and 0, while the charges of the ions of the supporting electrolyte are 1 and -1. Consequently the convolution limiting current is expected to be -2.39 μC/s$^{1/2}$. In Fig. 2.5.11 the convolution current is presented for the 3 cases. It can be observed tht the limiting current regardless of the magnitude of the uncompensated resistance effect remanins unchanged. However the shape of the potential dependent convolution

[15]Current due to the charge transport that is related to ions and the existence of potential gradient in the solution. To limit migrational transport of the ions that are components of the redox system examined in the cell, excess of supporting electrolyte is added to the solution [13].

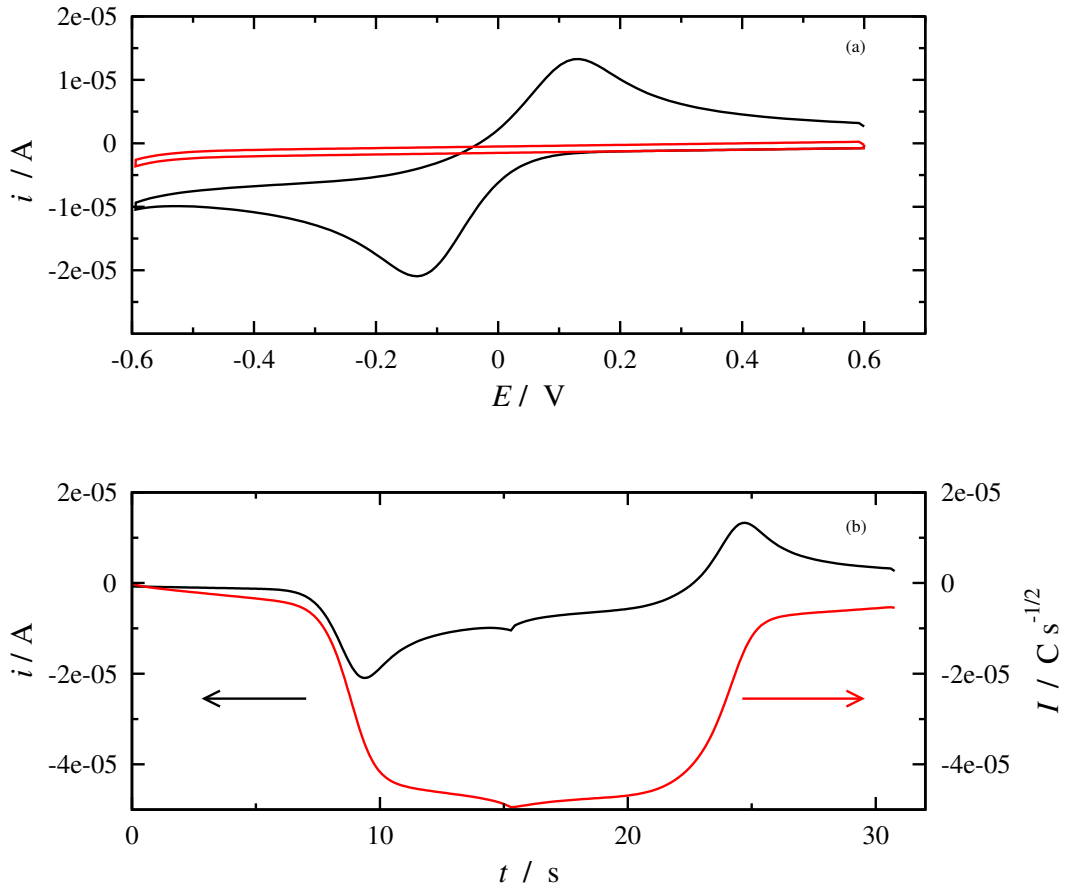

Figure 2.5.9: Effect of the capacitance. (a) Cyclic voltammogram and (b) convolution voltammogram of the redox species (balck) and capacitance current (red) for a scan rate of 50 mV/s. Parameters: $D_{\mathrm{A}} = 1 \times 10^{-9}$ m^2/s, $D_{\mathrm{B}} = 1.2 \times 10^{-9}$ m^2/s, $E^0 = 0$ V, $k^0 = 5 \times 10^{-6}$ m/s, $c^0 = 1$ mol/m^3, $a = 0.5$, $n = 1$ and $S = 1.257 \times 10^{-5}$ m^2.

current changes.

The correction of the uncompensated resistance is achievable in the case the resistance of the solution between the working and the reference electrode is known. In the present example, the specific conductivity of the electrolyte is

$$\bar{\sigma} = F^2 \sum_{k=1}^{3} z_k^2 c_k \frac{D_k}{RT} = 0.7586 \ \ \mathrm{S/m}$$

Consequently the resistance between the working and the reference electrode is,

$$R_\Omega = \frac{l}{A\bar{\sigma}} = 1.679 \times 10^6 \cdot l$$

where l is the distance expressed in m.

Thus the resistance shall be equal to 8.397×10^3, 3.359×10^4 and 6.717×10^4 Ω, for distances 5, 20 and 40 mm, respectively. The real eelctrode potential results from the

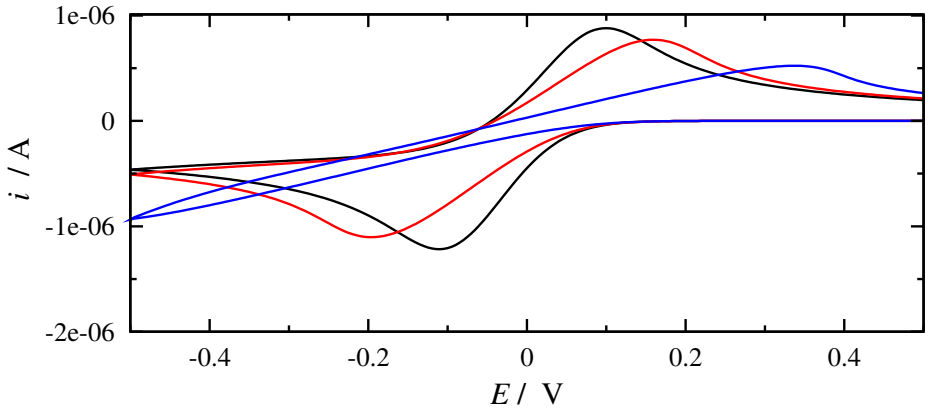

Figure 2.5.10: Effect of the supporting electrolyte concentration on a cyclic voltammogram of a quasi reversible reaction for a distance of 5 mm between the reference electrode and the working electrode, analyte concentration 1×10^{-3} M and electrode surface 0.00785 cm^2. Supporting electrolyte concentrations: 0.1 (black), 0.01 (red) and 0.001 M (blue).

following equation,

$$E = E_{\text{vs.ref}} - i \cdot R_{\Omega}$$

In Fig. 2.5.12 the corrected cyclic voltammograms are presented. One can see that the potential values where the peak potential values are the same. Moreover, the correction makes up for the peak potential values only and not for the magnitude of the peaks, which remains downgraded and the distance between the electrode increases.

In Fig 2.5.12 (b) one can find the convolution current resulting from the analysis of the aforementioned corrected. The slopes nod seem to bear a stronger similarity thatn before, but still a better approximation than before the correction.

Now the theoretical calculation of the solution resistance is usually inaccurate as the exact distances and the real diffusion coefficients are not known. The resistance value however can be determined with precision by using Electrochamical Impedence Spectrosopy (EIS), a subject that is not going to be addressed here however.

Another factor that shall be examined and affects both the cyclic voltammograms and the convolution analysis is the *electrode geometry*. In Fig. 2.5.13 the concentration and current distributions are presented for the cases of a disc electrode of different radii - 0.5, 2 and 8 mm. It is visible that the smaller the electrode, the more we cannot reach the case where the electrode surface is uniformly accessible by ions, as a contribution of the currents in the axial direction is observed as well. This means that the error in the assumption of an 1 dimensional problem becomes larger.

The effect of the electrode radius on a cyclic voltammograms is visible in Fig. 2.5.14 (a), for an irreversible reaction. It is worth to notice the deformation as well as the increase in the current density as the electrode surface becomes smaller. In Fig. 2.5.14(b) the respective convolution currents are observed, where it is obvious that the limiting convolution current can be determined only for the larger electrode where the approximation of an one-dimensional problem is satisfied better.

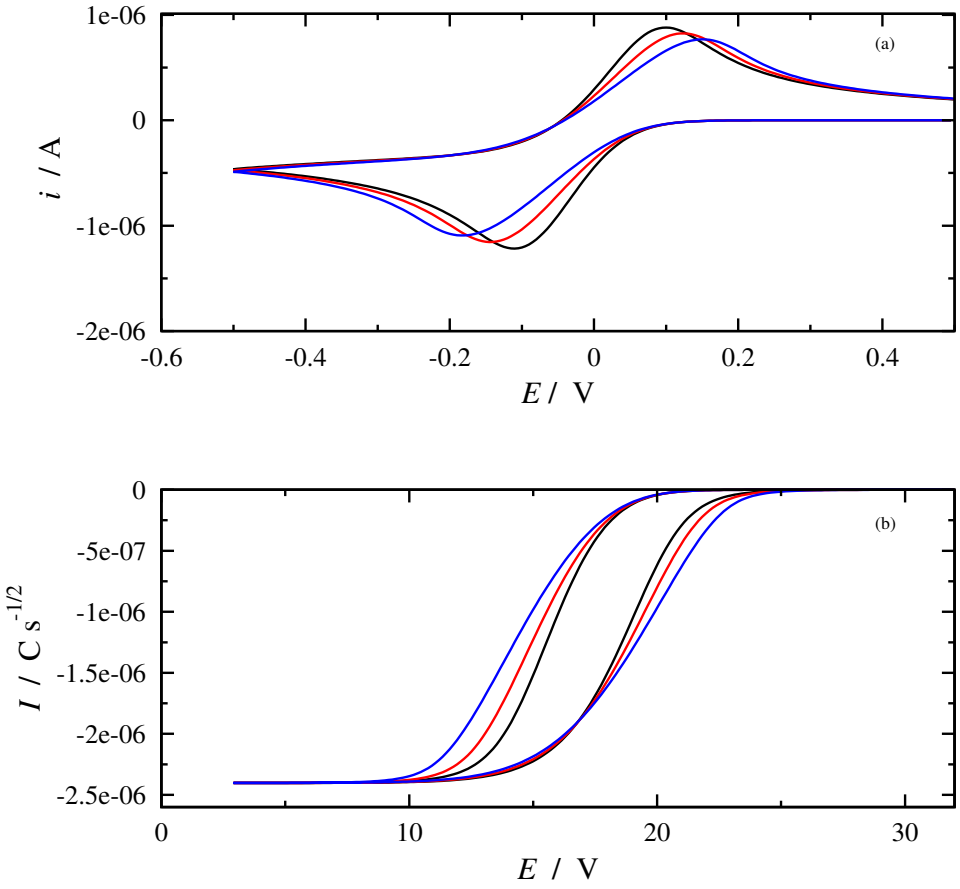

Figure 2.5.11: Effect of the distance between working and reference electrodes of a quasi reversible reaction for an analyte concentration 1×10^{-3} M, supporting electrolyte concentration 0.1 M and electrode surface 0.00785 cm^2. Electrode distance values: 5 (black), 20 (red) and 40 mm (blue).

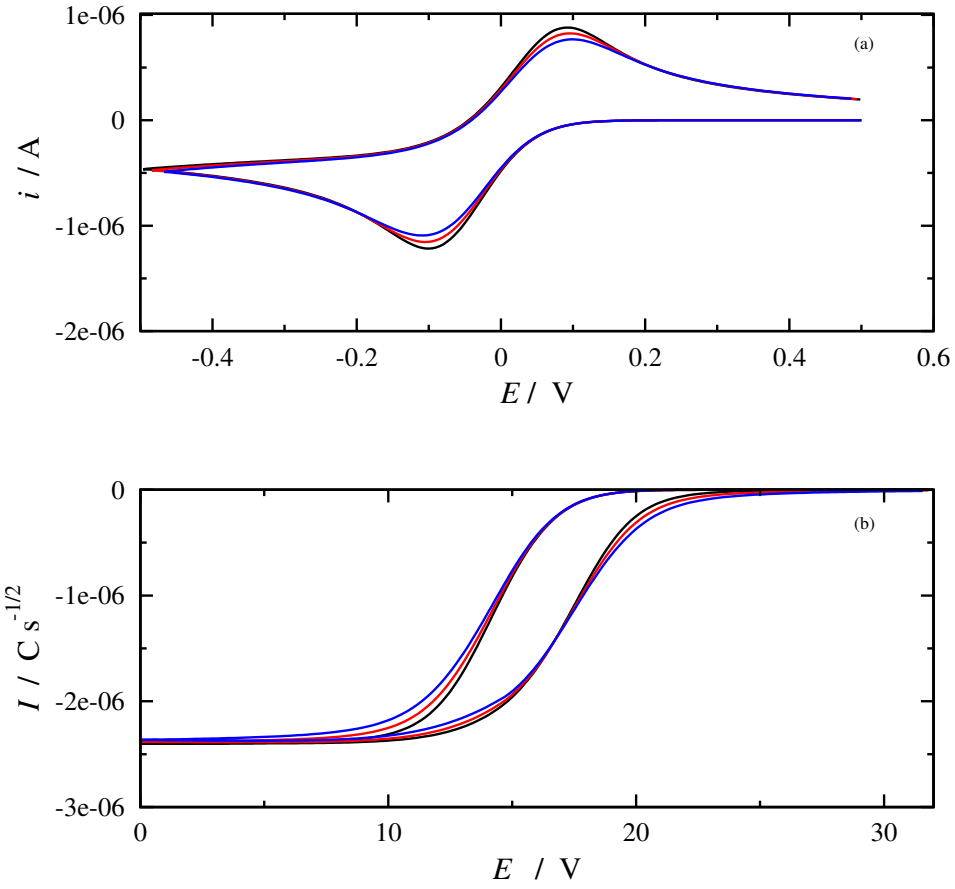

Figure 2.5.12: Cyclic voltammograms corrected for the uncompensated resistance for a quasi reversible reaction for an analyte concentration 1×10^{-3} M, supporting electrolyte concentration 0.1 M and electrode surface 0.00785 cm^2. Electrode distance values: 5 (black), 20 (red) and 40 mm (blue).

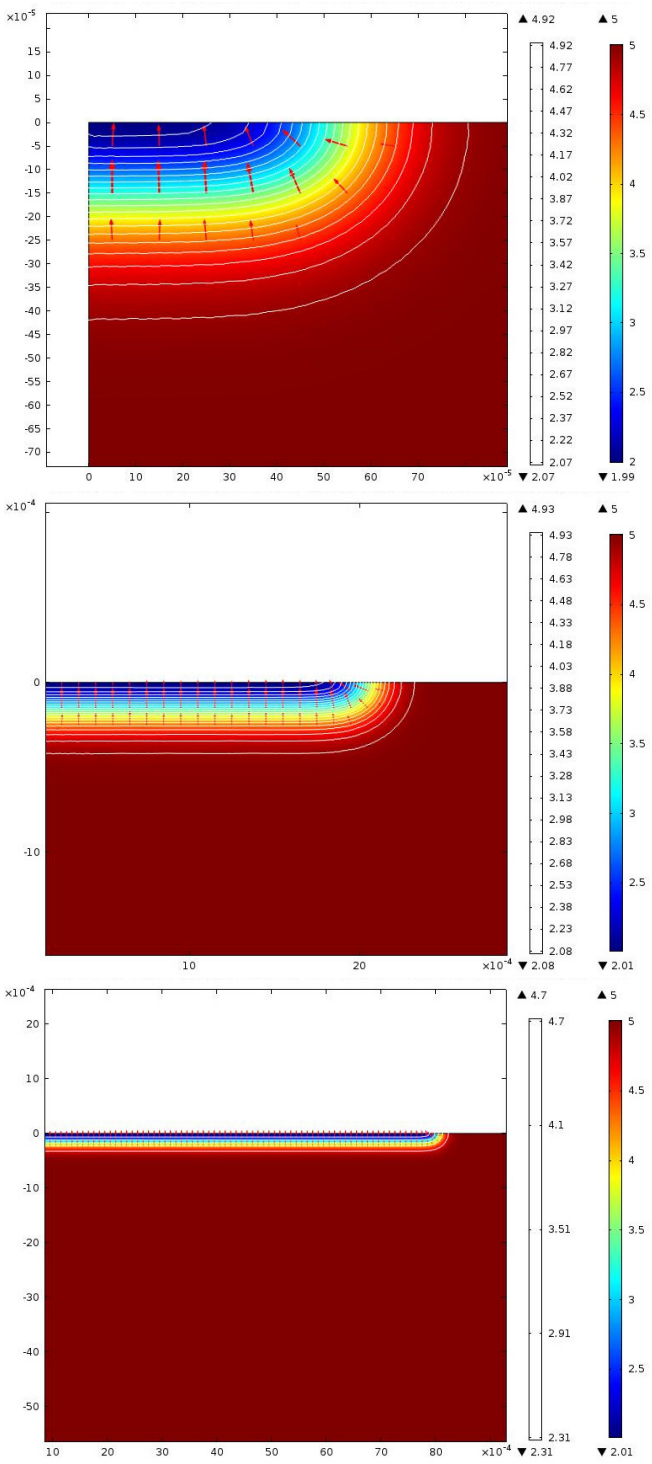

Figure 2.5.13: Spatial concentration distributions and ionic currents around an electrode surface for electrode radius of 0.5, 2 and 8 mm. The color legend refers to the concentration and the arrows to the ionic currentss.

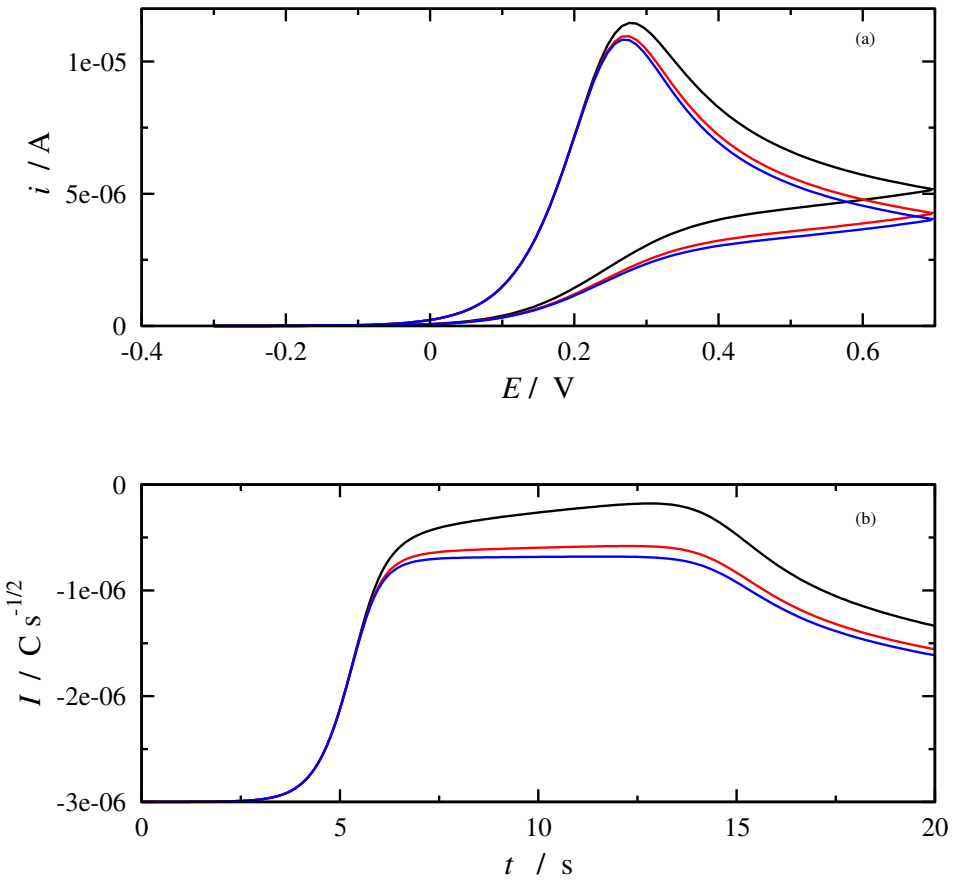

Figure 2.5.14: (a) Cycliv voltammograms and (b) Convolution current for an irreversible electrochemical reaction for different electode radii of a disc electrode surface. Radii values: 0.5, 2 and 8 mm.

2.5.4 Sequential and multistep reactions

At this point, we shall examine what happens with convolution voltammetry in sequential and multistep elelctrochemical reactions.

In the following examples it has been assumed that:

- The solution contains sufficient electrolyte so that the electromigration and the uncompensated resistance are eliminated
- The capacitance current has been subtracted
- Uncompensated resistance has been corrected
- The electrode is sufficiently large so that the effects of radial contribution can be ignored.

The kinetic scenario that will accompany us in this section is the following,

$$\mathrm{A} + \mathrm{e} \underset{k_{-1}}{\overset{k_1}{\rightleftharpoons}} \mathrm{R}$$
$$\mathrm{R} + \mathrm{e} \underset{k_{-2}}{\overset{k_2}{\rightleftharpoons}} \mathrm{B}$$

where k_i are the potential dependent kinetic constants.

In the case where the intermediate R is detectable experimentally the above scenario expresses 2 different subsequent electrochemical reactions, while when it is not detectable, it expresses the following reaction mechanism,

$$\mathrm{A} + 2\mathrm{e} \underset{k_{\mathrm{a}}}{\overset{k_{\mathrm{c}}}{\rightleftharpoons}} \mathrm{B}$$

where k_{c} and k_{a} are the apparent potential dependent kinetic constants which are defined by the k_i in a way that depends on their relative values. We shall come back to this point later on.

To get a better understanding of the difference between successive reactions and multi-step reactions in cyclic voltammetry we need to map the possible cyclic voltammograms in every case. In the following scenarios examined the parameters that have been assumed are $D_{\mathrm{A}} = 1 \times 10^{-9}$ m^2/s, $D_{\mathrm{R}} = 1.3 \times 10^{-9}$ m^2/s, $D_{\mathrm{B}} = 1.2 \times 10^{-9}$ m^2/s and transfer coefficient for both cases $a = 0.5$. Moreover, the potential is scanned linearly from $E_{\mathrm{I}} = 0.8$ V to $E_{\mathrm{R}} = -0.8$ V (cathodic scan) and the other way around during the respective anodic scan. For each step we shall consider that the current is given rom the following equations

$$i_1 = AFk_1^0(c_{\mathrm{R}} e^{\frac{(1-a)F}{RT}(E-E_1^0)} - c_{\mathrm{A}} e^{-\frac{aF}{RT}(E-E_1^0)}) \tag{2.5.47}$$
$$i_2 = AFk_2^0(c_{\mathrm{B}} e^{\frac{(1-a)F}{RT}(E-E_2^0)} - c_{\mathrm{R}} e^{-\frac{aF}{RT}(E-E_2^0)}) \tag{2.5.48}$$

where the concentrations are the ones on the electrode surface. The surface of the electrode is A. It is obvious that Butler-Volmer law has been assumed,

$$\begin{aligned} k_1(E) &= k_1^0 e^{-\frac{aF}{RT}(E-E_1^0)} \\ k_{-1}(E) &= k_1^0 e^{\frac{(1-a)F}{RT}(E-E_1^0)} \\ k_2(E) &= k_2^0 e^{-\frac{aF}{RT}(E-E_2^0)} \\ k_{-2}(E) &= k_2^0 e^{\frac{(1-a)F}{RT}(E-E_2^0)} \end{aligned} \tag{2.5.49}$$

where E_1^0 and E_2^0 are the formal electrode potentials of each step. Since the individual reactions express the mechanism of the whole reaction the formal potential is given by Luther's law,

$$E^0 = \frac{E_1^0 + E_2^0}{2}$$

given that for the whole reaction $n = 2$, while for the individual ones $n_1 = n_2 = 1$. Moreover, if the individual reactions express the steps of the whole reaction the total current shall be expressed by the following expression,

$$i = 2Fk^0(c_{\mathrm{B}} e^{\frac{b_{\mathrm{a}}F}{RT}(E-E^0)} - c_{\mathrm{A}} e^{\frac{-b_{\mathrm{c}}F}{RT}(E-E^0)})$$

where both k^0 and b_{a}, b_{c} depend on the relative values of k_i. We shall get back to this point later on. If the individual reactions express just two successive reactions, then the current shall be expressed as $i = i_1 + i_2$.

In Fig. 2.5.15(a) the case where the kinetic constants are equal - $k_1^0 = k_2^0 = 1 \times 10^{-6}$ m/s - and $E_1^0 = 0.4$ V, $E_2^0 = 0.2$ V is presented.[16] For a large scan rate of 500 mV/s two cathodic and two anodic peaks occur. In this case the kinetics for both the first and the second reaction are irreversible. As the scan rate lowers the kinetics of both reactions tend towards quasi-reversibility and for the lowest scan rate examined, that is 0.1 mV/s, the kinetics of both reactions can be characterized as reversible.

The cyclic voltammograms presented in Fig. 2.5.15(a) reveal two successive electrochemical reactions and not a multi-step one. If one observes closely the scanning the intermediated R resulting from the reduction of A (first cathodic peak), is reduced to B (second cathodic peak). Moreover, the intermediate R that is produced during the oxidation of B (first anodic peak) is oxidized again to A (second anodic peak).

The fact that the intermediate R is detectable can be be shown by taking a look at the surface concentration profiles in Fig. 2.5.15(b) where the surface concentration profiles of all the species is presented for a scan rate of 10 mV/s.[17] It is obvious that for these values of kinetic constants and scan rates, the life time of the intermediate is rather considerable as the concentration reaches high values during the potential scan.

For the analysis of the voltammograms in Fig. 2.5.15(a) several paths can be considered. According to the theory of cyclic voltammetry since the kinetics are not reversible,

[16] In this Figure the current is normalized with the square root of the scan rate for reasons of visualization

[17] For comparison reason the time is the x-axis is the dimensionless one $\tau = tvF/RT$.

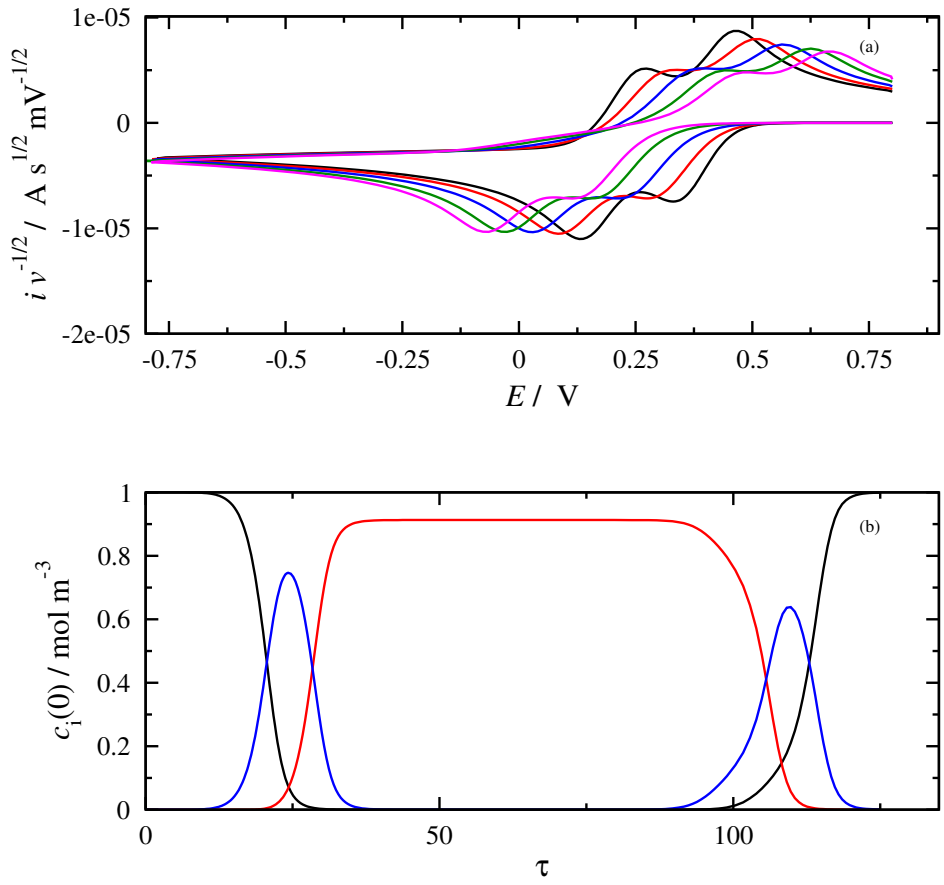

Figure 2.5.15: Sequential reactions. (a)Cyclic voltammograms normalized with the square root of the scan rate for $k_1^0 = k_2^0 = 1 \times 10^{-6}$ m/s, $E_1^0 = 0.4$ V, $E_2^0 = 0.2$ V at different scan rate values. 0.1 (black), 1 (red), 10 (blue) 100 (green) and 500 mV/s (magenta) (b) Surface concentration of A (black), B(red) and R (blue) for $v = 10$ mV/s.

the dependence on the potential is a function of the scan rate according to the following equation,

$$E_{\mathrm{pc},i} = E_i^0 - 0.78\frac{RT}{a_i F} + \frac{RT}{a_i F}\ln k_i^0 \sqrt{\frac{RT}{a_i F D}} + \frac{RT}{a_i F}\ln v^{-1/2}$$

Consequently, a diagram of the peak potential of an action versus the logarithm of the inverse scan rate has to be linear. From this slope the transfer coefficient.Then, for a known transfer coefficient , in general one can calculate the kinetic constant of the respective reaction can be calculated. this however requires knowing of the formal potential and diffusion coefficient.

In another approach if convolution is applied, the transfer coefficient can be easily extracted. After the convolution current is calculated, and I_{L} is determined, the $\ln \frac{I_{\mathrm{L}}-I}{i}$ diagram is designed. From the slopes of this diagram the respective transfer coefficients result.

In Fig. 2.5.16(a) one can find the currents together with the respective convolution currents for scan rates of 1 and 100 mV/s normalized with the electrode surface. It

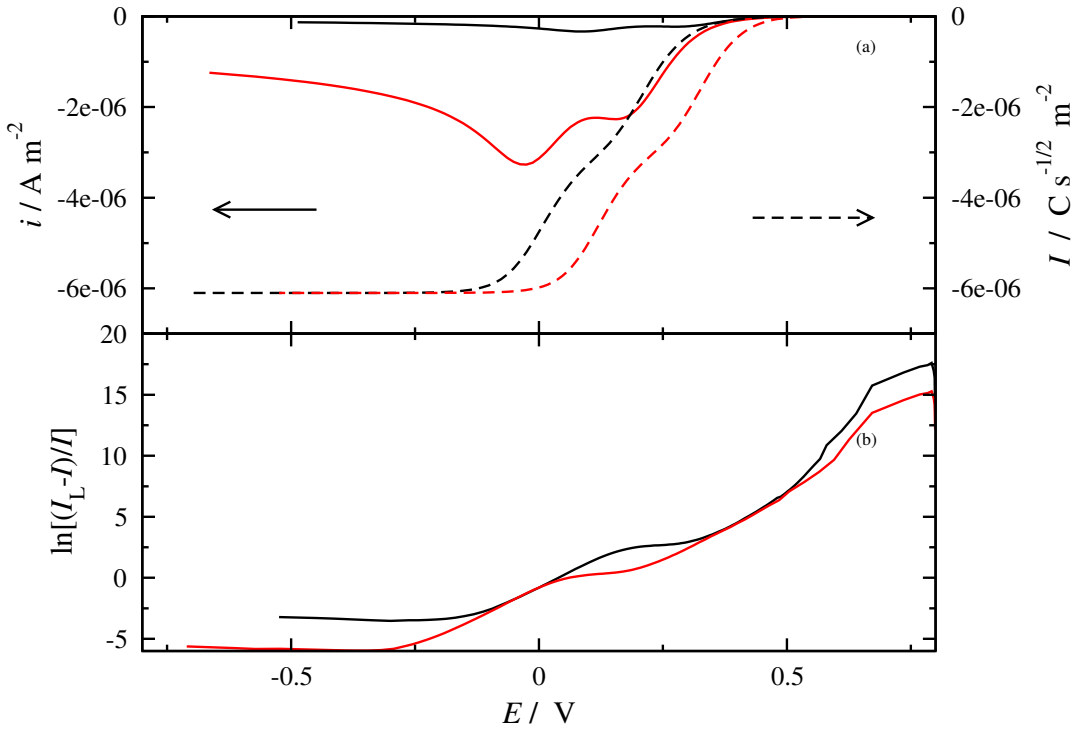

Figure 2.5.16: Sequential reactions. (a)Cyclic voltammograms (full lines) and convolution current (dashed lines) for $k_1^0 = k_2^0 = 1 \times 10^{-6}$ m/s, $E_1^0 = 0.4$ V, $E_2^0 = 0.2$ V at different scan rate values (b) Diagrams for the estimation of a. Scan rates examined: 1 (black) and 100 mV/s (red).

is noticeable that the limiting convolution current has a value of -6.1 C/s$^{1/2}$m^2. This value is the same as the theoretical one,

$$I_{\mathrm{L}} = nF\sqrt{D_{\mathrm{A}}}c^0 = 2 \times 96485 \times \sqrt{10^{-9}} \times 1 = -6.1 \quad \mathrm{C/s^{1/2}m^2}$$

It is also observable that the convolution current ahs a "step— which corresponds to the existence of two seperate cathodic peaks in the voltammograms.

Now in Fig. 2.5.16(b) the dependence of $\ln \frac{I_{\mathrm{L}}-I}{I}$ against the potential is presented. Two linear regions can be found with the more anodic one reflecting the first reaction while the more cathodic one the second. The calculated slope for the first reaction is 22 while for the second 20.3 (the theoretical one is 19.46).

If the procedure introduced in the quasi reversible case, one can calculate the half wave potential of the second reaction - an approximation for E_2^0 that is. From the cyclic voltammogram one can conclude that $E(i = 0) \approx 0.18$ V and from the convolution current $I(i = 0) \approx -5.3$ C/s$^{1/2}$m^2. From the aforementioned values we get that $E_{1/2,2} \approx 0.2$ V.

Now let's continue the analysis of the same kinetic scenario considering that the intermediate is not detectable - its concentration remains practically zero during the measurement. Moreover, we shall consider that its concentration is very small and practically remains unchanged in time (in comparison to the concentrations of A and

B),

$$\frac{dc_{\mathrm{R}}}{dt} \approx 0 \tag{2.5.50}$$

Under these assumptions, the two-step reaction is under steady state conditions, *i.e.* the rate of the first step is equal to that of the second one.This becomes obvious in the case the kinetic law for the intermediate is written,

$$\frac{dc_{\mathrm{R}}}{dt} = r_1 - r_2 \tag{2.5.51}$$

thus, using Eq. (2.5.50),

$$r_1 = r_2 \tag{2.5.52}$$

where r_i is the rate of its step. From Eq. (2.5.52), we have,

$$k_1(E)c_{\mathrm{A}} - k_{-1}(E)c_{\mathrm{R}} = k_2(E)c_{\mathrm{R}} - k_{-2}(E)c_{\mathrm{B}} \tag{2.5.53}$$

consequently the concentration of the intermediate R at each time shall be,

$$c_{\mathrm{R}} = \frac{k_1(E)}{k_{-1}(E) + k_2(E)}c_{\mathrm{A}} + \frac{k_{-2}(E)}{k_{-1}(E) + k_2(E)}c_{\mathrm{B}} \tag{2.5.54}$$

Substituting the expression of c_{R} in the expression of the rate of either the first or the second step the reaction rate that occurs under steady state is

$$r = r_1 = r_2 = \frac{k_1(E)k_2(E)}{k_{-1}(E) + k_2(E)}c_{\mathrm{A}} - \frac{k_{-1}(E)k_{-2}(E)}{k_{-1}(E) + k_2(E)}c_{\mathrm{B}} \tag{2.5.55}$$

But from Faraday's law we have that $i = -nAFr$, thus for the Faradaic current and $n = 2$),

$$i = 2AF[k_{\mathrm{a}}(E)c_{\mathrm{B}} - k_{\mathrm{c}}(E)c_{\mathrm{A}}] \tag{2.5.56}$$

where the apparent kinetic constants are given from the following expressions,

$$k_{\mathrm{a}}(E) = \frac{k_{-1}(E)k_{-2}(E)}{k_{-1}(E) + k_2(E)} \tag{2.5.57}$$

$$k_{\mathrm{c}}(E) = \frac{k_1(E)k_2(E)}{k_{-1}(E) + k_2(E)} \tag{2.5.58}$$

The following cases are distinguished,

- If $k_{-1}(E) \gg k_2(E)$ then for the rate we have,

$$r = \frac{k_1(E)k_2(E)}{k_{-1}(E)}c_{\mathrm{A}} - k_{-2}(E)c_{\mathrm{B}} = K_1(E)k_2(E)c_{\mathrm{A}} - k_{-2}(E)c_{\mathrm{B}} \tag{2.5.59}$$

  where $K_1 = k_1/k_{-1}$. One can observe that the rate depends only on the kinetic constants of the second step. in this case, the second step is the one determining the rate.

  The current shall be given by the expression,

$$i = 2SF[k_{-2}(E)c_{\mathrm{B}} - K_1(E)k_2(E)c_{\mathrm{A}}] \tag{2.5.60}$$

  From the above equation and the Eq. (2.5.49) one can understand that:

– The apparent anodic kinetic constant is k_{-2},

$$k_{\mathrm{a}}(E) = k_2^0 e^{\frac{(1-a)F}{RT}(E-E_2^0)}$$

meaning that if the second step is the rate determining and the anodic exponent b_{a} will be,

$$b_{\mathrm{a}} = \frac{(1-a)F}{RT} = 38.92 \times (1-a)$$

at 298.15 K. For $a = 0.5$ the value of the exponent is 19.46.

– The apparent cathodic kinetic constant is $K_1 k_2$,

$$k_{\mathrm{c}}(E) = \frac{k_1^0 e^{-\frac{aF}{RT}(E-E_1^0)} k_2^0 e^{-\frac{aF}{RT}(E-E_2^0)}}{k_1^0 e^{\frac{(1-a)F}{RT}(E-E_1^0)}} = k_2^0 e^{-\frac{F}{RT}[(1+a)E - aE_2^0 - E_1^0]}$$

Using Luther's law, the above correlation becomes,

$$k_{\mathrm{c}}(E) = k_2' e^{-\frac{(1+a)F}{RT}(E-E^0)}$$

where k_2' is given by the expression,

$$k_2' = k_2^0 e^{-\frac{F}{RT}(aE^0 - 0.5E_1^0)}$$

meaning that if the second step is the rate determining one, the cathodic exponent b_{c} shall be,

$$b_{\mathrm{c}} = \frac{(1+a)F}{RT} = 38.92 \times (1+a)$$

at 298.15 K. For $a = 0.5$ the value of the exponent is 58.38.

- If $k_{-1}(E) \ll k_2(E)$ then what is valid for the rate is,

$$r = k_1(E)c_{\mathrm{A}} - \frac{k_{-1}(E)k_{-2}(E)}{k_2(E)}c_{\mathrm{B}} = k_1(E)c_{\mathrm{A}} - K_2(E)k_{-1}(E)c_{\mathrm{B}} \tag{2.5.61}$$

where $K_2 = k_{-2}/k_2$. One can observe that the rate depends only on the kinetic constants of the first step. In this case the first step is the rate determing one.

The current shall be given by the expression,

$$i = 2AF[K_2(E)k_{-1}(E)c_{\mathrm{B}} - k_1(E)c_{\mathrm{A}}] \tag{2.5.62}$$

From the above expression and Eq. (2.5.49) one can conclude that:

– the apparent anodic kinetic constant is $K_2 k_{-1}$,

$$k_{\mathrm{a}}(E) = \frac{k_2^0 e^{\frac{(1-a)F}{RT}(E-E_2^0)} k_1^0 e^{\frac{(1-a)F}{RT}(E-E_1^0)}}{k_2^0 e^{-\frac{aF}{RT}(E-E_2^0)}} = k_1^0 e^{\frac{F}{RT}[(2-a)E - E_1^0 + aE_1^0 - E_2^0]}$$

Using Luther's law the above expression can be written as follows,

$$k_{\mathrm{a}}(E) = k_1' e^{\frac{(2-a)F}{RT}(E-E^0)}$$

where the constant k_1' is given by the expression,

$$k_1' = k_1^0 e^{-\frac{aF}{RT}(E^0 - E_1^0)}$$

This means that if the first step is the rate determining one, the anodic exponent b_{a} shall be,

$$b_{\mathrm{a}} = \frac{(2-a)F}{RT} = 38.92 \times (2-a)$$

at 298.15 K. For $a = 0.5$ the value of the exponent is 58.38.

– The apparent cathodic kinetic constant is k_1,

$$k_{\mathrm{c}}(E) = k_1^0 e^{-\frac{aF}{RT}(E-E_1^0)}$$

This means that if the first step is the rate determining one, the cathodic exponent b_{c} shall be,

$$b_{\mathrm{c}} = \frac{aF}{RT} = 38.92 \times a$$

at 298.15 K. For $a = 0.5$ the value of the exponent is 19.46.

At this point one important point needs to be made. As already mentioned, the relative values of $k_{-1}(E)$ and $k_2(E)$ are responsible for the rate determining step. However, in a voltammetric experiment the values of $k_{-1}(E)$ and $k_2(E)$ are determined by the by the potential value as it is scanned linearly in time. This means that the rate determining step is not defined solely by the values of k_1^0 and k_2^0 but from the values that $k_{-1}(E)$ and $k_2(E)$ get for every potential value. In other words during an experiment the relation of these constants can be kept (e.g. $k_{-1}(E)$ remains always smaller than $k_2(E)$) or change (e.g. for a potential window $k_{-1}(E)$ is greater than $k_2(E)$ and in another region smaller). The analysis of the anodic and cathodic exponents and their dependence from the potential can reveal a possible change in the mechanism in a potential region.

Another point that is worth mentioning is the following. Assuming a reduction is studied, this means we start from a solution containing only A and we scan towards negative potential values. However, $k_{-1}(E)$ is the oxidation kinetic constant of R and is given by the expression,

$$k_{-1}(E) = k_1^0 e^{\frac{(1-a)F}{RT}(E-E_1^0)}$$

Consequently we can expect that as the potential E becomes more negative, $k_{-1}(E)$ decreases constantly. On the other hand, $k_2(E)$ is the reduction kinetic constant of R towards B and is given by the expression,

$$k_2(E) = k_2^0 e^{-\frac{aF}{RT}(E-E_2^0)}$$

Consequently, we expect that as the potential E becomes more negative, $k_2(E)$ constantly increases. Thus, one would expect that during the cathodic scan $k_2(E) \gg k_{-1}(E)$ is always valid, meaning that the 1st step is always the rate determining one.

However, it should be noted that the values of $k_{-1}(E)$ and $k_2(E)$ are not determined by the value of E but from the difference $E - E_i^0$. Thus, if the formal potential of the second step is more anodic than that of the first one, it is possible that $k_{-1}(E) \gg k_2(E)$, at least in a potential range. The different cases shall be discussed in the examples that follow.

In Fig. 2.5.17 the diagrams for $k_1^0 = 10^{-8}$ m/s, $k_2^0 = 10^{-5}$ m/s, $E_1^0 = 0.2$ V, $E_2^0 = 0.1$ V are presented. One can observe that during the cathodic scan the voltammogram appears to have only one irreversible peak at about -0.3 V. From the surface concentration diagrams the reaction seems to be under steady state conditions during the cathodic scan as the concentration of the intermediate R is very small and constant comparably to the ones of the species A and B for the first 32 s. From the diagram of the dependencies of $k_{-1}(E)$ and $k_2(E)$ from the potential, it can be concluded that during the current increase of the reduction peak $k_{-1}(E) \ll k_2(E)$. Consequently the first step is the rate determining one. Since the first one is the rate determining step, the cathodic exponent should be $b_c = aF/RT \approx 19.8$ at 293.15 K, when a is 0.5. The slope analysis can be found in Fig. 2.5.17 (c) where it is estimated that the slope of $\ln \frac{I_L - I}{i}$ against potential is 20.458, really close to the theoretically expected one.

In Fig. 2.5.17 the diagrams for $k_1^0 = 10^{-3}$ m/s, $k_2^0 = 10^{-6}$ m/s, $E_1^0 = -0.4$ V, $E_2^0 = 0.3$ V are presented. One can observe again that in the cathodic scan of the cyclic voltammogram only one irreversible peak appears at about -0.35 V. From the surface concentration diagrams steady state can be ascertained as the concentration of the intermediate E is very small and stable in comparison to the concentrations of A and B.

From the diagram that concerns the dependencies of $k_{-1}(E)$ and $k_2(E)$ from the potential, it can be concluded that almost in the whole region of current increase of the cathodic peak $k_{-1}(E) \gg k_2(E)$. Consequently the second step is the rate determining one.

Since the second step is the rate determining, the cathodic exponent should be$b_c = (1 + a)F/RT \approx 58$ at 298.15 K, since a is 0.5. The analysis of the slope in Fig. 2.5.17 (b) of $\ln \frac{I_L - I}{I}$ against the potential is 54.151, very close to the theoretical one.

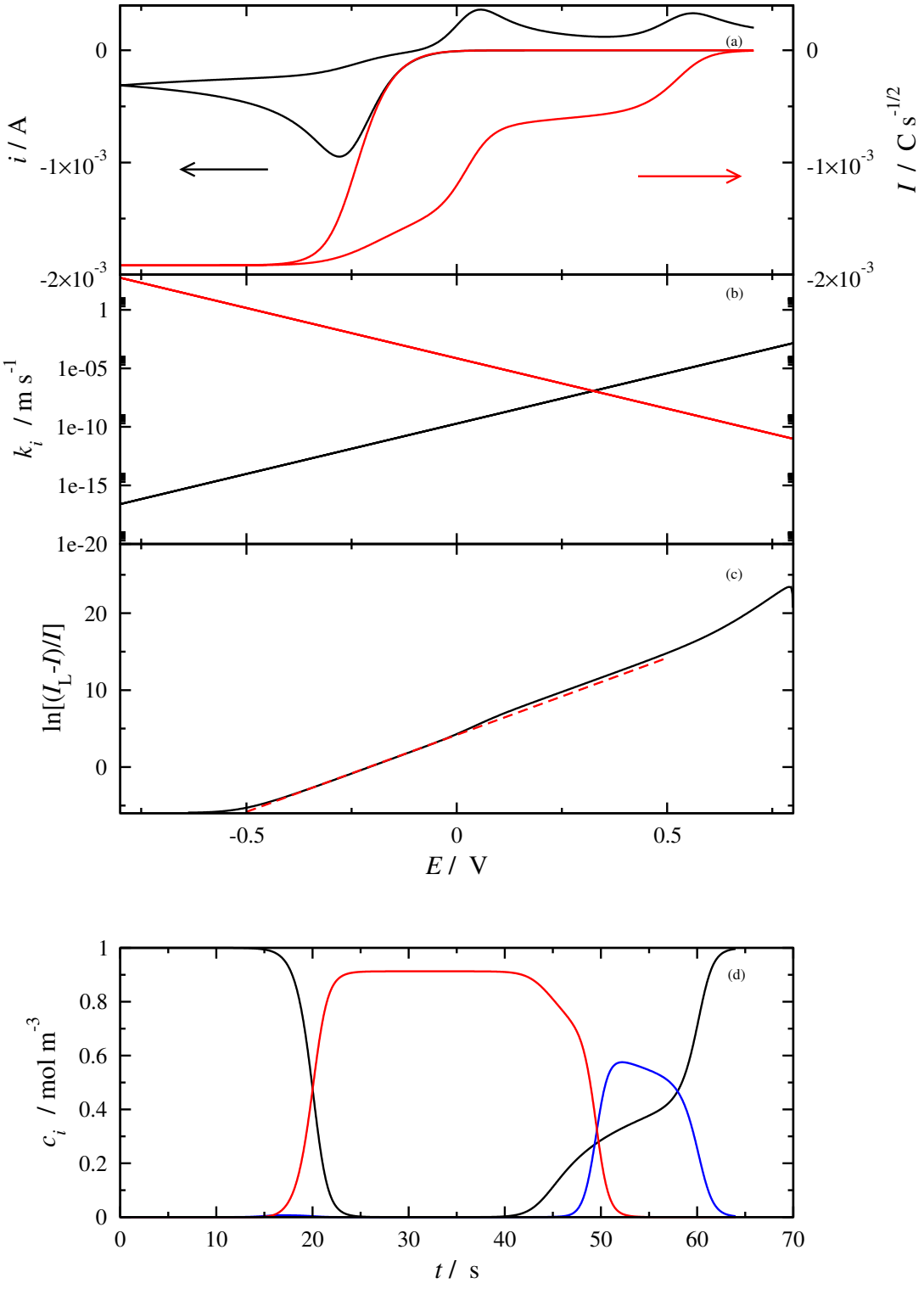

Figure 2.5.17: (a) Cyclic voltammogram (black) and the respective convolution current (red) of a multistep reaction. (b) Kinetic constants k_1 (black) and k_2 (red) for the same reaction (c) Dependence of $\ln \frac{I_L - I}{I}$ against the potential (d) Surface conentrations profile. c_A (black), c_A (red) and c_R (blue). and Parameter values: $k_1^0 = 10^{-8}$ m/s, $k_2^0 = 10^{-5}$ m/s, $E_1^0 = 0.2$ V, $E_2^0 = 0.1$ V.

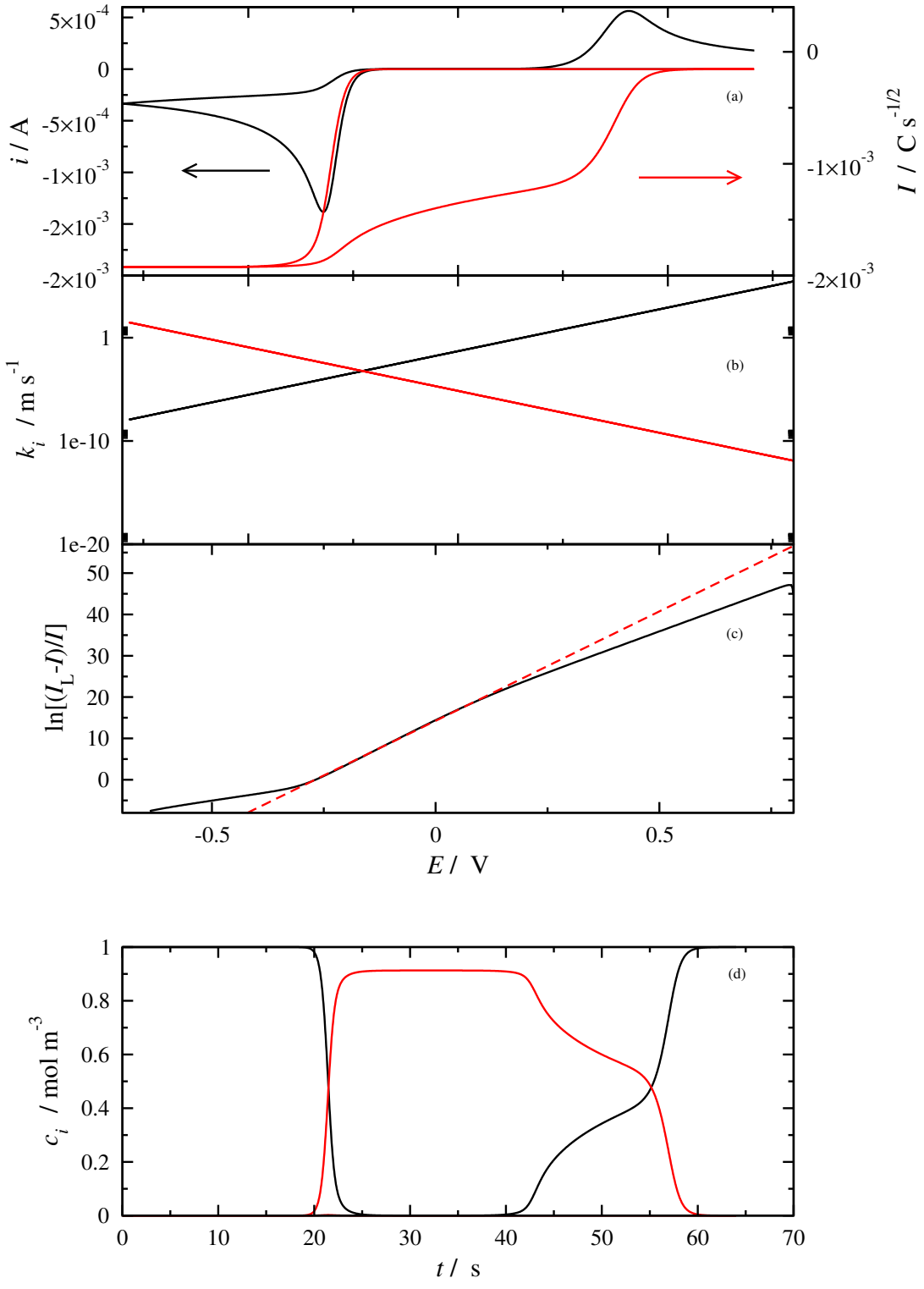

Figure 2.5.18: (a) Cyclic voltammogram (black) and the respective convolution current (red) of a multistep reaction. (b) Kinetic constants k_1 (black) and k_2 (red) for the same reaction (c) Dependence of $\ln \frac{I_L - I}{I}$ against the potential (d) Surface concentrations profile. c_A (black), c_A (red) and c_R (blue). and Parameter values: $k_1^0 = 10^{-3}$ m/s, $k_2^0 = 10^{-6}$ m/s, $E_1^0 = -0.4$ V, $E_2^0 = 0.3$ V.

Bibliography

[1] B. Ermentrout. *Simulating, analyzing, and animating dynamical systems: a guide to XPPAUT for researchers and students*. SIAM, 2002.

[2] L. Meites, P. Zuman, and H.W. Nurnberg. Recommended terms, symbols, and definitions for electroanalytical chemistry (recommendations 1985). *Pure Appl. Chem.*, 57(10):1491–1505, 1985.

[3] A. Ševčik. Oscillographic polarography with periodical triangular voltage. *Collect. Czech. Chem. Commun.*, 13:349–377, 1948.

[4] H. Matsuda and Y. Ayabe. Zur theorie der Randles-Sevčikschen kathodenstrahl-polarographie. *Z. Elektrochem.*, 59:494–503, 1955.

[5] Ch. G. Bell, C. A. Anastassiou, D. O'Hare, K. H. Parker, and J. H. Siggers. Large-amplitude ac voltammetry: Theory for reversible redox reactions in the "slow scan limit approximation". *Electrochim. Acta*, 56:6131–6141, 2011.

[6] S. O. Engblom, J. C. Myland, K. B. Oldham, and A. L. Taylor. Large amplitude ac voltammetry - a comparison between theory and experiment. *Electroanalysis*, 13:626–630, 2001.

[7] H. Adamson, A. M. Bond, and A. Parkin. Probing biological redox chemistry with large amplitude Fourier transformed ac voltammetry. *Chem. Commun.*, 53:9519–9533, 2017.

[8] A. J. Bard and L. R. Faulkner. *Electrochemical Methods: Fundamentals and Applications*. John Willey & Sons, New York, 1980.

[9] C. I. Mooring and H. L. Kies. A.C. voltammetry at large amplitudes. a simplified theoretical approach. *J. Electroanal. Chem.*, 78:219–227, 1977.

[10] S. O. Engblom, J. C. Myland, and K. B. Oldham. Must ac voltammetry employ small signals? *J. Electroanal. Chem.*, 480:120–132, 2000.

[11] J.-M. Savéant. *Elements of Molecular and Biomolecular Electrochemistry*. Wiley-Interscience, New Jersey, 2006.

[12] José M. Rodríguez M. A convolution algorithm for linear-sweep voltammetric data at unequaly spaced times. *Comput. Chem.*, 15(3):235–236, 1991.

[13] A. J. Bard, Gy. Inzelt, and F. Scholz. *Electrochemical dictionary*. Springer Science & Business Media, 2008.

3. Voltammetry of Immobilized Species

In this chapter, an analysis shall be made concerning an immobilized on an electrode surface electroactive species. The treatment will again be side by side for cyclic voltammetry and the corresponding cases in FTacV. The study will start from an one step reaction of an electroactive species, moving on to two step reactions. After that, what shall be studied is the coupling of the redox reaction of the immobilized species with a reaction that concerns a species free in the bulk solution. More specifically the Michaelis-Menten kinetics of an immobilized enzyme shall be thoroughly analyzed as well as various cases of an electrochemical-chemical (EC) mechanism.

All the results in this chapter are computational from solving the differential and/or respective integral equations in each case. As in the case of free species, XXPaut was used for solving differential equations [1]. After this chapter is over, one shall have a basic understanding of FTacV in comparison with cyclic voltammetry regarding various scenarios of redox reactions of immobilized species. A methodology to extract kinetic constants - both electrochemical and chemical - using FTacV is introduced which shall be quite useful in the experimental section of this thesis with the study of immobilized enzymes.

3.1 One Step Reaction

3.1.1 General formulation for CV and FTacV

Starting from the simplest case of an one step electrochemical reaction, we shall begin by considering an electrochemical reaction having a standard (or formal) electrode potential E^0, where both oxidized (Ox) and reduced species (Red) are *immobilized* on the electrode surface (Fig. 3.1.1),

$$\mathrm{Ox} + ne \underset{k_a}{\overset{k_c}{\rightleftharpoons}} \mathrm{Red} \tag{3.1.1}$$

where n is the number of exchanged electrons, k_c the cathodic kinetic constant and k_a the anodic one. The units for both kinetic constants are 1/s. Let us denote as Γ^0 the initial surface concentration of Ox species and assume a Butler-Volmer law for the rate constants,

$$k_c = k^0 e^{-\frac{anF}{RT}(E-E^0)} \tag{3.1.2}$$

$$k_a = k^0 e^{\frac{(1-a)nF}{RT}(E-E^0)} \tag{3.1.3}$$

where k^0 is the standard rate constant and a the transfer coefficient.

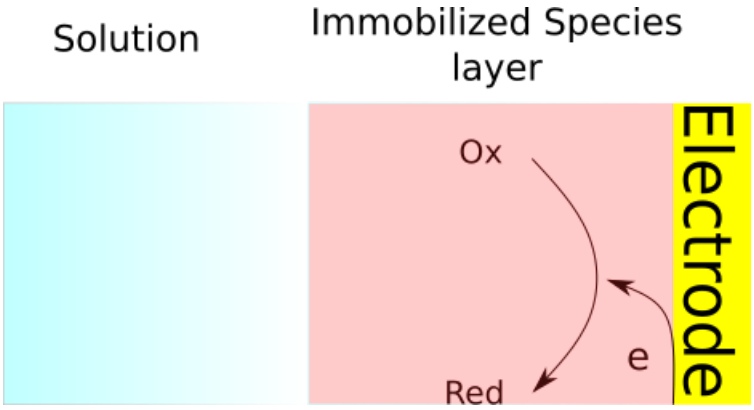

Figure 3.1.1: Immobilized species reaction scheme. The oxidized form, Ox, of the immobilized on the electrode surface electroactive species gets an electron from the electrode surface and is reduced to its reduced form, Red.

3.1.2 Cyclic voltammetry of immobilized species

For the case of cyclic voltammetry, it has been well estabished that the dimensionless expression of the Faradaic current during the redox reaction of the immobilized species can be given from Eq. (3.1.4) as a funtion of dimensionless time [2],

$$\psi_{CV,F} = k_{cv} \exp(-\alpha\xi)\{1 - [1 + \exp(-\xi)] \int_0^{\tau_{CV}} \psi_{CV,F} d\eta\} \tag{3.1.4}$$

where,

$$\psi_{CV,F} = \frac{i}{FS\Gamma^0 \frac{Fv}{RT}} \qquad \text{(dimensionless current for cyclic voltammetry)}$$

$$\xi = \frac{F}{RT}(E - E^0) \qquad \text{(dimensionless potential)}$$

$$\tau_{CV} = \frac{FV}{RT}t \qquad \text{(dimensionless time for cyclic voltammetry)}$$

$$k_{CV} = \frac{RT}{F}\frac{k^0}{v} \qquad \text{(kinetic parameter for cyclic voltammetry)}$$

Regarding the rest of the symbols appearing in the dimensionless magnitudes, F corresponds to the Faraday constant, S to the electrode surface, Γ^0 to the total surface concentration, E the applied electrode potential, E^0 the formal potential, v the scan rate, t the time, T the temperature and k^0 the standard electron transfer kinetic constant.

The sweep of the dimensionless potential, together with the progress of the surface coverage and the resulting dimensionless current as a function of the dimensionless time for a large value of the kinetic parameter k_{CV} , are presented in Fig. 3.1.2. It can be observed that, as the dimensionless potential goes to more cathodic values, the surface coverage θ - that reflects the ratio of the surface concentration of the oxidized form of the immobilized species to the initial surface concentration - lowers until it reaches the value of zero, meaning that the species is fully reduced. During this cathodic scan, a peak appears at the negative values of the dimensionless current, corresponding to the reduction of the immobilized species. The peak for large values of k_{CV} appears at the standard potential of the redox species (indicated by the dashed line in Fig. 3.1.2). The cathodic scan stops when the dimensionless potential reaches its lower limit, and then the scan reverses towards the initial potential. As the dimensionless potential increases, the coverage value also goes up to the point it reaches its maximum value of one, signifying the regeneration of the oxidized form of the immobilized species. Moreover during the anodic scan, positive dimensionless currents appear, with a maximum point again at the value of the standard potential of the species (also indicated by the dashed line in Fig. 3.1.2).

Since it is more common to represent cyclic voltammograms as an expression of potential, instead of time, the cyclic voltammogram of Fig. 3.1.2) as a funtion of potential is presented in Fig. 3.1.3 (black line). The case examined, which is that of large k_{CV}, corresponding to a reversible redox reaction. In such a case, the peak of the dimensionless current corresponds to a value of 0.25 [2]. If this value were to be translated into an expression with dimensions, it would be written as in Eq. (3.1.5), which shows that the peak current, $i_{\mathrm{p,CV}}$ is proportional to the scan rate, v,

$$i_{\mathrm{p,CV}} = 0.25 F S \Gamma^0 \frac{Fv}{RT} \tag{3.1.5}$$

Moreover, for fast kinetics, no separation is observed in the oxidation and reduction peak, as they both fall at the value of the standard potential.

But the case of fast kinetics is not the most common one encountered in nature. More often the redox reaction of immobilized species fall into the category of slower kinetics, which corresponds to lower values of k_{CV}. It is apparent from the expression of k_{CV} either due to lower values of the standard kinetic constant, or due to increasing scan rate. As k_{CV} decreases, the voltammogram transcends from a quasi-reversible state where the peaks are not well seperated and the value of the peak lowers (red and blue line in Fig. 3.1.3), to an irreversible state, where the peaks are well separated and reach a value of $i_{\mathrm{p,CV}} = 0.368a$ (green, orange, magenta and violet lines in Fig. 3.1.3). If the value were translated into an expression with dimensions it would be written as in Eq. (3.1.6),

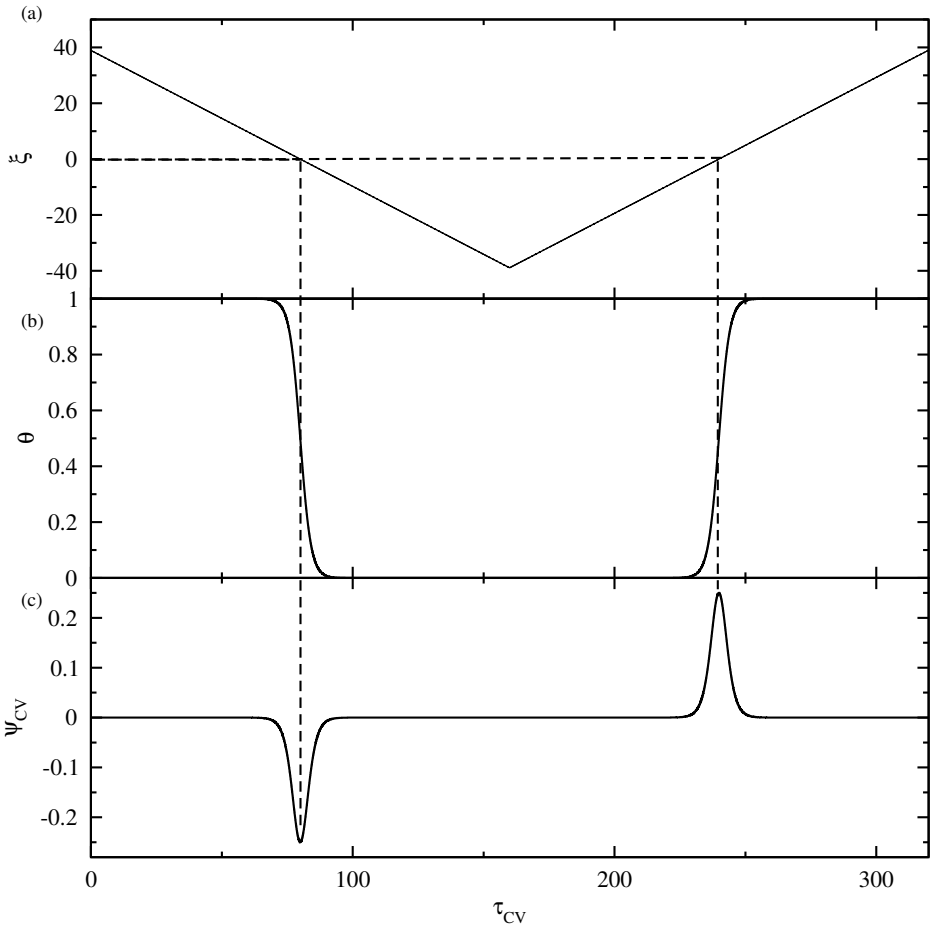

Figure 3.1.2: Example of cyclic voltammetry for an immobilized species. (a) dimensionless potential ξ against dimensionless time τ_{CV} (b) surface coverage θ against dimensionless time τ_{CV} (c) dimensionless current $\psi_{\mathrm{CV,F}}$ against dimensionless time τ_{CV}.

$$i_{\mathrm{p,CV}} = 0.368 aFS\Gamma^0 \frac{Fv}{RT} \tag{3.1.6}$$

There are also expressions which correspond to the shift of the anodic and cathodic peak as well as the half-height peak widths of the voltammograms in the irreversibility region. At this point, the dimensionless expressions shall not be presented and we shall proceed with the dimensional quantities. The values of the anodic $E_{\mathrm{p,a}}$ and the cathodic potential $E_{\mathrm{p,c}}$ are presented in Eq. (3.1.7) and (3.1.8), respectively,

$$E_{\mathrm{CV,a,p}} = E^0 + \frac{RT}{aF} \ln\left(\frac{RT}{(1-a)F}\frac{k^0}{v}\right) \tag{3.1.7}$$

$$E_{\mathrm{CV,c,p}} = E^0 + \frac{RT}{aF} \ln\left(\frac{RT}{aF}\frac{k^0}{v}\right) \tag{3.1.8}$$

The expressions for the half-height peak widths for the anodic $\Delta E_{\mathrm{p,a}}$ and $\Delta E_{\mathrm{p,c}}$ are found in Eq. (3.1.9) and (3.1.10), respectively,

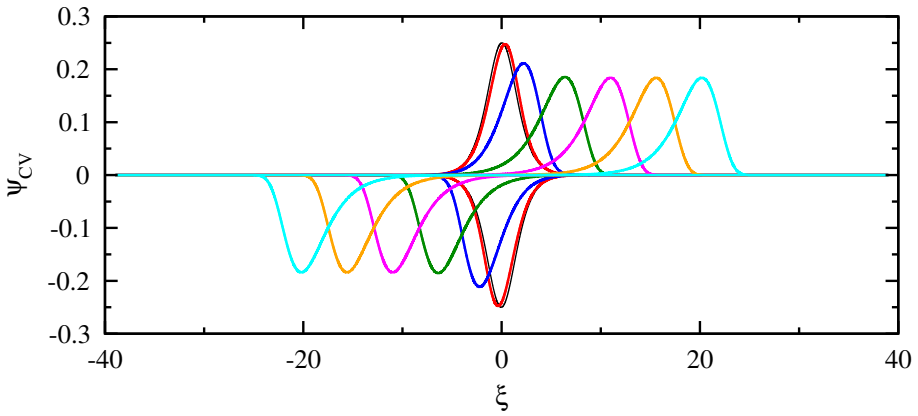

Figure 3.1.3: Dimensionless cyclic voltammograms of a one electron one step reaction for immobilized species for $\alpha_0 = 0.5$, $\xi^0 = 0$ and $k_{\rm CV} = 10$ (black), 1 (red), 0 (blue), 0.1 (green), 0.01 (magenta), 0.001 (orange) and 0.0001 and (cyan)

$$\Delta E_{\rm CV,a,p} = 2.46\frac{RT}{(1-a)F} \tag{3.1.9}$$

$$\Delta E_{\rm CV,c,p} = 2.46\frac{RT}{aF} \tag{3.1.10}$$

3.1.3 FTacV of immobilized species

Before we shall continue to the case of FTacV, we should note at this point that for the immobilized species, two different approaches were followed giving identical results. In the first approach, the kinetic equations for the coverage of the immobilized species were integrated and the ac-voltammograms were determined. Ac-voltammograms were Fourier transformed and the signal in the frequency domain was filtered by applying a rectangular window around each integer multiple of the perturbation frequency. The filtered signals were inverse Fourier transformed to the time domain and thus the harmonics were obtained. Now, in the second approach, the ac-voltammograms were obtained directly from the corresponding integral equation and filtered in the time-domain by a 10th order Butterworth filter around each integer multiple of the perturbation frequency. A Hilbert transform was applied in order to obtain the envelope of each harmonic[1].

Intergration of the kinetic equation for the coverage

Examining the kinetics of Eq. (3.1.1) one can understand that the rate r for this electrochemical reactions is

$$r = k_{\rm c}\Gamma_{\rm Ox} - k_{\rm a}\Gamma_{\rm Red} \tag{3.1.11}$$

[1]The latter method was used as an alternative to the Fourier transform of the voltammographic signal and gives identical results.

where Γ_{Ox} and Γ_{Red} the surface concentrations of Ox and Red respectively. By defining as surface coverage, θ, the ratio $\frac{\Gamma_{\mathrm{Ox}}}{\Gamma^0}$ and taking into account that at each time,

$$\Gamma^0 = \Gamma_{\mathrm{Ox}}(t) + \Gamma_{\mathrm{Red}}(t) \tag{3.1.12}$$

the rate from Eq. (3.1.11) becomes,

$$r = k_{\mathrm{c}}\Gamma_{\mathrm{Ox}} - k_{\mathrm{a}}\Gamma_{\mathrm{Ox}}(1-\theta) \tag{3.1.13}$$

Thus,

$$\frac{\mathrm{d}\Gamma_{\mathrm{Ox}}}{\mathrm{d}t} = -r \tag{3.1.14}$$

$$\frac{\mathrm{d}\theta}{\mathrm{d}t} = -k_{\mathrm{c}}\theta + k_{\mathrm{a}}(1-\theta) \tag{3.1.15}$$

Now, since the Faradaic current i_{F} can be expressed as,

$$i_{\mathrm{F}} = -nFr \tag{3.1.16}$$

where F is the Faraday constant, the Faradaic current can be expressed as in the following expression,

$$i_{\mathrm{F}} = nF\Gamma^0[k_{\mathrm{a}}(1-\theta) - k_{\mathrm{d}}\theta] \tag{3.1.17}$$

Assuming Butler-Volmer kinetics now as mentioned in the beginning of the chapter, the Faradaic current now becomes,

$$i_{\mathrm{F}} = nF\Gamma^0 k^0[(1-\theta)e^{\frac{(1-a)F}{RT}(E-E^0)} - \theta e^{\frac{(1-a)F}{RT}(E-E^0)}] \tag{3.1.18}$$

Now, assuming a cyclic voltammetry experiment where the potential starts from an initial value E_{I} and is scanned linearly towards more cathodic potentials against time at a certain scan rate v , and the scan is reversed at a time t_{R}, the applied potential can be expressed as in Eq. (3.1.19),

$$E = E_{\mathrm{I}} - vt_{\mathrm{R}} + v|t - t_{\mathrm{R}}| \tag{3.1.19}$$

When it comes to FTacV together with the scan sweep, a sinusoidal perturbation $A\sin 2\pi ft$ is imposed, where A and f are the perturbation amplitude and frequency respectively, and the scan is reversed at a time t_{R}, the applied potential can be expressed as in Eq.(3.1.20),

$$E = E_{\mathrm{I}} - vt_{\mathrm{R}} + v|t - t_{\mathrm{R}}| + A\sin 2\pi ft \tag{3.1.20}$$

At this point we shall introduce the dimensionless quantities for FTacV in the following equations,

$$\tau_{\mathrm{ac}} = ft \qquad \text{(dimensionless time for FTacV)}$$
$$a_0 = \frac{AF}{RT} \qquad \text{(dimensionless amplitude)}$$
$$k_{\mathrm{ac}} = \frac{k^0}{f} \qquad \text{(kinetic parameter for FTacV)}$$
$$\psi_{\mathrm{ac,F}} = \frac{i}{\Gamma^0 F f} \qquad \text{(dimensionless current for FTacV)}$$
$$\sigma = \frac{Fv}{RTf} \qquad \text{(dimensionless scanrate for FTacV)}$$

The dimensionless time here is a function of the frequency - and not of the scan rate as in cyclic voltammetry - indicating that the time scale that matters in this method is that of the frequency and not that of real time. This assumption stands as long as the method is independent of the scan rate, as discussed in the previous chapter. The dimensionless amplitude, undergoes a transition similar to that of the dimensionless potential. The dimensionless current is yet again dependent on the frequency and not the scan rate. Moreover it is evident that the current density is proportional to the frequency. Finally, the dimensionless kinetic parameter k_{ac} is only dependent on the frequency as well for a given value of amplitude, and as the frequency increases, k_{ac} decreases, giving less reversible kinetics. From this dimensionless analysis, it is rather obvious that the frequency is equivalent to the scan rate in a cyclic voltammetry experiment, as it influences the kinetic parameter and the current density in the same way as the scan rate does in cyclic voltammetry.

The dimensionless expressions for the applied potential and the current density as an expression of the surface coverage can thus be expressed as in Eq. (3.1.21) and (3.1.22), respectively,

$$\xi = \xi_{\mathrm{I}} - \sigma\tau_{\mathrm{R}} + \sigma|\tau_{\mathrm{ac}} - \tau_{\mathrm{R}}| + A_0 \sin 2\pi\tau_{\mathrm{ac}} \tag{3.1.21}$$
$$\psi_{\mathrm{ac,F}} = k(e^{(1-a)\xi}(1-\theta) - e^{(-a\xi)}\theta) \tag{3.1.22}$$

And this concludes the first approach regarding the integration of the kinetic equation for the coverage.

Integral Equation solving

Now, if we go back to Eq. (3.1.17) and take a different path we can produce a time dependent expression of the coverage. Starting from $\frac{\mathrm{d}\theta}{\mathrm{d}t} = \frac{i}{nF\Gamma^0}$ the coverage can be expressed as,

$$\theta(t) = \theta_0 + \int_0^t \frac{i}{nF\Gamma^0}\mathrm{d}t$$

where θ_0 is the initial coverage for the Ox species. For θ_0=1 one can derive that,

$$\theta(t) = 1 + \int_0^t \frac{i}{nF\Gamma^0}\mathrm{d}t \tag{3.1.23}$$

It is also obvious that,

$$1 - \theta(t) = -\int_0^t \frac{i}{nF\Gamma^0}\mathrm{d}t \tag{3.1.24}$$

Now, using these expressions of θ and putting them back in Eq. (3.1.17) the derived current expression is,

$$i_{\mathrm{ac,F}} = -nF\Gamma^0[k_{\mathrm{a}}\int_0^t \frac{i}{nF\Gamma^0}\mathrm{d}t - k_{\mathrm{a}}(1 + \int_0^t \frac{i}{nF\Gamma^0}\mathrm{d}t)] \tag{3.1.25}$$

Assuming once again Butler-Volmer kinetics, the above expression changes to,

$$\begin{aligned} i_{\mathrm{ac,F}} = -nF\Gamma^0 k^0[e^{\frac{(1-a)F}{RT}(E-E^0)}\int_0^t \frac{i}{nF\Gamma^0}\mathrm{d}t - \\ e^{\frac{-aF}{RT}(E-E^0)}(1 + \int_0^t \frac{i}{nF\Gamma^0}\mathrm{d}t)] \end{aligned} \tag{3.1.26}$$

By substituting the same dimensionless magnitudes for FTacV as the ones introduces in the previous section, the dimensionless form of the current is,

$$\psi_{\mathrm{ac,F}} = -k_{\mathrm{ac}}[e^{(1-a)\xi}\int_0^\tau \psi_{\mathrm{ac,F}}\mathrm{d}\tau - e^{-a\xi}(1 + \int_0^\tau \psi_{\mathrm{ac,F}}\mathrm{d}\tau)] \tag{3.1.27}$$

which shall be solved together with the dimensionless potential as reported in Eq. (3.1.21).

The filtered voltammogram around the h-th integer multiple of the frequency f is obtained by applying the appropriate filter $w_h(\tau)$ on $\psi(\tau)$, in the time-domain, *i.e.*,

$$\hat{\psi}_h(\tau) = \psi(\tau) * w_h(\tau) \tag{3.1.28}$$

where the asterisk represents the convolution. Finally, the h-th harmonic is most commonly represented as the envelope of $\hat{\psi}_h(\tau)$, which can be obtained as follows,

$$\psi_h(\tau) = |\hat{\psi}_h + jH(\hat{\psi}_h)| \tag{3.1.29}$$

where $H(\cdot)$ is the Hilbert transform and $j = \sqrt{-1}$. Under the assumption of potential-independent specific capacitance, harmonics higher than one do not include any capacitive contribution.

In Fig. 3.1.4 one can find the dependence of the dimensionless potential, surface coverage and dimensionless current for FTacV against the dimensionless time, similar to the correspondind dependencies for cyclic voltammetry presented in Fig. 3.1.2. These dependencies shall not be analyzed yet, as we will return to them later in this chapter.

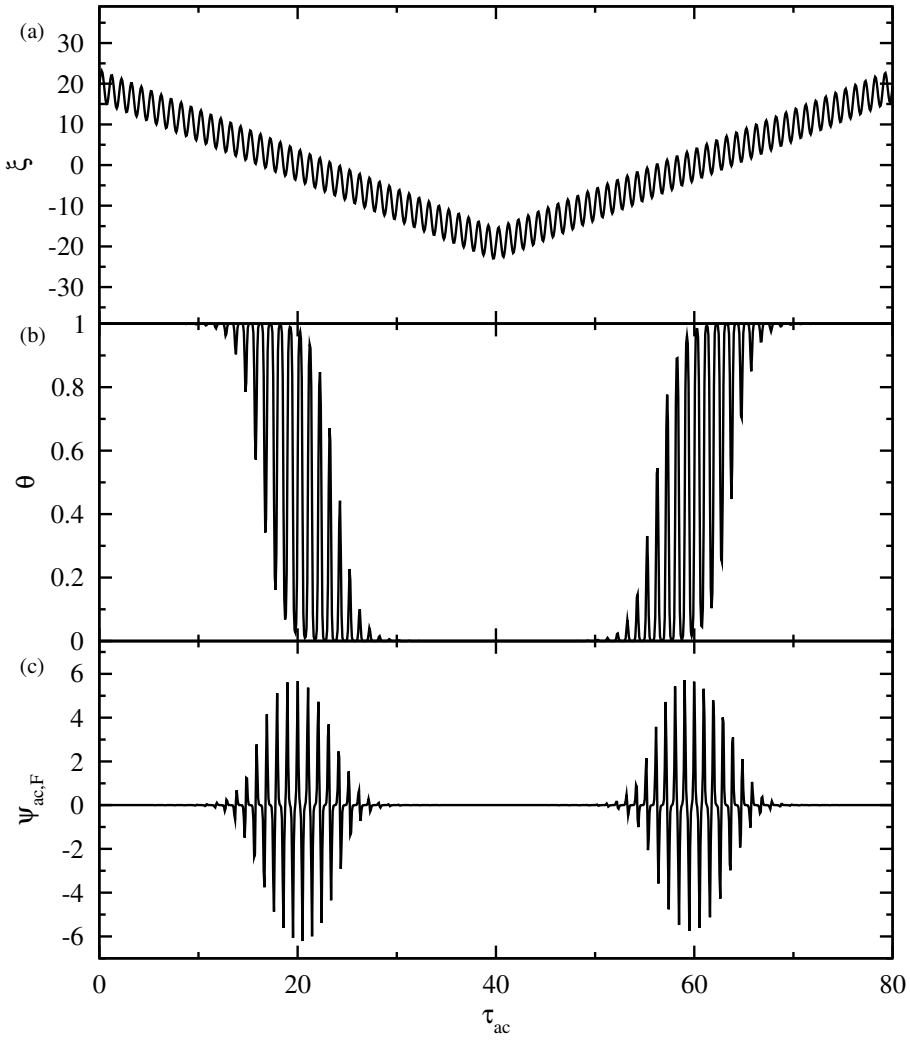

Figure 3.1.4: Example of FTacV for an immobilized species for $\alpha_0 = 3.892$ (a) dimensionless potential ξ against dimensionless time $\tau_{\rm ac}$, (b) surface coverage θ against dimensionless time $\tau_{\rm ac}$, (c)dimensionless current ψ against dimensionless time $\tau_{\rm ac}$.

Analysis

We shall move to the results extracted from the above analysis. For $|\xi_{\rm I}| \gg 0$ and under the condition of independence on scan rate, the harmonics depend on one experimental parameter when solving the dimensionless problem, namely the the perturbation amplitude a_0, and two kinetic parameters, namely the rate constant $k_{\rm ac}$ and the transfer coefficient a. In principle, the reaction is considered as "fast" or reversible if $k_{\rm ac}$ is large (large k^0 and/or small f) and "slow" or irreversible if $k_{\rm ac}$ is small (small k^0 and/or large f). For values of $k_{\rm ac}$ between these two limits, the reaction is considered quasi-reversible.

Reversible Systems

As long as the independence of the scan rate holds, we begin with the analysis that concerns the chief observables in the case of a reversible reaction of an immobilized electroactive species.

In order to study this case let us revert to an analytic solution of Eq. (3.1.27), when $k_{\rm ac} \to \infty$. In such a case, Eq. (3.1.27) becomes,

$$-e^{\xi(\tau)} \int_0^\tau \psi_{\rm ac,F}(s)ds = 1 + \int_0^\tau \psi_{\rm ac,F}(s)ds$$

resulting in the Faradaic component of a reversible ac-voltammogram,

$$\psi_{\rm ac,F} = \xi'(\tau) \frac{e^{\xi(\tau)}}{(1+e^{\xi(\tau)})^2} \tag{3.1.30}$$

The raw voltammograms - before any process - for three different dimensionless amplitudes are presented in Fig. 3.1.5, together with surface coverage against time. As the dimensionless amplitude increases, the raw voltammograms increase in both magnitude and width, whereas the coverage always varies between the values of 0 and 1. The difference in the surface coverage in the cases of cyclic voltammetry and FTacV, is that in the first case the coverage is a single line regardless of the manipulation of the parameters, while in the second one the theta is "spread" across time, and this "spread" increases as the amplitude goes up. This can be explained in the sense that as the potential is scanned, and apart from the linear sweep, a perturbation also takes place which forces the potential to swing between values as it is scanned.

This could be more easily understood with an example using parameters in their form with dimensions. Assuming an $E^0 = 0$, a potential sweep going from 500 to -500 mV , we examine what happens when the potential ramp reaches a value of 150 mV. If the perturbation amplitude is at 100 mV , the potentials around the selected one will be among 250 and 50 mV, thus no oxidation or reduction will take place yet as the formal potential has not yet been surpassed. Now, in the case where the applied amplitude is 200 mV the potential varies between 350 and -50 mV, thus oxidations and reductions around the formal potential start occurring despite the linearly applied potential not having yet reached such values where these reactions would be feasible. Then in the case of an amplitude of 300 mV the potential would vary from 450 to -150 mV, thus the redox reaction would become more intense as the overpotential would increase as well.

Regarding the analysis of a reversible system of an immobilized species, an example can be found in Fig. 3.1.6 for different values of dimensionless amplitudes. The first six harmonics that occur after the direct and inverse FFT can be found in Fig. 3.1.6 (b). The distinct features for the odd and even harmonics (as in the case of a free reversible species) are the width at the half of the maximum of the principal peak and the displacement of the principal peak respectively, as the amplitude increases. In the zoomed in areas of the Fig. 3.1.6(b) these dependencies are visualized and pointed out. For the second harmonic the displacement of the principal peak towards more negative potentials is shown. Accordingly the other principal peak of the second harmonic is

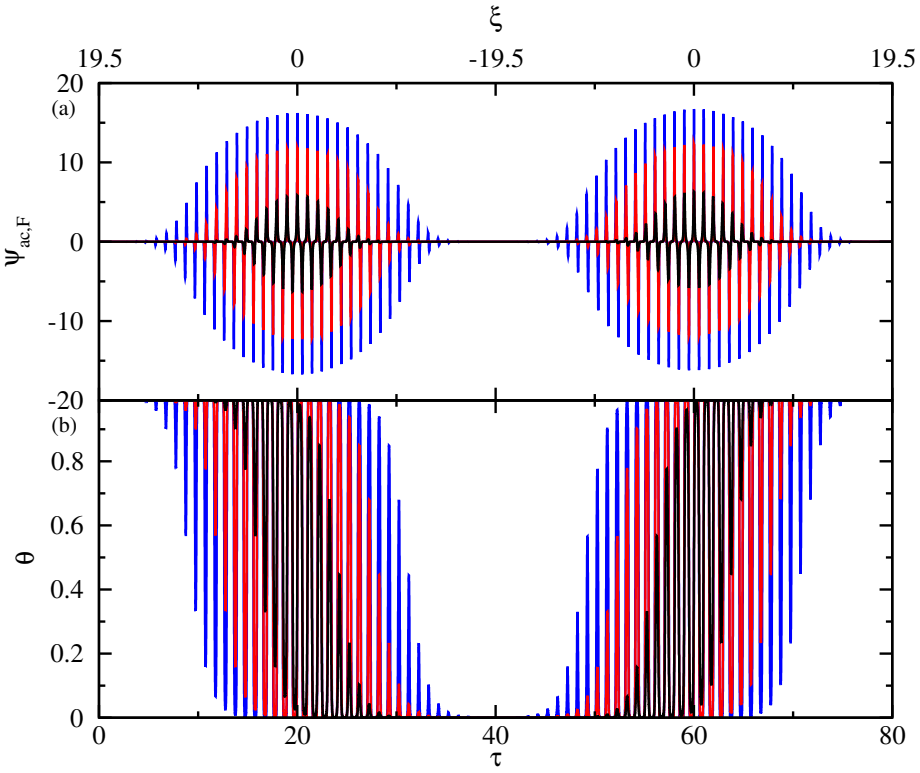

Figure 3.1.5: (a)Unprocessed FTacV voltammogram for immobilized species, (b) surface coverage θ against τ of immobilized species for σ 0.9735, ξ^0 0, k 20 and α_0 3.892 (black), 7.786 (red) and 11.678 (blue).

displaced towards more positive values. As an example for the odd harmonics, the width at the half of the maximum is shown for the 3rd harmonic. A quantification of the aforementioned features are presented in Fig. 3.1.7(a) and 3.1.7(b) for all the harmonics up to the sixth. Fig. 3.1.7(a) refers to the odd harmonics while 3.1.7(b) to the even ones.

Next, in Fig. 3.1.8 the maximum height of the principal peak(s) of each harmonic is presented. The increasing trend is similar to that of a free electroactive species, schematically at least, with a very intense increase with the amplitude that reads to a saturation value at high amplitudes. A difference that can be spotted is the region of large amplification, which for a free species is between 80 and 220 mV for one electron and 50 and 180 mV for two electrons, whereas for an immobilized species it can considered from 100 to 275 mV at 298.15 K. By fitting these regions to equation 3.1.31 the values in Table 3.1 occur.

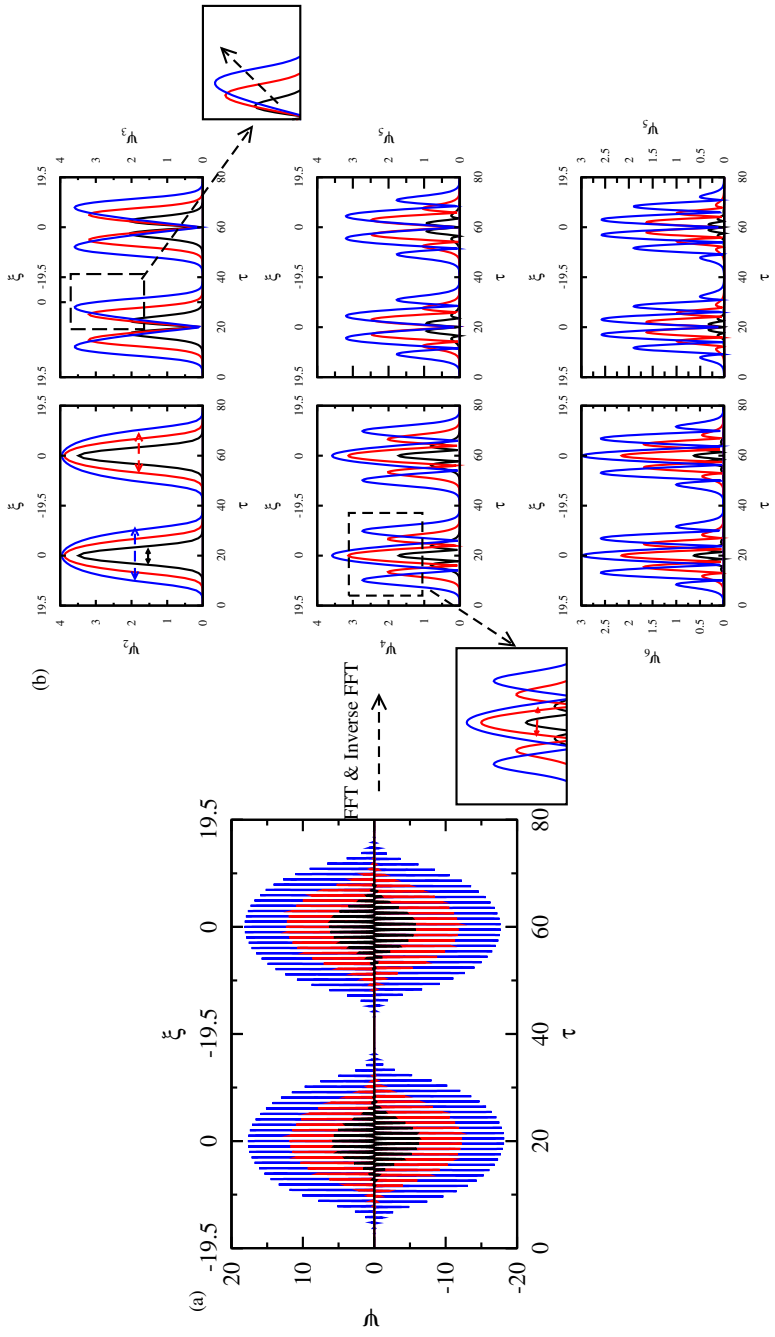

Figure 3.1.6: (a)Unprocessed FTacV voltammogram for immobilized species σ 0.9735, ξ^0 0, k 20 and α_0 3.892 (black), 7.786 (red) and 11.678 (blue) (b) 1st through 6th harmonic after process with FFT and inverse FFT.

Table 3.1: Fitting parameters for Eq. (3.1.31) in the region from $\alpha_0 = 1.946$ to 12.650

h	a_h	b_h
2	1.578	3.293
3	1.691	4.386
4	1.829	7.297
5	1.937	9.256
6	2.046	12.262

$$\ln \psi_{\mathrm{p},h} = a_h - \frac{b_h}{\alpha_0} \tag{3.1.31}$$

By looking more closely to Fig. 3.1.8 the saturation dimensionless currents coincide for the 2nd and 3rd harmonic, whereas saturation for harmonics higher than the 4th has yet to be reached at an α_0 value of 19.462, which signifies that theoretically there is room for further amplification of the signal, something hard to achieve in practice due to probably evoking other reactions if such high amplitudes are applied. For example, when using a glassy carbon electrode examining a substance with an E^0 at -100 mV vs Ag|AgCl, KCl sat, when using an amplitude of 600 mV at 298.15 K (α_0 23.353) at an acidic pH in an aqueous solution, while scanning cathodically the potential, due to the large perturbation, proton reduction will also be present in the signal, thus rendering the analysis more tricky due to the interpolation of two electrochemical reactions.

Quasi Reversible and Irreversible Systems

Up to this point only the case of the reversible immobilized electroactive species has been described, but of equal -if not of more - interest are the systems that their kinetics is not as fast.

By solving Eq. (3.1.29) one can determine the regions of reversibility, quasi-reversibility and irreversibility are further determined by the value of the perturbation amplitude a_0 and the dimensionless standard rate constant k_{ac}. The effect of a_0 on the height of the principal peak, $\psi_{\mathrm{p},h}$, of each harmonic up to the 6th is presented in Fig. 3.1.9, for $a = 0.5$ and $\sigma = 1$. It can be observed that for small values of k_{ac}, the height of the principal peak is rather small, whereas for large values, $\psi_{\mathrm{p},h}$ tends to a limiting value. It has to be noticed that the trend just described concerns the dimensionless height of the corresponding harmonic. The effect of perturbation amplitude is also evident from the plots of Fig. 3.1.9. Large values of a_0 induce a wider range of k where the limiting value of $\psi_{\mathrm{p},h}$ is observed, that is, shift the system towards the region of reversibility.

Now, in order to get a better understanding of the waveform of the harmonic, in Fig. 3.1.10 and 3.1.11 an immobilized species for different values of k_{ac} is examined at an α_0 3.894 and 11.68 respectively. At 3.894 (which translates at 100 mV at 298.15 K) as the k_{ac} lowers in all six harmonics, the magnitude drops drastically, and as the order of harmonic order increases, the decrease of the magnitude goes further down. At this amplitude, when it comes to the first harmonic, the peak of the harmonic falls one order

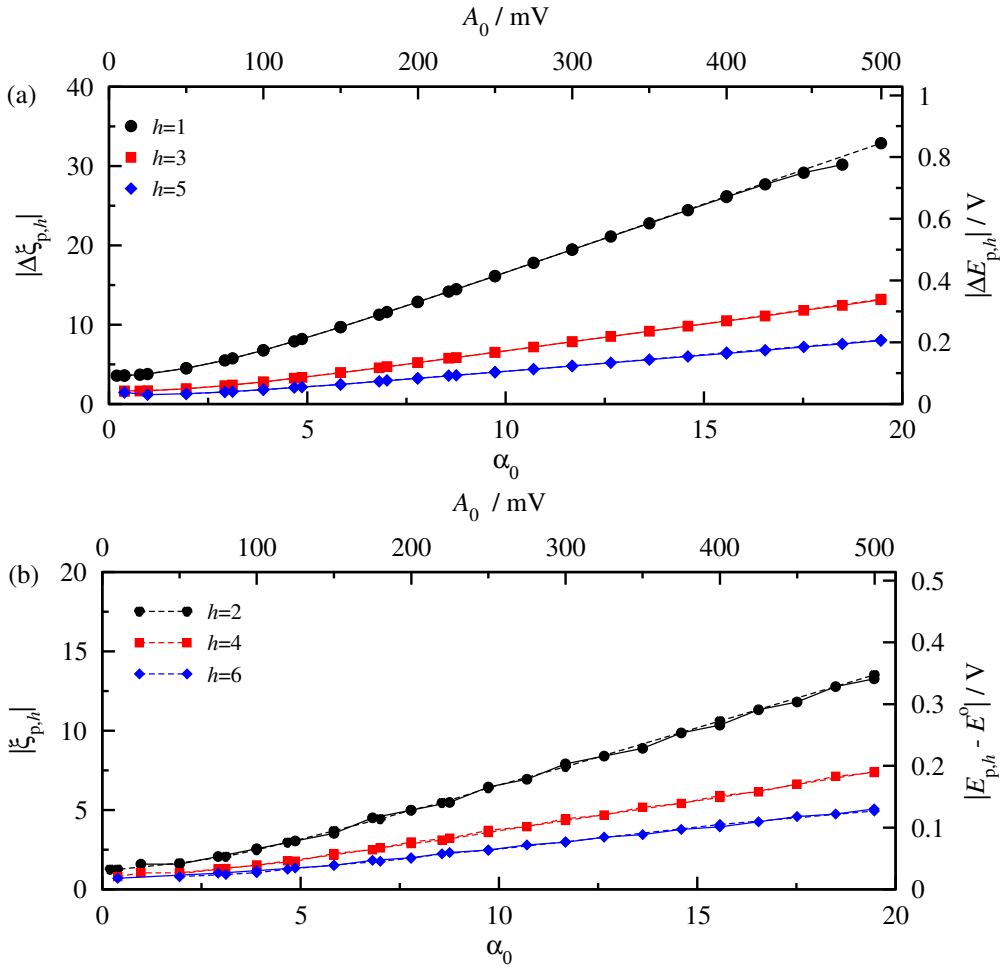

Figure 3.1.7: (a) Width at half maximum for the principal peaks of the odd harmonics and (b) peak potential of the principal peaks of the even harmonics, as a function of the perturbation amplitude α_0 at $T = 298.15$ K. Dashed lines refer to the results of the free species, while full lines to the result of the immobilized.

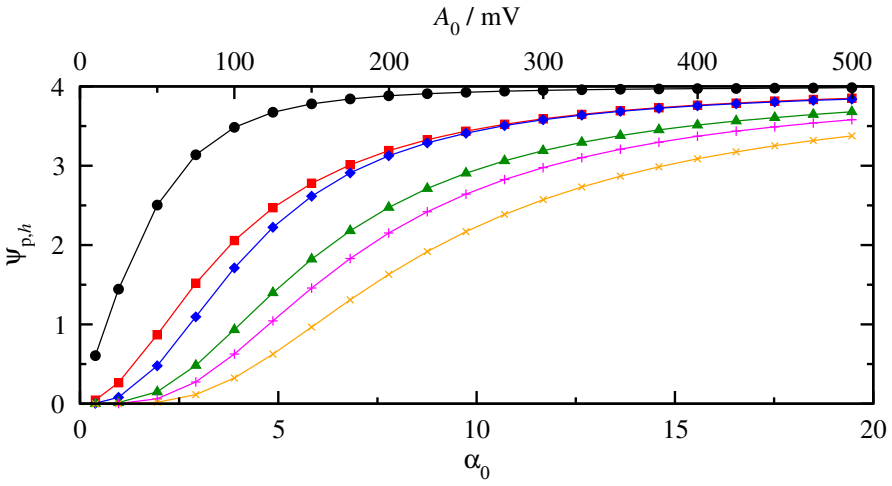

Figure 3.1.8: Maximum peak height, as a function of the perturbation amplitude α_0, together with the dimensional amplitude for $T = 298.15$ K for a reversible reaction. 1st (black circles), 2nd (red squares), 3rd (blue diamonds), 4th (green triangles), 5th (magenta plus) and 6th harmonic (orange x).

of magnitude, whereas in the 6th harmonic, 3 orders, in the transition from a totally reversible to a totally reversible case. Moreover, for lower k_{ac} values a deformation of the peaks occur leading to a small uniform peak for all the harmonics, which starts to displace as the k_{ac} decreases further.

In Fig. 3.1.11, where the same parameters at a higher amplitude (11.68 which translates to 300 mV at 298.15 K), looking at all the harmonics one could tell that the k has a smaller effect at the maximum of the harmonics. Yet, still when it comes to the 6th harmonic, a decrease of 2 orders of magnitude is still observable when comparing the reversible and the irreversible case.

Moreover, by taking a look in Fig. 3.1.10 and Fig. 3.1.11, one could observe that 3 zones are distinguishable. The reversible, the quasi-reversible and the irreversible, with the reversible zone remaining unchanged regardless of the α_0, while the limits of the quasi reversible and the irreversible can be altered.

In the case of the quasi-reversible kinetics, two regions can once again be distinguished. The 1st one extending where the principal peak in the odd peak decreases but still hasn't been displaced and the region where the harmonics start deforming until they reach the irreversible state. Now, regarding the shift of the dominant peak of the odd harmonics, the dependence can be found in Fig. 3.1.12

It is evident that for large values of k_{ac} the principal peak of the odd harmonics is observed at $\xi = 0$, that is, at E^0. As k_{ac} becomes smaller, a cathodic (anodic) shift of the principal cathodic (anodic) peak occurs, its value depending on a_0. This effect is depicted in Fig. 3.1.12. It is observed that the region of k where the potential of the principal peak is equal to the standard (or formal) potential is wider for large values of a_0. Moreover, for small values of k a linear dependence in observed in these

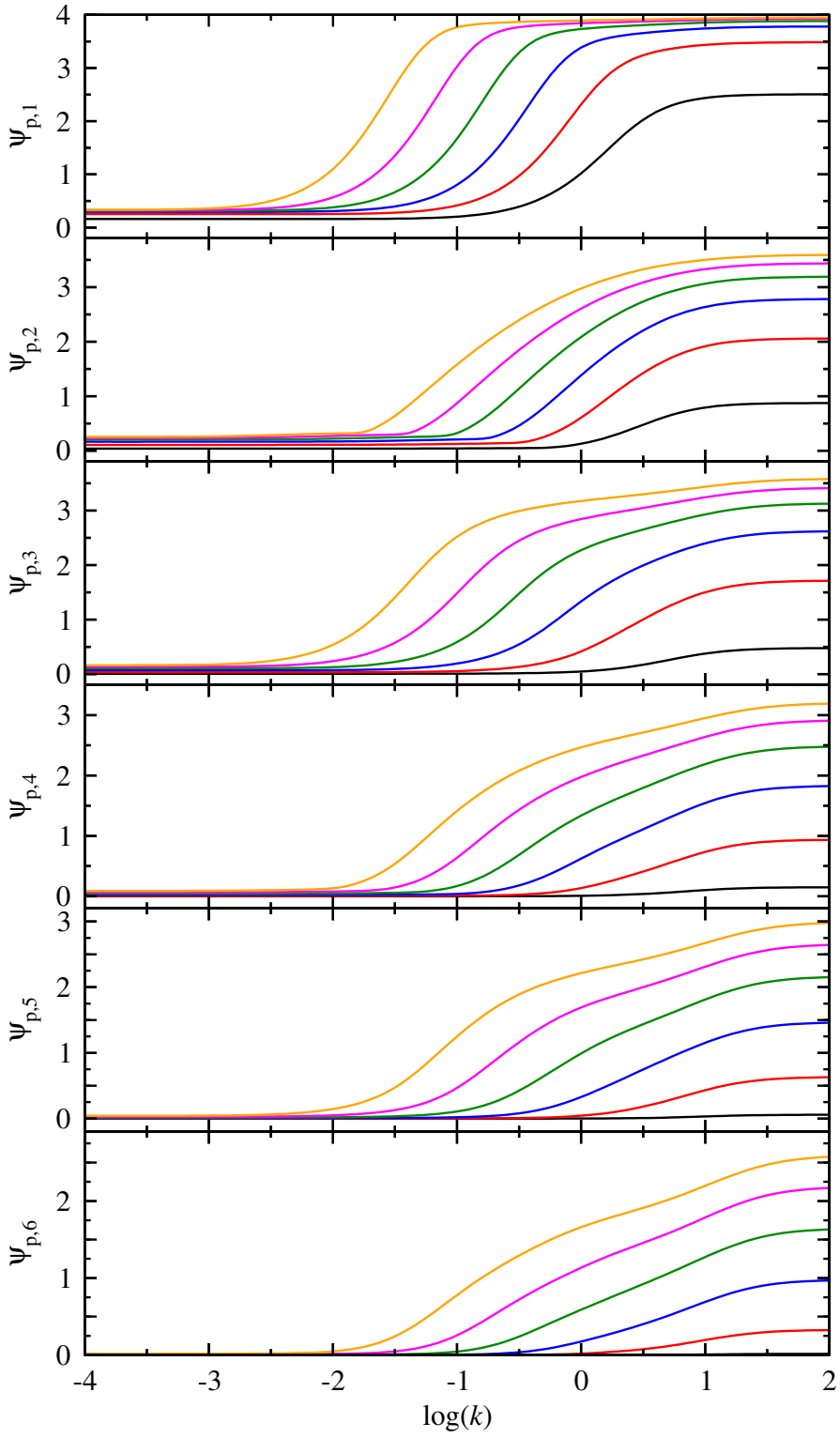

Figure 3.1.9: Maximum peak height for, as a function of the dimensionless kinetic constant k_{ac} for different dimensionless amplitudes for harmonics 1 through 6, for an immobilized species. α_0 values: 1.947 (black), 3.959 (red), 5.939 (blue), 7.919 (green), 9.898 (orange) and 11.878 (magenta).

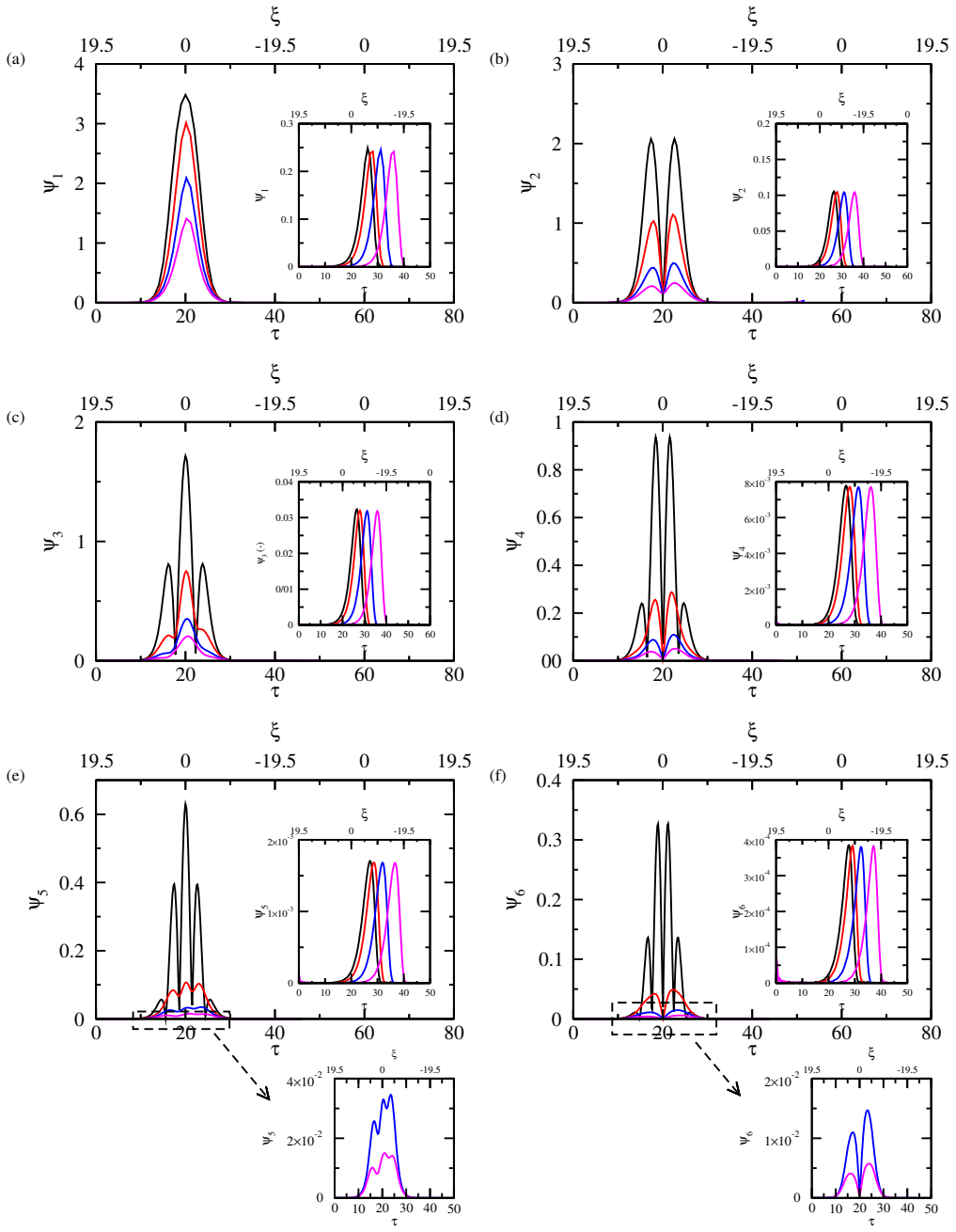

Figure 3.1.10: 1st through 6th harmonic of immobilized species for σ 0.9735, ξ^0 0, α_0 3.894 and k_{ac} 500 (black line), 2 (red line), 0.85 (blue line) and 0.5 (magenta line). In the insert diagramms the values for k are 0.01 (black line), 0.005 (red line), 0.001 (blue) line and 0.0001 (magenta line).

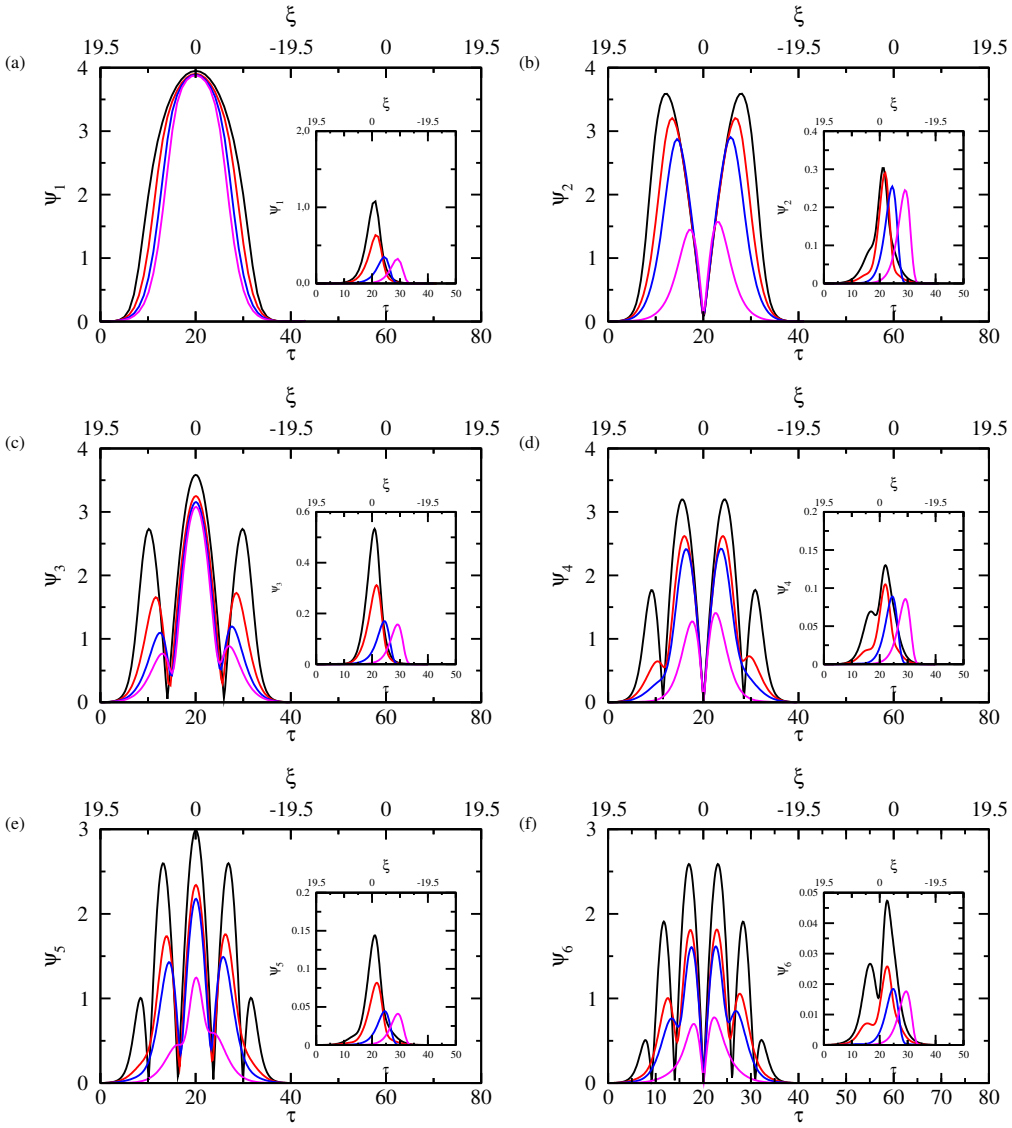

Figure 3.1.11: 1st through 6th harmonic of immobilized species for σ 0.9735, ξ^0 0, α_0 11.68 and k_{ac} 500 (black line), 2 (red line), 0.85 (blue line) and 0.5 (magenta line). In the insert diagramms the values for k are 0.01 (black line), 0.005 (red line), 0.001 (blue) line and 0.0001 (magenta line).

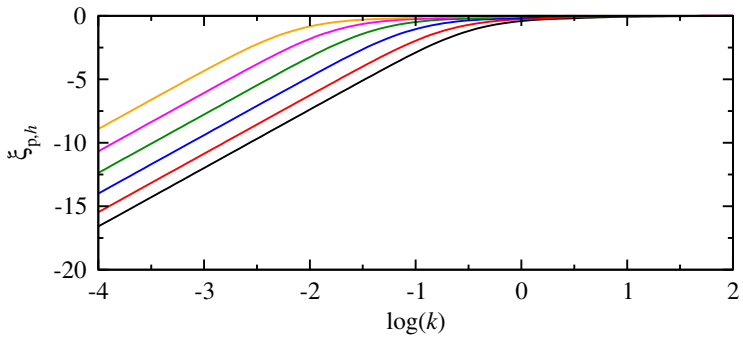

Figure 3.1.12: Principal peak potential as a function of the kinetic constant k of the odd harmonics for $a = 0.5$, $\sigma = 1$ and perturbation amplitude. α_0 values: 1.947 (black), 3.959 (red), 5.939 (blue), 7.919 (green), 9.898 (orange) and 11.878 (magenta).

Table 3.2: Values of β, Eq. (3.1.32), for different values of a_0

a_0	A_0 (mV at 298 K)	β
1.947	$50/n$	0.93
3.894	$100/n$	1.48
5.842	$150/n$	2.20
7.789	$200/n$	3.04
9.736	$250/n$	3.88
11.683	$300/n$	4.47

semi-logarithmic plots, the slope being $2.303/a$,

$$\xi_{p,h} = \frac{\beta}{a} + \frac{2.303}{a}\log(k) \tag{3.1.32}$$

where β depends on the perturbation amplitude. Indicative values of β for different values of a_0 are presented in Table 3.2.

The regions reversibility, quasi reversibility with no peak displacement and irreversibility for different amplitudes can be found in Table 3.3.

The irreversible case does not admit an analytic solution, but the problem is rather simplified. Thus, for slow kinetics (small values of k_{ac}), where the anodic and the

Table 3.3: Kinetic regions for immobilized species

α_0	Reversible	Quasi reversible with no Peak Displacement	Irreversible
3.959	k>100	100<k<2	k<-0.7
5.939	k>100	100<k<2	k<-1
7.919	k>100	100<k<2	k<-1.25
9.898	k>100	100<k<1	k<-1.7
11.878	k>100	100<k<1	k<-2

cathodic reaction are fully separated, Eq.(3.1.27) is written,

$$\psi_{\mathrm{ac,F}}(\tau) = -ke^{-a\xi(\tau)}\left(1 + \int_0^{\tau} \psi_{\mathrm{ac,F}}(s)ds\right)$$

The above equation can be written as an initial value problem,

$$\frac{d\psi_{\mathrm{ac,F}}}{d\tau} = -\left(a\xi'(\tau) + ke^{-a\xi(\tau)}\right)\psi_{\mathrm{ac,F}} \tag{3.1.33}$$

with initial condition, $\psi_{\mathrm{ac,F}}(0) = -ke^{-a\xi_{\mathrm{I}}}$. Here, it has been assumed that the potential scan is cathodic.

The effect of the perturbation amplitude a_0 on the height of the principal peaks of the harmonics is presented in Fig. 3.1.13(a). The trend is similar to the one observed in the case of the effect of a_0 on the height of the principal peaks of the harmonics for the reversible case. The difference here is that as the order of the harmonic increases, the increase of the height of the principal peak is less and less prominent and for harmonics above the third one, the dependencies fail to reach a saturation point for the amplitudes examined, that is, up to $514/n$ mV at 298 K.

The potential of the principal peak as a function of a_0 is presented in Fig. 3.1.13(b). For large amplitude values, the peak value for all the harmonics reach a common value, while for low amplitudes, the peak positions varies.

In Fig. 3.1.13(c) The half maximal width of the irreversible harmonics against the dimensionless perturbation amplitude is visualized. As one can only see one line in the diagram, it can be deducted that this quantity seems to be independent of the harmonic. For very large values of a_0 obeys the relation,

$$\Delta\xi_{\mathrm{p},h} = \frac{2.46}{a} \tag{3.1.34}$$

similarly to the case of cyclic voltammetry.

The results presented in this section can be utilized for the determination of E^0, a and k^0. Up to this point, we have worked with the dimensionless forms of the corresponding quantities. Now for a more practical approach, as a guide for one to extract the kinetic parameters from experimental data, we shall implement the respective dimensional versions of these quantities. Still all the results presented remain results of simulations.

Let us consider the case where the real surface area of the electrode A, and the initial surface concentration of reacting species Γ^0 are unknown. Let us consider a number of exchanged electrons $n = 1$.

Regarding the experiment that needs to be conducted, a series of large amplitude ac-voltammograms are recorded for a given perturbation amplitude A_0 and different frequencies f. The voltammograms are analyzed and a series of harmonics I_h is obtained. Let us suppose that the third harmonic $h = 3$ is free of capacitance contributions. A plot of I_3/f as a function of tf or electrode potential E would be as the one presented in Fig. 3.1.14(a) where $A_0 = 150$ mV. It is observed that for high frequencies the reaction is irreversible, for intermediate frequencies the reaction is quasi-reversible and

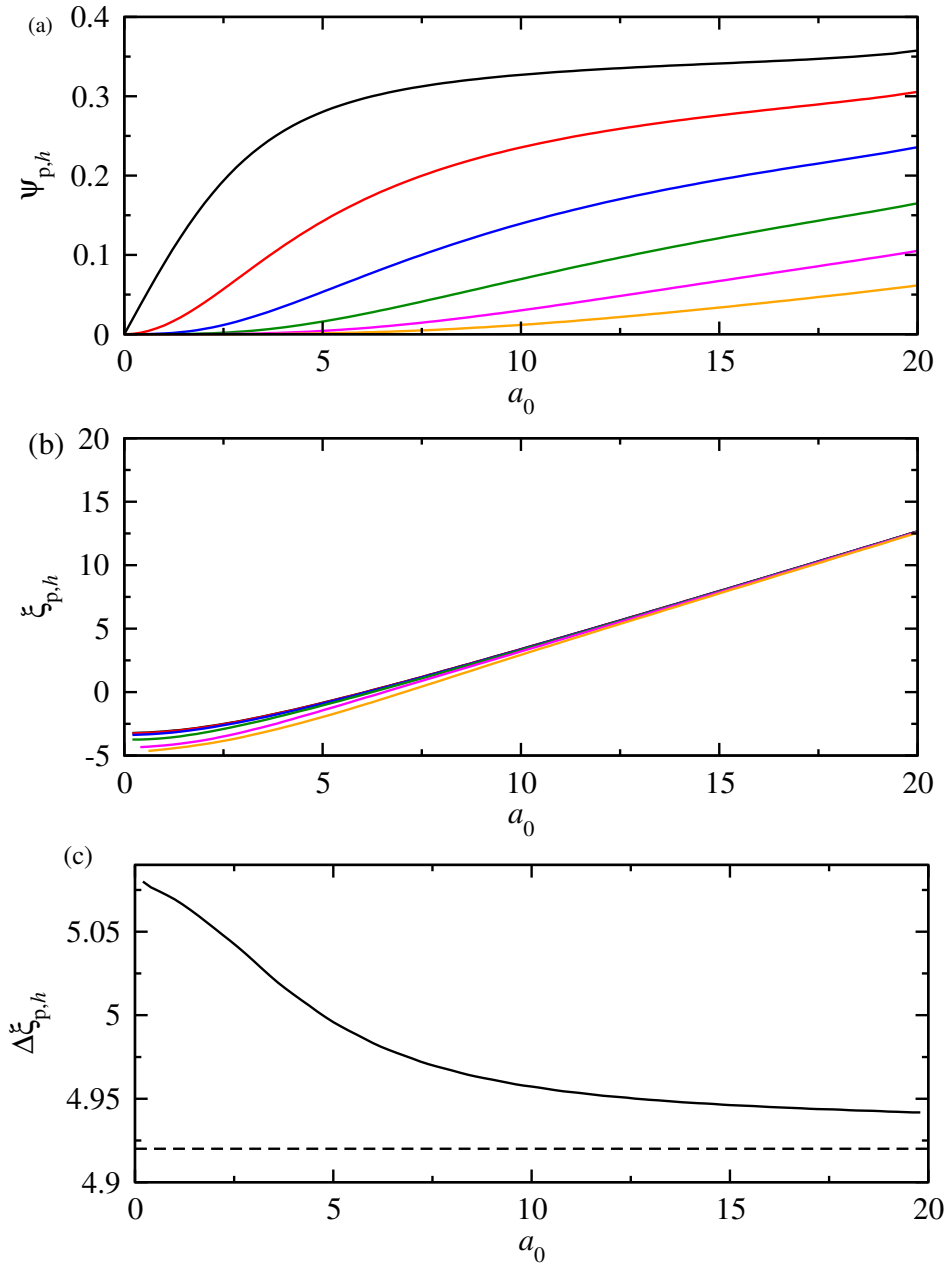

Figure 3.1.13: Irreversible reaction. (a)Dimensionless peak height $\psi_{p,h}$, (b) Dimenionles peak potential potential $\xi_{p,h}$ and (c) dimensinless half maximal width of the principal peak of the harmonics $\Delta\xi_{p,h}$ as a function of the perturbation amplitude a_0. Parameter values: $a = 0.5$, $\sigma = 1$ and $\mu = 0$. 1st (black), 2nd (red), 3rd (blue), 4th (green), 5th (magenta) and 6th harmonic (orange).

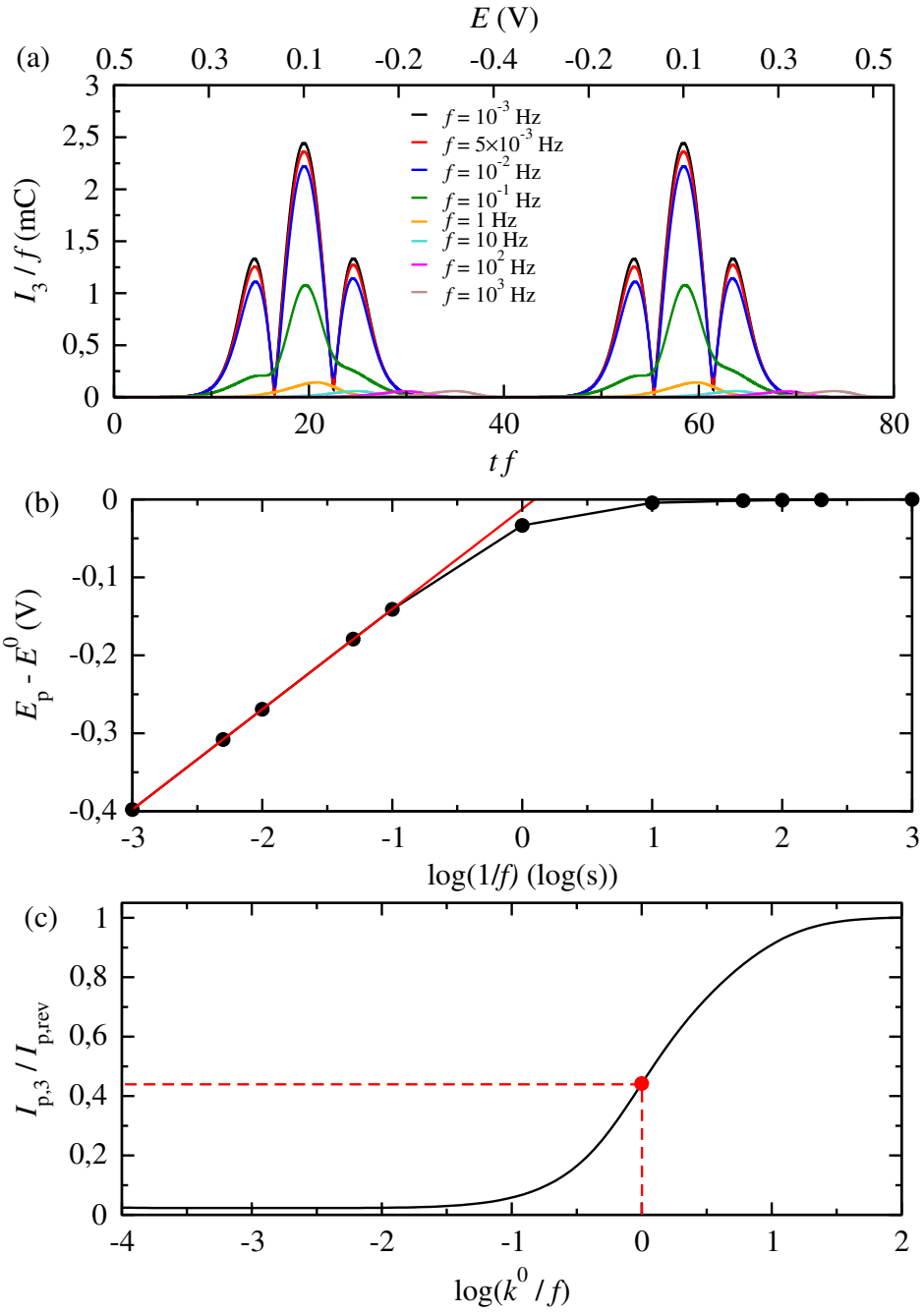

Figure 3.1.14: Methodology for determining thermodynamic and kinetic parameters. (a) Third harmonics for different frequencies f, for the determination of E^0 and $I_{\mathrm{p,rev}}$, (b) shift of the potential of the principal peak for the determination of a and (c) dependence of the normalized principal peak height for the specific a for the determination of k^0. Perturbation amplitude $A_0 = 150$ mV.

for low frequencies the reaction tends to complete reversibility. In the specific example presented in this figure, harmonics for $f \geq 10$ Hz are irreversible, for $0.1 \leq f \leq 10$ Hz are quasi-reversible and for $f \leq 0.01$ Hz tend to reversibility.

By taking a close look at Fig. 3.1.14(a) and (b) it can be seen that for values of the kinetic constant reaching the reversibility (*i.e.* for $f \leq 0.01$ Hz), the principal peak potential value corresponds to the standard (or formal) electrode potential. Thus, one can rather easily determine the standard potential of an immobilized species, as even in the quasi reversible region, the peak value is not shifted. In the case of the classical cyclic voltammetry, as the system enters the quasi reversibility region, the peaks start shifting away from the formal potential. In the case of the example presented in Fig. 3.1.14 E^0 can be estimated at a value of 0.1 V.

Since the formal potential was determined, the methodology to extract the standard rate constant and the transfer coefficient shall be introduced. As a first step, from the limiting value of the height of the principal peak when the system reaches reversibility, the quantity $I_{\mathrm{p,rev}}/f = 2.44$ mC is determined (black curve, corresponding to $f = 0.001$ Hz).

As a second step, the shift of the potential of the principal peak is plotted as a function of the logarithm of the inverse frequency. The corresponding plot is presented in Fig. 3.1.14(b). It is observed that the plot is linear for high frequencies, since in this frequency range the reaction is irreversible. By linear regression in this region, a slope of 0.1285 is found corresponding to a transfer coefficient $a = \frac{\ln(10)}{0.1285}\frac{RT}{F} = 0.46$ at 298 K, based on the dimensional form of Eq. 3.1.32.

As a third step, a quasi-reversible harmonic is chosen and the ratio $I_{\mathrm{p},3}/I_{\mathrm{p,rev}}$ is calculated. For this specific example, the harmonic corresponding to $f = 0.1$ Hz is used, where $I_{\mathrm{p},3}/I_{\mathrm{p,rev}} = 0.442$ (green curve in Fig. 3.1.14(a)). This value is used for the determination of k^0, from the graph presented in Fig. 3.1.14(c), which is a normalized version of Fig. 3.1.9 for $a = 0.46$. In this working example k^0 is determined to be 0.1 s^{-1}. The case of a quasi reversible harmonic was chosen, because, as it can be seen in Fig. 3.1.14(c), the region of great amplification in this plot corresponds to the quasi-reversible region. If one worked in either reversible or the irreversible region, the differences would be smaller, thus the error in the estimation would increase.

It should also be noted, that the curve in Fig. 3.1.14(c) was plotted for a given transfer coefficient value of 0.46. This methodology requires for somebody to calculate the curve for the extracted transfer coefficient. Otherwise if a curve for a transfer coefficient value of 0.5 was used (Fig. 3.1.14), the k^0 would be determined to be 0.08 s^{-1} instead of 0.1 s^{-1}, which could be considered a good approximation when it comes to a real experimental system.

The proposed procedure has been demonstrated for the 3rd harmonic. In order to ascertain the validity of the model assumptions, exactly the same methodology can be performed for other harmonics, in order to validate that the extracted values of k^0 and a coincide for all harmonics, taking into account that they are deprived of the capacitance contribution.

Additional validation can be achieved by chosing different frequencies in the quasi-reversible region to calculate the ratio $I_{\mathrm{p},h}/I_{\mathrm{p,rev}}$ and by using this value in a plot corresponding to that of Fig. 3.1.14(c). Apparently, the choice of f must be such as

the value of $I_{p,h}/I_{p,rev}$ falls in the steep part of this sigmoid curve. Hence, if the model assumptions a met, the estimated values should coincide for any chosen frequency in the quasi-reversible region.

An alternative for the determination of the kinetic parameters, when E^0 is known, is based solely in the curve of Fig. 3.1.14(b). The intercept of the linear part of this curve, is -0.0123. Using Eq. (3.1.32),

$$\log(k^0) = \frac{anF}{2.303RT}(-0.0123) - \frac{\beta}{2.303}$$

where a has been determined from the slope and $\beta = 2.2$ for $A_0 = 150$ mV, see Table 3.2. The derived value is $k^0 = 0.1$ s^{-1}, as expected.

The proposed methodology can be applied, in principle, for the determination of any value of the kinetic constant. Nevertheless, several issues emerge when k^0 is relatively small. For the specific example presented above, the determination of $I_{p,rev}$ requires an application of a small frequency signal. As a result, the duration of the experiment is large, since the scan rate must be small. Moreover, the height of the recorded harmonics will be small (notice that the harmonics in Fig. 3.1.15(a) are divided by the perturbation frequency).

Therefore, if k^0 is relatively is small, the following methodology is proposed. As before, a series of ac-voltammograms is recorded for different frequency values and a given perturbation amplitude A_0. An example is presented in Fig. 3.1.15(a) where the 3rd harmonics are shown for different frequencies and $A_0 = 150$ mV. The harmonic for $f = 0.1$ Hz is quasi-reversible (orange curve) whereas the rest of the harmonics are irreversible. As can be seen, when irreversibility is reached the electrochemical response reaches again a limiting value which can be exploited. From these curves, the height of the irreversible peak is found to be $I_{p,irr}/f = 0.56$ mC.

As a second step, a plot similar to that of Fig. 3.1.14(b) will give $a = 0.46$. Finally, the quasi-reversible harmonic for $f = 0.1$ Hz is chosen and the ratio $I_{p,irr}/I_{p,3}$ is found to be equal to 0.39. This value is used for the determination of k^0, from the graph presented in Fig. 3.1.15(b), which is actually another representation of the corresponding graph in Fig. 3.1.14(c) for $a = 0.46$. Therefore, in this case, the kinetic constant is found to be $k^0 = 0.01$ s^{-1}. Again, at this point, depending on the transfer coefficient estimated, the respective theoretical curve shall be calculated.

In this case as well, the validity of the model can be ascertained by repeating the methodology for different harmonics, comparing the extracted values. Moreover, a validity check can be based on the choice of different frequencies in the quasi-reversible region in order to extract $I_{p,irr}/I_{p,h}$ and implementing this value on a curve corresponding to that of Fig. 3.1.15(b).

In real experimental cases, the above analysis is valid only if the assumptions of the model are closely met. More specifically, Butler-Volmer law shall apply, the immobilized species must behave as a Langmuirian monolayer and a dispersion of the electrochemical transfer rates should not be dispersed. In the case where kinetic or thermodynamic dispersion is present, more elaborate models shall be considered [3]. Indeed, in the presence of kinetic or thermodynamic dispersion, the dependence of chief observables such as peak height and half maximal peak on scan rate or frequency may be different,

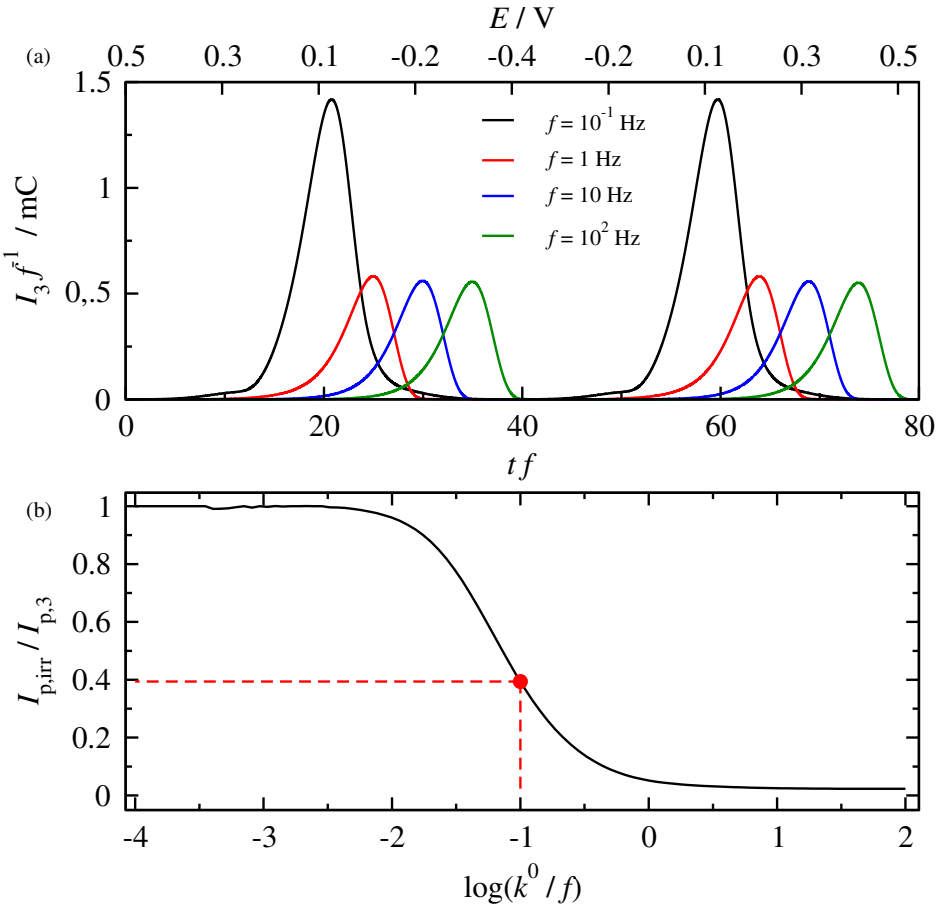

Figure 3.1.15: Methodology for determining kinetic parameters. (a) Third harmonics for different frequencies f, for the determination of $I_{\mathrm{p,irr}}$, and (b) dependence of the normalized principal peak amplitude for the specific a for the determination of k^0. Perturbation amplitude $A_0 = 150$ mV.

both in dc and ac voltammetry. In these cases, deviations of the estimated kinetic constant and formal electrode potential from their actual value are expected, as suggested recently by comparing experimental findings with direct numerical simulations [4, 5]. The influence of kinetic and thermodynamic dispersion on dc and ac voltammograms has been analyzed thoroughly [6], as well as the differences observed when Marcus-Hush theory is applied instead of the Butler-Volmer law [7].

3.1.4 Transfer Coefficient

In this section, the transfer coefficient a is examined. The case of a reversible reaction is not examined in this section, as the transfer coefficient has no role in any of the harmonics and the chief observables remain unchanged, no matter its value since the kinetics play no role in such systems.

The case of a quasi reversible reaction for different ransfer coefficients is presented in Fig. 3.1.16, where a dimensionless kinetic constant of 10 is used. For each harmonic only the oxidation peak is presented. In each panel in this Fig. 3.1.16, on the left side transfer coefficients of 0.2, 0.35 and 0.5 are presented, while on the left on 0.5, 0.65 and 0.8. For the first harmonic, no drastic change appears to occur with the change of the transfer coefficient. In the second harmonic, for a lower than 0.5 the first dominant peak remains at the same levels, whereas the second decreases a bit. For a higher than 0.5, the inverse behavior is observed. For the third harmonic the transfer coefficient has almost no impact on the dominant peak but also acts accordingly to the second harmonic as when it comes to the two smaller peaks. Regarding the fourth harmonic, as the a decreases, left dominant peak rises until the whole voltammogram becomes a uniform peak whereas the for a higher than 0.5, the exact opposite happens. The same logic goes for the 6th harmonic. Finally, when it comes to the fifth harmonic the tendency described in the third one becomes more prominent, and for transfer coefficients closer to 0 and 1 respectively, a uniform peak is observed.

3.1.5 Chemically Irreversible reaction

In this section we shall examine the case where the reaction is chemically irreversible, thus the reduced form of the immobilized species cannot return back to its oxidized state. At first, the case of cyclic voltammetry shall be examined. By rendering the oxidation term of Eq 3.1.18 equal to zero, the current expression becomes as in Eq. 3.1.35.

$$i = F\Gamma k^0 \mathrm{e}^{[\frac{(1-a)F}{RT}(E-E^0)](1-\theta)] } \tag{3.1.35}$$

By solving Eq. 3.1.35 and rendering the current and the potential dimensionless with the use of the dimensionless quantities introduced in the cyclic voltammetry analysis, the resulting voltammograms are the ones that appear in Fig. 3.1.17. The peak shifts as a function of the kinetic constant, but remains unchanged in magnitude. The absolute value of the peak of the dimensionless current is 0.184, the same as in the case of an irreversible reaction.

When it comes to FTacV, the dimensionless expression of the current presented in Eq. (3.1.22) is rewritten as in Eq. (3.1.36), where the oxidation term is yet again

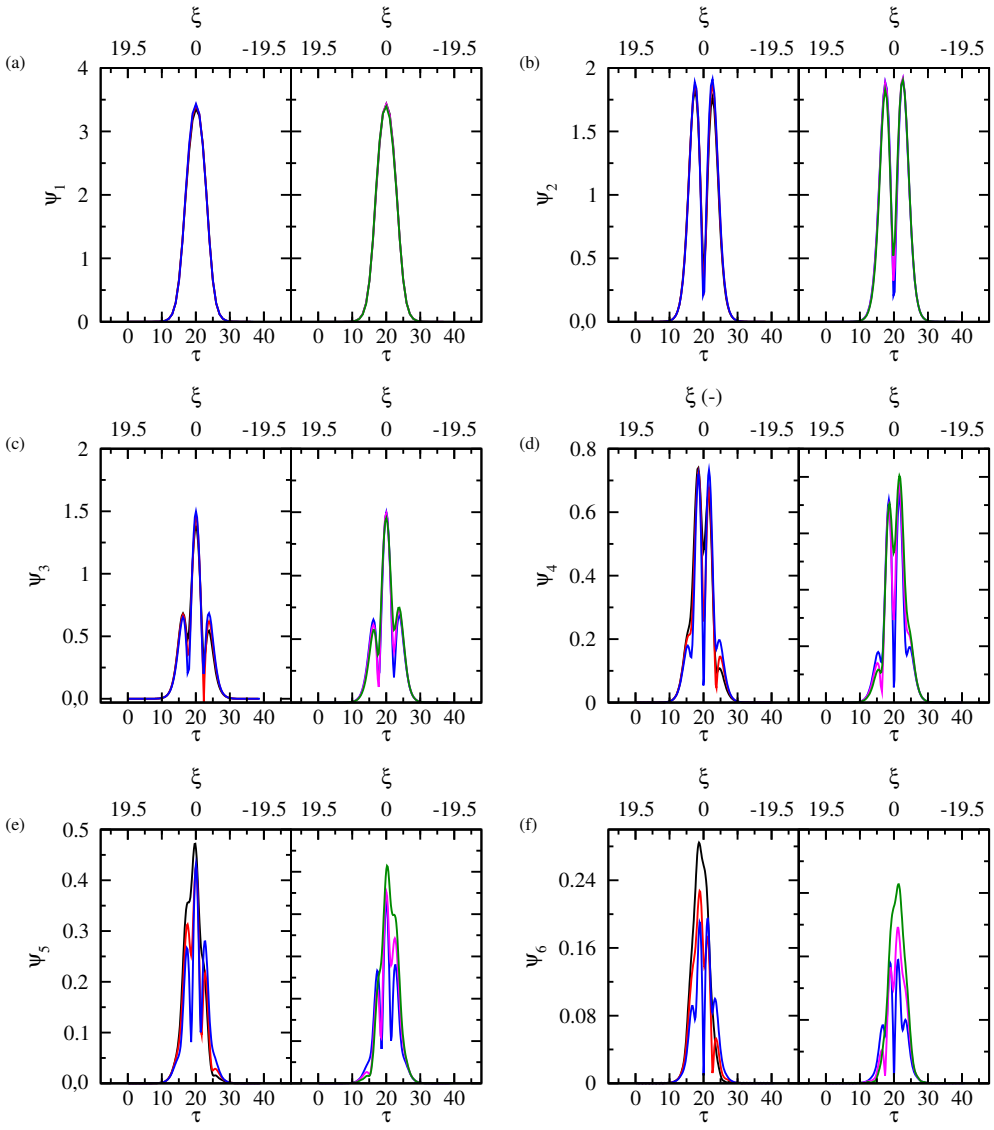

Figure 3.1.16: (a) - (e) 1st through 6th harmonic for an immobilized species α_0 3.959, σ 0.9735, ξ^0 0 and k_{ac} 10. values for a 0.2 (black line), 0.35 (red line), 0.5 (blue line), 0.65 (magenta line) and 0.8 (green line).

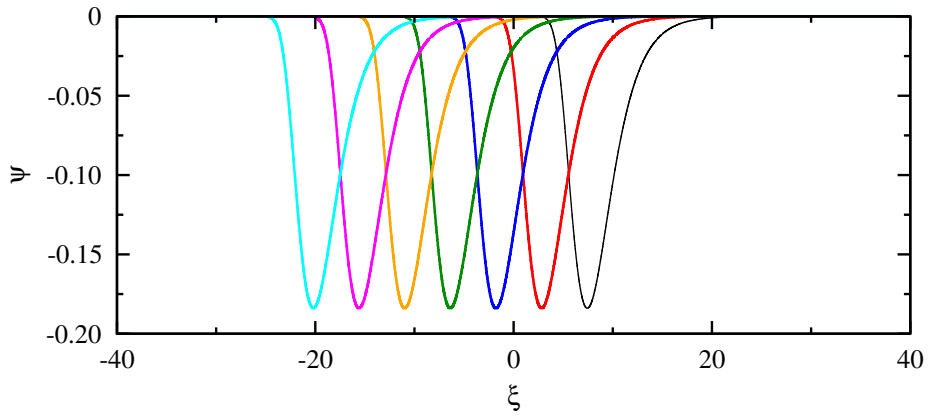

Figure 3.1.17: One step chemically irreversible reaction: Dimensionless cyclic voltammograms of immobilized species for σ= 0.4868, ξ^0= 0 and k_{cv} = 10 (black), 1 (red), 0 (blue), 0.1 (green), 0.01 (orange), 0.001 (magenta) and 0.0001 (cyan).

ommited,

$$\psi = -k_{ac} e^{-a\xi} \theta \tag{3.1.36}$$

By simulating of an FTacV experiment based on Eq. (3.1.36) and performing the necessary analysis, in Fig. 3.1.18 the effect of the kinetics on the 5th harmonic for a chemically irreversible reaction is presented at an amplitude of 3.959. Only one peak is visible in this case in the forward scan while, nothing is visible in the reverse scan. Moreover, as the kinetics get slower, the peak is displaced towards more cathodic potentials. The same trend is observed for all the other harmonics as well (results not shown). The trend of the peak shift is shown in Fig. 3.1.20(a). A linear trend of the peak potential against the logarithm of the kinetic constant is observed. One notable aspect of this case is that the shift of all the harmonics has the exact same trend.

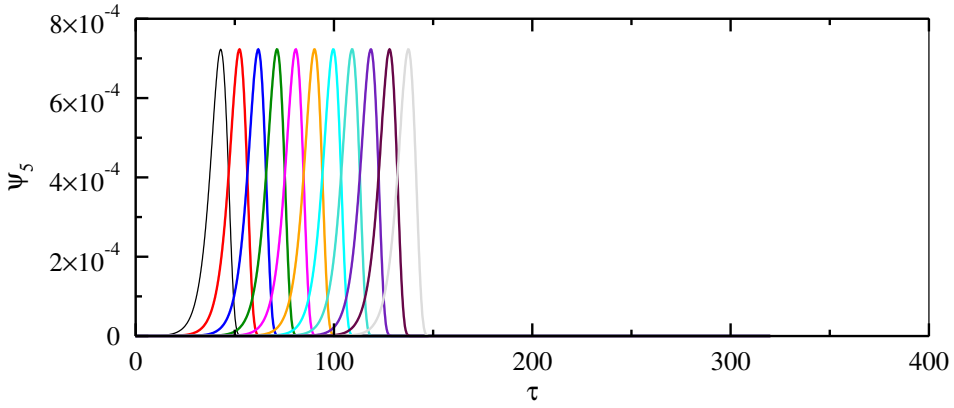

Figure 3.1.18: 5th Harmonic of chemically irreversible immobilized species for α_0 = 3.959, σ = 0.4868, a= 0.5, ξ^0 = 0 and k_{ac} = 1000 (black), 100 (red), 10 (blue), 1 (green), 0.1 (magenta), 0.01 (orange), 0.001 (violet), 1 × 10^{-4} (cyan), 1 × 10^{-5} (indigo), 1 × 10^{-6} (maroon) and 1 × 10^{-7} (grey).

In Fig. 3.1.19, the 5th harmonic of a chemically irreversible reaction at a k_{ac} value

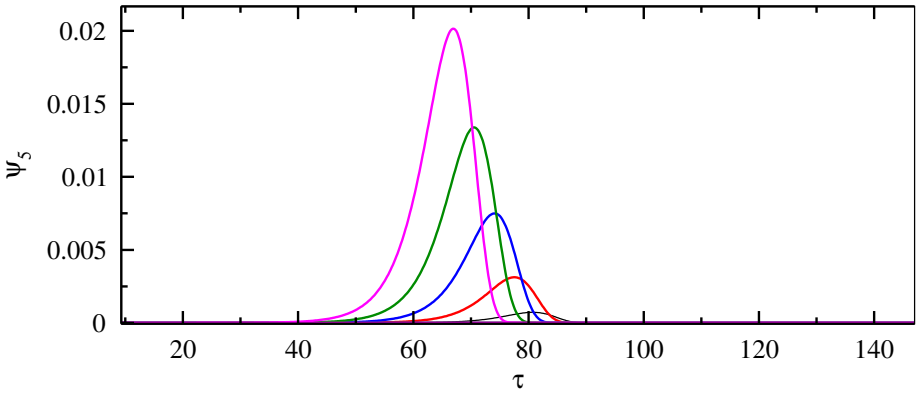

Figure 3.1.19: 5th Harmonic of chemically irreversible immobilized species for $\sigma = 0.4868$, $a = 0.5$, $\xi^0 = 0$, $k_{ac} = 0.1$ and $\alpha_0 = 3.959$ (black), 5.839 (red), 7.785 (blue), 9.731 (green) and 11.677 (magenta).

of 0.1, at different amplitude values. As the amplitude increases, it is evident that the magnitude of the harmonic increases and the peak potential shifts towards more anodic values. The shift of the peak against the logarithm of the kinetic constant for different amplitudes is presented in Fig. 3.1.18(b). It is reminded that the peak shift is independent of the order of the harmonic.

3.2 Two Step Reaction

3.2.1 Two Reversible Reactions

In the case of a two step reaction, the scenario changes slightly, with the reactions being described in Eqs. (3.2.1) and (3.2.2), where in the first step A is reduced to B and then B is reduced to C. The dimensionless kinetic constants corresponding to the two steps are k_1 and k_2 while the dimensionless formal potentials ξ_1^0 and ξ_2^0, respectively. The surface coverages in this case are defined as $\theta_1 = \frac{\Gamma_A}{\Gamma_{tot}}$ and $\theta_2 = \frac{\Gamma_C}{\Gamma_{tot}}$, and Γ_{tot} is equal to the sum $\Gamma_A + \Gamma_B + \Gamma_C$. The surface coverage of B is defined as $1 - \theta_1$-θ_2. Definitions for the dimensionless current and dimensionless scan rate remain the same. The dimensionless current expressions for each step are expressed as in Eqs. (3.2.3) and (3.2.4). The total dimensionless current ψ_{tot} is the sum of ψ_1 and ψ_2. Therefore,

$$A + e \underset{}{\overset{k_1^0}{\rightleftharpoons}} B \tag{3.2.1}$$

$$B + e \underset{}{\overset{k_2^0}{\rightleftharpoons}} C \tag{3.2.2}$$

and,

$$\psi_1 = k_1(e^{(1-a)\xi_1}(1 - \theta_1 - \theta_2) - e^{(-a\xi_1)}\theta_1) \tag{3.2.3}$$

$$\psi_2 = k_2(e^{(1-a)\xi_2}\theta_2 - e^{(-a\xi_2)}(1 - \theta_1 - \theta_2)) \tag{3.2.4}$$

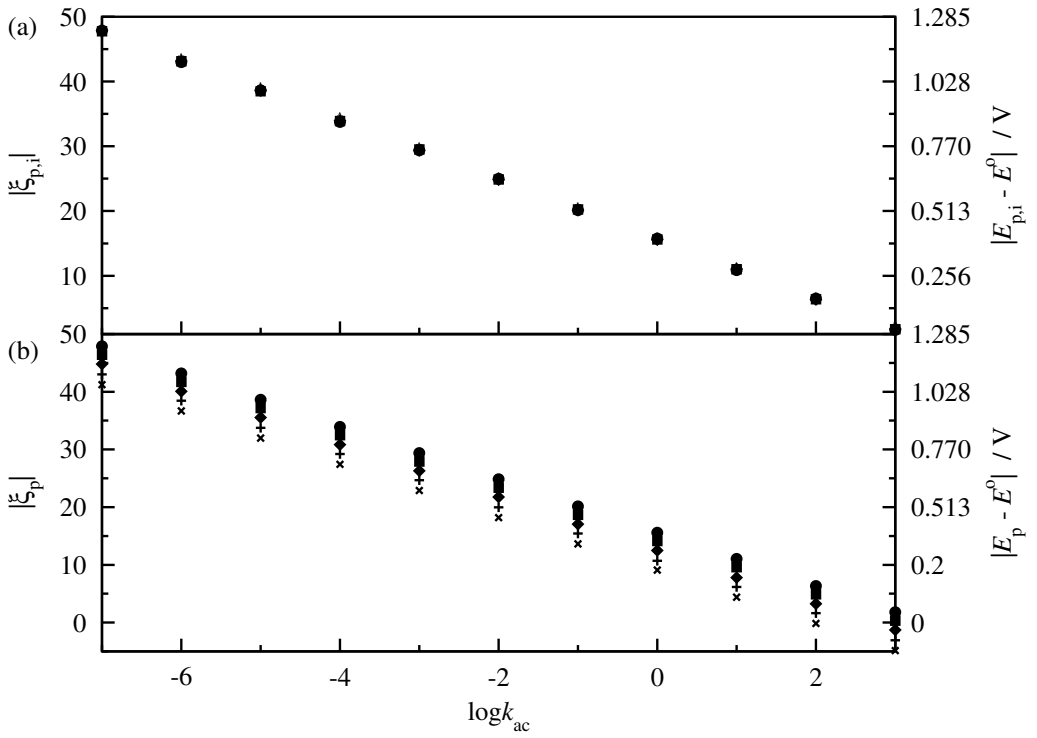

Figure 3.1.20: Displacement of peak for chemically irreversible immobilized species against logk_{ac} for (a) $\alpha_0 = 3.959$ 1st (circle), 2nd (square), 3rd (diamond), 4th (plus), 5th (x) and 6th harmonic (char) (b) 5th harmonic for $\alpha_0 = 3.959$ (circle), 5.839 (square), 7.785 (diamond), 9.731 (plus) and 11.677 (x).

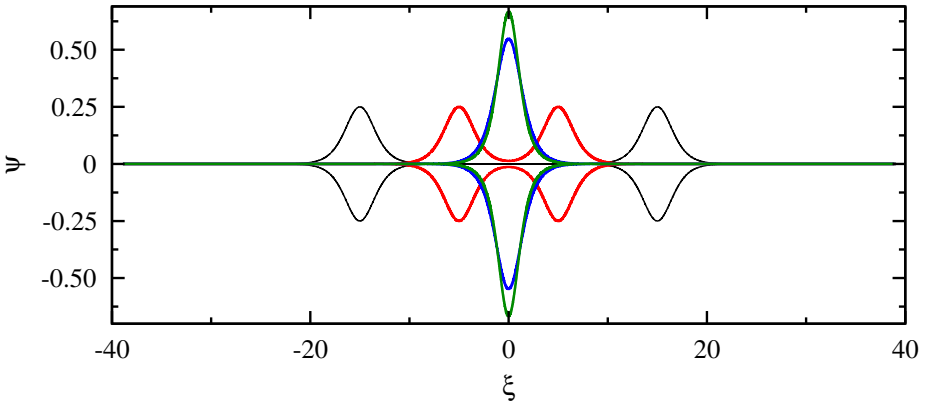

Figure 3.2.1: Two step reaction: Dimensionless cyclic voltammograms of immobilized species for σ=0.4868, k_1=k_2=100, ξ_1^0 = 15 and ξ_2^0 = -15 (black line), ξ_1^0 = 5 and ξ_2^0 = -5 (red line), ξ_1^0 = 0.5 and ξ_2^0 = -0.5 (blue line), ξ_1^0 = ξ_2^0 = 0 (green line).

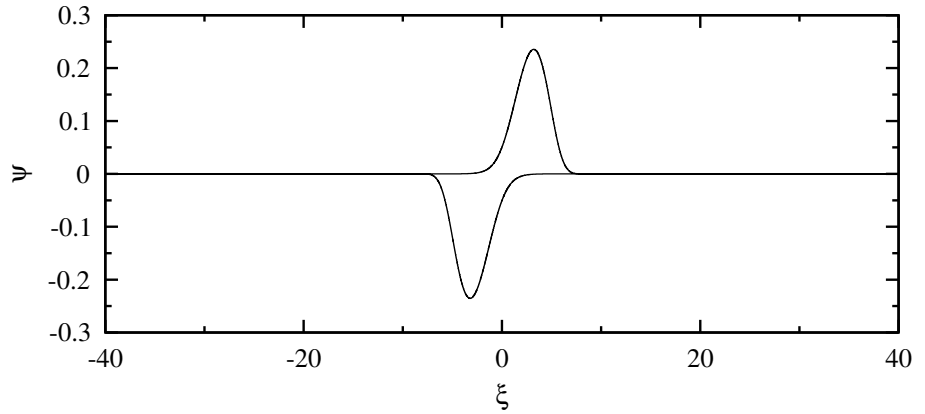

Figure 3.2.2: Two step reaction: Dimensionless cyclic voltammograms of immobilized species for σ=0.4868, k_1=k_2=100, ξ_1^0 = -15 and ξ_2^0 = 15.

Again, first the scenario will be examined for cyclic voltammetry and then for FTacV. In Fig. 3.2.1 the dimensionless cyclic voltammograms are presented for a two step reaction, with both steps reversible and the standard potential of the second being more negative than the standard potential of the first. When the two formal potentials are well separated it seems like having two cyclic voltammograms with the characteristics discussed before. As the two standard potential get closer, the two voltammograms start to intertwine forming one voltammogram, the peak height of which is more than two times the peak of the seperate voltammograms, in the case the two steps have the same standard potential. The case in which the standard potential of the second step is more positive than one of the first one is depicted in Fig. 3.2.2. In this case the peaks are not symmetrical regarding the potential, but the cathodic and the anodic peaks have the same absolute value at 0.235, which is different than the value of the irreversible one step reaction.

In Fig. 3.2.3 the 5th harmonic for different scenarios is presented in case both steps have very fast kinetics. Only the 5th harmonic is presented as all the other harmonics

have a similar trend. In Fig. 3.2.3(a) we have the case of two well separated steps with the the ξ^0 of the second step being more cathodic than the one of the first ($\xi_1^0 = 15$ and $\xi_2^0 = -15$) at different amplitudes. The maxima of each peak correspond to that of a single step fast reversible reaction and as the amplitude increases the harmonics widen. In such a case, no problem arises in the analysis of the peaks, as the same things that are valid for a one step fast reversible electrochemical reaction, are valid for each step separately. This is as long as the harmonics of the steps are well separated and do not interfere. So, experimentally, when one faces a two step reaction with separated peaks, he shall pay attention to the amplitude used, so that the harmonics do not widen to the extend that they start to interfere with each other.

In Fig. 3.2.3(b) we have the case where we go from two well separated steps (black and red line) to the case where the two steps tend to appear as one (blue line) and finally in the case where the two peaks have the same dimensionless formal potentials. In the latter case, schematically the harmonic resembles that of a single step reaction, but the peak dimensionless current of the harmonic is about 3.7 times higher than that of the single step reaction (2.23 vs 0.609 respectively). This difference could act as a diagnostic for the electron transfer mechanism, as if one harmonic appears a single electron transfer but the peak dimensionless current is higher than the expected, probably the reaction is a two-step one.

The last case examined when we have two steps and both are fast and reversible is presented in Fig. 3.2.3(c) for different amplitudes. Here, the dimensionless potential of the second step is more anodic than that of the first step ($\xi_1^0 = -15$ and $\xi_2^0 = 15$). Schematically, what is presented does not resemble the conventional 5th harmonic of an immobilized species, as the ones presented up to now, as for higher amplitudes only one peak is presented, while for the lowest amplitude (3.892) a rather unconventional pattern arises. In this case, the peaks cannot be separated and the only feature that can be extracted is that the dominant peak corresponds to the average of the dimensionless formal potentials, but this is still not a safe assumption.

3.2.2 One Reversible and One Irreversible Reaction

In this section a slightly different scenario shall be examined than the one in the previous section. The difference is that the second step is irreversible, thus C cannot be oxidized back to B. The only equation that changes is Eq. (3.2.4) which is transformed to Eq. (3.2.5). 1st through th harmonic of the forward scan of such a case is presented in Fig. 3.2.5.

$$\psi_2 = k_1 e^{(-a\xi_2)}(1 - \theta_1 - \theta_2) \tag{3.2.5}$$

The reverse scan is not shown as the second step is chemically irreversible and C cannot be oxidized back to B, leading to zero current densities. The fixed parameters in this example are $\sigma = 0.4868$, $\alpha_0 = 3.892$, $\xi_1^0 = 0$, $\xi_2^0 = 5$, $k_1 100$ while k_1 varies from 10 down to 0.0001. For high k_2 values one peak of low magnitude appears for all the harmonics. As k_2 value increases, this peak shifts towards more cathodic potentials, increasing in magnitude, and starting to resemble a reversible kinetics situation. This

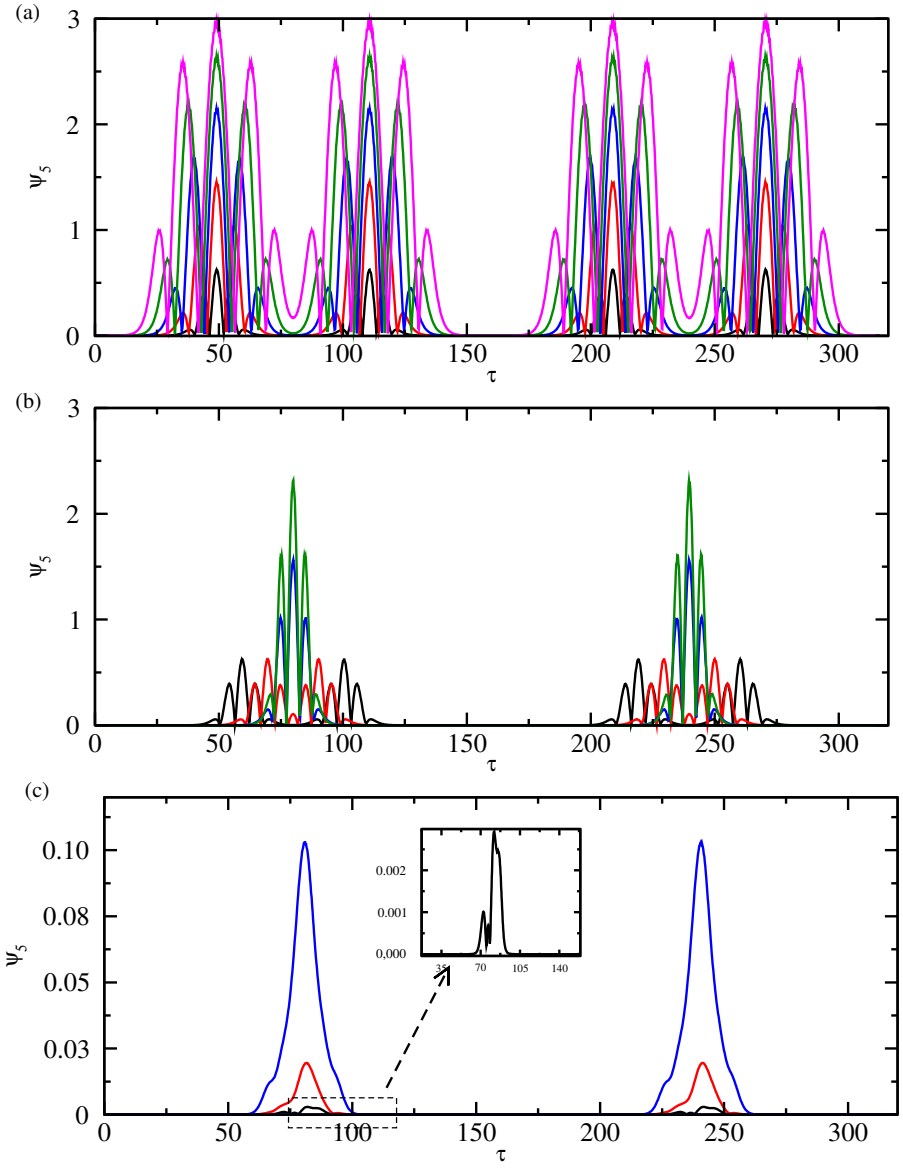

Figure 3.2.3: Different cases of a two step reaction with both steps being electrochemically reverisble (k_1=k_2=100): (a) Well seperated steps with $\xi_1^0 = 15$ and $\xi_2^0 = -15$ for different α_0 valuees. $\sigma = 0.4868$, $\alpha_0 = 3.892$ (black), 5.839 (red), 7.785 (blue), 9.731 (green) and 11.677 (magenta) (b) Decreasing seperation of the steps at $\alpha_0 = 3.892$ and different pairs of ξ^0 values. $\sigma = 0.4868$, $\xi_1^0 = 5$ and $\xi_1^0 = -5$ (red), $\xi_1^0 = 0.5$ and $\xi_2^0 = -0.5$ (blue) and $\xi_1^0 = \xi_2^0 = 0$ (green) (c) Well seperated steps but with inverse ξ^0 values at different amplitudes. $\sigma = 0.4868$, $\xi_1^0 = -15$ and $\xi_2^0 = 15$ at $\alpha_0 = 3.892$ (black), 5.839 (red), 7.785 (blue).

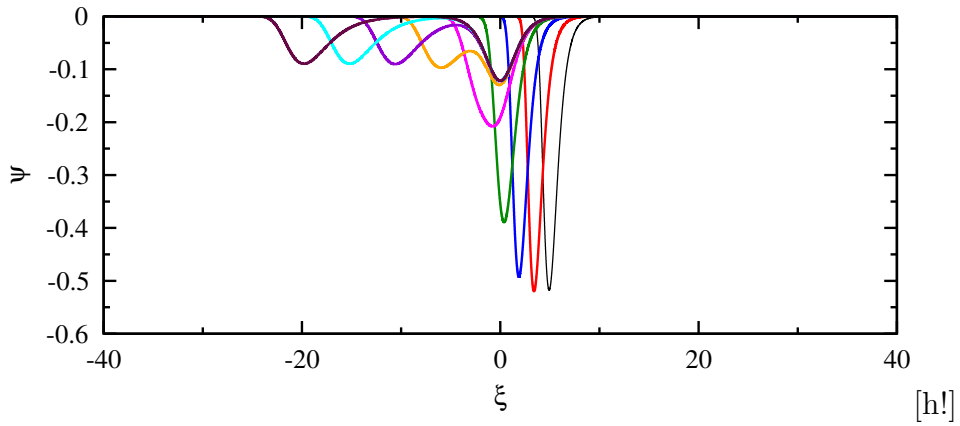

Figure 3.2.4: Two step reaction, with the second being chemically irreversible: Dimensionless cyclic voltammograms of immobilized species for $\sigma = 0.4868$, $\xi_1^0 = 0$, $\xi_2^0 = 5$, $k_1 = 100$ and $k_2 = 100$ (black), 10 (red), 1 (blue), 0.1 (green), 0.01 (magenta), 0.001 (orange), 1×10^{-4} (violet), 1×10^{-5} (cyan) and 1×10^{-6} (brown).

is due to the fact that the chemically irreversible reaction shifts towards more cathodic peaks when its kinetics get slower, just like in Section 3.1.5, revealing the first fast and reversible step. when the two steps get separated, the second step is almost invisible due to the fact that the magnitude of an irreversible reaction in FTacV is order of magnitudes smaller than the one of a reversible one. Experimentally, such a separation can be achieved by increasing the frequency of the experiment, so that the effective kinetic constant k_2 (equal to $k_2^0)/f$) gets lowered to a relatively small value and shift the peak of this step more cathodically. Technically, if one would increase the frequency from 1 to 100 Hz, the k_2 value would be lowered 2 orders of magnitude.

By looking at the harmonics, while the two harmonics are still intertwined, a mix up can occur while interpreting the results. Focusing at the green line of the 5th harmonic ($k_2 = 0.01$) 4 peaks are visible with the two dominant having about the same magnitude, which could lead one to think that it corresponds to the 4th harmonic instead of the fifth one.

3.3 Michaelis-Menten mechanism

3.3.1 Kinetic analysis

A kinetic analysis shall be made regarding a kinetic scenario according to which an electroactive enzyme, immobilized on an electrode surface, reacts with a substrate being free in the solution. This is necessary due to the fact that no such analysis has been presented in the literature under FTacV conditions. The reactions included in the scenario are depicted in Fig. 3.3.1. According to this reaction scheme, an electroactive enzyme (E_1 oxidized form, E_2 reduced form) is immobilized in a layer on the surface of an inert electrode. The substrate S is free in the solution and reacts according to a

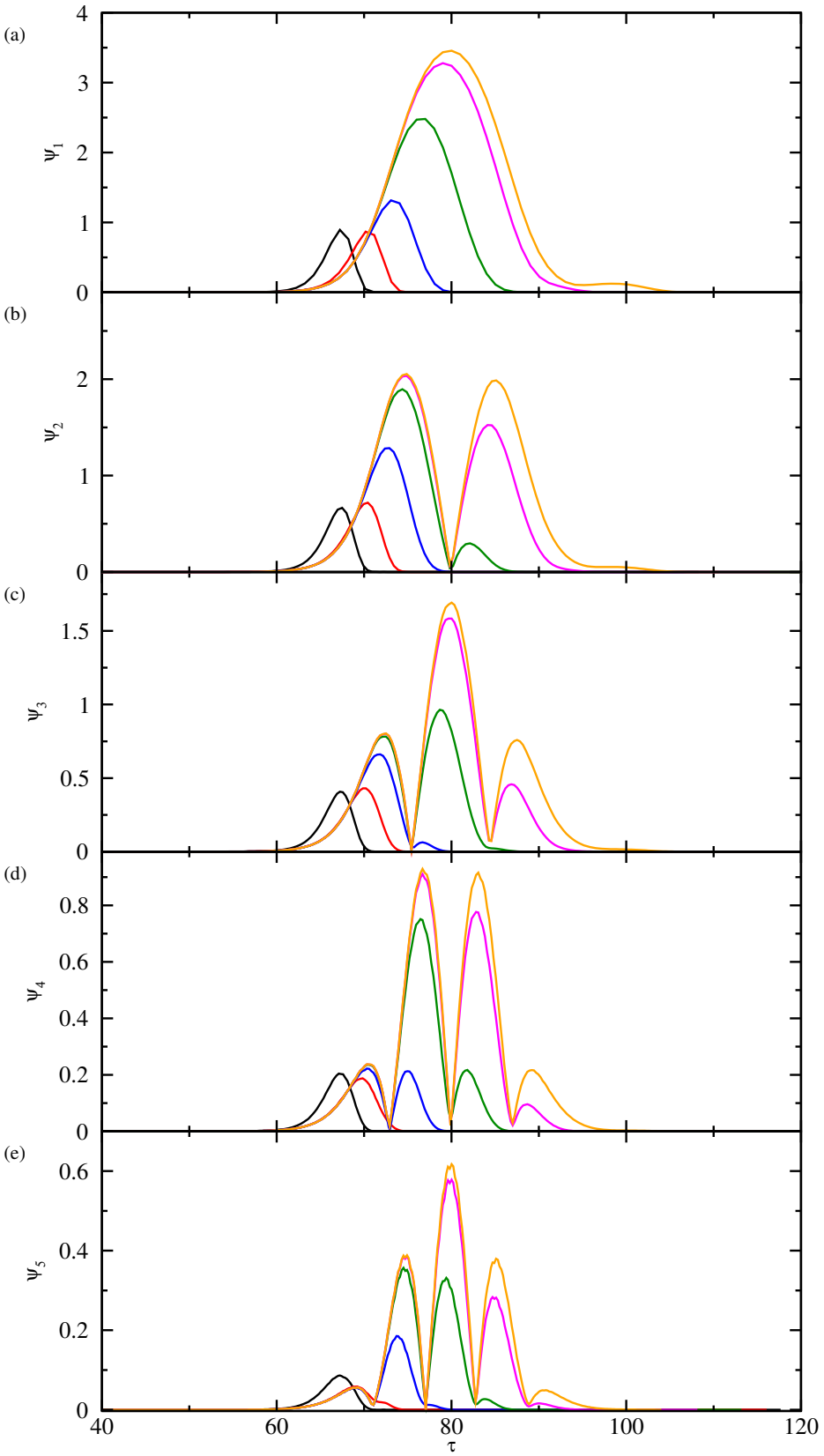

Figure 3.2.5: (a) - (e) 1st through 5th harmonic for a two step reaction with the first being chemically reversible and the second chemically irreversible. $\sigma = 0.4868$, $\alpha_0 = 3.892$, $\xi_1^0 = 0$, $\xi_2^0 = 5$, $k_1 = 100$ and $k_2 = 10$ (black), 1 (red), 0.1 (blue), 0.01 (green), 0.001 (magenta), 0.0001 (orange).

Michaelis-Menten mechanism,

$$\mathrm{E_1} + \mathrm{S} \underset{k_{-1}}{\overset{k_1}{\rightleftharpoons}} \mathrm{E_1S} \tag{3.3.1}$$

$$\mathrm{E_1S} \xrightarrow{k_2} \mathrm{E_2} + \mathrm{P} \tag{3.3.2}$$

$$\mathrm{E_2} \overset{k^0}{\rightleftharpoons} \mathrm{E_1} + \mathrm{e} \tag{3.3.3}$$

where k^0 is the standard rate constant of the electrochemical redox reaction on the electrode surface, k_1, k_{-1} and k_2 the reaction rate constants of the respective chemical steps. More specifically, the oxidized form of the enzyme $\mathrm{E_1}$ reacts with the substrate S, producing the product P and the reduced form of the enzyme $\mathrm{E_2}$. From this particular reduced form, the enzyme is oxidized electrochemically by the application of a sufficient anodic potential, producing again the oxidized form $\mathrm{E_1}$ which can again react with the substrate S.

Assuming practically constant concentration of the substrate c_S, the kinetic equations are written as follows,

$$\frac{d\Gamma_{\mathrm{E_1S}}}{dt} = r_1 - r_2 \tag{3.3.4}$$

$$\frac{d\Gamma_{\mathrm{E_2}}}{dt} = r_2 - r_3 \tag{3.3.5}$$

where $\Gamma_{\mathrm{E_1S}}$ and $\Gamma_{\mathrm{E_2}}$ are the surface concentrations of the corresponding species and t corresponds to time.

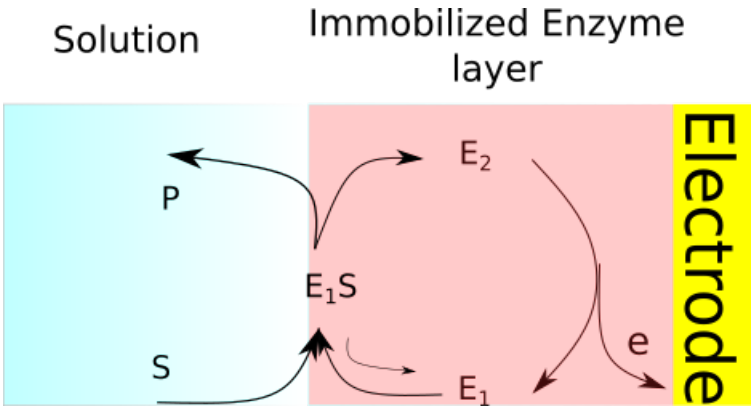

Figure 3.3.1: Reaction scheme of an immobilized electroactive enzyme. The oxidized form of the enzyme, $\mathrm{E_1}$, reacts with the substrate that is free in the solution, S, giving the enzyme's reduced form, $\mathrm{E_2}$ which can be then oxidized again.

The reaction rates r_i in Eqs. (3.3.4) and (3.3.5) are given by,

$$r_1 = k_1(\Gamma^0 - \Gamma_{E_1S} - \Gamma_{E_2})c_s - k_{-1}\Gamma_{E_1S} \tag{3.3.6}$$

$$r_2 = k_2\Gamma_{E_1S} \tag{3.3.7}$$

$$r_3 = k^0[\Gamma_{E_2}e^{\frac{(1-a)F}{RT}(E-E^0)} - (\Gamma^0 - \Gamma_{E_1S} - \Gamma_{E_2})e^{-\frac{aF}{RT}(E-E^0)}] \tag{3.3.8}$$

In the rate expressions above, $\Gamma_{E_1} = \Gamma^0 - \Gamma_{E_1S} - \Gamma_{E_2}$ is the surface concentration of the oxidized form of the enzyme, Γ^0 the initial surface concentration of the enzyme, E the electrode potential and E^0 the formal electrode potential of the electrochemical step. The rest of the symbols have their usual meaning.

In the case of an FTacV experiment, the electrode potential E is also time dependent. In the presence of double layer specific capacitance C_{dl} and uncompensated resistance R_s between the working and reference electrode, E will be given by the charge balance equation (*i.e.* the total current is the algebraic sum of the Faradaic and capacitance current),

$$AC_{dl}\frac{dE}{dt} = \frac{V - E}{R_s} - AFr_3 \tag{3.3.9}$$

where A is the surface area of the electrode and V is the applied potential. In Eq. (3.3.9), the left hand term corresponds to the capacitance current whereas the first right hand term is the total current and the second hand term is the Faradaic current. For a FTacV experiment, the applied potential V is given by,

$$V(t) = V_I + vt_R - v|t - t_R| + A_0\sin(2\pi ft) \tag{3.3.10}$$

corresponding to a sinusoidal signal, superimposed to a triangular wave. In this equation, V_I is the initial potential, v the scan rate, $t_R = |V_I - V_R|/v$ the reversal time for V_R reversal potential and A_0, f the perturbation amplitude and frequency, respectively. The current, recorded during the experiment is the total current,

$$I(t) = \frac{V(E) - E(t)}{R_s} \tag{3.3.11}$$

In the absence of uncompensated resistance R_s, the electrode potential is given by Eq. (3.3.10), by setting $V(t) = E(t)$, $V_I = E_I$ and $V_R = E_R$ and the recorded current is the algebraic sum of the Faradaic and capacitance current,

$$I = AFr_3 + AC_{dl}\left[v\frac{t - t_R}{|t - t_R|} + 2\pi fA_0\cos(2\pi ft)\right] \tag{3.3.12}$$

where the capacitance current has been obtained by differentiating Eq. (3.3.10).

Equations (3.3.4), (3.3.5) and (3.3.9), describe a typical cyclic voltammetry experiment for $A_0 = 0$, as in the absence of a perturbation on the potential, the classical dc voltammogram is obtained. In the case of $A_0 = 0$ and $v = 0$ the applied potential is constant, thus leading to the simulation of a chronoamperometric experiment. Both equations stand for constant c_S. During a FTacV experiment, the effect of capacitance current will be eliminated for harmonic components higher than one, provided that the capacitance is independent of the electrode potential.

3.3.2 Dimensional analysis

As can be seen from Eqs. (3.3.4)-(3.3.8) and (3.3.10), the kinetics of the reaction depend on four kinetic constants, the formal potential of the electrochemical step and the transfer coefficient as well as three adjustable parameters, namely, the initial enzyme concentration, the substrate concentration, the scan rate, the perturbation amplitude and frequency. The number of parameters to be considered for the the analysis of the kinetics can be reduced by performing a dimensional analysis. In order to do so, the following transformations are introduced,

$$\begin{aligned}
\tau &= tf && \text{(dimensionless time)}\\
u &= \frac{F}{RT}V && \text{(dimensionless applied potential)}\\
\xi &= \frac{F}{RT}(E-E^0) && \text{(dimensionless electrode potential)}\\
\theta_{\mathrm{E_1S}} &= \Gamma_{\mathrm{E_1S}}/\Gamma^0 && \text{(surface coverage of the intermediate)}\\
\theta_{\mathrm{E_2}} &= \Gamma_{\mathrm{E_2}}/\Gamma^0 && \text{(surface coverage of the reduced form of the enzyme)}\\
\hat{c}_{\mathrm{S}} &= c_{\mathrm{S}}/K_{\mathrm{M}} && \text{(dimensionless substrate concentration)}\\
\psi &= \frac{i}{f\Gamma^0 F} && \text{(dimensionless current density)}\\
\hat{r}_i &= \frac{r_i}{f\Gamma^0} && \text{(dimensionless rate)}
\end{aligned}$$

where $K_{\mathrm{M}} = (k_{-1}+k_2)/k_1$ is the Michaelis constant.

By introducing the dimensionless quantities in Eqs. (3.3.6)-(3.3.8) and replacing in Eqs. (3.3.4) and (3.3.5) we get the following set of equations for the temporal evolution of the reaction intermediate and the coverage of the reduced form of the enzyme,

$$\frac{\tau_{\mathrm{MM}}}{\tau_{\mathrm{AC}}}\frac{d\theta_{\mathrm{E_1S}}}{d\tau} = \hat{c}_{\mathrm{S}}(1-\theta_{\mathrm{E_2}}-\theta_{\mathrm{E_1S}}) - \theta_{\mathrm{E_1S}} \tag{3.3.13}$$

$$\frac{d\theta_{\mathrm{E_2}}}{d\tau} = \tau_{\mathrm{AC}}k_2\theta_{\mathrm{E_1S}} - \tau_{\mathrm{AC}}k^0\left[\theta_{\mathrm{E_2}}e^{(1-a)\xi} - (1-\theta_{\mathrm{E_2}}-\theta_{\mathrm{E_1S}})e^{-a\xi}\right] \tag{3.3.14}$$

Moreover, by introducing the dimensionless quantities in the charge balance equation, Eq. (3.3.9), the following equation governs the temporal evolution of the dimensionless potential,

$$\frac{d\xi}{d\tau} = \frac{\tau_{\mathrm{AC}}}{\tau_{\mathrm{RC}}}(u-\xi) - \beta\tau_{\mathrm{AC}}k^0\left[\theta_{\mathrm{E_2}}e^{(1-a)\xi} - (1-\theta_{\mathrm{E_2}}-\theta_{\mathrm{E_1S}})e^{-a\xi}\right] \tag{3.3.15}$$

where $\beta = \Gamma^0F^2/RTC_{\mathrm{dl}}$. Three different time constants appear in Eqs. (3.3.13)-(3.3.15). The time constant $\tau_{\mathrm{AC}} = 1/f$ is determined by the frequency of the FTacV experiment. The time constant $\tau_{\mathrm{RC}} = AC_{\mathrm{dl}}R_{\mathrm{s}}$ is determined by the experimental setup (surface area and solution conductivity). Finally, the time constant $\tau_{\mathrm{MM}} = 1/(k_{-1}+k_2) = 1/(k_1K_{\mathrm{M}})$ is determined by the rate constants of the chemical steps of the reaction.

The variation of the dimensionless applied potential is written in the form of Eq. (3.3.16), by introducing the dimensionless quantities in Eq. (3.3.10),

$$u = u_{\mathrm{I}} + \frac{\tau_{\mathrm{AC}}}{\tau_{\mathrm{CV}}}\tau_{\mathrm{R}} - \frac{\tau_{\mathrm{AC}}}{\tau_{\mathrm{CV}}}|\tau-\tau_{\mathrm{R}}| + \alpha_0\sin(2\pi\tau) \tag{3.3.16}$$

where $\alpha_0 = A_0 F/RT$ is the dimensionless perturbation amplitude. A forth time constant is introduced here, $\tau_{CV} = RT/Fv$, determined by the scan rate. The dimensionless total current $\Psi = \frac{I}{fA\Gamma^0 F}$ is obtained from Eq. (3.3.11),

$$\Psi(\tau) = \frac{\tau_{AC}}{\tau_{RC}} \frac{(u(\tau) - \xi(\tau))}{\beta} \tag{3.3.17}$$

In the absence of uncompensated resistance, the electrode potential is given by Eq. (3.3.16), by setting $u(\tau) = \xi(\tau)$, $u_I = \xi_I$ and $u_R = \xi_R$ and the recorded current is the algebraic sum of the Faradaic and capacitance current,

$$\Psi(\tau) = \hat{r}_3 + \frac{1}{\beta}\left[\frac{\tau_{AC}}{\tau_{CV}} \frac{\tau - \tau_R}{|\tau - \tau_R|} + 2\pi\alpha_0 \cos(2\pi\tau)\right] \tag{3.3.18}$$

where $\hat{r}_3 = \tau_{AC} r_3/\Gamma^0$ is the dimensionless Faradaic current.

As mentioned above, four different time constants are involved in Eqs. (3.3.14) - (3.3.17). The time constant of the ac perturbation, $\tau_{AC} = 1/f$, the time constant of the catalytic reaction $\tau_{MM} = 1/k_1 K_M = 1/(k_{-1} + k_2)$, the time constant of the linear sweep $\tau_{CV} = RT/Fv$ and the time constant of the RC circuit, $\tau_{RC} = AC_{dl}R_s$.

The time constant τ_{MM} can vary several orders of magnitude, whereas τ_{RC} is about 1.2×10^{-4} s for a typical experiment involving an electrode with $A \approx 0.1$ cm^2, $C_{dl} \approx 40 \times 10^{-6}$ F/cm^2 and $R_s \approx 30\ \Omega$. On the other hand, τ_{AC} and τ_{CV} are determined solely by controllable variables, the former by the frequency of the perturbation and the later by the scan rate. For typical values of scan rate, ranging from 0.1 to 1000 mV/s, τ_{CV} varies from about 250 to 0.025 s whereas τ_{AC} varies from 0.01 to 10 s in typical FTacV experiments. For reasons discussed thoroughly in the past the condition $\tau_{CV} \gg \tau_{AC}$ must be fulfilled when implementing the FTacV technique. Thus, the time constants are arranged as follows,

$$\tau_{CV} \gg \tau_{AC} \gg \tau_{RC}$$

with τ_{MM} lying anywhere in the above range.

Inspection of the dimensionless equations reveals also that the effective catalytic constant is $k_{cat} = \tau_{AC} k_2$, that is, its value can be tuned by the perturbation frequency.Large values of τ_{AC} (small frequency values) increase the value of the effective catalytic rate constant. The same is true for the effective heterogeneous constant $k_{het} = \tau_{AC} k^0$, that is, large values of τ_{AC} (small frequency values) render the electrochemical step more reversible. On the other hand, small value of τ_{AC} (large frequency values), decrease the value of the effective catalytic rate constant and render the electrochemical step less reversible.

Finally, it can be noticed that the dimensionless ratio of the catalytic time constant to the time constant of the ac perturbation τ_{MM}/τ_{AC} is introduced in the equation describing the temporal evolution of the reaction intermediate E_1S, see Eq. (3.3.13). It is evident that the steady state condition for the reaction intermediate tends to be fulfilled when $\tau_{MM}/\tau_{AC} \ll 1$, that is when τ_{MM} is small (large values of $k_{-1} + k_2$) and τ_{AC} is large (small frequency values).

Therefore, for small values of τ_{MM} and large values of τ_{AC}, the reaction mechanism should proceed according to the steady state approximation. It is rather straight forward to show that when $\hat{r}_1 = \hat{r}_2 = \hat{r}_3 = \hat{r}$, the dimensionless rate of the reaction will

be,

$$\hat{r} = \tau_{\mathrm{AC}} k_2 \frac{\hat{c}_{\mathrm{S}}}{1 + \hat{c}_{\mathrm{S}} + e^{-\xi} + \hat{c}_{\mathrm{S}} \frac{k_2}{k^0} e^{(a-1)\xi}} \tag{3.3.19}$$

The equation above is the analytic expression of the dimensionless ac - voltammogram under steady state conditions, when the electrochemical step is quasi-reversible or irreversible and the capacitance current is ignored.

Furthermore, if the catalytic steps are in steady state, $r_1 = r_2$ and the electrochemical step is at equilibrium $r_3 = 0$, *i.e.* the electrochemical reaction is reversible, then the dimensionless rate of the reaction will be,

$$\hat{r} = \tau_{\mathrm{AC}} k_2 \frac{\hat{c}_{\mathrm{S}}}{1 + \hat{c}_{\mathrm{S}} + e^{-\xi}} \tag{3.3.20}$$

Exactly the same rate equation is obtained if a very large value of k^0 is considered in Eq. (3.3.19), *i.e.* when the condition $k^0 \gg \hat{c}_{\mathrm{S}} k_2$ is fulfilled. Equation (3.3.20) is the analytic expression of the ac - voltammogram, when the chemical steps are at steady state conditions, the electrochemical step is Nernstian and the capacitance current is ignored.

Since the analytic expressions of the ac - voltammograms are known, the chief observables of FTacV can be calculated easily by performing the typical analysis. The fact that Eqs. (3.3.19) and (3.3.20) are valid only when the capacitance current is ignored is of no importance because the chief observables chosen in this work are the maximum of harmonics higher than one, $\psi_{h,\mathrm{p}}$ and the shift of the corresponding potential $\xi^* = \frac{F}{RT}(E_{h,\mathrm{p}} - E^0)$ as a function of the substrate concentration $\hat{c}_{\mathrm{S}}$. Both observables are independent of the capacitance current when the harmonic is higher than one.

As can be seen from Eq. (3.3.19), the dependence of the normalized ac - voltammogram $\hat{r}/\tau_{\mathrm{AC}} k_2$ on substrate concentration $\hat{c}_{\mathrm{S}}$ depends only on the ratio k_2/k^0. Therefore, the dependence of the chief observables will depend only on this ratio of the rate constants. The dependence of the maximum of the 3rd harmonic, $\psi_{3,\mathrm{p}}/\tau_{\mathrm{AC}} k_2$, for different values of k_2/k^0, is presented in Fig. 3.3.2(a).

For $k_2/k^0 \ll 1$, the electrochemical step is practically reversible within the range of substrate concentrations presented and the dependence resembles a Michaelis-Menten relation. For $k_2/k^0 < 1$, the normalized maximum $\psi_{3,\mathrm{p}}/\tau_{\mathrm{AC}} k_2$ increases for small values of $\hat{c}_{\mathrm{S}}$ and decreases for larger values. The reason for this response is as follows: for small values of substrate concentration the factor $\hat{c}_{\mathrm{S}} k_2/k^0$ in Eq. (3.3.19) remains small and the electrochemical step is practically reversible. For higher substrate concentrations this factor increases even when the ratio k_2/k^0 is small, thus rendering the electrochemical step quasi-reversible. Since it is known that the maxima of quasi-reversible harmonics are smaller than the maxima of the corresponding reversible, $\psi_{3,\mathrm{p}}/\tau_{\mathrm{AC}} k_2$ decreases for large values of $\hat{c}_{\mathrm{S}}$. For large values of k_2/k^0, where the traces practically overlap, a maximum is not observed within the chosen range of substrate concentrations and the dependence resembles a Michaelis-Menten relation. In this case, the electrochemical step is irreversible and the maxima of the harmonics tend to a fixed value as the substrate concentration increases.

The corresponding Lineweaver-Burk-like plots are presented in Fig. 3.3.2(b). It can be observed that for both small and large value of k_2/k^0, the ordinate at zero abscissa

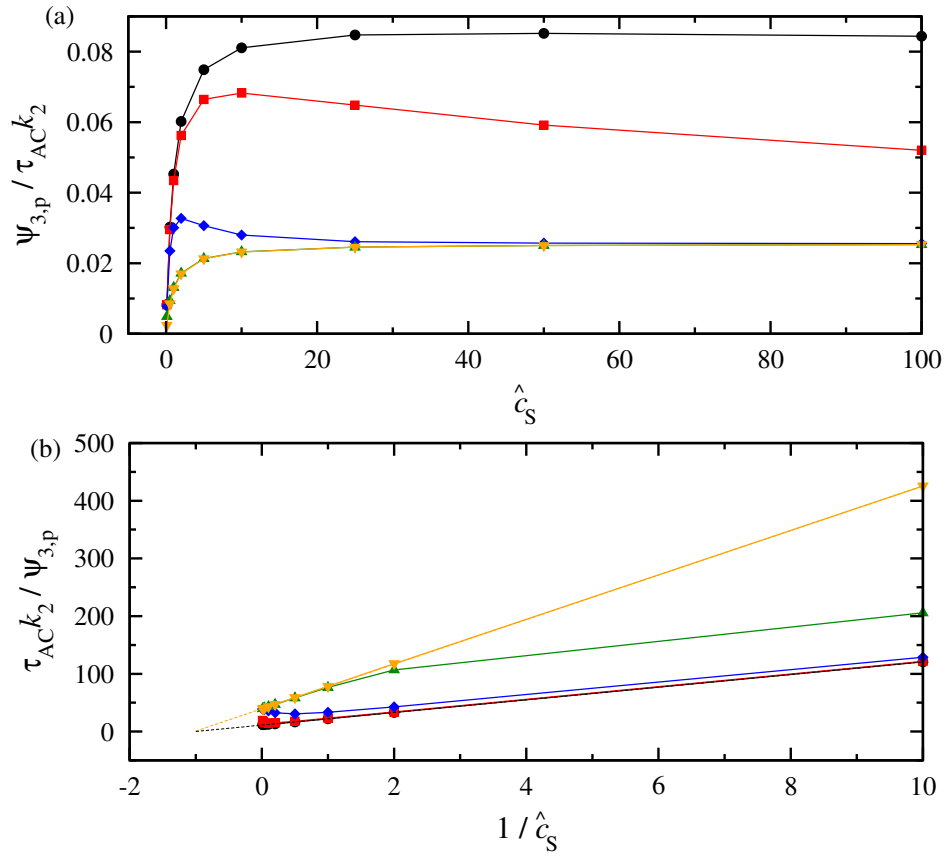

Figure 3.3.2: Computational results under steady state conditions: (a) Maxima of the normalized 3rd harmonic, $\psi_{3,p}/\tau_{AC}k_2$, as a function of the dimensionless substrate concentration, $\hat{c}_S$ and (b) corresponding Lineweaver-Burk-like plots, for ratio of kinetic constants $k_2/k^0 = 0.01$ (black circles), 0.1 (red squares), 1 (blue diamonds), 10 (green triangles up), 100 (orange triangles down). Parameter values $\alpha_0 = 3.895$, $\tau_{CV} = 2.567$ s and $a = 0.5$.

is -1, that is $1/c_s$ is equal $-1/K_M$ taking into account that $\hat{c}_S$ corresponds to c_s/K_M. It is interesting to realize that K_M is accessible whether the electrochemical step is fast (nerstian) or slow (quasi-reversible), provided that the steady state approximation is fulfilled.

Indicative 3rd harmonics are presented in Fig. 3.3.3(a), for different values of k_2/k^0 and $\hat{c}_S = 1$. For $k_2/k^0 > 1$, the dominant anodic peak is shifted anodically and its amplitude is relatively low (black and red curves), since they correspond to an irreversible electrochemical step. For $k_2/k^0 < 1$ the dominant anodic peak is shifted cathodically and its amplitude is high (green curve), since it corresponds to a reversible electrochemical step. The dependence of the shift of the dominant anodic peak, ξ^*, of the 3rd harmonic as a function of $\hat{c}_S$, for different values of k_2/k^0, is presented by the symbols in Fig. 3.3.3(b). It can be observed that for values of $k_2/k^0 > 1$, the peak is shifted anodically, the effect being more profound as the ratio of the rate constants is large, *i.e.* the heterogeneous rate constant is smaller than the catalytic

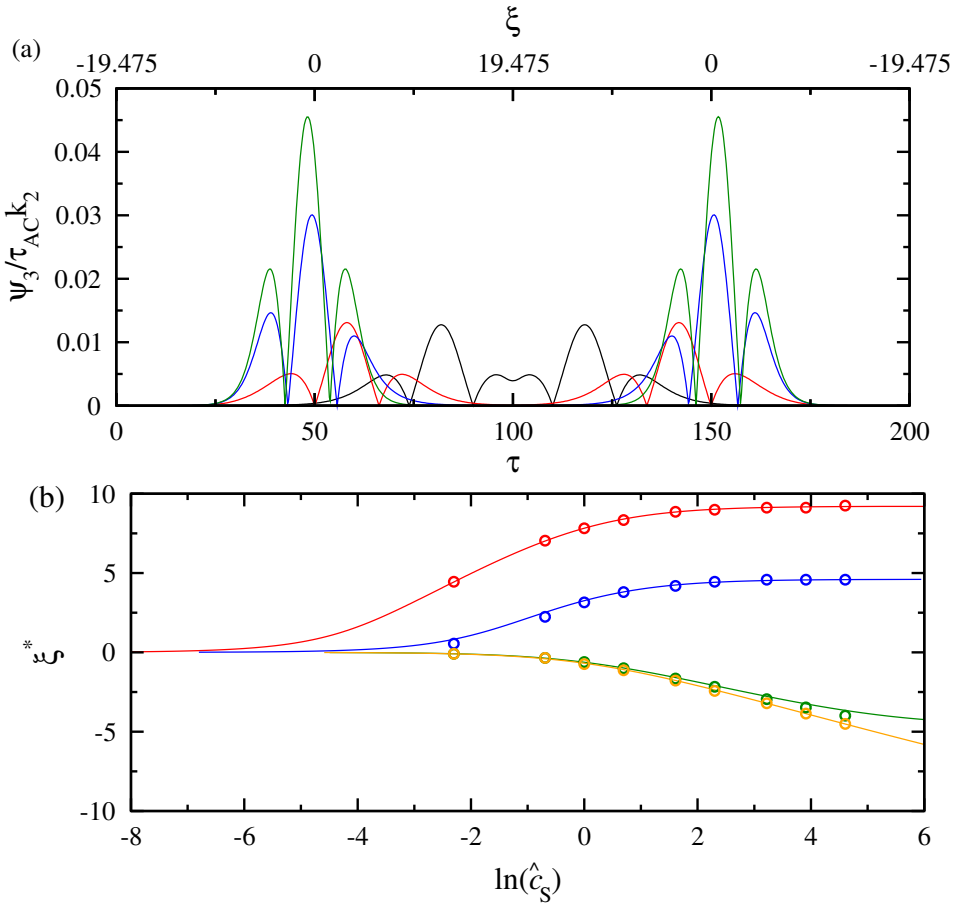

Figure 3.3.3: Computational results under steady state conditions: (a) Normalized third harmonics for ratio of kinetic constants $k_2/k^0 = 1000$ (black), 100 (red), 1 (blue) and 0.1 (green), and dimensionless substrate concentration $\hat{c}_S = 1$ and (b) shift of the anodic dominant peak ξ^* of the 3rd harmonic as a function of the logarithm of the dimensionless substrate concentration $\hat{c}_S$ for ratio of kinetic constants $k_2/k^0 = 100$ (red), 10 (blue), 0.1 (green) and 0.01 (orange). Parameter values $\alpha_0 = 3.895$, $\tau_{CV} = 2.567$ s and $a = 0.5$.

rate constant. On the other hand, when $k_2/k^0 < 1$, the peak is shifted cathodically whereas the dependence on $\hat{c}_S$ is not so profound. It is evident that a cathodic shift of the dominant peak of the 3rd harmonic is a signature of the relation between the catalytic and heterogeneous rate constant. The analysis of the peak shift displacement is one of the most interesting features of such a system, since it can give an indication of the ratio of k_2/k^0 and could be proven useful in the interpretation of experimental results.

The maximum of the dominant peak of the odd harmonics is observed at the half wave potential of the ac-voltammogram. Thus, the dependence of ξ^* on substrate concentration can be calculated directly from Eq. (3.3.19), by setting $\hat{r}(\xi^*) = \frac{\hat{r}_{max}}{2} = \frac{\tau_{AC} k_2 \hat{c}_S}{2(1+\hat{c}_S)}$, as can be seen by the continuous lines in Fig. 3.3.3(b).

Now, for the case of a reversible electrochemical step, the normalized rate $\hat{r}/\tau_{AC}k_2$ depends only on $\hat{c}_S$, Eq. (3.3.20). Typical third harmonics for this case are presented in Fig. 3.3.4(a). As can be seen in this figure, increase of $\hat{c}_S$ results in an increase of the principal peak of the harmonic, as well as a cathodic shift of the anodic peak potential. Both effects are drastic for small values of substrate concentrations and saturate as $\hat{c}_S$ is increased. The effect of $\hat{c}_S$ of the maximum of all harmonics up to the 5th is presented in Fig. 3.3.4(b). It can be observed that a saturation is observed at high values of substrate concentration. On the other hand, first order kinetics are revealed for small $\hat{c}_S$ values. These plots resemble Michaelis-Menten kinetics, as can be verified by the corresponding Lineweaver-Burk-like plots, presented in Fig. 3.3.4(c). The dependence of the inverse normalized rate versus the inverse substrate concentration is linear and the ordinate value at zero abscissa is -1, that is $-1/K_M$. The cathodic shift of the dominant anodic peak, ξ^*, of the odd harmonics is presented by the symbols in Fig. 3.3.4(d). A linear dependence is observed between ξ^* and the logarithm of $(1+c_S)$, which follows directly from Eq. (3.3.20),

$$\xi^* = -\ln(1+\hat{c}_S) \tag{3.3.21}$$

by setting $\hat{r}(\xi^*) = \frac{\hat{r}_{max}}{2} = \frac{\tau_{AC} k_2 \hat{c}_S}{2(1+\hat{c}_S)}$, since the maximum of the dominant peak of the odd harmonics is observed at the half wave potential of the ac-voltammogram. All the above results are valid for the observed current, provided that the uncompensated resistance tends to zero.

3.3.3 Numerical analysis

FTacV under steady state conditions for the reaction intermediate

The results presented in Sec. 3.3.2 are valid when the steady state approximation for the reaction mechanism is fulfilled. In this section the kinetic equations, Eqs. (3.3.14) and (3.3.13), will be investigated in order to elucidate the conditions under which this approximation is valid. The analysis will be restricted to the 3rd harmonic and it will be assumed that the uncompensated resistance tends to zero. The influence of the uncompensated resistance will be presented at the end of this section.

Let us consider the case where $\tau_{MM} = 0.001$ s, $k^0 = 1$ s^{-1} and $k_2 = 100$ s^{-1}, *i.e.* the electrochemical step is quasi-reversible due to the relatively low value of k^0. The only controllable parameters are τ_{AC} and α_0, provided that $\tau_{CV} \gg \tau_{AC}$, in order to

assure the independence of the scan rate. The dependence of the maximum of the 3rd harmonic, $\psi_{3,\mathrm{p}}$, on the substrate concentration $\hat{c}_{\mathrm{S}}$ is presented in Fig. 3.3.5(a), for different values of τ_{AC} and $\alpha_0 = 3.895$. It can be observed that a drastic increase of $\psi_{3,\mathrm{p}}$ at small $\hat{c}_{\mathrm{S}}$ values is followed by a saturation at large $\hat{c}_{\mathrm{S}}$ values. Moreover, the value $\psi_{3,\mathrm{p}}$ increases for increasing values of τ_{AC} (decreasing values of frequency). The corresponding Lineweaver-Burk-like plots, together with the curves corresponding to steady state conditions (dotted straight lines), are presented in Fig. 3.3.5(b). It is evident that for large values of τ_{AC}, the steady state condition is achieved within the whole range of $\hat{c}_{\mathrm{S}}$ and the abscissa at zero ordinate is -1, that is $-1/K_{\mathrm{M}}$. As τ_{AC} decreases, the abscissa at zero ordinate deviates from -1.

The results presented in Figs. 3.3.5(a) and (b) correspond to the case of $\tau_{\mathrm{AC}} = 0.001$ s and $k_2 = 100$ s^{-1}, that is $k_{-1} = 900$ s^{-1}, where steady state conditions are fulfilled only for large values of τ_{AC} (small frequency values). Steady state conditions are achieved within a wider range of frequencies if $k_{-1} < k_2$, as can be seen in the example presented in Figs. 3.3.5(c) and (d), where $k_2 = 900$ s^{-1}, $\tau_{\mathrm{MM}} = 0.001$ s and $k^0 = 1$ s^{-1}. It can be observed once again that a drastic increase of $\psi_{3,\mathrm{p}}$ at small $\hat{c}_{\mathrm{S}}$ values is followed by a saturation at large $\hat{c}_{\mathrm{S}}$ values. Moreover, the value $\psi_{3,\mathrm{p}}$ increases for increasing values of τ_{AC} (decreasing values of frequency). From the corresponding Lineweaver-Burk-like plots it is evident that for every τ_{AC} value, the steady state condition is achieved within a range of $\hat{c}_{\mathrm{S}}$ and the abscissa at zero ordinate is -1, that is $1/c_{\mathrm{s}}$ is equal to $-1/K_{\mathrm{M}}$.

The value of τ_{AC} determines also the dependence of the shift of the dominant anodic peak ξ^* on substrate concentration. As can be seen in the result presented in Fig. 3.3.6(a) for $k^0 = 1$ s^{-1} and $k_2 = 100$ s^{-1}, for relatively small values of τ_{AC} (relatively large frequency) ξ^* does not follow the trend predicted under the steady state treatment (continuous curve). As τ_{AC} increases (the frequency decreases) the dependence of ξ^* on the logarithm of substrate concentration tends to the steady state prediction.

By comparing Figs. 3.3.5(b) and (d), it is realized that relatively large values of τ_{AC} (small frequency values) are required in order to achieve steady state conditions and access the K_{M} value when $k_2 < k_{-1}$. For these values of τ_{AC}, the amplitude of the harmonics, $i_{h,\mathrm{p}} = F\Gamma^0\psi_{h,\mathrm{p}}/\tau_{\mathrm{AC}}$, is rather low, introducing a difficulty in the analysis of real experimental data, specially for small values of substrate concentration. This obstacle can be overcome by increasing the perturbation amplitude. An example is presented in Fig. 3.3.6(b) for the most extreme case of $\tau_{\mathrm{AC}} = 10$ s. The curve depicted by circles is obtained for $\alpha_0 = 3.895$ whereas the curve depicted by squares for $\alpha_0 = 11.685$. It is evident that the perturbation amplitude can amplify the signal, thus rendering the analysis more feasible, even for large values of τ_{AC} and small values of substrate concentration.

FTacV for reversible electrochemical step

The case of a reversible electrochemical step under steady state conditions have been treated in Sec. 3.3.2. Here, an analysis will be attempted for the case of a large heterogeneous rate constant $k^0 = 10^4$ s^{-1}, fulfilling the condition of reversibility, catalytic rate constant $k_2 = 100$ s^{-1} and $\tau_{\mathrm{MM}} = 0.001$ s, fulfilling the steady state approximation for the reaction intermediate.

The dependence of $\psi_{3,\mathrm{p}}$ on $\hat{c}_{\mathrm{S}}$ is shown in Fig. 3.3.7(a) for three different values of τ_{AC}. The effect is more evident in the corresponding Lineweaver-Burk-like plots of Fig. 3.3.7(b), where the curves corresponding to steady state conditions are presented also (dotted lines). For $\tau_{\mathrm{AC}} = 0.5$ s, steady state is hardly achieved for relatively high values of substrate concentration. As τ_{AC} is increased, *i.e.* the perturbation frequency decreases, steady state conditions are satisfied within a wide range of $\hat{c}_S$ values and K_{M} is, in principle accessible. In Fig. 3.3.7(c), the shift of the dominant anodic peak is presented (discrete points) together with the theoretical prediction, Eq. (3.3.21). It is to be observed that all cases tend to follow a linear relation between ξ^* and $\ln(1+\hat{c}_S)$.

According to the discussion presented in Sec. 3.3.3, steady state conditions are hard to achieve for small values of k_2, even if k^0 is very large. Therefore, when the electrochemical step is reversible and τ_{MM} is small, small values of the catalytic rate constant introduce a difficulty in applying the method. In such a case, very small frequency values have to be used, together with large amplitude values. On the other hand, for relatively large values of the catalytic rate constant, the method can be applied with relatively high frequencies and moderate amplitudes. In such a case, first order kinetics are expected to be observed for small substrate concentrations and the Michaelis constant can be accessed from large substrate concentrations via Lineweaver-Burk-like plots.

FTacV under transient conditions for the reaction intermediate

When $\tau_{\mathrm{MM}}/\tau_{\mathrm{AC}}$ is large, the steady state condition cannot be fulfilled for the reaction intermediate, $\mathrm{E_1S}$ (see Eq. 3.3.13). Under this condition, the chemical step cannot follow the potential perturbation and each step of the mechanism, both chemical and electrochemical, occur with a different rate.

Two typical examples are presented in Fig. 3.3.8(a) for $\tau_{\mathrm{MM}} = 1$ s, $\tau_{\mathrm{AC}} = 1$ s, $k_2 = 0.5$ s^{-1} and $k^0 = 1$ s^{-1} (black circles) and 0.05 s^{-1} (red squares). It is observed that when $k_2/k^0 < 1$, the maximum of the 3rd harmonic decreases for increasing values of $\hat{c}_{\mathrm{S}}$, a clear evidence that this case does not follow steady state conditions (see also the corresponding Lineweaver-Burk-like plot of Fig. 3.3.8(b)). A more confusing case is when $k_2/k^0 > 1$, where the maximum of the 3rd harmonic increases for increasing values of $\hat{c}_{\mathrm{S}}$ and finally reaches a limiting value. Both this plot and the corresponding Lineweaver-Burk-like plot of Fig. 3.3.8(b) resemble the case of steady state kinetics, even though this is not the case. In principle, these plots cannot be used for the determination of kinetic parameters based on the equations derived from the corresponding analysis. Nevertheless, the dependence of $\psi_{3,\mathrm{p}}$ on $\hat{c}_{\mathrm{S}}$ for small substrate concentrations tends to be linear and, in principle, could be used as an analytical tool for the detection of the substrate.

Effect of uncompensated ohmic resistance

The effect of uncompensated ohmic resistance, *i.e.* the potential drop between the working and reference electrode, can be studied by varying the time constant τ_{RC}, while keeping the parameter β constant. For an electrode area of 0.1 cm^2 and specific

capacitance 40×10^{-6} F/cm^2, typical values of τ_{RC} for well designed experiments are expected to be around 1.2×10^{-4} s (resistance 30 Ω). For low solution conductivity, τ_{RC} can be about 8×10^{-4} s (resistance 200 Ω).

Typical examples of the effect of uncompensated ohmic resistance under steady state conditions for $\tau_{\mathrm{MM}} = 0.001$ s, $k_2 = 900$ s^{-1}, $k^0 = 1$ s^{-1} and $\tau_{\mathrm{AC}} = 1$ s, are presented in Fig. 3.3.9. In this figure, black circles represent the ideal case of complete absence of uncompensated resistance. As can be seen in Fig. 3.3.9(a), when the resistance is relatively high, $\tau_{\mathrm{RC}} = 8 \times 10^{-4}$ s (green triangles), the dependence of $\psi_{3,\mathrm{p}}$ on substrate concentration deviates from the ideal situation. For $\tau_{\mathrm{RC}} = 4 \times 10^{-4}$ s the effect of uncompensated resistance is less profound (blue squares) whereas for $\tau_{\mathrm{RC}} = 1.2 \times 10^{-4}$ s (red asterisks), corresponding to the case of a well designed experiment, the curves practically overlap. The effect of uncompensated ohmic resistance on the corresponding Lineweaver-Burk-like curves can be observed in Fig. 3.3.9(b).

It can be concluded that high values of solution resistance have a drastic effect on the amplitude of the harmonics, but this effect can be diminished in a well designed experiment where the solution conductivity is sufficiently high and the reference electrode is placed near the surface of the working electrode.

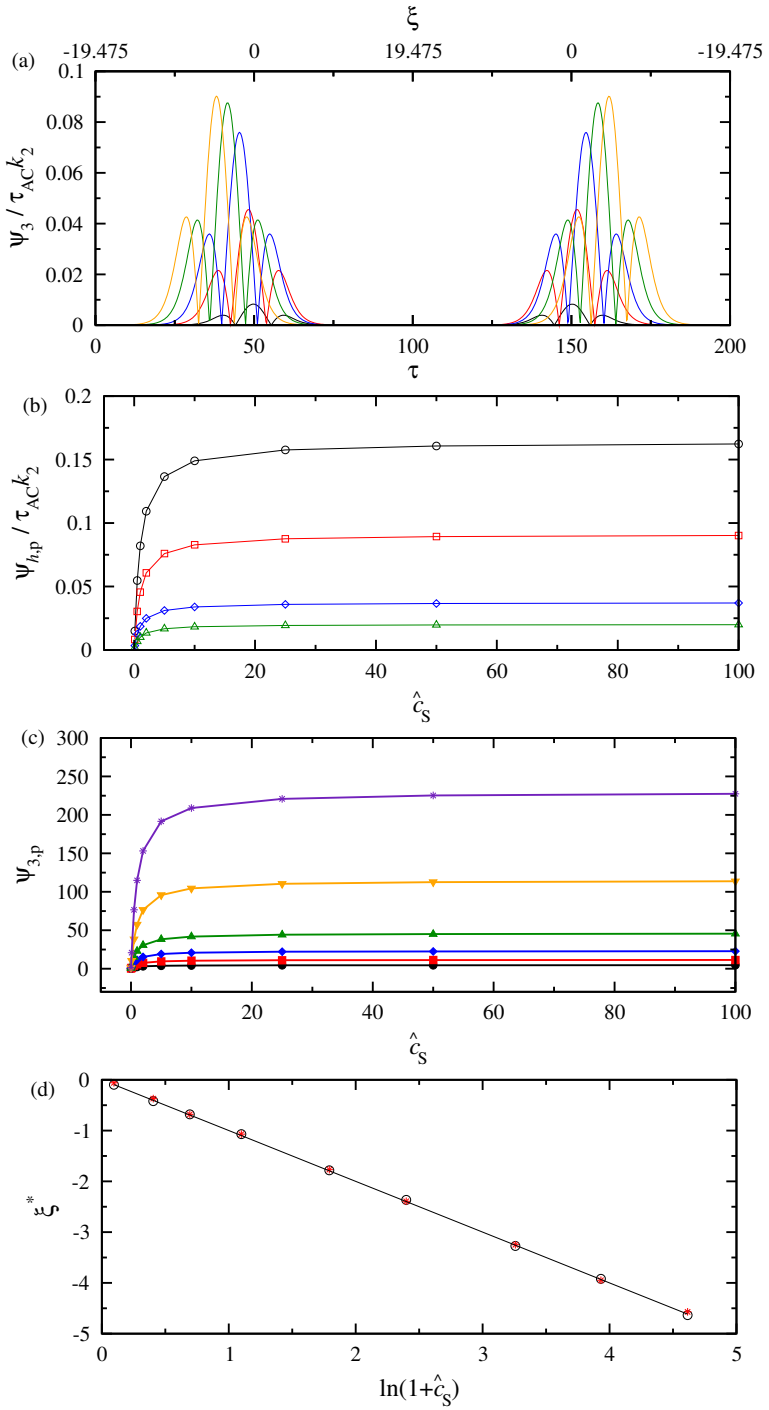

Figure 3.3.4: Computational results under steady state conditions with reversible electrochemical step: (a)Normalized third harmonics for dimensionless concentration $\hat{c}_S = 0.1$ (black), 1 (red), 5 (blue), 25 (green) and 100 (orange), (b) Normalized maximum $\psi_{h,p}/\tau_{AC}k_2$ of the 2nd (black circles), 3rd (red squares), 4th (blue diamonds) and 5th (green triangles) harmonics, (c) corresponding Lineweaver-Burk-like plots and (d) shift of the anodic dominant peak ξ^* of the 3rd (black circles) and 5th (red asterisks) harmonics as a function of the logarithm of $1 + \hat{c}_S$. Parameter values $\alpha_0 = 3.895$, $\tau_{CV} = 2.567$ s

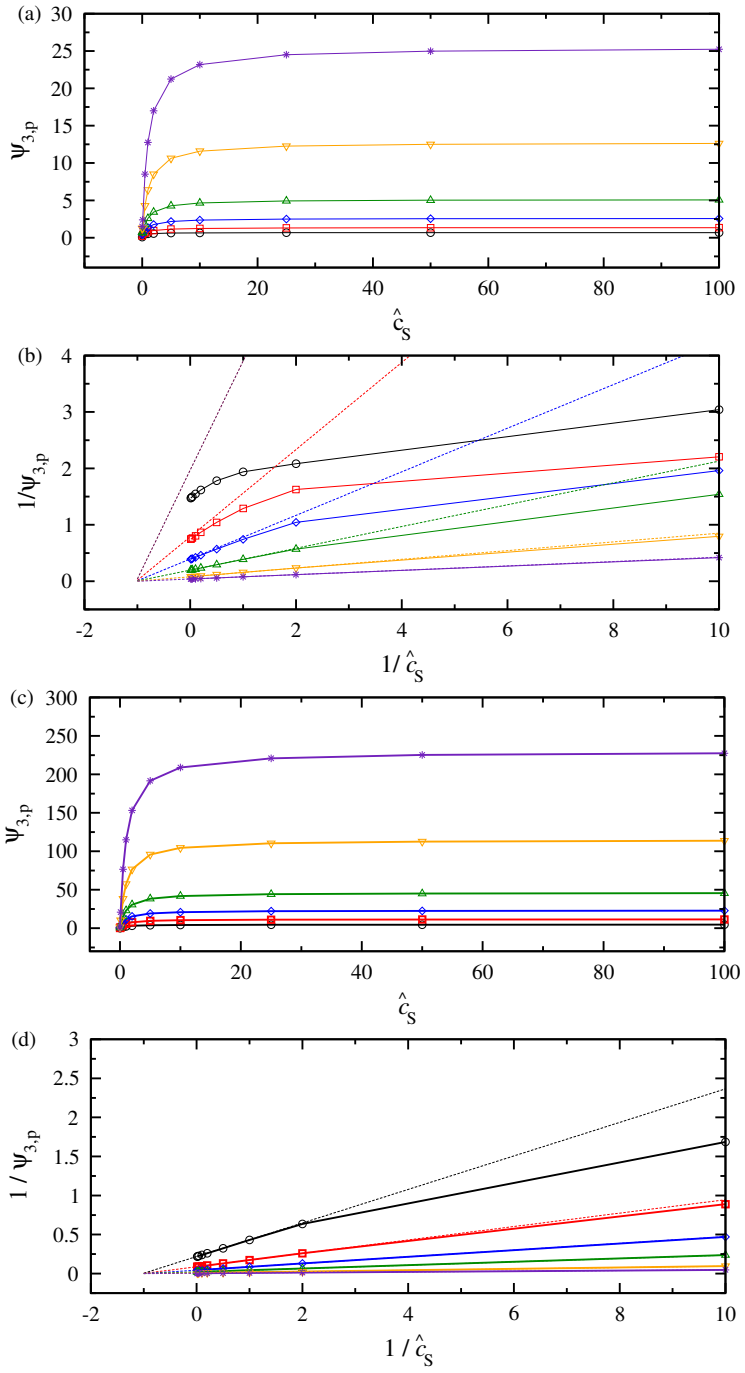

Figure 3.3.5: Computational results under steady state conditions for the reaction intermediate: (a) Dependence of the maximum of the 3rd harmonic $\psi_{3,\mathrm{p}}$ on the substrate concentration $\hat{c}_\mathrm{S}$ for kinetic constant $k_2 = 100$ s^{-1} and (b) corresponding Lineweaver-Burk-like plots, for different time constant τ_AC values. (c) Dependence of the maximum of the 3rd harmonic $\psi_{3,\mathrm{p}}$ on the substrate concentration $\hat{c}_\mathrm{S}$ for kinetic constant $k_2 = 900$ s^{-1} and (d) corresponding Lineweaver-Burk-like plots, for different values of time constant τ_AC. Values of $\tau_\mathrm{AC} = 0.2$ s (black circles), 0.5 s (red squares), 1 s (blue diamonds), 2 s (green triangles up), 5 s (orange triangles down), 10 s (purple asterisks). Parameter values, $k^0 = 1$ s^{-1}, $\tau_\mathrm{MM} = 0.001$ s and $a = 0.5$.

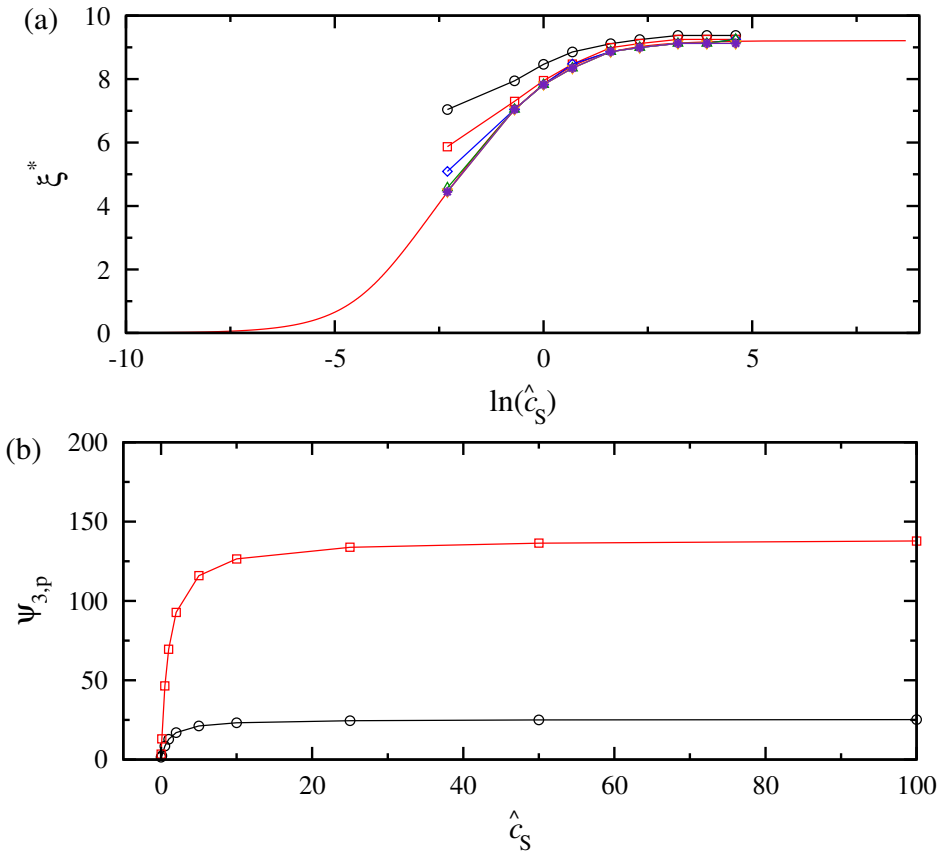

Figure 3.3.6: Computational results under steady state conditions for the reaction intermediate: (a) Effect of time constant τ_{AC} on the shift of the anodic dominant peak ξ^*, $\tau_{AC} = 0.2$ s (black circles), 0.5 s (red squares), 1 s (blue diamonds), 2 s (green triangles up), 5 s (orange triangles down), 10 s (purple asterisks). (b) Effect of the dimensionless perturbation amplitude α_0 on the maxima of the 3rd harmonic for time constant $\tau_{AC} = 10$ s, $\alpha_0 = 3.895$ (black circles) and 11.685 (red squares). Parameter values, $k^0 = 1$ s^{-1}, $k_2 = 100$ s^{-1}, $\tau_{MM} = 0.001$ s and $a = 0.5$.

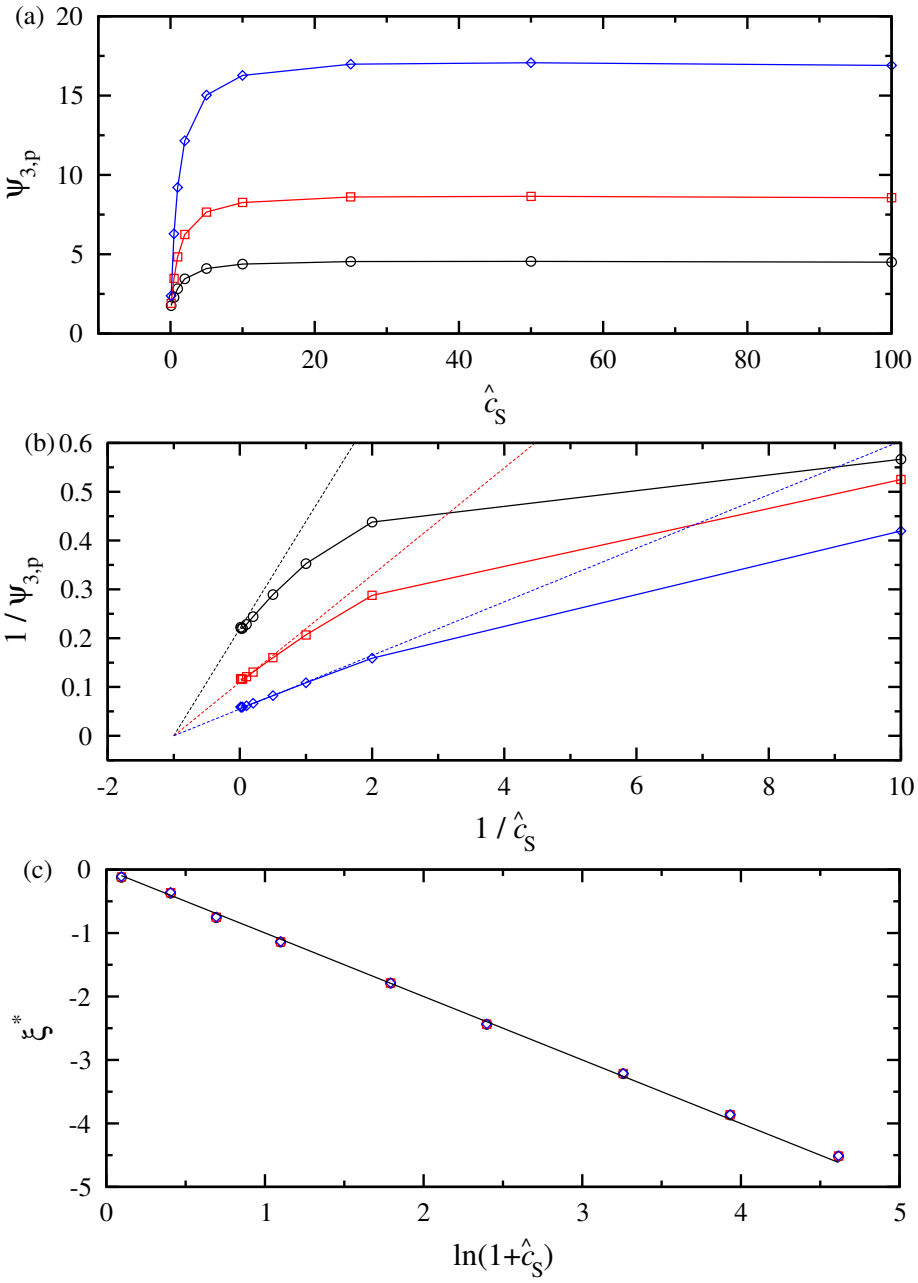

Figure 3.3.7: Computational results for reversible electrochemical step: (a) Dependence of the dominant anodic peak of the 3rd harmonic $\psi_{3,\mathrm{p}}$ on dimensionless concentration of the substrate $\hat{c}_\mathrm{S}$, (b) corresponding Lineweaver-Burk-like plots and (c) shift of the anodic dominant peak ξ^*, for time constant $\tau_\mathrm{AC} = 0.5$ s (black circles), 1 s (red squares) and 2 s (blue diamonds). Parameter values, $k^0 = 10^4$ s^{-1}, $k_2 = 100$ s^{-1}, $\tau_\mathrm{MM} = 0.001$ s, $\alpha_0 = 3.895$ and $a = 0.5$.

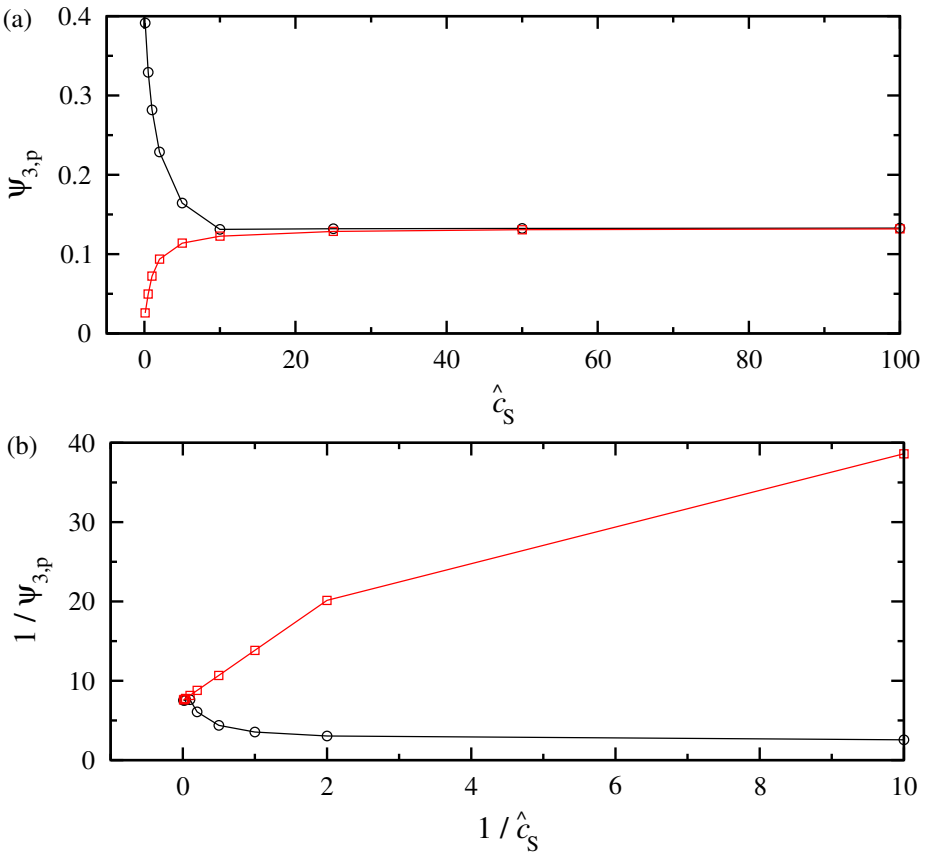

Figure 3.3.8: Computational results under transient conditions for time constant $\tau_{MM} = 1$ s, $\tau_{AC} = 1$ s and kinetic constant $k_2 = 0.5$ s^{-1}. (a) Dependence of the maximum of the 3rd harmonic $\psi_{3,p}$ on substrate concentration $\hat{c}_S$ and (b) corresponding Lineweaver-Burk-like plots, for kinetic constant $k^0 = 1$ s^{-1} (black circles) and 0.05 s^{-1} (red squares). Parameter values: $\tau_{CV} = 2.567$ s, $\alpha_0 = 3.895$ and $a = 0.5$.

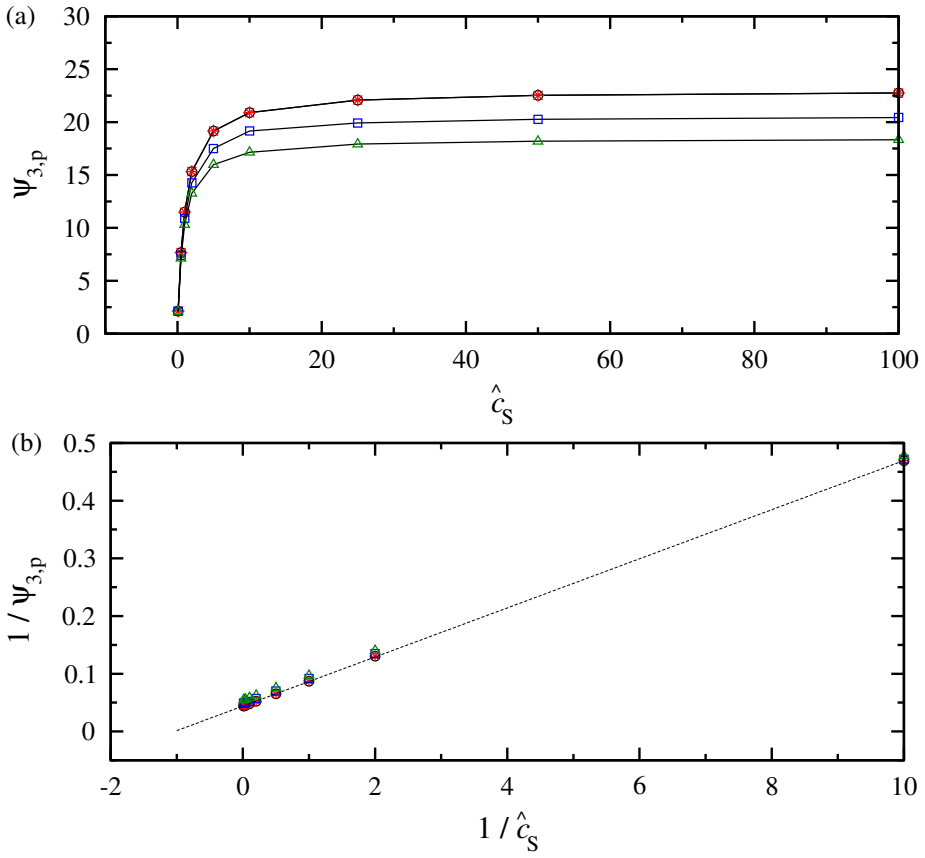

Figure 3.3.9: Computational results in the presence of uncompensated ohmic resistance for kinetic constants $k_2 = 900$ s^{-1}, $k^0 = 1$ s^{-1} on the (a) dependence of the maximum of the 3rd harmonic $\psi_{3,\mathrm{p}}$ on substrate concentration $\hat{c}_\mathrm{S}$ and (b) corresponding Lineweaver-Burk-like curves, in the absence of solution resistance (black circles) and for time constant $\tau_\mathrm{RC} = 1.2 \times 10^{-4}$ s (red asterisks), 4×10^{-4} s (blue squares) and 8×10^{-4} s (green triangles). Parameter values, $\tau_\mathrm{MM} = 0.001$ s, $\tau_\mathrm{AC} = 1$ s, $\tau_\mathrm{CV} = 2.567$ s, $\alpha_0 = 3.895$ and $a = 0.5$.

3.4 EC Mechanism for immobilized species

Let us assume a chemical species E_1 (oxidized form) which is immobilized in a monolayer on an electrode surface and can be reduced to E_2 (reduced form) by receiving one electron from the electrode. Then the reduced form E_2 can react with a chemical species S, that is diffused to the electrode surface, forming a surface bound species E_2S,

$$E_1 + e \underset{}{\overset{k^0}{\rightleftharpoons}} E_2 \tag{3.4.1}$$

$$E_2 + S \xrightarrow{k_1} E_2S \tag{3.4.2}$$

where k^0 is the standard rate constant of the electrochemical redox reaction on the electrode surface, k_1 the reaction kinetic constant of the second step (Fig. 3.3.1).

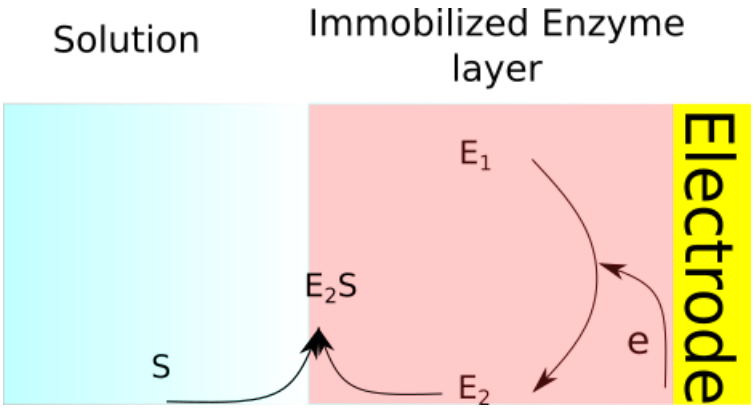

Figure 3.4.1: EC mechanism for immobilized species reaction scheme. The oxidized form of the immobilized species E_1 is reduced to E_2 and then reacts with the free in the solution species S to form the species E_2S.

Assuming practically constant concentration of the free in the solution substrate c_S, the kinetic equations are written as follows,

$$\frac{d\Gamma_{E_1}}{dt} = r_1 \tag{3.4.3}$$

$$\frac{d\Gamma_{E_2S}}{dt} = r_2 \tag{3.4.4}$$

where Γ_{E_1} and Γ_{E_2S} are the surface concentrations of the corresponding species and t corresponds to time.

The reaction rates r_i in Eqs. (3.4.3) and (3.4.4) are given by,

$$r_1 = k^0[(\Gamma^0 - \Gamma_{E_1} - \Gamma_{E_2S})e^{\frac{(1-a)F}{RT}(E-E^0)} - \Gamma_{E_1}e^{-\frac{aF}{RT}(E-E^0)} \tag{3.4.5}$$

$$r_2 = k_1\Gamma_{E_1}c_s \tag{3.4.6}$$

$$\tag{3.4.7}$$

In the rate expressions above, $\Gamma_{E_2} = \Gamma^0 - \Gamma_{E_1} - \Gamma_{E_2S}$ is the surface concentration of the reduced form of the enzyme, Γ^0 the initial surface concentration of the enzyme, E the electrode potential and E^0 the formal electrode potential of the electrochemical step. The rest of the symbols have their usual meaning.

As can be seen from Eqs. (3.4.3)-(3.4.6), the kinetics of the reaction depend on one kinetic constant, the formal potential of the electrochemical step and the transfer coefficient as well as five adjustable parameters, namely, the initial immobilized species concentration and the substrate concentration. The scenario shall be examined with both cyclic voltammetry and FTacV. In the case of cyclic voltammetry there is one more parameter, that of scan rate, while if FTacV other than the scan rate, the perturbation frequency and amplitude also have a role in the system.

The number of parameters to be considered for the analysis of the kinetics can be reduced by performing a dimensional analysis. Some parameters have the same dimensionless form in both cyclic voltammetry and FTacV. In order to do so, the following transformations are introduced[2],

$$\tau = t\frac{Fv}{RT} \qquad \text{(dimensionless time for cyclc voltammetry)}$$

$$\tau = tf \qquad \text{(dimensionless time for FTacV)}$$

$$\xi = \frac{F}{RT}(E - E^0) \qquad \text{(dimensionless electrode potential)}$$

$$k = \frac{k^0 RT}{Fv} \qquad \text{(dimensionless electron transfer constant for cyclic voltammetry)}$$

$$k = \frac{k^0}{f} \qquad \text{(dimensionless electron transfer constant forFTacV)}$$

$$\theta_{E_2S} = \Gamma_{E_2S}/\Gamma^0 \qquad \text{(surface coverage of the formed complex)}$$

$$\theta_{E_1} = \Gamma_{E_1}/\Gamma^0 \qquad \text{(surface coverage of the oxidized form of the species)}$$

$$k_{r1,CV} = \frac{k_1 RT}{c_S FV} \qquad \text{(dimensionless kinetic constant } k_1 \text{ for cyclic voltammetry)}$$

$$k_{r1,FTacV} = \frac{k_1}{c_S f} \qquad \text{(dimensionless kinetic constant } k_1 \text{ for FTacV)}$$

$$\psi = \frac{i}{\frac{Fv}{RT}\Gamma^0 F} \qquad \text{(dimensionless current density for cyclic voltammetry)}$$

$$\psi = \frac{i}{f\Gamma^0 F} \qquad \text{(dimensionless current density for FTacV)}$$

$$\hat{r}_i = \frac{r_i RT}{Fv\Gamma^0} \qquad \text{(dimensionless rate for cyclic voltammetry)}$$

$$\hat{r}_i = \frac{r_i}{f\Gamma^0} \qquad \text{(dimensionless rate for FTacV)}$$

For the dimensionless time, the dimensionless electron transfer constant, the dimensionless rates and the dimensionless current, the same symbol shall be used despite the different dimensional analysis.

[2]In this section the same symbols shall be used for cyclic voltammetry and FTacV for reasons of simplicity

By introducing the dimensionless quantities in Eqs. (3.4.5) and (3.4.6) and replacing in Eqs. (3.4.3) and (3.4.4) we get the following set of equations for the temporal evolution of the formed complex and the coverage of the oxidized form of the enzyme,

$$\frac{d\theta_{\mathrm{E_1}}}{d\tau} = -k\left[(1-\theta_{\mathrm{E_1}}-\theta_{\mathrm{E_2S}})e^{(1-a)\xi}-\theta_{\mathrm{E_1}})e^{-a\xi}\right] \tag{3.4.8}$$

$$\frac{d\theta_{\mathrm{E_2S}}}{d\tau} = k_{\mathrm{r1}}(1-\theta_{\mathrm{E_1}}-\theta_{\mathrm{E_2S}}) \tag{3.4.9}$$

The resulting dimensionless rates for reactions 3.4.1 and 3.4.1 are presented in the following equations.

$$\hat{r}_1 = k\left[(1-\theta_{\mathrm{E_1}}-\theta_{\mathrm{E_2S}})e^{(1-a)\xi}-\theta_{\mathrm{E_1}})e^{-a\xi}\right] \tag{3.4.10}$$

$$\hat{r}_2 = k_{\mathrm{r1}}(1-\theta_{\mathrm{E_1}}-\theta_{\mathrm{E_2S}}) \tag{3.4.11}$$

3.4.1 Numerical analysis

Taking into account the aforementioned dimensionless quantities we shall begin the analysis by the employment of cyclic voltammetry. In Fig. 3.4.2 one can find the dimensionless cyclic voltammograms for simple EC mechanism at various values of the dimensionless kinetic constant $k_{\mathrm{r1,CV}}$ in the case the electrochemical reaction is reversible ($k = 100$). In order to get a better understanding of the sequence of the voltammograms, separate close-ups of the oxidation and the reduction peaks are also presented in the same figure.

Starting from the oxidation peak for scan limits extending from $\xi_{\mathrm{I}} = 40$ to $\xi_{\mathrm{R}} = -40$, a steep decrease of the peak is observed for low values of $k_{\mathrm{r1,CV}}$, finally vanishing at a value of $k_{\mathrm{r1,CV}} = 0.01$. Next, regarding the reduction peak, as long as the oxidation peak is still apparent, there is no change neither in its value nor its position. For values of $k_{\mathrm{r1,CV}}$ higher than 0.01, the peak starts increasing and shifts towards more anodic potentials. This can be explained by taking into account that as $k_{\mathrm{r1,CV}}$ increases, the chemical reaction starts consuming the product of the electrochemical reaction, and effectively the apparent mechanism of the reaction becomes,

$$\mathrm{E_1} + \mathrm{e} \xrightarrow{k_{\mathrm{r1,CV}}} \mathrm{E_2S} \tag{3.4.12}$$

(3.4.13)

resulting in an irreversible voltammogram. The shape of the voltammogram at very high values of $k_{\mathrm{r1,CV}}$ also resembles that of a one-way electrochemical reaction.

After the general description of the aspects of the voltammograms, we head back to take a closer look at the oxidation peak. This gradually decreasing peak $\psi_{\mathrm{p,CV}}$ is plotted against the logarithm of $k_{\mathrm{r1,CV}}$ in Fig. 3.4.2(a). Also the normalized current peak with the peak in the absence of substrate $\psi_{\mathrm{p,CV}}/\psi^0_{\mathrm{p,CV}}$ is plotted in Fig. 3.4.2(b). The initial scope of such diagrams was to be used in order to extract the kinetic constant of the

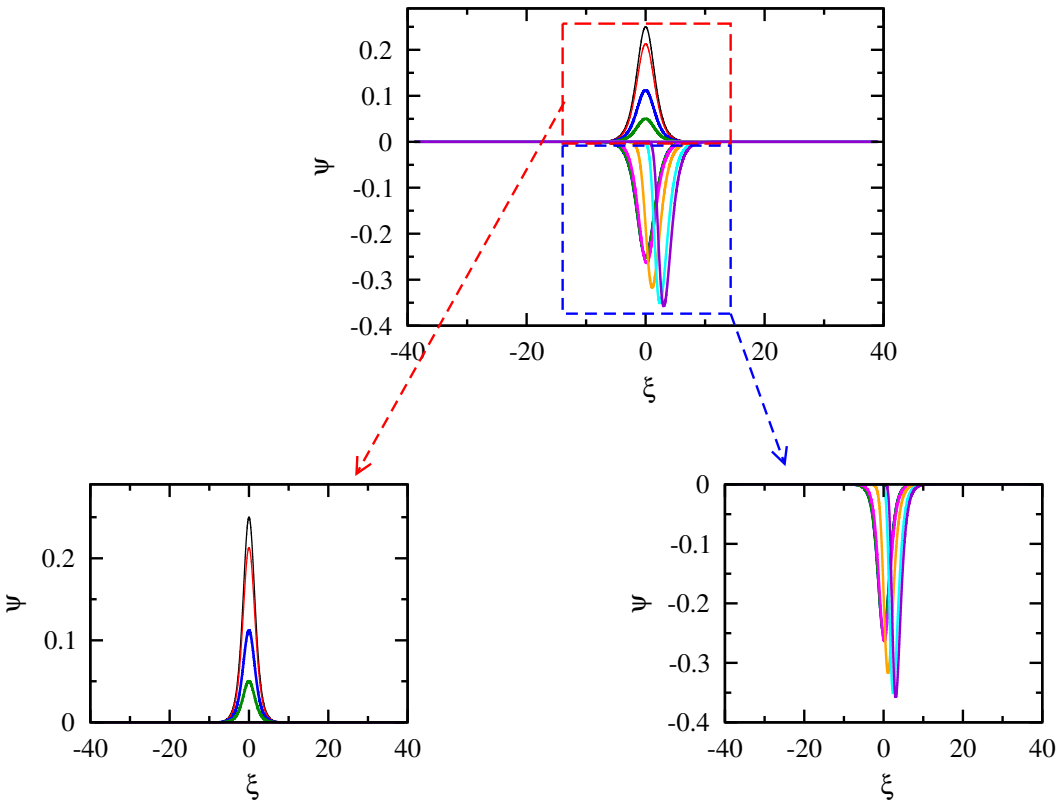

Figure 3.4.2: Dimensionless cyclic voltammograms for a EC mechanism of an immobilized species for various dimensionless kinetic constant $k_{\mathrm{r1,CV}}$. $k = 100$ and $k_{\mathrm{r1,CV}} = 0$ (black line), 0.001 (red line), 0.005 (blue line), 0.01 (green line), 0.1 (magenta line), 1 (orange line), 5 (cyan line) and 10 (violet line). $\xi_{\mathrm{I}} = 40$ to $\xi_{\mathrm{R}} = -40$.

chemical reaction by rendering dimensionless the experimental value of the oxidation peak of such a system. But from further analyzing a couple of problems occurred. The first is that all this takes into account the assumption that the first cycle is used and the second that the peak is independent of the scan limits. The second one is the more serious one since it shows that this approach lacks universality. Regarding the scan limits, it will be further analyzed later in this work.

In Fig. 3.4.4, the anodic shift of the reduction peak $\xi_{\mathrm{p,CV}}$ is plotted against the logarithm of $k_{\mathrm{r1,CV}}$. For small values of $k_{\mathrm{r1,CV}}$ there is no shif of the peak, while for large values of $k_{\mathrm{r1,CV}}$, a linear dependence is observed.

Now, back to the oxidation peak $\psi_{\mathrm{p,CV}}$ of the first cycle for low values of $k_{\mathrm{r1,CV}}$. At this point the effect of the scan limits of the voltammograms is examined. The Napierian logarithm of the oxidation peak is plotted against the $k_{\mathrm{r1,CV}}$ for four different potential limits in Fig. 3.4.5. For all these cases, a linear dependence is observed with all dependencies having the same intercept but different slopes. The intercept for all the cases has a value of -1.386 wich corresponds to a value of ln 0.25 (0.25 is the peak value in the absence of the chemical reaction step). The change of the slope is attributed to the change of scan limits. As the limits increase, reduction lasts longer, thus more time for the second reaction to occur. Consequently, the decrease of the peaks is sharper

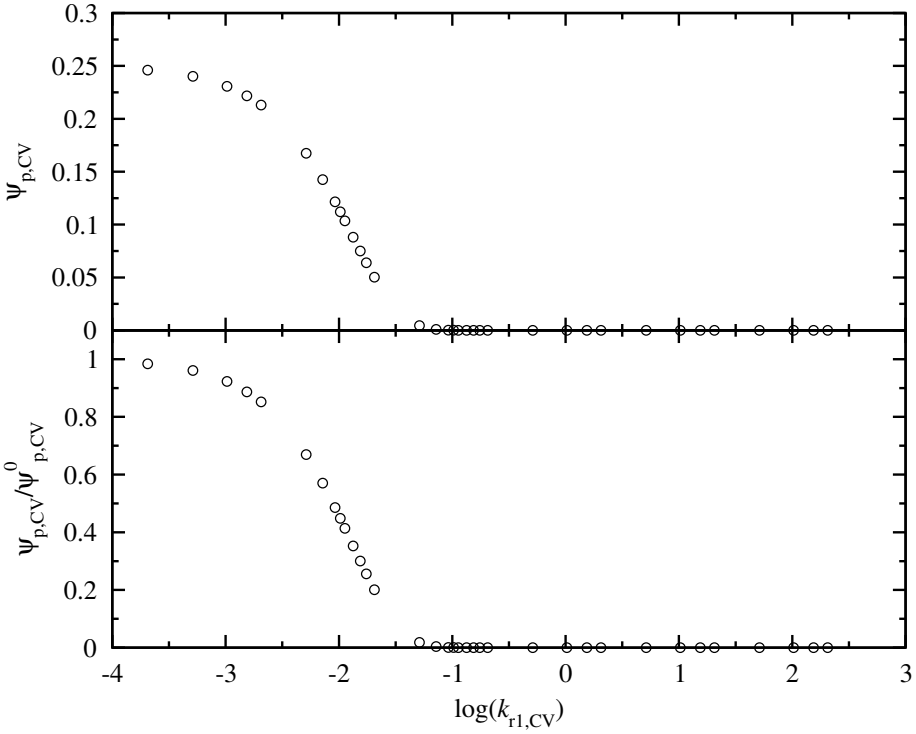

Figure 3.4.3: $\psi_{\mathrm{p,CV}}$ and $\psi_{\mathrm{p,CV}}/\psi^0_{\mathrm{p,CV}}$ *vs* $\log(k_{\mathrm{r1,CV}})$ for an EC of immobilized species. $\xi_{\mathrm{I}} = 40$ to $\xi_{\mathrm{R}} = -40$.

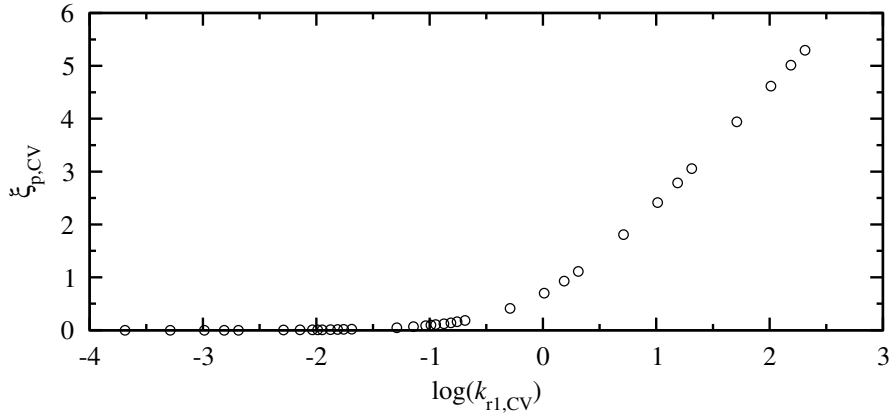

Figure 3.4.4: $\xi_{\mathrm{p,CV}}$ *vs* $\log(k_{\mathrm{r1,CV}})$ for simple EC mechanism of an immobilized species. Scan limits $\xi_{\mathrm{I}} = 40$ to $\xi_{\mathrm{R}} = -40$

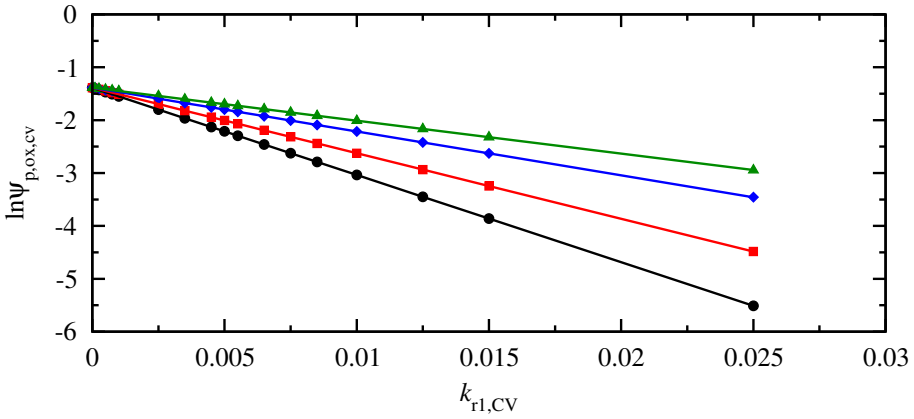

Figure 3.4.5: Napierian logarithm of the oxidation peak of the first cycle for an EC mechanism of immobilized species against the kinetic constant $k_{\mathrm{r1,CV}}$ for different potential limits. $\xi_{\mathrm{I}} = 40$ to $\xi_{\mathrm{R}} = -40$ (black circles), $\xi_{\mathrm{I}} = 30$ to $\xi_{\mathrm{R}} = -30$ (red squares), $\xi_{\mathrm{I}} = 20$ to $\xi_{\mathrm{R}} = -20$ (blue diamonds) and $\xi_{\mathrm{I}} = 15$ to $\xi_{\mathrm{R}} = -15$ (green triangles).

and for larger scan limits, the slope is higher.

From this aspect, cyclic voltammetry cannot be used as the method by using the oxidation peak of the first cycle to extract the kinetic information directly. The next thing that will be considered is if information can be obtained in the case of continuous cycles. An example of such a case is presented in Fig. 3.4.6. In Fig. 3.4.6(a), a series of a large number of voltammograms against time is presented. It is evident that as the number of cycles increases, the peak height decreases. In order to get a clearer picture of the voltammograms, a close-up in the first 15.5 cycles can be found in Fig 3.4.6(b). For an even better understanding this series of voltammograms are presented against the potential in Fig. 3.4.6(c).

After having examined the general outlook of the voltammograms over the course of time, the surface coverage of the three forms that can coexist on the electrode surface during such an experiment are presented in Fig. 3.4.7(a). As the cycles progress in time the surface coverages of $\mathrm{E_1}$ and $\mathrm{E_2}$ ($\theta_{\mathrm{E_1}}$ and $1 - \theta_{\mathrm{E_1}} - \theta_{\mathrm{E_2S}}$, respectively) decrease over time, while that of $\mathrm{E_2S}$ ($\theta_{\mathrm{E_2S}}$) goes the other way. Moreover, the coverages seem to have a step-like form, which is due to the fact that as the time progresses we have an infinite succession of fully oxidizing and reducing the the immobilized species. When the species is in its reduced form, the chemical step of the EC mechanism is unlocked, thus, at this point the surface coverage $\theta_{\mathrm{E_2S}}$ increases while $1 - \theta_{\mathrm{E_1}} - \theta_{\mathrm{E_2S}}$ decreases. During the periods when the immobilized species is in its oxidized form, the chemical reaction does not proceed and thus, $\theta_{\mathrm{E_2S}}$ is constant.

In Fig. 3.4.7(b) the dimensionless rate of the chemical step is shown. While the species is in its oxidized form the rate is 0 while when in its reduced form, the rate takes a certain value which lowers as the time progresses due to the consumption of $\mathrm{E_2}$. The rate of the electrochemical step is not depicted as it is similar to cyclic voltammograms.

Then,in order to see if there is a clear correlation between the the oxidation peak of each cycle and the surface coverage, a plot of $\psi_{\mathrm{p,CV}}$ against $1 - \theta_{\mathrm{E_1}} - \theta_{\mathrm{E_2S}}$ is constructed in Fig. 3.4.8. The value of the surface coverage corresponds to the peak of the coverage

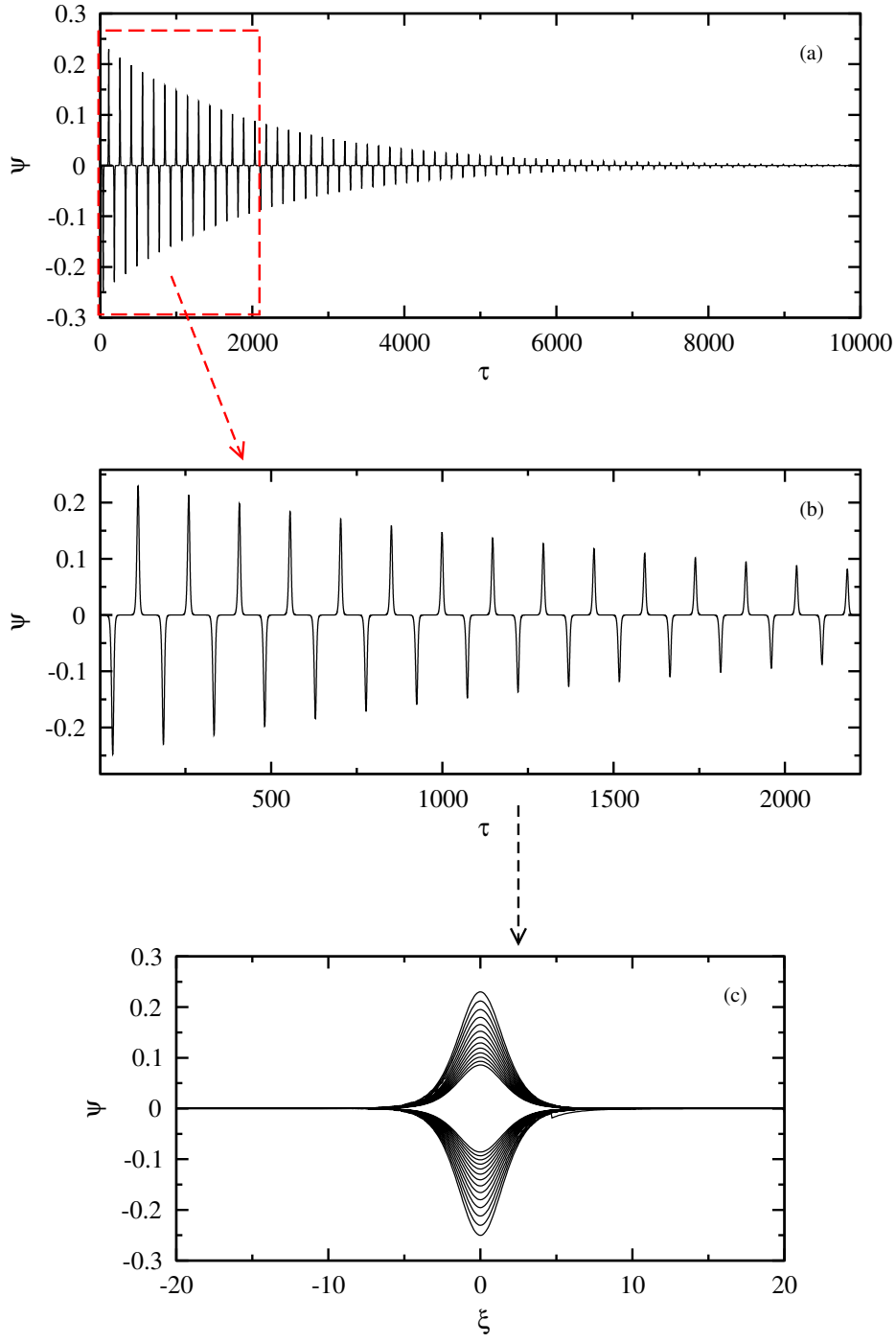

Figure 3.4.6: (a) Cyclic voltammograms against time of continuous circles for simple EC mechanism of an immobilized species for $k_{\mathrm{r1,CV}} = 0.001$. (b) Enlarged region for the first 15 circles. (c) Cyclic voltammograms against potential for the first 15.5 circles.

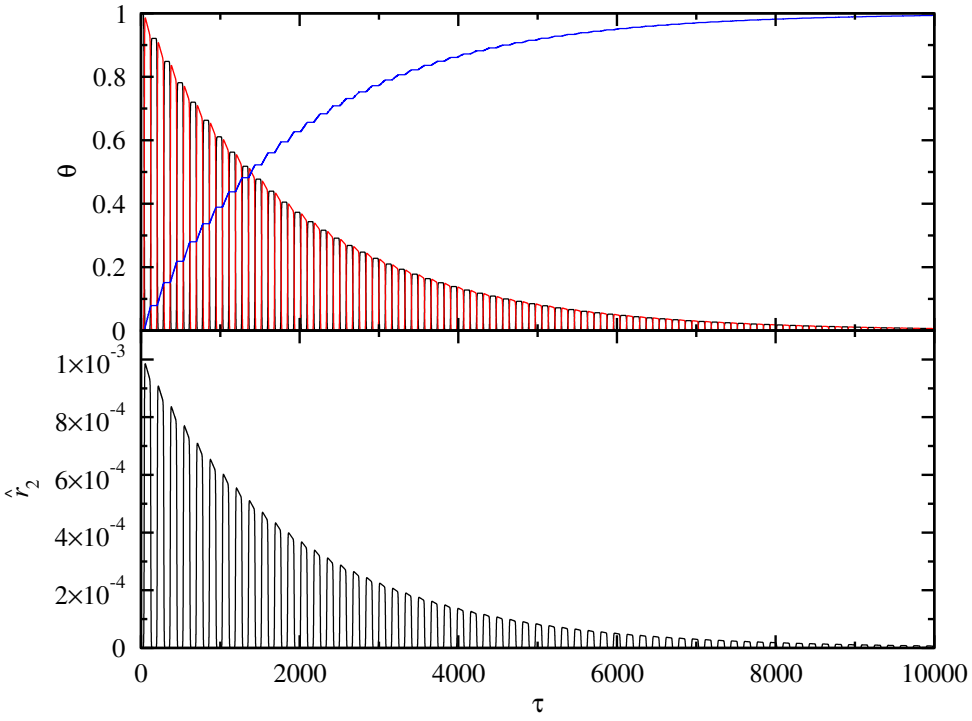

Figure 3.4.7: (a) Surface coverages of immobilized species against time for a EC mechanim of immobilized species for $k_{\mathrm{r1,CV}} = 0.001$ and $\xi_{\mathrm{init}} = 20$ to $\xi_{\mathrm{final}} = -20$. θ_1 (black line), 1-$\theta_{\mathrm{E_1}} - \theta_{\mathrm{E_2S}}$ (red line) and $\theta_{\mathrm{E_2S}}$ (blue line). (b) dimensionless rate $\hat{r}_2$ against time under the same conditions.

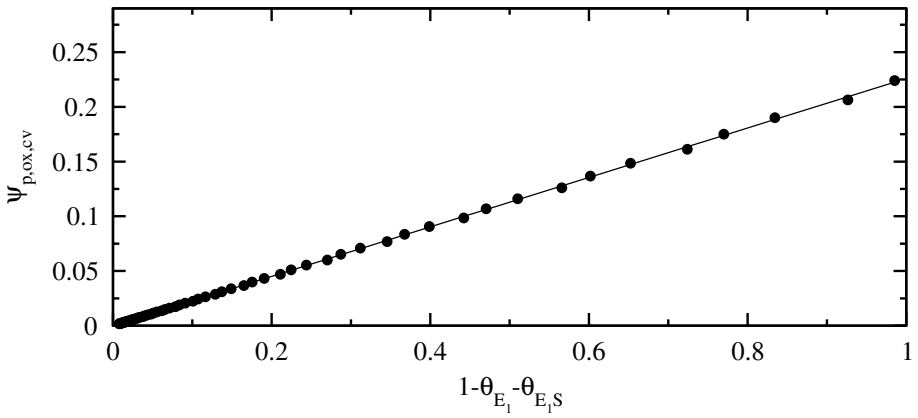

Figure 3.4.8: Oxidation peak of progressing cycles for simple EC mechanism of immobilized species against surface coverarage $1-\theta_{\mathrm{E}_1}-theta_{\mathrm{E}_2\mathrm{S}}$ for $k_{\mathrm{r1,CV}}=0.001$ and $\xi_{\mathrm{I}}=20$ to $\xi_{\mathrm{R}}=-20$.

of the reduced form of the immobilized species during each cycle. A linear dependence is observed, so, a direct correlation of the decrease of the surface coverage can be obtained by using the values of the measured current in an experiment.

Next, an attempt is made to overcome the disadvantages of using the oxidation peak of the first cycle of an experiment, by exploiting the successive oxidation peaks of multiple cycles. The Naeperian logarithm of the oxidation peak against time for different potential limits for $k_{\mathrm{r1,CV}}=0.001$ is presented in Fig. 3.4.9. An an initial glimpse, the trend seems to be the exact same, regardless of the the scan limits used. From the slope of the fitting, directly the value of $k_{\mathrm{r1,CV}}$ is extracted, as in all cases it corresponds to 0.001. Regarding the intercept, depending on the limits used, a slight variation is observed with no obvious trend of physical meaning. Regardless of the intercept though, the Naeperian logarithm of the oxidation peak can be expressed as linear expression of time from which the $k_{\mathrm{r1,CV}}$ can be directly extracted, ignoring the intercept which is a function of the scan limits. Therefore,

$$\ln\psi_{\mathrm{p,CV}}=f(\xi_{\mathrm{I}},\xi_{\mathrm{R}})-k_{\mathrm{r1,CV}}\tau \tag{3.4.14}$$

Rendering now, this equation dimensional, the above equation can be rewritten as,

$$i_{\mathrm{p,CV}}=q\mathrm{e}^{k_1 t} \tag{3.4.15}$$

where q is a constant which includes the scan limits, the surface concentration, the temperature and the scan rate. However in an experimental where the sole scope is to extract the kinetic constant of the chemical step of the reaction k_1 this constant does not affect the desired result.

In Fig.-3.4.10 the same type of plot is depicted as in Fig. 3.4.9, at fixed scan limits but different $k_{\mathrm{r1,CV}}$ values, so as to confirm that the slope is indeed the kinetic constant value. Again, linear dependence is observed with the slope being the $k_{\mathrm{r1,CV}}$ and the slope slightly depending on the $k_{\mathrm{r1,CV}}$ as well. Thus, we reach a formula similar to the one previously introduces with the difference that the intercept in the dimensionless

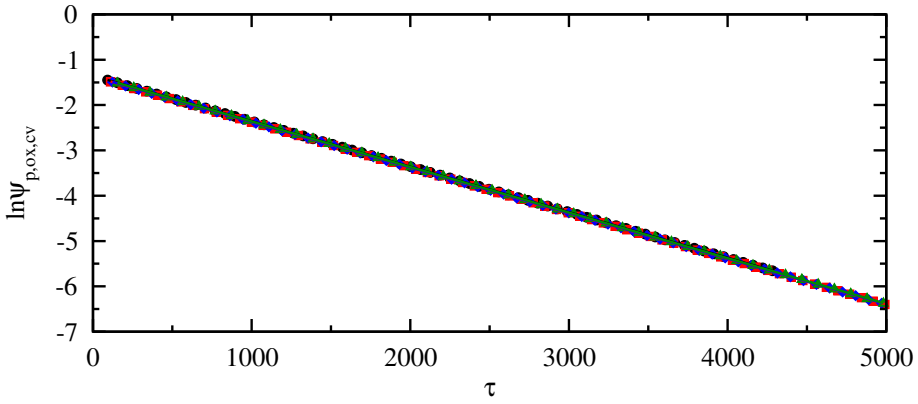

Figure 3.4.9: Napierian logarithm of the oxidation peak of progressing cycles for simple EC mechanism of immobilized species against time for different potential limits for $k_{\mathrm{r1,CV}} = 0.001$. $\xi_{\mathrm{I}} = 15$ to $\xi_{\mathrm{R}} = -15$ (black circles), $\xi_{\mathrm{I}} = 18$ to $\xi_{\mathrm{R}} = -18$ (red squares), $\xi_{\mathrm{I}} = 20$ to $\xi_{\mathrm{R}} = -20$ (blue diamonds) and $\xi_{\mathrm{I}} = 30$ to $\xi_{\mathrm{R}} = -30$ (green triangles).

form and the q constant in the dimensional one depend also on the kinetic constant of the chemical reaction, whithout have an impact on the way that $k_{\mathrm{r1,CV}}$ can be extracted from the oxidation peaks on successive experiments,

$$\ln \psi_{\mathrm{p,CV}} = g(\xi_{\mathrm{I}}, \xi_{\mathrm{R}}, k_{\mathrm{r1,CV}}) - k_{\mathrm{r1,CV}}\tau \tag{3.4.16}$$

and,

$$i_{\mathrm{p,CV}} = q\mathrm{e}^{k_1 t} \tag{3.4.17}$$

Next up in line, is to check if the chief observables of an FTacV experiment can work in the same way as the one in cyclic voltammetry. The first five harmonics resulting from an FTacV experiment for simple EC mechanism of an immobilized species at a dimensionless amplitude of 3.892 and various $k_{\mathrm{r1,FTacV}}$ are presented in Fig. 3.4.11. As in the case of cyclic voltammetry, looking at the oxidation peak, it drastically decreases as the kinetic constant increases, and it has already vanished at a value of $k_{\mathrm{r1,FTacV}} = 0.1$.

Up to this point, a dimensionless kinetic constant value of 0.01, the reduction peak is in tact with no significant changes, but a larger values, and in the absence of the oxidation peak, it starts decreasing is size and slightly deforming. This comes in contrast to the case of cyclic voltammetry where the reduction peak increases and shifts to more anodic values, but for FTacV, this behavior comes natural When $k_{\mathrm{r1,FTacV}}$ reaches very high values, the two-step reaction is essentially rendered in an apparent one step irreversible reaction, and the signals of irreversible reactions in FTacV drop significantly in magnitude in comparison to the reversible ones.

Regarding the dominant peak of the odd harmonics for five different amplitudes, diagrams similar to those of cyclic voltammetry (Fig. 3.4.3) are presented in Fig. 3.4.12. The trend appears to be similar to that of cyclic voltammetry for the oxidation peak of the first cycle, however, this approach suffer the same problems as the ones previously discussed, that is that such diagrams depend strongly on the scan limits.

In Fig. 3.4.15, the progress of the 5th harmonic in time of an FTacV experiment for $\alpha_0 = 3.892$, $\xi_{\mathrm{I}} = 20$ to $\xi_{\mathrm{R}} = -20$, $k_{\mathrm{r1,FTacV}} = 0.001$ is presented. There is also a zoom

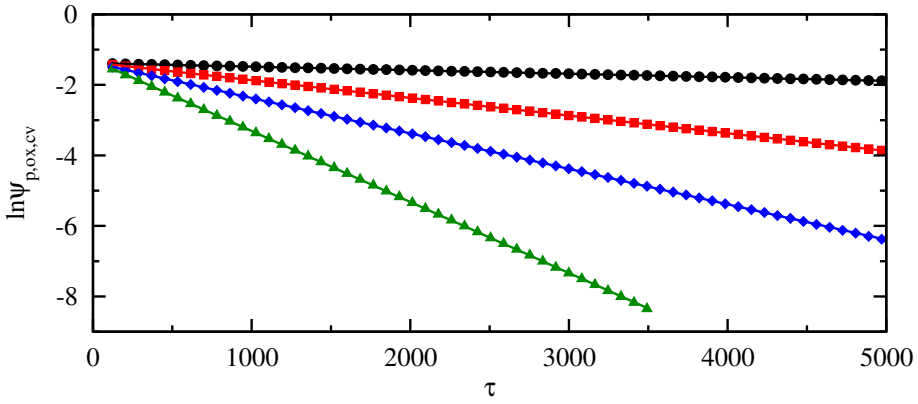

Figure 3.4.10: Naeperian logarithm of the oxidation peak of progressing cycles for a EC mechanism of immobilized species against time for different kinetic constants for $\xi_{\mathrm{I}} = 20$ to $\xi_{\mathrm{R}} - 20$. $k_{\mathrm{r1,CV}} = 0.0001$ (black circles), 0.0005 (red squares), 0.001 (blue diamonds) and 0.002 (green triangles).

in the first six cycles. One can clearly see that a trend of decrease is present as the one in found in cyclic voltammetry.

The surface coverages of the possible forms of the immobilized species alongside the dimensionless rate of the chemical step, are presented in Fig. 3.4.14(a) and 3.4.14(b), respectively. The same pattern is observed as the one in cyclic voltammetry. The difference is that in the surface coverages and the rate, a perturbation is also observed due to the potential perturbation applied in FTacV.

Taking into account the trend observed in cyclic voltammetry for the oxidation peak over the course of successive cycles, two more parameters are examined, namely the order of the harmonic and the perturbation amplitude. As can be noted in Figs. 3.4.15 and 3.4.16 a linear dependence is still observed both when the order of the odd harmonic as well as the perturbation amplitude are examined. In all the cases the slope of the diagram corresponds to the $k_{\mathrm{r1,FTacV}}$ and the only thing that changes is the intercept. Thus, other than the parameters that affect the intercept of such diagrams other than the ones already mentioned in cyclic voltammetry are these two. Consequently, the dependence of the dominant oxidation peak of the odd harmonic for FTacV, in the dimensionless and the dimensional form are presented below,

$$\ln \psi_{\mathrm{ip,FTacV}} = h(\xi_{\mathrm{init}}, \xi_{\mathrm{final}}, k_{\mathrm{r1,FTacV}}, \alpha_0) - k_{\mathrm{r1,FTacV}}\tau \tag{3.4.18}$$

and,

$$i_{\mathrm{ip,FTacV}} = q\mathrm{e}^{k_1 t} \tag{3.4.19}$$

. Still solely, by exploiting the oxidation peak of the current the kinetic constant of the chemical reaction can be extracted by fitting the above equations to the experimental data. It should be noted that even though this analysis holds for a reversible electrochemical reaction, this analysis can also be applied for the examination of quasi reversible cases of the electrochemical step [8].

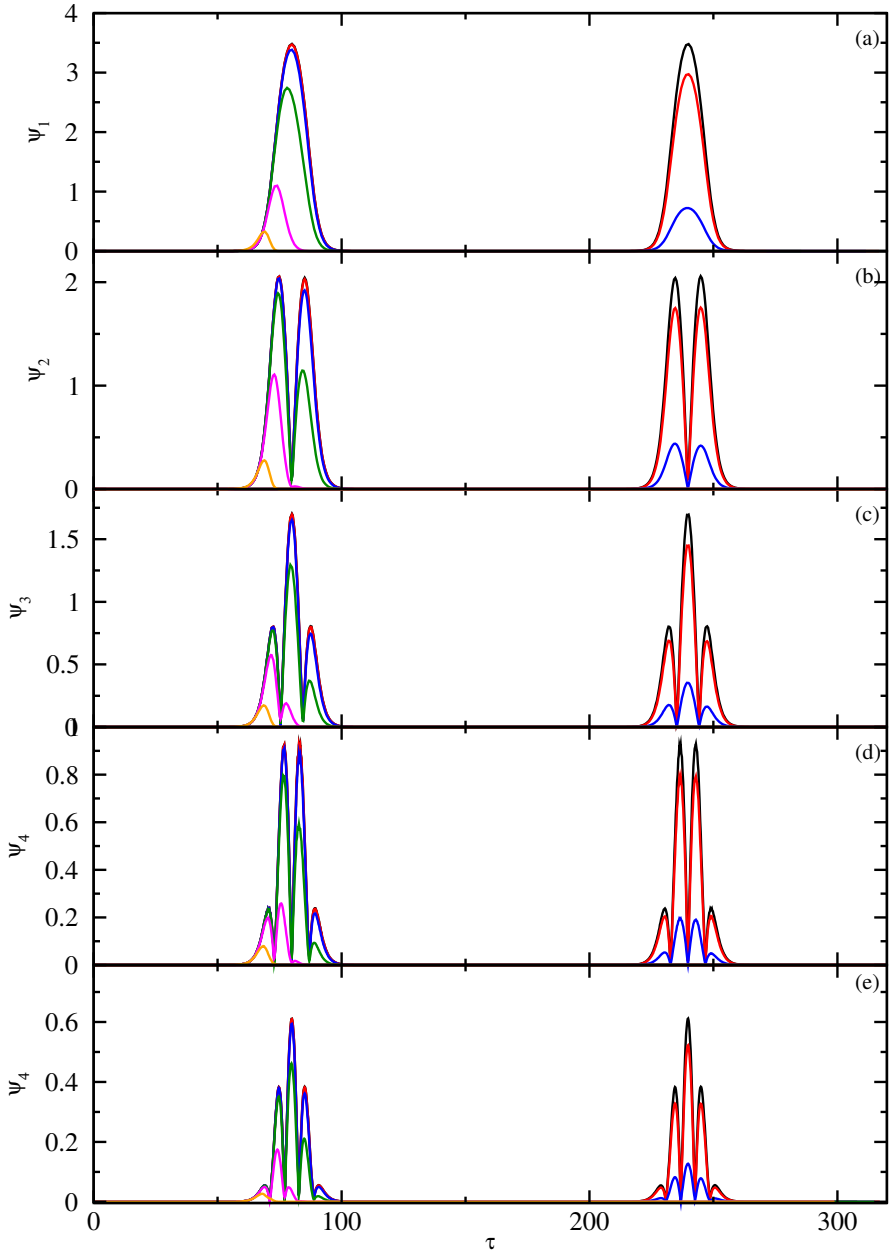

Figure 3.4.11: 1st through 5th harmonic (a) -(e) for an EC mechanism of an immobilized species. $\sigma = 0.4868$, $\alpha_0 = 3.892$,$\xi_{\mathrm{I}} = 40$ to $\xi_{\mathrm{R}} = -40$, $k = 100$ and $k_{\mathrm{r1,FTacV}} = 0$ (black line), 0.001 (red line), 0.01 (blue line), 0.1 (green line), 1 (magenta line) and 10 (orange line).

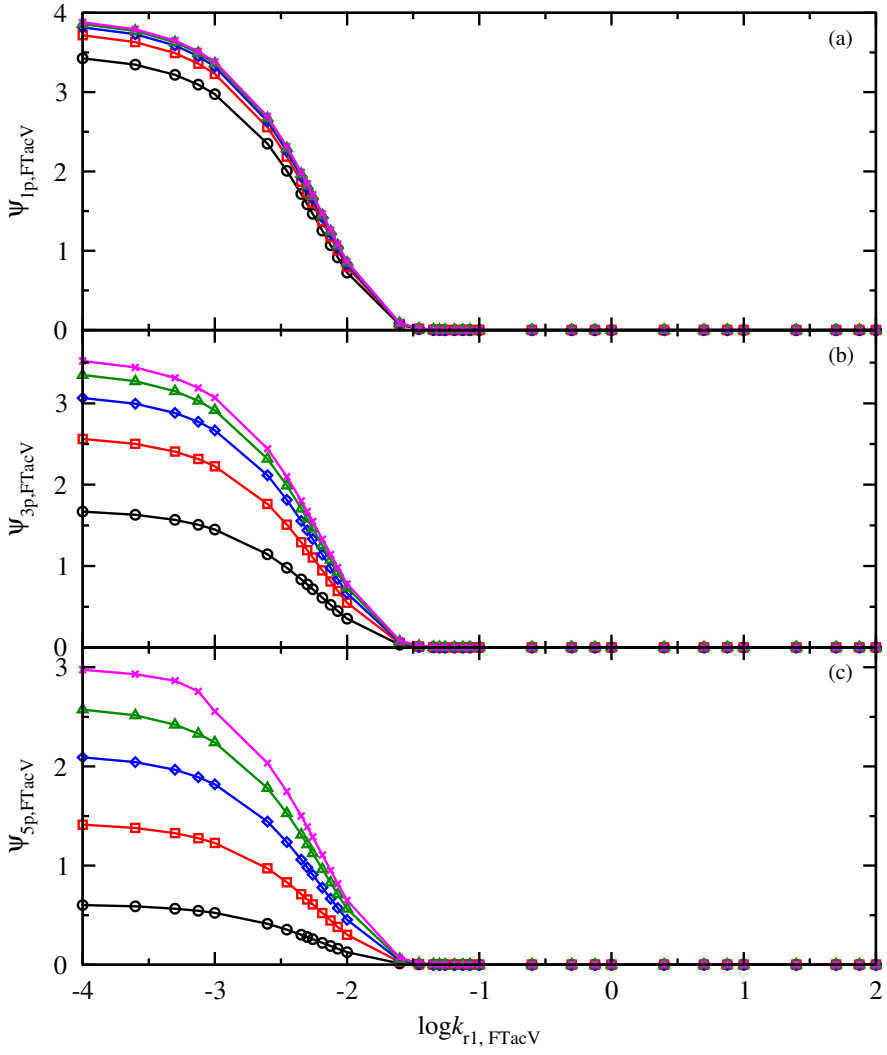

Figure 3.4.12: Dimensionless oxidation peak $\psi_{p,FTacV}$ against $\log k_{\mathrm{r1,FTacV}}$ of (a) 1st (b) 3rd and (c) 5th harmonic for an EC mechanism of an immobilized species for different dimensionless amplitudes for $\xi_{\mathrm{I}} = 40$ 40 to $\xi_{\mathrm{R}} = -40$. $\alpha_0 = 3.892$ (black circles), 5.839 (red squares), 7.784 (blue diamonds), 9.731 (green triangles) and 11.677 (magenta x).

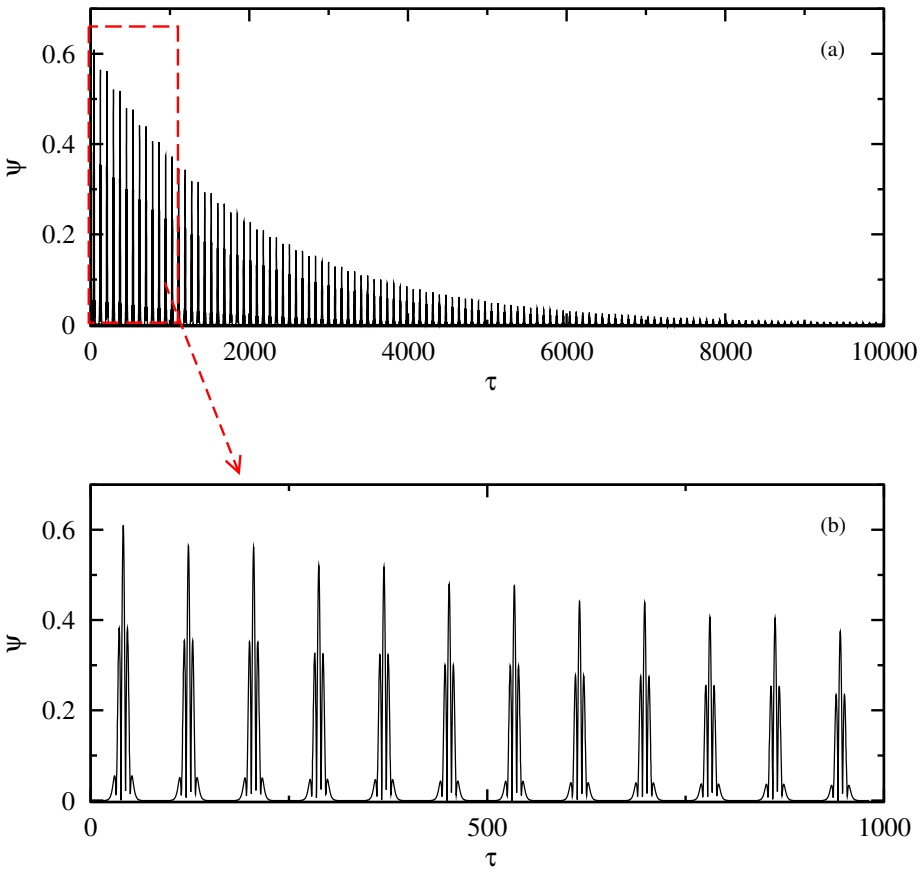

Figure 3.4.13: (a) 5th harmonic FTac voltammograms against time of continuous circles for an EC mechanism of an immobilized species for $k_{\mathrm{r1,FTacV}} = 0.001$, $\alpha_0 = 3.892$ and $\xi_{\mathrm{I}} = 20$ to $\xi_{\mathrm{R}} = -20$. (b) Zoom in the first 6 circles.

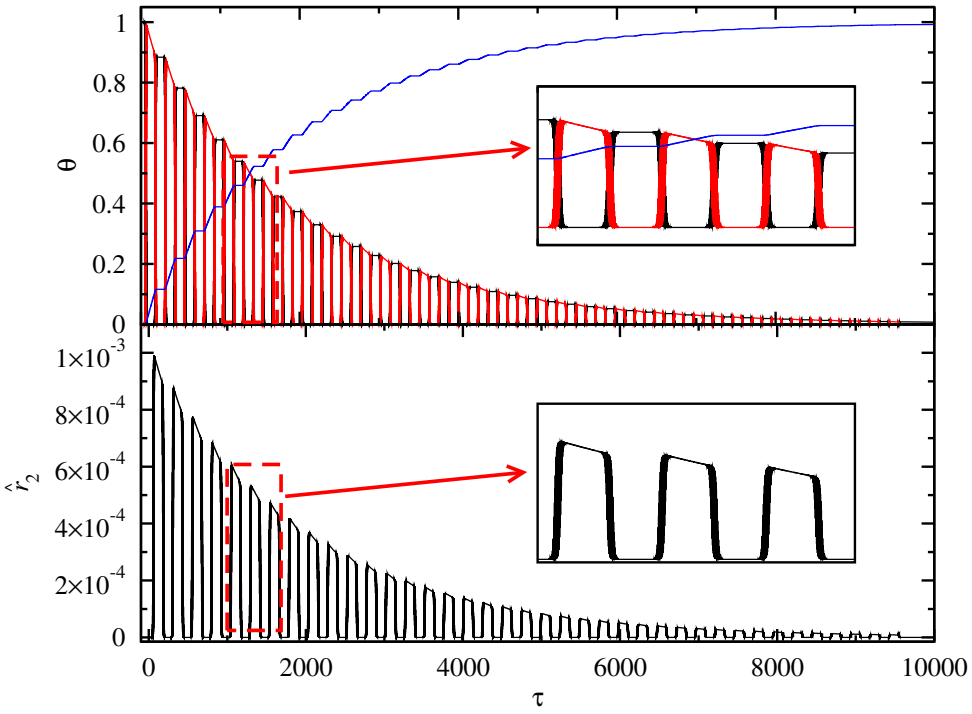

Figure 3.4.14: (a) Surface coverages of immobilized species against time for an EC mechanism of immobilized species for $k_{\mathrm{r1,CV}} = 0.001$ and $\xi_{\mathrm{I}} = 30$ to $\xi_{\mathrm{R}} = -30$ and amplitude 3.892. θ_1 (black line), $1 - \theta_{\mathrm{E_1}} - \theta_{\mathrm{E_2S}}$ (red line) and $\theta_{\mathrm{E_2S}}$ (blue line). (b) dimensionless rate $\hat{r}_2$ against time under the same conditions.

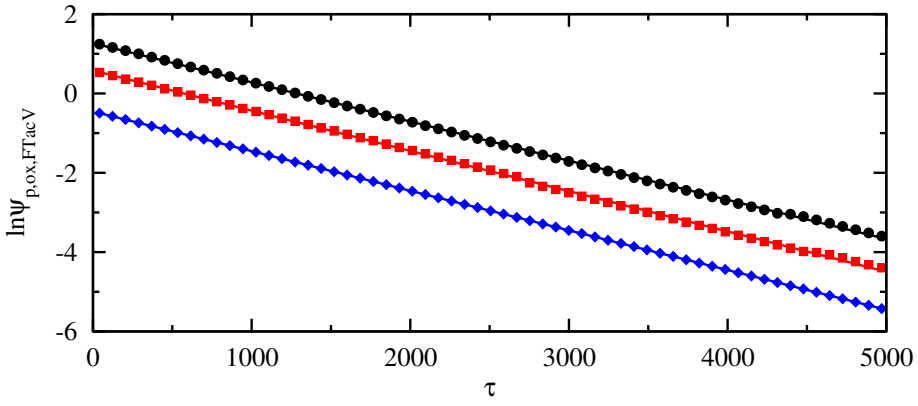

Figure 3.4.15: Napierian logarithm of the oxidation peak of progressing cycles for an EC mechanism of immobilized species against time for $\alpha_0 = 3.892$, $\xi_{\mathrm{I}} = 20$ to $\xi_{\mathrm{R}} = -20$, $k_{\mathrm{r1,FTacV}} = 0.001$ for different harmonics. 1st harmonic (black circles), 3rd harmonic (red squares) and 5th harmonic (blue diamonds).

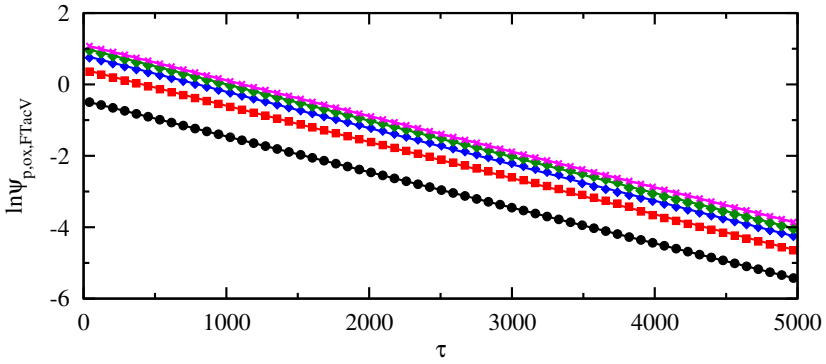

Figure 3.4.16: Naeperian logarithm of the oxidation peak of the 5th harmonic of progressing cycles for an EC mechanism of immobilized species against time for $\xi_{\mathrm{I}} = 20$ to $\xi_{\mathrm{R}} = -20$, $k_{\mathrm{r1,FTacV}} = 0.001$ for different amplitudes. Amplitude values 3.892 (black circles), 5.839 (red squares) 7.784 (blue diamonds) 9.731 (green triangles) and 11.677 (magenta x).

3.4.2 Mechanistic analysis

Considering the same mechanism, a mechanistic approach shall be made.

Firstly, we shall consider the case where the electrochemical reaction is reversible, *i.e.* Nernst law applies,

$$\frac{\Gamma_{\mathrm{E_1}}}{\Gamma_{\mathrm{E_2}}} = e^{\frac{F}{RT}(E-E^0)} \tag{3.4.20}$$

Since, $\mathrm{E_1}$, $\mathrm{E_2}$ and $\mathrm{E_2S}$ are immobilized,

$$\Gamma^0 = \Gamma_{\mathrm{E_1}}(t) + \Gamma_{\mathrm{E_2S}}(t) + \Gamma_{\mathrm{E_2}}(t) \tag{3.4.21}$$

By using Eq. (3.4.21), Eq. (3.4.20) is written,

$$\Gamma_{\mathrm{E_2}}(t) = \frac{\Gamma^0 - \Gamma_{\mathrm{E_2S}}(t)}{1 + e^{\frac{F}{RT}(E-E^0)}} \tag{3.4.22}$$

The rate of the product production will be,

$$r_2 = \frac{d\Gamma_{\mathrm{E_2S}}}{dt} = k_1 c_{\mathrm{S}} \Gamma_{\mathrm{E_2S}}(t)$$

or, by using Eq. (3.4.22),

$$\frac{d\Gamma_{\mathrm{E_2S}}}{dt} = k_1 c_{\mathrm{s}} \frac{\Gamma^0 - \Gamma_{\mathrm{E_2S}}(t)}{1 + e^{\frac{F}{RT}(E-E^0)}} \tag{3.4.23}$$

The rate of change of Γ_2 is obtained by differentiating Eq. (3.4.22). Thus,

$$\frac{d\Gamma_{\mathrm{E_2}}}{dt} = -(\Gamma^0 - \Gamma_{\mathrm{E_2S}}) \frac{k_1 c_{\mathrm{s}} + \frac{F}{RT} E' e^{\frac{F}{RT}(E-E^0)}}{(1 + e^{\frac{F}{RT}(E-E^0)})^2} \tag{3.4.24}$$

The rate of change of $\Gamma_{\mathrm{E_1}}$ is obtained by differentiating Eq. (3.4.21),

$$\frac{d\Gamma_{\mathrm{E_1}}}{dt} = -\frac{d\Gamma_{\mathrm{E_2}}}{dt} - \frac{d\Gamma_{\mathrm{E_2S}}}{dt}$$

that is,

$$\frac{d\Gamma_{E_1}}{dt} = \frac{\Gamma^0 - \Gamma_{E_2S}}{(1 + e^{\frac{F}{RT}(E-E^0)})^2}(\frac{F}{RT}E' - k_1 c_S)e^{\frac{F}{RT}(E-E^0)} \tag{3.4.25}$$

The current density will be,

$$\frac{i}{F} = \frac{d\Gamma_{E_1}}{dt}$$

Thus, from Eq. (3.4.25),

$$I = SF\frac{\Gamma^0 - \Gamma_{E_2S}}{(1 + e^{\frac{F}{RT}(E-E^0)})^2}\Big(\frac{F}{RT}E' - k_1 c_S\Big)e^{\frac{F}{RT}(E-E^0)} \tag{3.4.26}$$

where S is the electrode surface area. We observe that the current depends on the analytic form of $\Gamma_P(t)$ as well as the potential program $E(t)$. Thus,

- For a cathodic linear scan,

  $$E(t) = E_I - vt$$

  the current is written,

  $$I = -SF\frac{\Gamma^0 - \Gamma_{E_2S}}{(1 + e^{\frac{F}{RT}(E-E^0)})^2}\Big(\frac{Fv}{RT} + k_1 c_S\Big)e^{\frac{F}{RT}(E-E^0)} \tag{3.4.27}$$

- For an anodic linear scan,

  $$E(t) = E_R + vt$$

  the current is written,

  $$I = AF\frac{\Gamma^0 - \Gamma_{E_2S}}{(1 + e^{\frac{F}{RT}(E-E^0)})^2}\Big(\frac{Fv}{RT} - k_1 c_S\Big)e^{\frac{F}{RT}(E-E^0)} \tag{3.4.28}$$

In order to write the analytic dependence of I on potential or time, the analytic form of $\Gamma_{E_2S}(t)$ must be determined.

The analytic form of $\Gamma_{E_2S}(t)$ is obtained by solving Eq. (3.4.23).

- For a cathodic scan, Eq. (3.4.23) is written,

  $$\frac{d\Gamma_{E_2S}}{dt} = k_1 c_S\frac{\Gamma^0 - \Gamma_{E_2S}(t)}{1 + e^{\frac{F}{RT}(E_i - vt - E^0)}} \tag{3.4.29}$$

  This equation can be solved by separation of the variables,

  $$\Gamma_{E_2S}(t) = \Gamma^0 - C(1 + e^{-\frac{F}{RT}(E-E^0)})^{-\frac{k_1 c_S RT}{Fv}}$$

  The integration constant C is determined by the value of Γ_{E_2S} at the time instant t_i, *i.e.* when the potential is equal to E_i. Hence,

  $$\Gamma_{E_2S}(t) = \Gamma^0 - (\Gamma^0 - \Gamma_{E_2S}(t_i))(1 + e^{-\frac{F}{RT}(E-E^0)})^{-kc_A\frac{RT}{Fv}} \tag{3.4.30}$$

  Here, it has been assumed that $e^{-\frac{F}{RT}(E_i - vt_i - E^0)} \to 0$.

- For an anodic scan, Eq. (3.4.23) is written,

$$\frac{d\Gamma_{\mathrm{E_2S}}}{dt} = k_1 c_{\mathrm{S}} \frac{\Gamma^0 - \Gamma_{\mathrm{E_2S}}(t)}{1 + e^{\frac{F}{RT}(E_{\mathrm{r}} + vt - E^0)}} \tag{3.4.31}$$

This equation can be solved by separation of the variables,

$$\Gamma_{\mathrm{E_2S}}(t) = \Gamma^0 - C(1 + e^{-\frac{F}{RT}(E-E^0)})^{\frac{k_1 c_{\mathrm{S}} RT}{Fv}}$$

The integration constant C is determined by the value of $\Gamma_{\mathrm{E_2S}}$ at the time instant t_{r}, *i.e.* when the potential is equal to E_{r}. Hence,

$$\Gamma_{\mathrm{E_2S}}(t) = \Gamma^0 - (\Gamma^0 - \Gamma_{\mathrm{E_2S}}(t_{\mathrm{r}}))\Big(\frac{1 + e^{-\frac{F}{RT}(E-E^0)}}{1 + e^{-\frac{F}{RT}(E_{\mathrm{r}}-E^0)}}\Big)^{k_1 c_{\mathrm{S}} \frac{RT}{Fv}} \tag{3.4.32}$$

It is to be observed that the analytic expressions of $\Gamma_{\mathrm{p}}(t)$ depend on the values of $\Gamma_{\mathrm{p}}(t_{\mathrm{i}})$ (*i.e.* the surface concentration of P at the beginning of the cathodic scan) and $\Gamma_{\mathrm{p}}(t_{\mathrm{r}})$ (*i.e.* the surface concentration of P at the beginning of the anodic scan).

For the *first cathodic scan*, that is for $t \in [0, t_{\mathrm{r}}]$, $t_{\mathrm{i}} = 0$ and $\Gamma_{\mathrm{E_2S}}(t_{\mathrm{i}}) = 0$. Thus, Eq. (3.4.30) is written,

$$\Gamma_{\mathrm{E_2S}}(t) = \Gamma^0 - \Gamma^0(1 + e^{-\frac{F}{RT}(E-E^0)})^{-kc_{\mathrm{A}} \frac{RT}{Fv}}$$

The value of $\Gamma_{\mathrm{E_2S}}$ at $t = t_{\mathrm{r}}$ is,

$$\Gamma_{\mathrm{E_2S}}(t_{\mathrm{r}}) = \Gamma^0 - \Gamma^0(1 + e^{-\frac{F}{RT}(E_{\mathrm{r}}-E^0)})^{-k_1 c_{\mathrm{S}} \frac{RT}{Fv}}$$

Now, for the *first anodic scan*, that is for $t \in [t_{\mathrm{r}}, 2t_{\mathrm{r}}]$, the value of $\Gamma_{\mathrm{E_2S}}(t_{\mathrm{r}})$ is known and Eq. (3.4.32) is written,

$$\Gamma_{\mathrm{E_2S}}(t) = \Gamma^0 - \Gamma^0\Big[\frac{1 + e^{-\frac{F}{RT}(E-E^0)}}{(1 + e^{-\frac{F}{RT}(E_{\mathrm{r}}-E^0)})^2}\Big]^{k_1 c_{\mathrm{R}} \frac{RT}{Fv}}$$

At the end of the first anodic scan $t_{\mathrm{i}} = 2t_{\mathrm{r}}$. Therefore,

$$\Gamma_{\mathrm{E_2S}}(t_{\mathrm{i}}) = \Gamma^0 - \Gamma^0\Big[\frac{1 + e^{-\frac{F}{RT}(E_{\mathrm{i}}-E^0)}}{(1 + e^{-\frac{F}{RT}(E_{\mathrm{r}}-E^0)})^2}\Big]^{k_1 c_{\mathrm{S}} \frac{RT}{Fv}}$$

Now, for the *second cathodic scan*, that is for $t \in [2t_{\mathrm{r}}, 3t_{\mathrm{r}}]$, the value of $\Gamma_{\mathrm{P}}(t_{\mathrm{i}})$ is known. Equation (3.4.30) is written,

$$\Gamma_{\mathrm{E_2S}}(t) = \Gamma^0 - \Gamma^0\Big[\frac{1 + e^{-\frac{F}{RT}(E-E^0)}}{(1 + e^{-\frac{F}{RT}(E_{\mathrm{r}}-E^0)})^{-2}}\Big]^{-k_1 c_{\mathrm{S}} \frac{RT}{Fv}}$$

At the end of the second cathodic scan, *i.e.* at $3t_{\mathrm{r}}$, the value of $\Gamma_{\mathrm{E_2S}}$ is,

$$\Gamma_{\mathrm{E_2S}}(t_{\mathrm{r}}) = \Gamma^0 - \Gamma^0[(1 + e^{-\frac{F}{RT}(E_{\mathrm{r}}-E^0)})^3]^{-k_1 c_{\mathrm{S}} \frac{RT}{Fv}}$$

Therefore, by using Eq. (3.4.32) for the *second anodic scan*, that is for $t \in [3t_{\rm r}, 4t_{\rm r}]$, we get,

$$\Gamma_{\rm E_2S}(t) = \Gamma^0 - \Gamma^0\Big[\frac{1+e^{-\frac{F}{RT}(E-E^0)}}{(1+e^{-\frac{F}{RT}(E_{\rm r}-E^0)})^4}\Big]^{k_1 c_{\rm S}\frac{RT}{Fv}}$$

It is to be observed that, if $n = 1, 2, \ldots$ is the number of the corresponding scan, the following equations hold,

- For the n-th cathodic scan, $E(t) = E_{\rm i} - v[t - 2(n-1)t_{\rm r}]$,

$$\Gamma_{\rm E_2S}(t) = \Gamma^0 - \Gamma^0\Big[\frac{1+e^{-\frac{F}{RT}(E-E^0)}}{(1+e^{-\frac{F}{RT}(E_{\rm r}-E^0)})^{2(1-n)}}\Big]^{-k_1 c_{\rm S}\frac{RT}{Fv}} \tag{3.4.33}$$

- For the n-th anodic scan, $E(t) = E_{\rm r} + v[t - (2n-1)t_{\rm r}]$,

$$\Gamma_{\rm E_2S}(t) = \Gamma^0 - \Gamma^0\Big[\frac{1+e^{-\frac{F}{RT}(E-E^0)}}{(1+e^{-\frac{F}{RT}(E_{\rm r}-E^0)})^{2n}}\Big]^{k_1 c_{\rm S}\frac{RT}{Fv}} \tag{3.4.34}$$

The above equations can be written in dimensionless form by setting, $\theta_{\rm E_2S} = \frac{\Gamma_{\rm E_2S}}{\Gamma^0}$, $\xi = \frac{F}{RT}(E - E^0)$, $\xi_{\rm R} = \frac{F}{RT}(E_{\rm r} - E^0)$ and $k_{\rm r_1,CV} = k_1 c_{\rm S}\frac{RT}{Fv}$. Therefore,

- For the n-th cathodic scan,

$$\theta_{\rm E_2S} = 1 - \Big[\frac{1+e^{-\xi}}{(1+e^{-\xi_{\rm R}})^{2(1-n)}}\Big]^{-k_{\rm r_1,CV}} \tag{3.4.35}$$

- For the n-th anodic scan,

$$\theta_{\rm E_2S} = 1 - \Big[\frac{1+e^{-\xi}}{(1+e^{-\xi_{\rm R}})^{2n}}\Big]^{k_{\rm r_1,CV}} \tag{3.4.36}$$

An example of the dependence of $\theta_{\rm E_2S}$ on ξ for four cycles is presented in Fig. 3.4.17, for $k_{\rm c_1,CV} = 0.01$.

Using $\psi = \frac{IRT}{AF^2 v\Gamma^0}$ as well as the above dimensionless variables and parameters, the dimensionless current is written,

- For the cathodic scans,

$$\psi = -\Big[\frac{1+e^{-\xi}}{(1+e^{-\xi_{\rm R}})^{2(1-n)}}\Big]^{-k_{\rm c_1,CV}}\frac{(1+k_{\rm c_1,CV})e^{\xi}}{(1+e^{\xi})^2} \tag{3.4.37}$$

- For the anodic scans,

$$\psi = \Big[\frac{1+e^{-\xi}}{(1+e^{-\xi_{\rm R}})^{2n}}\Big]^{k_{\rm r_1,CV}}\frac{(1-k_{\rm r_1,CV})e^{\xi}}{(1+e^{\xi})^2} \tag{3.4.38}$$

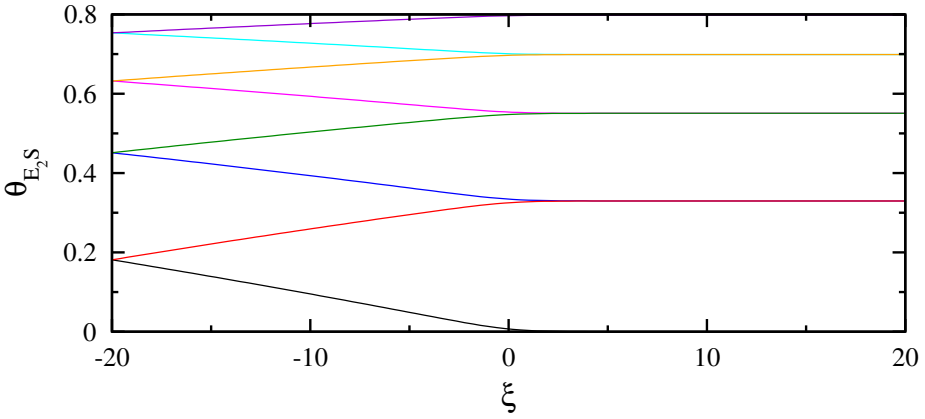

Figure 3.4.17: Dependence of $\theta_{\mathrm{E_2S}}$ on ξ for four cycles and $k_{\mathrm{c_1,CV}} = 0.01$.

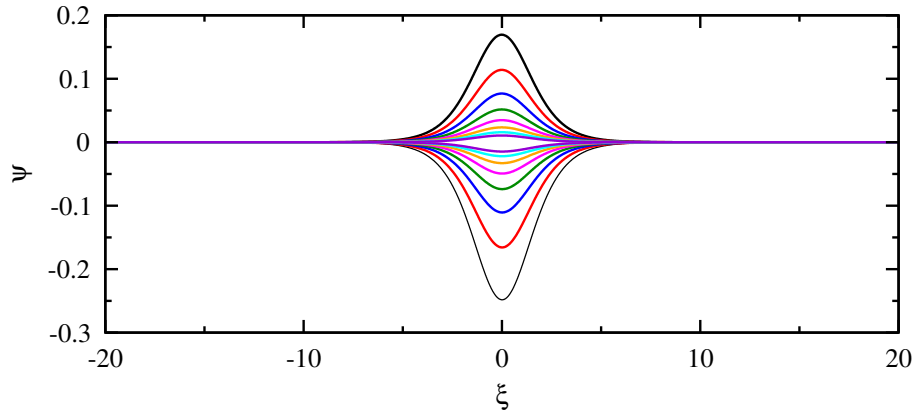

Figure 3.4.18: Dependence of ψ on ξ for eight cycles and $k_{\mathrm{c_1,CV}} = 0.01$.

The cyclic voltammogram is presented in Fig. 3.4.18. The potential of the anodic current peak can be obtained by differentiation. Thus,

$$\xi_{\mathrm{p,CV,a}} = \ln(1 - k_{\mathrm{r_1,CV}})$$

that is,

$$E_{\mathrm{CV,a,p}} = E^0 + \ln\left(1 - k_1 c_{\mathrm{S}} \frac{RT}{Fv}\right) \tag{3.4.39}$$

It is to be noticed that a maximum of the anodic peak exists only if,

$$k_1 < \frac{Fv}{RTc_{\mathrm{S}}}$$

that is for $k_1 < 38.95\frac{v}{c_{\mathrm{S}}}$ at 298 K.

The potential of cathodic current peak can be obtained, once again, by differentiation. Thus,

$$\xi_{\mathrm{CV,p,c}} = \ln(1 + k_{\mathrm{r_1,CV}})$$

that is,

$$E_{\mathrm{CV,p,c}} = E^0 + \ln\left(1 + k_1 c_{\mathrm{S}} \frac{RT}{Fv}\right) \tag{3.4.40}$$

The anodic and cathodic peak potential is independent of the number of cycles, n.

For small values of k, both anodic and cathodic peak potentials are $E_{\mathrm{p,a}} \approx E_{\mathrm{p,c}} \approx E^0$. In such a case, the anodic peak current is,

$$\psi_{\mathrm{p,CV,a}} \approx \left[\frac{2}{(1+e^{-\xi_{\mathrm{R}}})^{2n}}\right]^{k_{\mathrm{r_1,CV}}} \frac{1}{4}$$

Since $e^{-\xi_{\mathrm{R}}} \gg 1$ the above equation is written,

$$\ln \psi_{\mathrm{p,CV,a}} = \ln \frac{2^{k}{}_{\mathrm{r_1,CV}}(1 - k_{\mathrm{r_1,CV}})}{4} + 2\xi_{\mathrm{R}} k_{\mathrm{r_1,CV}} n \tag{3.4.41}$$

or, in dimensional parameters,

$$\ln I_{\mathrm{p,CV,a}} = B + 2n \frac{E_{\mathrm{R}} - E^0}{v} k_1 c_{\mathrm{s}} \tag{3.4.42}$$

But, $2(E_{\mathrm{r}} - E^0)/v = t_{\mathrm{p,c}} - t_{\mathrm{p,a}}$, where $t_{\mathrm{p,a}}$ and $t_{\mathrm{p,a}}$ are the time instances where the n-th anodic and cathodic peaks appear. Therefore, the equation relating the height of the anodic peak with the time instance when it appears is,

$$\ln I_{\mathrm{p,cv,a}} = B - nk_1 c_{\mathrm{s}}(t_{\mathrm{p,a}} - t_{\mathrm{p,c}}) \tag{3.4.43}$$

The slope of the linear plot of $\ln I_{\mathrm{p,a}}$ *vs.* $t_{\mathrm{p,a}}$ can serve for the evaluation of k_1 (for known c_{s}). It is interesting to notice that the slope is independent of the electrode surface and the value of the formal electrode potential.

An example of the dependence of $\psi_{\mathrm{P,CV,a}}$ on n for eight cycles and $k_{\mathrm{r_1,CV}} = 0.01$ is shown in Fig. 3.4.19. From this plot, the slope was found to be -0.396. Taking into account that $\xi_{\mathrm{R}} = -20$, the estimation of $k_{\mathrm{r_1,CV}}$ is,

$$k_{\mathrm{r_1,CV}} = -\frac{0.396}{2\xi_{\mathrm{R}}} = \frac{0.396}{2 \times 20} = 0.0099$$

which is a rather good approximation of the original value.

For a large amplitude Fourier transform ac voltammetry, the potential program is written,

$$\xi(t) = \frac{2\xi_{\mathrm{i}}}{\pi} \mathrm{asin}\left[\sin\left(\frac{2\pi(\tau + \tau_{\mathrm{r}}/2)}{2t_{\mathrm{r}}}\right)\right] + a_0 \sin(2\pi\tau) \tag{3.4.44}$$

where the dimensionless time is defined now as $\tau = tf$. The evolution of the coverage of the product is written,

$$\frac{d\theta_{\mathrm{E_2S}}}{d\tau} = k_{\mathrm{r_1,CV}} \frac{1 - \theta_{\mathrm{E_2S}}(\tau)}{1 + e^{\xi(\tau)}} \tag{3.4.45}$$

and the Faradaic current is,

$$\psi = \frac{1 - \theta_{\mathrm{E_2S}}}{(1+e^{\xi})^2}(\xi' - k_{\mathrm{c_1,CV}})e^{\xi} \tag{3.4.46}$$

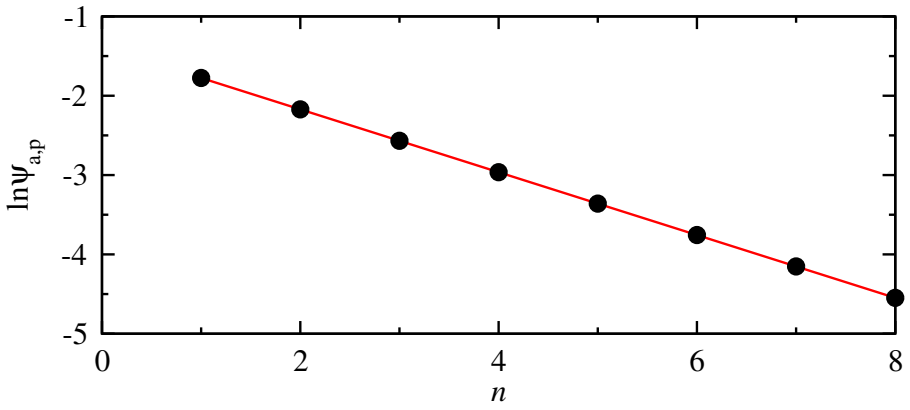

Figure 3.4.19: Dependence of $\psi_{\mathrm{a,p}}$ on n for eight cycles and $k_{\mathrm{c_1,CV}} = 0.01$.

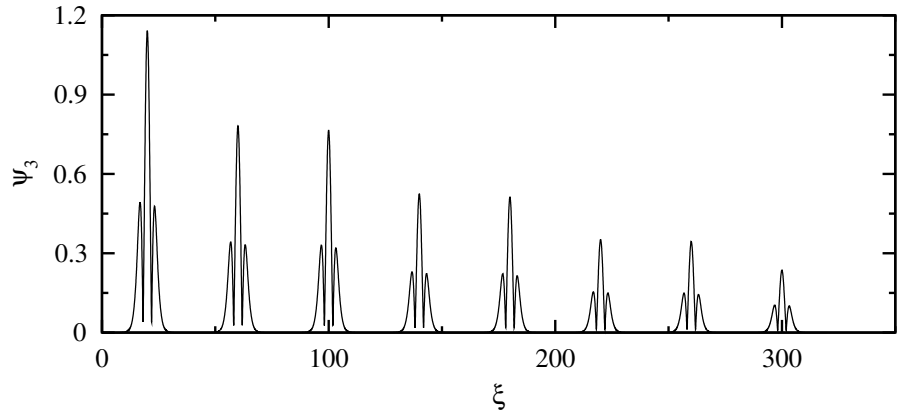

Figure 3.4.20: Dependence of ψ_3 on τ for four cycles and $k_{\mathrm{c_1,CV}} = 0.01$.

where now, $k_{\mathrm{r_1,CV}} = k_1 c_{\mathrm{R}}/f$ and $\psi = \frac{I}{AF\Gamma^0 f}$. The derivative of ξ is[3],

$$\xi'(\tau) = -\mathrm{sgn}\left[\sin\left(\frac{2\pi\tau}{2\tau_{\mathrm{r}}}\right)\right] + 2\pi a_0 \cos(2\pi\tau)) \tag{3.4.47}$$

Unfortunately, Eq. (3.4.45) cannot be solved analytically, so we must turn to numerical solutions.

The envelope of the 3rd harmonic, ψ_3, for $n = 4$, $k_{\mathrm{c_1,CV}} = 0.01$ and $a_0 = 3$ is presented in Fig. 3.4.20. In this figure, the first triplet corresponds to the first cathodic scan, the second triplet to the first anodic scan, the third triplet to the second cathodic scan etc.

[3]The signum function (sgn) - that appears in the equation - of a real number x is defined as follows:

- -1, if $x < 1$
- 0, if $x = 1$
- 1, if $x > 1$

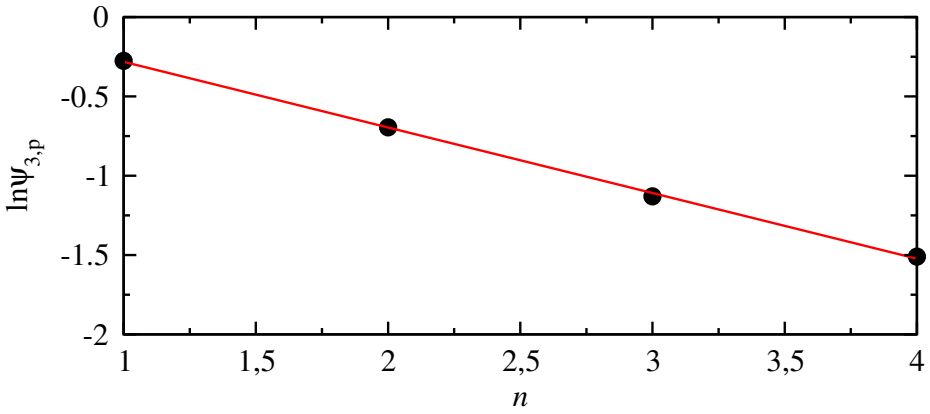

Figure 3.4.21: Dependence of the anodic $\psi_{3,\mathrm{p}}$ on n for four cycles and $k_{\mathrm{c}_1,\mathrm{CV}} = 0.01$.

The dependence of the height of the principal anodic peak of the 3rd harmonic, $\psi_{3,\mathrm{p}}$ on the cycle number n is presented in Fig. 3.4.21. The slope of this plot is -0.399. Taking into account that $\xi_{\mathrm{R}} = -20$, the estimation of $k_{\mathrm{c}_1,\mathrm{CV}}$ is,

$$k_{\mathrm{c}_1,\mathrm{CV}} = -\frac{0.399}{2\xi_{\mathrm{R}}} = 0.0099$$

which is a good estimation of the kinetic constant.

Bibliography

[1] José M. Rodríguez M. A convolution algorithm for linear-sweep voltammetric data at unequaly spaced times. *Comput. Chem.*, 15(3):235–236, 1991.

[2] J.-M. Savéant. *Elements of Molecular and Biomolecular Electrochemistry*. Wiley-Interscience, New Jersey, 2006.

[3] C. Léger, A. K. Jones, S. P. J. Albracht, and F. A. Armstrong. Effect of a dispersion of interfacial electron transfer rates on steady state catalytic electron transport in [NiFe]-hydrogenase and other enzymes. *J. Phys. Chem. B*, 106(50):13058–13063, 2002.

[4] M. Robinson, K. Ounnunkad, J. Zhang, D. Gavaghan, and A. M. Bond. Models and their limitations in the voltammmetric parameterization of the six-electron surface-confined reduction of $[PMo_{12}O_{40}]_3$- at glassy carbon and boron-doped diamond electrodes. *ChemElectroChem*, 6(21):5499–5510, 2019.

[5] M. A. Rahman, S.-X. Guo, M. Laurans, G. Izzet, A. Proust, A. M. Bond, and J. Zhang. Thermodynamics, electrode kinetics, and mechanistic nuances associated with the voltammetric reduction of dissolved $[n\text{-}Bu_4N]_4[PW_{11}O_{39}$ $\{Sn(C_6H_4)C{\equiv}C(C_6H_4)(N_3C_4H_{10})\}]$ and a surface-confined diazonium derivative. *ACS Appl. Energy Mater.*, 3(4):3991–4006, 2020.

[6] G. P. Morris, R. E. Baker, K. Gillow, J. J. Davis, D. J. Gavaghan, and A. M. Bond. Theoretical analysis of the relative significance of thermodynamic and kinetic dispersion in the dc and ac voltammetry of surface-confined molecules. *Langmuir*, 31(17):4996–5004, 2015.

[7] G. P. Stevenson, R. E. Baker, G. F. Kennedy, A. M. Bond, D. J. Gavaghan, and K. Gillow. Access to enhanced differences in Marcus–Hush and Butler–Volmer electron transfer theories by systematic analysis of higher order ac harmonics. *PCCP*, 15(6):2210–2221, 2013.

[8] S.-X. Guo, A. M. Bond, and J. Zhang. Fourier transformed large amplitude alternating current voltammetry: Principles and applications. *Review of Polarography*, 61:21–32, 2015.

4. Description and electrochemical study of lytic polysaccharide monooxygenases (LPMOs)

The scope of this chapter is the study of some of the mechanistic aspects of lytic polysaccharide monooxygenases (LPMOs) with the use of electrochemical methods. In the beginning of the chapter an introduction to the LPMOs and their classification is made, followed by an overview of their mechanism and the methods employed for their characterization.

As a next step the methodologies and the biochemical protocols followed for their expression and purification are presented. Finally, the produced LPMOs are studied electrochemically with direct electron transfer and their interaction with phosphoric acid swollen cellulose (PASC) while immobilized on a modified electrode surface is examined.

4.1 An introduction to LPMOs

4.1.1 Families

Lytic polysaccharide monooxygenases (LPMOs) are copper-dependent enzymes that cleave polysaccharides through an oxidative mechanism. They are major contributors to the recycling of carbon in nature and are currently used in the biorefinery industry and are commonly used in synergy with cellulases to enhance biomass deconstruction [1]. LPMOs are classified as Auxiliary Activities (AAs) in the Carbohydrate Active enZyme database (CAZy). They are divided into seven families (AA9 – 11 and AA13 – 16), based on their sequence similarities. Most of the LPMOs studied thoroughly belong to the AA9 and AA10 families [2]. In this work the main focus will be on LPMOs belonging to the AA9 family, although information on the other families shall be provided as well.

AA9

Regarding the AA9 LPMOs, their main source are fungi. This family possesses catalytic activity over a wide range of substrates including cellulose, cello-oligosaccharides, glucomannan, mixed-linkage glucan, xylan, xylo-oligosaccharides and xyloglucan. Regarding their regioselectivity, C1-specific, C4-specific and mixed C1-C4 LPMOs have been discovered releasing either products with an additional carboxyl group (lactonic acids) or gemdiols (hydrated form of corresponding 4-ketolaldoses), respectively.. It is the only family to have such a wide range of substrates and regioselectivity until now [2]. The fungi from which LPMOs from the AA9 family have been characterized based on cazy.org include *Aspergillus nidulans*, *Gloeophyllum trabeum*, *Heterobasidion irregulare*, L*entinus similis*, *Neurospora crassa*, *Podospora anserina* , *Thermothelomyces thermophila* and *Trichoderma reesei*.

Of interest in this work, are AA9 LPMOs deriving from the fungus *Thermothelomyces thermophila*, thus we shall pay a little more attention to enzymes originating from this particular fungus for now. One of the first LPMOs that comes from *Thermothelomyces thermophila* was reported by Dimarogona *et al* in 2012 [3] under the name *St*Cel61a[1]. At the time it was not recognised as an LPMO but as a glycoside hydrolase belonging to the GH61 family. Although rather weak hydrolytic activity on specific glucans and xylans was observed, it was noted that it could enhance lignocellulose hydrolysis when added to Celluclast or cellulases. Moreover, the enhancing effect was related to the lignin content of the substrate. This LPMO was later published as *Mt*LPMO9[2] and its synergism was examined with a thermostable processive *Mt*EG5 endoglucanase [4]. The regioselectivity of the enzyme is mixed C1-C4.

Another LPMO from *T. thermophila* belonging to the AA9 family is *Mt*LPMO9A that shows oxidative cleavage of xylan and cellulose with mixed C1-C4 regioselectivity [5]. *Mt*LPMO9B and *Mt*LPMO9C were expressed homologously in *Thermothelomyces thermophila* and were tested on regenerated amorphous cellulose (RAC), both in presence and absence of ascorbic acid and the and the products were analysed with HPAEC and MALDI-TOF MS. [6]. *Mt*LPMO9B gave only C1-oxidized gluco-oligosaccharides while *Mt*LPMO9C only C4-oxidized gluco-oligosaccharides Besides non-oxidized gluco-oligosaccharides. *Mt*LPMO9D was found to oxidize cellulose at the C1 position [7],*Mt*LPMO9E produces C4-oxidised cello-oligosaccharides , *Mt*LPMO9I is C1-specific [8] and *Mt*LPMO9J oxidizes at the C4 position and shows activity against cellulose, soluble cello- oligosaccharides and xyloglucan [9].

AA10

Regarding the members of the AA10 class, they originate from bacteria. Their activity include cellulose and chitin as substrates, while regarding their regioselectivity C1-specific and mixed C1-C4 AA10 LPMOs have been found [2]. Before identified as members of the AA10 family, they were generally known as chitin binding proteins (CBPs) and as carbohydrate-binding modules belonging to family CBM33.

[1] *Thermothelomyces thermophila* was known as *Sporotrichum thermophile* at the time.
[2] *Thermothelomyces thermophila* was known as *Myceliophthora thermophila* at the time

AA11

The AA11 LPMOs originate from fungi, are active on chitin and C1-specific[2]. In this category, only one LPMO has been fully characterized from *Aspergillus oryzae* [10]. It was expressed in *E. coli*. Its products were characterized with MALDI-TOF analysis showing chitinolytic activity with no activity on other substrates such as mannans, cellulose and starch.

AA13

The AA13 family LPMOs are produced fungi and they comprise a unique group of enzymes that are active on starch. They are C1-specific LPMOs[2]. 4 LPMOs of this family have been characterised up to now, one from *Neurospora crassa* [11], one from *Aspergillus nidulans* [12], one from *Aspergillus terreus* [13] and one from *Aspergillus oryzae* [14]. The LPMO from *Neurospora crassa* was shown to have activity on both amylose and amylopectin oxidizing the C1 position [11] while the one originating from *Aspergillus nidulans* was shown to have activity on n a recalcitrant 'retrograded' starch, predominantly releasing aldonic acid maltooligosaccharides [12].

AA14

AA14 LPMOs originate from fungi. They are active on xylan and have been found to be C1-specific [2]. LPMOs from this family were first expressed and characterized biochemically by Couturier *et al* in 2018 [15]. The first characterized members of this family originate from the white-rot basidiomycete fungus *Pycnoporus coccineus*, *Pc*AA14A and *Pc*AA14B, and they were heterologously expressed and produced in in *Pichia pastoris*. When examining their activity a wide range of polysaccharides including cellulose and xylans in the presence of ascorbic acid were tested, giving no activity. An interesting characteristic of this LPMO family is that they do not harbor any CBM module, indicating that they do not require specific binding to the flat crystalline cellulose surface to act. Initial findings suggest that AA14 can act upon xylan only when the latter is attached to crystalline cellulose rather than alone.

AA15

The AA15 LPMO family can be found in eykariota and viruses. These LPMOs are active on cellulose and chitin and have been found to be C1-specific [2]. 2 LPMOs of this family have been characterized up to now both from the insect *Thermobia domestica* [16]. *Td*AA15A was cloned andexpressed in *Escherichia coli* and its activity was assayed n microcrystalline cellulose (AVICEL® PH-101) and β-chitin (squid pen chitin) indicating a predominant C1-oxidation pattern and generation of C1-aldonic acids onboth substrates. It is worth noting that in this work different electron donors were explored including ascorbic acid, hydroquinone, gallic acid, pyrogallol, cystein, quinic acid, cysteine and coumaric acid and the maximum yield regarding the product formation was given by gallic acid and not ascorbic acid. In fact, ascorbic acid gave the worst yield out of the donors tested. *Td*AA15B was also produced and purified and what

was revelaed after analysis with MALDI-TOF MS was gallic acid-dependent formation of C1-oxidation products from both highly crystalline and partially amorphous chitin.

AA16

AA16 is the LPMO family which most recently discovered. This cluster of LPMOs shows similar biochemical characteristics to those of C1-acting enzymes of AA9 family, however their classification in a different family was based on bioinformatic analysis. These enzymes originate from fungi and are active on cellulose. They are C1-specific [2]. The first LPMO of this family was encountered by Filiatrault-Chastel *et al* [17]. It originated from the fungus *Aspergillus aculeatus* (AaAA16) and was produced to high level in *Pichia pastoris*. Its molecular weight is about 38 kDa with activity detected on cellohexaose and cellulosic substrates. Using HPAEC-PAD the release of a majority of non-oxidized products (DP2–DP5), and small peaks eluting at the same retention time as C1-oxidized products (DP2ox–DP4ox) was monitored.

4.1.2 Structure

Despite the fact that generally the different LPMO families show many differences in their sequences, their structure follows a general pattern. The core is built up by two β-sandwiches made up of anti-parallel strands making the LPMO structure resemble both fibronectin type III and immunoglobulin domains. On the aforementioned strands loops of various lengths and a varying number of short helices are connected. These loops have an effect on the substrate-recognizing surfaces of the LPMOs.

The most common characteristic regarding the LPMOs is their active center, containing a solvent-exposed type-2 copper center. This copper ion is coordinated by three nitrogen ligands provided by two fully conserved histidine residues (one of which is the N-terminal residue) that form a T-shaped histidine brace. When it comes to fungal LPMOS , the N-terminal histidine is N-methylated. Additionally, two water molecules in a fourth equatorial position and in the distal axial position, and a tyrosine/phenylalanine in the proximal axial position act as ligands for the copper ion.

Regarding the part of the LPMOs that differ from family to family, or even among members of the same family, this is the second coordination sphere. It is made up of residues close to the copper but not directly interacting with it. However, these residues may help shaping the active site and in coordinating the co-substrate.

The substrate-binding surface area of different LPMOs also varies in terms of the nature of amino acids of the flat surface binding areaEnzymes belonging to the AA9 family, generally have flat substrate-binding surfaces with solvent- exposed aromatic residues, while the ones belonging to the AA10 family have largely hydrophilic substrate-interacting surfaces with only one surface-exposed aromatic residue oriented in such a way that it can participate in stacking interactions [18].

4.1.3 Regioselectivity

The LPMOs in general can have different regioselectivity. More specifically, their action can cleave polyssacchirides leading to the oxidation of the C1 position generating a lactone, which is hydrated to a reducing-end aldonic acid or to the oxidation of the C4 position leading to non-reducing-end 4-ketoaldose formation, which will spontaneously hydrate to gemdiols in aqueous conditions. There are LPMOs which can cause the oxidation of both the C1 and C4 position leading to double oxidized products (Fig. 4.1.1) [19].

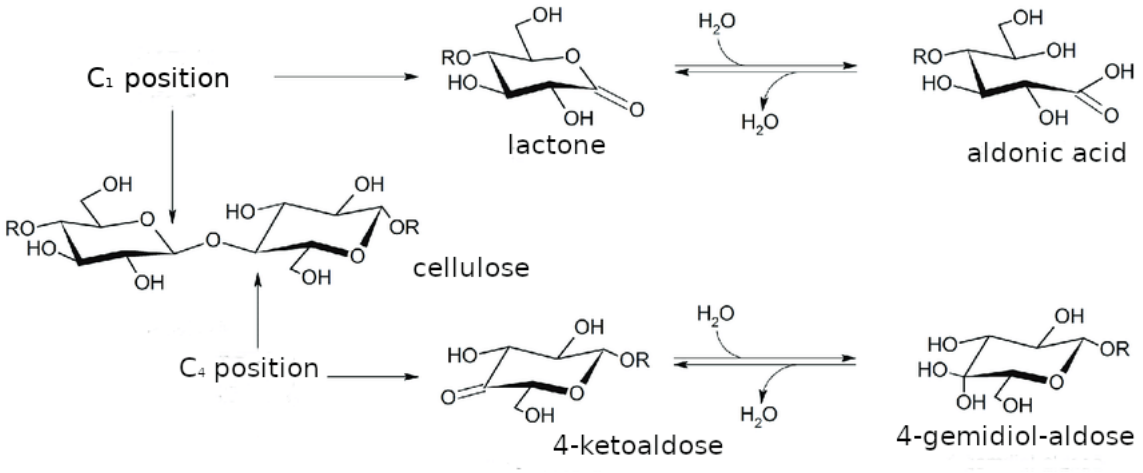

Figure 4.1.1: C1/C4-regioselectivity of LPMOs

4.1.4 Mechanisms

One of the main mysteries that remain unresolved regarding the LPMOs is their mechanism of action. When initially discovered they were thought to use O_2 as their co-substrate in order to cleave the bonds of the substrates they interact with. Recently, evidence has arisen claiming that their actual co-substrate is H_2O_2 and not O_2. In this section, an overview of the proposed mechanisms shall be presented.

We shall begin with the scenarios that assume that the co-substrate is O_2, under which the LPMOs were initially classified as monoxygenases. Still, in this case, variations exist, regarding the intermediats as well as the question wether O_2 binds before or after the substrate to the enzyme's active surface [20, 21].

Oxygen binds to Cu before the substrate

As a first step the enzyme is reduced from its oxidized state LPMO-Cu(II) to its reduced form LPMO-Cu(I) by an external electron donor.

$$\text{LPMO} - \text{Cu(II)} + e^- \rightleftharpoons \text{LPMO} - \text{Cu(I)} \tag{4.1.1}$$

Then O_2 binds to the reduced form LPMO-Cu(I) forming LPMO-Cu(II)-$OO^{\bullet -}$

$$\text{LPMO} - \text{Cu(I)} + \text{O}_2 \rightleftharpoons \text{LPMO} - \text{Cu(II)} - \text{OO}^{\bullet -} \tag{4.1.2}$$

Then the substrate RH binds to the LPMO-Cu(II)-$OO^{\bullet -}$ forming a complex LPMO-Cu(II)-$OO^{\bullet -}$-RH

$$\text{LPMO} - \text{Cu(II)} - \text{OO}^{\bullet -} + \text{RH} \rightleftharpoons \text{LPMO} - \text{Cu(II)} - \text{OO}^{\bullet -} - \text{RH} \tag{4.1.3}$$

Substrate binds to Cu befor O_2

As a first step again the enzyme is reduced from its oxidized state LPMO-Cu(II) to its reduced form LPMO-Cu(I) by an external electrode donor.

$$\text{LPMO} - \text{Cu(II)} + \text{e}^- \rightleftharpoons \text{LPMO} - \text{Cu(I)} \tag{4.1.4}$$

Then the substrate RH binds to the reduced form LPMO-Cu(I), forming a complex LPMO-Cu(I)-RH

$$\text{LPMO} - \text{Cu(I)} + \text{RH} \rightleftharpoons \text{LPMO} - \text{Cu(I)} - \text{RH} \tag{4.1.5}$$

After that, O_2 binds again to the LPMO-Cu(I)-RH complex forming LPMO-Cu(II)-$OO^{\bullet -}$-RH

$$\text{LPMO} - \text{Cu(I)} - \text{RH} + \text{O}_2 \rightleftharpoons \text{LPMO} - \text{Cu(II)} - \text{OO}^{\bullet -} - \text{RH} \tag{4.1.6}$$

After the binding

Regardless of what binds first, the result seems to be the same with the formation of the LPMO-Cu(II)-$OO^{\bullet -}$-RH superoxide intermediate. For the next step, again various scenarios have been proposed with the most plausible being the following one.

After the binding of the O_2 and the substrate on the active center, the LPMO then performs its catalytic cycle via two proton-coupled electron-transfer steps, leading to elimination of a water molecule and formation of an LPMO-Cu(II)-$O^{\bullet -}$-RH intermediate. The latter abstracts a H atom from the atom of the saccharide with a rapid, water-assisted hydroxyl rebound to the substrate, leading to formation of the product R-OH and regenerating the enzyme active state LPMO-Cu(I)

$$\text{LPMO} - \text{Cu(II)} - \text{OO}^{\bullet -} - \text{RH} + \text{H}^+ \rightleftharpoons \text{LPMO} - \text{Cu(II)} - \text{OOH}^- - \text{RH} \tag{4.1.7}$$

$$\text{LPMO} - \text{Cu(II)} - \text{OOH}^- - \text{RH} + \text{H}^+ \rightleftharpoons \text{LPMO} - \text{Cu(II)} - \text{O}^{\bullet -} - \text{RH} + \text{H}_2\text{O} \tag{4.1.8}$$

$$\text{LPMO} - \text{Cu(II)} - \text{O}^{\bullet -} - \text{RH} \rightleftharpoons \text{LPMO} - \text{Cu(I)} + \text{RH} \tag{4.1.9}$$

4.1.5 Electron Donors

Out of all the topics that remain unresolved regarding the mechanism of action of LPMOs, the one that all the groups working with LPMOs have agreed upon is that in order for the catalytic cycle to initiate, electrons shall be provided to the enzymes be an external donor. Now, regarding the nature of donors, several works have attempted to deal with the issue.

One of the early electron donors reported was the enzyme cellobiose dehydrogenase (CDH) [22, 23, 24]. One other commonly used molecule used as an electron donor and has been proven to be rather effective is ascorbic acid [4, 9].

Other enzymes that have been studied and were proven to be quite efficient include single-domain flavoenzymes and more specifically aryl-alcohol quinone oxidoreductases (AAQOs) from *Pycnoporus cinnabarinus* and an aryl-alcohol oxidase (AAO) from *Ustilago maydis* [25].

In another work by Westereng *et al*, low molecular weight lingin (LMWL) and high molecular weight lingin (HMWL) fragments were tested as electron donors. Oxidized products from *Tt*LPMO9E and *Pc*LPMO9D were found in samples containing both LMWL and HMWL, while in samples containing only one of the fragments, no activity was detected. Thus, it was proposed that a mechanism where water soluble compounds from LMWL shuttle electrons from HMWL to the active site of the LPMOS stands [26].

4.1.6 Characterization Methods

In order to assay the activity of LPMOs different approaches have been made over the years, as carbohydrates are rather difficult to analyze with the use of common chromatography or other usual detection methods since they are very polar molecules exhibiting similar structure characteristics and lack a right chromophore.[3]

Chromatographic approaches

While the carbohydrates remain unchanged in acidic and neutral pH values, when moving to very high pH regions (over 13) they become oxyanions [27]. A way to detect oxyanions is anion exchange chromatography using NaOH eluents.[4] Under alkaline conditions, native, C1, C4 and C1/C4 oxidized sugars are eluted in different elution times, making it possible to detect them.

The detection and quantification of carbohydrates in such a system is done with pulse amperometric detection (PAD) [27, 28, 29]. The working electrode used for the detection is a gold one. While it was known well before its application that carbonhydrates could be detected on gold electrodes at highly alkaline solutions, the fouling of the electrode at very high pH values by the oxidized products was an obstable. Thus a succession of different potentials were implemented in order to clean and restore the

[3] A region in the molecule where the energy difference between two separate molecular orbitals falls within the range of the visible spectrum.

[4] Glucose for example has a pK_a at a value of 12.28 and in a pH of more than 12, it shall be in equilibrium with its oxyanion [28].

electrode after the detection. the most common potential program used is that of a 4 potential wave form. Even a two potential waveform has been proposed, giving identical results [29].

The above system is one of the most commonly used systems for the detection of products from the action of LPMOs and its acronym is HPAEC-PAD standing for high performance anion exchange chromatography with pulsed amperomentric detection [27, 28]. The stationary phase in the chromatography column used in HPAEC-PAD is composed of essentially non-porous (microporous) poly-styrene-divinylbenzene beads chemically treated to create a cation-exchanger. These substrate beads are then treated (agglomerated) with smaller poly-styrene-divinylbenzene beads (<1 μm, the latex) that had quaternary amine groups (a strong anion-exchanger) on their surface. For the mobile phase when it comes to the separation of carbonhydrates only two types of mobile phases are required: sodium (or potassium) hydroxide and sodium acetate [28].

Westereng *et al* in 2013 made a comparison fo different chromatographic appo-raches for the identification and quantification of the products generated by the action of LPMOs [30]. HPAEC-PAD is reported to offer speed in the analysis, sensitivity and good separation of the products. Porous graphitized carbon liquid chromatography (PGC-LC) has the advantage of separating lactones from aldonic acids but as a draw-back, its strong retention of longer oligosaccharides is listed. This leads to limiting the study of oligosaccharides of intermediate length and could possibly lead to shortening the life time of the column. Regarding hydrophilic interaction liquid chromatography (HILIC), it is reported to offer shorter times and better separation that PGC-LC, but it is more sensitive to the changes in the composition of the solvent and its peaks are poor compared to HPAEC-PAD and PGC-LC.

In 2006 the same group accepting the dominance of HPAEC-PAD in the analysis of products derived from LPMOs, proposed PGC hyphenated with either charges aerosol detector (CAD) or mass spectrometry (MS) in order to overcome the instabilities of the C4 products of LPMOs in alkaline solution for the mobile phase of HPAEC-PAD [31].

Other Approaches

Other techniques for the detection of LPMO products are matrix assisted laser desorp-tion/ionization of flight mass spectromet (MALDI-TOF-MS) [5, 6] and Electrospray ionization mass spectrometry (ESI-MS) [31].

Moreover, three spectroscopic techniques have been proposed for monitoring the ac-tivity of LPMOs. Although two of them are based on their action as peroxygenases and not have a direct correlation to their oxidized products. The first of the spectroscopic approaches conerns the C_1 active LPMOs. The LPMO treated surface of the oxidized polyssachiride is first percipitated by centrifugation and the supenatant is disposed. After washing it with HEPES[5], a Ni^{2+} solution is added which is adsorbed on the ends of the treated polyssacchiride. Using pyrocatethol violet (PV) spectroscopically the change in the concentration of Ni^{2+} is estimated. This change is then correlated to the carboxyl groups of the substrate [32].

[5](4-(2-hydroxyethyl)-1-piperazineethanesulfonic acid) is a zwitterionic sulfonic acid buffering agent.

Regarding the other methods 2,6-dimethoxyphenol (2,6-DMP) and hydrocoerulignone were tested in the presence of H_2O_2 giving apparent Michaelis Menten constants for H_2O_2 in the range of a few μM [33, 34].

4.2 Expression of LPMOs

Starting this section, the biochemical methodologies regarding the enzyme production and purification shall be introduced. All LPMOs introduced in this work are a result of recombinant expression in *Pichia pastoris*. The two expression vectors used are pPICZαC and pGAPZαC.[6]

Three LPMOs can be found in this work. *Mt*LPMO9H (GenBank:XP_003661787.1)[7], *Fo*LPMO9 and *Mt*LPMO9G (GenBank: AEO54509.1). Of these *Fo*LPMO (GenBank: XP_018247071.1) and *Mt*LPMO9H are expressed in both pPICZαC and pGAPZαC, while *Mt*LPMO9G in pGAPZαC only. *Mt*LPMO9H [3], *Fo*LPMO9A expressed in pPICZαC have already be expressed in the laboratory of Biotechnology of the School of Chemical Engineering of the National Technical University of Athens, while *Mt*LPMO9H in pGAPZαC has been produced in LuleåTekniska Universitet, Sweden. Thus, the enzymes that are produced for the first time in this work, are *Fo*LPMO9 and *Mt*LPMO9G in pGAPZαC. Although all steps of production and purification will be introduced, according to the information given above, each enzyme underwent the respective stages.

In Table 4.2, one can find which enzyme is expressed in which vector is this work. The genes of the LPMOs that can be found in this work are reported in Appendix A.

Table 4.1: List of LPMO enzymes that were produced in this work together with the respective vector.

Enzyme	pPICZαC	pGAPZαC
*Mt*LPMO9H	✓	✓
*Fo*LPMO9	✓	✓
*Mt*LPMO9G	✗	✓

In Table 4.2, the theoretical molecular weights of the LPMOs can be found as estimated using ExPasy based on their aminoacid sequence. The actual molecular weight of the enzymes is also presented. The molecular weight for *Mt*LPMO9H is already known [4], the SDS-PAGE results[8] used for the estimation of the molecular weight of *Fo*LPMO9 are presented in Appendix B, while the biochemical characterization of *Mt*LPMO9G is not part of this work, thus, the SDS-PAGE results for this enzyme are not presented.

*Mt*LPMO9H and *Fo*LPMO9 are categorized as a C_1-C_4 LPMOs while *Mt*LPMO9G is a C_1 LPMO, based on their regioselectivity.

[6]It is actually a modified version of pGAPZαC, but this matter will be referred to later in this work.

[7]Previously reported as *St*Cel61a and *Mt*LPMO9.

[8]The process for SDS-PAGE is described later.

Table 4.2: Theoretical *vs* determined molecular weight for each LPMO.

Enzyme	Theoretical MW / kDa	Determined MW / kDa
*Mt*LPMO9H	34.94	65
*Fo*LPMO9	31.53	55
*Mt*LPMO9G	25.28	29

4.2.1 Expression Vectors

An expression vector is usually a plasmid or virus designed for gene expression in cells. The vector is used to introduce a specific gene into a target cell, and can commandeer the cell's mechanism for protein synthesis to produce the protein encoded by the gene. Expression vectors are the basic tools in biotechnology for the production of proteins.

The vector is engineered to contain regulatory sequences that act as enhancer and promoter regions and lead to efficient transcription of the gene carried on the expression vector. In this work the two vectors that shall be used are pPICZαC and pGAPZαC.

4.2.2 pPICZαC Vector

pPICZαC is a 3.3 kb expression vector which is used in order to express recombinant proteins in *Pichia pastoris*. They are expressed as a fusion to the C terminal peptide containing the *C-myc* epitope [9] and a polyhistidine (6-His) tag[10]. It allows methanol inducible expression of the gene of interest in *Pichia pastoris* strains including X33, GS115, SMD1168H, and KM71H. It contains the following elements

- Multiple cloning site[11]
- 5' fragment containing the AOX1 promoter[12] for regulated, methanol-induced expression of the gene of interest
- C-terminal peptide containing the *c-myc* epitope and a polyhistidine (6xHis) tag for detection and purification of a recombinant fusion protein
- Zeocin^{TM}[13] resistance gene

In Fig. 4.2.1 the map of the vector is presented, indicating its main features.

[9] *C-myc* epitope is a sequence of amino acids (Glu-Gln-Lys-Leu-Ile-Ser-Glu-Glu-Asp-Leu) that permits detection of your recombinant fusion protein with the Anti-myc Antibody or Anti-myc-HRP Antibody.

[10] A polyhistidine (6-His) tag permits purification of a recombinant fusion protein on metal-chelating resin.

[11] The multiple cloning site allows insertion of the gene into the expression vector.

[12] A 942 bp fragment containing the *AOX1 promoter* that allows methanol-inducible, high-level expression of the gene of interest in *Pichia*.

[13] Zeocin^{TM} is a member of the bleomycin/phleomycin family of antibiotics isolated from Streptomyces. Antibiotics in this family are broad spectrum antibiotics that act as strong anti-bacterial and anti-tumor drugs. They show strong toxicity against bacteria, fungi (including yeast), plants, and mammalian cells [35, 36].

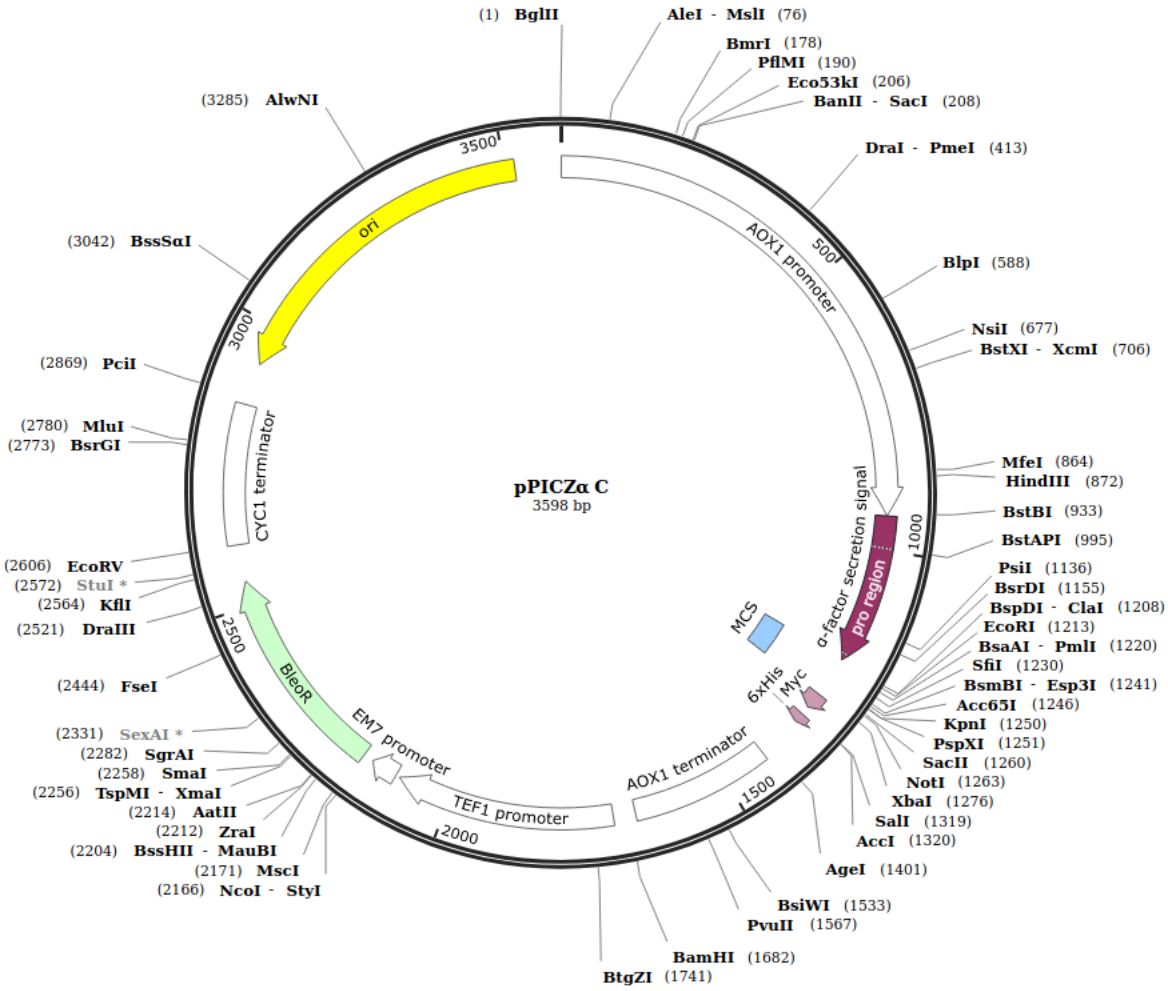

Figure 4.2.1: Map of pPICZaC expression vector

4.2.3 Modified pGAPZaC Vector

The glyceraldehyde-3-phosphate dehydrogenase (GAPDH) enzyme is constitutively expressed at high levels in many organisms, including *Pichia pastoris*. The promoter of the gene (GAP) encoding the GAPDH protein has recently been characterized and shown to express recombinant proteins to high levels in *Pichia pastoris*, depending on the carbon source used [37]. The level of expression seen with the GAP promoter (pGAP) can be slightly higher than that obtained with the AOX1 promoter. The pGAPZaC (3.1 kb) vector which uses the GAP promoter to constitutively express recombinant proteins in *Pichia pastoris*. Proteins can be expressed as fusions to a C-terminal peptide containing the myc epitope for detection and a polyhistidine tag for purification on metal-chelating resin. Selection of these vectors is based on the dominant selectable marker, Zeocin^{TM}, which is bifunctional in both *P. pastoris* and *E. coli*.

The vector is slightly modified in this work as the a-factor area has been ommited, so at the final sequence that is expressed one can find only the native signal peptide. In LPMOs the histidine found in position 1 (His1) is very important for their action, as it is one of the aminoacids taking part in the confortation of the active center of the enzyme, thus, keeping the native signal peptide in tact and cutting of the a factor correctly is of utmost importance of the enzyme's activity. It is also noted in the literature that when expressing LPMOs in Pichia pastoris the α factor is not cut correctly by the protease Ste B [38, 39].

Its map is presented in Fig. 4.2.2

It contains the following elements

- Multiple cloning site.
- GAP promoter[14]
- C-terminal peptide containing the *c-myc* epitope and a polyhistidine (6xHis) tag for detection and purification of a recombinant fusion protein
- Three reading frames to facilitate in-frame cloning with the C-terminal peptide
- Zeocin^{TM} resistance gene

4.2.4 Expression of synthetic Gene

Preparation

Now moving on to the expression of the synthetic genes for pGAPZaC[15] 4 ng of the gene containing the LPMO sequence with the native signal peptides[16] is received. Each

[14]The GAP promoter allows constitutive, high-level expression in Pichia in the presence of glucose [37].

[15]This procedure does not concern the enzymes expressed in pPICZa as they were only produced for the shake of this work.

[16]A signal peptide (sometimes referred to as signal sequence, targeting signal, localization signal, localization sequence, transit peptide, leader sequence or leader peptide) is a short peptide (usually 16-30 amino acids long) present at the N-terminus of the majority of newly synthesized proteins that are destined toward the secretory pathway.

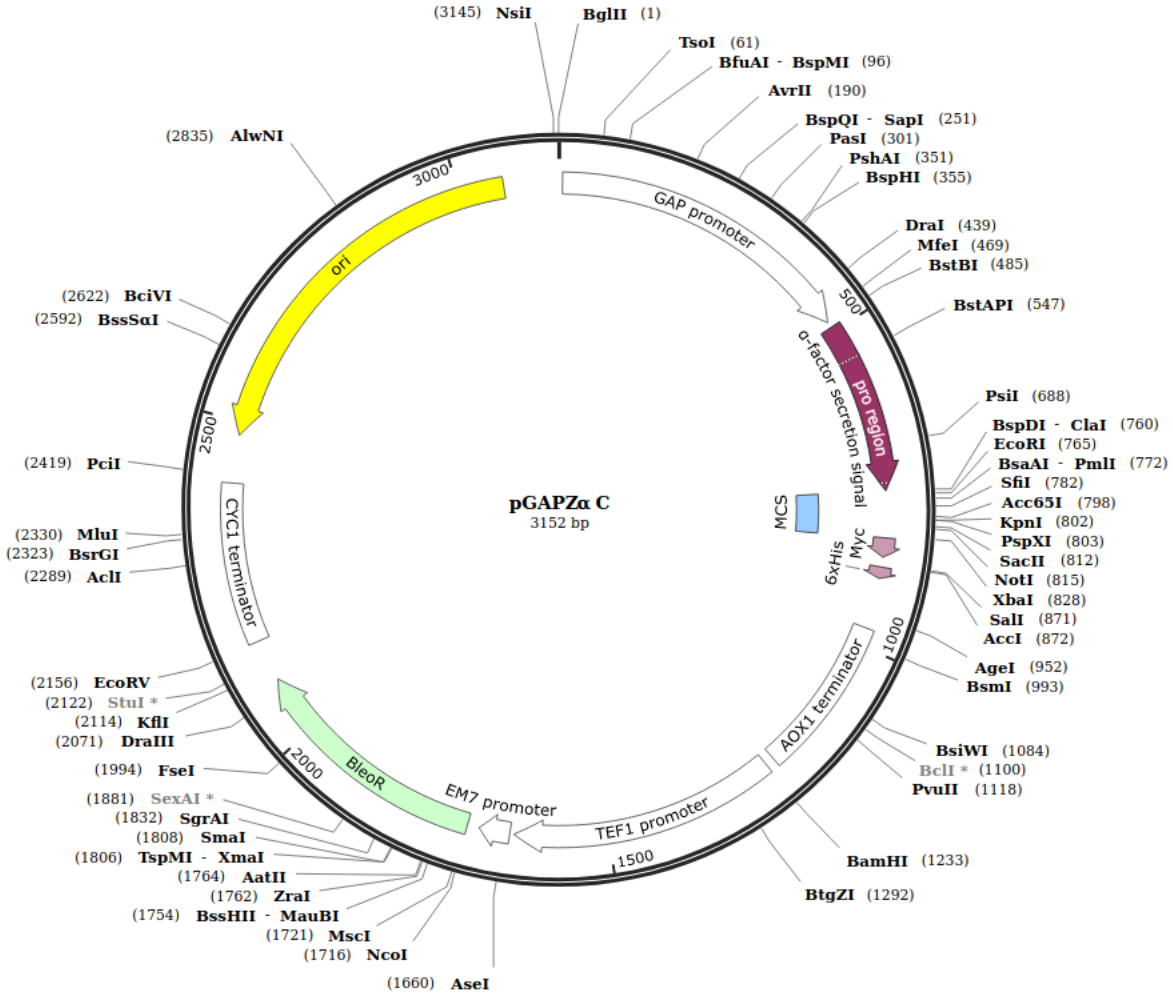

Figure 4.2.2: Map of pGAPZaC expression vector

sequence have the recognition areas of the restriction enzymes *BSTB1* and *Xba1* at its ends, so it can be cut off at these points easily with these commercial enzymes.

So after the recombinant gene is received, 500 μL of ultra pure sterilized water are added in the center of the plastic carrier containing the gene, and it is left to hydrate for 1 - 2 minutes. The hydrated gene is pipetted 5-6 times gently and then the plasmid is kept in the freezer at -20°C until it is further used.

The hydrated cells shall then be multiplied in *E. coli* top 10 cells, in order to get the plasmid in a larger quantity. The multiplication happens by transforming competent *E. coli* cells. These *E. coli* cells have been pretreated to be preamble to macromolecules.

Preparation of *E. coli* TOP10 competent cells

The prepared *E. coli* TOP10 cells are rendered susceptible to transformation chemically, based on the attractive interactions between the bacteria and the recombinant DNA. The cell membranes are positively charged when exposed to a $CaCl_2$ solution and then they are afterwards attracted to the negatively charged phosphate groups of the plasmid, making it thus easier for the plasmid to enter the bacterial cell. The transformed cells are then isolated in nutrition medium containing the antibiotic.

In order for the aforementioned procedure to be completed, the following steps shall be followed.

The *E. coli* TOP10 cells are firstly cultivated in a solid nutricient medium with antibiotic. The medium in this case is Luria-Bertani broth (LB) and it includes

- 10 g/L tryptone
- 5 g/L yeast
- 10 g/L yeast (In case of low salinity LB (LS-LB) the concentration is 5 g/L)
- The pH is adjsuted to 7.4 with the addition of 0.1 M NaOH[17]
- 25 μL/100 mL Zeocin^{TM}

A colony of *E. coli* TOP10 cells is inoculated in 5 mL of liquid LB medium containing streptomycin and are then incubated at 37°C while stirred at 180 rpm for about 16 hrs. This is considered to be a preculture. After the incubation, 1 mL of the preculture is used as an inoculation for 100 mL of LB, a quantity which is then incubated until the OD reaches a value between 0.4 and 0.8 ($\simeq$2 hrs).

The flask containing the culture is then transfered in ice for about 30 min. The cells are then centrifuged (1500 x g) at 4 °C for 5 min and the cells are resuspended in 12 mL of sterilized cold 0.1 M $MgCl_2$ solution.

After that the cells are centrifuged again under the same conditions and are then resuspended in 4 mL of 1 M $CaCl_2$ cold sterilized solution.

The resuspended cells are then stored at 4 °C for 16 hrs increasing their transformation yield. After the addition of 1.9 mL 50% w/w glycerol solution, aliquots of 0.1 mL are made and they are then stored in sterilized plastic centrifuge tubes of 2 mL.

[17]Higher pH and high salts concentration render Zeocin^{TM} inactive, thus the pH is adjusted around a value of 7.4.

Transformation of competent cells with heat shock

The resulting competent cells that have been pretreated with $MgCl_2$ in the previous stage are used for the transformation of the recombinant plasmids of interest.

One aliquot of *E. coli* TOP10 cells is taken from the fridge out of the -80 °C where they are stored and they are left in ice in order to unfreeze.

- 5 μL of the plasmid are pipetted gently with circular movements in the Top10 cell aliquot.
- The new mix is left to rest fro 30 min in the ice.
- Then the mix is heated for 1 min 20 s at 42 °C and it is then put back in the ice.
- 0.2 mL of LB liquid is then added to the mix and it is incubated at 30 °C for 1 hr. This is what will be referred to as the transformation mix from now on.
- Then 100-200 μL of the transformation mix are added in Petri Dishes containing low salt LB medium. In this case the medium also contains 1.5 % w/v agar so as to solidify and 25 mg/100 mL Zeocin^{TM}.
- The Petri dishes are left overnight at 37 °C for about 16 hrs.
- Then 5-7 of the resulting colonies are selected and are added to 5 mL of LS-LB liquid medium containing Zeocin^{TM} and are incubated for 16 hrs at 37 °C under stirring at 200 rpm -One colony per 5 mL of LS-LB.

Plasmid Recovery and Clone Analysis

After the incubation, with the use of the Nucleospin Plasma Kit, the high copy plasmid DNA is isolated from *E. coli*.

- The culture media from *E. coli* is centrifuged and the supernatant is disposed.
- Then the cells are resuspended by adding 250 μL of the addition of A1 buffer which contains chelating factors (EDTA), thus entrapping the ions and the RNAses to ensure that RNA contamination is avoided.
- Then 250 μL of A2 buffer are added. A2 is the lysis buffer, which contains the surfactants SDS causing holes in the cell membranes and unfolds the DNA helixes.
- The resulting mixture is then mixed by gently inverting the tube containing 6-8 times.[18] The mix is the incubated at room temperature for 5 min.
- Then 300 μL of A3 are added and again the mixture is gently inverted upside down 8 to 10 times. A3 is the neutralization buffer that drops the pH leading the DNA to fold back again. The plasmidic DNA returns back to normal while the genomic does not.

[18] Intense mixing could lead to the shearing of the genomic DNA.

- The mixture is the centrifuged for 5 min. The supernatant should be clear at this point.
- Then special tubes with a separation membrane are used. The supernatant is decanted in this tube. It is centrifuged for 1 min and the flow through is thrown away.
- 500 μL of washing solution are then added and centrifuged for 2 min and the flow through is thrown away.
- 400 μL of A4 buffer are then added and centrifuged for 1 min. A4 contains ethanol, so that macromolecules, contaminants and metabolites are washed away. Then it is centrifuged again for 1 min.
- Then the flow through is once again thrown away and then what remains is centrifuged again for 2 min.
- Finally the flow through is again thrown away and 50 μL of AE buffer are added and then it is centrifuged once again for 1 min. The flow through now is what is kept. This buffer's pH is slightly alkalic and entraps plasmidic DNA.

DNA electrophoresis in Agarose Gel

As DNA is uniformly negatively charged, under an electric field applied on an horizontal agarose gel, the DNA moves towards the positive pole of the electrophoresis apparatus, at a speed inversely proportional to its size. The gel density as well as the applied applied voltage are adjusted based on the size of the molecules that shall be separated.[19] Moreover, the shape of the nucleotides has also a role in the applied conditions.[20]

In this case, a 1 % w/v gel shall be used. Thus, 0.5 g of agarose are added in 50 mL of a Tris/Borate/EDTA (TBE) solution. Agarose is dissolved by heating after added in the TBE solution. It is then left at room temperature until it reaches about 60 °C and then a few μL of Midori Green are added.[21]

A stock solution of 10 times concentrated TBE solution (10x TBE) shall include 54 g/L Tris, 27.5 g/L boric acid, 20 mL/L 0.5 EDTA. It's pH is adjusted to a value of 8.

The gel is then left to solidify in the electrophoresis apparatus. 50 mL of TBE are than added in the apparatus and the samples are loaded in the gel.

Plasmid Linerization

Before the transformation of the competent yeast cells, a linearization of the plasmid shall be done.

The plasmid is digested by taking advantage of the unique identification site of the pGAP promoter allowing the insertion of the expression cassette to the genome of *P. pastoris*.

[19] The gel density ranges from 0.7 % w/v for big DNA molecules up to 2 % w/v for small ones.
[20] an uncut plasmid shall run slower a cut one.
[21] DNA/RNA stain for in gel or poststaining.

This way the recombinant plasmid is added to the yeast *P. pastoris*.

The digestion occurs with the use of the restriction enzyme *BlnI* (or *AvrII*). 5 μL of sterilized ultrapure water, together with 5 μL of the restriction enzyme, 10 μL of the commercial enzyme buffer and 80 μL of the plasmid are mixed and are then incubated at 37 °C for 3 hours. After clean up with the appropriate kit, the linearized plasmid is ready to be transformed to *P. pastoris*.

Electroporation Procedure

During the step of electroporation, the conductivity and the preamability of the cell membrane are increased by imposing an electric pulse. This way a substrate can enter the cell membrane. During the pulse, for a few instances, pores occur in the cell membrane (40-120 nm) through which the plasmid can enter the yeast membrane and then get integrated in its DNA.

Preparationg of *Pichia pastoris* Wild type X33 yeast cells are incubated in liquid YPD medium[22] for 20 hrs at 30 °C under stirring at 180 rpm.

In this case, 4 Erlenmeyer flasks of 250 mL shall be needed. 1 g of glucose is added to each flask. Then 200 mL solution including a 1% yeast extract and 2% peptone are prepared.[23] These are sterilized separately at 121 °C for 20 min. Then the solution is added to the glucose, it is distributed equally to the 4 flasks and when room temperature is reached, X33 cells are inoculated in the flasks.[24] The flasks are left to incubate at 30 °C overnight under stirring at 180 rpm.

When this step is over, 10 mL of the preculture medium are inoculated in the main culture. For the main culture 2 1 L flasks are needed. 3 g are put inside the flasks. Now a 600 mL solution including 1% yeast extract and 2% is prepared. They are again sterilized separately and the solution is equally distributed in the two flasks. When they reach room temperature, they are inoculated with the aforementioned 10 mL of the preculture medium and are incubated at 30 °C under stirring at 180 rpm for 3-4 hrs until its O.D. 600 nm reaches a value between 1.3 and 1.4.

When this feat is achieved, a process of 4 rounds of centrifugation follows (1500 × g for 5 min at 4 °C for each round.)

- In the first round about 250 mL of the main culture are centrifuged.
- In the second round, the precipitate is resuspended in 250 mL of ice cold sterilized ultrapure water and the resuspended cells are then centrifuged again.
- In the third round, the precipitate is resuspended in 150 mL of ice cold sterilized ultrapure water and the resuspended cells are then centrifuged again.
- In the fourth round, the precipitate is resuspended in 12 mL of ice cold sterilized 1 M sorbitol solution[25] and the resuspended cells are then centrifuged again.

[22] YPD (Yeast, peptone, dextrose) contains 1 % yeast, 2 % peptone, 2 % glucose.
[23] Ultrapure water (Millipore 18.2 MΩ·cm) is used for the yeast peptone solution
[24] If the temperature is high, the inserted cells shall die and not grow.
[25] The sorbitol is dissolved in ultrapure water in order to make this solution.

- Then, the precipitate is resuspended again in 0.6 mL of ice cold sterilized 1 M sorbitol solution.

Until the transformation procedure begins, the cells are left in the ice.

Electroporation Final Stage

- 80 μL of the final suspension which includes the competent X33 cells are mixed with 30 μL of the linearized DNA
- The mix is then transfered to the electroporation cuvette and is left there at 4 °C for 5 min.
- Then with the electroporation apparatus (Bio-Rad MicroPulser Electroporator (BioRad, Life Science Research)), the pulse is imposed
- Right after that 1 mL of sorbitol is added to the mix which is transferred to a sterile plastic carrier and is incubated at 30 °C for 1-2 hrs.
- Then the mix is distributed to 3-4 Petri Dishes containing YPDS[26] solid medium with Zeocin^{TM} at a concentration of 100 mg/mL and are left to incubate at 30 °C for 3-4 days.

4.2.5 Failed Plate Assays

In order to chose which colony shall be further used to produce and purify the enzymes, a usual practice is to take advantage of established plate assays.

In order to distinguish which clone is the most efficient to chose from the ones that occurred in the YPDS plates. For LPMOs, there is no established plate assay, thus, an effort was made to create one. Two methods were tested, and both failed. Nevertheless, they shall be reported in this work in order to be avoided or modified in the future.[27]

Plate assay with a polysaccharidic substrate

A number of colonies depending on the transformation yield are transferred to Petri dishes with solid nutricient MGY (minimal medium) with 0.5 % PASC. MGY contains glucose that induces the expression of the LPMO.

The MGY constituents are:

- 1.34% Yeast Nitogen Base (YNB) (For 100 mL 3.4 g YNB w/o ammonium sulfate with amino acids + 10g g ammonium sulfate are dissolved or 13.4 g YNB with ammonium sulfate and amino acids)
- 0.005% amino acids (if using YNB without amino acids)

[26] YPDS (Yeast, peptone, dextrose, sorbitol) contains 1 % yeast, 2 % peptone, 2 % glucose and 1 M sorbitol.

[27] Since the plate assays did not work, 8 to 10 colonies were selected, and small cultures were used in order to screen which colony would have a higher enzyme yield.

- 0.5% glucose
- 0.5% PASC (phosphoric-acid swollen cellulose)
- 1.5% agar

After 24 hrs of incubation at 30 °C

- 10 mL of Congo Red[28] 1% w/v solution are poured onto the dishes and they are incubated for 15 min
- The Congo Red solution is disposed and 10 mL of 1M NaCl solution are added for the discoloration
- Incubation for 5 min and the previous step is repeated until visible discolored rings appear around the colonies. These colonies are supposed to be the ones that produced an active form of the enzyme.

The X33 wild type was used as a negative strain.

An alternative version of this assay was conducted by injecting some μL of 1 mM ascorbic acid on each colony letting it dry, before the addition of Congo Red. It is needless to say, that this test did not give any results.

Plate assay with 2,6-dimethoxyphenol (2,6-DMP)

A number of colonies depending on the transformation yield are transferred to Petri dishes with solid nutricient MGY (minimal medium) with 2mM 2.6-DMP (DMP is added added after the sterilization of the other constituents). MGY containes glucose that induces the expression of the LPMO.

After 24 hrs of incubation at 30 °C in the absence of light, for the detection of peroxidase activity, a few μL of 1 mM H_2O_2. The plates are incubated for some time in the absence of light at 30 °C, until a difference in the color in the are around the colony appears.

4.2.6 Enzyme Production

In this section, the methods for the enzyme production for both vectors shall be analyzed. The procedure is divided in the Agar stock cultures, where the colonies grow in solid YPD medium - this stage is the same for both vectors - while the stages of the preculture and the main culture differ.

We shall start with the Agar stock cultures which is common for both expression systems, and then the section will be separated in two parts, each corresponding to one vector system.

[28] Congo Red interacts with polysaccharides containing contiguous β-(1$\longrightarrow$4)-linked D-gluco or D-xylopyranosyl units yielding a vivid red color, leaving unstained the areas that contain cleaved oligosaccharides released by the activity of cellulases and hemicellulases. Handling of Congo Red must be conducted with care as Congo Red is carcinogenic due to the presence of aromatic amine groups. Details of the supplier on the material safety data sheet should be taken into consideration prior to any experiment.

Agar stock cultures

In order to initiate the process a Agar stock cultures is needed. For the Agar stock cultures the medium needed is YPD consisting of 2% agar, 1% yeast, 2% peptone, 2% glucose (dextrose) and 100 mg/mL Zeocin^{TM}.

For two Petri dishes of Agar stock cultures, 50 mL of YPD medium are needed.In one sterilization bottle 50 mL of deionized water 1 g of agar, 0.5 g of yeast extract and 1 g of peptone are dissolved. Then in a different sterilization bottle, 1 g of of glucose is added and both carriers are put in an autoclave for 20 min at 121 °C. [29]

After the sterilization is over, the mix with the agar, the yeast extract and the peptone is added to the glucose and is stirred until the glucose is dissolved. When the temperature of the mix goes down, 50 μL of Zeocin^{TM} are added to the mixture and the final mixture is equally distributed to the 2 petri dishes and they are left to solidify. After the medium is solidified, it is inoculated with the desired carrier which will grow.

The petri dishes are left for two days at 30°C under ventilation.

All of the above processes are carried out under sterilized conditions.

pGAPZαC as a *Pichia pastoris* expression vector of a recombinant protein

Preculture Medium

The growth medium in both the preculture and the culture is YPD (1% yeast, 2% peptone, 2% glucose).

For a preculture volume of 100 mL 1 g of yeast, 2 g of peptone and 2 g of peptone are needed. Firstly the yeast is dissolved in deionized water and afterwards the peptone is added to be dissolves as well. In 2 Erlenmeyer flasks of 250 mL, 1 g of glucose is added.

The Erlenmeyer flasks with the glucose and the 100 mL mixture of peptone and yeast are sterilized separately in an autoclave at 121°C for 20 min. Afterwards, 50 mL of the peptone-yeast mixture are added in each Erlenmeyer flask and they are left to reach room temperature.[30] After they reach room temperature they are inoculated. The flasks are then left overnight in incubators at 28 °C and 200 rpm.

Main Culture

For 0.5 L culture of YPD medium the procedure goes as follows. In 450 mL of deionized water 5 g of yeast and 10 g of peptone are dissolved. In order to reach the final volume of 0.5 L 50 mL of 1 M phosphate buffer pH 6 should be added. (The final concentration of the buffer in the culture will be 100 mM).

10 g of glucose are added in a 2 L Erlenmeyer flasks. The buffer, the peptone-yeast mixture and the glucose are sterilized separately in an autoclave at 121 °C for 20 min. Then the constituents are mixed in the Erlenmeyer flask and is left to cool down until

[29]The glucose is sterilized separately because in case it was dissolved together with the rest of the constituents, it would be polymerized.

[30]The flasks are left to reach room temperature because otherwise the cells of the inoculation would die.

it reaches room temperature. After that they are a inoculated with the preculture medium.

For the inoculation a sample from each flask of the preculture is taken and is diluted 1:100. Their optical density is measured at 600 nm. After that, the necessary volume needed to be added to the main culture is calculated so as the optical density is equal to 1 at each Erlenmeyer flask of the main culture.[31]

The culture is not fed. It is incubated at 30 °C under stirring at 180 rpm for 4-5 days.

pPICZαC as a *Pichia pastoris* expression vector of a recombinant protein

In the case that pPICZαC is used as an expression vector, there are some differences in the media of the preculture and the main culture as well as some procedures.

Preculture Medium

The preculture medium (BMGY) consists of 1% yeast, 2% peptone, 100 mM phosphate buffer pH 6, 1.34% YNB, 4×10^{-5} Biotin and 0.5% v/v glycerol.

Culture

The main culture medium (BMMY) consists of 1% yeast, 2% peptone, 100 mM phosphate buffer pH 6, 1.34% YNB, 4×10^{-5} Biotin and 0.5% v/v methanol.

For 125 mL of YNB 8.5 g Yeast Nitrogen Base and 25 g Ammonium Sulfate are needed.

For 1 L culture medium:

- For the BMGY, in 140 mL of diionized water 2 g of yeast and 4 g of peptone are dissolved. 20 mL phosphate buffer 100 mM ph 6, 20 mL YNB, 400 μL Biotin and 20 mL of glycerol 10% are prepared.

- The same procedure for the preculture is followed when it comes to the optical density calculations. The difference in this case is that the preculture is centrifuged in sterilized carriers and then the yeast is resuspended in water and then the main cultures are inoculated.

[31] For example, if the optical of the diluted sample of one flask corresponding to the preculture is 0.200 abs, then

$$c_1V_1 = c_2V_2 \tag{4.2.1}$$

where

$$c_1 = c_1'100 \tag{4.2.2}$$

Regarding the indexes, 1 refers to the preculture and 2 to the main culture and c_1' to the diluted sample.

After doing the calculation, V_1 corresponds to 15 mL, and considering that the volume does not change significantly for this application, 15 mL from the preculture are added to the main culture.

- For the main culture, 10 g of yeast and 20 g of peptone are dissolved in 800 mL of water. 2 mL of Biotin, 100 mL of YNB, 100 mL phosphate buffer 100 mM ph 6 are also prepared. They are separated into 2 Erlenmeyer flasks of 2 L. 2.5 mL of methanol are added in each flask. The culture lasts for 4 to 5 days.

4.2.7 Purification

In order to purify the enzyme produced, the main culture containing the enzyme has to be condensated first.

The culture is centrifuged for 10 min so that the cells are separated from the medium. Afterwards, the separated medium goes through common filter paper and it then undergoes filtration under vacuum with filters with pores 0.8 and 0.2 μm.

When the filtering is over, the medium is condensed to a volume of about 50 mL using an Amicon Ultrafiltration system and a 10 kDa membrane.[32]

Then, under normal circumstances, the enzyme should be captured by an IMAC - Talon column. In order for this feat to be achieved, dialysis has to be performed to the condensed culture medium in a Talon pH 8 solution.

Firstly, 700 mL of Talon pH 8 10x solution are prepared with ultrapure water, of which the 400 mL are diluted into a final volume of 4 L with deionized water.

The Talon pH 8 10x solution consists of 500 mM Tris, 3 M NaCl, and an adequate volume of HCl for the pH to be adjusted to a value of 8.

The condensated medium containing the enzyme is enclosed in a dialysis membrane, which was pretreated by being drenched for about 30 min in water which had boiled. It is left for at least 7 hours in the diluted Talon buffer.

The next day, after the dialysis is over, the condensated medium goes through a separation column in order for the enzyme to be isolated from the rest of the medium. Around 1 L of the diluted Talon buffer (solution A) and 100 mL of the diluted buffer with 100 mM imidazole (solution B) should be prepared.

- At first, ultrapure water goes through the column.
- Then, solution A goes through the column at a volumetric rate of 2.5 mL/min so that about 10-20 column volumes (CV) have passed through the column. The the sample containing the enzyme is loaded at a rate of 1 mL/min to the column.
- After that, the column is washed with solution A until the absorbance reaches zero after it has peaked.[33] This escalation of the absorption is due to the impurities that weren't withheld by the column.
- The next step is the loading of solution B at a rate of 2 mL/min so that the enzyme detaches from the column in order to be collected The flow though collection stops when the absorption indication reaches zero again.

[32] This is the rate determining step of the situation which can take up to 7 h for a medium volume of 1 L the culture medium and using 2 Amicon systems simultaneously. In the case of a 0.5 L culture medium and using 2 Amicon systems, the process takes about 4 hours for the enzymes treated in this work.

[33] About 10 column volumes are usually enough.

- Then solution A goes through the column again at a rate of 2.5 mL/min until 10 column volumes have passed through it.

Then 5 L of Tris-HCl pH 8 20 mM are prepared in order to put the enzyme for dialysis again overnight.

In case of *Fo*LPMO9 wich could not be isolated by IMAC, ion exchange column is needed, a Q-sepharose column is used instead and the procedures differs as follows: the first dialysis occurs in Tris-HCl pH 8 20 mM and the flow though after the sample loading is collected instead. Then the TrisHCl pH 8 20 mM with 100 mM NaCl is used to clean up the column. The protein in this case is not thoroughly purified and no second dialysis is needed to be performed. For more details one shall refer to the Appendix B.

4.2.8 Sodium Dodecyl Sulphate Polyacrylamide Gel Electrophoresis, SDS-PAGE

The main purpose of this stage of the procedure is so as to ascertain the existence of proteins in a sample, the purity of a protein after the purification step as well as to estimate relative molecular mass of a protein.

In this method in order to separate protein molecules a polyacrylamide gel is used, which is chemically inactive so as not to interact with the proteins. The polymerism of the acrylamide is achieved with the use of Ammonium Persulfate (APS) and the initiator Tetramethylethylenediamine (TEMED).

The movement of the proteins inside the gel during the electrophoresis is achieved through 2 gels one on top of the other. The first one is the stacking gel on which the samples are loaded. Due to its lower concentration in polyacrylamide, bigger pores occur, allowing the protein molecules, regardless of their size, to get aligned so that they can all move forward to the next gel (resolving gel). In the resolving gel, the separation depending on the molecular weight is achieved.

The electrophoresis apparatus is the Mini-Protean3 from Biorad.

The stacking gel consists of 3.0 mL ultrapure water, 3.75 mL 0.25M Tris/SDS 0.2% (pH 6.8), 0.75 mL 40% bis –acrylamide (30:1), 20 μL TEMED and 60 μL 10% APS (w/v).

The resolving gel consists of 3.5 mL ultrapure water, 9.4 mL 0.25M Tris/SDS 0.2% (pH 6,8), 5.8 mL 40% bis –acrylamide (30:1), 30 μL TEMED and 90 μL 10% APS (w/v).

The experimental procedure followed is described below

- The constituents of the resolving gel are mixed and then the resulting mix is poured between two glass plates. It is left to solidify for about 30 min
- The constituents of the stacking gel are then mixed and the resulting mix is poured between the glass plates on top of the resolving gel. Then a special comb is placed in order to form the loading slots. It is then left to solidify for about 30 min.

- The glass plates are then placed in the electrophoresis apparatus, which is then filled with SDS running buffer 1X.
- The comb is removed and the samples are loaded.[34]
- Together with the samples, the corresponding SDS-Page ladder is used so that the molecular weight of the proteins can be determined.
- the applied current is about 35 mA per gel and in order to get the separation and the gel is left to run for as long as it takes.

4.2.9 Isoelectric focusing - Polyacrylamide gel electrophoresis, IEF-PAGE

Isoelectric focusing - Polyacrylamide gel electrophoresis, (IEF-PAGE) is a protein separation method based on their isoelectric point (pI). The gels used in this method are manufactured in such a way that when electric field is applied each protein will move to its isoelectric point. The electrophoresis apparatus used was from Phastsystem. The gels used were already manufactured and covered a pH range from 3 to 9. The isoelectric point ladder used had a pH range from 3.5 to 9.3.

After the electrophoresis was over, the gel was placed in a 20 % tetrachloroacetic acid solution for 5 min and then it was placed for 2 min in the destaining solution. Then, the protein staining was done with Coomassie Brilliant Blue G-250. The gel was placed in the staining solution Coomassie Brilliant Blue G-250 fro 1 hr and then in the destaining solution for 20 min.

4.3 Preliminary Analysis

Regarding the mechanistic study of LPMOs , aspects of the first step of the reaction where the enzyme is reduced by an electron donor, shall be examined extensively in the next chapter. The study of LPMOs in the present chapter shall focus more on their interaction with their substrate and more specifically with PASC.

Since the polyssacharidic substrates that interact with the LPMOs are not electrochemically active on an electrode surface in the operating conditions of LPMOs, these enzymes cannot be studied through mediated electron transfer. Thus, the approach chosen was to immobilize the LPMOs and attempt direct electron transfer, which is always a challenge when it comes to redox enzymes due to the distance between the enzymes' active center and the electrode surface. However, in the case of the LPMOs the active site lies on their surface. Thus, direct electron transfer concerning this class of enzymes while immobilized on an electrode surface is more promising than when using other enzymes such as peroxidases which have their active site buried within their

[34]The samples need to be prepared beforehand. 20 μL of the enzyme together with 5 μL of the loading buffer are boiled for 5-7 min. The loading buffer contains the SDS surfactant that breaks the disulfidic bridges and the proteins shall seem like a monomer molecule. Moreover the proteins are charged negatively.

structure. Thus, in this section a first attempt is made to immobilize LPMOs on a glassy carbon electrode with the use of Nafion^{TM} in order to examine the feasibility of direct electron transfer. Then another matrix is used for a more stable immobilization so as to further study the enzymes and their interactions with their substrates.

So in order to study these enzymes with electrochemical methods, a first step is to use a simple immobilization method to examine if it is feasible to observe electron transfer between the LPMOs and the electrode.

The enzymes used in the preliminary experiments are *Mt*LPMO9H and *Fo*LPMO9 expressed in pPICZαC. The electrode used was a common glassy carbon electrode and the immobilization matrix was Nafion^{TM} perfluorinated resin solution used in the experiments concentration was 5 wt% in lower aliphatic alcohols and water (Aldrich).

A single compartment 3 electrode cell was used consisting of a disk glassy carbon electrode (GC) with a surface of 0.785 mm^2 as working electrode, a 1.6 mm diameter Pt coated titanium rod as a counter electrode, and an Ag|AgCl, KCl sat. reference electrode (+0.197 V vs NHE). The aqueous solution of about 3 mL consisted either of 1 M Na_2SO_4 (98 %, Merk) as supporting electrolyte or 100 mM tartrate buffer (pH 5) (PENTA).

Voltammetric measurements were performed by a PAR 263A Potentiostat connected to an AFG 5101 Tektronix programmable arbitrary function generator. All solutions were deaerated for at least 10 min before the experiments in order to avoid oxygen reduction on the electrode surface or even possible catalytic currents in the case that the mechanism for the action of the LPMOs that ultimately holds is that of oxygen reacting with the enzymes. Nitrogen gas was also purged over the solution during measurement. The temperature of the cell was kept at a specific value during measurement with the use of a thermostated bath (FALC WB-MD5). The temperature of the cell was recorded during the measurement, in order to assure that it remained constant. The analysis of the data from the FTacV experiments was performed by a program developed in our lab.

The glassy carbon electrode was polished on a cloth with successive use of a 0.3 μm and 0.05 μm Al_2O_3. The electrode was then washed with distilled water and subsequently sonicated in distilled water for 5 min. After the sonication, the electrode was again washed with distilled water. An enzyme volume of 1 μL was left on the surface of the glassy carbon electrode to dry for about 15 min at room temperature. The procedure was repeated once more in order to increase the enzyme surface concentration on the electrode. Subsequently, 1 μL of Nafion^{TM} was left to dry above the deposited enzyme in order to complete the immobilization.

4.3.1 Cyclic Voltammetry

A first approach to ascertain electron transfer between the LPMOs and the electrode surface is by using common cyclic voltammetry. A commonly used supporting electrolyte is Na_2SO_4 1 M with a pH value of 7. The cyclic voltammetry experiments of *Fo*LPMO9 are pictured in Fig. 4.3.1. By taking a quick look at this figure without focusing on the details it is rather clear that the capacitance is the dominant feature in both subfigures. More specifically, the cyclic voltammograms of a Nafion^{TM}-*Fo*LPMO9

modified glassy carbon electrode versus a Nafion™ only modified glassy carbon electrode are depicted in Fig. 4.3.1(a). Cyclic voltammetry was conducted in 1 M Na_2SO_4 at 20 °C between 600 mV and -600 mV, with 600 mV being the initial potential. By comparing the voltammogram of a Nafion™ only modified electrode with that of the *Fo*LPMO9-Nafion™ electrode, one oxidative broad peak is observed near 180 mV and a reductive one at -50 mV. The problem which arises from these peaks is that they are not intense enough to perform an analysis and their separation is about 230 mV possibly indicating a non-reversible electron transfer. In Fig. 4.3.1(b), some voltammograms of the *Fo*LPMO9-Nafion™ electrode, under the aforementioned conditions and different scan rates, are depicted. It is evident that for high scan rates the electrode capacitance deforms the cyclic voltammogram, making it hard to analyze, whereas for lower scan rates, the reduction peak becomes even less intense. Thus, it was rendered necessary to use another technique in order to study and prove the LPMOs' direct electron transfer.

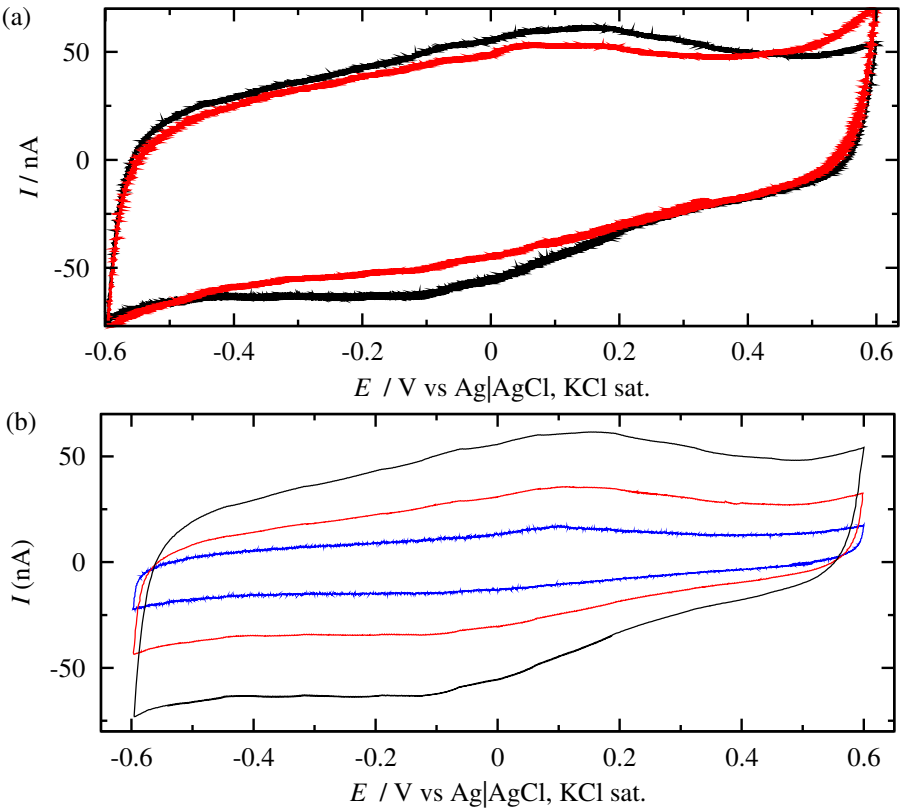

Figure 4.3.1: (a) Cyclic voltammograms of GC-Nafion™ electrode (red curve) and *Fo*LPMO9 immobilized on a GC electrode with the use of Nafion™ (black curve) at 100 mV/s in 1 M Na_2SO_4 deaerated solution at 20 °C. (b) Cyclic voltammograms of *Fo*LPMO9 immobilized on a GC electrode with the use of Nafion™ at different scan rates in 1 M Na_2SO_4 deaerated solution at 20 °C.

4.3.2 FTacV

The next step was to use FTacV to examine *Fo*LPMO9, so as to eliminate capacitance currents. A perturbation amplitude A_0 of 330 mV and a frequency f of 9 Hz are employed in order to get an intense signal. In Fig. 4.3.2(a) and (b), the third and fifth harmonics are presented, respectively. The scan is performed between 700 and -500 mV vs Ag|AgCl with initial potential 700 mV at a scan rate v of 50 mV/s. One can observe well defined peaks for both harmonics. In the third harmonic the capacitance is not yet eliminated and the response is affected whereas, in the fifth harmonic the capacitance component is diminished. In Fig. 4.3.2(a) and (b), the blank voltammograms refer to Nafion^{TM} only modified glassy carbon electrode. As can seen, they do not present any systematic pattern or well-defined peaks corresponding to electractive species that reminiscence the standard voltammograms derived from an analysis of FTacV data. In the present work, as a matter of convenience, the odd harmonics are presented, as they exhibit maxima where the redox potentials appear, whereas even harmonic exhibit minima.

The above results indicate that direct electron transfer as well as the determination of $E^{0\prime}$[35] seems to be possible for LPMOs immobilized on a GC electrode with the Nafion^{TM} polyelectrolyte. For the initial experiments Na_2SO_4 was used as a supporting electrolyte at a concentration of 1 M. Since LPMOs are studied biochemically in buffered solutions of certain pH, the next experiments shall be conducted in a tartrate buffer solution. The analysis will be performed in the next section for a pH value of 5 using tartrate buffer.

Now, since the biochemical experiments for LPMOs from the fungi *T. thermophila* and *F. oxysporum* are conducted in slightly acidic pH, a value of pH 5 was chosen in order to conduct a more elaborate study. Other pH values were not examined as these are only preliminary experiments that concern the feasibility of direct electron transfer. On the other hand the temperature was a factor taken into consideration in order to see the behaviour of an immobilized enzyme closer to its operational conditions.

The temperature range examined for *Fo*LPMO9 is between 23 and 47 °C, since *F. oxysporum* is a mesophilic fungus. In Fig. 4.3.3, the fifth harmonic from the FTacV analysis is presented for the *Fo*LPMO9 at $v = 50$ mV/s, $A = 330$ mV, $f = 9$ Hz in deaerated 100 mM tartrate buffer pH 6, at 23, 29, 39 and 47 °C.

The corrected values for the reductive, oxidative and formal potential are presented in Table 4.3. These values have been obtained by taking into account the temperature coefficient -1.01 mV/°C of the Ag|AgCl, KCl sat. reference electrode , assuming to be constant for all temperatures studied. The difference between E_{ox} and E_{red} for lower temperatures is about 10 mV whereas for 47 °C it is about 5 mV. The mean value of the oxidation and the reduction peaks is calculated and is then regarded as the formal standard potential of the enzyme at each temperature.

The same procedure was followed for *Mt*LPMO9H with the difference being the temperature range examined, since it originates from a thermophilic fungus. In Fig. 4.3.4, the 5th harmonic is depicted for various temperatures.

[35]Regarding the experimental results the term formal potential shall be used, instead that of the standard potential, as the relative activities differ from unity.

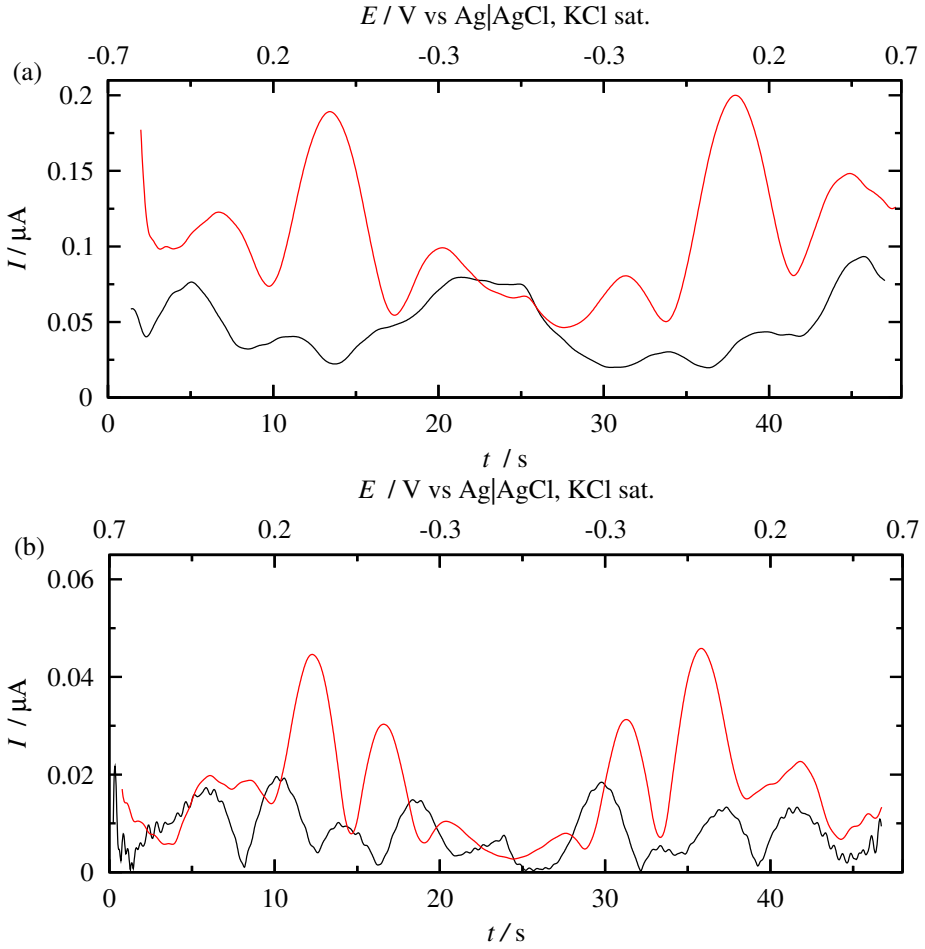

Figure 4.3.2: (a) FTacV 3rd harmonic and (b) FTacV 5th harmonic of *Fo*LPMO9 immobilized on a GC electrode with the use of Nafion^{TM} (red curve) and a GC electrode covered solely with Nafion^{TM} (black curve) for $v = 50$ mV/s, $A_0 = 330$ mV and $f = 9$ Hz in deaerated 1 M Na_2SO_4 solution at 20 °C

Table 4.3: Reduction, oxidation and apparent formal potentials for *Fo*LPMO9 immobilized on a GC electrode with the use of Nafion^{TM} for a $v = 50$ mV/s and $A_0 = 330$ mV in deaerated 100 mM tartrate buffer pH 5. Potential values are versus Ag|AgCl, KCl sat.

T(°C)	E_{ox} (mV)	E_{red} (mV)	$E^{\circ\prime}_{app}$ (mV)
23 ± 1.0	79.7 ± 0.8	69.1 ± 0.8	74.4 ± 0.9
27 ± 1.0	84.3 ± 6.9	71.6 ± 1.0	77.9 ± 3.8
29 ± 1.0	84.7 ± 1.0	74.7 ± 1.0	79.7 ± 0.9
33 ± 1.0	86.0 ± 5.6	76.7 ± 1.0	81.3 ± 2.9
39 ± 1.0	88.9 ± 1.0	80.9 ± 1.0	84.9 ± 0.6
42 ± 1.0	90.5 ± 1.7	81.9 ± 1.0	86.2 ± 1.4
47 ± 1.0	88.0 ± 2.1	82.7 ± 2.1	85.3 ± 1.1

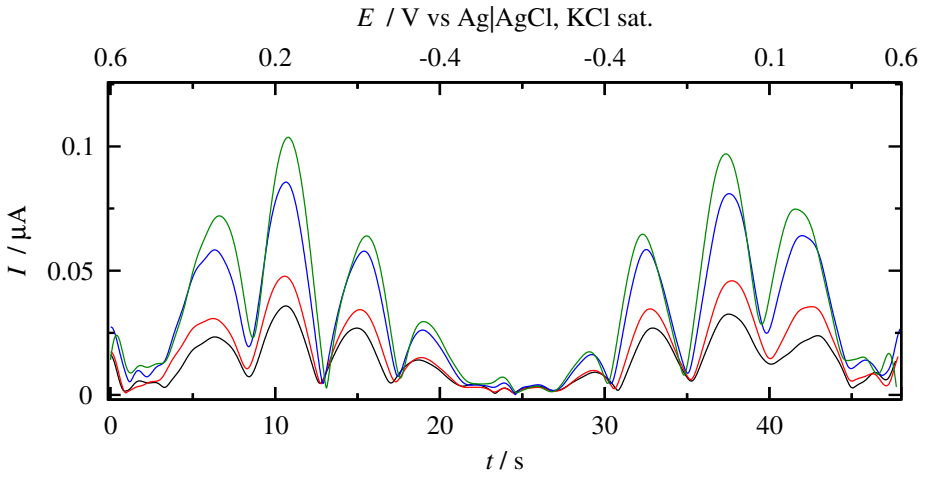

Figure 4.3.3: FTacV 5th Harmonic of *Fo*LPMO9 immobilized on a GC electrode with the use of Nafion^{TM} for $v = 50$ mV/s, $A_0 = 330$ mV, $f = 9$ Hz in deaerated 100 mM tartrate buffer pH 6 at different temperatures. $T = 23$ (black), 29 (red), 39 (blue) and 47 °C (green).

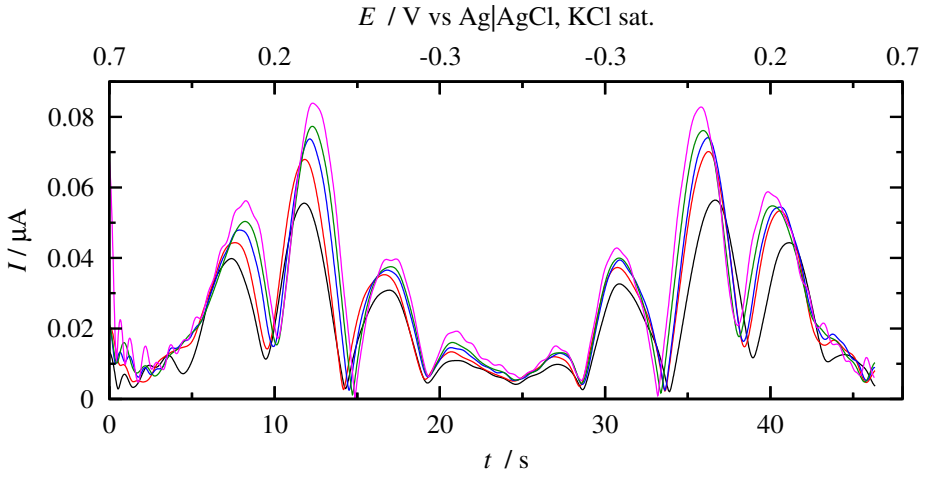

Figure 4.3.4: FTacV 5th Harmonic of *Mt*LPMO9H immobilized on a GC electrode with the use of Nafion^{TM} for $v = 50$ mV/s, $A = 330$ mV and $f = 9$ Hz in deaerated 100 mM tartrate buffer pH 6 at different temperatures. $T = 30$ (black), 37 (red), 44 (blue), 50 (green) and 57 °C (magenta).

Table 4.4: Reduction, oxidation and apparent formal potentials for *Mt*LPMO9H immobilized on a GC electrode with the use of Nafion^{TM} for $v = 50$ mV/s, $A_0 = 330$ mV in deaerated 100 mM tartrate buffer pH 6. Potentials are versus Ag|AgCl, KCl sat.

T(°C)	E_{red} (mV)	E_{ox} (mV)	$E^{0\prime}_{app}$ (mV)
30 ± 1.0	115.4 ± 0.8	134.1 ± 1.5	124.7± 0.9
37 ± 1.0	112.7 ± 2.7	126.3 ± 2.3	119.5± 1.8
44 ± 1.0	116.3 ± 1.9	125.9 ± 2.4	121.1± 1.5
50 ± 1.0	122.0 ± 14.1	117.2 ± 0.3	119.6± 7.1
57 ± 1.0	112.9 ± 1.6	118.6 ± 2.0	115.8± 1.3

The corrected potentials regarding the temperature, corresponding to *Mt*LPMO9 are presented in Table 4.4.

The potentials reported up to this point are affected by the polyelectrolyte the enzymes are entrapped inside. The paramaters that affect the potential values are the pH and the concentration of the buffer solution and the Nafion^{TM} concentration used. However, the value of interest is that of a free enzyme. Thus, in order to get a better approximation of the formal potential E$^{0\prime}$ of the *Mt*LPMO9H and *Fo*LPMO9 the following expression shall be used.

$$E^{0\prime}_{app} = E^{0\prime} + \frac{RT}{nF}\ln\frac{c_s}{c_p} - 2.303\frac{RT}{nF}\text{pH} \tag{4.3.1}$$

where c_s and c_p are the concentrations of the supporting electrolyte cations in the solution and the polyelectrolyte respectively. The concentration c_p is essentially constant and in this case can be considered equal to $[SO_3^-]_p$, which is the concentration of the sulfonate groups inside the polyelectrollyte. $E^{0\prime}_{app}$ refers to the $E^{0\prime}$ value which is affected by the immobilization matrix.

Taking into account an average molecular weight for the Nafion^{TM} polyeletrolyte to be 5×10^5 g mol^{-1}, and its concentration at 5% w/v, its molecular concentration is estimated at 1×10^{-4} M, which can be treated as equal to $[SO_3^-]_p$ and thus equal to c_p. The supporting electrolyte which was used in the case of *Fo*LPMO9 and *Mt*LPMO9H was 0.1 M and the pH value was 5. Consequently the corrected $E^{0\prime}$ values are presented in Tables 4.5 and 4.6 respectively.

4.4 Alternate Immobilization methdod

4.4.1 *Mt*LPMO9H

After the ascertainment of the feasibility of direct electron transfer of LPMOs with an electrode surface, a more stable immobilization matrix was desired in this work. Thus, an attempt was made to exploit the His-Tag incorporated in the LPMO structure taking advantage of its affinity to metal ions such as nickel and cobalt.

In order to manufacture this matrix, 1 g of commercial functionalized Multi-wall Carbon Nanotubes (MWCNTs) (HONGWUNEMATERIAL, item No: C933-MC, China)

Table 4.5: Corrected formal potentials for *Fo*LPMO9 immobilized on a GC electrode with the use of Nafion^{TM} for $v = 50$ mV/s, $A_0 = 330$ mV in deaerated 100 mM tartrate buffer pH 5. Potentials are versus Ag|AgCl, KCl sat.

T(°C)	$E^{0\prime}$ (mV)
23 ± 1.0	191.2 ± 0.9
27 ± 1.0	197.1 ± 3.8
29 ± 1.0	199.7 ± 0.9
33 ± 1.0	202.8 ± 2.9
39 ± 1.0	208.9 ± 0.6
42 ± 1.0	211.3 ± 1.4
47 ± 1.0	212.2 ± 1.1

Table 4.6: Corrected formal potentials for *Mt*LPMO9H immobilized on a GC electrode with the use of Nafion^{TM} for $v = 50$ mV/s, $A_0 = 330$ mV in deaerated 100 mM tartrate buffer pH 5. Potentials are versus Ag|AgCl, KCl sat.

T(°C)	$E^{0\prime}$ (mV)
30 ± 1.0	245.1± 0.9
37 ± 1.0	242.3± 1.8
44 ± 1.0	247.0± 1.5
50 ± 1.0	247.9± 7.1
57 ± 1.0	246.8± 1.3

were added in a 150 ml solution with 20 % mol acetic acid. The solution was stirred for 20 min at 120 °C for further functionalization. The solution was left to dry overnight at 90 °C until dry powder was collected. The powder was centrifuged 5 times with deionized water until the supernatant had a pH value of ≃7.0. This step ensured the removal of acetic acid excess. The dry functionalized commercial MWCNTs (f-MWCNT) were left to dry at 90 °C. Subsequently, the f-MWCNTs were mixed with 150 ml deionized water and 0.4227 mg of $(CH_3COO)_2Co{\cdot}_4H_2O$ (MERCK) leading to a 10 % Co and solution that was then subjected to sonication at a low-frequency (20 kHz)using a Hielscher (UIP500hd) sonicator (probe tip diameter of 22 mm) for 1h. The solution was further left to dry and centrifuged (as described above) for the collection of the final product. The Cobalt functionalized MWCNTs (Co-f-MWCNTs) were stored in a desiccator at room temperature.

In order to test the matrix, 0.005 g were dissolved in 100 μL of Nafion^{TM} perfluorinated resin solution. Its concentration was 5 wt% in lower aliphatic alcohols and water. The mixture was sonicated for about 15 min. 2 μL of the matrix were taken and diluted with 8 μL of Tris HCl pH 8, 20 mM. 2 μL of this mix were taken and left to dry at room temperature, on the electrode surface of a disk GC electrode (3 mm diameter). The modified electrode was tested at a scan rate of 100 mV/s in a 3 electrode compartment cell with acetate buffer, pH 6 500 mM as a supporting electrolyte.

The cyclic voltammograms were recorder under different potential windows. By taking a close look at Fig. 4.4.1, when using a potential window ranging from 800 to

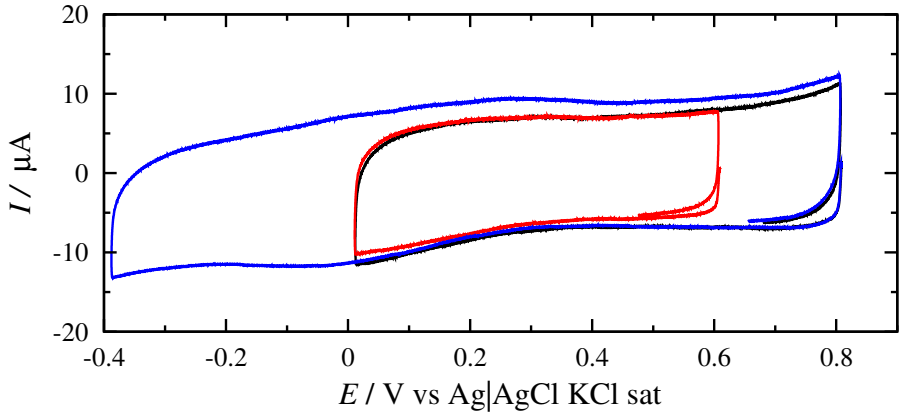

Figure 4.4.1: Cyclic voltammograms of the Co-f-MWCNTs modified electrode in an acetate buffer pH 6, 500 mM at 100 mV/s for different scan limits. 0.8 to -0 V (black), 0.6 to -0 V (red) and 0.8 to -0.4 V (blue)

0 mV vs Ag|AgCl, KCl sat., at room temperature, no apparent peaks appear. Thus, this region can be regarded as safe to work with this electrode. When scanning more cathodically, a pair of faint, wide and irreversible peaks appear somewhere between 0 and 200 mV, and the capacitance increases as well. Thus, a safe region to work with the Co-f-MWCNTs modified electrode, without the interference of other peaks at a pH of 6, is between 800 to 0 mV vs Ag|AgCl, KCl sat. For higher potentials, an increase of the current is observed. The solution was deaeriated during the experiment.

Then, 2 μL of Co-f-MWCNTs were taken and were mixed with 8 μL of *Mt*LMPO9H of concentration 5.5 mg/mL in Tris HCl pH 8, 20 mM. 2 μL of this mix was left to dry on the GC electrode surface. The resulting cyclic voltammogram of the modified with the enzyme electrode is presented in Fig. 4.4.2. By taking a close look at the voltammogram one can observe a set of two redox peak. One cathodic at 0.210 V and one anodic at 0.253 V. Thus, the peak separation is estimated at 43 mV which could be considered close to reversibility for an immobilized species. Moreover, the signal is still governed by capacitance, making it difficult to work with it in a cyclic voltammetry experiment. This capacitance can also be responsible for the peak separation and the deformation of the voltammogram.

The next experiment to be conducted was FTacV, in order to get a pure Faradaic signal deprived of capacitance. FTacV was performed on the Co-f-MWCNTs *Mt*LPMO9H mix on a glassy carbon electrode for $A_0 = 250$ mV, $f = 1$ Hz and $v = 5$ mV s^{-1} over a course of 20 cycles at 25 °C in a pH 6 0.5 M acetate buffer. The 5th harmonic from this experiment for the first and the 20th cycle is presented in Fig. 4.4.3. In this figure one can observe a typical 5th harmonic corresponding to a quasi reversible reaction.

Thus, from this experiment it can be concluded that with this matrix indeed a pure Faradaic signal can be obtained with this immobilization without the use of extreme perturbation amplitudes or frequencies. Moreover, a rather satisfactory stability was achieved at a relatively low scan rate, as 20 cycles could be obtained without any significant change at 25 °C. The stability at higher temperatures shall be examined later in this work.

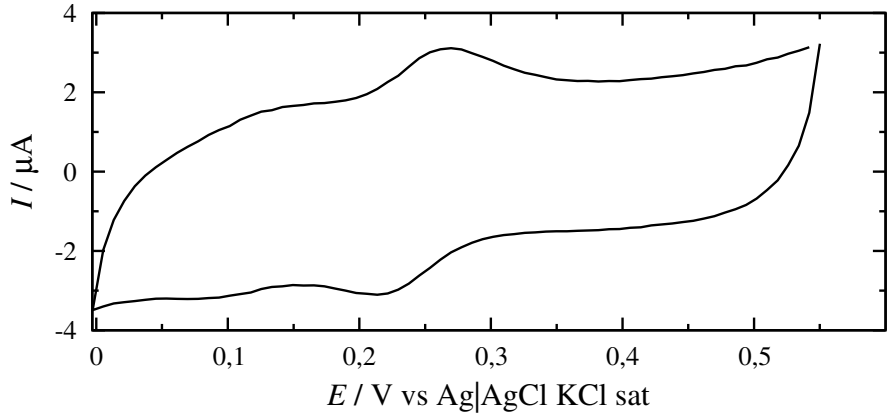

Figure 4.4.2: Cyclic voltammograms of Co-f-MWCNTs *Mt*LPMO9H mix on a glassy carbon electrode in a 0.5 M acetate buffer at 50 mV/s at 25 °C

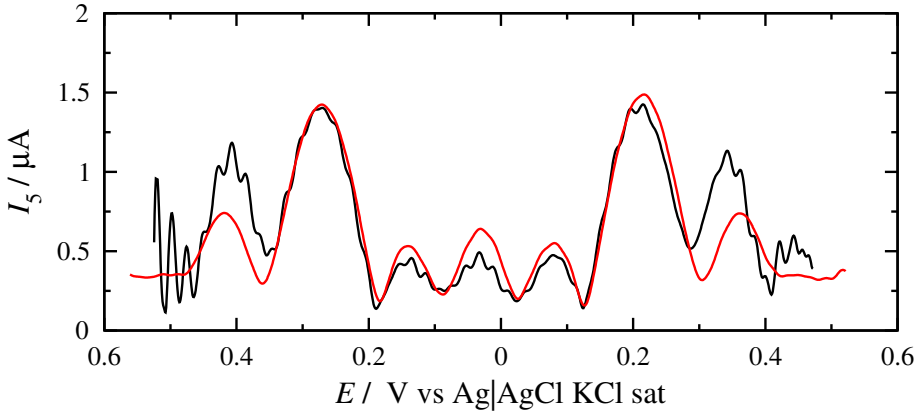

Figure 4.4.3: 5th harmonic of Co-f-MWCNTs *Mt*LPMO9H mix on a glassy carbon electrode in a 0.5 M acetate buffer for $A_0 = 250$ mV, $f = 1$ Hz and $v = 5$ mV s^{-1}. The black curve corresponds to the 1st cylce while the red to the 20th.

Continuing the electrochemical study of *Mt*LPMO9H, FTacV was performed for different frequencies at A_0 = 250 mV in order to apply the methodology introduced in Sec. 3.1.3 and extract the standard electron transfer kinetic constant k^0. In Fig. 4.4.4(a) the anodic scan of the immobilized *Mt*LPMO9H for frequency values of 5, 2, 1, 0.5, 0.2 and 0.1 Hz at room temperature are presented. For the higher frequencies employed, a typical 5th harmonic of a quasi-reversible system is depicted and as the frequency decreases the signal reflects more and more that of a reversible one. From the dominant peak of the 5th harmonic the apparent formal potential $E^{0\prime}_{app}$ can be estimated at 232 mV vs Ag|AgCl, KCl sat, a value very similar to the one of the formal potential estimated in Table 4.6.[36]

Going back to Fig. 4.4.4, where the normalized with the frequency anodic scan of the 5th harmonic of the immobilized *Mt*LPMO9H is presented, by employing the methodology introduced in Sec.3.1.3, one can conclude that by a frequency value of 0.1 Hz reversibility is achieved as no further increase for the dominant peak is observed. A slight increase is observed for the more anodic part of the harmonic, but this is probably due to the background of the matrix itself. Nevertheless, the dominant peak is not considered to be affected and the analysis is considered independent.

he same analysis is performed for the 4th harmonic in Fig. 4.4.5(a). Again as in the case of the 5th harmonic, in the higher frequencies a typical quasi reversible system is observed. The normalized 4th harmonics are presented in Fig. 4.4.5(b). For the lower frequencies employed in this harmonic, the two dominant peaks are symmetrical, reminding even more the behavior of a reversible reaction. The interference observed in the 5th harmonic around 0.4 V is almost not noticed in this case as the main part of the dominant peak starts at more cathodic potentials, having a more clear picture of the pure Faradaic signal of the immobilized enzyme in this case.

Back to the extraction of k^0 for *Mt*LPMO9H the ration of the normalized current peak for 5 Hz to the normalized peak of the reversible peak for 0.1 Hz shall be used. For the complete methodology to be used, experiments should have been conducted at very high frequencies to render the system irreversible and extract the transfer coefficient a. However, at very high frequencies, there were interferences due to the non linearity of the capacitance, making impossible to extract the transfer coefficient value.

Consequently, the working curves that shall be used will be the ones assuming a transfer coefficient 0.5. The deviation of the value shall not be of great importance as looking at the quasi reversible harmonics at higher frequencies the deformation that appears is not such that would indicate a transfer coefficient beyond the range of 0.4-0.6. Thus, using the working curves presented in Fig. 4.4.6 for the 4th and the 5th harmonic, the resulting value is $k^0 = 2.86 \pm 0.1$ s^{-1}.

Moving on, the interaction of *Mt*LPMO9H with PASC is to be examined, taking into account the scenario which implicates that the substrate binds to the enzyme before

[36]Taking into consideration the correction introduced earlier when Nafion^{TM} is implicated in the immobilization of an electroactive species, the formal potential should be estimated at 290 mV. However, this correction concerns a species entrapped in a Nafion^{TM} matrix, while in this case the enzyme is immobilized on the electrode surface through a Co-f-MWCNTs matrix and Nafion^{TM} is solely a supporting medium which helps with the stabilization of the matrix on the electrode surface. Thus the expression for the formal potential correction shall not be applied here.

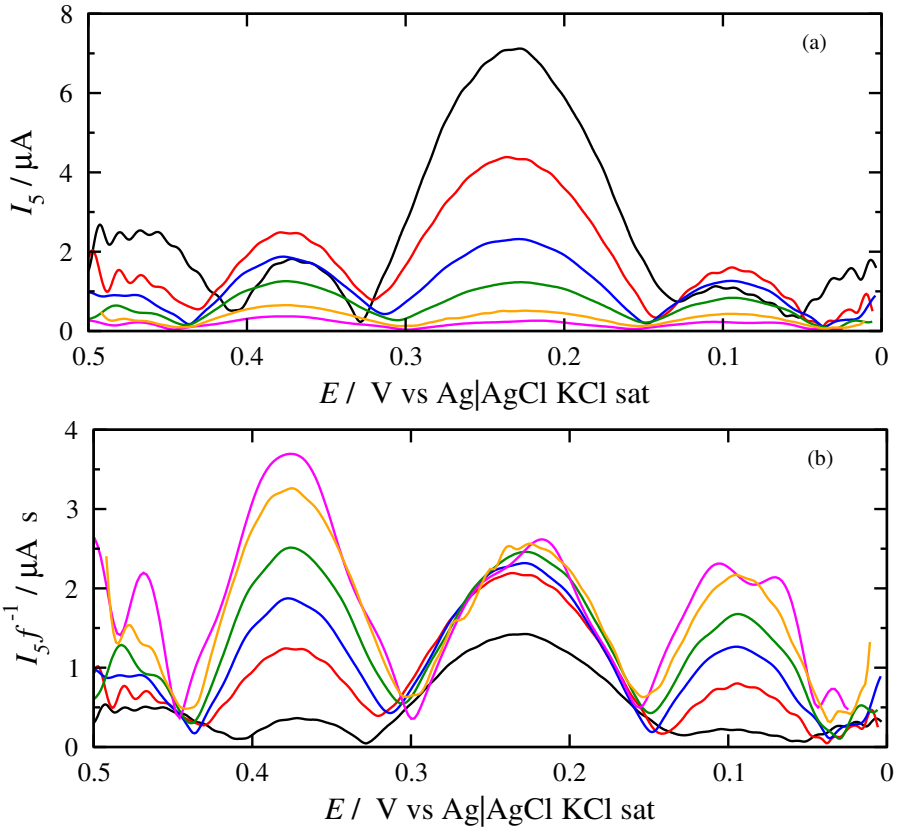

Figure 4.4.4: (a) 5th harmonic (b) normalized 5th harmonic of Co-f-MWCNTs *Mt*LPMO9H mix on a glassy carbon electrode in a 0.5 M acetate buffer for $A_0 = 250$ mV and $f = 5$ (black), 2 (red), 1 (blue), 0.5 (green), 0.2 (orange) and 0.1 Hz (magenta).

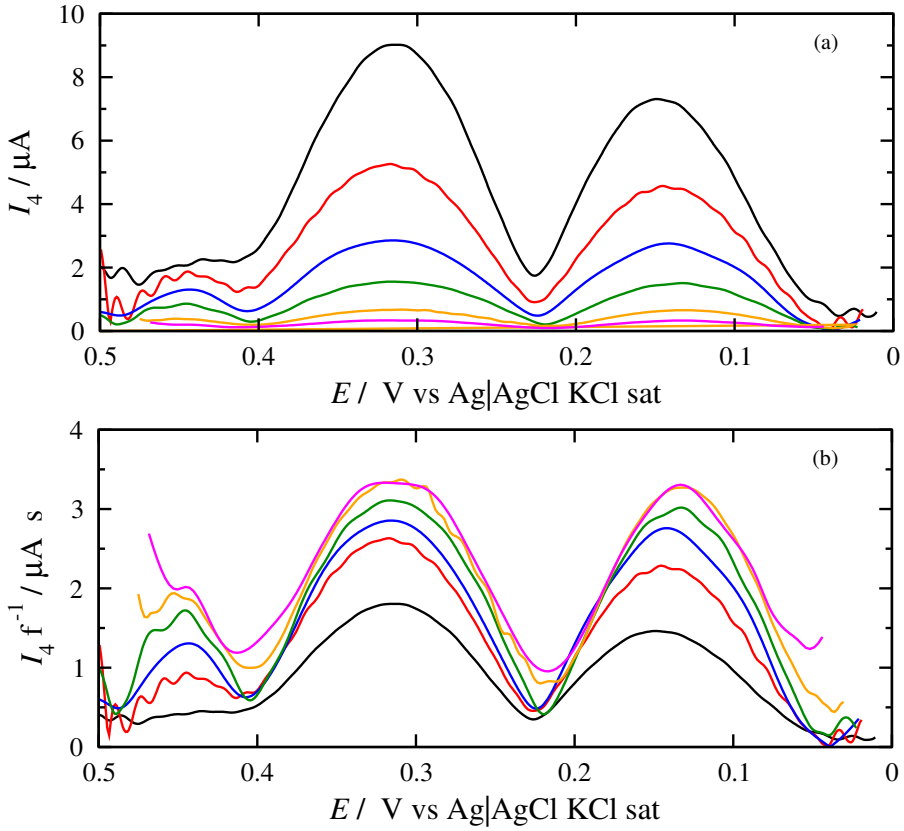

Figure 4.4.5: (a) 4th harmonic (b) normalized 4th harmonic of Co-f-MWCNTs *Mt*LPMO9H mix on a glassy carbon electrode in a 0.5 M acetate buffer for $A_0 = 250$ mV and $f = 5$ (black), 2 (red), 1 (blue), 0.5 (green), 0.2 (orange) and 0.1 Hz (magenta).

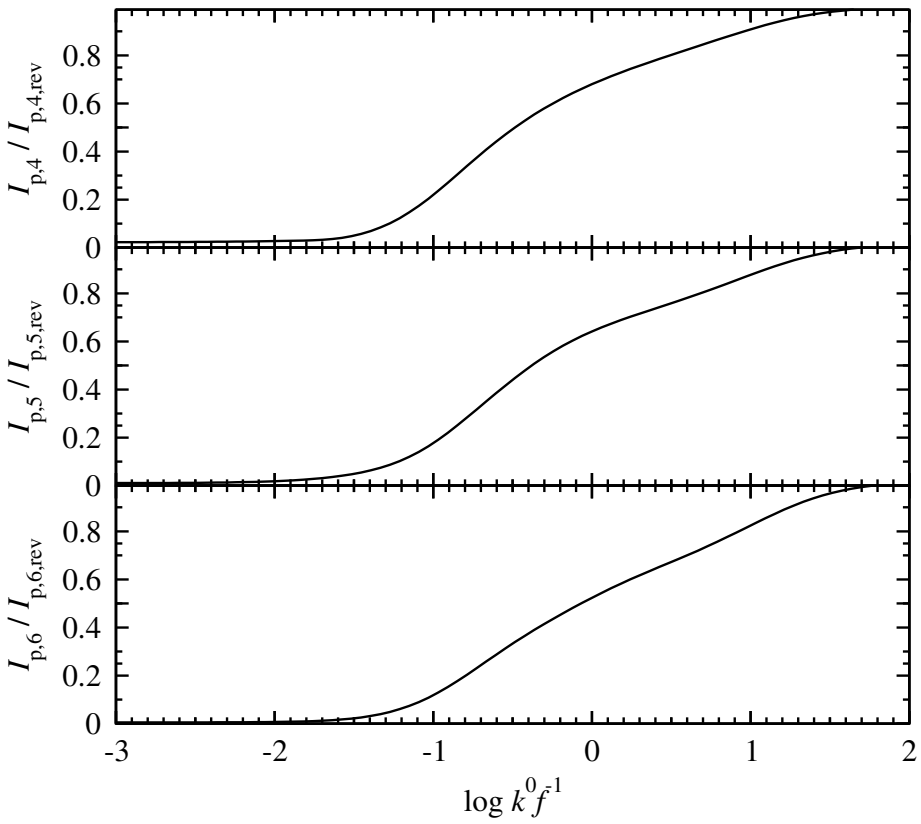

Figure 4.4.6: Working curves for 4th, 5th and 6th harmonic for $a = 0.5$.

the O_2 and/or H_2O_2 does. For the interpretation of the results the EC mechanism for immobilized species introduced in Sec. 3.4 shall be exploited.

As a first the stability of *Mt*LPMO9H while immobilized on the glassy carbon electrode was affirmed, so that to assure any decrease observed during the experimental process would be attributed solely to the reaction of the immobilized enzyme with the free in the solution species.

In Fig. 4.4.7(a) and (b) multiple cycles of the third and the fifth harmonic respectively of *Mt*LPMO9H while immobilized on the glassy carbon electrode at 30 °C are presented. The potential is scanned cathodically from 0.5 to 0 V and then back again to 0.5 V. The scan rate employed was 10 mV s^{-1} and the perturbation amplitude and frequency were 5 Hz and 250 mV respectively. As one can observe from these figures, the LPMO was stable and no degradation was observed for 6 cycles. After that a slight decrease in the signal started appearing, so it was decided that at this temperature under these scanning conditions the limit would be 6 cycles when performing the experiment in the presence of PASC. Moreover one could observe in Fig. 4.4.7(a) that the capacitance is still present in the signal and not yet completely eliminated, where as in Fig. 4.4.7(b) one could claim that in the 5th harmonic the capacitance current presence is negligible. The reason why by the 3rd harmonic capacitance is not fully eliminated is due to the non linearity of the the capacitance in the scanning limits tested, thus leading to the need of higher harmonics for its elimination. Moreover from the shape of the voltammograms one can claim that the electrochemical kinetics under these experimental conditions fall into the quasi-reversible region 25 °C. Thus the theory for the EC mechanism which was developed in the in Sec. 3.4 shall be valid.

The next step in this work was to add PASC in the solution so that and examine the decrease of the electrochemical signal. In Fig. 4.4.8(a) and (b) the 3rd and the 5th harmonic are presented respectively in the presence of 0.04 g/L PASC for multiple cycles under the same experimental conditions as in the previous experiment. One can observe that in both harmonics as the cycles go by there is an observable decrease in the peaks. However, in the case of the 3rd harmonic the decrease seems to be less prominent. This is also reflected in Fig. 4.4.8(c) where the anodic oxidation peak is plotted against time for the harmonics. The resulting slope for the third harmonic is -0.000375 while for the 5th is -0.000623 indicating a probable underestimation in the slope in the case of the 3rd harmonic. This could be probably attributed to the fact that the capacitance is yet to be fully eliminated by the 3rd harmonic and has a negative effect on the magnitude of the slope.

In order to investigate this matter further the fourth harmonic was also investigated. In Fig 4.4.9(a) the fourth harmonic resulting from the analysis of the same experiment can be found. The decrease of both the anodic dominant peaks shall be examined in this case. Then, in Fig 4.4.9(b) the linear dependencies of these two peaks are plotted against the time. The resulting slopes -0.000647 and -0.000583 which are closer to the the values found for the 5th harmonic, reinforcing the argument that the value of the slope in the third harmonic is underestimated due to the presence of capacitance currents.

From this analysis of the 4th and 5th harmonic for the 30 °C the resulting k value is 0.031 $\pm$ 0.0003 s^{-1}. The same process shall be followed now for higher temperatures

Table 4.7: Kinetic constant k of PASC binding to MtLPMO9H for different temperatures.

T (°C)	k (L g^{-1} s^{-1})
30	0.00061 ± 0.00005
35	0.00823 ± 0.0016
40	0.00867 ± 0.0005
45	0.0129 ± 0.002
50	0.0153 ± 0.003

as the MtLPMO9H has an optimum operation temperature at 50 °C.

One problem that was encountered at higher temperatures was the instability of the immobilized enzyme when a slow scan rate was employed and not more than 5 stable cycles could be obtained. So, for higher temperatures higher scan artes were used and more specifically 50 mV s^{-1} for 35 and 40 °C and 75 mV s^{-1} for 45 and 50 °C. The blank 5th harmonics of each temperature are presented in Fig. 4.4.10, where no significan change is observed for cycles 1 through 8 for all the temperatures under the chosen experimental conditions. Only small fluctuations within the expected experimental error range are visible.

After that, under the respective scan rate conditions, with the rest remaining the same, PASC was added in order to examine the decrease of the anodic oxidation peak for the 4th and the 5th harmonic. Indicatively, the results for the 45 °C experiments are presented in Fig 4.4.11. The 4th and the 5th harmonics are depicted in Fig 4.4.11(a) and (b) respectively where the decrease of anodic peak is rather evident even in such smaller time intervals in comparison to the ones depicted for the 30 °C, as in the former case the scan rate was 10 mV s^{-1} whereas now it 75 mV s^{-1}. The dependecies of the anodic peaks against the time are presented in Fig. 4.4.11(c).

Following the same procedure for all the temperatures, the extracted kinetic constants are presented in Table 4.4.1, where an increasing trend is observes as the temperature goes up.

An attempt for an Arrhenius type plot was then made in Fig. 4.4.12 where indeed a linear dependence is observed when the Napierian logarithm of the kinetic constant ($\ln k$) is plotted against the inverse temperature (T). From the slope the activation energy can be estimated at 37 kJ/mol.

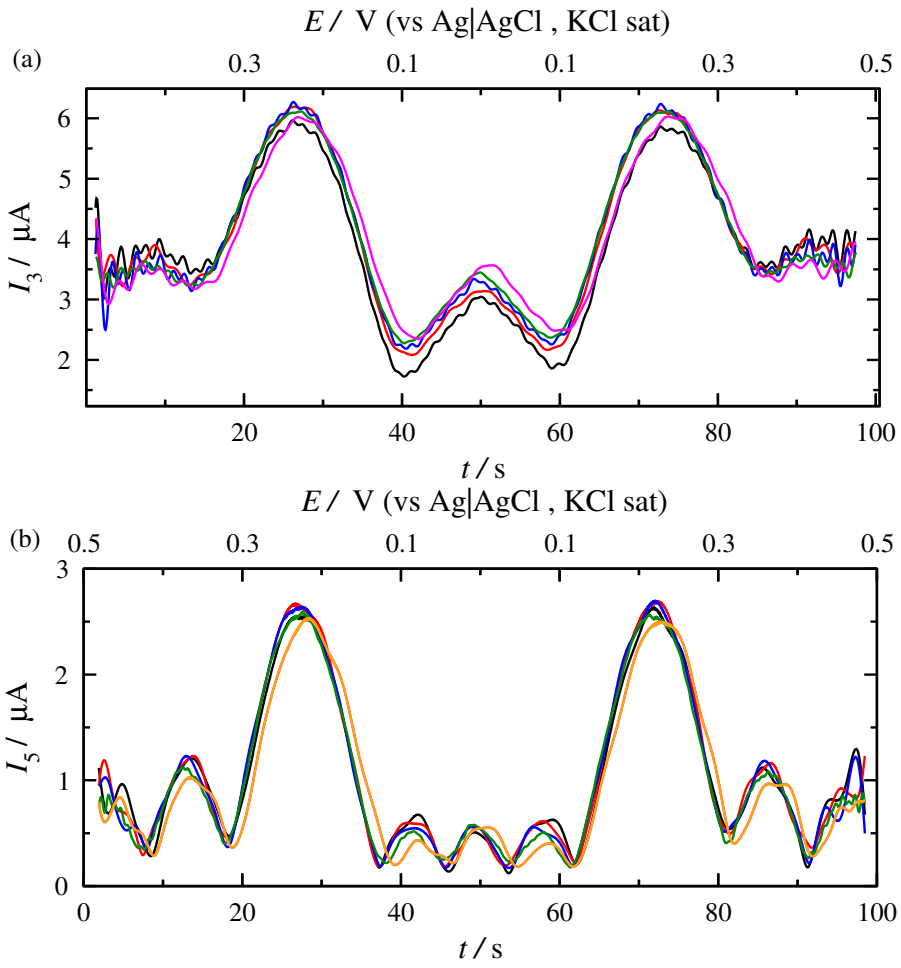

Figure 4.4.7: (a) 3rd and (b) 5th harmonic of Co-f-MWCNTs *Mt*LPMO9H mix on a glassy carbon electrode in an acetate buffer 500 mM pH 6, 500 mM at $v = 10$ mV s^{-1}, $f = 5$ Hz and $A_0 = 250$ mV at 30 °C. Cycles: 1st (black), 2nd (red), 3rd (blue), 4th (green), 5th (magenta) and 6th (orange)

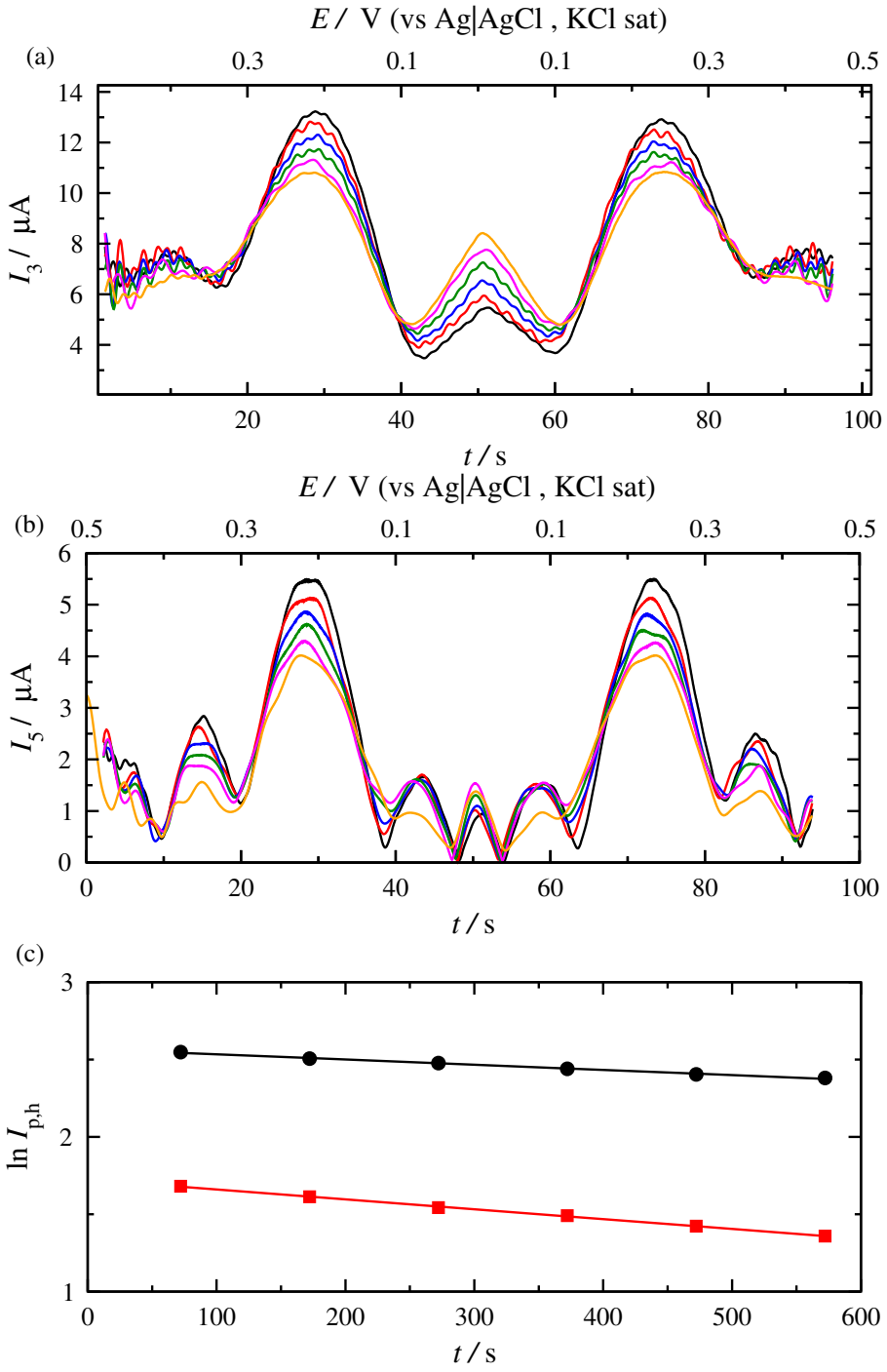

Figure 4.4.8: (a) 3rd and (b) 5th harmonic of Co-f-MWCNTs *Mt*LPMO9H mix on a glassy carbon electrode in an acetate buffer 500 mM pH 6, 500 mM at v = 10 mV s^{-1}, f = 5 Hz and A_0 = 250 mV in the presence of 0.04 g/L PASC at 30 °C. Cycles: 1st (black), 2nd (red), 3rd (blue), 4th (green), 5th (magenta) and 6th (orange) (c) Denendence of the Napierian logarithm of the oxidation peak ($\ln I_{p,h}$) against time (t) for 3rd (black circles) and 5th (red squares) harmonic.

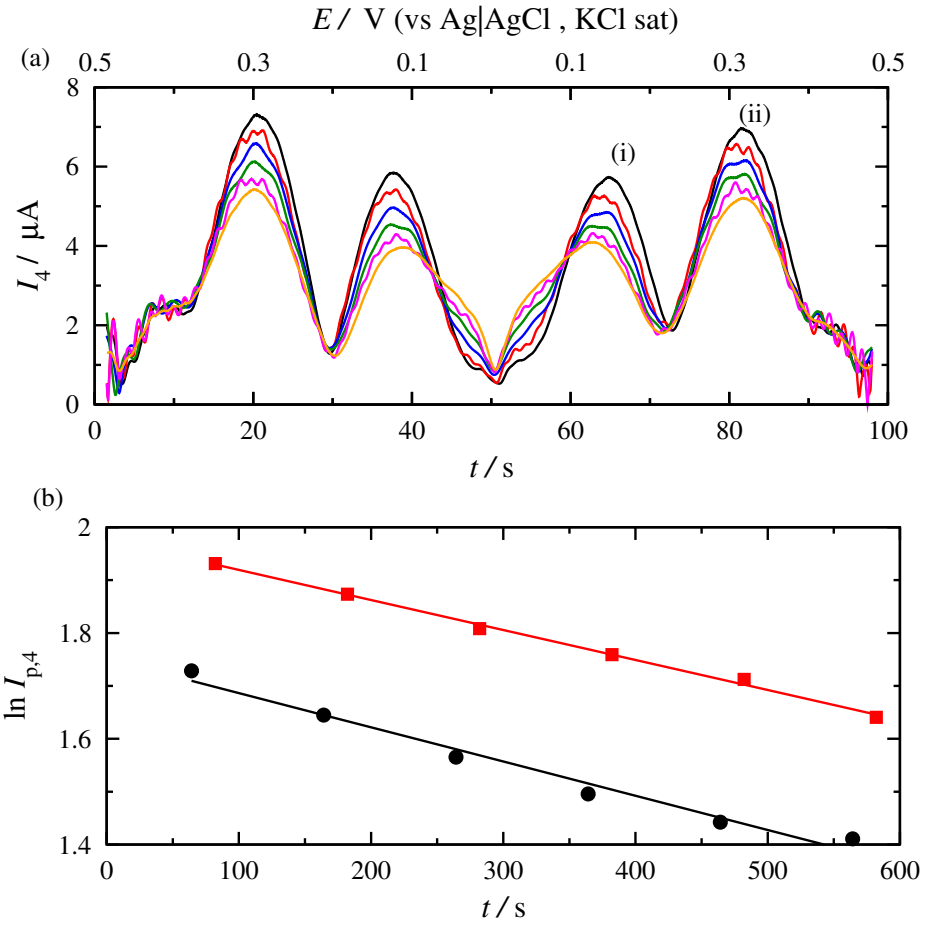

Figure 4.4.9: (a) 4th harmonic of Co-f-MWCNTs *Mt*LPMO9H mix on a glassy carbon electrode in an acetate buffer 500 mM pH 6, 500 mM at $v = 10$ mV s^{-1}, $f = 5$ Hz and $A_0 = 250$ mV in the presence of 0.04 g/L PASC at 30 °C. Cycles: 1st (black), 2nd (red), 3rd (blue), 4th (green), 5th (magenta) and 6th (orange) (b) Denendence of the Napierian logarithm of the oxidation peak i (black circles) and ii (red squares) ($\ln I_{p,h}$) against time (t).

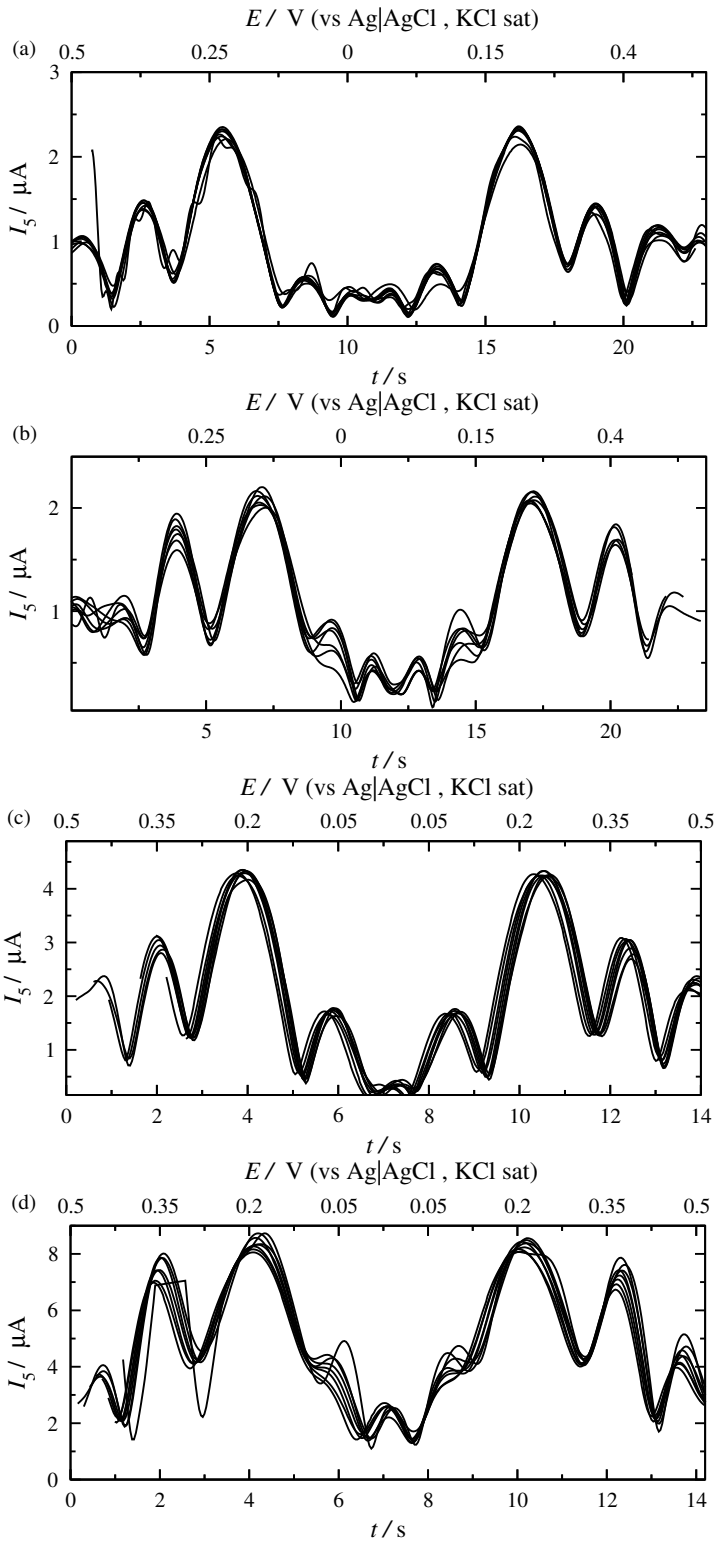

Figure 4.4.10: 5th harmonic of Co-f-MWCNTs *Mt*LPMO9H mix on a glassy carbon electrode in an acetate buffer 500 mM pH 6, 500 mM at $f = 5$ Hz and $A_0 = 250$ mV at (a) 35, (b) 40, (c) 45 and (b) at 50 °C for cycles 1 through 8. The scan rate v for 35 and 40 °C is 50 mV s^{-1} while for 45 and 50 °C is 75 mV s^{-1}.

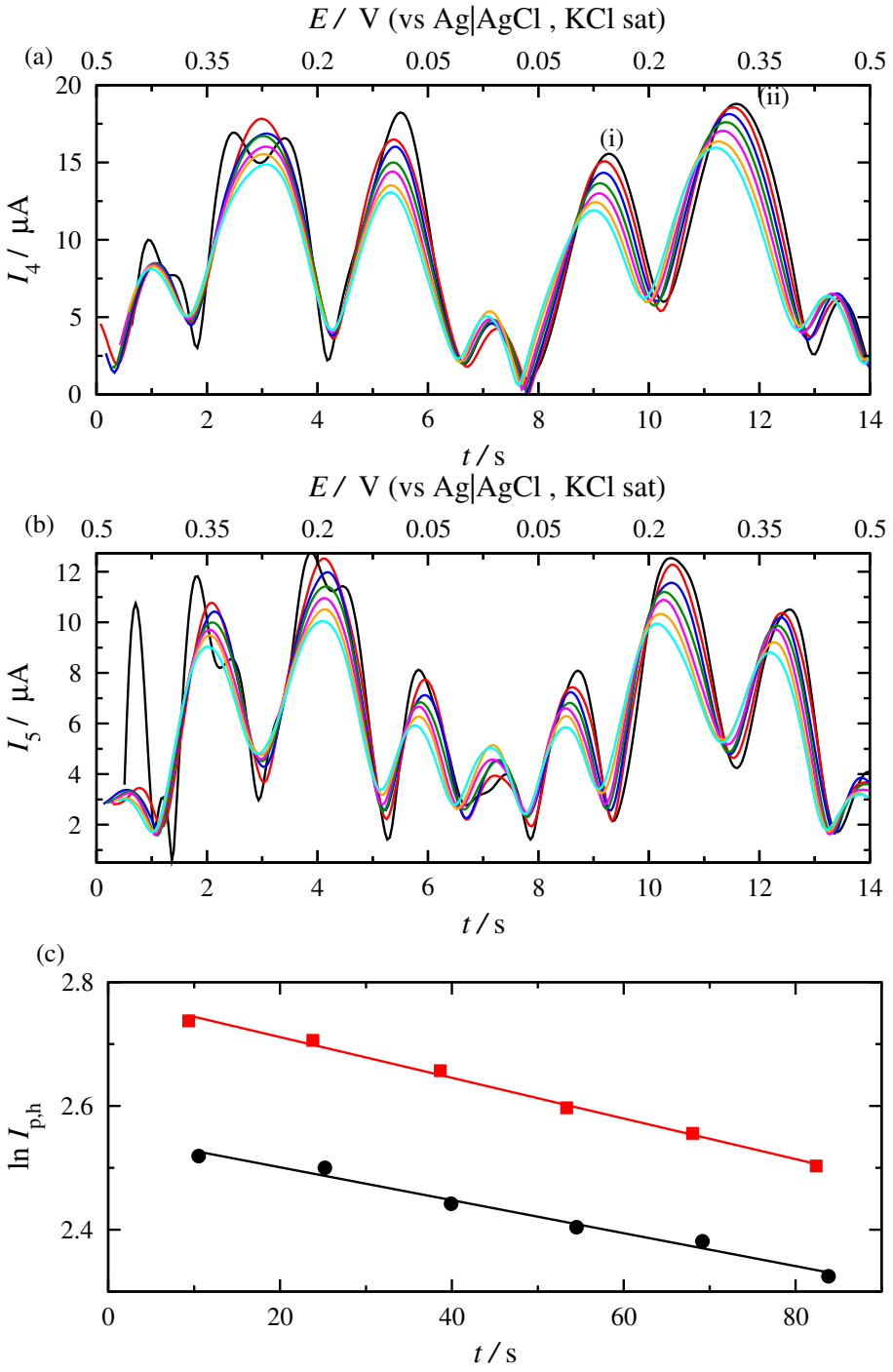

Figure 4.4.11: (a) 4th and (b) 5th harmonic of Co-f-MWCNTs *Mt*LPMO9H mix on a glassy carbon electrode in an acetate buffer 500 mM pH 6, 500 mM at $v = 75$ mV s^{-1}, $f = 5$ Hz and $A_0 = 250$ mV at 45 °C in the presence of 0.2 g/L PASC. Cycles: 1st (black), 2nd (red), 3rd (blue), 4th (green), 5th (magenta), 6th (orange) and 7th (cyan). (c) Denendence of the Napierian logarithm of the oxidation peak ($\ln I_{p,h}$) against time (t) for the 4th (red circles) and 5th harmonic (black squares).

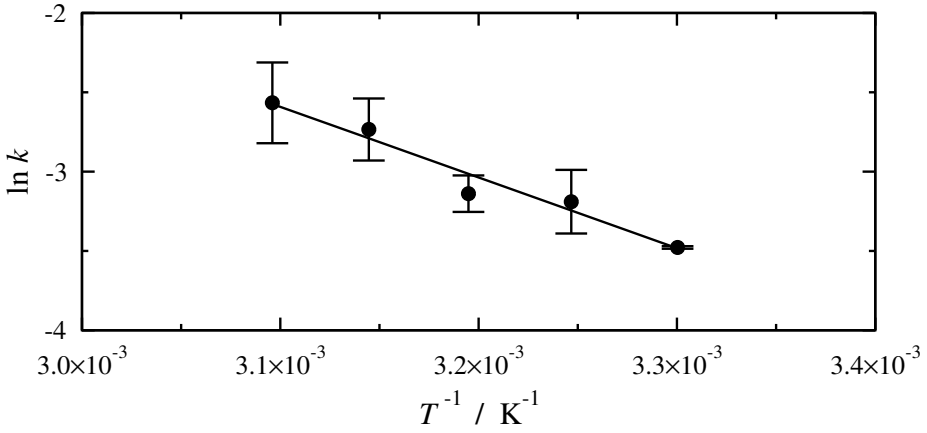

Figure 4.4.12: Napierian logarithm of the kinetic constant ($\ln k$) against the inverse temperature (T) for MtLPMO9H.

4.4.2 *Mt*LPMO9G

The next enzyme to be examined electrochemically is *Mt*LPMO9G. The initial concentration of this LPMO was 5.5 mg/L and again was mixed in a 8:2 ratio with Co-f-MWCNTs. Then, 2 μL of this mix were left to dry on the electrode surface. FTacV is again performed in a a pH 6 0.5 M acetate buffer for A_0 = 250 mV and different frequencies, f = 5, 2, 1, 0.5, 0.2 and 0.1 Hz. The anodic scan of the 5th harmonic of the immobilized LPMO is presented in Fig. 4.4.13(a) and the respective normalized with the frequency harmonics in Fig. 4.4.13(b).

Again in this case the reversibility is achieved for a frequency of 0.1 Hz with the difference here compared to *Mt*LPMO9H being that the peak ratio of the normalized harmonic for 5 Hz against the normalized reversible peak is lower, eventually leading to a lower value of k^0 but we shall get back to this later. It can also be observed that the interference appearing around the 0.4 V giving rise to the more anodic part of the harmonic at lower frequencies is also present in this enzyme.

Then the respective process has been followed for the 4th and the 6th harmonic as well in Fig. 4.4.14 and Fig 4.4.15 respectively. Again for the lower frequencies typical even harmonics of a reversible reaction can be observe. What is of interest here is that the saturation in the increase of the 6th harmonic is not achieved. This is due to the fact that as the order of the harmonic increases, it is more difficult to achieve reversibility and lower frequencies are needed to be employed.

Regarding now the k^0 value, the mean value extracted from the 4th and the 5th harmonic is 0.91 $\pm$ 0.1 s^{-1}, which is indeed lower than the one of *Mt*LPMO0H as predicted earlier.

After the k^0 extraction, the next step was again to examine the interaction of the enzyme with PASC. The T examined were 30, 35, 40, 45 and 50 °C. Regarding the other experimental conditions the frequency was 5 Hz and the amplitude 250 mV and the scan rate 50 mV s^{-1} for 30 and 35 °C, 62.5 mV s^{-1} for 45°C and 75 mV s^{-1} for 45 and 50 °C. The PASC concentration was 0.2 g/L in all the cases. An example for the decrease of the signal of the 4th, 5th and 6th harmonic as the cycles go by in the presence of PASC are presented in Fig. 4.4.16 at 50 °C. As one can observe, the decrease of the dominant peak in all three cases that the capacitance is eliminated is steady. A quantification of this decrease is presented in Fig 4.4.17. The dominant peak for the even harmonics is the second anodic dominant one. The slopes extracted are -0.0037, -0.0034 and -0.0037 for the 4th, 5th and 6th harmonic respectively indicating a good agreement between the harmonics.

The kinetic constant values extracted from each harmonic are presented in Table 4.4.2.

An attempt for an Arrhenius type plot was again made in Fig. 4.4.18 where indeed a linear dependence is observed when the Napierian logarithm of the kinetic constant ($\ln k$) is plotted against the inverse temperature (T). From the slope the activation energy can be estimated at 36.1 kJ/mol.

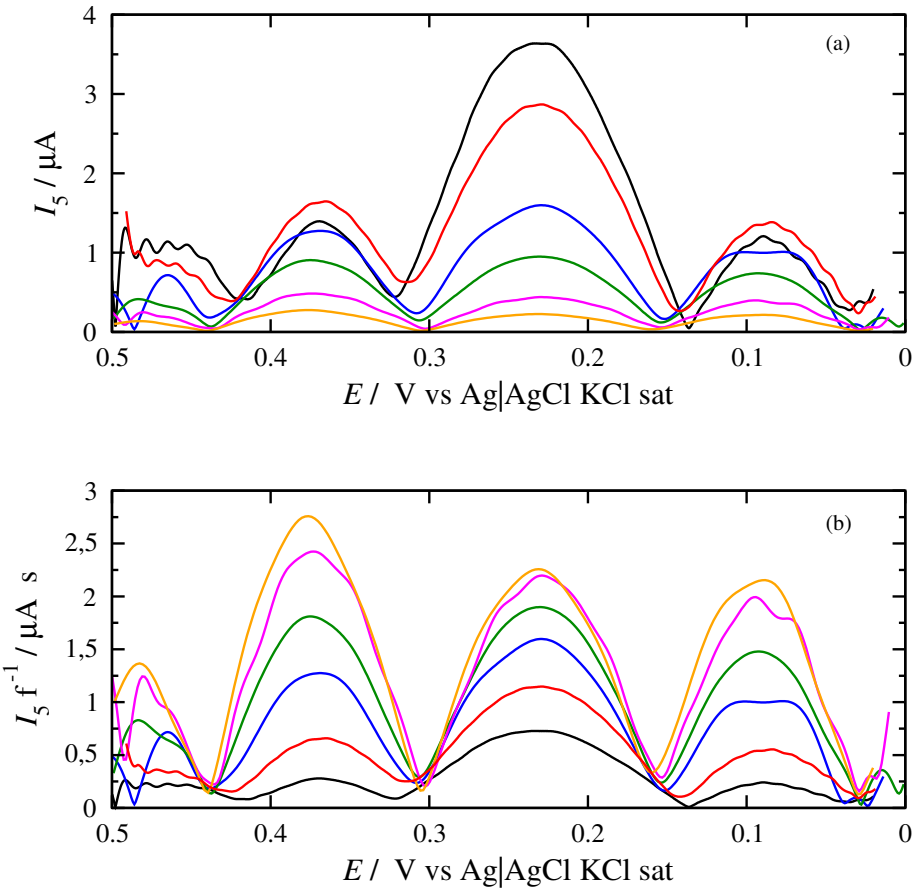

Figure 4.4.13: (a) 5th harmonic (b) normalized 5th harmonic of Co-f-MWCNTs *Mt*LPMO9G mix on a glassy carbon electrode in a pH 6 0.5 M acetate buffer for A_0 = 250 mV and f = 5 (black), 2.5 (red), 1 (blue), 0.5 (green), 0.2 (orange) and 0.1 Hz (magenta).

Table 4.8: Kinetic constant k of PASC binding to *Mt*LPMO9G for different temperatures.

T (°C)	k (L g^{-1} s^{-1})
30	0.0071 ± 0.0007
35	0.009 ± 0.0008
40	0.0118 ± 0.0002
45	0.0145 ± 0.006
50	0.0173 ± 0.002

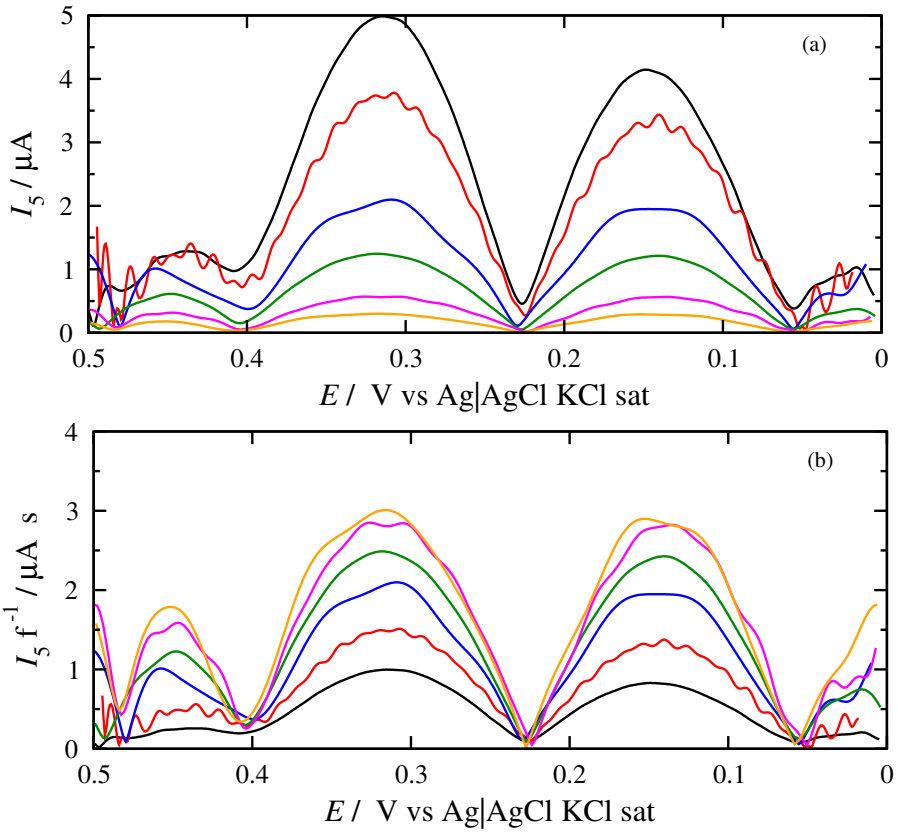

Figure 4.4.14: (a) 4th harmonic (b) normalized 4th harmonic of Co-f-MWCNTs *Mt*LPMO9G mix on a glassy carbon electrode in a pH 6 0.5 M acetate buffer for $A_0 = 250$ mV and $f = 5$ (black), 2 (red), 1 (blue), 0.5 (green), 0.2 (orange) and 0.1 Hz (mangenta).

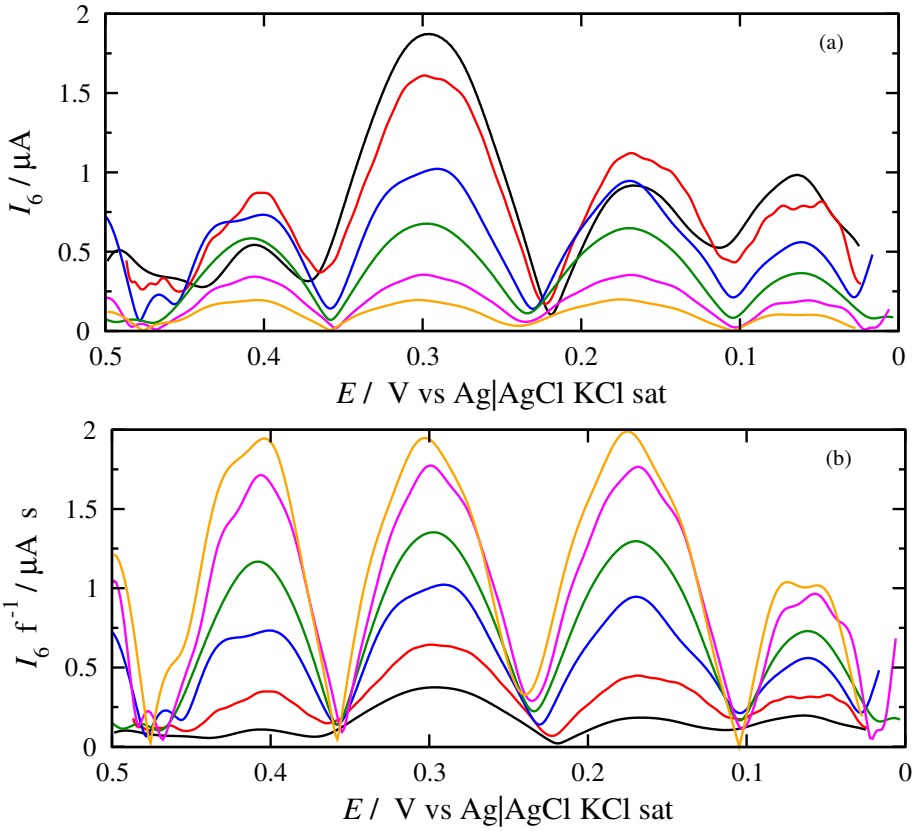

Figure 4.4.15: (a) 6th harmonic (b) normalized 6th harmonic of Co-f-MWCNTs *Mt*LPMO9G mix on a glassy carbon electrode in a 0.5 M acetate buffer for $A_0 = 250$ mV and $f = 5$ (black), 2 (red), 1 (blue), 0.5 (green), 0.2 (orange) and 0.1 Hz (magenta).

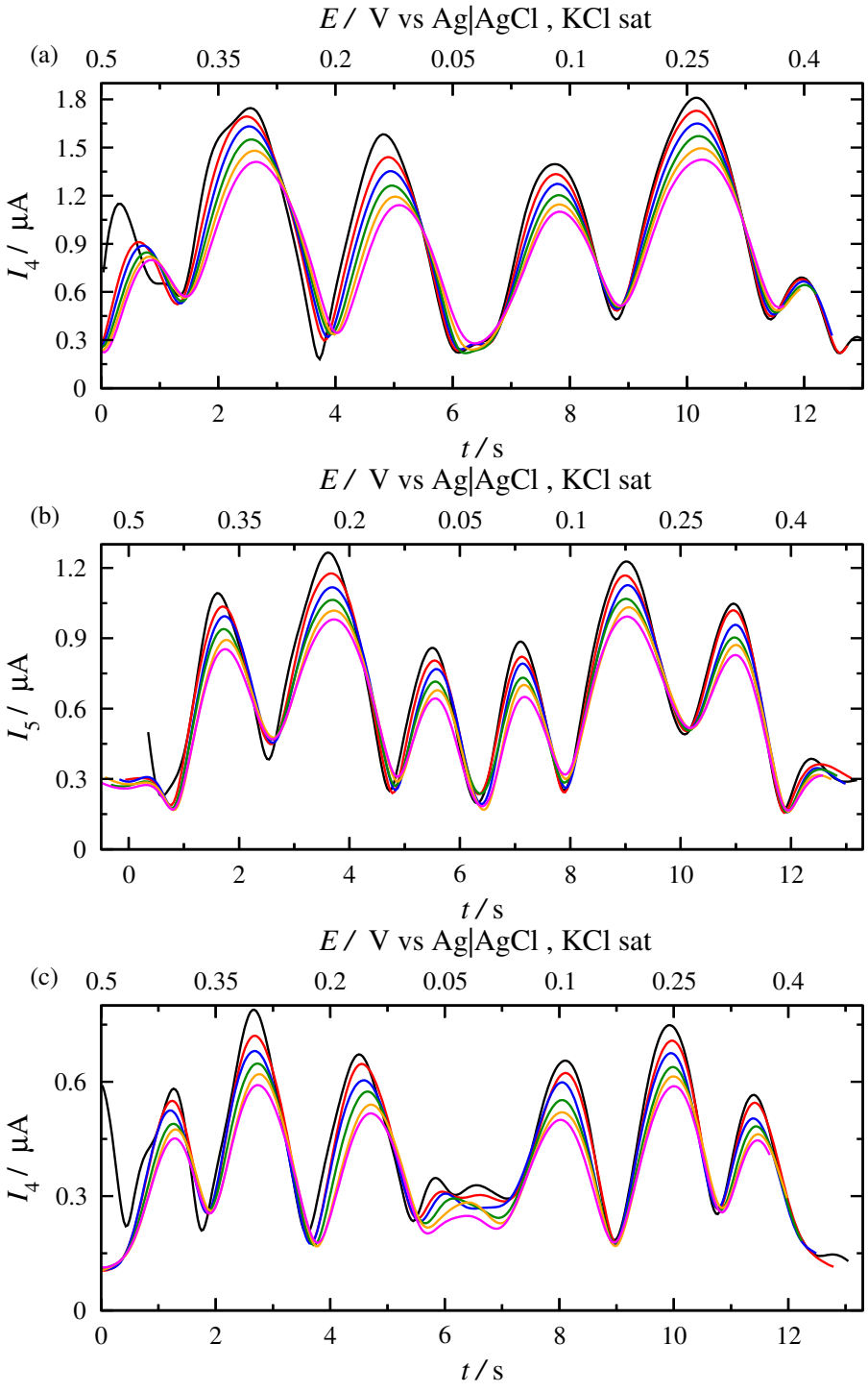

Figure 4.4.16: (a)4th and (b) 5th harmonic and (c) 6th of Co-f-MWCNTs *Mt*LPMO9G mix on a glassy carbon electrode in an acetate buffer 500 mM pH 6, 500 mM at v = 75 mV s^{-1}, f = 5 Hz and A_0 = 250 mV at 50 °C and 0.2 g/L PASC. Cycles: 1st (black), 2nd (red), 3rd (blue), 4th (green), 5th (magenta), 6th (orange) and 7th (cyan).

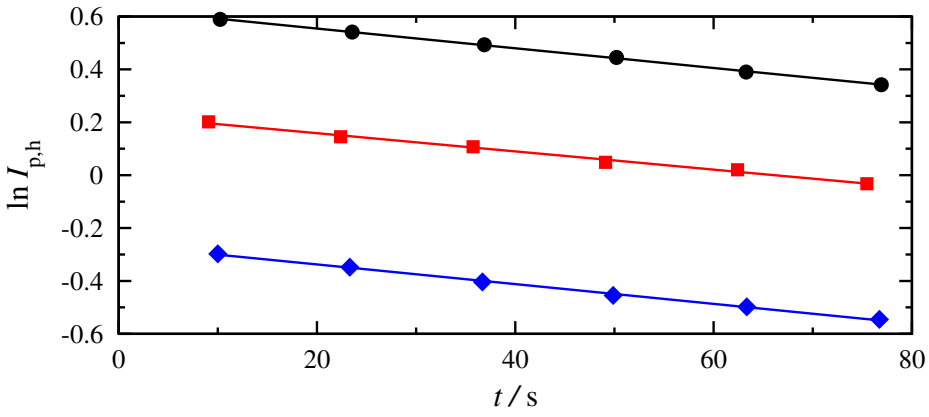

Figure 4.4.17: Denendence of the Napierian logarithm of the oxidation peak ($\ln I_{p,h}$) against time (t) for the 4th (black circles), 5th (red squares) and 6th harmonic (blue diamonds) of *Mt*LPMO9G at 50°C.

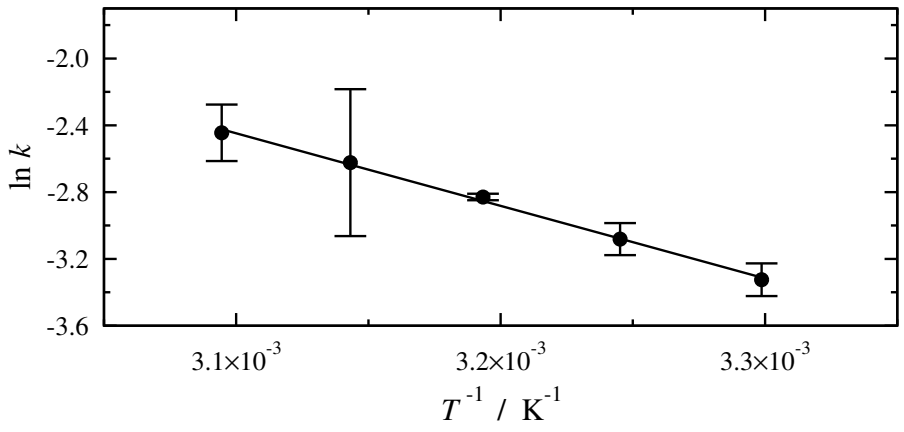

Figure 4.4.18: Napierian logarithm of the kinetic constant ($\ln k$) against the inverse temperature (T) for *Mt*LPMO9G.

Table 4.9: Kinetic constant k of PASC binding to *Fo*LPMO9 for different temperatures.

T (°C)	k (L g^{-1} s^{-1})
30	0.0042 ± 0.00009
35	0.0097 ± 0.001
40	0.011 ± 0.003
45	0.0159 ± 0.002

4.4.3 *Fo*LPMO9

The last LPMO to be examined in this work with the new immobilization method was *Fo*LPMO9. The same procedure was followed as in the two previous enzymes, with the main difference being in the Co-f-MWCNTs matrix - *Mt*LPMO9G ratio used 1:1.[37]

The anodic scan of the 5th harmonics of the immobilized *Fo*LPMO9 are presented in Fig. 4.4.19(a) along with the normalized harmonics in Fig. 4.4.19(b) for $A_0 = 250$ mV and $f = 5$, 2, 1 and 0.5 Hz.

The apparent formal potential extracted from the dominant peak of the 5th harmonic is at 210 mV. Regarding the extraction of the k^0 value from the normalized 5th harmonics, the reversibility is achieved for $f = 0.5$ Hz and the value is estimated at 12.3 s^{-1}. This value is higher than the one extracted for the two previous LPMOs. This is probably due to this enzyme not being glycosylated and having a low molecular weight, making the access to the active site easier than in the other two cases.

Regarding its interaction with PASC, it was studied at 30, 35, 40 and 45 °C at $A_0 = 250$ mV and $f = 5$. The scan rates used were 50 mV s^{-1} for 30 and 35 °C, while 75 mV s^{-1} for 40 and 45 °C. The PASC concentration was again 0.2 g/L in all the experiments.

An example of the decrease of the 5th harmonic as the cycles go by at 35 °C can be found in Fig. 4.4.20(a) while the quantification of the decrease is presented in Fig 4.4.20(b). The extracted kinetic consntants can be found in Table 4.4.3 while the activation energy was estimated at 67.6 kJ mol^{-1} from Fig. 4.4.20.

[37] *Fo*LPMO9 showed a lack of affinity during the purification with the cobalt ion column, thus in an attempt for a more stable result, higher concentration of the matrix was used.

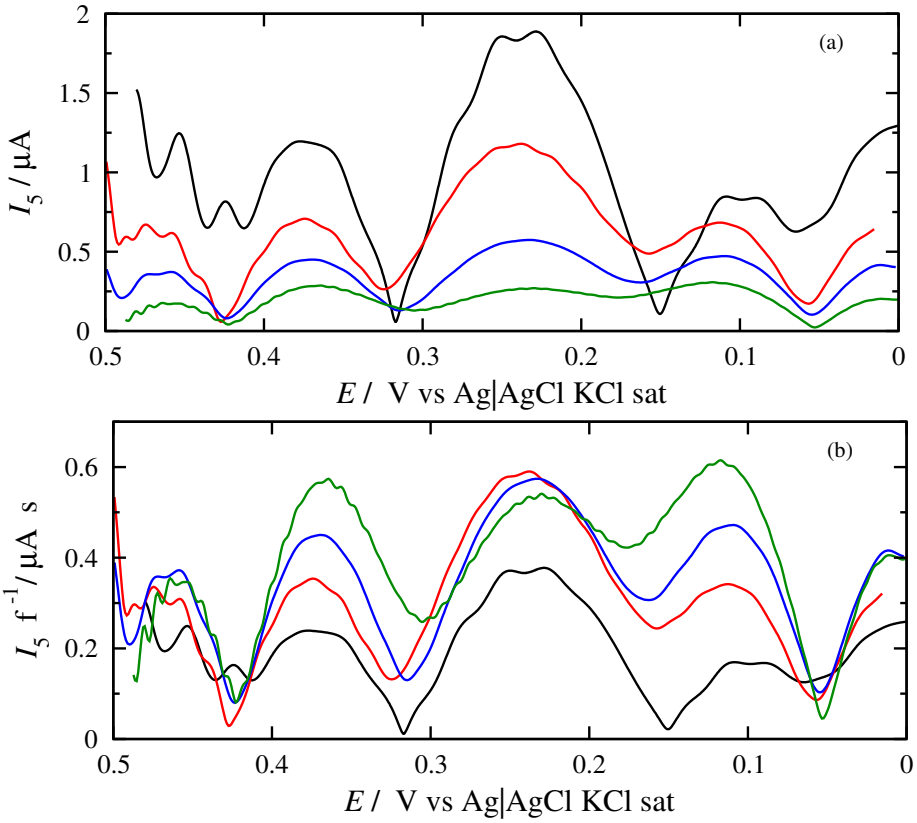

Figure 4.4.19: (a) 5th harmonic (b) normalized 5th harmonic of Co-f-MWCNTs *Mt*LPMO9G mix on a glassy carbon electrode in a 0.5 M acetate buffer for $A_0 = 250$ mV and $f = 5$ (black), 2.5 (red), 1 (blue) and 0.5 (green).

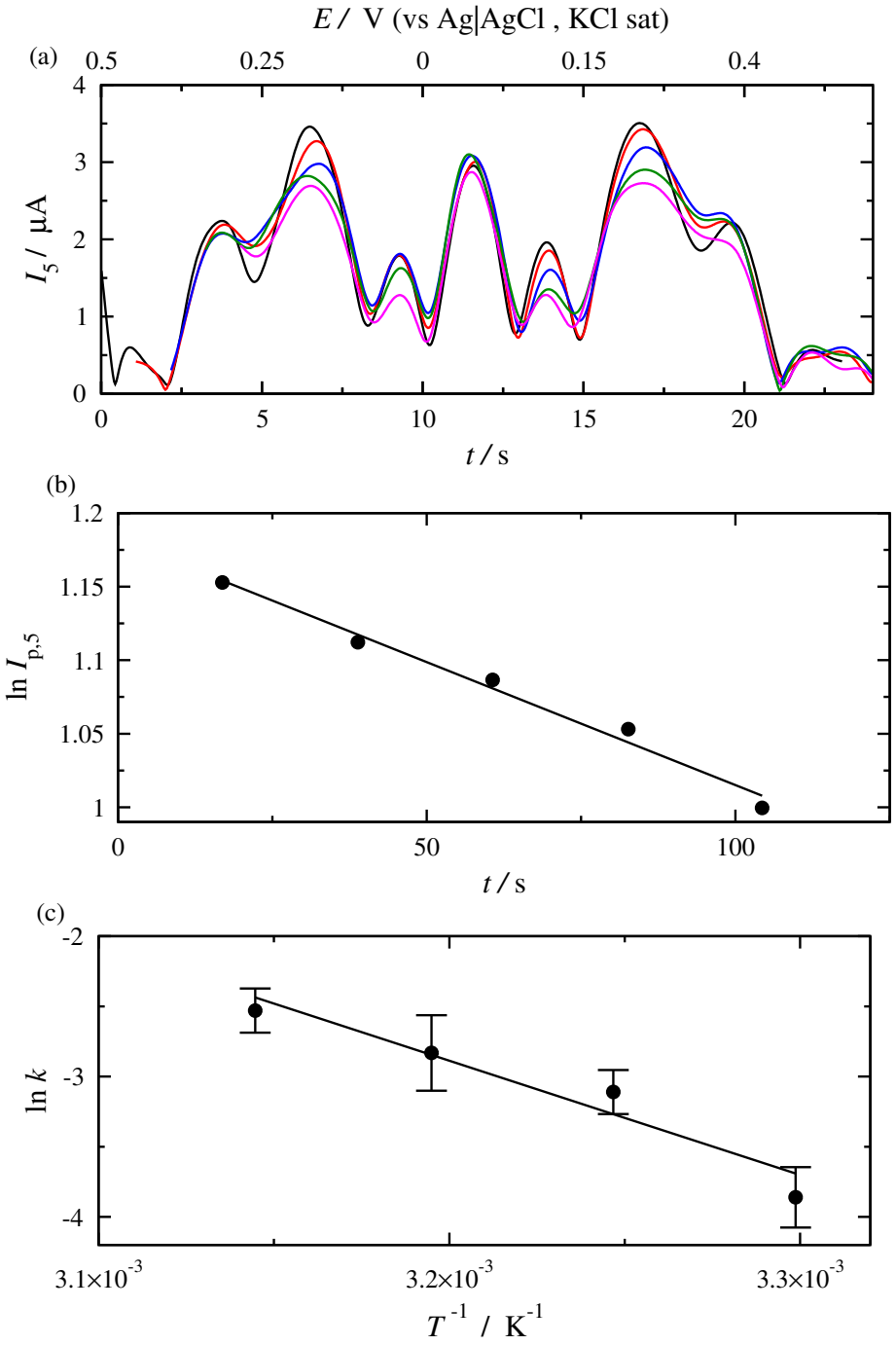

Figure 4.4.20: (a) 5th harmonic of Co-f-MWCNTs *Fo*LPMO9 mix on a glassy carbon electrode electrode in an acetate buffer 500 mM pH 6, 500 mM at $v = 75$ mV/s, $f = 5$ Hz and $A_0 = 250$ mV at 35 °C. Cycles: 1st (black), 2nd (red), 3rd (blue), 4th (green), 5th (magenta). (b) Denendence of the Napierian logarithm of the oxidation peak ($\ln I_{\mathrm{p},5}$) against time (t) (c) Napierian logarithm of the kinetic constant ($\ln k$) against the inverse temperature (T).

Bibliography

[1] C. Moreau, S. Tapin-Lingua, S. Grisel, I. Gimbert, S. Le Gall, V. Meyer, M. Petit-Conil, J.-G. Berrin, B. Cathala, and A. Villares. Lytic polysaccharide monooxygenases (LPMOs) facilitate cellulose nanofibrils production. *Biotechnol. Biofuels*, 12(1):1–13, 2019.

[2] Z. Forsberg, A. A. Stepnov, G. Kruge Nærdal, G. Klinkenberg, and V. G.H. Eijsink. Engineering lytic polysaccharide monooxygenases (LPMOs). Method. Enzymol. 2020.

[3] M. Dimarogona, E. Topakas, L. Olsson, and P. Christakopoulos. Lignin boosts the cellulase performance of a GH-61 enzyme from *Sporotrichum Thermophile*. *Bioresour. Technol.*, 110:480 – 487, 2012.

[4] A. Karnaouri, M. N. Muraleedharan, M. Dimarogona, E. Topakas, U. Rova, M. Sandgren, and P. Christakopoulos. Recombinant expression of thermostable processive *Mt*EG5 endoglucanase and its synergism with *Mt*LPMO from *Myceliophthora thermophila* during the hydrolysis of lignocellulosic substrates. *Biotechnol. Biofuels*, 10(1):126, 2017.

[5] M. Frommhagen, S. Sforza, A. H. Westphal, J. Visser, S. W. A. Hinz, M. J. Koetsier, W. J. H. van Berkel, H. Gruppen, and M. A. Kabel. Discovery of the combined oxidative cleavage of plant xylan and cellulose by a new fungal polysaccharide monooxygenase. *Biotechnol. Biofuels*, 8(1):101, 2015.

[6] M. Frommhagen, M.J. Koetsier, A.H. Westphal, J. Visser, S.W.A. Hinz, J.-P. Vincken, W.J.H. Van Berkel, M.A. Kabel, and H. Gruppen. Lytic polysaccharide monooxygenases from *Myceliophthora thermophila* C_1 differ in substrate preference and reducing agent specificity. *Biotechnol. Biofuels*, 9(1), 2016.

[7] M. Frommhagen, A. H. Westphal, R. Hilgers, M. J. Koetsier, S. W. A. Hinz, J. Visser, H. Gruppen, W. J. H. van Berkel, and M. A. Kabel. Quantification of the catalytic performance of C_1-cellulose-specific lytic polysaccharide monooxygenases. *Appl. Microbiol. Biotechnol.*, 102(3):1281–1295, 2018.

[8] P. Sun, M. Frommhagen, M. Kleine Haar, G. van Erven, E. J. Bakx, W. J. H. van Berkel, and M. A. Kabel. Mass spectrometric fragmentation patterns discriminate C_1- and C_4-oxidised cello-oligosaccharides from their non-oxidised and reduced forms. *Carbohydr. Polym.*, 234:115917, 2020.

[9] M. A .S. Kadowaki, A. Varnai, J. K. Jameson, A. E. T. Leite, A. J. Costa-Filho, P. S. Kumagai, R. A. Prade, I. Polikarpov, and V. G. H. Eijsink. Functional characterization of a lytic polysaccharide monooxygenase from the thermophilic fungus *Myceliophthora thermophila*. *PloS one*, 13(8):e0202148, 2018.

[10] G. R. Hemsworth, B. Henrissat, G. J. Davies, and P. H. Walton. Discovery and characterization of a new family of lytic polysaccharide monooxygenases. *Nat. Chem. Biol.*, 10(2):122–126, 2014.

[11] V. V. Vu, W. T. Beeson, E. A. Span, E. R. Farquhar, and M. A. Marletta. A family of starch-active polysaccharide monooxygenases. *PNAS*, 111(38):13822–13827, 2014.

[12] L. L. Leggio, T. J. Simmons, J. C. N. Poulsen, K. E. H. Frandsen, G. R. Hemsworth, M. A. Stringer, P. Von Freiesleben, M. Tovborg, K. S. Johansen, L. De Maria, P. V. Harris, C. L. Soong, P. Dupree, T. Tryfona, N. Lenfant, B. Henrissat, G. J. Davies, and P. H. Walton. Structure and boosting activity of a starch-degrading lytic polysaccharide monooxygenase. *Nat. Commun.*, 6(1):1–9, 2015.

[13] L. Nekiunaite, T. Isaksen, G. Vaaje-Kolstad, and M. Abou Hachem. Fungal lytic polysaccharide monooxygenases bind starch and β-cyclodextrin similarly to amylolytic hydrolases. *FEBS Lett.*, pages 2737–2747, 2016.

[14] S. J Muderspach, T. Tandrup, K. E. H. Frandsen, G. Santoni, J. C. N. Poulsen, and L. L. Leggio. Further structural studies of the lytic polysaccharide monooxygenase *Ao*AA13 belonging to the starch-active AA13 family. *Amylase*, 3(1):41–54, 2019.

[15] M. Couturier, S. Ladevèze, G. Sulzenbacher, L. Ciano, M. Fanuel, C. Moreau, A. Villares, B. Cathala, F. Chaspoul, K.E. Frandsen, A. Labourel, I. Herpoël-Gimbert, S. Grisel, M. Haon, N. Lenfant, H. Rogniaux, D. Ropartz, G.J. Davies, M.-N. Rosso, P.H. Walton, B. Henrissat, and J.-G. Berrin. Lytic xylan oxidases from wood-decay fungi unlock biomass degradation. *Nat. Chem. Biol.*, 14(3):306–310, 2018.

[16] F. Sabbadin, G. R. Hemsworth, L. Ciano, B. Henrissat, P. Dupree, T. Tryfona, R. D. S. Marques, S. T. Sweeney, K. Besser, L. Elias, G. Pesante, Y. Li, A. A. Dowle, R. Bates, L. D. Gomez, R. Simister, G. J. Davies, P. H. Walton, N. C. Bruce, and S. J. McQueen-Mason. An ancient family of lytic polysaccharide monooxygenases with roles in arthropod development and biomass digestion. *Nat. Commun.*, 9(1):756, February 2018.

[17] C. Filiatrault-Chastel, D. Navarro, M. Haon, S. Grisel, I. Herpoël-Gimbert, D. Chevret, M. Fanuel, B. Henrissat, S. Heiss-Blanquet, A. Margeot, and J.G. Berrin. AA16, a new lytic polysaccharide monooxygenase family identified in fungal secretomes. *Biotechnol. Biofuels*, 12(1):1–15, 2019.

[18] Z. Forsberg, A. A. Stepnov, G. K. Nærdal, G. Klinkenberg, and V. G. H. Eijsink. Engineering lytic polysaccharide monooxygenases (LPMOs). 2020.

[19] B. Danneels, M. Tanghe, H.-J. Joosten, T. Gundinger, O. Spadiut, I. Stals, and T. Desmet. A quantitative indicator diagram for lytic polysaccharide monooxygenases reveals the role of aromatic surface residues in *Hj*LPMO9A regioselectivity. *PloS one*, 12(5):e0178446, 2017.

[20] L. Bertini, R. Breglia, M. Lambrughi, P. Fantucci, L. De Gioia, M. Borsari, M. Sola, C.A. Bortolotti, and M. Bruschi. Catalytic mechanism of fungal lytic polysaccharide monooxygenases investigated by first-principles calculations. *Inorg. Chem.*, 57(1):86–97, 2018.

[21] P. H. Walton and G. J. Davies. On the catalytic mechanisms of lytic polysaccharide monooxygenases. *Curr. Opin. Chem. Biol.*, 31:195 – 207, 2016.

[22] T. C. Tan, D. Kracher, R. Gandini, C. Sygmund, R. Kittl, D. Haltrich, B. M. Hällberg, R. Ludwig, and C. Divne. Structural basis for cellobiose dehydrogenase action during oxidative cellulose degradation. *Nat. Commun.*, 6:7542, 2015.

[23] J. S. M. Loose, Z. Forsberg, D. Kracher, S. Scheiblbrandner, R. Ludwig, V. G. H. Eijsink, and G. Vaaje-Kolstad. Activation of bacterial lytic polysaccharide monooxygenases with cellobiose dehydrogenase. *Protein Sci.*, 25(12):2175–2186, 2016.

[24] G. Courtade, R. Wimmer, Å. K. Røhr, M. Preims, A. K. G. Felice, M. Dimarogona, G. Vaaje-Kolstad, M. Sørlie, M. Sandgren, R. Ludwig, and V. G. H. Eijsink. Interactions of a fungal lytic polysaccharide monooxygenase with β-glucan substrates and cellobiose dehydrogenase. *PNAS*, 113(21):5922–5927, 2016.

[25] S. Garajova, Y. Mathieu, M. R. Beccia, C. Bennati-Granier, F. Biaso, M. Fanuel, D. Ropartz, B. Guigliarelli, E. Record, H. Rogniaux, Henrissat B., and J. G. Berrin. Single-domain flavoenzymes trigger lytic polysaccharide monooxygenases for oxidative degradation of cellulose. *Sci. Rep.*, 6:28276, 2016.

[26] B. Westereng, D. Cannella, J. W. Agger, H. Jørgensen, M. L. Andersen, V. G. H. Eijsink, and C. Felby. Enzymatic cellulose oxidation is linked to lignin by long-range electron transfer. *Sci. Rep.*, 5(1):1–9, 2015.

[27] J. S. Rohrer. High-performance anion-exchange chromatography with pulsed amperometric detection for the determination of oligosaccharides in foods and agricultural products. ACS Publications, 2003.

[28] J. S. Rohrer, L. Basumallick, and D. Hurum. High-performance anion-exchange chromatography with pulsed amperometric detection for carbohydrate analysis of glycoproteins. *Biochemistry (Moscow)*, 78(7):697–709, 2013.

[29] D. Kotnik, M. Novič, W. R. LaCourse, and B. Pihlar. Cathodic re-activation of the gold electrode in pulsed electrochemical detection of carbohydrates. *J. Electroanal. Chem.*, 663(1):30–35, 2011.

[30] B. Westereng, J. W. Agger, S. J. Horn, G. Vaaje-Kolstad, F. L. Aachmann, Y. H Stenstrøm, and V. G. Eijsink. Efficient separation of oxidized cello-oligosaccharides generated by cellulose degrading lytic polysaccharide monooxygenases. *J. Chromatogr. A*, 1271(1):144–152, 2013.

[31] B. Westereng, M. Ø. Arntzen, F. L. Aachmann, A. Várnai, V. G. H Eijsink, and J. W. Agger. Simultaneous analysis of C_1 and C_4 oxidized oligosaccharides, the products of lytic polysaccharide monooxygenases acting on cellulose. *J. Chromatogr. A*, 1445:46–54, 2016.

[32] D. Wang, J. Li, A. C. Y. Wong, F. L. Aachmann, and Y. S. Y. Hsieh. A colorimetric assay to rapidly determine the activities of lytic polysaccharide monooxygenases. *Biotechnol. Biofuels*, 11(1):215, 2018.

[33] E. Breslmayr, M. Hanžek, A. Hanrahan, C. Leitner, R. Kittl, B. Šantek, C. Oostenbrink, and R. Ludwig. A fast and sensitive activity assay for lytic polysaccharide monooxygenase. *Biotechnol. Biofuels*, 11(1):1–13, 2018.

[34] E. Breslmayr, S. Daly, A. Požgajčić, H. Chang, T. Rezić, C. Oostenbrink, and R. Ludwig. Improved spectrophotometric assay for lytic polysaccharide monooxygenase. *Biotechnol. Biofuels*, 12(1):283, 2019.

[35] P. Muslant, A. Gatignol, M. Dalens., and G. Tiraby. Phleomycin resistance as a dominant selectable marker in CHO cells. *Somatic Cell and Molecular Genetics volume*, 14:243–252, 1988.

[36] M. Baron, J. P. Reynes, D. Stassi, and G. Tiraby. A selectable bifunctional β-galactosidase: phleomycin-resistance fusion protein as a potential marker for eukaryotic cells. *Gene*, 114(2):239 – 243, 1992.

[37] H. R. Waterham, M. E. Digan, P. J. Koutz, S. V. Lair, and J. M. Cregg. Isolation of the *Pichia pastoris* glyceraldehyde-3-phosphate dehydrogenase gene and regulation and use of its promoter. *Gene*, 186(1):37 – 44, 1997.

[38] R. Daly and M. T. Hearn. Expression of heterologous proteins in *Pichia pastoris*: a useful experimental tool in protein engineering and production. *J Mol Recognit.*, 18(2):119–38, 2005.

[39] C. Moreau, S. Tapin-Lingua, S. Grisel, I. Gimbert, S. Le Gall, V. Meyer, M. Petit-Conil, J.G. Berrin, B. Cathala, and A. Villares. Lytic polysaccharide monooxygenases (LPMOs) facilitate cellulose nanofibrils production. *Biotechnol Biofuels*, 12(2):156, 2019.

5. An electrochemical interpretation of the interaction between LPMOs and potential electron donors

A part of this work focused on understanding the interactions of LPMOs with electron donors and the electrochemical characterization of these donors. It is reminded at this point that in order for the catalytic cycle of an LPMO to start, the enzyme needs to be reduced by an external electron donor. This donor has to be characterized by a lower formal potential of that of the LPMO in order for the reduction to be feasible.

The first step was to electrochemically study ascorbic acid, which is a universally accepted donor for LPMOs. Based on the prevailing scenarios concerning the oxidation of ascorbic acid on an electrode surface, cyclic volammetry, convolution voltammetry and FTacV were employed. The experimental results were then compared to computational ones in order to get a better grasp of what could be the most plausible scenario of the voltammographic pattern observed.

Then, based on the reactivity of as electron donors to *Mt*LPMO9H at a pH value of 6 at 50°C, pyrogallol, gallic acid, methyl gallate, caffeic acid, sinapic acid, syringealdehyde, vanillin, ferulic acid, *p*-coumaric acid, vanillic acid and *p*-hydroxybenzoic acid were examined with cyclic voltammetry and FTacV. The voltammetric results together with data and mechanisms proposed in the literature were exploited and a pattern in the behavior of the compounds regarding their reactivity with the LPMO is interpreted. Moreover the interaction of *Mt*LPMO9H with lignin from wheat straw as an electron donor is examined and an interpretation of its interaction with the enzyme is given.

Experimental

*Mt*LPMO9H was incubated with various potential electron donors at 50° C under stirring (1000 rpm), using 1 % w/v PASC as a substrate. The enzyme to substrate ratio was 50 mg/g substrate and the final electron donor concentration was 2 mM. Two sets of blank reactions were also incubated, in the absence of either the electron donor or the enzyme. The analysis of the reaction products was performed using a high-performance anion-exchange chromatography (HPAEC), using a CarboPac PA-1

(4×250 mm, Dionex) column with a pulsed amperometric detector (PAD) equipped with a gold electrode. 25 μL of samples were injected and the reaction products were eluted at 1 mL/min with initial conditions set to 0.1 M NaOH (100% eluent A). This step was succeeded by a linear gradient toward 10% eluent B (1 M NaOAc in 0.1 M NaOH) after 10 min and 30% B after 25 min; a 5 min exponential gradient to 100% B followed. Between separate injections, a 10 min stabilization step (100% A) was interjected. Integration of chromatograms was performed using Chromeleon 6.0 software.

Voltammetric experiments were performed in a single compartment three electrode cell consisting of a disk glassy carbon electrode (GC) with a surface of 0.0706 cm^2 as working electrode, a 1.6 mm diameter Pt coated titanium rod as a counter electrode, and an Ag|AgCl, KCl sat. reference electrode (+0.197 V vs NHE). As a supporting electrolyte sodium acetate buffer was used. The sodium acetate was purchased by Panreac and the acetic acid by Chem-Lab NV.

Voltammetric measurements were performed by a PAR 263A Potentiostat connected to an AFG 5101 Tektronix programmable arbitrary function generator. The temperature of the cell was kept at a specific value during measurement with the use of a thermostated bath (FALC WB-MD5). The temperature of the cell was recorded during the measurement, in order to assure that it remained constant.

Before each measurement the glassy carbon electrode was polished on a cloth with the use of a 0.3 μm and 0.05 μm Al_2O_3. The electrode was then washed with distilled water and subsequently sonicated in distilled water for 5 min. After the sonication, the electrode was again washed with distilled water.

All solutions were freshly prepared before each set of experiments.

5.1 HPAEC-PAD

The elution patterns of the reactions for the different potential electron donors are presented in Fig. 5.1.1. They are divided into two categories. The ones that gave non oxidized and oxidized products (Fig. 5.1.1(a)) and the ones that did not (Fig. 5.1.1(b)). Taking a close look at these elution patterns one can observe that ascorbic acid, caffeic acid, gallic acid methyl gallate and pytogallol interacted rather effectively with the LPMO giving intense peaks for both C_1 and C_4 oxidized products, while sinapic acid gave evidently less intense peaks. On the other hand, the elution patters where *p*-coumaric acid, ferulic acid, *p*-hydroxybenzoic acid, syringaldehyde, vanillic acid and vanillin were used as electron donors gave no detectable oxidized products, signifying very restricted to no reactivity towards the *Mt*LPMO9H.

For the compounds that succeeded as electron donors, a quantitative comparison shall be made regarding the non oxidized, the C_1 and the C_4 oxidized products that resulted from the respective reactions with the LPMOs. This comparison is made based on the integration of the surface area beneath the peaks corresponding to the respective oxidized products. The results are presented in Table 5.1.

Summing up the results of the HPAEC-PAD analysis, nine different monophenols, one dihydroxybenzene (caffeic acid), three trihydroxybenzenes (gallic acid, pyrogallol and methyl-gallate) and ascorbic acid were evaluated for their ability to provide elec-

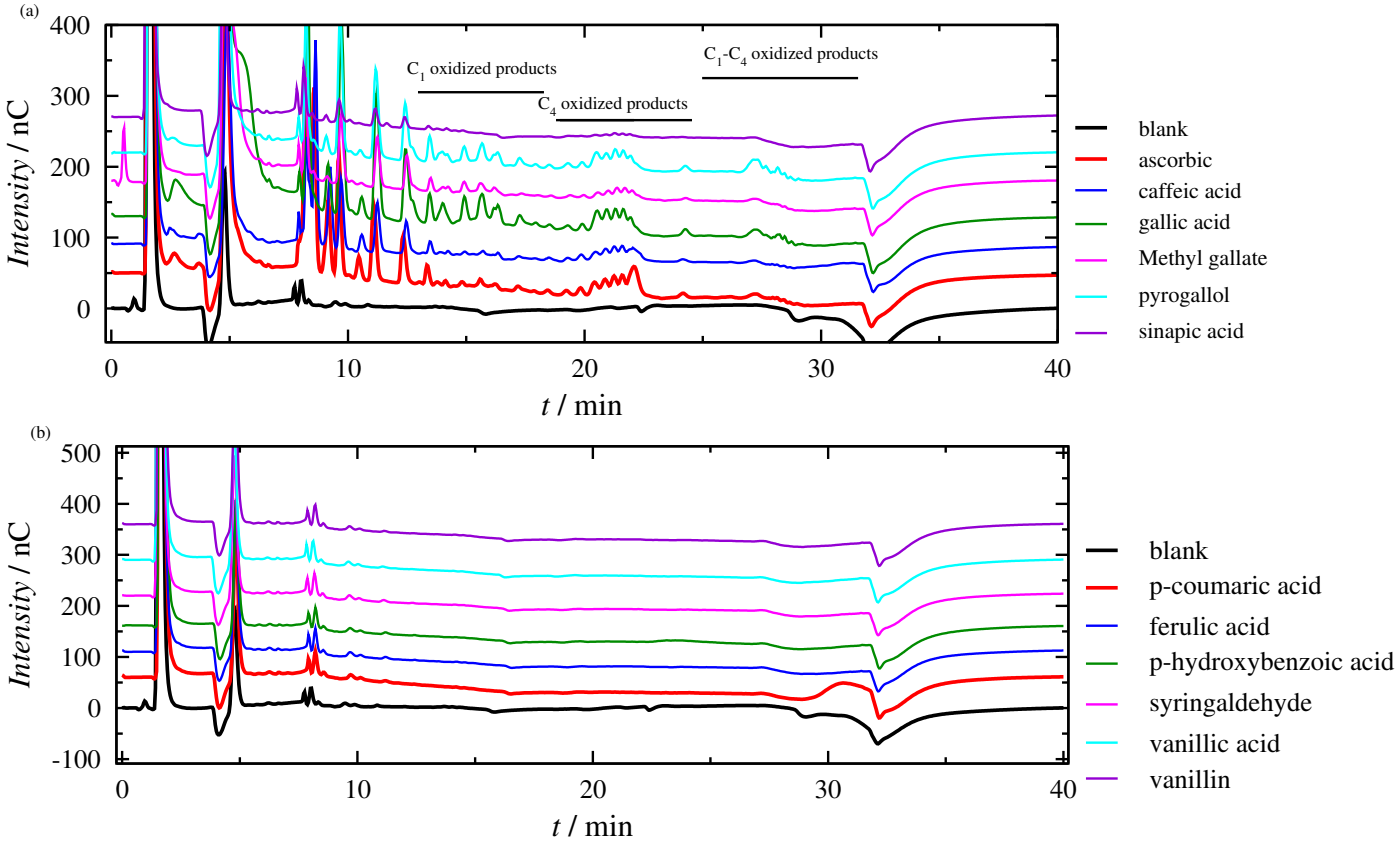

Figure 5.1.1: HPAEC-PAD elution patterns of PASC after a 14 h incubation with *Mt*LPMO9H (50 mg/g substrate) for different electron donors. (a) blank (black), ascorbic acid (red), caffeic acid (blue), gallic acid (green), methyl gallate (magenta), pyrogallol (cyan) and sinapic acid (purple). (b) blank (black), *p*-coumaric acid (red), ferulic acid (blue), *p*-hydroxybenzoic acid (green), syringaldehyde (magenta), vanillic acid (cyan) and vanillin (purple).

Table 5.1: Quantification of non-oxidized, C_1 and C_4 oxidized products from the reaction of *Mt*LPMO9H with PASC as a substrate after a 14 h incubation for different electron donors together with the % relative activity compared to ascorbic acid. All quatities are measured in nC min^{-1}. Assignment according to [1].

Electron donor	Non-oxidized prod.	%	C_1 prod.	%	C_4 prod.	%
Ascorbic Acid	231.95	100	14.19	100	32.43	100
Caffeic Acid	162.95	70	9.26	65	23.83	73
Gallic Acid	274.58	118	47.99	338	40.16	123
Methyl Gallate	78.25	34	15.41	109	18.36	56
Pyrogallol	144.60	62	30.83	217	31.79	98
Sinapic Acid	34.10	15	4.81	34	13.05	40

trons to support the oxidative activity of *Mt*LPMO9H on PASC. Gallic acid, pyrogallol and methyl-gallate, all with three hydroxyl groups attached to the benzene ring, promoted efficiently the activity of LPMO and leaded to the highest yield of C1-oxidized oligosaccharides. Caffeic acid, a benzenediol compound, as well as sinapic acid could provide electrons to the active site of the enzyme, but were not as successful as benzenetriols, while upon addition of all residual monophenols no activity of LPMO was detected.

5.2 Ascorbic acid

We shall begin this chapter with the electrochemical examination of ascorbic acid. Typical voltammograms of the oxidation of ascorbic acid on an electrode surface have been a subject of scientific interest in the past, with different approaches followed.

One of the earliest works regarding the oxidation of ascorbic acid dates back to the distant 1933 with an attempt to measure the formal potential of ascorbic acid in various pH values. In the aforementioned work the observed $E^{0\prime}$ is reported [2]. In 1985 Karabinas *et al.* studied the oxidation of ascorbic acid on a hanging drop mercury electrode in citric acid - pottasium acetate buffer at a pH of 7.4. In this work it was concluded that the oxidation of ascorbic acid is a 2 electron reversible process followed by a fast irreversible chemical reaction [3].

One of the most cited works in the subject of the oxidation of ascorbic acid is that of Hu and Kuwana one year later, where cyclic voltammetry and convolution voltammetry was performed in a solution containing ascorbic acid with glassy carbon as a working electrode. In this work a sequence of one reversible one electron and an irreversible one electron reactions is proposed instead of 2 electron reversible process followed by a fast irreversible chemical reaction [4].

Other works dealing with the mechanism of the oxidation of ascorbic acid and the determination of the formal potentials of the intermediate steps on a more theoretical level can be found in references [5, 6, 7, 8, 9]. Most recent experimental work around the oxidation of ascorbic acid revolve around the detection of the substance on modified electrodes [10, 11, 12, 13].

The scenarios that shall be examined is a modification of that of Hu and Kuwana with the addition of disproportionation[1] and the other is that of Karabinas *et al.*

Cyclic Voltammetry and Convolution

Before examining the scenarios the experimental results and their analysis shall be first presented starting with cyclic and convolution voltammetry. A set of cyclic voltammograms of ascorbic acid at different scan rates can be found in Fig. 5.2.1. The scanning starts at -0.3 V and goes on anodically to 1.0 V and then returns to -0.3 V. The concentration of the ascorbic acid is 5 mM and a 500 mM acetate buffer at a pH of 6 is used as a supporting electrolyte. The scan rates examined range from 25 to 250 mV/s. In

[1] The scenario of Hu and Kuwana alone without the addition of disproportionation is also examined indirectly, but the results were not satisfactory.

the voltammograms only one distinct peak is observed during the anodic scan, while no peak is observed in the respective cathodic scan. These results are in accordance with the literature [3, 4]. Thus the assumption concerning the mechanism that the steps are either a two step reversible oxidation followed by an irreversible chemical reaction or the oxidation consist of a reversible one electron and a subsequent one step irreversible electron stands.

Now based on the anodic scan, convolution voltammetry analysis is performed. In Fig. 5.2.2 (a) an anodic scan for 100 mV/s of ascorbic acid together with the respective convoluted voltammogram are presented. The same analysis is performed for the other scan rates as well. The limiting current for the convoluted voltammograms I_{L} is independent of the scan rate indicating an electrochemical - chemical - electrochemical (ECE) or elecrohemical - disproportionation - elecrochemical (E-DISP-E) process that does not interfere significantly in the scan rate used, $v = 0.025 - 0.25$ V s^{-1}. The value of the I_{L} is calculated at 165.05 ($\pm$ 8.87) μC s$^{-1/2}$. In addition, by plotting the current value at the oxidation peak against the square root of the respective scan rate, a linear correlation is observed, signifying no adsorption of the electrochemical species can be considered significant interfering with the process (Fig. 5.2.2 (b)). The peak width was found to be $E_{\mathrm{p}} - E_{\mathrm{p/2}} = 82.3$ mV, corresponding to a value of $E_{\mathrm{p}} - E_{\mathrm{p/2}} = 3.2RT/F$, for $T = 298.15$ K.

The value of the effective diffusion coefficient D_{eff} is approximated by fitting the function,

$$c_{\mathrm{A}}(0) = \frac{I_{\mathrm{L}} - I}{2FAD^{1/2}} \tag{5.2.1}$$

to the value of $c^*_{\mathrm{A}} = 5$ mM, see Fig. 5.2.2(c). The mean value obtained is ($\pm$ 0.059) $\times 10^{-5}$ cm^2, as shown in Table 5.2. This value is rather underestimated in comparison to the value of 0.81 cm^2 s^{-1} reported for the ascorbate anion by Shamim and Bakin [14].

The dependence of the effective rate constant k_{eff} on the potential difference $E - E^{0\prime}$ is shown in Fig. 5.2.2(d). For this plot the bibliographic value of $E^{0\prime} = -0.09$ V vs. Ag| AgCl (KCl sat.) is used, corresponding to pH 6,

$$k_{\mathrm{eff}} = D_{\mathrm{eff}}^{1/2} \frac{i}{I_{\mathrm{L}} - I} \tag{5.2.2}$$

Two, rather distinct linear regions are observed, one at low potentials, $E < 0.02$ V and the other at higher potentials $E > 0.04$ V. From this plot, two different effective transfer coefficients can be calculated, one at low potentials being $\beta_{\mathrm{a},1} = 1.38$ and another at high potentials $\beta_{\mathrm{a},2} = 0.52$, see Table 5.2. These values are in good agreement with the values reported by Hu and Kuwana [4], for the same system in pH 2. According to the same authors, the change of the value of the apparent Tafel coefficients is due to the change of the rate determining step of the reaction mechanism. More specifically, for low potentials, the rate determining step is the second electron transfer step whereas for higher potentials the first electron transfer step is rate determining.[2]

[2]The change in the mechanism takes place due to the dependence of the k_i on the electrode potential.

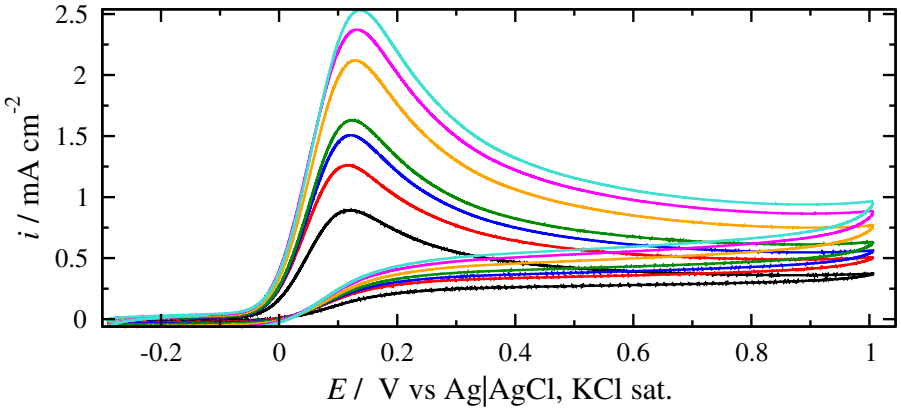

Figure 5.2.1: Cyclic voltammograms of 5 mM ascorbic acid in 500 mM acetate buffer pH 6 at various scan rates at 25 °C. v values: 25 (black), 50 (red), 75 (blue) 100 (green), 150 (orange), 200 (magenta) and 250 mV/s (cyan).

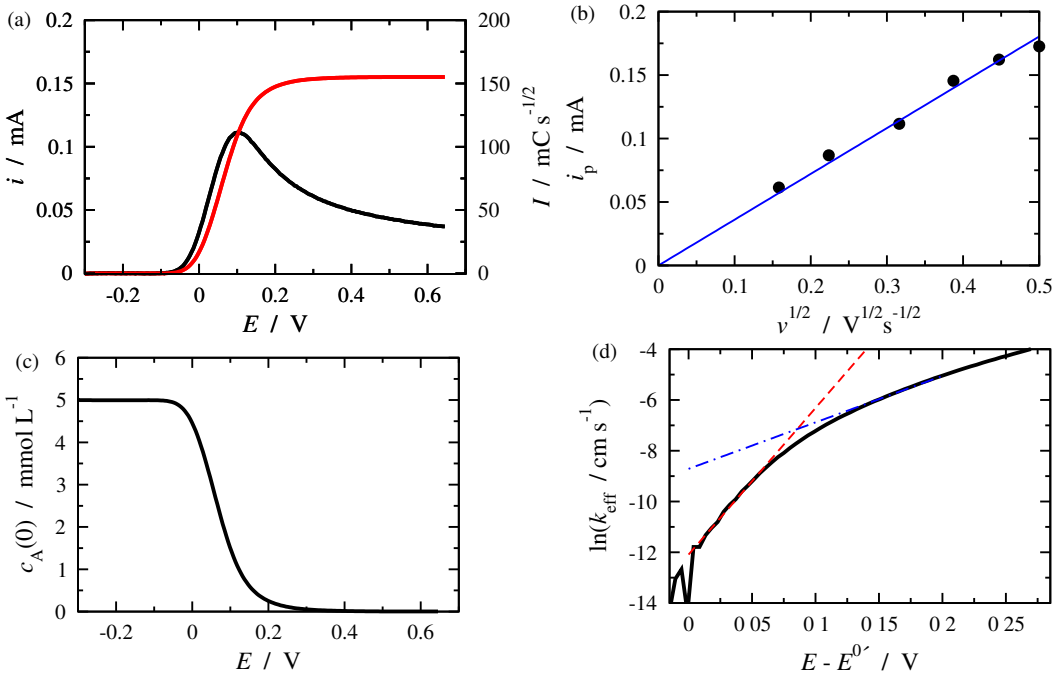

Figure 5.2.2: (a) Linear (black) and convolution (red) potenial sweep voltammogram, (b) i_p against v-1/2 (c) surface concentration of ascorbate ions and (d) effective rate constant. Parameters: concentration of ascorbic acid $c_\mathrm{A}^* = 5$ mM in acetate buffer pH 6, scan rate $v = 0.1$ V s^{-1}, electrode area $S = 0.0706$ cm^2.

Table 5.2: Experimental quantities obtained for scan rates v = 0.025, 0.05, 0.1, 0.15, 0.2, 0.25 V s^{-1}.

Symbol	Value	Description
I_L	165.05 (± 8.87) μC $s^{-1/2}$	limiting convolution current
$E_p - E_{p/2}$	82.3 (± 4.3) mV	peak width
D_{eff}	0.59 (± 0.06) $\times 10^{-5}$ cm^2 s^{-1}	effective diffusion coefficient
$\beta_{a,1}$	1.38 (± 0.13)	effective transfer coefficient (low potentials)
$k^0_{eff,1}$	4.8(±0.4) $\times 10^{-6}$ cm s^{-1}	effective rate constant (low potentials)
$\beta_{a,2}$	0.52 (± 0.06)	effective transfer coefficient (high potentials)
$k^0_{eff,2}$	1.1(±0.4) $\times 10^{-4}$ cm s^{-1}	effective rate constant (high potentials)

FTacV

Supplementary to the above experimental procedure, FTacV was also performed on ascorbic acid.

In Fig. 5.2.3 harmonics 2 through 5 are presented for the LA-FTacV experiments of 5 mM ascorbic acid in acetate buffer pH 6 0.5 M at 1 Hz and 3 different A_0 (100, 150 and 200 mV). As one familiar with this technique could observe, the pattern does not correspond to that of a usually reported reversible or quasi reversible electrochemical reaction. For the anodic scan going from -300 mV to 1000 mV the two characteristic peaks of the second harmonic appear, though rather disproportional with the second one being barely visible for the lowest amplitude. Regarding the third harmonic, the middle peak of the triplet is not the dominant one, as the first one is more intense and gets even more intense as the amplitude increases. Now when it comes to the 4th and 5th harmonic, they do not resemble by any means the usually reported ones. The 4th appears to have 3 peaks with the middle one being the dominant while the 5th has 4 disproportianl pekas. Moreover, in all the harmonics there is a shift towards more negative potentials with the increase of the amplitude regarding the corresponding dominant peak.

According to the mechanism based on disproportionation, the observed signal is an interplay of a quasi reversible (electochemically), reversible (chemically) reaction and an irreversible (chemically) electrochemical reaction. The cathodic shift of the dominant peak is an indication of the strong presence of the chemically irreversible electrochemical reaction. Regarding the cathodic scan going from 1 V to -300 mV, some peaks are observed, which resemble those of the anodic scan, though smaller in magnitude. This observation comes to a contrast with the cyclic voltammetry experiments where nothing is observed in the cathodic scan of the ascorbic acid. This is attributed to the fact that during the cathodic scan, due to the perturbation of the potential both anodically and cathodically, both oxidations and reductions occur, leading to small but observable oxidation currents, whereas in the classical cyclic voltammetry this is not possible.

Regarding the scenario which is based on the consumption of the resulting electrochemical species right after a two electron reversible reaction, it is possible that the

expected pattern could be one resembling the experimental data, as via the irreversible chemical step, the electrochemical reaction is also practically rendered irreversible.

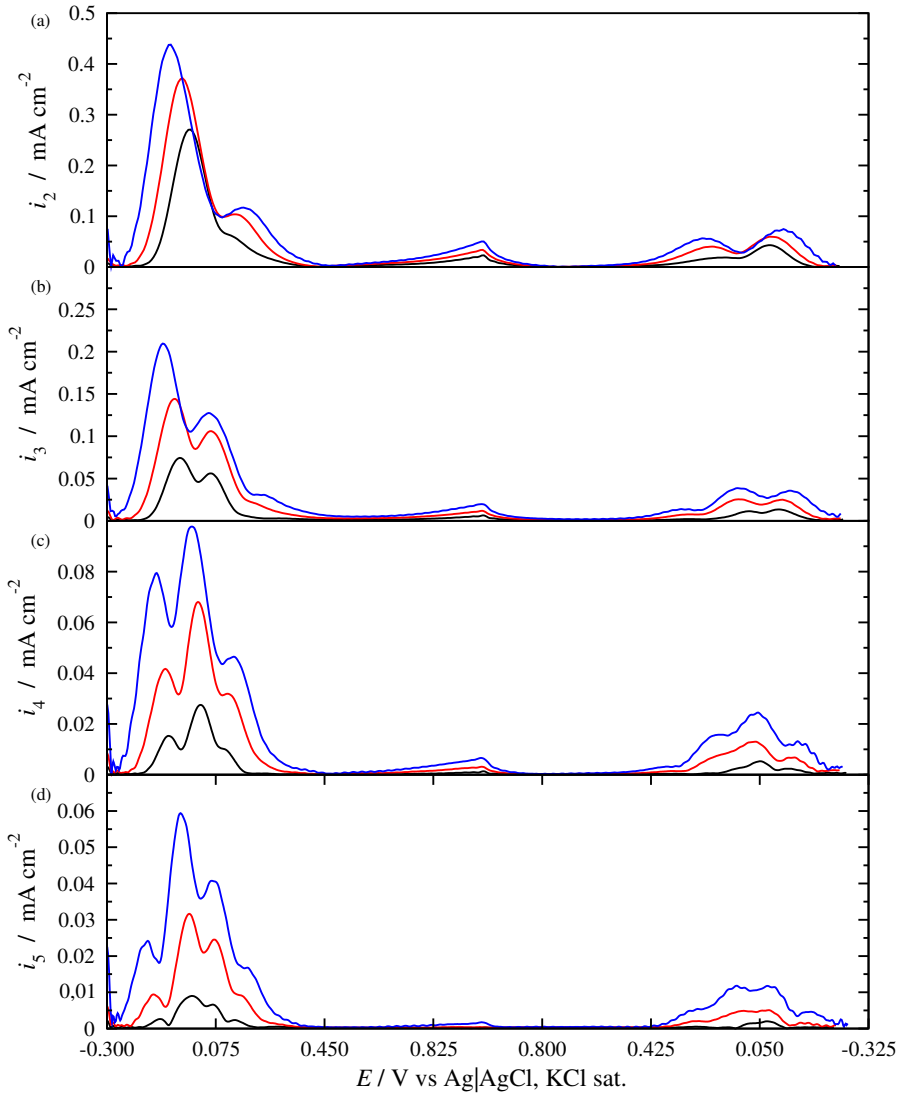

Figure 5.2.3: (a)-(d) 2nd through 5th harmonic of ascorbic acid 5 mM acetate buffer pH 6 0.5 M at $v = 15$ mV/s, $f = 1$ Hz and $A_0 = 100$ (black), 150 (red) and 200 mV (blue) at 25 °C.

Proposed Mechanism based on disproportionation

In order to explain the experimental results, the two proposed mechanisms shall be discussed in further detail. The first one is the one that implicated the interference of the disproportionation of the intermediate radical of ascorbic acid.

According to the Pourbaix diagram proposed by Tu *et al.* [7], ascorbic acid is mainly in the form of ascrobate ions in pH 6. Moreover, during the first electron transfer,

ascorbate radicals are formed which can disproportionate rapidly to dehydroascrobic acid and ascrobate ions (possibly via a dimer structure). Thus, for the interpretation of the experimental findings, the following reaction mechanism is proposed,

$$\mathrm{HA^-} \underset{k_{-1}}{\overset{k_1}{\rightleftharpoons}} \mathrm{A^{-\bullet}} + \mathrm{H^+} + \mathrm{e} \tag{5.2.3}$$

$$\mathrm{A^{-\bullet}} \xrightarrow{k_2} \mathrm{A} + \mathrm{e} \tag{5.2.4}$$

$$2\mathrm{A^{-\bullet}} + 2\mathrm{H^+} \xrightarrow{k_\mathrm{D}} \mathrm{HA^-} + \mathrm{A} \tag{5.2.5}$$

The mass balance equations are written,

$$\frac{\partial c_\mathrm{A}}{\partial t} = D_\mathrm{A}\frac{\partial^2 c_\mathrm{A}}{\partial x^2} + r_\mathrm{D} \tag{5.2.6}$$

$$\frac{\partial c_\mathrm{B}}{\partial t} = D_\mathrm{B}\frac{\partial^2 c_\mathrm{B}}{\partial x^2} + r_\mathrm{D} \tag{5.2.7}$$

$$\frac{\partial c_\mathrm{R}}{\partial t} = D_\mathrm{R}\frac{\partial^2 c_\mathrm{R}}{\partial x^2} - 2r_\mathrm{D} \tag{5.2.8}$$

where $c_\mathrm{A}(x,t) = [\mathrm{HA^-}]$ is the concentration of ascorbate anions, $c_\mathrm{B}(x,t) = [\mathrm{A}]$ the concentration of dehydroascorbic acid and $c_\mathrm{R}(x,t) = [\mathrm{A^{-\bullet}}]$ the concentration of the reaction intermediate. The rate of the disproportionation reaction is,

$$r_\mathrm{D} = k_\mathrm{D} c_\mathrm{R}^2 \tag{5.2.9}$$

where the concentration of hydrogen ions is included in the rate constant.

The initial conditions of the above problem are,

$$c_\mathrm{A}(x,0) = c_\mathrm{A}^* \tag{5.2.10}$$

$$c_\mathrm{B}(x,0) = 0 \tag{5.2.11}$$

$$c_\mathrm{R}(x,0) = 0 \tag{5.2.12}$$

where c_A^* is the bulk concentration of ascorbate anions.

The boundary conditions far from the electrode surface are,

$$c_\mathrm{A}(x\to\infty,t) = c_\mathrm{A}^* \tag{5.2.13}$$

$$c_\mathrm{B}(x\to\infty,t) = 0 \tag{5.2.14}$$

$$c_\mathrm{R}(x\to\infty,t) = 0 \tag{5.2.15}$$

whereas, at the electrode surface,

$$D_\mathrm{A}\frac{\partial c_\mathrm{A}}{\partial x}\bigg|_{x=0} = \frac{i_1}{F} \tag{5.2.16}$$

$$D_\mathrm{B}\frac{\partial c_\mathrm{B}}{\partial x}\bigg|_{x=0} = -\frac{i_2}{F} \tag{5.2.17}$$

$$D_\mathrm{R}\frac{\partial c_\mathrm{R}}{\partial x}\bigg|_{x=0} = -\frac{i_1}{F} + \frac{i_2}{F} \tag{5.2.18}$$

The local current densities are given by a Volmer-type dependence of the kinetic constants k_1, k_{-1} and k_2 on electrode potential,

$$i_1 = Fk_1^0\left[c_{\mathrm{A}}(0,t)e^{\frac{(1-a_1)F}{RT}(E(t)-E_1^{0\prime})} - c_{\mathrm{R}}(0,t)e^{-\frac{a_1F}{RT}(E(t)-E_1^{0\prime})}\right] \tag{5.2.19}$$

$$i_2 = Fk_2^0 c_{\mathrm{R}}(0,t)e^{\frac{(1-a_2)F}{RT}(E(t)-E_2^{0\prime})} \tag{5.2.20}$$

where k_i^0 and $E_i^{0\prime}$ is the heterogeneous kinetic constant and formal electrode potential, respectively, at a given concentration of hydrogen ions. The total current is the algebraic sum of the local currents, *i.e.*, $I = A(i_1 + i_2)$, where A is the electrode area.

For the formal potentials at a given pH, we consider the following relations,

$$\begin{aligned} E_1^{0\prime} &= E_1^0 - 0.059\mathrm{pH} \\ E_2^{0\prime} &= E_2^0 \\ E^{0\prime} &= \frac{E_1^0 + E_2^0}{2} - 0.029\mathrm{pH} \end{aligned}$$

where $E^{0\prime}$ is the formal electrode potential of the overall two-electron reaction[3] [7, 8, 9].

Considering a value of $E_1^0 \approx 0.73$ V and $E_2^0 \approx -0.180$ V the corresponding formal potentials are calculated for pH 6 (acetate buffer) versus the Ag|AgCl (KCl sat) reference electrode (potential 0.199 V vs NHE), at 0.180 V and -0.360 V respectively..

Now that the model for the first mechanism has been fully analyzed we shall move on to the fitting of the experimental data. At first, an attempt was made to fit the data to the cyclic voltammogram. The problem that occured when using the scenario of Hu and Kuwana as it is, with potentials close to the ones found in the literature, the decay of the current after the peak was rather sharp compared to the experimental data regardless of the combination of kinetic constants, transfer coefficients and diffusion coefficients used. This lead to the conclusion that one more reaction shall be included in the mechanism. An attempt was then made to include the disproportionation of the intermediate radical of the ascorbic acid and a cyclic voltammogram very close to the experimental was extracted Fig. 5.2.4. The parameters used for the fitting were $E_1^0 = 180$ mV, $E_2^0 = -360$ mV, $k_1^0 = 3 \times 10^{-4}$ m/s, $k_2^0 = 2 \times 10^{-7}$ m/s, $v = 100$ mV/s, $a = 0.61$, $D = 0.55 \times 10^{-5}$ cm^2/s, $k_{\mathrm{dis}} = 1.5 \times 10^{10}$ L mol^{-1}s^{-1} and a comparison of the theoretical and experimental cyclic voltammograms is presented in Fig. 5.2.4. It should be noted here, that a similar voltammogram to the experimental can be found numerically without disproportionation but with pairs of E_1^0, k_1^0 and E_2^0, k_2^0, that do not correspond to the literature values, regarding the formal potentials.

By using the data of the cyclic voltammogram fit, another attempt was made then to fit the results to the FTacV experiments. The results of the fit are presented in Fig. 5.2.5. For $A_0 = 100$ mV harmonics 2 through 5 are presented, while for 150 and 200 mV, indicatively the 4th and 5th harmonics are shown, with their corresponding fits. It is important to note here that although other combinations of kinetic constants and formal potentials close to the ones reported in the literature without the effect of the disproportionation, cyclic voltammograms very similar to the experimental ones

[3] H^+ is not implicated in the second step of the reaction, thus the value is regarded constant regardless of the pH value.

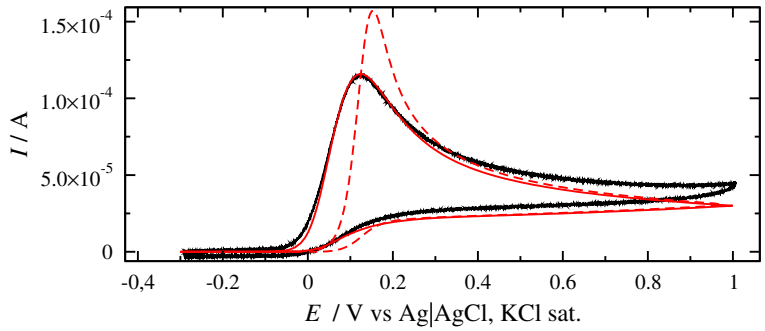

Figure 5.2.4: Experimental cyclic voltammogram of ascorbic acid 5 mM acetate buffer pH 6 0.5 M at 100 mV/s without capacitance extraction (black) at 25 °C. Computational cyclic voltammogram of the proposed mechanism with disproportionation (red) and without disproportionation (dashed red). Fitting parameters $E_1^0 = 180$ mV, $E_2^0 = -360$ mV, $k_1^0 = 3 \times 10^{-4}$ m/s, $k_2^0 = 2 \times 10^{-7}$ m/s, $v = 100$ mV/s, $a = 0.61$, $D = 0.55 \times 10^{-5}$ cm^2/s, $k_{\text{dis}} = 1.5 \times 10^{10}$ L mol^{-1}s^{-1}.

were obtained, when the parameters where fitted to the FTacV experiments, the results were not the expected and rather observable differences appeared.

Although the fit depicted in Fig. 5.2.5 is very close to the experimental data, some features of the voltammogram were not approximated very precisely giving the benefit of the doubt to this approach.

Proposed Mechanism based on the consumption of the oxidized product.

Karabinas *et al.* proposed in their work an EC mechanism scenario in which a two electron reversible reaction of ascorbic acid is suceeded by an irreversible chemical reaction consuming the oxidized product [3]. This scenario can be simply summarized as follows

$$\mathrm{A} \overset{k^0}{\rightleftharpoons} \mathrm{B} + 2\mathrm{H}^+ + 2\mathrm{e} \tag{5.2.21}$$

$$\mathrm{B} \xrightarrow{k_\mathrm{C}} C \tag{5.2.22}$$

where A is the reduced form of the ascorbic acid (ascorbate anions) , B the oxidized form after the two electron oxidation (dehydroascorbic acid) and C the final product. For reasons of simplicity the chemical reaction is treated as a first order one.

The mass balance of the problem shall be written as The mass balance equations

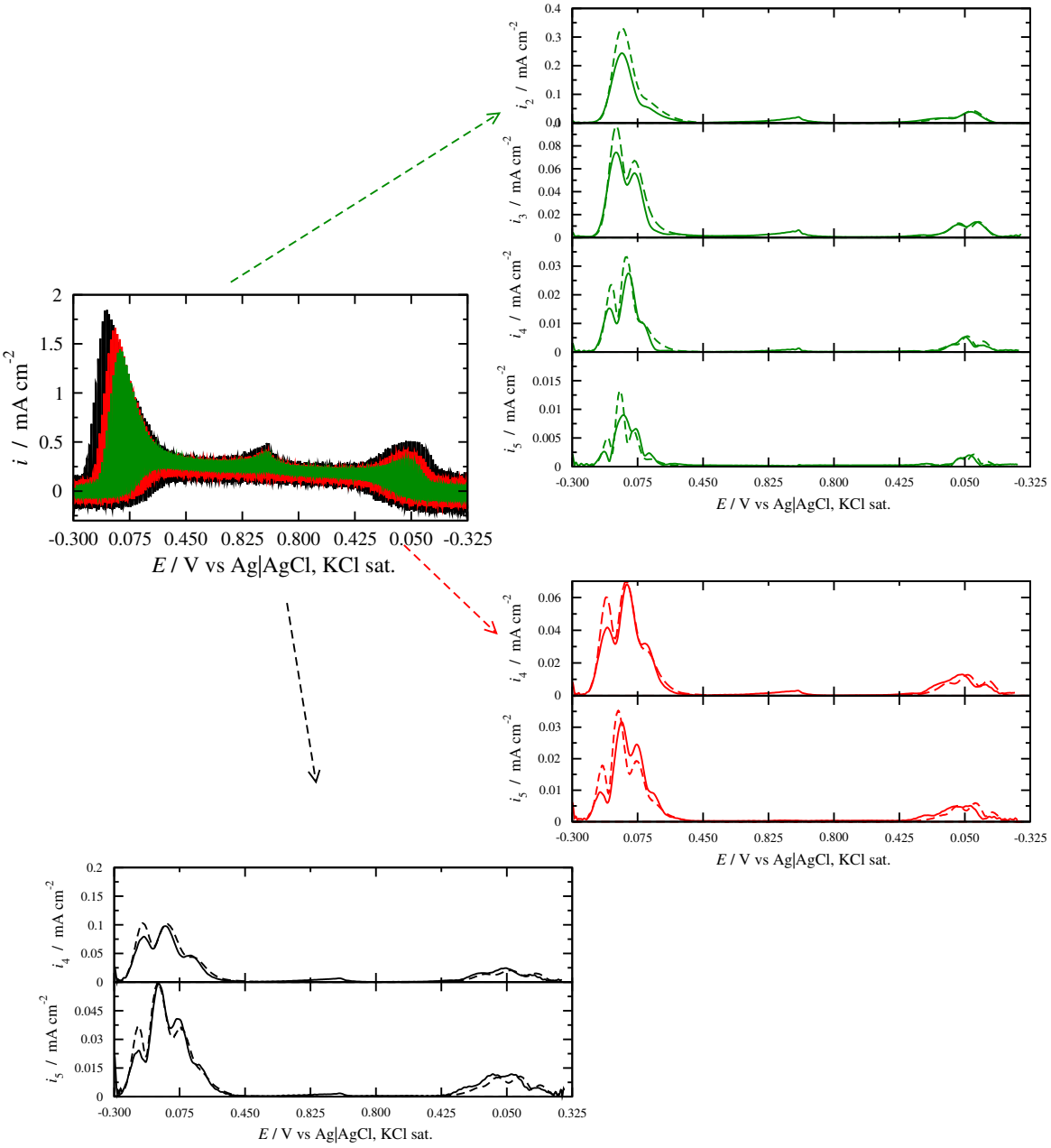

Figure 5.2.5: Experimental *vs* theoretical voltammograms for disoproportionation mechanism of ascorbic acid 5 mM acetate buffer pH 6 0.5 M at $v = 15$ mV/s, $f = 1$ Hz and $A_0 = 100$ (green), 150 (red) and 200 mV (black) at 25 °C. The experimental values are presented with full lines while the theoretical ones with dashed lines. Fitting parameters $E_1^0 = 180$ mV, $E_2^0 = -360$ mV, $k_1^0 = 3 \times 10^{-4}$ m/s, $k_2^0 = 2 \times 10^{-7}$ m/s, $v = 100$ mV/s, $a = 0.61$, $D = 0.55 \times 10^{-5}$ cm^2/s, $k_{\text{dis}} = 1.5 \times 10^{10}$ L mol^{-1}s^{-1}.

are written,

$$\frac{\partial c_{\mathrm{A}}}{\partial t} = D_{\mathrm{A}} \frac{\partial^2 c_{\mathrm{A}}}{\partial x^2} \tag{5.2.23}$$

$$\frac{\partial c_{\mathrm{B}}}{\partial t} = D_{\mathrm{B}} \frac{\partial^2 c_{\mathrm{B}}}{\partial x^2} - r_{\mathrm{C}} \tag{5.2.24}$$

$$\tag{5.2.25}$$

where $c_{\mathrm{A}}(x,t)$ is the concentration of ascorbate anions, $c_{\mathrm{B}}(x,t)$ the concentration of dehydroascorbic acid. The rate of the consumption reaction is,

$$r_{\mathrm{c}} = k_{\mathrm{c}} c_{\mathrm{B}} \tag{5.2.26}$$

where the concentration of hydrogen ions is included in the rate constant.

The initial conditions of the above problem are,

$$c_{\mathrm{A}}(x,0) = c_{\mathrm{A}}^{*} \tag{5.2.27}$$

$$c_{\mathrm{B}}(x,0) = 0 \tag{5.2.28}$$

$$c_{\mathrm{C}}(x,0) = 0 \tag{5.2.29}$$

where c_{A}^{*} is the bulk concentration of ascorbate anions.

The boundary conditions far from the electrode surface are,

$$c_{\mathrm{A}}(x \to \infty, t) = c_{\mathrm{A}}^{*} \tag{5.2.30}$$

$$c_{\mathrm{B}}(x \to \infty, t) = 0 \tag{5.2.31}$$

$$c_{\mathrm{R}}(x \to \infty, t) = 0 \tag{5.2.32}$$

whereas, at the electrode surface,

$$D_{\mathrm{A}} \frac{\partial c_{\mathrm{A}}}{\partial x}\bigg|_{x=0} = \frac{i_1}{F} \tag{5.2.33}$$

$$D_{\mathrm{B}} \frac{\partial c_{\mathrm{B}}}{\partial x}\bigg|_{x=0} = -\frac{i_2}{F} \tag{5.2.34}$$

Now let is move on to the fitting of the experimental data based on this scenario. As indicated by convolution voltammetry, for potentials over 40 mV the rate determining step is the first one if one would assume two separate one electron reactions instead of an one step two electrons one. Based on this, the formal potential that will be assumed in this scenario is that used for the first step in the previous section. For values $k^0 = 4.2 \times 10^{-4}$ m/s $v = 100$ mV/s, $a = 0.61$, $D = 0.55 \times 10^{-5}$ cm^2/s and $k_{\mathrm{C}} = 1 \times 10^5$ 1/s [4] one can see in Fig. 5.2.6 that the computational voltammogram approximates the experimental one really well, to the same degree as the previous scenario (Fig. 5.2.4). Now the critical point is the fitting of the FTacV experiments.

[4]The value of the k_{C} used in the theoretical calculation indicated basically the order of magnitude of the constant, rather than the exact value. In order to have visible changes in the voltammogram the kinetic constant had to vary orders of magnitude, thus an attempt for a more precise kinetic constant would not be useful.

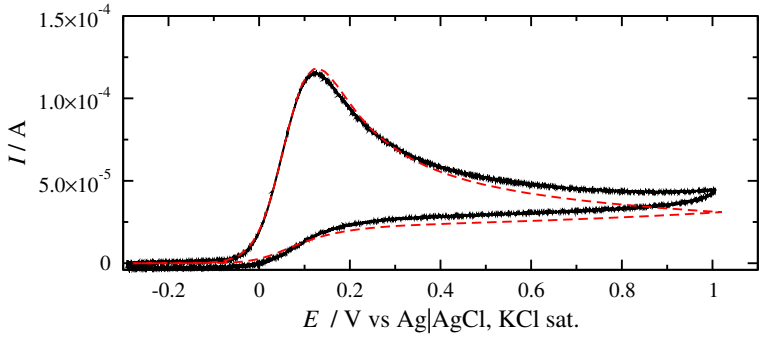

Figure 5.2.6: Experimental cyclic voltammogram of ascorbic acid 5 mM acetate buffer pH 6 0.5 M at 100 mV/s without capacitance extraction (black) at 25 °C. Computational cyclic voltammogram of the mechanism of the 2nd scenario with consumption (dashed red). Fitting parameters $E_1^0 = 180$ mV, $k^0 = 4.2 \times 10^{-4}$ m/s, $v = 100$ mV/s, $a = 0.61$, $D = 0.55 \times 10^{-5}$ cm^2/s, $k_C = 1 \times 10^5$ 1/s.

By taking a look at Fig. 5.2.7, one would agree that with this approach, the features that were not approximated correctly in the previous scenario are now corrected. This is an indication the the proposed scenario by Karabinas *et al.* is closer to the oxidation of ascorbic acid on an electrode surface, although much simpler.

In both cases though, the value of the formal potential extracted is that of 180 mV vs Ag|AgCl, KCl sat. lower than that of *Mt*LPMO9H (245 mV vs Ag|AgCl, KCl sat), making it feasible for the electron transfer thermodynamically. This oxidation path proposed is pretty straightforward with no side reactions that could affect the activity of *Mt*LPMO9H, explaining why it acts consistently well in LPMOs in a lab scale.

5.3 Caffeic Acid

As a next step, phenolic compounds that were tested with *Mt*LPMO9H in order to check their reactivity as electron donors were examined electrochemically. First the electron donors that showed a relatively high yield of oxidized products shall be presented.

The first one in the list is caffeic acid (3,4-Dihydroxycinnamic acid) which showed a reactivity at a level of 59 to 70% regarding the non-oxidized and oxidized products in comparison to ascorbic acid when acting as an electron donor to the LPMO. In Fig. 5.3.1 the cyclic voltammograms of a 2.5 mM caffeic acid solution at various scan rates are presented. A 500 mM acetate buffer at a pH of 6 is used as a supporting electrolyte. The scan rates examined range from 25 to 250 mV/s. The potential is scanned from -0.3 anodically up to 1 V and then cathodically back to -0.3 V. During the anodic scan a peak appears at about 220 mV, the magnitude of which increases with the increase of the scan rate. During the cathodic scan, a reduction peak arises around 120 mV. At a first glance, and if scan rates lower than 100 mV/s had not been examined, one would characterize the reduction and oxidation peak as a set of quasi-reversible peaks of the two electron oxidation and reduction of caffeic acid. However, as the scan rate

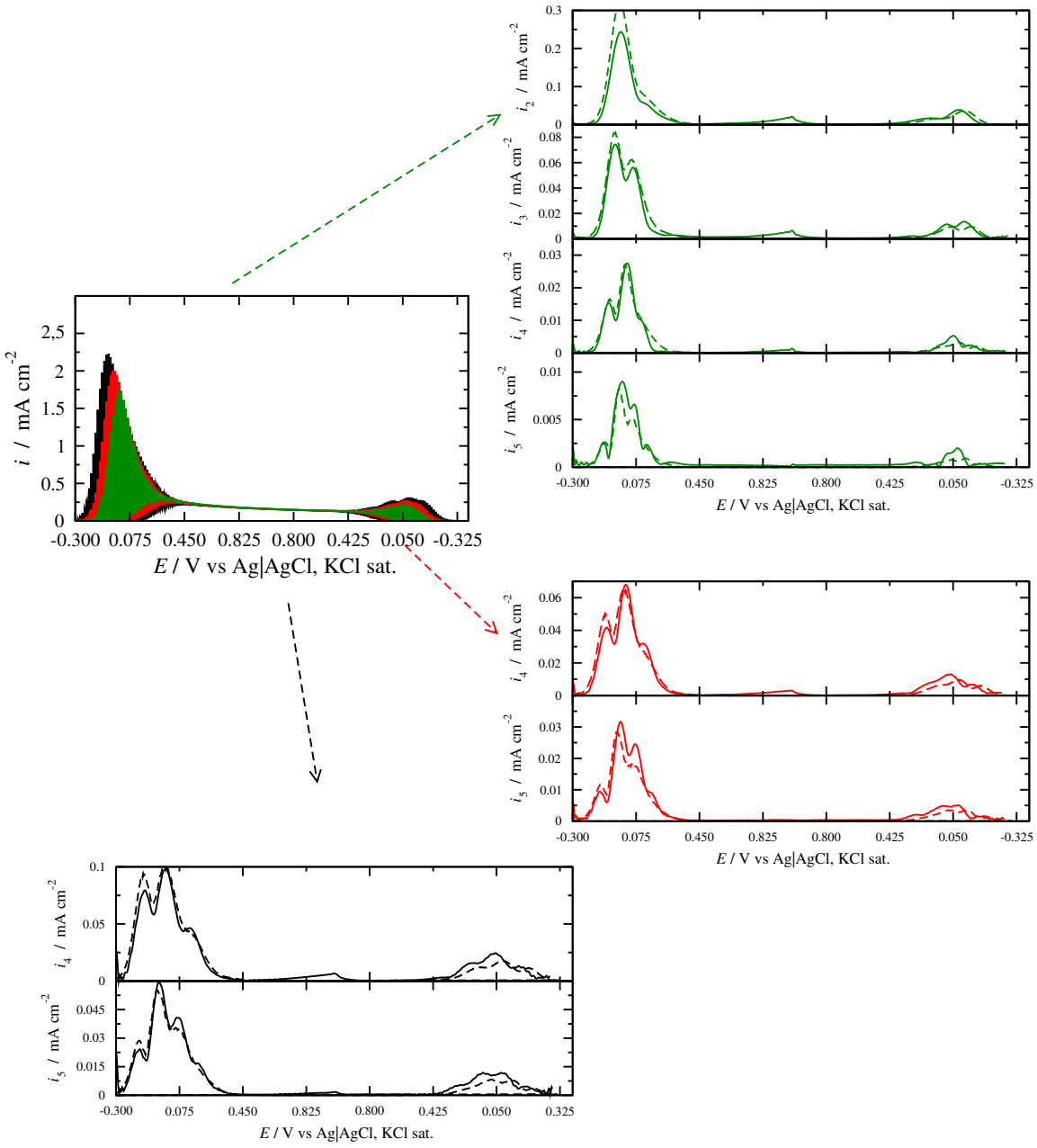

Figure 5.2.7: Experimental vs Theoretical voltammograms of ascorbic acid 5 mM acetate buffer pH 6 0.5 M at $v = 15$ mV/s, $f = 1$ Hz and $A_0 = 100$ (green), 150 (red) and 200 mV (black) at 25 °C. The experimental values are presented with full lines while the theoretical ones with dashed lines.Fitting parameters $E_1^0 = 180$ mV, $k^0 = 4.2 \times 10^{-4}$ m/s, $v = 100$ mV/s, $a = 0.61$, $D = 0.55 \times 10^{-5}$ cm^2/s, $k_C = 1 \times 10^5$ 1/s.

is decreasing, it can be assumed that the quantity of the reduced species is consumed and rendered to a form that cannot be reduced, thus the peak is almost diminished at 25 mV/s.

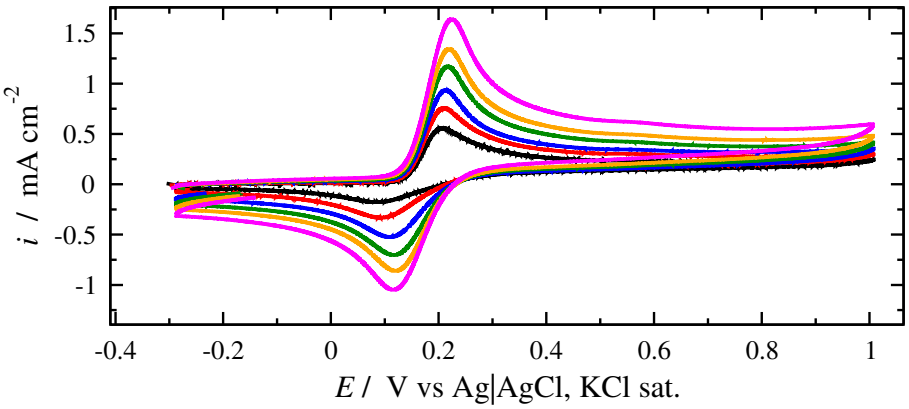

Figure 5.3.1: Cyclic voltammograms of 2.5 mM caffeic acid in 500 mM acetate buffer pH 6 at various scan rates at 25 °C. v values: 25 (black), 50 (red), 75 (blue) 100 (green), 150 (orange), 200 (magenta) and 250 mV/s (cyan).

In 2001 Hotta *et al.* while examining some polyphenolic antioxidants, including caffeic acid, observed with flow column electrolysis experiments that while at low pH values the number of electrons exchanged for the oxidation of caffeic acid were 2 for higher pH values, higher numbers of electrons were acquired, indicating further reactions occuring. It was assumed then this was due to the oxidation of polymerized products of caffeic acid, as in higher pH values, semi-quinones resulting from the oxidation of caffeic acid are thermodynamically more stable and polymerization reactions can preferably occur [15]. Moreover, Arakawa *et al.* in 2004 using on-line electrochemistry / electrospray ionization mass spectrometry, while examining caffeic acid, detected dimer products for applied potentials aroung 0.7 V and trimers for potentials at 1 V, reinforcing the claims of Hotta *et al.* [16].

Based on the aforementioned claims together with the experimental results from the cyclic voltammograms, it can be concluded that the anodic peak is indeed due to the 2 electron oxidation of caffeic acid, but the cathodic peak is rather distorted especially at lower scan rates, due to the fact that polymerization of the resulting products of the oxidation of caffeic acid occurs as a result of the pH and the high overpotential applied.

In order to further explore the redox reaction of caffeic acid on a glassy carbon electrode, FTacV experiments were performed at a frequency f of 1 Hz and various amplitudes ranging from 100 to 300 mV. Harmonics 2 through 5 are presented in Fig. 5.3.2. The scan rate employed is 15 mV/s so that a frequency of 1 Hz can be used satisfying the independence of the experiment from the scan rate. The scanning limits are the same as the ones employed for cyclic voltammetry. From all the harmonics it can be concluded safely that a distorted picture of a quasi reversible reaction can be distinguished during the anodic scan. The distortion is more evident as the amplitude increases on the more anodic part of each harmonic as it appears to be smaller in

magnitude than the left one. This could be due to the polymerized products of caffeic acid being formed, thus not letting the signal expand to its full potential through the whole voltammogram. Regardless of the possible deformation of the magnitude of the principal peak of the odd harmonics, considering that no displacement is observed, a formal potential value can be extracted at 180 mV. This value shall be attributed to the two step electron reaction of the oxidation of caffeic acid.

During the cathodic scan, it can be seen that the magnitude of the cathodic peak is far less impactful than that of the anodic scan. This can be attributed to the same reasons as the one mentioned for the simple cyclic voltammogran. It should be mentioned as well at this point, that the scanning employed for FTacV is slower than the ones used for the cyclic voltammetry experiments, making the overall effect of the polymerization of the products of the oxidation of caffeic acid more prominent.

Based on these observations and the data from the literature, a reaction scheme for the oxidation of caffeic acid on an electrode surface is presented in Fig. 5.3.3. At first the reduced form of caffeic acid undergoes an one electron transfer forming a semi-quinone (B), with a standard rate constant $k^0_{1,\text{caffeic}}$

$$\mathrm{A} \overset{k^0_{1,\text{caffeic}}}{\rightleftharpoons} \mathrm{B} + \mathrm{e}^- + \mathrm{H}^+ \tag{5.3.1}$$

The formal potential of this step will be regarded as the one extracted from the FTacV experiments, whith a potential low enough to act as an electron donor for *Mt*LPMO9H.

After the aforementioned first step, two other paths are possible. One is the further oxidation of B to a quinone (C) with a standard rate constant $k^0_{2,\text{caffeic}}$

$$\mathrm{B} \overset{k^0_{2,\text{caffeic}}}{\rightleftharpoons} \mathrm{C} + \mathrm{e}^- + \mathrm{H}^+ \tag{5.3.2}$$

while the other one is for two semi quinones to react together to form a dimer D at a reaction constant k_{caffeic}

$$2\mathrm{B} \xrightarrow{k_{\text{caffeic}}} \mathrm{D} \tag{5.3.3}$$

Finally the formed dimer undergoes an irreversible electrochemical oxidation with a standard rate constant $k^0_{3,\text{caffeic}}$

$$\mathrm{D} \xrightarrow{k^0_{3,\text{caffeic}}} \mathrm{E} + 4\mathrm{e}^- + 4\mathrm{H}^+ \tag{5.3.4}$$

The oxidation of the possibly formed dimer was not detectable initially with the experimental parameters used. For this reason this substance was further examined with FTacV for $A_0 = 100$ mV anf $f = 1$, 3 and 5 Hz. The corresponding 5th harmonic is presented in the (Fig. 5.3.4). Going into further detail, the signal focuses on the cathodic scan where a set of peaks appear around 250 mV, which is not visible during

the anodic scan and becomes more intense as the frequency increases. This set of peaks could be attributed to the formed dimer and is detected during the cathodic scan as it has not been formed during the anodic scan. Moreover, if the formal potential lies around where the extra peaks can be found, the potential different between the LPMO and the dimer is rather marginal, making their interaction non feasible.

Thus, first step of the oxidation of caffeic acid has a formal potential that allows the reduction of *Mt*LPMO9H (180 mV *vs* 245 mV). Moreover, the formal potential is similar to that of the ascorbic acid and the yield in non-oxidized and oxidized products is comparable. Finally, the possible formed dimers from the anodic oxidation of caffeic acid cannot contribute to the reduction of *Mt*LPMO9H as their formal potential probably lies around 250 mV.

5.4 Pyrogallol, Gallic acid and Methyl Gallate

After caffeic acid, next up in line to be examined electrochemically are pyrogallol (Benzene-1,2,3-triol), gallic acid (3,4,5-trihydroxybenzoic acid) and methyl gallate (Methyl 3,4,5-trihydroxybenzoate). All three of them have similar structures with three hydroxyl groups in the same positions in the benzene ring and they differ in the substuent in one particular position. Consequently a similar mechanism is expected for all three compounds. When reacting with *Mt*LPMO9H pyrogallol and gallic acid gave a higher yield of non oxidized and C_1 oxidized products than ascorbic acid, while methyl gallate gave a comparable yield in C_1 oxidized products and lower yield in C_4 oxidized and non oxidized products when compared to ascorbic acid.

Pyrogallol

In Fig. 5.4.1 the cyclic voltammograms of a 5 mM pyrogallol solution at various scan rates are presented. A 500 mM acetate buffer at a pH of 6 is used as a supporting electrolyte. The scan rates examined range from 25 to 250 mV/s. The potential is scanned from -0.3 anodically up to 1 V and then cathodically back to -0.3 V. During the anodic scan a peak appears at about 260 mV, that increases with scan rate. Moreover, contrary to what was seen in the previous two compounds examined, a second small peak appears more anodic than the first one. Regarding the second peak, the explanation that the expected two electron transfer is seen in two steps with no other reaction interfering cannot be plausible, as in such a case the second peak is supposed to be of greater magnitude in comparison with the first one. During the cathodic scan no peak is observed indicating consumption of the species resulting from the anodic oxidation of pyrogallol.

Although it was stated that the second peak could not be attibuted to a second oxidation step due to its magnitude, that would be under the circumstances that the product of the first step was not consumed. However, since no reduction peaks are observed, it could be safe to assume that that the product of the first step of the anodic oxidation of pyrogallol is indeed probably dimerized as in the case of caffeic acid and thus consumed. It is also worth noting that when the scan rate lowers, the second peak

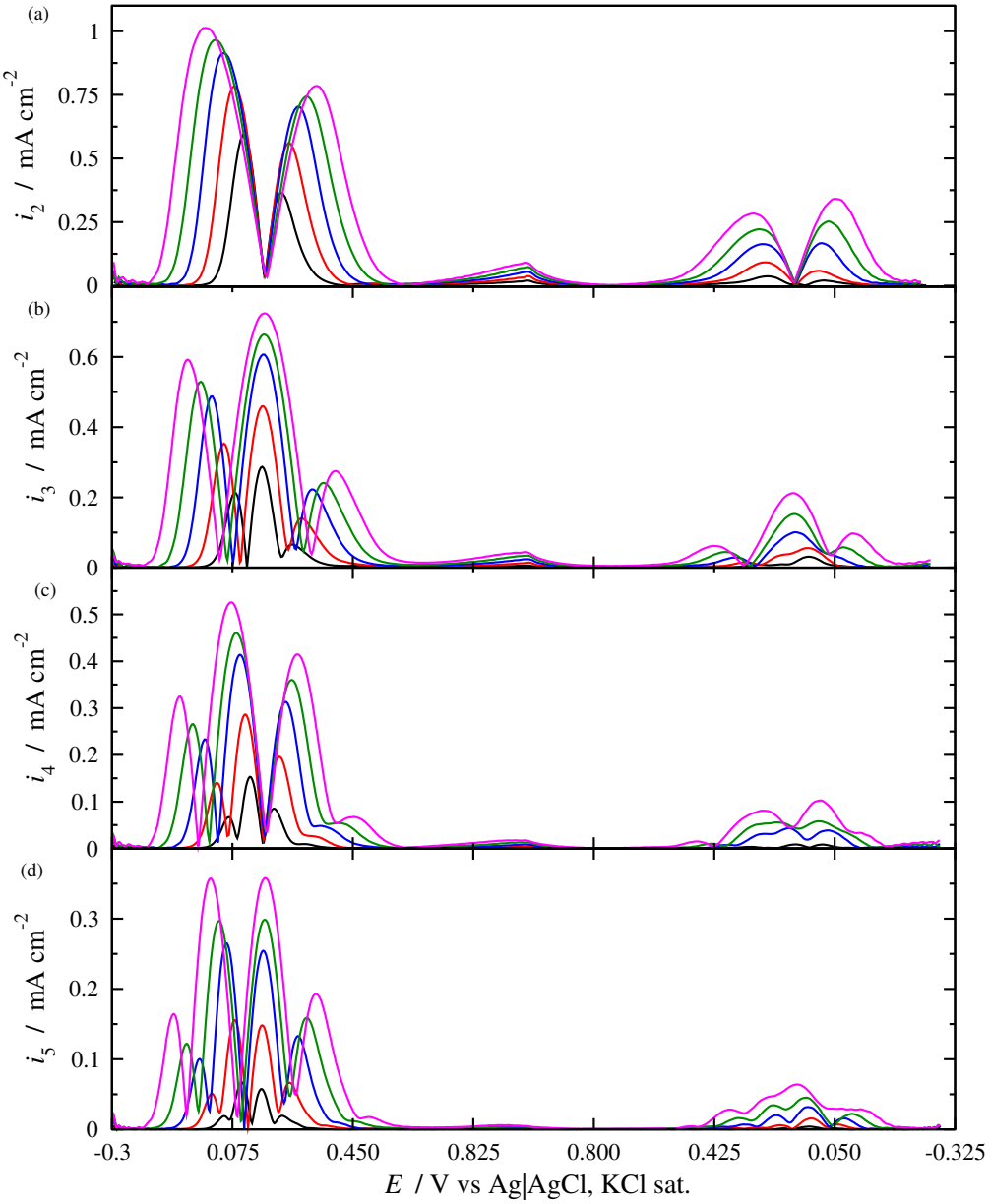

Figure 5.3.2: (a)-(d) 2nd through 5th harmonic of caffeic acid 2.5 mM acetate buffer pH 6 0.5 M at $v = 15$ mV/s, $f = 1$ Hz and $A_0 = 100$ (black), 150 (red), 200 (blue), 250 (green) and 300 mV (magenta) at 25 °C.

diminishes, while as the scan rate increases, it becomes more and more prominent. This indicates, that whatever can be found in the second step, becomes more intense when the potential is swept faster and other chemical reactions do not have the time to take place. Moreover, since the first and the second step of the oxidation are well seperated, the intermediate reaction shall have more "room" to act and consequently no reduction peak can be found in the reverse scan, contrary to what is seen in the caffeic acid case. Now taking into account the work of Hotta *et al.* [17] in which it was observed that more than two electrons take place during pyrogallol's scavenging activity,

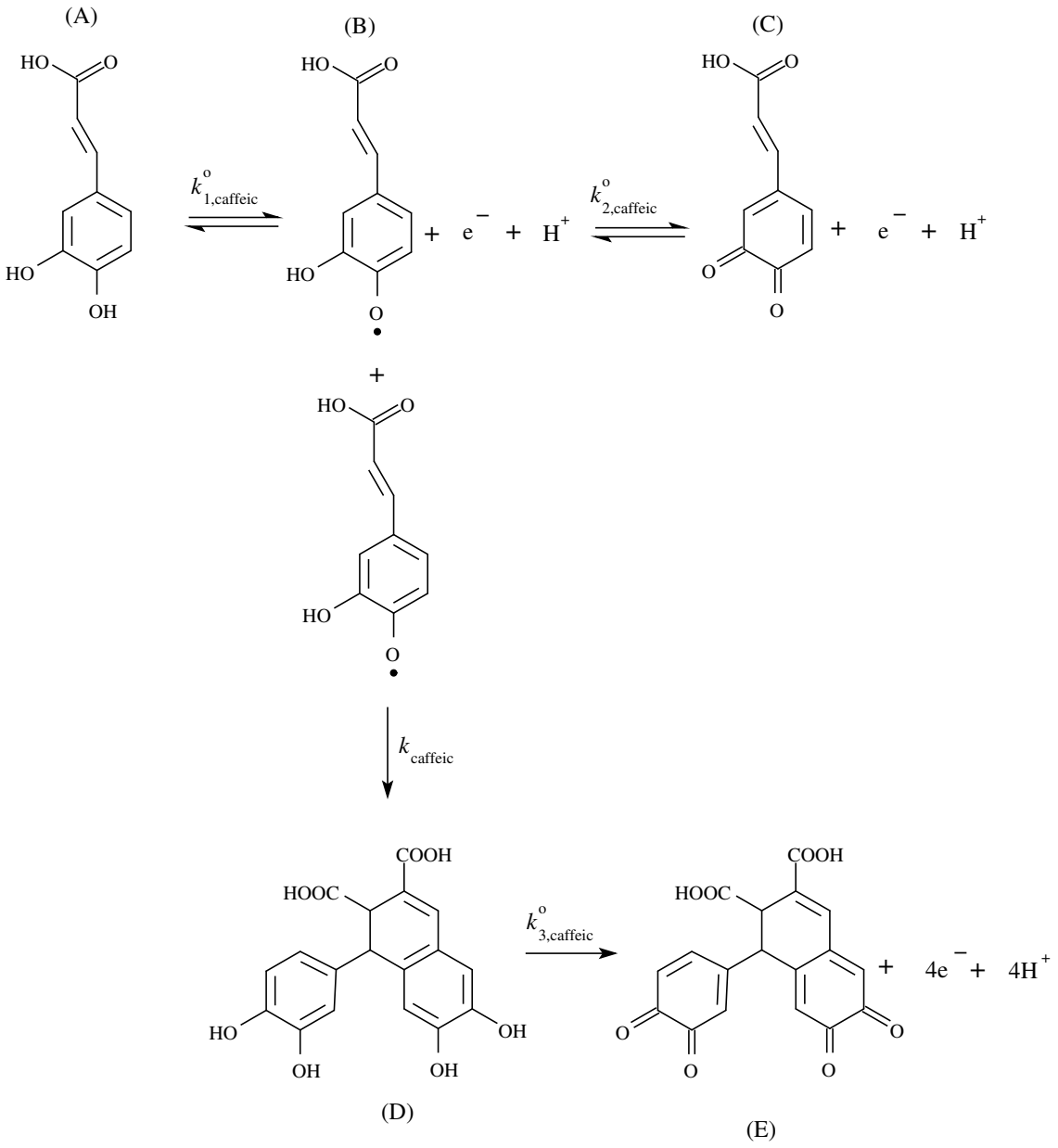

Figure 5.3.3: Caffeic Acid oxidation pathway.

indicating the formation of dimers, as well the mechanisms supported by Ryan *et al.* [18], Yamamura and Nishiyama [19] and Careganto *et al.* [20], indeed after the first step of the oxidation of pyrogallol, in near neutral and basic pH values, dimerization occurs, not letting the second step of the oxidation unfolding to its fullest.

Pyrogallol is also examined with FTacV for different frequencies at a constant amplitude and for different amplitudes at a constant frequency 5.4.2(a) and (b) respectively. The scan rate used is 15 mV/s so that a frequency of 1 Hz can be used satisfying the independence of the experiment from the scan rate. The scanning limits are the same

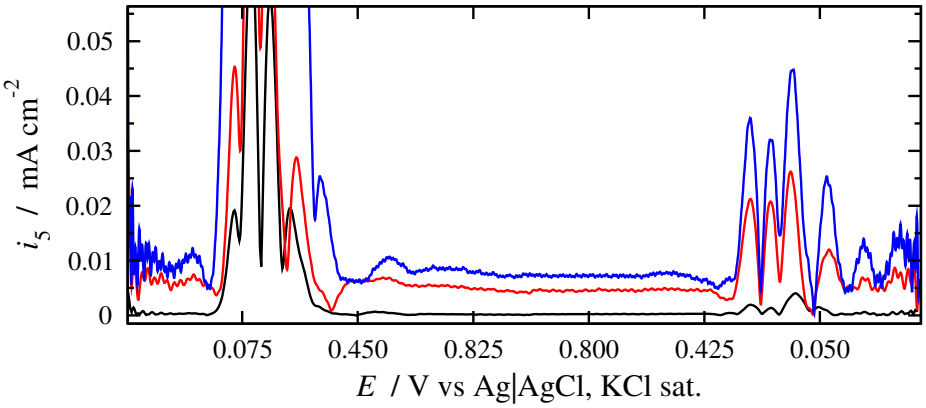

Figure 5.3.4: 5th harmonic of caffeic acid 2.5 mM in 500 mM acetate buffer pH 6 at $v = 15$ mV/s, $A_0 = 100$ and $f = 1$ (black), 3 (red) and 5 Hz (blue) at 25 °C.

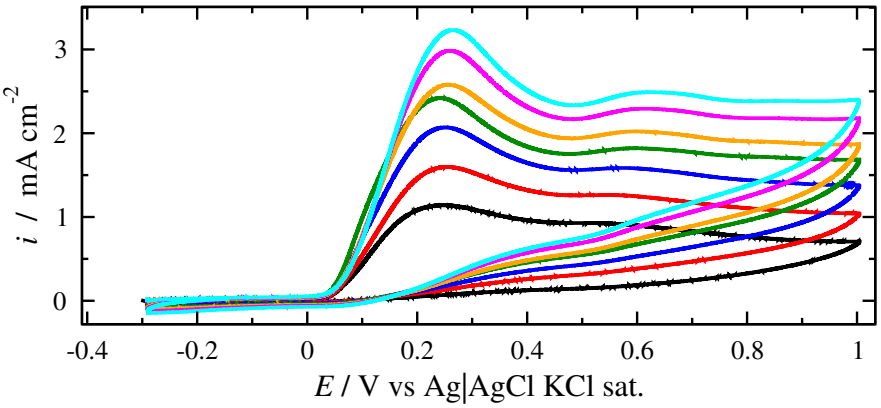

Figure 5.4.1: Cyclic voltammograms of 5 mM pyrogallol in 500 mM acetate buffer pH 6 at various scan rates at 25 °C. v values: 25 (black), 50 (red), 75 (blue) 100 (green), 150 (orange), 200 (magenta) and 250 mV/s (cyan).

as the ones employed for cyclic voltammetry. The first thing one can observe while manipulating both the amplitude and the frequency is that during the reverse scan a small set of peaks appear, though they could be described rather faint in comparison to those of the anodic scan. This is nonetheless a feature missing in the cyclic voltammograms. It can be attributed to the fact that due to the potential perturbation during the scanning, both oxidation and reduction reactions occur, thus the first step of the oxidation of pyrogallol can be observed to some extend. Now back to the peak at the oxidation scan. For $A_0 = 100$ mV and $f = 1$ Hz what seems like a distorted 5th harmonic of a reversible reaction can be observed. On a first glance, this asymmetry observed would be attributed to the symmetry coefficient in a "normal" system and the deformation would worsen as the frequency increased. However, in this case when frequency increases, the system resembled more the waveform of a reversible 5th harmonic. This suggests that what can be observed a harmonic corresponding to the reversible oxidation of the first step of the oxidation of pyrogallol. At high frequencies, the increase

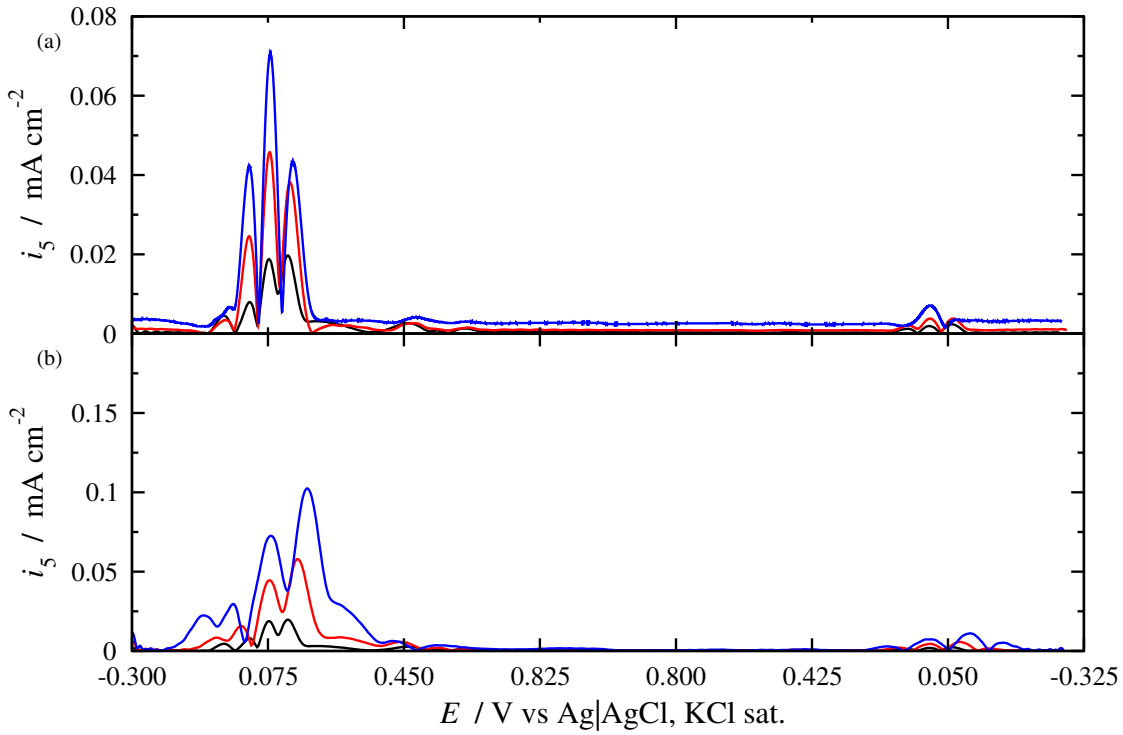

Figure 5.4.2: 5th harmonic of 5 mM pyrogallol in 500 mM acetate buffer pH 6 at 25 °C (a) for different frequencies: $v = 15$ mV/s, $A_0 = 100$ mV and $f = 1$ (black), 5 (red) and 8 Hz (blue) (b) for different amplitudes: $v = 15$ mV/s, $f = 1$ Hz and A_0 100 (black), 150 (red) and 200 mV (blue).

of reversible reactions is more evident than that of the irreversible ones, implying that what distorts the harmonic in the lower frequencies is an irreversible electrochemical reaction, probably the oxidation of the formed dimer. From the dominant peak of the anodic scan, the formal potential of the first step of the oxidation of pyrogallol can be estimated at 86 mV vs. Ag| AgCl (KCl sat), making it possible for pyrogallol to act as an electron donor for *Mt*LPMO9H.

Looking at what happens when the frequency is steady at 1 Hz and the amplitude increases, is that the deformation of the left side of the voltammogram becomes more evident indicating that the irreversible reaction interferes even more with this part of the harmonic. As the amplitude increases, the oxidation of pyrogallol starts earlier on during the scan, meaning that the possible dimers can be formed earlier than when scanning at a lower amplitude, thus interfering more intensely.

Gallic Acid

In Fig. 5.4.3 the cyclic voltammograms of a 5 mM gallic solution solution at various scan rates are presented. A 500 mM acetate buffer at a pH of 6 is used as a supporting electrolyte. Again, the scan rates examined range from 25 to 250 mV/s. The potential is scanned from -0.3 anodically up to 1 V and then cathodically back to -0.3 V. The behaviour observed is similar to that of pyrogallol. During the anodic scan a peak

appears at about 282 mV, that increases with the scan rate. Then s second small peak appears right after the first one at about 650 mV and during the cathodic scan no peak is apparent. The difference with the pyrogallol voltammogram is that the first peak is slightly sharper and slightly more anodically shifted. Thus, the same mechanism is assumed for the explanation of the voltammogram, as expected due to their similar structure. Moreover, Hotta *et al.* [17] again when it came to gallic acid they observed that more than two electrons take place during its scavenging activity, indicating the formation of dimers.

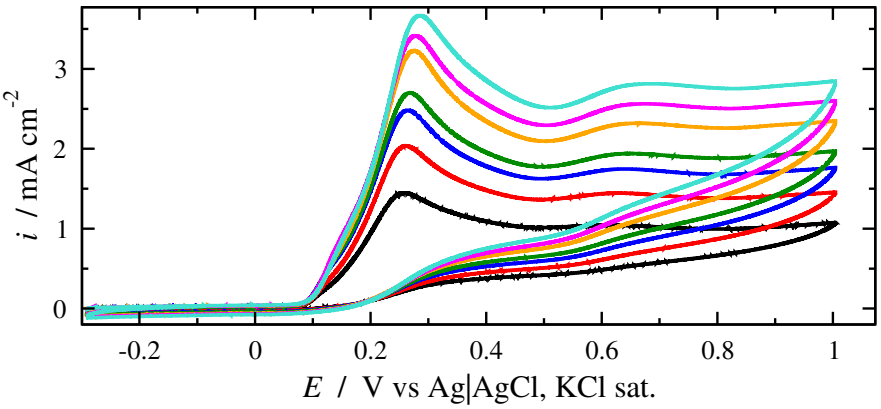

Figure 5.4.3: Cyclic voltammograms of 5 mM gallic acid in 500 mM acetate buffer pH 6 at various scan rates at 25 °C. v values: 25 (black), 50 (red), 75 (blue) 100 (green), 150 (orange), 200 (magenta) and 250 mV/s (cyan).

In Fig. 5.4.4 the 5th harmonics of a solution consisting 5 mM gallic acid in 500 mM acetate buffer pH 6 for v = 15 mV/s, A_0 = 100 mV and different frequencies are presented. It can be seen that just like in the case of pyrogallol, when increasing the frequency a set of peaks arise resembling that of a reversible reaction. Then, on the right part of the harmonic, a single peak interferes, that distorts the signal less as the frequency increases. This is probably due to the dimer that is formed and its irreversible oxidation. Contrary to pyrogallol, what seems to be deformed now is the more anodic side of the voltammogram, indicating that what is oxidized and interferes has a more positive potential than the first step of the oxidation of gallic acid. Lastly, the formal potential of the first step of the oxidation of gallic acid can be estimated from the dominant peak of the fifth harmonic at a value of 74 mV vs. Ag| AgCl (KCl sat), again low enough to act as an electron donor for *Mt*LPMO9H.

Methyl Gallate

Now in Fig. 5.4.3 the cyclic voltammograms of a 5 mM methyl gallate solution at various scan rates are presented. A 500 mM acetate buffer at a pH of 6 is used as a supporting electrolyte. The scan rates examined range from 25 to 250 mV/s. Again, the potential is scanned from -0.3 anodically up to 1 V and then cathodically back to -0.3 V. The behavior observed is similar to that of pyrogallol and gallic acid with one

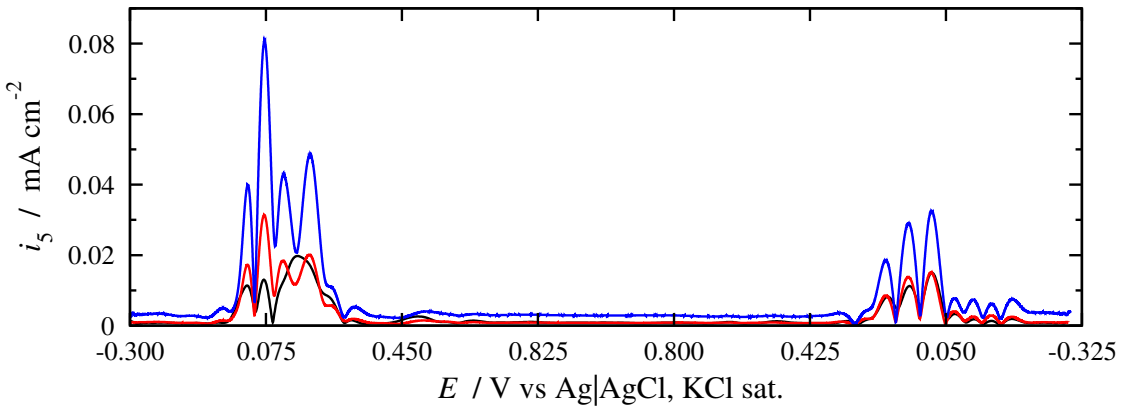

Figure 5.4.4: 5th harmonic of 5 mM gallic acid in 500 mM acetate buffer pH 6 at 25 °C for $v = 15$ mV/s, $A_0 = 100$ mV and $f = 3$ (black), 12 (red) and 18 Hz (blue).

peak at 195 mV and a shoulder that could resemble a peak at 0.3 V. One would argue that another shoulder can be found around 600 mV. Regarding the shoulder around 0.3 V it can be observed that as the scan rate increases, it becomes less and less evident, contrary to the one at 600 mV which could be defined as more intense as the scan rate increases. Based on the mechanism proposed for pyrogallol and gallic acid, the first shoulder probably corresponds to the irreversible oxidation of the formed dimer during the anodic scan, while the second is due to the second step of the oxidation of methyl gallate. Again during the cathodic scan no peak is observed indicating that what was produced during the anodic scan was irreversibly consumed chemically.

In Fig. 5.4.6 the 5th harmonics of a solution consisting 5 mM methyl gallate in 500 mM acetate buffer pH 6 for $v = 15$ mV/s, $A_0 = 100$ mV and different frequencies are presented. It can be seen that just like in the case of pyrogallol and gallic acid, when increasing the frequency a set of peaks arise resembling that of a reversible reaction. Interferences on the right side of the harmonic can be observed probably due to the oxidation of the formed dimer. This deformation is prominent at potentials higher thatn 250 mV, indicating that whatever is formed and is oxidized in this region, is not eligible to act as an electron donor for *Mt*LPMO9H. Lastly, the formal potential of the first step of the oxidation of gallic acid can be estimated from the dominant peak of the fifth harmonic at a value of 180 mV vs. Ag| AgCl (KCl sat), again low enough to act as an electron donor for *Mt*LPMO9H.

General mechanism proposed benzenetriols

Since all three compounds have a similar structure and probably follow a similar oxidation path and based on the general mechanism proposed by Namamura and Nishiyama [19] as well as the experimental findings, a proposed mechanism can be found in Fig. 5.4.7.[5]

[5]The proposed dimer is a general form of a dimer that could occur from the reactions and not an experimentally confirmed one. The correct structure is a matter of discussion and the present form serves only an indicative dimer that could possibly occur.

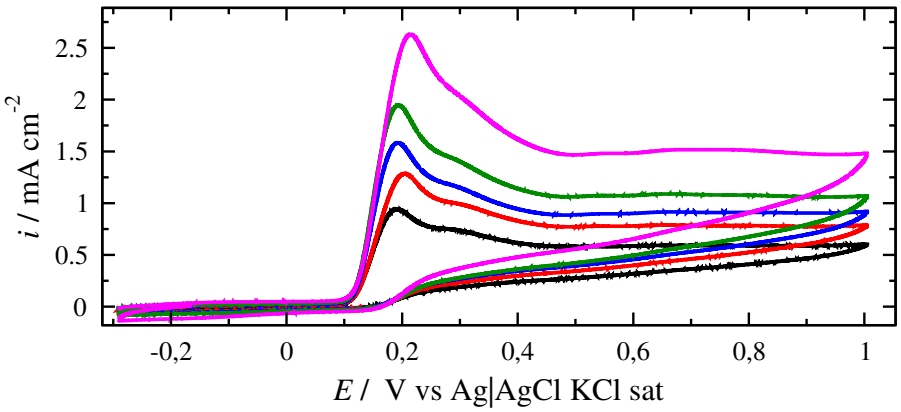

Figure 5.4.5: Cyclic voltammograms of 5 mM methyl gallate in 500 mM acetate buffer pH 6 at various scan rates at 25 °C. v values: 25 (black), 50 (red), 75 (blue) 100 (green), and 200 mV (magenta).

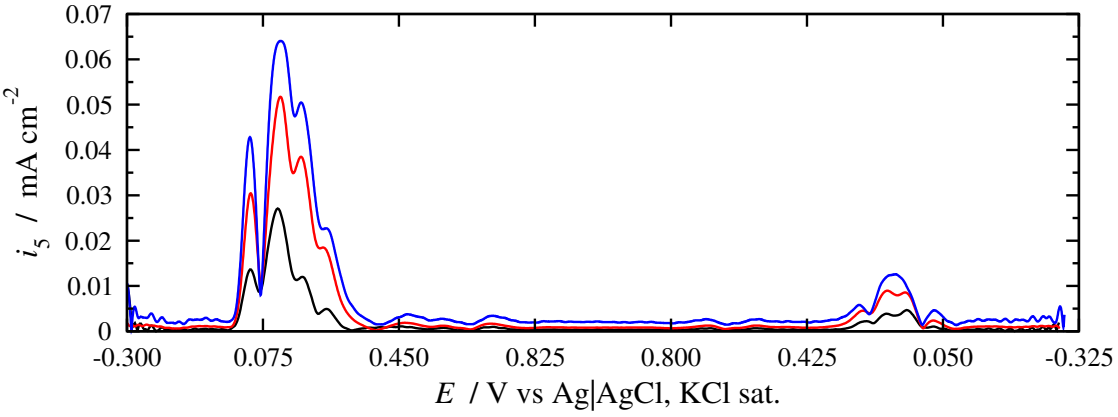

Figure 5.4.6: 5th harmonic of 5 mM gallic acid in 500 mM acetate buffer pH 6 at 25 °C for $v = 15$ mV/s, $A_0 = 100$ mV and $f = 1$ (black), 3 (red) and 5 Hz (blue).

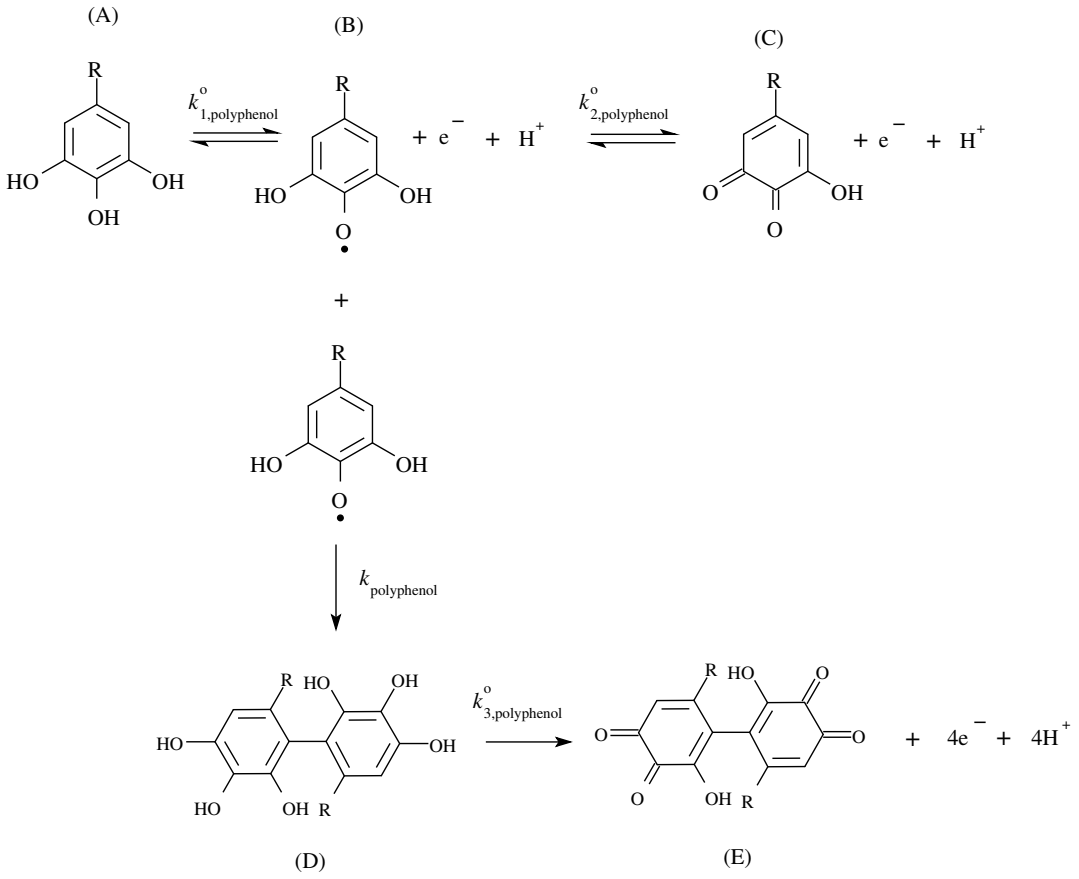

Figure 5.4.7: Indicative oxidation pathway of pyrogallol, gallic acid and methy gallate.

At first the reduced form of the polyphenol undergoes an one electron transfer forming a semi-quinone (B), with a standard rate constant $k^0_{1,\text{polyphenol}}$

$$\text{A} \overset{k^0_{1,\text{polyphenol}}}{\rightleftharpoons} \text{B} + \text{e}^- + \text{H}^+ \tag{5.4.1}$$

Then, again two other paths are possible. One is the further oxidation of B to a quinone (C) with a standard rate constant $k^0_{2,\text{polyphenol}}$

$$\text{B} \overset{k^0_{2,\text{polyphenol}}}{\rightleftharpoons} \text{C} + \text{e}^- + \text{H}^+ \tag{5.4.2}$$

while the other one is for two semi quinones to react together to form a dimer D at a reaction constant $k_{\text{polyphenol}}$

$$2\text{B} \xrightarrow{k_{\text{polyphenol}}} \text{D} \tag{5.4.3}$$

Finally the formed dimer undergoes an irreversible electrochemical oxidation with a standard rate constant $k^0_{3,\text{polyphenol}}$

$$\text{D} \xrightarrow{k^0_{3,\text{polyphenol}}} \text{E} + 4\text{e}^- + 4\text{H}^+ \tag{5.4.4}$$

The formal potential of the first step of all the 3 polyphenols examined in this section are estimated at values which render the reaction of the reduction of *Mt*LPMO9H feasible. However, what changes between these 3 is the potential that the possibly formed dimer probably appears. For gallic acid and pyrogallol, the deformation extra anodic peaks appear at potentials lower than that of *Mt*LPMO9H, meaning that the formed dimers can thermodynamically act as an electron sink for the enzyme as well. This can explain the higher yields in C_1 oxidized products for these two in comparison to ascorbic acid. On the other hand, regarding, methyl gallate which showed similar yields with ascorbic acid in C_1 oxidized products, the indications showed that the formed dimer could not act as an external electron donor for the LPMO.

5.5 Sinapic Acid

Next up in line for examination is sinapic acid (3-(4-hydroxy-3,5 -dimethoxyphenyl) prop- 2-enoic acid). When examined as a donor for *Mt*LPMO9H it gave a 15-34% activity in comparison to ascorbic acid regarding the non-oxidized and oxidized products. An anodic oxidation path of sinapic acid has been proposed by Nishiyama *et al.* [21].

The first step is an one electron oxidation of the sinapic acid forming a radical (B), with a standard rate constant $k^0_{1,\text{sinapic}}$,

$$\text{A} \overset{k^0_{1,\text{sinapic}}}{\rightleftharpoons} \text{B} + \text{e}^- + \text{H}^+ \tag{5.5.1}$$

The two formed radicals react together forming a dimer (C) undergoing an intramolecular transformation to a more stable form. This form can be further oxidized in an irreversible reaction to its final form E at a standard rate constant $k^0_{2,\text{sinapic}}$,

$$2\text{B} \xrightarrow{k_{1,\text{sinapic}}} \text{C} \tag{5.5.2}$$

$$\text{C} \xrightarrow{k_{2,\text{sinapic}}} \text{D} \tag{5.5.3}$$

$$\text{D} \xrightarrow{k^0_{2,\text{sinapic}}} \text{E} + 2\text{e}^- + 2\text{H}^+ \tag{5.5.4}$$

In Fig. 5.5.2 the cyclic voltammograms of 1 mM sinapic acid at various scan rate are presented. A 500 mM acetate buffer at a pH of 6 is used as a supporting electrolyte. The scan rates examined range from 50 to 150 mV/s. The potential is scanned from -0.2 anodically up to 0.8 V and then cathodically back to -0.2 V. Two peaks seem to appear at all scan rates with second more prominent than the first one. The first peak shall be attributed to the reaction from Eq. (5.5.2) while the second to that of Eq. (5.5.4).

In Fig. 5.5.3 the 5th harmonics resulting from FTacV performed on 1 mM sinapic acid in 500 mM acetate buffer pH 6 at 25 °C for $v = 10$ mV/s, $A_0 = 150$ mV at different frequencies are depicted. Again at the highest frequency examined one can relatively clearly see a quasi-reversible reaction arising which shall be attributed to the first step of the oxidation of sinapic acid. Then, what seems like an irreversible second reaction appears which shall be attributed to the oxidation of the dimer. The formal potential of the first step is estimated at 120 mV vs. Ag| AgCl (KCl sat) which makes it a valid electron donor for an *Mt*LPMO9H. However, no clear information regarding can be obtained for the irreversible oxidation of the dimer, even though from the deformation of the FTac voltammogram of the first step at more anodic potentials, it could be concluded that its formal potential lies higher than a value 250 mV, thus making it rather difficult, if not non feasible, for an interaction between sinapic acid and *Mt*LPMO9H to occur. Consequently thermodynamically, one could say that from the first step of the oxidation of sinapic acid, LPMO can thermodynamically obtain electrons, however, during the formed dimer is probably not in the position to contribute to the enzyme's reduction.

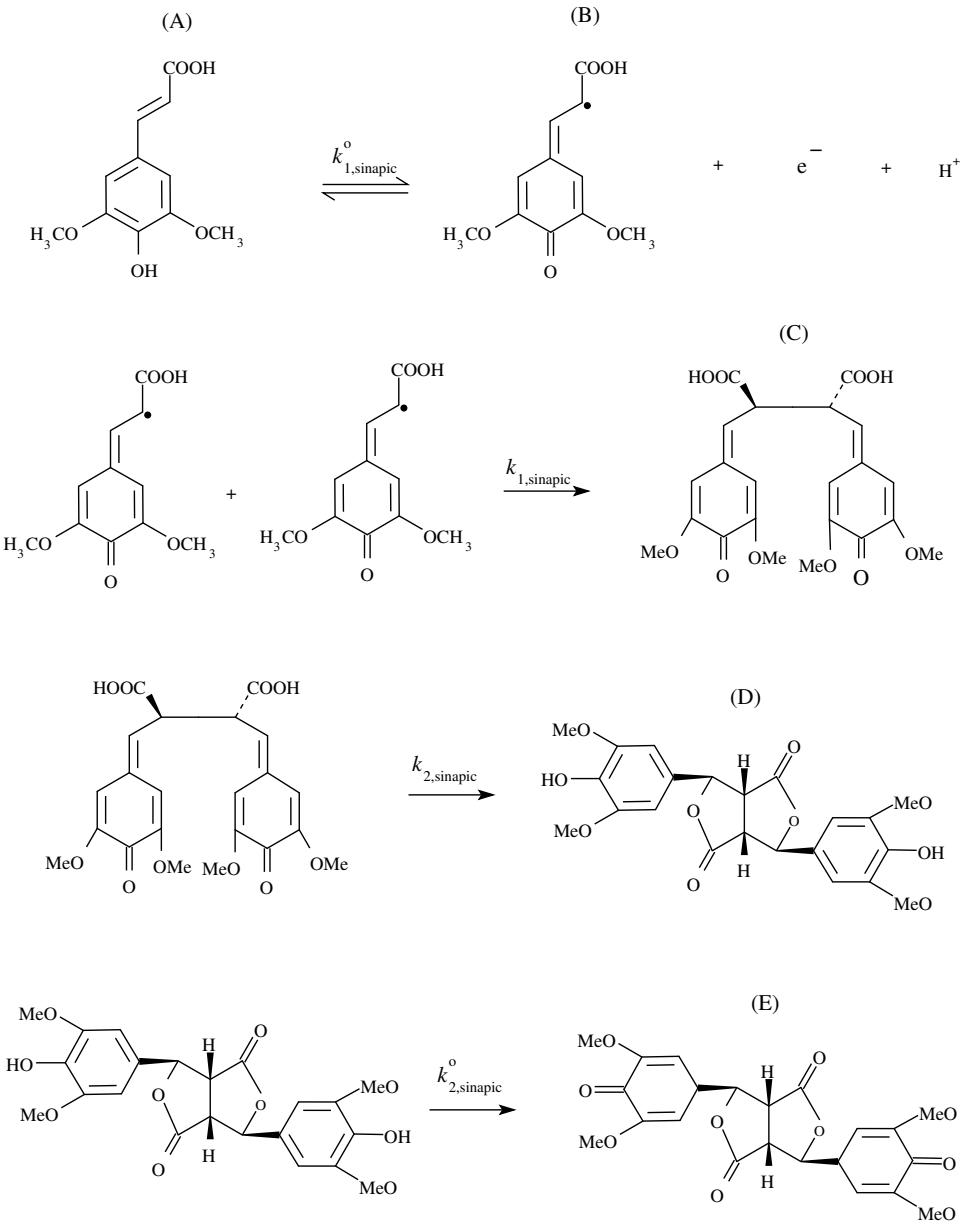

Figure 5.5.1: Sinapic oxidation pathway.

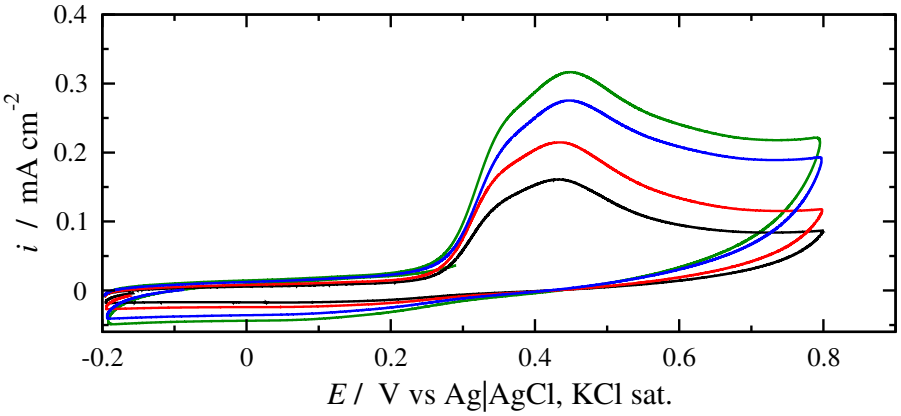

Figure 5.5.2: Cyclic voltammograms of 1 mM sinapic acid in 500 mM acetate buffer pH 6 at various scan rates at 25 °C. v values: 50 (black), 75 (red), 125 (blue) and 150 mV s^{-1} (green).

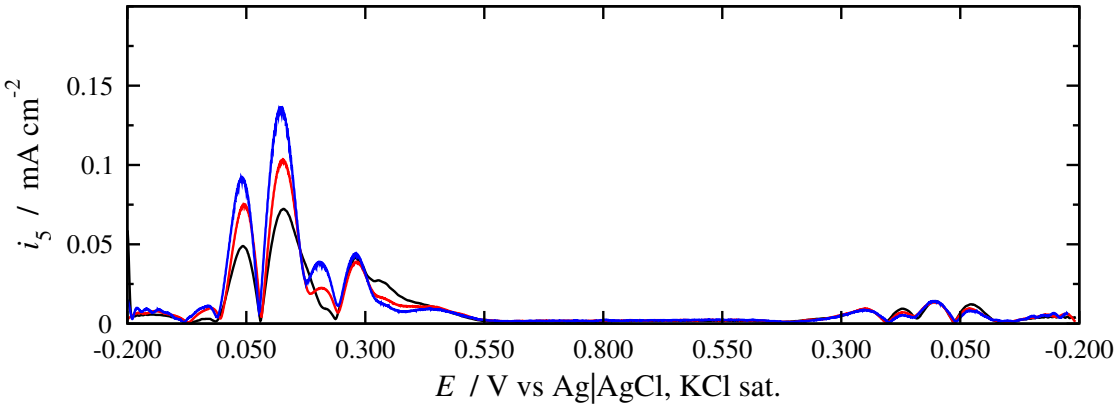

Figure 5.5.3: 5th harmonic of 1 mM sinapic acid in 500 mM acetate buffer pH 6 at 25 °C for $v = 10$ mV/s, $A_0 = 150$ mV and $f = 3$ (black), 5 (red) and 7 Hz (blue).

5.6 Syringaldehyde

The next phenolic compound to be examined is syringaldehyde (4-Hydroxy-3,5- dimethoxybenzaldehyde) which gave a yield of 20% yield of oxidized products compared to ascorbic acid when reacting with *Fo*LPMO9. The unexpected thing about this compound is that its electroactive behavior did not resemble the precious molecules studied.

The voltammograms of syringaldehyde at different scan rates appear in Fig. 5.6.1. A 500 mM acetate buffer pH 6 is used as a supporting electrolyte. The potential is scanned from -0.2 anodically to 0.8 V and then back to -0.2 V. While scanning anodically, a shoulder appears around 0.2 V and then a clear peak around 0.34 V. Going back cathodically during the reverse scan, a rather clear peak appears at -0.3 V. As one can observe the oxidation and reduction peaks are very close to each other. The mean distance of the oxidation and reduction peaks are 31 mV with a standard deviation at 6 mV. This is a clear indication of a 2 electron reversible reaction as the criteria for one to be characterized as such in the case of a free in a solution species is that the oxidation and the reduction peak should have a distance 29 mV. The formal potential of this reaction is estimated at 329 mV. The mystery remains on what is the first shoulder.

FTacV experiments were also performed on syringaldehyde but did not give more information as the second reaction was dominant again overshadowing the first one. The results thus are not presented since they would not add anything to the analysis.

Regarding the mechanism of the oxidation of syringaldehyde Kawai *et al.* studied the oxidation of methoxylated benzyl alcohol in the presence of a laccase from *Coriolus versicolor* in the presence of syringaldehyde and by studying the products of the reactions, they proposed a mechanism of the oxidation of syringaldehyde [22]. Based on what they reported in combination a reaction scheme is proposed in Fig. 5.6.2.

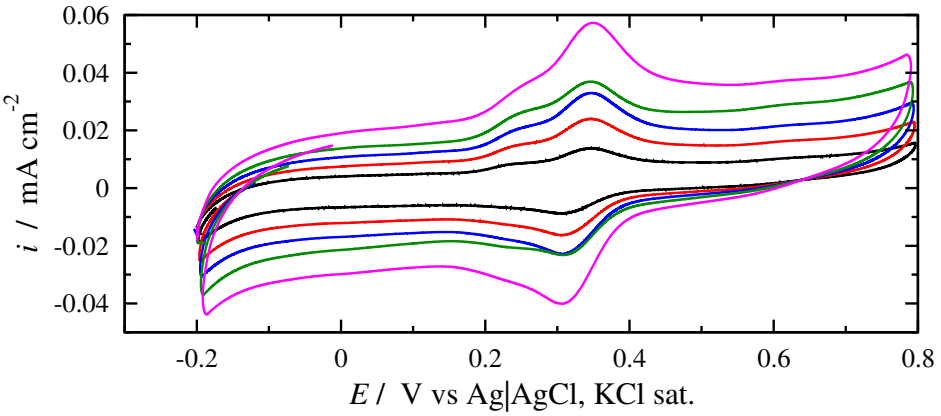

Figure 5.6.1: Cyclic voltammograms of 2 mM syringaldehyde in 500 mM acetate buffer pH 6 at various scan rates at 25 °C. v values: 25 (black), 50 (red), 75 (blue), 100 (green) and 150 mV (magenta).

The first shoulder found in the cyclic voltammogram is probably attributed to the oxidation of of syringaldehyde (A) to a phenoxy radical (B), with a standard rate

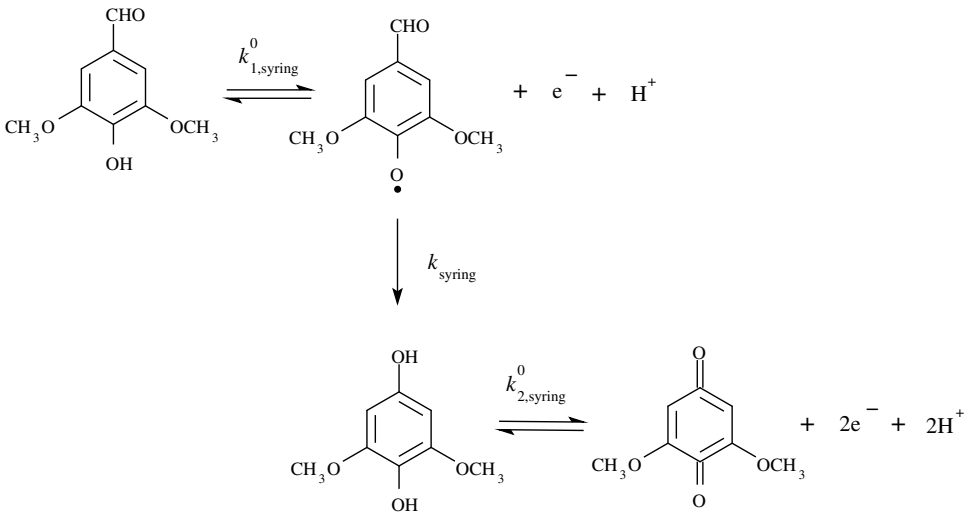

Figure 5.6.2: Syringealdehyde oxidation pathway.

constant $k^0_{1,\text{syring}}$. In case this is indeed a reversible reaction, based on the shoulder of the voltammograms which could corresponds to the oxidation peak, the formal potential of the first step should be found somewhere around 230 mV, marginally lower than the formal potentials of an LPMO, thus making it rather difficult, if not non feasible, for an interaction between sinapic acid and *Mt*LPMO9H to occur,

$$\mathrm{A} \overset{k^0_{1,\text{syring}}}{\rightleftharpoons} \mathrm{B} + \mathrm{e}^- + \mathrm{H}^+ \tag{5.6.1}$$

In the next step the phenoxyl radical (B) is converted to 2,6-dimethoxy-p-hydroquinone (C),

$$\mathrm{B} \xrightarrow{k_{\text{syring}}} \mathrm{C} \tag{5.6.2}$$

Then the 2,6-dimethoxy-p-hydroquinone (C) can be reversibly oxidized to 2,6-dimethoxy-p-benzoquinone (D),

$$\mathrm{C} \overset{k^0_{2,\text{syring}}}{\rightleftharpoons} \mathrm{D} + 2\mathrm{e}^- + 2\mathrm{H}^+ \tag{5.6.3}$$

5.7 Donors that did not work sufficiently

Moving on, we shall proceed with the phenolic compounds that did not work as electron donors with *Mt*LPMO9H, giving no yield in oxidized products. These are ferulic acid ((2E)-3-(4-hydroxy-3-methoxyphenyl)prop-2-enoic acid), vanillin (4-Hydroxy-3-methoxybenzaldehyde), *p*-coumaric acid ((2E)-3-(4-Hydroxyphenyl)prop-2-enoic acid), *p*-hydroxybezoic acid and vanillic acid (4-Hydroxy-3-methoxybenzoic acid). The voltammograms of all these compounds are presented alltogether at different scan rates under the same condition in Fig. 5.7.1.

Starting with ferulic acid, the cyclic voltammograms can be found in Fig 5.7.1 (a). The scanning starts at -0.3 V ending at 1.0 V and then going back to 0.3 V. The concentration of ferulic acid is 2.5 mM and the supporting electrolyte is a 500 mM acetate buffer pH 6. Only one broad peak is observed at a potential value of 0.46 V - quite higher that the peaks observed in the previous compounds. Assuming a kinetic scenario similar to the ones for the other phenolic compounds examined, that is a first step as an oxidation to a semi-quinone and a subsequent dimerization, the FTac voltammograms presented in Fig. 5.7.2 could be explained. A deformed oxidation peak appears around 0.25 V but not many conclusions can be reached. In this compound, the reverse scan is quite visible compared to the previous substances examined and a rather clear 5th harmonic is visible. If we consider it to correspond to the quasi reversible reduction of the first step of the mechanism, the formal potential is then calculated at 240 mV, a value higher than the ones of the other electron donors examined in this work. This potential comes close to the value of the potential of *Mt*LPMO9H, thus explaining possibly lack of interaction.

Regarding the rest of the compounds examined, looking the voltammograms examined in Fig. 5.7.1, the oxidation of all of them starts at potentials considerably higher that ($\geqslant$400 mV) of those that worked with *Fo*LPMO9A and their oxidation peak can be found at potentials higher that 500 mV. This is an indication that these compounds give electrons more difficult. Morever it is an indication that their formal potential is higher that the one of the LPMOs, thus making it imposible to work as electron donors. Supplementary claims to this is again the work of Hotta *et al.* in which ferulic acid, *p*-coumaric acid, *p*-hydroxybenzoic acid and vanillic acid showed lower electron scavenging activities indicating lower reducing capacitance [17].

5.8 Lignin as an electron donor

In this section of the thesis we shall examine the interaction of *Mt*LPMO9H with lignin isolated from wheat straw as an electron donor. Again the substrate that shall be used is PASC. The wheat straw used in this work was pretreated hydrothermally in a microwave digestion equipment at 195 °C for 15 min as described in the work of Matsakas and Christakopoulos [23]. The treated lignin will be referred to as HT-A-WS.

The feasibility of the reaction of *Mt*LPMO9H with HT-A-WS as an electron donor and PASC as a substrate was ascertained with the use of HPAEC-PAD. The enzyme was incubated with HT-A-WS at a concentration of 3 % w/v in a 400 mL final concentration

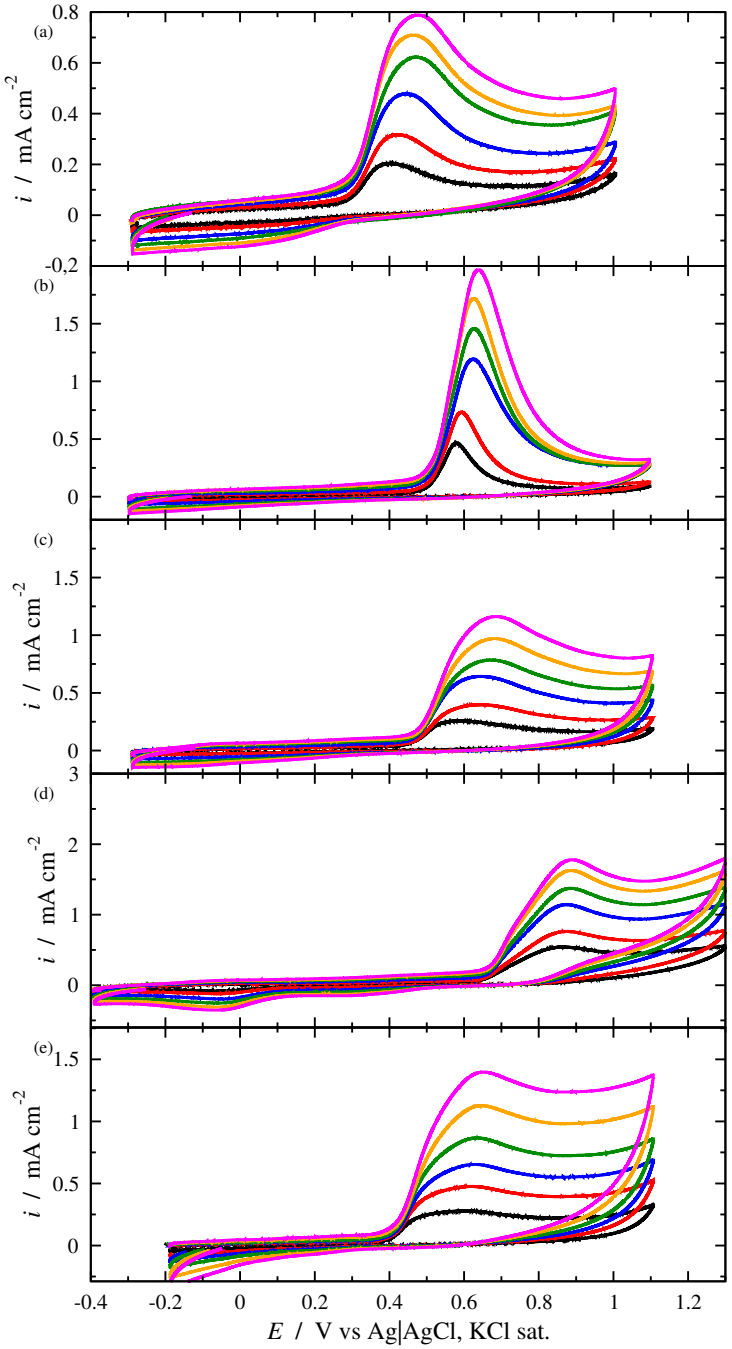

Figure 5.7.1: Cyclic voltammograms of 5 mM of phenolic compounds that did not work sufficiently as electron donors to *Fo*LPMO9A in 500 mM acetate buffer pH 6 at 25 °C at different v values. 25 (black), 50 (red), 75 (blue) 100 (green), and 200 mV s^{-1} (magenta) (a) ferulic acid (b) vanillin (c) *p*-coumaric acid (d) *p*-hydroxybenzoic acid (e) vanillic acid.

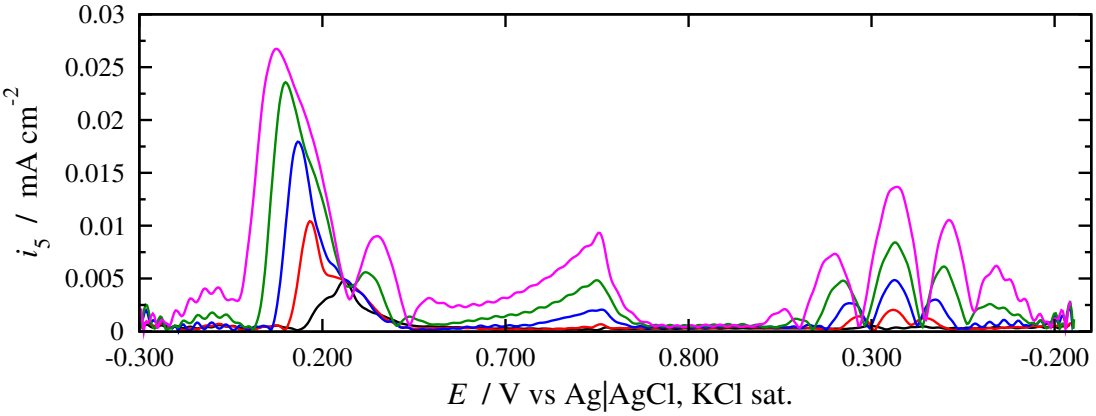

Figure 5.7.2: 5th harmonic of 2.5 mM ferulic acid in 500 mM acetate buffer pH 6 at 25 °C for v = 20 mV/s, f = 1 Hz and A_0 = 100 (black), 150 (red), 200 (blue), 250 (green) and 300 mV (orange).

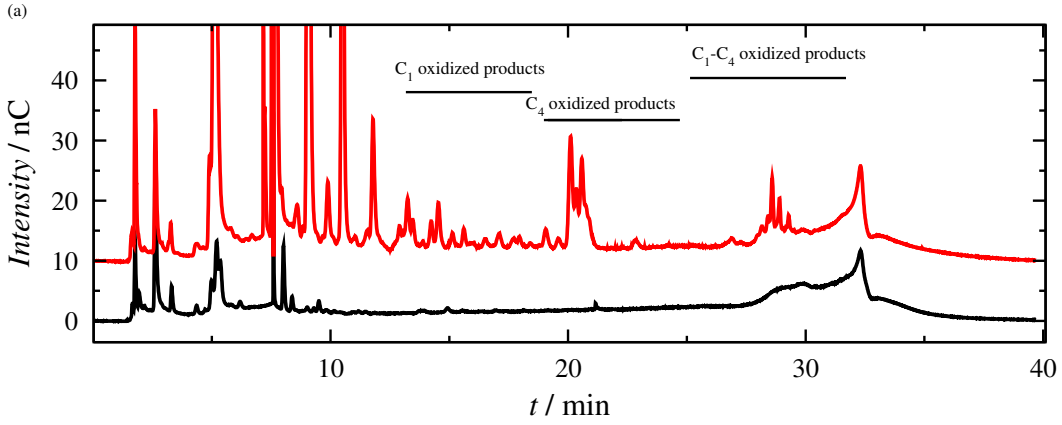

Figure 5.8.1: HPAEC-PAD elution patterns of PASC after a 24 h incubation with *Mt*LPMO9H (30 mg/g substrate) without (black) and with HT-A-WS (red).

reaction volume. The enzyme loading was 30 mg of enzyme per g of substrate. The buffer used was a 100 mM phosphate citrate buffer at a pH value of 6. The incubation took place at 50 °C for 24 h under agitation at 1100 rpm. A blank measurement was also run in the absence of lingin.

The HPAEC-PAD elution pattern is presented in Fig. 5.8.1, where, C_1, C_4 and C_1-C_4 products are indicated in the figure. It is rather obvious that HT-A-WS worked as an electron donor for *Mt*LPMO9H.

As a next step HT-A-WS was studied electrochemically. The lignin was immobilized on a 1 mm diameter glassy carbon disk electrode. It was first dissolved in absolute ethanol at a concentration of 2×10^{-3} mg/mL. 1 μL of this solution was left to dry on the surface of the electrode for a few minutes. This procedure was repeated two more times to increase the surface concentration of the lignin. After that 1 μL of Nafion^{TM} was left to dry above the lignin on the electrode surface for few minutes.

The cyclic voltammograms of HT-A-WS immobilized on a glassy carbon electrode

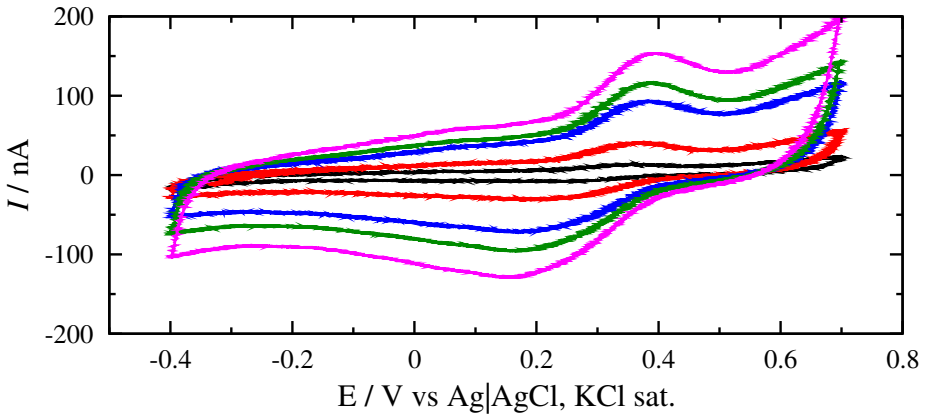

Figure 5.8.2: Cyclic voltammograms of immobilized HT-A-WS on a glassy carbon electrode using Nafion^{TM} in a pH 5 0.1 M tartrate buffer at 50 °C for v = 10 (black), 20 (red), 50 (blue), 70 (green) and 100 mV s^{-1}. (magenta).

in a pH 5 0.1 M tartrate buffer at 50 °C is presented in Fig. 5.8.2. Before recording these voltammograms, about 10 cycles were performed at 100 mV/s, until a stable cyclic voltammogram was achieved. The potential is scanned anodically from -0.4 to 0.7 V and then cathodically back to -0.4 V. During the anodic scan for v = 10 mV s^{-1} the anodic peak appears at 0.357 V and shifts towards more anodic potentials as the scan rate increases while the cathodic peak appears at 0.281 V and shifts to more cathodic potentials as the scan rate increases.

Regarding the interpretation of the voltammetric behaviour of lignin contains 15–30 free phenolic OH groups per 100 of C_9 units in softwoods and 10–15 groups in hardwoods [24]. When oxidation of this phenolic hydroxyl group occurs, the first step is the formation of a phenoxy radical I followed by de-methoxylation and formation of an o-quinone II. Phenoxy radicals can also recombine and form new C–C and O–O bonds leading to cross-link-ing of the lignin structure [25]. The redox peak is attributed to the quinone/hydroquinone couple.

In order to get an estimation of the apparent formal potential of FTacV was also performed for A_0 = 110 mV, v = 50 mV s^{-1} and f = 12.3 Hz. the 5th harmonic is presented in Fig.5.8.3. From the dominant peak of the 5th harmonic, the apparent formal potential is estimated at 346 mV, a value higher that the one of *Mt*LPMO9H, making it thermodynamically impossible for the lignin to give electrons to the enzyme. This lack of feasibility of the reaction between the lignins and the LPMOs based on the calculated formal potentials does not exclude the possibility of another oxidation path of the lignins that is not detectable electrochemically. Additionally, it has been proposed that the exchange of electrons between the lignin and the LPMOs is not direct but occurs through the use of lower molecular weight compounds [26].

To further ascertain that the LPMOs are indeed capable of utilizing the phenolic compounds released in the reaction medium,more experiments was conducted. HT-A-WS lignin was incubated either alone or in the presence of *Mt*LPMO9H in citrate–phosphate buffer 100 mM pH 5 for 24 h at 50 °C under agitation and the reaction mixtures were then centrifuged. The supernatants were collected and analyzed with

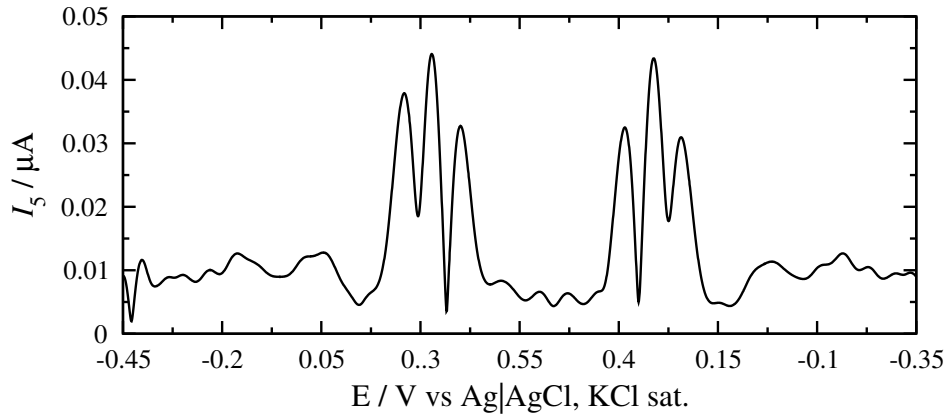

Figure 5.8.3: 5th harmonic of immobilized HT-A-WS on a glassy carbon electrode using Nafion^{TM} in a pH 5 0.1 M tartrate buffer at 50 °C for $v = 50$, $A_0 = 110$ mV and $f = 12.3$ Hz.

cyclic voltammetry and FTacV.

The supernatant after the lignin incubation without the enzyme (supernatant 1) was immobilized on the glassy carbon electrode. Both cyclic voltammetry and FTacV were performed under the same conditions as for the immobilized lignins.

To further ascertain that the LPMOs are indeed capable of utilizing the phenolic compounds released in the reaction medium,more experiments was conducted. HT-A-WS lignin was incubated either alone or in the presence of *Mt*LPMO9H in citrate–phosphate buffer 100 mM pH 5 for 24 h at 50 °C under agitation and the reaction mixtures were then centrifuged. The supernatants were collected and analyzed with cyclic voltammetry and FTacV.

The supernatant after the lignin incubation without the enzyme (supernatant 1) was immobilized on the glassy carbon electrode. Both cyclic voltammetry and FTacV were performed under the same conditions as for the immobilized lignins. In Fig. 5.8.4(a), the cyclic voltammograms of supernatant 1 are depicted at different scan rates and it is evident that a second redox peak couple appears around 20 mV apart from the one around 300 mV, that is the one corresponding to the redox couple observed at the voltammetric experiments of HT-A-WS immobilized on the electrode surface.

FTacV was also performed on supernatant 1 (Fig. 5.8.5) and comparing it to the 5th harmonic of HT-A-WS (Fig.5.8.3) a second set of peaks is arising at around 20 mV in the supernatant, reinforcing the indication of the cyclic voltammogram that a second redox peak appears. These results indicate that some electroactive compounds, possibly from the bulk lignin structure could be released in the solution during the incubation and the electron transfer is possible through them. With the potential of the second redox couples more negative than that of *Mt*LPMO9H, one could assume that the reduction of the LPMO by the lignin is indeed feasible. The supernatant of lignin incubated with *Mt*LPMO9H (supernatant 2) is also analyzed with cyclic voltammetry under the same conditions (Fig. 5.8.4(b)), showing that the second redox couple is less evident, indicating that the couple has reacted and been consumed (oxidized). The results indicate that LPMOs are capable of oxidizing the lignin-derived electroactive

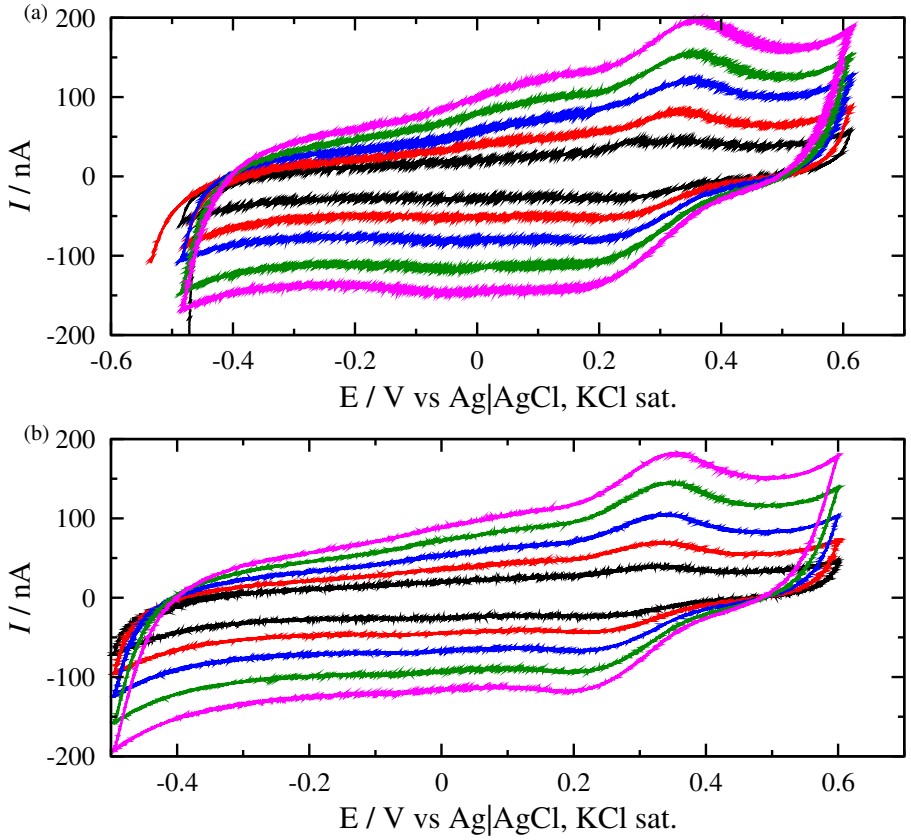

Figure 5.8.4: Cyclic voltammograms of supernatants after (a) lignin and (b) lignin in the presence of *Mt*LPMO9H incubation in 0.1 M phosphate-citrate buffer pH 5 for 24 h at 50°C, at 30 (black), 60 (red), 100 (green), 150 (orange) and 200 (magenta) mV/s in deaerated 0.1 M pH 5 tartrate buffer at 50°C

compounds released in the reaction, is a thermodynamically feasible process, indicating that these compounds act as the initial reducing agents that trigger the action of the enzymes.

Both supernatants and precipitates were tested as electron donors for *Mt*LPMO9H, with PASC as a substrate using HPAEC-PAD. Looking at the elution patterns in Fig. 5.8.6 one can observe that the supernatant can act as a reducing agent and support the release of oxidized sugars from PASC. The sugars yield was much lower when lignin was used, which is attributed to the consumption (oxidation) of the free phenolic compounds that terminated the reaction. Interestingly, when the lignin precipitate was used, only traces of oxidized sugars are detected. These results lead to the assumption that LPMOs do not use directly the bulk lignin as an electron donor, but the small molecules that are possibly released in the buffer instead.

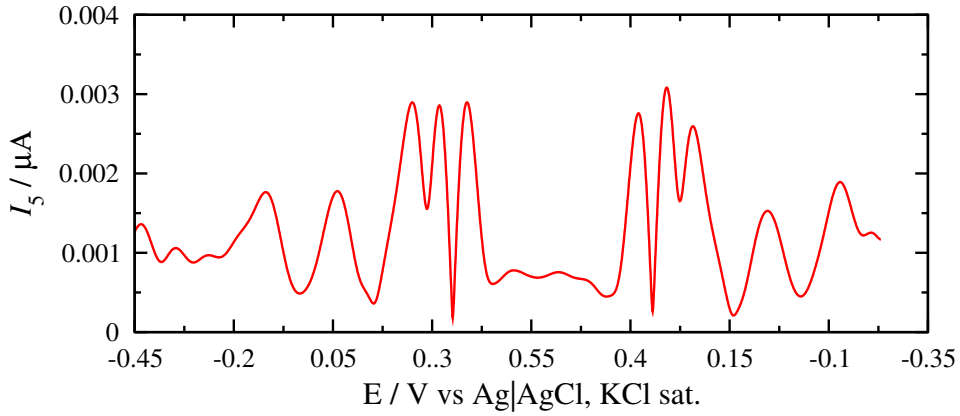

Figure 5.8.5: 5th Harmonic of supernatant 1 immobilized on a glassy carbon electrode with the use of Nafion^{TM} for $v = 50$, $A_0 = 110$ mV and $f = 12.3$ Hz in deaerated 0.1 M pH 5 tartrate buffer at 50°C.

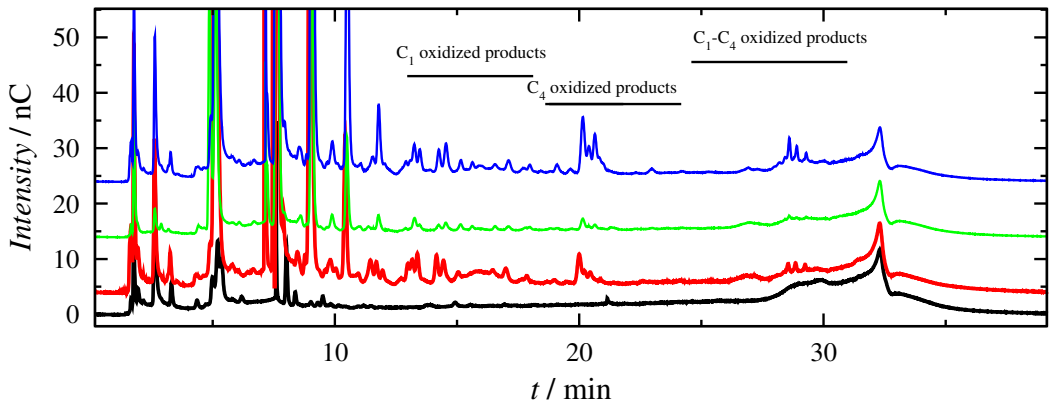

Figure 5.8.6: HPAEC-PAD elution patterns: PASC after a 24 h incubation with *Mt*LPMO9H (30 mg/g substrate) without lignin (black). Lignin was pre-incubated in buffer for 24 h, then the supernatant was added to PASC together with *Mt*LPMO9 and incubated for another 24 h(red). Lignin was pre-incubated in buffer for 24 h, then the precipitant was added to PASC together with *Mt*LPMO9H and incubated for another 24 h (green). PASC was pre-incubated with lignin for 24 h, then MtLPMO9 was added and incubated for another 24 h (blue).

Bibliography

[1] A. Karnaouri, M. N. Muraleedharan, M. Dimarogona, E. Topakas, U. Rova, M. Sandgren, and P. Christakopoulos. Recombinant expression of thermostable processive *Mt*EG5 endoglucanase and its synergism with *Mt*LPMO from *Myceliophthorathermophila* during the hydrolysis of lignocellulosic substrates. *Biotechnol. Biofuels*, 10(1):126, 2017.

[2] H. Borsook and G. Keighley. Oxidation-reduction potential of ascorbic acid (vitamin C). *PProc Natl Acad Sci U S A.*, 19(9):875, 1933.

[3] P. Karabinas, D. Sazou, and D. Jannakoudakis. —comparative electrochemical study of L-ascorbic acid and dihydroxyfumaric acid on a mercury electrode in neutral media. *Bioelectrochem. Bioenerg.*, 14(4-6):469–478, 1985.

[4] I. Feng Hu and T. Kuwana. Oxidative mechanism of ascorbic acid at glassy carbon electrodes. *Anal. Chem.*, 58(14):3235–3239, 1986.

[5] Y. I Tur'yan and R. Kohen. Formal redox potentials of the dehydro-L-ascorbic acid/L-ascorbic acid system. *J. Electroanal. Chem.*, 380(1-2):273–277, 1995.

[6] Y. Nishikawa and T. Kurata. Interconversion between dehydro-L-ascorbic acid and L-ascorbic acid. *Biosci. biotech. biochem.*, 64(3):476–483, 2000.

[7] Y. J. Tu, D. Njus, and H. B. Schlegel. A theoretical study of ascorbic acid oxidation and HOO/O_2- radical scavenging. *Org. Biomol. Chem.*, 15(20):4417–4431, 2017.

[8] T. Matsui, Y. Kitagawa, M. Okumura, and Y. Shigeta. Accurate standard hydrogen electrode potential and applications to the redox potentials of vitamin C and NAD/NADH. *J. Phys. Chem. A*, 119(2):369–376, 2015.

[9] M. D. Lovander, J. D. Lyon, D. L. Parr IV, J. Wang, B. Parke, and J. Leddy. Critical review—electrochemical properties of 13 vitamins: a critical review and assessment. *J. Electrochem. Soc.*, 165(2):G18, 2018.

[10] S. A. Wring, J. P. Hart, and B. J. Birch. Voltammetric behaviour of ascorbic acid at a graphite—epoxy composite electrode chemically modified with cobalt phthalocyanine and its amperometric determination in multivitamin preparations. *Anal. Chim. Acta*, 229:63–70, 1990.

[11] I. G. Casella and M. R. Guascito. Electrocatalysis of ascorbic acid on the glassy carbon electrode chemically modified with polyaniline films. *Electroanalysis*, 9(18):1381–1386, 1997.

[12] J. B. Raoof, R. Ojani, H. Beitollahi, and R. Hossienzadeh. Electrocatalytic determination of ascorbic acid at the surface of 2, 7-bis (ferrocenyl ethyl) fluoren-9-one modified carbon paste electrode. *Electroanalysis*, 18(12):1193–1201, 2006.

[13] W. Ren, H. Q. Luo, and N. B. Li. Simultaneous voltammetric measurement of ascorbic acid, epinephrine and uric acid at a glassy carbon electrode modified with caffeic acid. *Biosens. Bioelectron.*, 21(7):1086–1092, 2006.

[14] M. Shamim and S. M. A. Baki. Diffusion measurements in aqueous L-ascorbic acid solutions. *Aust. J. Chem.*, 33(8):1857–1861, 1980.

[15] H. Hotta, H. Sakamoto, S. Nagano, T. Osakai, and Y. Tsujino. Unusually large numbers of electrons for the oxidation of polyphenolic antioxidants. *Biochim. Biophys. Acta, Gen. Subj.*, 1526(2):159–167, 2001.

[16] R. Arakawa, M. Yamaguchi, H. Hotta, T. Osakai, and T. Kimoto. Product analysis of caffeic acid oxidation by on-line electrochemistry/electrospray ionization mass spectrometry. *J. Am. Soc. Mass Spectrom.*, 15(8):1228–1236, 2004.

[17] H. Hotta, S. Nagano, M. Ueda, Y. Tsujino, J. Koyama, and T. Osakai. Higher radical scavenging activities of polyphenolic antioxidants can be ascribed to chemical reactions following their oxidation. *Biochim. Biophys. Acta, Gen. Subj.*, 1572(1):123–132, 2002.

[18] M. D. Ryan, A. Yueh, and W. Y. Chen. The electrochemical oxidation of substituted catechols. *J. Electrochem. Soc.*, 127(7):1489, 1980.

[19] S. Yamamura and S. Nishiyama. Anodic oxidation of phenols towards the synthesis of bioactive natural products. *Synlett*, 2002(04):0533–0543, 2002.

[20] P. Caregnato, P. M. D. Gara, G. N. Bosio, M. C. Gonzalez, N. Russo, M. Michelini, and D. O. Mártire. Theoretical and experimental investigation on the oxidation of gallic acid by sulfate radical anions. *J. Phys. Chem. A.*, 112(6):1188–1194, 2008.

[21] A. Nishiyama, H. Eto, Y. Terada, M. Iguchi, and S. Yamamura. Anodic oxidation of 4-hydroxycinnamic acids and related phenols. *Chemical and pharmaceutical bulletin*, 31(8):2845–2852, 1983.

[22] S. Kawai, T. Umezawa, and T. Higuchi. Oxidation of methoxylated benzyl alcohols by laccase of *Coriolus versicolor* in the presence of syringaldehyde. *Wood research : bulletin of the Wood Research Institute Kyoto University*, 76:10–16, 1989.

[23] L. Matsakas and P. Christakopoulos. Fermentation of liquefacted hydrothermally pretreated sweet sorghum bagasse to ethanol at high-solids content. *Bioresour. Technol.*, 127:202–208, 2013.

[24] E. Sjostrom. *Wood chemistry: fundamentals and applications*. Gulf professional publishing, 1993.

[25] G. Milczarek. Preparation and characterization of a lignin modified electrode. *Electroanalysis: An International Journal Devoted to Fundamental and Practical Aspects of Electroanalysis*, 19(13):1411–1414, 2007.

[26] B. Westereng, D. Cannella, J. W. Agger, H. Jørgensen, M. L. Andersen, V. G. H. Eijsink, and C. Felby. Enzymatic cellulose oxidation is linked to lignin by long-range electron transfer. *Sci. Rep.*, 5(1):1–9, 2015.

6. Interaction of TtLMCO1 with epinephrine

The scope of the chapter is to immonibilize a laccase like multi copper oxidase from the fungus *Thermothelomyces thermophila* in order to achieve direct electron transfer and then examine its interaction with a neurotransmitter as a substrate. The enzyme examined is *Tt*LMCO1 which has been recently been expressed and purified [1].

Beginning this chapter, an introduction to the multicopper oxidases and laccases shall be made, regarding their mechanisms as well as their exploitation up to now, regarding electrochemical studies with direct electron transfer.

Experimentall, after its electrochemical activity is ascertained while immobilized on a pyrolytic carbon electrode with Nafion^{TM} as an immobilization matrix, the electrochemical behavior of free in the solution epinephrine is examined on both glassy carbon and pyrolytic carbon electrode. Finally, the interaction of the immobilized enzyme and the free in the solution epinephrine - acting as a substrate - is studied. Also the application of the theory of probing an immobilized redox enzyme reacting with a free in the solution substrate following a Michaelis-Menten kinetic scheme is examined.

6.1 Multicooper oxidases

Multicopper oxidases (MCOs) comprise a rather diverse group of enzymes that couple the oxidation of a variety of substrates to the reduction of molecular oxygen using Cu ions as cofactors [2, 3].

The main components of their active center are [3, 4]

- One "blue"[1] type 1 (T1) Cu center
- One trinuclear cluster including:
  - A "normal" mononuclear type 2 (T2) Cu site

[1]The T1 Cu center is referred to as "blue" due to its strong absorption at 600 nM in the UV-Vis spectrum [5]

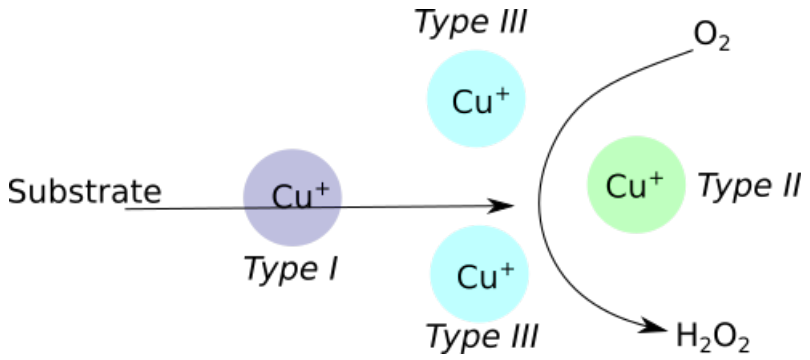

Figure 6.1.1: Schematic representation of MCO mechanism.

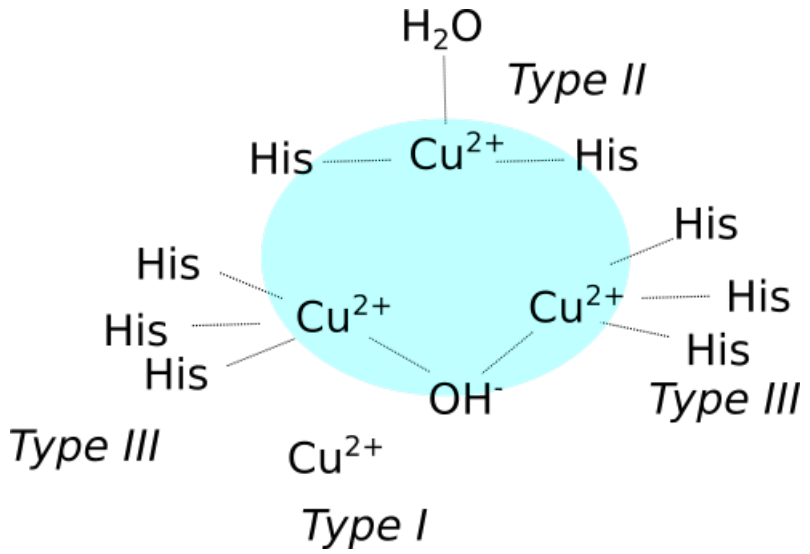

Figure 6.1.2: Schematic representation of the active center of a MCO.

– A binuclear type 3 (T3) Cu center, binding and reducing O_2

Regarding its mechanism, the mononuclear T1 Cu accepts electrons from a wide variety of phenolic substrates transferring the trinuclear center. Then molecular oxygen binds to the trinuclear centre and, following the transfer of four electrons, is reduced to two molecules of water [6]. A more vivid illustration of this mechanism can be found in Fig. 6.1.1.

For purely informative reasons, let us take a close look at the structure of the active center of a MCO, see Fig. 6.1.2. The T1 copper has a distorted tetrahedral coordination with three ligands (one cysteine and two histidines), while the T2 copper is generally coordinated by two histidines and a water or hydroxide ion. T3 copper is coordinated by three histidines. A T2 copper ion and a pair of T3 copper ions form a trinuclear copper cluster (TNC), which is the active site for O_2 reduction. A hydroxyl ion bridges the T3 copper ion pair.

Some of the main MCO classes are:

- Ceruloplasmin - EC 1.16.3.1 - (ferroxidase), a 6-domain enzyme oxidizing different

inorganic and organic substances

- Laccase - EC 1.10.3.2 - (p-benzenediol: oxygen oxidoreductases), a 3-domain enzyme which oxidizing different phenols and diamines.
- Ascorbate oxidase - EC 1.10.3.3 -, a 3-domain enzyme. Its main substrate is ascorbic acid
- Nitrite reductase - EC 1.7.2.1 -, a 2-domain enzyme containing type-1 and type-2 copper centres.

Of these categories we shall pay a bit more attention to the laccases, as the enzyme examined in this work is laccase-like oxidase. A few introductory information shall be provided and then a quick overview of the electrochemical study of laccases will be presented.

6.1.1 Laccases overview

Laccases(E.C. 1.10.3.2, p-benzenediol: oxygen oxidoreductases) are multicopper oxidases which catalyze the oxidation of various phenolic compounds as well as amines while simultaneously catalysing the reduction of molecular oxygen to water. They are mostly encountered as monomeric, secreted glycoproteins, around 60–70 kDa in size, with acidic pI [7]. Up to now, laccases have been encountered in a variety of organisms, such as bacteria, fungi, plants and insects [8]. Thermostable laccases have been isolated from Basidiomycetes, Ascomycetes and bacterial species. More information on thermostable laccases can be found in [9].

Laccases of fungal origin, as the one examined in this work, are mainly extracellular , and they are involved in a number of different physiological processes, including wood degradation and delignification, virulence, pathogenesis, pigmentation, and fruiting body formation [10].

Regarding their active center's structure, they follow the typical coordination of a MCO as described above. Regarding some more specific characteristics of laccases, the topology of the T1 copper–binding site is formed by two His[2] and one Cys[3] equatorial residues in trigonal coordination with the Cu atom, and two additional weakly– or non–coordinating residues in an axial position [11]. A Met[4] is usually found in one of these axial ligands of low redox potential, E^0, around 0.3 to 0.5 V versus normal hydrogen electrode (NHE) bacterial and plant laccases, coordinating to the T1 copper center, contrary to most fungal ones, which include a Leu[5] or Phe[6] [7, 12]. The existence of Met as a fourth coordinating axial ligand at the T1 Cu center, or its replacement by a Phe or a Leu, might affect, to a certain extent, the E^0 of the enzyme. Laccases with non–coordinating residues at this position generally have higher E^0, and they are thus

[2]Histidine
[3]Cysteine
[4]Methionine
[5]Leucine
[6]Phenylalanine

capable of oxidizing a wider array of substrates [11]. High E^0 basidiomycete laccases (0.5 - 0.8 V versus NHE) usually have a Phe, and medium E^0 ascomycete laccases (0.4 - 0.7 V versus NHE) have Leu [13, 11]. However, this observation is not to be taken as a general rule, since for example, the M. thermophila laccase, containing Leu in this position, has still a lower E^0 than *Bacillus subtilis* CotA laccase [14].

When it comes to their study with electrochemical methods, one of the first attempts to achieve direct electron transfer, *i.e.* reduction on an electrode material, of a laccase was when a laccase was absorbed on a pyrolytic carbon electrode surface. This was reported by Lee *et al.* in 1984 while examining the catalysis of oxygen [15]. Later, in 1998 the blue copper oxidase from *Polyporus versicolor* was abdorbed on an edge plane pyrolytic carbon electrode [16]. Again, the reduction of molecular oxygen was examined and the laccase modified electrode was also tested under anaerobic conditions.

Other studies revealing direct electron transfer between a laccase confined on an electrode surface include cyclic voltammetry on a laccase purified from acetone-dried powder from the lac[7] of the Japanese lacquer tree *Rhus vernicifera* embedded within a polymeric film of an anionic exchange resin containing tributylmethyl phosphonium chloride (TBMPC) bound to polystyrene, cross-linked with 1% (w/v) divinylbenzene [17]. In this work a E^0 of about 400 mV vs NHE is reported at a pH value of 7. Typical problems of high capacitance currents are clearly stated in this work.

In 2005 Shleev et al. reported direct electron transfer from a laccase originating from the fungus *Trametes hirsuta* on a capillar gold electrode with the enzyme free in the solution. The concentration of the enzyme used was rather high at a value of 10 mg/mL. In the voltammograms no evident peaks arised, with only the backgroung current being visible in the absence of a O_2. Nevertheless, when the molecular oxygen was present, the background current was somewhat deformed resembling sigmoidal currents, indication of a reaction occuring between the enzyme and the molecular oxygen [18].

Another interesting work on the intermolecurlar electron transfer of laccases is that of Ivnitski and Atanassov [19]. A laccase from *Trametes versicolor* is examined while immobilized on a carbon electrode using a matrix of glutaraldehyde and a cationic polyethylenimine (PEI) polymer. With the use of cyclic voltammetry two sets of peaks were detected with the first one being attributed to the T2/T3 center at 250 mV vs Ag|AgCl, 3 M KCl and the second one to the T1 center at $\approx$ 540 mV.

In another work, the His-Tag of a recombinant laccase was exploited for the immobilization of the enzyme on a gold surface covered by NTA-terminated alkanethiols [20].

More recent research examining on direct electron transfer of laccases has focused on more applied approaches such as the use of laccases in biosensing for the detection of various phenolic compounds, giving less significance ot the mechanistic aspect and kinetics of the immobilized laccases [21, 22].

Taking into account that direct electron transfer of laccases is indeed possible, a laccase-like multicopper oxidase from *Thermothelomyces thermophila* shall be examined in this work.

[7] Lac is the resinous secretion of a number of species of lac insects, of which the most commonly cultivated is *Kerria lacca*.

6.1.2 *Tt*LMCO1

Before moving to the experimental section of this Chapter, a few details of *Tt*LMCO1 shall be noted as published recently [1]. *Tt*LMCO1 was isolated first by A. Zerva et al. This LMCO originated from the thermophilus fungus *Thermothelomyces thermophila* and was expressed in *Pichia pastoris* using the vector pPICZαA[8] Various substrates were reported to have been tested in the publication including cathechol, 2,6 dimethoxyphenol, pyrogallol, guaiacol, L-DOPA, ABTS and L-ascorbic acid.

Other tested substrates such as epinephrine, showed somewhat promising results but still its substrate range was deemed rather narrow.

Its molecular weight was estimated at 75 kDa with SDS-Page gel electrophoresis and the pI value was found at a value of 4. Its optimum temperature for enzymatic activity towards ABTS[9] as a reference was found to be at 50°C, while its optimum pH was at a value of 4. Thus, it was classified as a thermophilic acidic enzyme.

Most of its activity was found to be kept at high salt concentrations [10], an important factor, as the supporting electrolyte in electrochemical experiments requires rather high salt concentrations so as to avoid incompensated resistance and electromigration currents.

6.2 Experimental Process

Voltammetric experiments were performed in a single compartment three electrode cell consisting of a disk pyrolytic graphite electrode (PGE) (Alfa Aesar) as working electrode, a Pt wire as a counter electrode (ALS Co.), and a Ag|AgCl, KCl sat. reference electrode (+0.197 V vs NHE) (ALS Co.). The aqueous solution of about 20 mL consisted of 0.5 M acetate buffer (various pH) as supporting electrolyte. The sodium acetate was purchased by Panreac and the acetic acid by Chem-Lab NV. Nafion^{TM} perfluorinated resin solution used in the experiments concentration was 5 wt% in lower aliphatic alcohols and water (Aldrich).

Voltammetric measurements were performed by a PAR 362 Potentiostat connected to a Rigol DS1047Z, which was used as a sinusoidal perturbation generator. All solutions were deaerated for at least 10 min before the experiments in order to avoid oxygen reduction on the electrode surface or even possible catalytic currents. Nitrogen gas was also purged over the solution during measurement. The temperature of the cell was kept at a specific value during measurement with the use of a thermostated bath. The temperature of the cell was recorded during the measurement, in order to assure that it remained constant.

The enzyme *Tt*LMCO1 was produced and purified to homogeneity as described in the previous chapter. More information can be found here [23]. After the purification the enzyme was divided in aliquots of 500 μL and was stored at -15 °C until used.

[8] The experimental procedure for the expression in pPICZαA is the same as the one described for pPICZαC in the previous chapter. The difference is that 0.25 mM of Cu_2SO_4 are added in the main culture for the expression of this particular enzyme.

[9] 2,2'-azino-bis(3-ethylbenzothiazoline-6-sulfonic acid.

[10] 0.1 M NaCl.

Each aliquot was stored for a maximum time of 5 days at 4 °C after its first use. The concentration of the purified enzyme was about 1.5 mg/mL. The pyrolytic graphite electrode was polished on a cloth with the use of a 0.3 μm alumina, after it was polarized in $HClO_4$ for 10 min at -2.5 V. The electrode was then washed with distilled water and subsequently sonicated in distilled water for 5 min. After the sonication, the electrode was again washed with distilled water. An enzyme volume mixed with Nafion^{TM} in a volume ratio of 1:1 was left on the surface of the pyrolytic graphite electrode to dry for about 15 min at room temperature. The amount of enzyme-Nafion^{TM} mixture was 10 μL and by taking into account the molecular weight 75 kDa of the *Tt*LMCO1 and the electrode surface of 0.48 cm^2, an estimate for the maximum surface concentration was calculated at 1×10^{-10} mol/cm^2. The activity of the enzyme before immobilization was assayed with ABTS substrate and was found 3.33 ± 0.21 U/L as described in the work of Zerva *et al.* [1] at room temperature.

All experiments were repeated three times and all epinephrine solutions were freshly prepared before each set of experiments.

6.2.1 Pyrolytic Carbon surface determination

*Tt*LMCO1 was immobilized on a pyrolytic carbon electrode. The choice of this material was based on the fact that in some works it was reported that laccases can be absorbed on such an electrode [15, 16]. Other attempts were made with the use of glassy carbon electrode as well as a plate gold electrode, but the efforts did not give off results that were convincing enough to insist and carry on with these materials.

Since the surface of pyrolytic carbon is not even, the geometrical one does not coincide with the real electroactive surface. And since it is useful to convert current values to current densities by dividing with the real surface area of an electrode, as a first step in this study, the surface is estimated. For this, linear sweep voltammograms of 5 mM $[Fe(CN)_6]^{3-}$ in 1 M Na_2SO_4 at $T = 25$ °C for different scan rates is performed between 0.7 and -0.2 V. The voltammograms are presented in Fig. 6.2.1(a) for scan rated of 5, 10, 25, 50 and 100 mV/s. Higher values of scan rated were not used, as the system started deviating from reversible kinetics. Based on the Randles-Sevcik equation

$$I_p = 2.69 \times 10^5 n^{3/2} S D_{ox}^{1/2} C_{ox} v^{1/2} \tag{6.2.1}$$

and the value of the diffusion coeffient found in the literature $D_{ox} = 0.896 \times 10^{-5}$ cm^2/s, the surface area S shall be estimated. By plotting the reduction peaks against the inverse square root of the respective scan rate, Fig. 6.2.1 (b), the resulting electroactive surface is estimated at 0.48 cm^2. Thus, from now on, all current densities presented in this chapter when pyrolytic carbon is used a working electrode will have been calculated based on this value.

6.2.2 *Tt*LMCO1 electrochemical activity ascertation

After having estimated the working electrode surface area, the next step of the experimental procedure is to ascertain if direct electron transfer is feasible by immobilizing

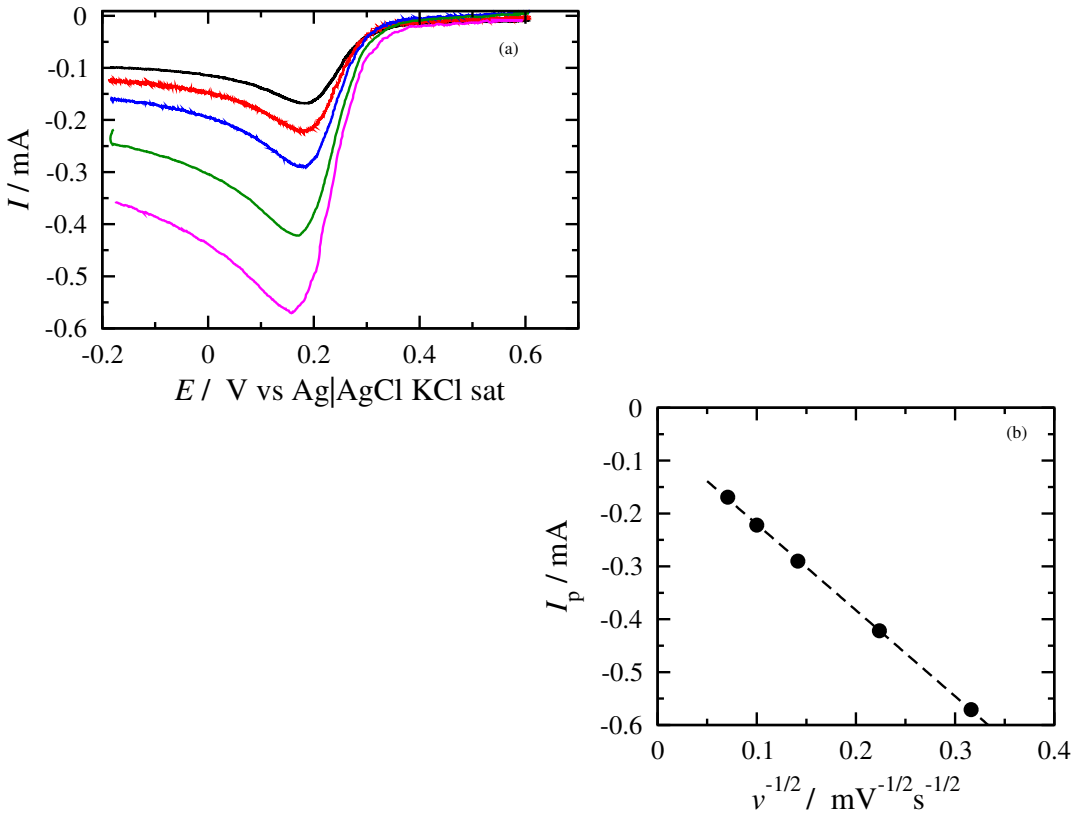

Figure 6.2.1: (a) Linear sweep voltammograms of 5 mM $[Fe(CN)_6]^{3-}$ in 1 M Na2SO4 at $T = 25$ °C with pyrolytic carbon as a working electrode for $v = 5$ (black), 10 (red), 25 (blue), 50 (green) and 100 mV/s (magenta) (b) peak current I_p against the inverse scan rate $v^{-1/2}$ together with the corresponding linear fit.

*Tt*LMCO1 on a pyrolytic graphite electrode surface.

The 5th harmonic component of FTacV voltammograms for different temperatures of *Tt*LMCO1 immobilized with Nafion^{TM} on pyrolytic graphite, are presented in Fig. 6.2.2. The potential is scanned from 0.6 to -0.2 V at an A_0 value of 300 mV and a frequency f value of 5 Hz. The scan rate used is 20 mV/s and the experiment is considered independent of this parameter.

The dominant peak presented is rather clear for both the oxidation and the reduction and it can be observed that its magnitude decreases as the temperature rises. This could be attributed to the immobilization in a Nafion^{TM} matrix which might not be the ideal one for this enzyme while entrapped in this particular polyelectrolyte, since it might be partially denaturated as the temperature increases. It can nevertheless be ascertained that direct electron transfer is indeed feasible between *Tt*LMCO1 and the pyrolytic graphite electrode. The redox action monitored is attributed to the copper in the T1-site of the enzyme which is responsible for the oxidation of the substrates interacting with laccases.

From the values of the dominant peak, the formal potential $E^{0\prime}_{app}$ [11] at each examined

[11] It is reminded here that $E^{0\prime}_{app}$ refers to the $E^{0\prime}$ value which is affected by the immobilization matrix.

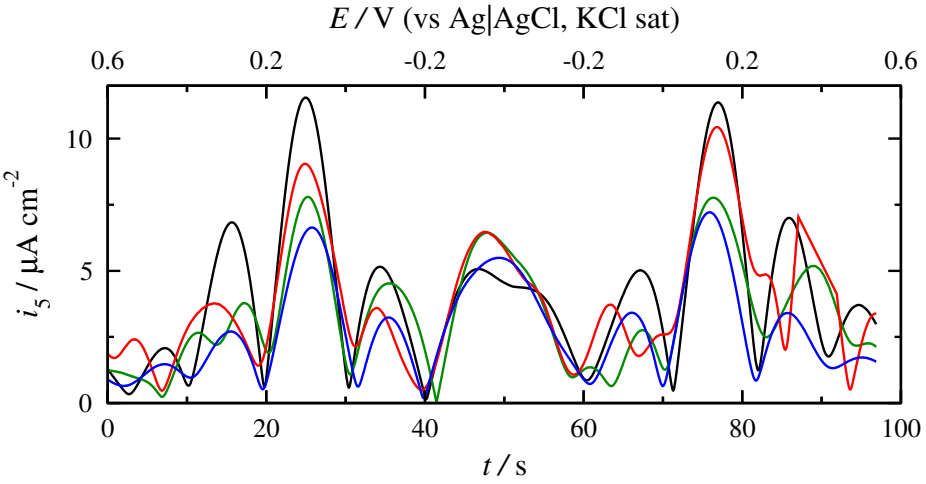

Figure 6.2.2: Experimental results: 5th harmonic of *Tt*LMCO1 immobilized with Nafion^{TM} on a pyrolytic graphite electrode in acetate buffer 500 mM pH 5. $f = 5$ Hz, $A_0 = 300$ mV, $v = 20$ mV/s and $T = 30$ (black), 35 (red), 40 (green) and 45 °C (blue).

Table 6.1: $E^{0\prime}_{app}$ for *Tt*LMCO1 immobilized on a pyrolytic graphite electrode with the use of Nafion^{TM} for $f = 5$ Hz, $v = 20$ mV/s and $A_0 = 330$ mV in deaerated 500 mM acetate buffer pH 5. Potential values are versus NHE.

T (°C)	$E^{0\prime}_{app}$ (mV)
30 ± 1	317 ± 5
35 ± 1	324 ± 2
40 ± 1	313 ± 8
45 ± 1	317 ± 12
50 ± 1	295 ± 5

temperature along with their standard deviations can be found in Table 6.1. The presented values are versus the normal hydrogen electrode (NHE). The correction for the temperature change of the reference electrode is also taken into account [24]. No significant change in the potential value is observed to 45 °C while there is a shift of about 20 mV at 50 °C. Acidic pH values are also examined at 30 °C and are presented in Table 6.2. Decrease in the pH values indicate a shift of the formal potential to more anodic values. This temperature and pH ranges were chosen considering the enzyme's stability and catalytic activity while free in a solution [1].

By taking into consideration the correction of the apparent formal potential from Eq. (4.3.1) the apparent formal potentials from Tables 6.1 and 6.2 are corrected in Tables 6.3 and 6.4.

The redox potential of laccases and related multicopper oxidases covers a wide range of values, from low (340-430 mV) plant laccases from *Cucurbita pepo* and *Rhus vernicifera* respectively [25] to middle-redox potential laccases (465 mV for *Thermothelomyces thermophila* blue laccase [26]), up to high-redox potential Basidiomycete laccases, such as 650 mV for *Pleurotus ostreatus* laccase [27], and 790 mV for laccases from

Table 6.2: $E^{0\prime}_{app}$ for *Tt*LMCO1 immobilized on a pyrolytic graphite electrode with the use of Nafion^{TM} for $T = 30$ °C, $v = 20$ mV/s and $A_0 = 300$ mV in deaerated 500 mM acetate buffer for various pH values. Potential values are versus NHE.

pH	$E^{0\prime}_{app}$ (mV)
5 ± 0.1	317 ± 5
4.6 ± 0.1	359 ± 3
4 ± 0.1	382 ± 5
3.6 ± 0.1	425 ± 6
3.1 ± 0.1	446 ± 2

Table 6.3: Corrected formal potentials for *Tt*LMCO1 immobilized on a pyrolytic graphite electrode with the use of Nafion^{TM} for $f = 5$ Hz, $v = 20$ mV/s and $A_0 = 330$ mV in deaerated 500 mM acetate buffer pH 5. Potential values are versus NHE.

T (°C)	$E^{0\prime}$ (mV)
30 ± 1	437 ± 5
35 ± 1	446 ± 2
40 ± 1	437 ± 8
45 ± 1	443 ± 12
50 ± 1	423 ± 5

Trametes species [26]. Bacterial laccases usually lie in the low-to medium redox potential, with formal potential values ranging from 525 mV for CotA laccase from *Bacillus subtilis* [28] and 440 mV for CueO laccase from *E.coli* [29]. Therefore, it appears to be a low-potential laccase, which is also reflected in the relatively narrow substrate range of the enzyme [1]. This property can be exploited in biosensor applications, where selectivity plays a key role in the selection of a suitable biocatalyst for the detection and quantification of the target compound.

6.2.3 Epinephrine Voltammetry

The next step, before having the enzyme interacting with epinephrine, is to examine epinephrine alone from an electrochemical point of view.

The first experiment concerning epinephrine is cyclic voltammetry on a glassy carbon electrode. Test experiments were conducted first on a rather usual electrode such as glassy carbon, since we had no previous electrochemical experience with this substance before. Consequently, it was deemed better for our understanding to see how it works alone on an electrode that is easy to prepare and get reproducible results.

In Fig. 6.2.3 (a) cyclic voltammograms of a 5 mM epinephrine solution with 500 mM acetate buffer pH 5 as a supporting electrolyte are presented at various scan rates ranging from 25 and reaching 500 mV/s. All voltammograms start at -0.5 V reach an upper limit og 1.2 V, go back to -0.5 V and end an 0.2 V. Between each cycle the glassy carbon electrode was polished with 0.3 μm alumina powder on a slighlty wet pad.

Table 6.4: Corrected formal potentials for *Tt*LMCO1 immobilized on a pyrolytic graphite electrode with the use of Nafion™ for $T = 30$ °C, $v = 20$ mV/s and $A_0 = 300$ mV in deaerated 500 mM acetate buffer for various pH values. Potential values are versus NHE.

pH	$E^{0\prime}$ (mV)
5 ± 0.1	437 ± 5
4.6 ± 0.1	455 ± 3
4 ± 0.1	442 ± 5
3.6 ± 0.1	461 ± 6
3.1 ± 0.1	452 ± 2

While scanning anodically during the first scanbefore 0.25 V no peak is detected. After that something that seems like an irreversible peak starts arising, with the peak being found around 550 mV. While returning back to cathodic potential, around -0.1 V a reduction peak arises. If the scan ended at -0.5 V of the first scan, one would be mistaken and state that the reduction peak is the respective peak of the oxidation peak found while scanning anodically. However, during the second cycle an oxidation peak can be found at about -0.05 V, which problaly corresponds to the oxidation of what was reduced during the cathodic scan.

In Fig. 6.2.3 (b), the cyclic voltammogram of epinephrine under the same conditions at 100 mV/s for 4 cycles is presented. It can be observed that from the second cycle and after the dominant peak around 0.55 V at the anodic scan is decreasing, signifying that it is consumed at the are near the electrode surface during each cycle. Moreover, the peak redox couple around -0.05 and -0.1 V persists in existing as the cycles go on, meaning that the substance that is formed after the oxidation of epinephrine is rather stable. Moreover, a small peak can be found around 0.25 V after the second cycle.

FTacV was also performed in a 5 mM epinephrine solution with 500 mM acetate buffer pH 5 as a supporting electrolyte at v of 10 mV/s, $f = 1$ Hz and $A_0 = 100$ mV. The potential is scanned between -0.5 and 1.2 V. The 3rd and the 5th harmonic are presented in Fig.6.2.4 (a) and (b) respectively. During the anodic scan, around 0.4-0.5 V a set of peak arises that does not reminiscence neither a clearly irrversible electrochemical reaction, nor a typical waveform of a quasi reversible harmonic. The harmonics resemble either a sequence of two electrochemical reaction where the formal potential of the second step is more negative than that of the first one, or a sequence where a chemical step follows the electrochemical one nad consumes the products of the chemical one.

Then, around the end of the anodic scan what seems like an irreversible peak arises. In fact this is due to the oxidation of water at such a high applied potential. During the cathodic scan, a set of peaks arises around 0.4-0.5 V corresponding to the peaks observed during the anodic scan, but at a lower magnitude. Finally, what seems like a set of peaks of a quasi-reversible reaction can be observed around -0.1 V during the cathodic scan, reflecting the set of peaks found in the cyclic voltammogram during the cathodic scan of the first cycle and the anodic of the second.

Taking into account the data from the cyclic voltammogram and the FTacV, and taking into account the mechanism prosposed for the oxidation of epinephrine proposed

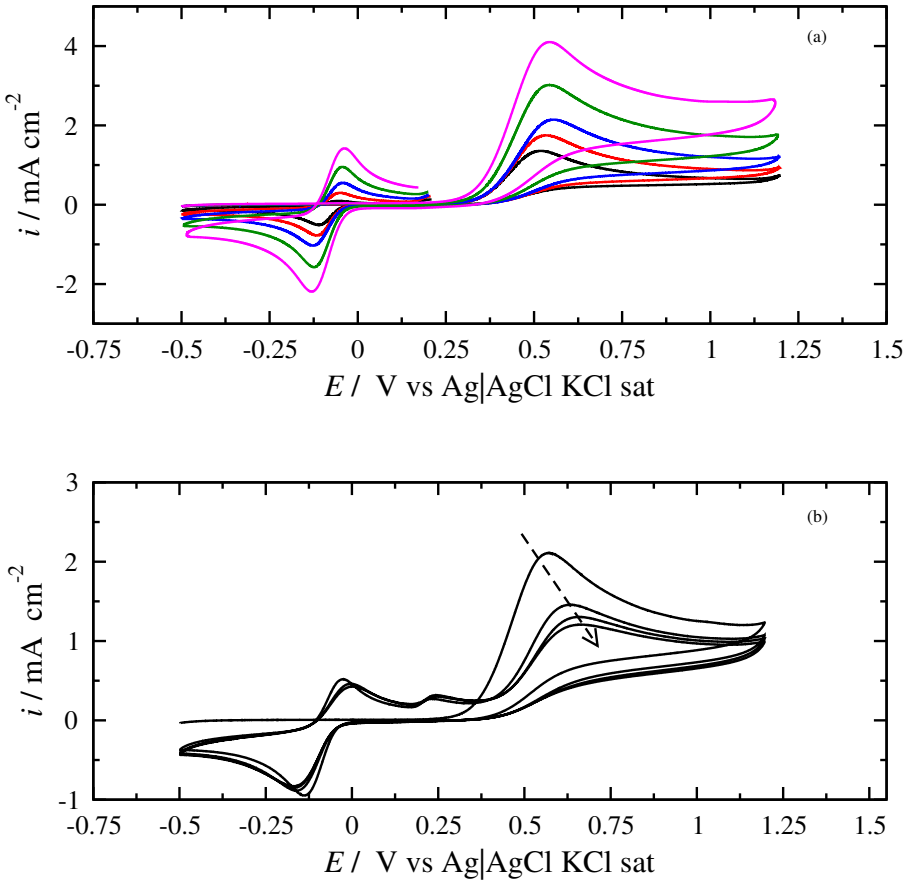

Figure 6.2.3: (a) Cyclic voltammograms of 5 mM epinephrine in 500 mM acetate buffer pH 5 for $T = 30$ °C and $v = 25$ (black), 50 (red), 100 (blue), 200 (green) and 500 mV/s (magenta) with glassy carbon as a working electrode (b) Multiple cycles at $v = 100$ mV/s under the same experimental conditions.

in 1966 [30].

More specifically, the peak that occurs around +0.55 V corresponds to the oxidation of adrenaline to the open-chain quinone. Then the cyclization reaction occurs leading to the formation of adrenochrome. This is the reason why during the cathodic scan, no reduction peak occurs nowhere near the region 0.5 V [12]. The oxidized form of epinephrine turns into this cyclized form with a different formal potential, and the redox reaction of this cyclized form appears near -0.1 mV as a quasi reversible reaction. A scheme of the reactions taking place can be seen in Fig. 6.2.5.

After having examined epinephrine on a glassy carbon electrode, and knowing that one redox peak appears near 0.5 V and since the peaks appearing for *Tt*LMCO1 are around 0.1 V, the next step is to focus on the oxidation peak of epinephrine using FTacV on a pyrolytic carbon electrode. The limits of detection shall be addressed as

[12]In the work of Hawley *et al* a small reduction peak disproportional to the oxidation one appears earlier in the scan, but the pH examined is lower and some protonated quinone has not undergone cyclization and is free to be reduced.

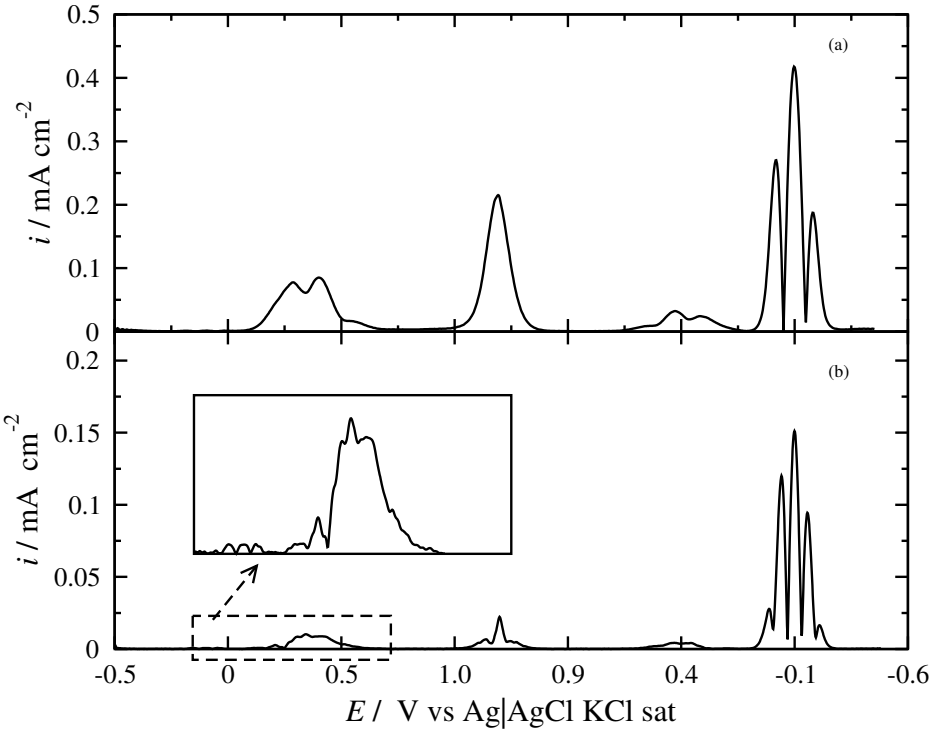

Figure 6.2.4: (a) 3rd and (b) 5th harmonic of 5 mM epinephrine in 500 mM acetate buffer pH 5 for $T = 30$ °C and $v = 10$ mV/s, $f = 1$ Hz, $A_0 = 100$ mV with glassy carbon as a working electrode

well as the expected waveform. In Fig. 6.2.6(a) and (b) 0.5 mM epinephrine in 500 mM acetate buffer pH 5 for $T = 30$ °C scanning from 0 to 0.8 V are examined for different amplitudes and frequencies respectively. It can be observed that as the amplitude and the frequency increase, the magnitude of the signal also increases up to a certain point. Beyond 250 mV and 9 Hz the increase in not as significant, as it is expected, since for higher amplitudes a saturation is expected in the signal increase and for a free species, the increase is proportional to the square root of the frequency and not to the frequency.

Then, for an amplitude of 250 mV and a frequency of 9 Hz the detection limits are examined. A linear correlation of the dominant peak value of the 3rd harmonic against the concentration is presented in Fig. 6.2.7. The detection of epinephrine under these conditions were found at 25 μM because for lower concentrations the signal was not clear and the peaks not distinguishable. Consequently, for concentrations lower than 25 μM it is safe to assume that the oxidation of epinephrine on the electrode surface shall not be detectable and shall not interfere.

6.2.4 Interaction of *Tt*LMCO1 with epinephrine

The next step is to examine the feasibility of monitoring the reaction of *Tt*LMCO1 with epinephrine by FTacV. The scenario assumed in this case is that starting from a potential more negative than the formal potential of the laccase and by sweeping the potential towards more positive values, the oxidized form of the enzyme, produced by

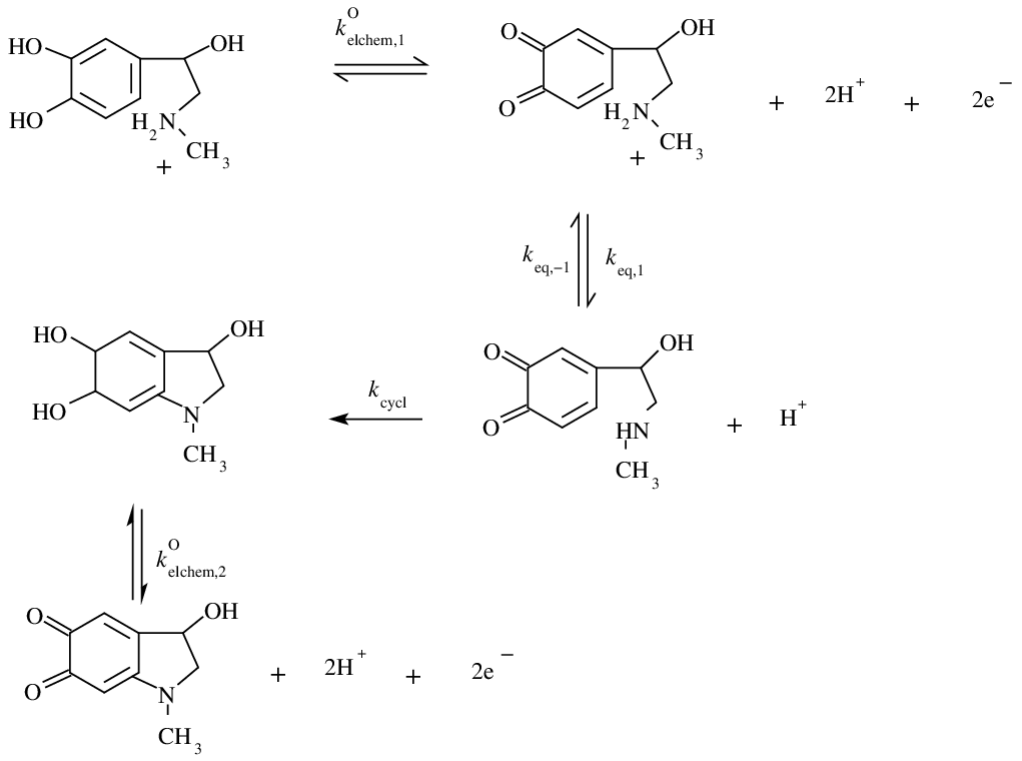

Figure 6.2.5: Epinephrine oxidation pathway.

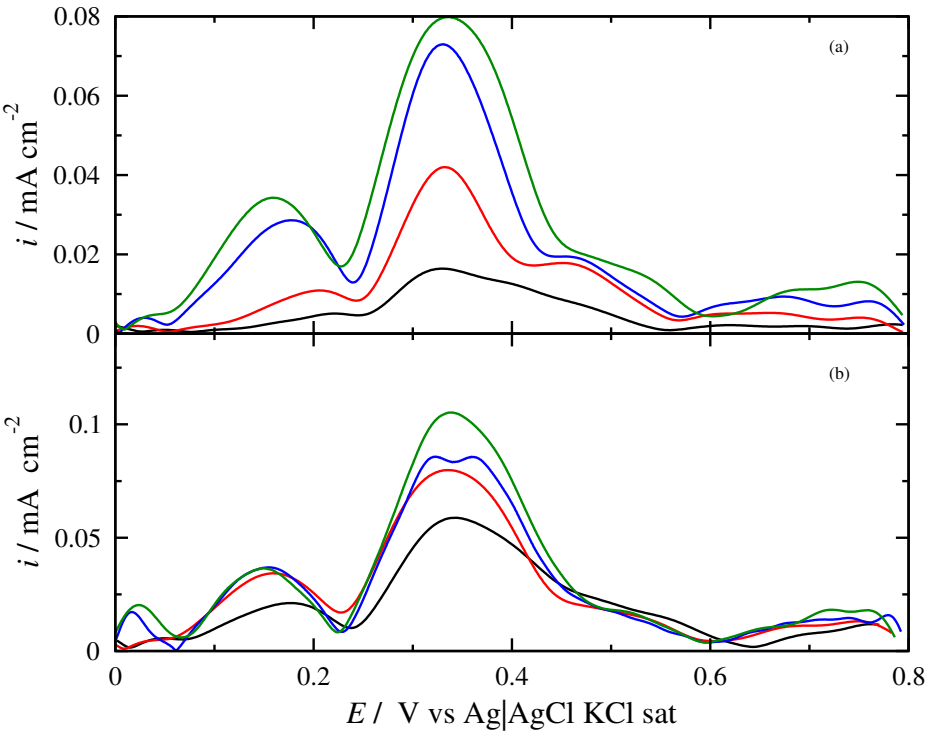

Figure 6.2.6: (a) 3rd harmonic of 0.5 mM epinephrine in 500 mM acetate buffer pH 5 for $T = 30$ °C and $v = 20$ mV/s, $f = 5$ Hz, $A_0 = 150$ (black), 200 (red), 250 (blue) and 300 mV (green) with pyrolytic carbon as a working electrode. (b)3rd harmonic of 0.5 mM epinephrine in 500 mM pH 5 for $T = 30$ °C and $v = 20$ mV/s, $A_0 = 250$ and $f = 3$ (black), 5 (red), 7 (blue) and 9 Hz (green) with pyrolytic carbon as a working electrode.

the electrochemical step, will react with the reduced form of the epinephrine, producing the reduced form of enzyme by the catalytic step. As the potential is scanned anodically, the reduced enzyme with be oxidized electrochemically and thus enter the catalytic cycle once again. The electrode is polarized before each experiment for 10 s at -300 mV in order to ensure that the enzyme is in its reduced form at the beginning of each cycle, as indicated by the proposed scenario.

A scan rate of 20 mV/s is chosen for the experiments, together with an amplitude of 300 mV. Regarding the amplitude, it was chosen as to ascertain clear signals of the electron transfer between the enzyme and the electrode, without at the same time evoking other reactions which could interfere with the enzymatic one, such as the proton reduction at cathodic potentials. Of the frequencies examined, those for 2, 1.5, 1.25 and 1 Hz were chosen to be presented, ensuring that the independence of the scan rate is achieved. Lower values of frequencies at lower scan rates were examined as well but the signals obtained were not clear enough to be processed, thus recognizing that for this particular system the lower limit of frequency that can be achieved is that of 1 Hz. Thus, for the next experiments, a frequency of 1 Hz was chosen.

The peak of the third harmonic, $i_{3,\mathrm{p}}$, at different concentrations of epinephrine, c_{S}, is presented in Fig. 6.2.8(a). An initial increase and a following plateau is observed

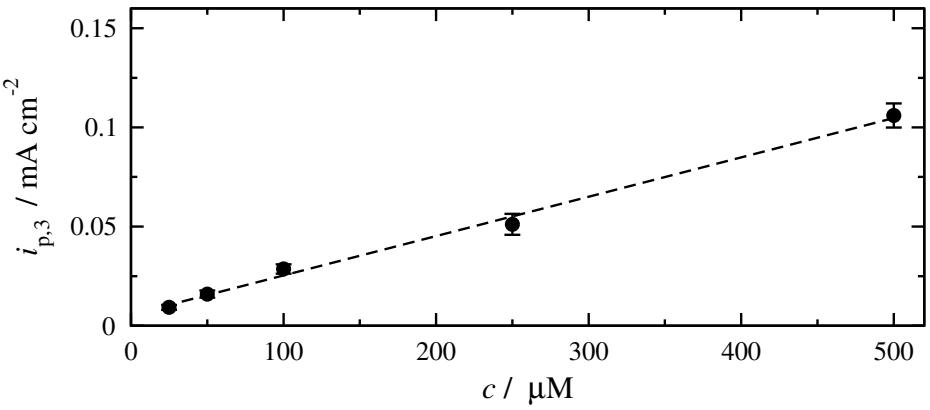

Figure 6.2.7: Peak of the 3rd harmonic $i_{p,3}$ against concentration c in 500 mM acetate buffer pH 5 for $T = 30$ °C and $v = 20$ mV/s, $f = 9$ Hz and $A_0 = 250$ mV together with the corresponding linear fit. Slope 0.198 mA cm^{-2} μM^{-1}., intercept 0.05 mA/cm^{-2} and $R^2 = 0.995$.

for all the frequencies, reminiscent of the behavior for the case of high k_2/k^0, as it is showcased in Fig. 3.3.5(a). By inverting the current and the substrate concentrations axes, Lineweaver-Burk-like plots are retrieved, Fig. 6.2.8(b), similar to those of Fig.3.3.5(b). Moreover, in case the current densities of the maxima of the peak of the third harmonic are normalized with the corresponding frequencies, Fig. 6.2.8(a) turns into Fig. 3.3.5(a), which corresponds to the trend depicted in Fig. 3.3.5(a), where the increase for the lower frequency (or equivalently higher τ_{AC}) is greater for the same substrate concentration.

By taking a close look at Fig. 6.2.8(d), the potential shift of the dominant anodic peak of the 3rd harmonic, $\Delta E^* = (E_{3,p} - E^{0\prime})$, for two frequencies, is plotted against the Naeperian logarithm of the substrate concentration, indicating a displacement towards more positive potentials as the concentration increases, similar to the trend depicted for high values of k_2/k^0 as it is shown in Fig.3.3.3(b). These results reinforce the argument that direct electron transfer is feasible, and that the immobilized enzyme reacts with the epinephrine in the solution. Although with the proposed analysis, numerical values have not been extracted for the kinetic constants of the enzyme, the fact that k_2 seems to be greater than the electron transfer kinetic constant is still a valuable finding. The initial experiments were performed at a pH of 5 and 25 °C for a potential range extending from -300 to 600 mV.

In order to extract the K_M, according to the methodology described in the previous sections, lower frequencies should be employed, which for this particular system were not applicable. If one was to be mislead by the similarity of the plots of Fig. 6.2.8 with steady state Michaelis-Menten kinetics, an extremely small Michaelis constant would

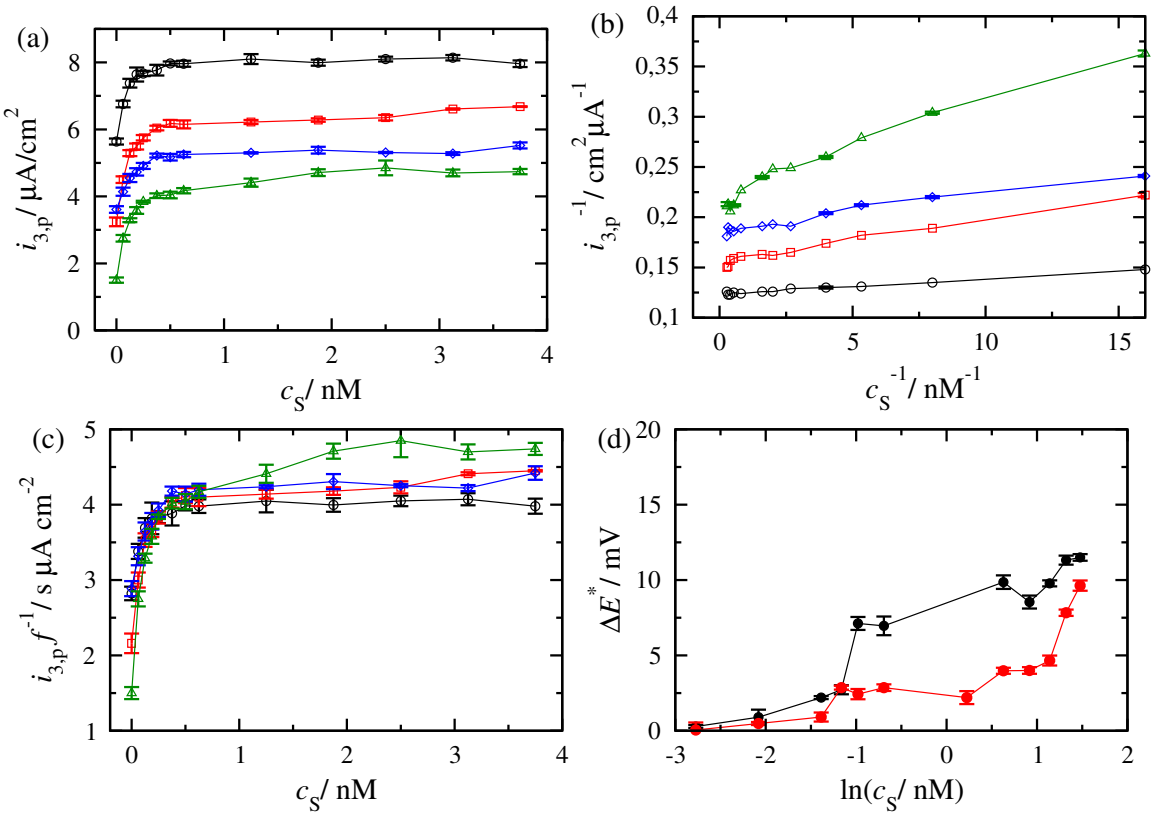

Figure 6.2.8: Experimental results: (a) peak of the 3rd harmonic $i_{3,\mathrm{p}}$ against substrate concentration c_{S} and (b) corresponding Lineweaver-Burk-like plot (c) Normalized peak of the 3rd harmonic $i_{3,\mathrm{p}}/f$ against substrate concentration c_{S} for the dominant peak of the 3rd harmonic of *Tt*LMCO1 immobilized with Nafion$^{\mathrm{TM}}$ on a pyrolytic graphite electrode in acetate buffer 500 mM, pH 5, $T = 25$ °C, $A_0 = 300$ mV, $v = 20$ mV/s for $f = 2$ (black), 1.5 (red), 1.25 (blue) and 1 Hz (green) (d) Shift of the dominant anodic peak ΔE^* against for the aforementioned conditions frequencies $f = 1$ (black) and 1.5 Hz (red).

be derived. This value would unusual for a laccase-type enzyme. However, still, the fact that the peak of the 3rd harmonic increases linearly at low substrate concentrations could be exploited as an application for an analytical technique regarding the determination of epinephrine. In case a Michaelis-Menten constant was to be extracted from the existing data, the value would be estimated at an order of magnitude of 10^{-11} M, which is extremely low to the ones that appear in the literature, and an indication that it cannot be extracted in the present case. It must be emphasized that, in the present work, we do not propose this specific electrode as a biosensor but we discuss the possibility to implement FTacV in a system consisting of an electroactive immobilized enzyme for the detection of a substrate in the solution, in the absence of a mediator. Consequently, the next experiments were designed in this aspect.

Regarding the pH and temperature conditions for the next experiments, an opti-

Table 6.5: Current density increase at saturation point percentage $(i_{sat} - i_{bl})/i_{bl}\%$ at different temperatures T at the saturation point of epinephrine additions.

T (°C)	$(i_{sat} - i_{bl})/i_{bl}\%$
30 ± 1	97.9 ± 8.1
35 ± 1	89.5 ± 5.9
40 ± 1	70.9 ± 5.6
45 ± 1	35.7 ± 3.3
50 ± 1	29.4 ± 7.5

mization attempt was made. By taking into account the value of the dominant peak at the saturation point against the dominant peak of the blank, the percentage of the current density is calculated for temperatures ranging from 30 to 50 °C and for pH values from 3.1 to 5. The temperature and pH choices are made based again on the data from the stability and performance of the enzyme while free in a solution. However the optimal conditions of the immobilized enzyme for this application are found to be at pH 4 and $T = 30$ °C, as can be seen in Tables 6.5 and 6.6 This can be attributed to a possible deformation of the enzyme while immobilized or the incompatibility of the enzyme and Nafion^{TM} polyelectrolyte at this temperature and pH range.

At the optimized conditions, the exact same process described above was executed and the results are presented in Fig. 6.2.9. The 3rd harmonics for different concentrations of epinephrine in the range of 0.065 to 1.25 nM are shown in Fig. 6.2.9(a).

As can be seen in Fig. 6.2.9(b), the linear region is extending from 0.065 to 0.265 nM. The sensitivity extracted from the linear region is 13.538 ± 0.2 μA/(cm^{2}nM), as taken from the equation that occurs form the linear response of the system ($i_{3,p} = 13.538c + 4.489$, $R^2 = 0.993$). For a signal to noise ratio equal to 3 the detection limit is calculated at 0.027 ± 0.014 nM, by taking into account the standard deviation of the blank at 0.12 μA/cm^2. As noted before, the linear region is not ample, however considering the amounts of epinephrine employed in this study, the sensitivity is rather high and the detection limit very low. These two, together with the comparably simple immobilization method, can account for the advantages of this approach, since trace amounts can be detected at considerable current densities. The low detection limit can be the asset of the method, as the increase of the current against the blank at extremely low concentrations can be used as an indication for the presence of this particular substance in solutions.

Table 6.6: Current density increase at saturation point percentage $(i_{sat} - i_{bl})/i_{bl}\%$ at different values of pH at the saturation point of epinephrine additions.

pH	$(i_{sat} - i_{bl})/i_{bl}\%$
5 ± 0.1	97.9 ± 8.1
4.6 ± 0.1	104.9 ± 9.1
4 ± 0.1	162.7 ± 9.6
3.6 ± 0.1	84.4 ± 25.7
3.1 ± 0.1	74.5 ± 15.4

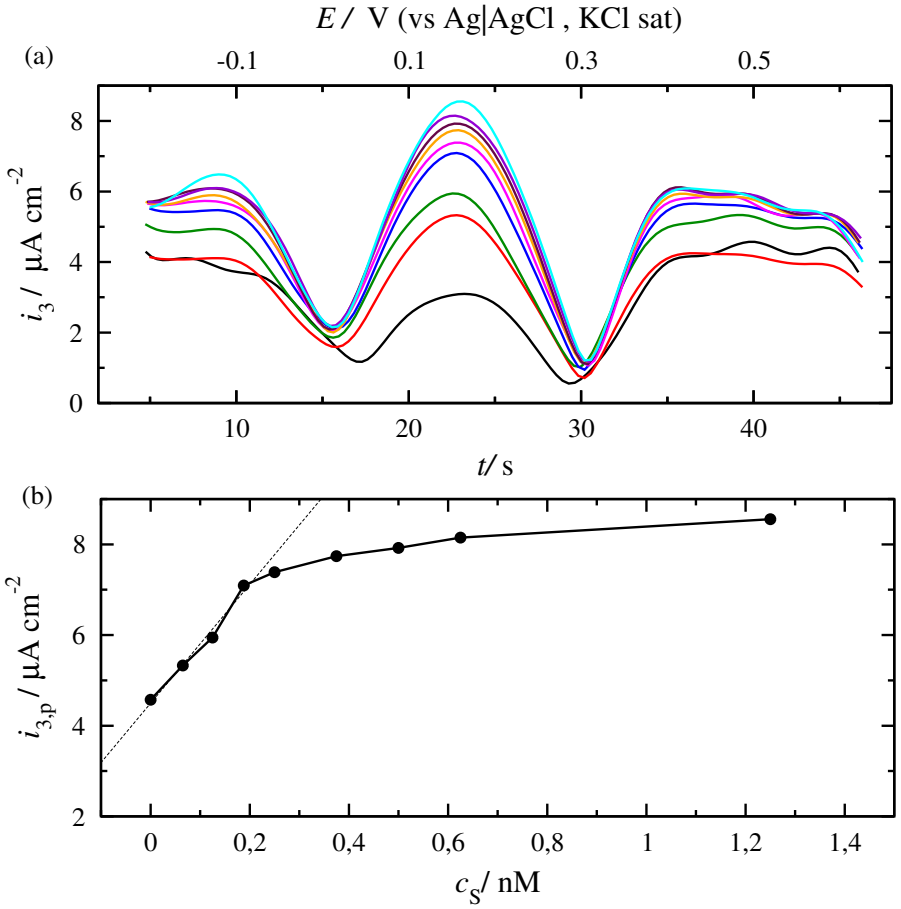

Figure 6.2.9: Experimental Results:(a) 3rd harmonic of *Tt*LMCO1 immobilized with Nafion^{TM} on a pyrolytic graphite electrode in acetate buffer 500 mM pH 4, $T = 30$ °C, $f = 1$ Hz, $A_0 = 300$ mV, $v = 20$ mV/s at different epinephrine concentrations: 0 (black line), 0.065 (red line), 0.125 (green line), 0.188 (blue line), 0.250 (magenta line), 0.375 (orange line), 0.500 (maroon line), 0.625 (violet line) and 1.25 nM (cyan line). (b) Dependence of the peak $i_{3,p}$ of the dominant peak of the 3rd harmonic as a function of substrate concentration c_S.

As pointed above, the scope of this section was to show that FTacV can be implemented for the detection of the substrate by the electroactive immobilized enzyme, in the absence of mediator. The detection is based on the fact that a linear region appears on the dependence of the maximum of the principal peak of the 3rd harmonic at quite low substrate concentrations. The study is limited to a solution containing solely epinephrine and a simple immobilization method. Typical characteristics of a biosensor such as operational and storage stability were not examined. Regarding the typical testing of inhibitors as the ones found in the literature, was not considered in this work. A new model shall be developed to predict the scenarios of inhibitors and a careful choice of substrates shall be made. For these reasons, the present work does not propose this specific modified electrode as a biosensor, at this level of understanding.

Nevertheless, if the present system is to be used as a biosensor, it is recommended that after each set of measurements, a fresh enzyme-Nafion^{TM} mixture to be utilized, since the amount of enzyme used is quite small and the immobilization method is straightforward, accomplished with a commercially available matrix. Indicative systems for electrochemical epinephrine detection are presented in Table 6.2.4.

Table 6.7: Electrochemical method, modified electrode, linear range, and limit of detection (L.O.D.) of epinephrine, real life samples and interference tested as found in literature

Method	Electrode	Linear Region	LOD	Real Sample Tested	Interferences Tested	Ref.
SWV	MWNT/EPPGE	0.5-100 nM	0.15 nM	blood plasma / urine	AA, DA, UA	[31]
Amperometry	MWNT/SDS/Carbon	0.1-1 μM	4.5 nM	adrenaline tartrate injection	Trp, Tyr, C, FA	[32]
CV	Carbon Fiber	10-100 ng/mL	7.8 ng/mL	Urine	NE, ephedrine	[33]
SWV	GNPs/PAn-LB GCE	0.4-10 μM	8 nM	human blood serum	AA, GLC, Glu, XAN	[34]
DPV	L-Cystein SAM GE	0.1-2 μM	10 nM	adrenaline injection	-	[35]
Amperometry	AuPt@GR	1.5-9.6 nM	0.9 nM	blood serum diluted with PBS	GLC, AA, UA, DA, 5-HT	[36]
Amperometry	PEDOT-PSS OECT	90-900 pM	90 pM	-	Try, Tyr, Gly, Cys, DA, AA	[37]
DPV	o-SWCNHs	2-2500 μM	0.1 μM	-	5-HT, NE, AA, UA	[38]
DPV	GN-NP/PET	5-100 μM	0.3 μM	synthetic urine sample	-	[39]
DPV	CPE/Fe_3O_4	0.4-270 μM	22 nM	human blood serum	Phe, CA	[40]
Amperometry	GQD-TMSPED-AuNCs	10nM-4 μM	10 nM	human urine sample	UA, AA, GLC, U	[41]
FTacV	Lac-Naf-PGE	0.065-0.265 nM	0.027 nM	-	-	Present Work

Method Abbreviations SWV: Square Wave Voltammetry, CV: Cyclic Voltammetry, DPV: Differential Pulse Voltammetry

Electrodes' abbreviations MWNT: Multi-Walled Carbon Nanotubes, EPPGE: Edge Plane Pyrolytic Graphite, SDS: Sodium Dodecyl Sulfate, GNP: Gold Nanoparticle, PAn-LB: Polyaniline Langmuir- Blodgett, GCE: Glassy Carbon Electrode, SAM: Self Assembly Monolayer, GE: Gold Electrode, GR: Graphene, PEDOT: Polyethylenedioxythiophene, PSS: Polystyrene Sulfonate, o-SWCNHs:Oxidized Single-Wall Carbon Nanohorns , PET: Polyethylene Terephthalate CPE: Carbon Paste electrode, GQD: Graphene Quantum Dots, TMSPED: N[3(trimethoxysilyl)propyl]ethylenediamine, AuNCs: Gold nanocrystals, RGO: Reduced Graphene Oxide, Irr-PANi: Irradiated Polyaniline, BSA: Bovine Serum Albumin, WRF: White Rot Fungi, Lac-Naf-PGE: Laccase Nafion^{TM} Pyrolytic Carbon , PPy-PVS: polypyrrole–polyvinylsulphonate

Interference abbreviations AA:Ascorbic Acid, DA: Dopamine, UA: Uric Acid, Trp: Tryptophan, Tyr: Tyrosine, Cys: Cysteine, FA: Folic Acid, NE: Norepinephrine, GLC: Glucose, Glu: Glutamic Acid, XAN: Xanthine, 5-HT: Serotonine, Gly: Glycine, Phe: Phenylalalanine, CL: Cellulose, U: Urea, CA: Citric Acid

Bibliography

[1] A. Zerva, E. Koutroufini, I. Kostopoulou, A. Detsi, and E. Topakas. A novel thermophilic laccase-like multicopper oxidase from thermothelomyces thermophila and its application in the oxidative cyclization of 2', 3, 4- trihydroxychalcone. *New Biotechnol.*, 49:10 – 18, 2019.

[2] U. M. Sundaram E. I. Solomon and T. E. Machonkin. Multicopper oxidases and oxygenases. *Chem. Rev.*, 96:2563–2606, 1996.

[3] H. Komori and Y. Higuchi. Structural insights into the O_2 reduction mechanism of multicopper oxidase. *The Journal of Biochemistry*, 158(4):293–298, 2015.

[4] I. Galli, G. Musci, and M. C. Bonaccorsi di Patti. Sequential reconstitution of copper sites in the multicopper oxidase CueO. *J. Biol. Inorg. Chem.*, 158(9):90–95, 2004.

[5] J. M. Guss and H. C. Freeman. Structure of oxidized poplar plastocyanin at 1.6 Å resolution. *J. Mol. Biol.*, 169:521 –563, 1983.

[6] I. Bento, L. O. Martinez, and M. Armenia Carrondo G. Gato Lopez. Dioxygen reduction by multi-copper oxidases; a structural perspective. *Dalton Transactions*, 21:3507–13, 2005.

[7] R. Reiss, J. Ihssen, M. Richter, E. Eichhorn, B. Schilling, and L. Thöny-Meyer. Laccase versus laccase-like multi-copper oxidase: a comparative study of similar enzymes with diverse substrate spectra. *PloS one*, 8(6):e65633, 2013.

[8] P. Baldrian. Fungal laccases – occurrence and properties. *FEMS Microbiol. Rev.*, 30(2):215–242, 2006.

[9] K. Hilden, T. K. Hakala, and T. Lundell. Thermotolerant and thermostable laccases. *Biotechnol. Lett.*, 31:1117, 2009.

[10] J. Yang, W. Li, T. B. Ng, X. Deng, J. Lin, and X. Ye. Laccases: Production, expression regulation, and applications in pharmaceutical biodegradation. *Front. Microb.*, 8:832, 2017.

[11] A. K. Sitarz, J. D. Mikkelsen, and A. S. Meyer. Structure, functionality and tuning up of laccases for lignocellulose and other industrial applications. *Crit. Rev. Biotechnol.*, 36(1):70–86, 2016.

[12] N. Hakulinen and J. Rouvinen. Three-dimensional structures of laccases. *Cell. Mol. Life Sci.*, 72(5):857–868, 2015.

[13] H. A. Ernst, L. J. Jørgensen, C. Bukh, K. Piontek, D. A. Plattner, L. H. Østergaard, S. Larsen, and M. J. Bjerrum. A comparative structural analysis of the surface properties of asco-laccases. *PloS one*, 13(11):e0206589, 2018.

[14] J. Zeng, Q. Zhu, Y. Wu, and X. Lin. Oxidation of polycyclic aromatic hydrocarbons using bacillus *Subtilis cota* with high laccase activity and copper independence. *Chemosphere*, 148:1–7, 2016.

[15] C. W. Lee, H.B. Gray, F.C. Anson, and B.G. Malmström. Catalysis of the reduction of dioxygen at graphite electrodes coated with fungal laccase A. *J. Electroanal. Chem.*, 172(1-2):289–300, 1984.

[16] M.H. Thuesen, O. Farver, B. Reinhammar, and J. Ulstrup. Cyclic voltammetry and electrocatalysis of the blue copper oxidase *Polyporus versicolor* laccase. *Acta Chem. Scand.*, 52(5):555–562, 1998.

[17] R. Santucci, T. Ferri, L. Morpurgo, I. Savini, and L. Avigliano. Unmediated heterogeneous electron transfer reaction of ascorbate oxidase and laccase at a gold electrode. *Biochem. J.*, 332(3):611–615, 1998.

[18] S. Shleev, A. Christenson, V. Serezhenkov, D. Burbaev, A. Yaropolov, L. Gorton, and T. Ruzgas. Electrochemical redox transformations of T1 and T2 copper sites in native trametes hirsuta laccase at gold electrode. *Biochem. J.*, 385(3):745–754, 2005.

[19] D. Ivnitski and P. Atanassov. Electrochemical studies of intramolecular electron transfer in laccase from *Trametes versicolor*. *Electroanalysis*, 19(22):2307–2313, 2007.

[20] V. Balland, C. Hureau, A. M. Cusano, Y. Liu, T. Tron, and B. Limoges. Oriented immobilization of a fully active monolayer of histidine-tagged recombinant laccase on modified gold electrodes. *Chem. Eur. J.*, 14:7186 – 7192, 2008.

[21] H. Chakroun Galai, I. Rassas, P. Namour, A. Bonhomme, S. Besbes Hentati, and N. Jaffrezic-Renault. A laccase/chitosan-lambda-carrageenan based voltammetric biosensor for phenolic compound detection. *Electroanalysis*, 32:732 – 740, 2020.

[22] C. Lou, T. Jing, J. Zhou, J. Tian, Y. Zheng, C. Wang, Z. Zhao, J. Lin, H. Liu, C. Zhao, and Z. Guo. Laccase immobilized polyaniline/magnetic graphene composite electrode for detecting hydroquinone. *International Journal of Biological Macromolecules*, 149:1130 – 1138, 2020.

[23] E. Topakas, M. Moukouli, M. Dimarogona, and P. Christakopoulos. Expression, characterization and structural modelling of a feruloyl esterase from the thermophilic fungus *Myceliophthora thermophila*. *Appl. Microbiol. Biotechnol.*, 94(6):399–411, 2012.

[24] Donald T Sawyer, Andrzej Sobkowiak, and Julian L Roberts. *Electrochemistry for chemists*. Wiley, 1995.

[25] M. Alcalde. Laccases: biological functions, molecular structure and industrial applications. In *Industrial enzymes*, pages 461–476. Springer, 2007.

[26] A. K. Sitarz, J. D. Mikkelsen, and A. S. Meyer. Structure, functionality and tuning up of laccases for lignocellulose and other industrial applications. *Crit. Rev. Biotechnol.*, 36:70–86, 2016.

[27] A. M. Garzillo, M. C. Colao, V. Buonocore, R. Oliva, L. Falcigno, M. Saviano, A. M. Santoro, R. Zappala, R. P. Bonomo, C. Bianco, P. Giardina, G. Palmieri, and G. Sannia. Structural and kinetic characterization of native laccases from *Pleurotus ostreatus*, *Rigidoporus lignosus*, and *Trametes trogii*. *J. Protein Chem.*, 20(3):191–201, 2001.

[28] Z. Chen, P. Duro, A. Fernandes, P. Hildebrandt, D. Murgida, S. Todorovic, M. Pereira, E. Melo, and L. O. Martins. Copper incorporation into recombinant cota-laccase from *Bacillus subtilis*: Characterization of fully copper loaded enzymes. *J. Biotechnol.*, 136:183–193, 2008.

[29] K. Y. Djoko, L. X. Chong, A. G. Wedd, and Z. Xiao. Reaction mechanisms of the multicopper oxidase cueo from *Escherichia coli* support its functional role as a cuprous oxidase. *J. Am. Chem. Soc.*, 132(6):2005–2015, 2010.

[30] M. D. Hawley, S. V. Tatawawadi, S. Piekarski, and R. N. Adarns. Electrochemical studies of the oxidation pathways of catecholamines. *J. Am. Chem. Soc.*, 89(6):447–450, 1967.

[31] R.N. Goyal and S. Bishnoi. Simultaneous determination of epinephrine and norepinephrine in human blood plasma and urine samples using nanotubes modified edge plane pyrolytic graphite electrode. *Talanta*, 84:78–83, 2011.

[32] T. Thomas, R.J. Mascarenhas, O.J.D. Souza, S. Detriche, Z. Mekhalif, and P. Martis. Pristine multi-walled carbon nanotubes/SDS modified carbon paste electrode as an amperometric sensor for epinephrine. *Talanta*, 125:352–360, 2014.

[33] P. Hernández, I. Sánchez, and L. Hernández F. Patón. Cyclic voltammetry determination of epinephrine with a carbon fiber ultramicroelectrode. *Talanta*, 46:985–991, 1998.

[34] L. Zou, Y. Li, S. Cao, and B. Ye. Gold nanoparticles/polyaniline Langmuir-Blodgett film modified glassy carbon electrode as voltammetric sensor for detection of epinephrine and uric acid. *Talanta*, 117:333–337, 2013.

[35] S.Fu Wang, D. Du, and Q.-C. Zou. Electrochemical behavior of epinephrine at L-cysteine self-assembled monolayers modified gold electrode. *Talanta*, 57:687–692, 2002.

[36] T.D. Thanh, J. Balamurugan, N.T. Tuan, H. Jeong, S.H. Lee, N.H. Kim, and J.H. Lee. Enhanced electrocatalytic performance of an ultrafine aupt nanoalloy framework embedded in graphene towards epinephrine sensing. *Biosens. Bioelectron.*, 89:750–757, 2017.

[37] N. Saraf, E.R. Woods, M. Peppler, and S. Seal. Highly selective aptamer based organic electrochemical biosensor with pico-level detection. *Biosens. Bioelectron.*, 117:40–46, 2018.

[38] F. Valentini, E. Ciambella, V. Conte, L. Sabatini, N. Ditaranto, F. Cataldo, G. Palleschi, M. Bonchio, F. Giacalone, Z. Syrgiannis, and M. Prato. Highly selective detection of epinephrine at oxidized single-wall carbon nanohorns modified screen printed electrodes (SPES). *Biosens. Bioelectron.*, 59:94–98, 2014.

[39] I.A. de Araujo Andreotti, L.O. Orzari, J.R. Camargo, R.C. Faria, L.H. Marcolino-Junior, M.F. Bergamini, A. Gatti, and B.C. Janegitz. Disposable and flexible electrochemical sensor made by recyclable material and low cost conductive ink. *J. Electroanal. Chem.*, 840:109–116, 2019.

[40] N.H. Arani, S.M. Ghoreishi, and A. Khoobi. Increasing the electrochemical system performance using a magnetic nanostructured sensor for simultaneous determination of L-tyrosine and epinephrine. *Anal. Methods*, 11:1192–1198, 2019.

[41] V. Vinoth, L.N. Natarajan, R.V. Mangalaraja, H. Valdes, and S. Anandan. Simultaneous electrochemical determination of dopamine and epinephrine using gold nanocrystals capped with graphene quantum dots in a silica network. *Microchim. Acta*, 186:12, 2019.

7. Overview and Conclusions

Concluding this work, an overview of what was reported throughout the text shall be made, pointing out the main conclusions reached. This work focuses on the utilization of electrochemical methods for the study of redox enzyme and their interaction with their substrates. Redox enzymes can be studied with either mediated electron transfer or direct electron transfer - if direct electron tranfer is possible and the active site of the enzyme is not burried inside its structure. In case that mediators cannot be used, direct electron transfer is the only solution and enzymes are needed to be immobilized on the electrode surface to achieve this. When using cyclic voltammetry capacitance currents overlap with the electrochemical signal. So, an alternate to cyclic voltammetry can be FTacV that reinforces the signal and through FFT the capacitance is eliminated. Despite the intensive work over the past decade on FTacV, a more intensive study is needed to extract the voltammographic patterns and chief-observables dependencies for various kinetic scnaerios. Such a study was performed in this work for both free and immobilized species. Experimentally, enzymes belonging to the LPMO family and one laccase-like multicopper oxidase were studied.

For the case of the reaction of free species using FTacV the main findings are,

- For the case of a reversible electrochemical reaction of free electroactive species a semi-analytical dimensionless solution was formulated, which can be solved with a simple iteration and not complex mathematical packages.

$$\psi_{\mathrm{ac}}(\tau) = \frac{n^2\Delta}{2\sqrt{\pi}}\Bigg\{\frac{1}{2}\frac{\sigma\frac{\tau-\tau_{\mathrm{R}}}{|\tau-\tau_{\mathrm{R}}|} + 2\pi\alpha_0\cos 2\pi\tau}{\cosh^2[0.5n(\xi_{\mathrm{I}} - \sigma\tau_{\mathrm{R}} + \sigma|\tau-\tau_{\mathrm{R}}| + \alpha_0\sin\tau)]} \sum_{j=1}\frac{\sigma\frac{\tau-(jh)^2-\tau_{\mathrm{R}}}{|\tau-(jh)^2-\tau_{\mathrm{R}}|} + 2\pi\alpha_0\cos 2\pi(\tau-(jh)^2)}{\cosh^2[0.5n(\xi_{\mathrm{I}} - \sigma\tau_{\mathrm{R}} + \sigma|\tau-(jh)^2-\tau_{\mathrm{R}}| + \alpha_0\sin 2\pi(\tau-(jh)^2))]}\Bigg\} + \mu\Big(\sigma\frac{\tau-\tau_{\mathrm{R}}}{|\tau-\tau_{\mathrm{R}}|} + 2\pi\alpha_0\cos 2\pi\tau\Big) \tag{7.0.1}$$

- The current peak is proportional to the square root of the frequency.
- The independence of the scan rate of FTacV was determined for harmonics up to the 5th as long as the applied frequency obeys to the following expression.

$$f \geq 0.77 \frac{nF}{RT} v \tag{7.0.2}$$

- The dependence of peaks of the harmonics follows a sigmoidal - like increase up to 300 mV (See Fig. 2.1.9) for both one and two electron transfer.
- The effect of the amplitude on the chief observables - width at half maximum of the prinicipal peak for the odd harmonics and peak potential of the principal peak for the even harmonics - was determined (Fig. 2.1.11). The dependence for amplitudes over 100 mV at 25 °C is linear. These observables can be used as criteria for the reversibility of an electrochemical reaction of a free species.
- The voltammographic patterns of the harmonics are determined for slower electrode kinetics, deviating for the reversibility (Fig. 2.1.14).
- The k^0 regions of reversibility, quasi reversibility and irreversibility for different amplitudes is also presented (Table 2.4).
- The dependence of the dominant peak of the harmonics against the electrode kinetics was extracted and presented in Fig. 2.1.16.
- In the irreversibility region, the dominant peak of the odd harmonics follows a linear trend against the logarith of the kinetic parameter

$$\xi_{\mathrm{p},h} = \frac{\beta_h}{a} + \frac{2.303}{a} \log k_{\mathrm{ac}} \tag{7.0.3}$$

  The symmetry coefficient can be determined from the slope of this dependence
- The voltammographic behaviour of a two step electron transfer using FTacV was also determined in the case of both steps being reversible (Fig. 2.2.2) and when the second step is irreversible (Fig. 2.2.4).
- Coupling an electrochemical with an irreversible chemical reaction (EC mechanism) was also studied and the effect of the kinetics of the chemical reaction on the odd harmonics is determined (Fig. 2.3.3).
- The homogenous catalytic scheme for FTacV was analyzed and the effect of the kinetics on the odd harmonic was presented (Fig 2.4.6-2.4.10). The increase of the current observed in the catalytic signal for cyclic voltammetry is not intense in FTacV and is observed only for very large values of the kinetic parameters.

For the case of the behaviour of immobilized species using FTacV, the main findings are,

- The dimensionless integral equation of the immobilized species

$$\psi_{\mathrm{ac,F}} = -k_{\mathrm{ac}}[e^{(1-a)\xi}\int_0^{\tau}\psi_{\mathrm{ac,F}}\mathrm{d}\tau - e^{-a\xi}(1+\int_0^{\tau}\psi_{\mathrm{ac,F}}\mathrm{d}\tau)] \tag{7.0.4}$$

  was solved

- For reversible systems the Faradaic current was given by

$$\psi_{\mathrm{ac,F}} = \xi'(\tau)\frac{e^{\xi(\tau)}}{(1+e^{\xi(\tau)})^2} \tag{7.0.5}$$

- The current peak was proportional to the frequency

- The dependence of peaks of the harmonics follow a sigmoidal - like increase up to 400 mV (See Fig. 3.1.8).

- The effect of the amplitude on the chief observables - width at half maximum of the prinicipal peak for the odd harmonics and peak potential of the principal peak for the even harmonics - is determined (Fig. 3.1.7). The dependence for amplitudes over 100 mV at 25 °C is linear. These observables can be used as criteria for the reversibility of an electrochemical reaction of an immobilized species.

- The dependence of the dominant peak of the harmonics against the electrode kinetics was extracted and presented in Fig. 3.1.9.

- In the irreversibility region, the dominant peak of the all the harmonics harmonics follows the same linear trend against the logarith of the kinetic parameter

$$\xi_{\mathrm{p},h} = \frac{\beta}{a} + \frac{2.303}{a}\log k_{\mathrm{ac}} \tag{7.0.6}$$

  The symmetry coefficient can be determined from the slope of this dependence

- The regions of reversibility, quasi reversibility and irreversibility for different amplitudes were also presented (Table 3.3).

- The standard (or formal) electrode potential can be determined for the potential of the principal peak of odd harmonics, at low perturbation frequency and high amplitude, while the system is reversible.

- The kinetic parameters, *i.e.* the transfer coefficient a and the heterogeneous rate constant k^0, can be determined for the "nomograms" relating the height of the principal peak(s) with the logarithm of the dimensionless rate constant k^0/f, for different perturbation amplitudes.

- Alternatively, the kinetic parameters can be determined from the slope and intercept of the dependence of the the principal peak potential of odd harmonics on the logarithm of the inverse of the frequency.

- The voltammographic behaviour of a two step electron transfer using FTacV was also determined in the case of both steps being reversible and when the second step is irreversible (Fig. 3.2.3).

- The dimensionless equations for the scenario of an immobilized enzyme reacting with a free in a solution substrate following a Michaelis-Menten reaction scheme are

$$\frac{\tau_{\mathrm{MM}}}{\tau_{\mathrm{AC}}}\frac{d\theta_{\mathrm{E_1S}}}{d\tau} = \hat{c}_{\mathrm{S}}(1-\theta_{\mathrm{E_2}}-\theta_{\mathrm{E_1S}}) - \theta_{\mathrm{E_1S}} \tag{7.0.7}$$

$$\frac{d\theta_{\mathrm{E_2}}}{d\tau} = \tau_{\mathrm{AC}}k_2\theta_{\mathrm{E_1S}} - \tau_{\mathrm{AC}}k^0\left[\theta_{\mathrm{E_2}}e^{(1-a)\xi} - (1-\theta_{\mathrm{E_2}}-\theta_{\mathrm{E_1S}})e^{-a\xi}\right. \tag{7.0.8}$$

- The dimensionless rate under steady state conditions is

$$\hat{r} = \tau_{\mathrm{AC}}k_2\frac{\hat{c}_{\mathrm{S}}}{1+\hat{c}_{\mathrm{S}}+e^{-\xi}+\hat{c}_{\mathrm{S}}\frac{k_2}{k^0}e^{(a-1)\xi}} \tag{7.0.9}$$

  end for the case of a reversible electrochemical reaction

$$\hat{r} = \tau_{\mathrm{AC}}k_2\frac{\hat{c}_{\mathrm{S}}}{1+\hat{c}_{\mathrm{S}}+e^{-\xi}} \tag{7.0.10}$$

- Under steady state conditions, the Michaelis Menten kinetic constant can be determined

- The dependence of the dominant peak potential depending on the kinetics is determined (Fig. 3.3.3)

- Under transient conditions, no kinetic information can be obtained directly (Fig. 3.3.8) and uncompensated resistance decreases the value of dominant peaks (Fig. 3.3.9).

- The EC mechanism of immobilized species was examined. For continuous cycles the dependence of the dominant peak against time can give the reation kinetic constant (Fig. 3.4.21). The slope of this dependence is unaffected from the order of the harmonic, the perturbation amplitude and the scan limits.

Regarding the experimental study of immobilized LPMOs, the main findings are,

- Three LPMOs from the AA9 family were expressed heterologously in *P. pastoris*, *Mt*LPMO9H (Gen Bank:XP_003661787.1), *Fo*LPMO9 and *Mt*LPMO9G (Gen-Bank: AEO54509.1). The expression vectors used were pPICZαC and pGAPZαC.

- *Mt*LPMO9H and *Fo*LPMO9 were immobilized on a glassy carbon electrode using Nafion$^{\mathrm{TM}}$ and direct electron transfer was ascertained using FTacV (Fig. 4.3.3 and 4.3.4).

- The formal potentials of *Mt*LPMO9H and *Fo*LPMO9 were determined (Tables 4.5 and 4.6).

- An alternate immobilization method, using modified with cobalt ions MWCNTs, taking advantage of the His-tag of the LPMOs for a more stable immobilization was performed.

- The stability at different temperatures using this method was ascertained Fig. 4.4.10.

- The k^0 was extracted for *Mt*LPMO9H, *Mt*LPMO9G and *Fo*LPMO9 at 2.86 $\pm$ 0.9, 0.91$\pm$ 1.8, 12.3$\pm$ 1.5 s^{-1} respectively.

- The kinetic constants from the interaction of *Mt*LPMO9H, *Mt*LPMO9G and *Fo*LPMO9 for different temperatures were extracted based on the EC mechanism scenario (Tables 4.4.1, 4.4.2 and 4.4.3 respectively).

Regarding the interaction of LPMOs with various possible electron donors the main findings are,

- *Mt*LPMO9H was incubated with ascrobic acid, caffeic acid, gallic acid, methyl gallate, pyrogallol, sinapic acid, syringaldehyde, ferulic acid, vanillin, p-coumaric acid, *p*-hydroxybenzoic acid and vanillic acid as electron donors and PASC as a substrate. Analysing the non oxidized and oxidized products with HPAEC-PAD ascrobic acid, caffeic acid, gallic acid, methyl gallate, pyrogallol and sinapic acid acted as electron donors while the others did not (Fig. 5.1.1 and Table 5.1).

- The oxidation of ascorbic acid in a pH of 6 corresponds to an one step two electron transfer followed by an irreversible chemical reaction. The formal potential of the oxidation of ascorbic acid was estimated at 180 mV vs Ag|AgCl (KCl sat.), making it a valid electron donor for *Mt*LPMO9H ($E^{0\prime} = 245$ mV vs Ag| AgCl (KCl sat.)) (Fig. 5.2.7). .

- The first step of the oxidation of caffeic acid has a formal potential of 180 mV vs Ag|AgCl (KCl sat.) making it eligible as an electron donor for *Mt*LPMO9H. The formed dimer has a higher formal potential and cannot act as an electron donor (Fig. 5.3.2 and 5.3.4).

- The first step of the oxidation of gallic acid, pyrogallol and methyl gallate has a formal potential of 75, 86 and 180 mV vs Ag|AgCl (KCl sat.) respectively. The increased activity when gallic acid and pyrogallol were used as electron donors when compared to ascorbic acid is attributed that the possible formed dimer during their anodic oxidation has a formal potential beneath the value of *Mt*LPMO9H and can act as an electron donor as well (Fig. 5.4.2, 5.4.4 and 5.4.6).

- The first step of the oxidation of sinapic acid has a formal potential of 120 mV vs Ag|AgCl (KCl sat.) making it eligible as an electron donor for *Mt*LPMO9H. The formed dimer has a higher formal potential and cannot act as an electron donor (Fig. 5.5.3).

- The first step of the oxidation of syringaldehyde has a formal potential very close to that of *Mt*LPMOH, making it hard to act as an electron donor (Fig. 5.6.1).
- The oxidation of p-coumaric acid, ferulic acid, p-hydroxybenzoic acid, vanillic acid and vanillin started at potentials higher than 0.3 V vs Ag|AgCl (KCl sat.), indicating high formal potentials explaining why they did not work with *Mt*LPMO9H (Fig. 5.7.1).
- *Mt*LPMO9H was tested with white straw lignin as an electron donor and PASC as a substrate giving oxidized products, detected with HPAEC-PAD (Fig. 5.8.1).
- The formal potential of the lignin indicates that it cannot work as an electron donor for *Mt*LPMO9H (Fig. 5.8.3).
- The interaction of *Mt*LPMO9H with the lignin happens through lower molecular weight compounds which are released from lignin.

Regarding the study of the interaction of a laccase like multi copper oxidase, *Tt*LMCO1, with epinephrine the main findings are,

- *Tt*LMCO1 was immobilized on a pyrolytic carbon electrode surface using Nafion^{TM}. The electrochemical interaction with the electrode was ascertained (Fig. 6.2.2) and the formal potential of the enzyme was extracted (Table 6.3).
- Epinephrine was studied with cyclic voltammetry and FTacV and its detection limit with FTacV was determined at 25 μM (Fig. 6.2.7).
- No quantitative kinetic data was extracted from the interaction of *Tt*LMCO1 with epinephrine.
- A low detection limit and a linear dependence in the subnanomolarity region (0.065 to 0.265 nM) for epinephrine were extracted when *Tt*LMCO1 is immobilized on the pyrolytic carbon electrode at pH 4 and $T = 30$ °C (Fig. 6.2.9).

Hence, with the use of the appropriate voltammetric technique and with the appropriate background to interprete the resulting signals, thorough study of redox enzymes that can perform direct electron transfer is indeed possible and kinetic constants can be extracted. Also the interaction of the redox enzymes with their substrates can be interpreted.

A. Appendix: LPMO Genes

A.1 *Mt*LPMO9H

MSKASALLAGLTGAALVAAHGHVSHIVVNGVYYRNYDPTTDWYQPNPPTVIGWT
AADQDNGFVEPNSFGTPDIICHKSATPGGGHATVAAGDKINIVWTPEWPESHIG
PVIDYLAACNGDCETVDKSSLRWFKIDGAGYDKAAGRWAADALRANGNSWLVQI
PSDLKAGNYVLRHEIIALHGAQSPNGAQAYPQCINLRVTGGGSNLPSGVAGTSL
YKATDPGILFNPYVSSPDYTVPGPALIAGAASSIAQSTSVATATGTATVPGGGG
ANPTATTTAATSAAPSTTLRTTTTSAAQTTAPPSGDVQTKYGQCGGNGWTGPTVC
APGSSCSVLNEWYSQCL

GenBank:XP_003661787.1

A.2 *Mt*LPMO9G

MKGLLGAAALSLAVSDVSAHYIFQQLTTGGVKHAVYQYIRKNTNYNSPVTDLTS
NDLRCNVGATGAGTDTVTVRAGDSFTFTTDTPVYHQGPTSIYMSKAPGSASDYD
GSGGWFKIKDWGADFSSGQATWTLASDYTATIPECIPPGDYLLRIQQLGIHNPW
PAGIPQFYISCAQITVTGGGSANPGPTVSIPGAFKETDPGYTVNIYNNFHNYT
VPGPAVFTCNGSGGNNGGGSNPVTTTTTTTTRPSTSTAQSQPSSSPTSPSSCT
VAKWGQCGGQGYSGCTVCAAGSTCQKTNDYYSQCL

GenBank: AEO54509.1

A.3 *Fo*LPMO9

MHCNLSLGVVAALLAGANAHGHVAKVIAGGKEYTGGIPHGAPSDAVGWAAGNQD
NGFVSPDAFKSADIICHKSAKPVSNAVVVAAGDVVTLKWDTWPESHHGPVTEYL
APVSGDFASINKQSLRWVKVAQKGLKSGSNPGDWASDDLIRDGFSWKFTVPKNL

KAGKYVLRHEIIGLHSAGQANGAQAYPQCINLEVTGSGGQAISGGGDFTTFYTP
TDPGILFNLYQSFSSYPIPGPAVRTI

GenBank: XP_018247071.1

B. Appendix: FoLPMO9 purification process

Due to the inability of *Fo*LPMO9 to be purified using ion metal affinity chromatography (IMAC), Ion exchange chromatography was examined as a option. The colums that were used where Q- Sepharose (anion exchange resin) and SP-Sepharose (cation exchange resin).

Ion exchange chromatography is one of the major methods of fractionation of labile biological substances exploiting the isoelectric point (pI) of an enzyme which is the pH at which the net charge of an enzyme is zero. Arginine, lysine and histidine contribute to positive charges, depending on the pH of the surrounding buffer. Any free N-terminal amine will also contribute to a positive charge below pH 8. Usually, aspartate, glutamate residues, and the C-terminal carboxyl group contribute to negative charges. Therefore, it is feasible to separate enzymes using either fixed positive charges on the stationary phase, anion exchanger, or fixed negative charges, cation exchanger. In general, anion exchange chromatography is carried out at pH values above the isoelectric point of the enzyme of interest, while cation exchange chromatography takes place below the isoelectric point, attracting positively charged enzymes. By simply changing the pH of elution buffer, the protein of interest can be collected[1].

In case the pI of an enzyme is already known, the correspoding methodology followed based on this value. A theoretical isoelectric point can be calculated based on the aminoacid sequence of the enzyme by using the pK values of amino acids [2]. The theoretical pI of *Fo*LPMO9 was estimated at 7.12 using Expasy.

IEF-PAGE was also performed on *Fo*LPMO9. Under normal circumstances a purified enzyme is needed in order to perform IEF-PAGE so that other proteins do not interfere and only one band is present in the electrophoresis gel. However, since there indications of deviation from the theoretically defined pI, IEF-PAGE was nonetheless performed assuming that the concentration of *Fo*LPMO9 was greater than the one of the other proteins expressed. Following the procedure described in Sec. 4.2.9, the resulting gel is presented in Fig. B.0.1. Only one band was present which was attributed to the presence of *Fo*LPMO9 with the isoelectric point being around a value of 5.6. Thus, theoretically for higher pH values *Fo*LPMO9 should have been purified for pH

Table B.1: Buffer solutions used in each pH and column for the isolation of *Fo*LPMO9

Colmunm	pH	Buffer
anion exchange	9	Tris-HCl
anion exchange	7	Tris-HCl
anion exchange	4	Piperazine
cation exchange	4	Lactic Acid
cation exchange	6	MES[1]
cation exchange	7	HEPES[2]
cation exchange	8	HEPES

values higher that 6.6 using anion exchange chromatography and for pH values lower than 4.6 using cation exchange chromatography.

The expreimental procedure followed for the investigation of which column and buffer shall be used for the purification of *Fo*LPMO9:

- 5 mL of the corresponding column resin was washed with ultrapure water water, centrifuged for 5 min .
- The supernatant water was disposed and the resin was resuspended in 10 mL of the respective buffer and was left overnight at 4 °C to equilibrate.
- The resins were centrifuged again for 5 min and the supernatant was disposed.
- Each resin was resuspended in 5 mL of the equilibrated *Fo*LPMO9 in the respective buffer.
- Then each resin was centrifuged for 5 min and the supernatant was collected (flow through - FT).
- Each resin was resuspended again in 5 mL of water and was then centrifuged for 5 min. The supernatant was collected again (wash).
- Each resin was again resuspended in the respective buffer wich this time included 500 mM NaCl so that in case the enzyme that would be bound to the resin would be detached from it and collected in the supernatant after the centrifugation.
- Each resin was again resuspended again in ultrapure water, was centrifuged for 5 min and was then stored in 20 % ethanol solution.

The pH conditions examined were 5, 7 and 9 for the anion exchange column and 4, 6, 7 and 8 for the cation exchange column.

The buffers used in each case are listed in Table B.

SDS-PAGE was performed in order to check if the enzyme was bound in the respective column. In Fig. B.0.2(a) a thick band is clearly visible around 28 kDa, which is very close to the theoretical molecular weight of 25.281 kDa. Thus, this is assumed to correspond to *Fo*LPMO9, while the smaller faint bands are due to the impurities

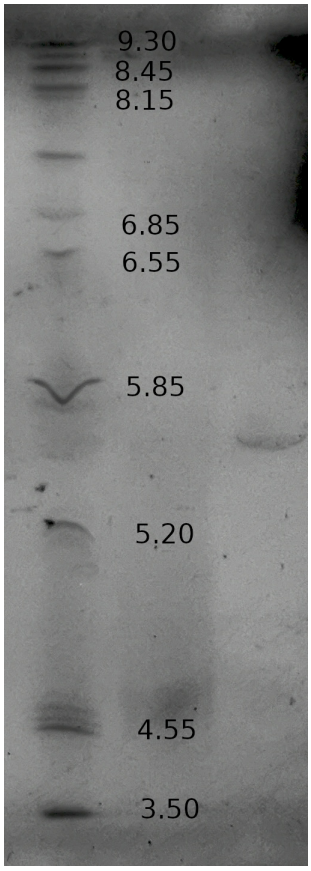

Figure B.0.1: IEF-PAGE of *Fo*LPMO9

and the other enzymes produced by *P. pastoris*. The next samples in the SDS-PAGE gels correspond to the couples of the sample before the interaction with the resin with the flow through (indicated with FT in the Figure).By looking at the samples of anion exchange chromatography the band at 28 kDa before and after the interaction with the resin, it is rather clear that little no amount of *Fo*LPMO9 was bound to the resin at any of the pH values tested. Theoretically this was expected for pH 4, but it should have been bound to pH 7 and 9. It is also pretty evident in all the cases that in the flow through only *Fo*LPMO9 is present as the other bands have disappeared. Regarding the cation exchange chromatography, as expected at pH values higher than 6 *Fo*LMPO9 in not bound to the resin. The only sign of hope in this case was pH 4 with the cation exchange resin, as in this case in the flow through the band for *Fo*LPMO9 is very faint, indicating that it was bound to the resin.

Thus from this analysis, there are two options for purifying *Fo*LPMO9, with the first one being using an anion exchange chromatography at a pH higher than 7, in order to hold all the impurities in the resin and get the enzyme in the flow through, while the other is to use cation exchange chromatography at a pH lower than 4 in order to bind the enzyme to the column and then detach it using the buffer with a high salt concentration.

Bibliography

[1] H. G Boman. Purification of enzymes by ion exchange chromatography. In *Modern Methods of Plant Analysis/Moderne Methoden der Pflanzenanalyse*, pages 393–415. Springer, 1963.

[2] B. Bjellqvist, G. J. Hughes, C. Pasquali, N. Paquet, F. Ravier, J.-C. Sanchez, S. Frutiger, and D. Hochstrasser. The focusing positions of polypeptides in immobilized ph gradients can be predicted from their amino acid sequences. *Electrophoresis*, 14(1):1023–1031, 1993.

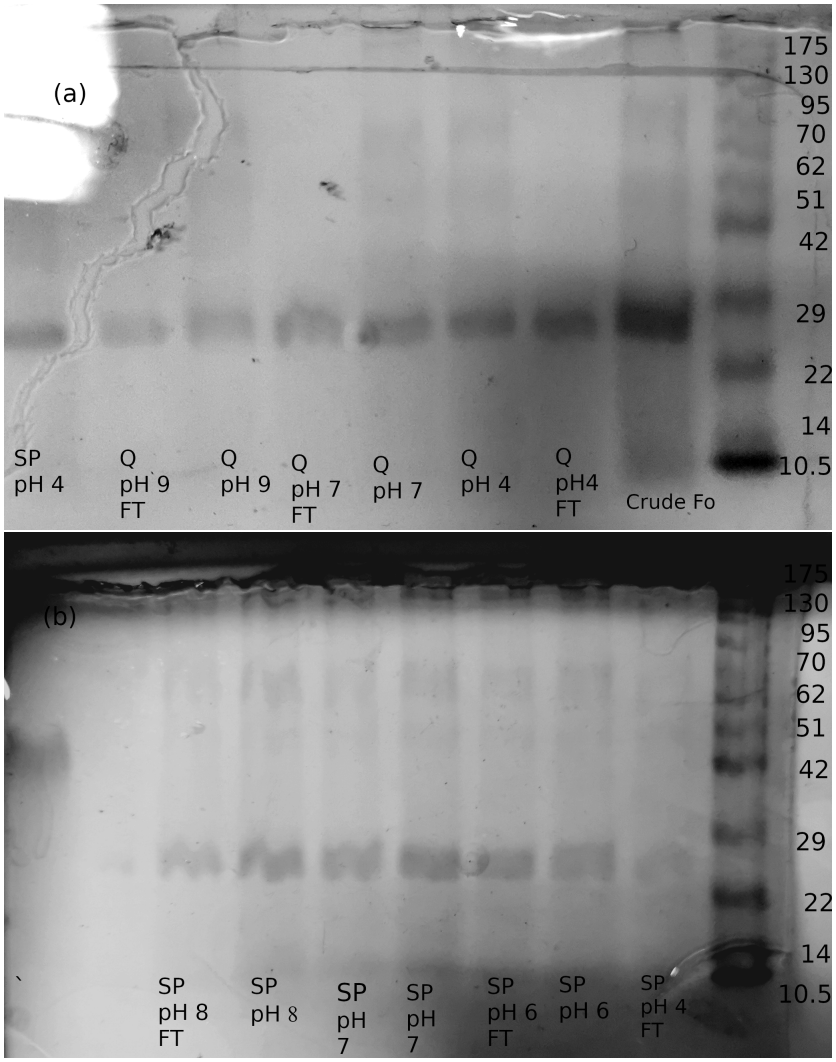

Figure B.0.2: SDS-PAGE of crude *Fo*LMPO9 and equilibrated *Fo*LPMO9 at the respective buffer and the flow through of *Fo*LPMO9 from each resin.

C. Appendix: PASC

This appendix includes the procedure followed for the preparation of the PASC (phosphoric acid swollen cellulose) which was used as a substrate for the experiments with the LPMOs [1].

The procedure is described bellow

- 4 g of Avicel®[1] are dissolved in 100 mL of phosphoric acid. At first a small quantity of acid is added. Then the Avicel® is being smashed for a few minutes. Then more phoshoric acid is added. The process of smashing is repeated. The procedure continues until all the acid is added.
- The Avicel®-phosphoric acid mixture is stirred at 4 °C for about one hour.
- Then 1900 mL of cold water are added in the mix. The resulting mix is left to be stirred for one more hour.
- The final 2 L volume is then filtrated so as the amorphous cellulose is extracted.
- The resulting amorphous cellulose is then washed
  - 4 times with ultrapure water
  - 2 times with 1% $NaHCO_3$ (The $NaHCO_3$ solution is prepared with ultrapure water as well)
  - 3 times with ultrapure water
- The thoroughly washed amorphous cellulose is then mixed with 300 mL of ultrapure water.

In order to assure that the process of PASC preparation is successful, a sample was checked against a sample of commercial AVICEL® with X-Ray Diffraction (XRD) for

[1] Avicel® is the trade name for microcrystalline cellulose that has been partially hydrolyzed with acid, and reduced to a fine powder. It disperses in water and has the properties of a gum.

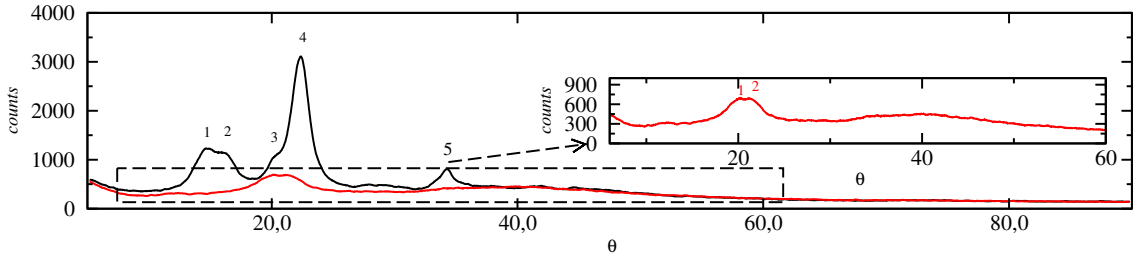

Figure C.0.1: X-Ray diffraction patterns of AVICEL (black) and PASC (red) for λ 1.54 at 40 kV and 40 mA used in the 2θ range 5 - 90° at a scanning speed of 0.026 °.

$\lambda = 1.54$ at 40 kV and 40 mA, in the 2θ range 5-90 ° at a scanning speed of 0.026 °/s. The XRD patterns and the respective annotated peaks are presented in Fig. C.0.1. The fact that no intense peaks appear in the PASC sample, signify the formation of amorphous cellulose from the microcrystalline cellulose.

Bibliography

[1] C. S. Walseth. Occurrence of cellulases in enzyme preparations from microorganisms. *Tappi*, 35(5):228–233, 1952.